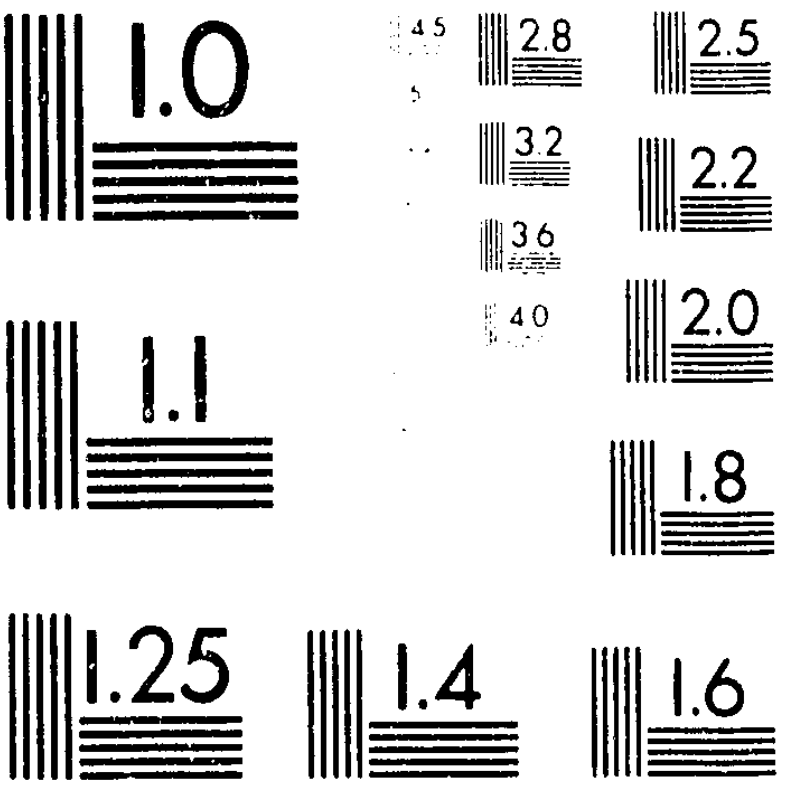

NEA/NSC/DOC(93)2
(INDC(JPN)-163/L)

JAERI-M
93-046

JAERI-M--93-046
JP9312190

PROCEEDINGS OF THE 1992 SYMPOSIUM ON NUCLEAR DATA

November 26-27, 1992, JAERI, Tokai, Japan

March 1993

(Eds.) Mamoru BABA* and Tsuneo NAKAGAWA

日 本 原 子 力 研 究 所
Japan Atomic Energy Research Institute

JAERI-Mレポートは，日本原子力研究所が不定期に公刊している研究報告書です．
入手の問合わせは，日本原子力研究所技術情報部情報資料課（〒319-11茨城県那珂郡東海村）あて，お申しこしください．なお，このほかに財団法人原子力弘済会資料センター（〒319-11茨城県那珂郡東海村日本原子力研究所内）で複写による実費頒布をおこなっております．

JAERI-M reports are issued irregularly.
Inquiries about availability of the reports should be addressed to Information Division Department of Technical Information, Japan Atomic Energy Research Institute, Tokai-mura, Naka-gun, Ibaraki-ken 319-11, Japan.

編集兼発行　日本原子力研究所
印　　刷　いばらき印刷㈱

JAERI-M 93-046

Proceedings of the 1992 Symposium on Nuclear Data
November 26-27, 1992, JAERI, Tokai, Japan

(Eds.) Mamoru BABA* and Tsuneo NAKAGAWA

Japanese Nuclear Data Committee
Tokai Research Establishment
Japan Atomic Energy Research Institute
Tokai-mura, Naka-gun, Ibaraki-ken

(Received February 5, 1993)

The 1992 Symposium on Nuclear Data was held at Tokai Research Establishment, Japan Atomic Energy Research Institute (JAERI), on 26th and 27th of November, 1992. The symposium was organized by Japanese Nuclear Data Committee and Nuclear Data Center, JAERI. In the oral session, a total of 15 papers were pesented under the sessions of present status of revision work of JENDL-3, adjustment of group constants, nuclear data in medium energy region, nuclear data evaluation method, integral data analyses and topics. In the poster session, presented were 25 papers concerning experiments, evaluations and benchmark tests of nuclear data. Activities of JNDC working groups were also displayed in the poster session. All of the 40 papers except the reports from JNDC working groups are compiled in this proceedings.

Keywords: Nuclear Data, Symposium, Proceedings, JENDL-3, Medium Energy Region, Adjustment, Experiment, Evaluation, Benchmark Test

---

* Tohoku University

JAERI-M 93-046

1992年核データ研究会報文集

1992年11月26日～27日，日本原子力研究所，東海村

日本原子力研究所東海研究所
シグマ研究委員会
（編）馬場　護*・中川　庸雄

（1993年2月5日受理）

1992年核データ研究会が，1992年11月26日と27日の両日，日本原子力研究所東海研究所において開かれた。この研究会は，日本原子力研究所のシグマ研究委員会と核データセンターが主催して開いたものである。口頭発表では，15件の論文が「ＪＥＮＤＬ－３改訂の現状」，「群定数の調整」，「中間エネルギーの核データ」，「核データ評価手法」，「積分データ解析」及びトピックスのセッションで報告された。ポスターセッションでは，核データの測定，評価，積分テストに関する25件の報告があった。シグマ委員会のワーキンググループの活動報告もポスターセッションで行われた。このレポートは，ワーキンググループの活動報告を除いて，全部で40件の報告をまとめたものである。

東海研究所：〒319 －11　茨城県那珂郡東海村白方字白根２－４
＊　東北大学

Program Committee

Mamomu BABA (Chairman)	Tohoku University
Satoshi CHIBA	Japan Atomic Energy Research Institute
Tetsuo IGUCHI	University of Tokyo
Norio KISHIDA	CRC Research Institute Inc.
Hideo KITAZAWA	Tokyo Institute of Technology
Kouichi MAKI	Energy Research Laboratory, Hitachi Ltd.
Tsuneo NAKAGAWA	Japan Atomic Energy Research Institute
Ken NAKAJIMA	Japan Atomic Energy Research Institute
Yutaka NAKAJIMA	Japan Atomic Energy Research Institute
Naoki YAMONO	Sumitomo Atomic Energy Industries Ltd.

プログラム委員会

馬場　護（委員長）	東北大学
千葉　敏	日本原子力研究所
井口　哲夫	東京大学
岸田　則生	（株）ＣＲＣ総合研究所
北沢　日出男	東京工業大学
真木　紘一	日立製作所エネルギー研究所
中川　庸雄	日本原子力研究所
中島　健	日本原子力研究所
中島　豊	日本原子力研究所
山野　直樹	住友原子力工業（株）

Contents

目　　次

1. Preface

The 1992 Symposium on Nuclear Data was held at Tokai Research Establishment, Japan Atomic Energy Research Institute (JAERI), on 26th and 27th of November, 1992. The symposium was organized by Japanese Nuclear Data Committee and Nuclear Data Center, JAERI. The program of the symposium is listed below. In the oral session, a total of 15 papers were presented under the sessions of present status of revision work of JENDL-3, adjustment of group constants, nuclear data in medium energy region, nuclear data evaluation methods, integral data analyses and topics. In the poster session, presented were 25 papers concerning experiments, evaluations and benchmark tests of nuclear data. Activities of JNDC working groups were also displayed in the poster session. All of the 40 papers except the reports from JNDC working groups are compiled in this proceedings.

Program of Oral Session

November 26 (Thursday)

11:00 Opening

11:00～11:10

1. Opening Address — R.Nakashima(Hosei Univ.)

11:10～11:55

2. Topic (1) — Chairman: Y.Kikuchi(JAERI)

Nuclear Data Studies in Korea [40+5] — B.Min(KAERI)

11:55～13:00 lunch

13:00～14:15

3. Present Status of Revision of JENDL-3 — Chairman: T.Yoshida(Toshiba)

3.1 Status of Data on Heavy Nuclei and Structural Materials Revised for JENDL-3.2 [35+10] — Y.Kikuchi(JAERI)

3.2 Present Status of JENDL-3 Gamma-Ray Production Data [25+5] — S.Igarasi(NEDAC)

14:15～15:00

4. Adjustment of Group Constants — Chairman: A. Zukeran(Hitachi)

LMFBR Cores using the JUPITER Analytical Results [35+10]

M.Ishikawa(PNC)

15:00～15:15 Coffee break

15:15～17:30

5. Nuclear Data in Medium Energy Region Chairman: M.Mizumoto(JAERI)

5.1 Study of Nuclear Reaction by Molecular Dynamics Methods [35+10]

H.Horiuchi(Kyoto Univ.)

5.2 Comparison of Theoretical Calculation Codes Applied to Nuclear Data Evaluation in the Intermediate Energy Region [25+5]

T.Fukahori(JAERI)

5.3 Integral Spallation Experiment with a Lead Assembly Irradiated with 500 MeV Protons [25+5]

H.Takada(JAERI)

5.4 Neutron Measurement for (p,Xn) Reaction with GeV Protons [25+5]

K.Ishibashi(Kyushu Univ.)

18:00～20:00

Reception (AKOGIGA-URA club)

November 27 (Friday)

9:00～10:15

6. Poster Session (odd number)

10:15～10:55

7. Topic (2) Chairman: T.Ohsawa(Kinki Univ.)

Collective Enhancement of Nuclear Level Density in the Frame of Interacting Boson Model [30+10]

A.Mengoni(JAERI)

10:55～12:05

8. Nuclear Data Evaluation Methods Chairman: S.Iwasaki(Tohoku Univ.)

8.1 Integrated Nuclear Data Evaluation System: INDES [25+10]

T.Nakagawa(JAERI)

8.2 Methods of Covariance Generation for Nuclear Data [30+10]

Y.Kanda

12:05～13:00 lunch

13:00～14:20

9. Topic (3) Chairman: T.Iguchi(Univ. of Tokyo)

9.1 P and T Violation in Neutron Resonance Reaction [30+10]

Y.Masuda(KEK)

9.2 Atomic and Nuclear Data for the Development of Soft X-ray and Gamma-ray Lasers [30+10]

H.Kitazawa(Tokyo Inst. Technol)

14:20～15:35

10. Poster Session (even number)

15:35～16:35

11. Integral Data Analyses Chairman: H.Takano(JAERI)

11.1 Measurement of Doppler Effect up to 2000°C at FCA [25+5]

S.Okajima(JAERI)

11.2 Integral Benchmark Tests of JENDL-3 and ENDF/B-VI [25+5]

K.Kobayashi(Hitachi)

16:35～16:45

12. Closing Address I.Kimura(Kyoto Univ.)

2. Papers Presented at Oral Session

2.1 Topic 1

2.1.1 Review of Nuclear Energy in Korea
－ Nuclear Data Study －

Byung-Joo Min

Korea Atomic Energy Research Institute
P.O. Box 7, Daeduk-Danji, Daejon, 305-606, Korea

Abstract: This report contains the review of nuclear energy and the plan of nuclear data researches in Korea.

1. Introduction

Up until the end of World War II, the Korean peninsula used to be installed with a total power generation capacity of 1722 MW, mostly of hydropower plants. However, 1524 MW or 89.5 % of it went behind the 38th parallel by which Korea was divided into two halves politically, economically and physically. To our surprise, the north abrubtly cut the power supply to the south on 14th of May 1948, which subsequently paralyzed the entire economic wheels and households in the south. To make the matter worse, almost all the remaining 11.5 % facilities, which had been trivial in capacities are usually operated to meet the peaking demand, were devastated during the Korean War. All such unfavourable situations forced Korea to suffer from tremendous shortage of electric power. To keep abreast with the ever-increasing demand for power, Korean electric power sector has made diehard efforts since the end of Korean War to develop power supply and transmission facilities and has resulted in an unprecedented record in such a way that the peak power supply in 1952 was 100 MW, that in 1968 was 1,000 MW, that in 1986 was 10,000 MW, and it is now approaching 25,000 MW range.

Since Korea is not blessed with natural resources, especially energy resources, the energy sector has been obliged to rely on mostly imported oil from abroad, and therefore we have not been free from oils grip. To get rid of

from abroad, and therefore we have not been free from oils grip. To get rid of this situation, we have employed our every possible means to develop nuclear power which can be considered to be a quasi-domestic energy. As a results, the lion's share of electric power is now supplied by fission energy from nine operating reactors.

To this end, the supreme priority has been placed on the manpower development, because nuclear energy is digged out of brain and not from underground. For instance, we had to pay $2,000 to a first-class specialist per day in addition to $10,000 for relocation for the specialist plus travelling expenses and hotel acoommodations as below.

Table 1 Expense list

Items	Expense
Daily pay	$2,000
Relocation fee	$7,000
Stand-bye fee	$3,000
First class round ticket and hotel charge	

For the training of our engineers and scientists in the area of nuclear fuel design and NSSS design, 50 % of training contents were filled in by vendor company's lecturers. For instance, about 10 week training out of 20 week preliminary training at our Research Institute was conducted by foreign vendor company's lectures. Needless to say, about 8 week introductory in-house training courses had been offered to the trainees prior to giving formal courses by the foreign specialists. After this 20 week course, all the trainees were sent to vendor company abroad for 6 month on-the-job trainning which was split into specialty areas according to each person's major.

The details of lecture contents by the foreign specialists and domestic training in case of training NSSS designers are listed as Table 2.

Table 2 NSSS designer's training courses

Training Course	Duration
Lectures on basic coursese by C-E specialists	4 Weeks
KEPCO simulator training and practice en situ	6 Weeks
Codes and standards course	4 Weeks
Safety analysis course	1 Week
Quality assurance course	1 Week
Training course at Yonggwang power plant	2 Weeks
Training course at Ulchin power plant	2 Weeks
On-the-Job training at C-E	6 months

In spite of much efforts and burdensome investment into nuclear sector, Korea has not yet been mature to the state of self-reliance in design, manufacture and analysis of nuclear software and hardware. In constant with the worldly trend of stagnant nuclear development, inter alia, in the advanced industrialized countries, resources-poor and energy-hungry Korea has been pursuing to enhance the domestic participation in technology and equipment manufacture in an attempt to attain the technological independence of nuclear power.

2. Development of Nuclear Power in Korea

Since the synchronization of Kori Nuclear Unit 1 in 1978, nine nuclear reactors have been in operation serving the nation with nearly 50 % of the power demand, and the status is as described in Table 3.

Table 3 Nuclear power plants in operation

Nuclear Unit	Reactor Type	Gross (MWe)	Form of Contract	NSSS Supllier	Operation Date
Kori 1	PWR	587	Tunrkey	Westinghouse	1978. 4
Kori 2	PWR	659	Tunrkey	Westinghouse	1983. 7
Wolsung 1	PHWR	679	Tunrkey	AECL	1983. 4
Kori 3	PWR	950	Component	Westinghouse	1985. 9
Kori 4	PWR	950	Component	Westinghouse	1986. 4
Yonggwang 1	PWR	950	Component	Westinghouse	1986. 8
Yonggwang 2	PWR	950	Component	Westinghouse	1987. 6
Ulchin 1	PWR	950	Component	Framatome	1988. 9
Ulchin 2	PWR	950	Component	Framatome	1989.12

The national medium-term nuclear development program calls for the completion of 18 additional nuclear units by year 2006. Last year, Canadian AECL was nominated as the successful supplier for Wolsung Unit 2 CANDU reactor which is identical to its sister Unit No.1, and the initial construction of this unit is now at full swing aiming at the completion by 1997. In addition, the contract for two o ;r CANDU units, namely, Wolsung 3 & 4, was awarded to AECL a few months ago, and its construction work is just at the commencing stage. These two heavy water reactors will also be synchronized before the turn of this century. Two other PWR units are approaching at the final stage of the negotiations, and it is scheduled to be signed sometimes in 1993. The schdule for the remaining nuclear units is as shown in the following Table.

Table 4 Nuclear power plants to be constructed

No	Nuclear Unit	Reactor Type	Gross(MWe)	Completion Date
1	Yonggwang 3	PWR	1,000	1995. 3
2	Yonggwang 4	PWR	1,000	1996. 3
3	Wolsung 2	PHWR	700	1997. 6 (Under construction)
4	Ulchin 3	PWR	1,000	1998. 6
5	Wolsung 3	PHWR	700	1998. 6 (Contracted)
6	Wolsung 4	PHWR	700	1999. 6 (Contracted)
7	Ulchin 4	PWR	1,000	1999. 6
8	Undecided	PWR	1,000	2000. 6
9	Undecided	PWR	1,000	2001. 6
10	Undecided	PWR	1,000	2002. 6
11	Undecided	PHWR	700	2002. 6
12	Undecided	PWR	1,000	2003. 6
13	Undecided	PHWR	1,000	2003. 6
14	Undecided	PWR	1,000	2003.10
15	Undecided	PWR	1,000	2004. 6
16	Undecided	PWR	1,000	2005. 6
17	Undecided	PWR	1,000	2006. 6
18	Undecided	PHWR	700	2006. 6

In 1991, the portion of nuclear power out of the total electricity accounted for about 47 percent. It is presumed that its share will become to be the majority share of electric power in the nation, when and if all these 18 additional units be constructed by 2006. The composition rate of nuclear power

to the total is estimated somewhat up and down with the gradual decrease toward the end of this century and increase afterwards as shown below.

Table 5 The composition rate of nuclear power to the total

Year	Nuclear Power (GWh)	Ratio of Nuclear Power to the Total (%)
1991	56,311	47.5
1993	53,905	37.9
1996	65,171	36.0
2001	104,379	43.3
2006	156,868	52.1

The pivotal element for the effective development of nuclear power program is to supply quality-assured manpower in time. Nuclear industry is complex and diversified in majors. Yet the number of enrollment of freshmen in the Department of Nuclear Engineering can be indicative of the status in nuclear manpower supply, and the details are as given below:

Table 6 Nuclear engineering in the universities

University	Year of Establishment	The Number of Students('1992)		
		Bachelor	Master	Ph. D
Hanyang Univ.	1958	50	20	5
Seoul National Univ.	1959	33	30	20
KyungHee Univ.	1979	60	14	2
Chosun Univ.	1985	55	8	
KAIST	1982		36	40

As shown in Table 6, five advanced institutions in Korea have the Department of Nuclear Engineering. To our regret, however, the quality of enrolling students has been somewhat degrading and is not reputed as the best sort, despite the fact that it used to be the top-notch in the earlier years.

In order to train and retrain the nuclear manpower, each nuclear organization has established in-house training center, where evening classes and other Ad Hoc Topics are taught intensively to cope with the on-going

projects, and such scheme has been highly appreciated.

The below gives a brief history on how Korea Atomic Energy Research Institute, which is the Mecca of nuclear academia and engineering, has been established and grown up until recently.

1959. 1.21	The Office of Atomic Energy (OAE) established
1959. 3. 1	The Atomic Energy Research Institute (AERI) established under OAE
1963.12.17	The Radiological Research Institute (RRI) established under OAE
1966.11.30	The Radiation Research Institute in Agriculture (RRIA) established under OAE
1968. 2.10	The Cancer Research Hospital (CRH) established under RRI
1973. 2.17	The Korea Atomic Energy Research Institute (KAERI) established by reorganizing from AERI
1975.11. 3	The Daeduk Engineering Center established as branch of KAERI
1976.12. 1	The Korea Nuclear Fuel Development Institute (KNFDI) established reorganizing The Daeduk Engineering Center
1980.12.19	KNFDI integrated into KAERI
1981. 1. 5	The Korea Atomic Energy Research Institute (Old KAERI) became The Korea Advanced Energy Research Institute (New KAERI)
1981.12.21	The Nuclear Safety Center established within KAERI
1989.12.30	The Korea Advanced Energy Research Institute renamed as The Korea Atomic Energy Research Institute
1990.11.19	The Nuclear Environment Management Center (NEMAC) established within KAERI.

The following are the current major projects at KAERI

1) Development of nuclear fuel cycle technology including radwaste management
2) Development of NSSS system design technology
3) Design and construction of a multi-purpose research reactor (KMRR)
4) Nuclear safety research together with basic nuclear-related research
5) Radioisotope applications and a cancer research hospital management
6) Nuclear manpower training
7) Support the Government in establishing nuclear policies.

KMRR project, one of the most important projects at KAERI, was started in 1985 and will be completed by 1994. KMRR is designed and constructed by KAERI's own efforts. KMRR project comprises the following researches:

1) Fuel and materials testing necessary to support the local manufacture of fuel and reactor components for PWR's and CANDU's.
2) The production of key radioisotopes, including ^{99}Tc, ^{131}I, ^{192}Ir, ^{60}Co, etc., and the production of neutron transmutation doped silicon.
3) Neutron activation analysis of nuclear-grade materials and other samples

of industrial R&D need, and basic and supplied research employing neutron beams, e.g., nuclear physics, solid state physics and metallargy.

4) Neutron radiography for scanning experimental power-reactor fuel performing non-destractive examinations of materials and components used in both nuclear and non-nuclear applications.

The following are the specifications of KMRR Design

- Reactor type : Open-Tank-In-Pool, LWR/HWR Hybrid
- Thermal Power : 30 MWth
- Fuel : U_3Si-Al, 19.75 w/o ^{235}U enriched
- Coolant : H_2O
- Moderator : H_2O/D_2O
- Reflector : D_2O
- Cooling Method : Convective Up-Flow
- Secondary Cooling : Cooling Tower
- Reactor Building : Confinement.

3. Nuclear Data in Korea

We are still relying on most of nuclear data from foreign countries. Nuclear data production and evaluation depend on other countries entirely. The activities of nuclear data compilation have been carried out for the past 10 years. Evaluated data from IAEA nuclear data section are processed by using computer codes and then applied to designing reactors.

Evaluated Data were introduced from the following countries:

Evaluated Data	Country
ENDF/B-IV, V, VI	USA
JENDL-2, 3.1	JAPAN
JEF-I	NEA
BROND	USSR

For generating multigroup constant data, the following processing codes were used:

ETOT, ETOG for LEOPARD (Thermal) code
ETOX for 1DX (Fast) code
FEDGROUP-C84 for NKNDL and KEDAK - format library
NJOY (Thermal, Fast, Shielding) for EBDF/B - format library

The following application libraries were used for each reactor:

Reactor Type	Library used
PWR	LEOPARD code
CANDU	WIMS/D code
KMRR	WIMS/D code
FBR	1DX, SPHINX code

Frankly speaking, research on nuclear data evaluation in Korea has not been performed to the extent of satisfactation. Although its importance is deeply recognized among the nuclear personnel, the manpower and budget for this are trivial, so to speak. Last year, we had an opportunity to use some computer codes for evaluation of nuclear data. The following 4 computer codes were introduced, and 3 of them are in operation on each computer system:

Code Name	Version	Operation	Computer system
CHUCKS	PC	applicable	PC
ABAREX	PC	applicable	PC
SAMMY	IBM	applicable	Cyber
GNASH	CRAY	not applicable	Workstation

Currently, the following developments are being processed at KAERI and so newly evaluated nuclear data are required

- Advanced LWR Development
- Advanced LWR and FBR Fuel Development
- Nuclear Transmutation Research.

For the successful evaluation of nuclear data, Korea will have to overcome the difficulties in manpower and financial constraints and will have to perform this important task in the collaboration with advanced countries including Japan.

References

1) "The 30th Anniversary of the First Korean Research Reactor Start-up", Special Lectures, KAERI & KNS (1992)

2) "Nuclear Industry in the Republic of Korea", KAIF (1990)

3) "KEPCO Annual Review", KEPCO (1992)

4) "KAERI Brochure", KAERI (1992)

5) "KMRR Brochure", KAERI (1992)

6) C.K. Lee, "The Fundamentals of Nuclear Power", KNS (1991)

7) C.K. Lee, Private Communications

2.2 Present Status of Revision of JENDL-3

2.2.1 Status of JENDL-3 Revision Work

Yasuyuki KIKUCHI and Tsuneo NAKAGAWA

Japan Atomic Energy Research Institute
Tokai-mura, Naka-gun, Ibaraki-ken 319-11

The data of JENDL-3 are now being revised by considering the feedback information from various benchmark tests. The main items to be revised are the resonance parameters, fission spectra and inelastic scattering cross sections of heavy nuclides and the total cross sections of shielding materials. The revision work will be hopefully completed in March 1993.

1. Introduction

Since the release of JENDL-3[1] in 1989, various benchmark tests[2-5] have so far been made and the data have been also used for various applications. It has been found that JENDL-3 predicts various neutronics problems much better than JENDL-2 as a whole. On the other hand, however, some drawbacks have become clear in JENDL-3 with accumulation of user's experience.

The drawbacks thus pointed out are not so serious that the new version, JENDL-4, is ungently required. Hence it was decided to revise the JENDL-3 data and release them as JENDL-3 Revision 2 (JENDL-3.2). This revision work is expected to be completed at the end of the 1992 fiscal year; i.e., March 1993.

This paper presents the status of revision work for mainly heavy and structural material nuclides. The status on the γ-ray production data is reported in another paper in the same symposium by S. Igarasi.[6]

2. Feedback from Benchmark Tests

Feedback informations to nuclear data from rather simple benchmark tests are described below.

2.1 Tests with Simple Systems[2]

Seven Critical systems with simple components and geometry, such as GODIVA, JEZBEL, FLATTOP, etc. were analyzed.

Good results were reported for Pu and ^{235}U cores. On the other hand, the predictions were not satisfactory for ^{233}U cores. It was suspected that the fission spectrum was too hard and the inelastic scattering cross sections were too high in ^{233}U.

2.2 FBR Benchmark Tests[3]

In FBR benchmark tests, much improvements were observed in prediction of Na void coefficients, reaction rate distributions, space dependence of C/R worth and Doppler coefficients. It was pointed out, on the other hand, that core size dependence of k_{eff} existed particularly in ^{235}U cores and anomalous behavior of k_{eff} in FCA-IX cores (^{235}U cores) particularly in C moderated ones.

They might suggest some problems of ^{235}U data in the unresolved resonance region.

2.3 Thermal Benchmark Tests[4]

Thermal critical assemblies such as TRX, BAPL and TCA were analyzed. It was observed that the k_{eff} values were underestimated by 0.5~0.8% for U-cores and by 0.3~0.5% for Pu-cores. This suggests also some problems in the resonance parameters particularly for ^{235}U. It was also pointed out that the ^{235}U capture resonance integral of JENDL-3 was 14% larger than that of ENDF/B-VI.

2.4 Shielding Benchmark[5]

Various shielding benchmark problems were analyzed so as to check the total and scattering cross sections of shielding materials. From the ORNL Broomstick experiments, problems were pointed out for the total cross sections of N, Na and Fe. From various deep penetration experiments, it was suggested that there existed some problems in the balance between the elastic and inelastic scattering cross sections in Fe.

2.5 Fusion Neutronics

From the view point of fusion neutronics, the ENDF-5 format adopted in JENDL-3 is not appropriate, since the energy-angular double differential cross sections (DDX) in file 6 are much required.

3. Revision Items

Considering the feedback from the benchmark tests and other user's comments, items listed in Table 1 were selected to be revised.

Among them, the DDX required from fusion neutronics will be provided as a JENDL special purpose file, JENDL Fusion file. The γ-ray production data will be discussed in another paper.[6]

4. Resonance Parameters of Heavy Nuclides

Most of the resolved resonance parameters of heavy nuclides except ^{238}U and ^{239}Pu were carried over from JENDL-2 with the single or multi-level Breit-Wigner formula. Recently parameter sets with the Reich-Moore formula become available, which were deduced by simultaneous fitting of high resolution transmission and fission cross section data. It was decided to adopt these Reich-Moore parameter sets as seen in Table 2.

^{233}U : New evaluation by Derrien[7] at JAERI

^{235}U : Evaluation by Leal et al.[8]; same as ENDF/B-VI up to 500 eV

^{238}U : Evaluation by Moxon et al.[9]; same as JEF-2
^{239}Pu : New evaluation by Derrien[10] up to 2.5 keV
^{241}Pu : Evaluation by Derrien and de Saussure[11]

The unresolved resonance parameters of ^{235}U were modified so as to reproduce the presently revised fission and capture cross sections. The upper energy of unresolved resonance region was extended to 150 keV for ^{238}U.

5. η-value of ^{235}U in the Thermal Region

It has been long discussed whether the η-value of ^{235}U is flat below 0.1 eV. Recently NEANSC International Evaluation Cooperation Working Group recommended that the η-value increased with energy, based on the recent measurements of η and α at Geel.[12,13] The revised resonance parameters could reproduce this tendency as seen in Fig. 1.

6. Fission and Capture Cross Sections of ^{235}U

It was pointed out that the capture cross section of ^{235}U might be too large in the unresolved resonance region. The α-value of JENDL-3 is compared with that of ENDF/B-VI as well as the measured data. JENDL-3 took account of all the existing data, while ENDF/B-VI looks to be evaluated mainly on the basis of the measurements by Adamchuk et al.[14] and by Corvi[15] and gives lower values.

The experimental conditions of the measurements have been checked by Matsunobu and it was concluded that the measurements by Adamchuk et al. and by Corvi were more reliable. A new evaluation was made on the basis of these two measurements as shown in Fig. 2.

The fission cross section is also being reevaluated on the basis of the data of Weston and Todd[16]. Figure 3 shows the preliminary result. The capture cross section will be derived from the α-value and the fission cross section.

7. ν and χ

The ν-value of ^{235}U was reevaluated on the basis of recent measurements which have structure below 100 keV.

The fission spectra of fissile nuclides have been systematically reviewed. For ^{233}U, more soft spectrum will be adopted. Applicability of the two temperature Madland-Nix model proposed by Ohsawa[17] is now under investigation.

8. Inelastic Scattering

The inelastic scattering cross sections of heavy nuclides are difficult to be measured, and there remain considerable uncertainties in the evaluated data. The JENDL-3 data were checked by comparing with the existing experimental data.

The evaluated values were found to be consistent with the measured data for ^{235}U and ^{239}Pu, and therefore were not changed. The values of ^{233}U were slightly modified

on the basis of the measured data of Smith et al.[18]

The inelastic scattering cross section of ^{238}U is still an open question and is being investigated as an item of the NEANSC International Evaluation Cooperation. Both the JENDL-3 and ENDF/B-VI data look higher than the measured data by Baba et al.[19] and by Kornilov[20] as seen in Fig. 4. The final decision will be made soon in the corresponding subgroup of the NEANSC International Evaluation Cooperation, and this decision will be adopted in JENDL-3.2.

9. Total Cross Sections of Shielding Materials

9.1 Sodium

The ORNL Broomstick experiments reveal that the uncollided flux is overestimated with JENDL-3 as is seen in Fig. 5. This suggests that the total cross section is too iow. The evaluation of JENDL-3 was based on the measurements of Cierjacks et al.[21]. On the other hand, Larson et al.[22] gave higher values as shown in Fig. 6. A new evaluation was made on the basis of the new measurements of Larson et al. The C/E values were much improved as seen in Fig. 5.

9.2 Iron

The Broomstick experiments show considerable underestimation of the uncollided flux calculated with JENDL-3 in the energy region below 3 MeV as seen in Fig. 7, while ENDF/B-IV gives fairly good C/E values.

The average total cross sections are nearly analogous between JENDL-3 and ENDF/B-IV. It was found, however, that the ENDF/B-IV shows sharper resonance structure than JENDL-3. The evaluation of JENDL-3 was made by tracing the high resolution experimental data of Cierjacks et al.[21] The experimental data might be smoothed out with the resolution function, and the true structure must be sharper. The ENDF/B-IV data might be unfolded, presumably considering the Broomstick benchmarks.

In order to unfold the JENDL-3 data so as to reproduce the Broomsteck results better, the following approximate methods were adopted:

$$\sigma_{J3}(E_0) = \int_{E_0-D}^{E_0+D} C\sigma_W(E)R(E)dE, \qquad (1)$$

where σ_{J3} : cross section of JENDL-3
$\sigma_W(E)$: cross section to be unfolded (same as σ_{J3} at the 1st iteration)
C : correction factor
R(E) : resolution function.

With this equation, the correction factor C is obtained and the modified cross section at E_0 is given as

$$\sigma_M(E_0) = C\times\sigma_W(E_0). \qquad (2)$$

The change of the cross section after 1 iteration is schematically shown in Fig. 8. It is seen that the peak becomes higher and the valley lower after the unfolding.

The total cross section thus modified is compared with the JENDL-3 data in Fig. 9. With the modified total cross section, the C/E values of Broomstick results are much improved as seen in Fig. 7.

The same correction was applied for Cr and Ni.

10. Concluding Remarks

Most of drawbacks in JENDL-3 pointed out from various benchmark tests are now being modified. The revised data are always being checked with benchmark tests using CATEX system[23], which predicts the effects of the cross section change on various integral quantities by using sensitivity coefficients.

Revision work will be hopefully completed in March 1993.

References

1) K. Shibata et al.: "Japanese Evaluated Nuclear Data Library, Version 3: JENDL-3", JAERI 1319 (1990).
2) D. Tian et al.: To be published in J. Nucl. Sci. Technol.
3) H. Takano et al.: Proc. Int. Conf. Phys. Reactors, April 1990, Marseille, Vol.3, PI-21 (1990).
4) H. Takano: Proc. 1991 Symposium on Nucl. Data, 28-29 Nov. 1991, Tokai, p.147, JAERI-M 92-027 (1992).
5) M. Kawai et al.: To be published as JAERI report.
6) S. Igarasi et al: Proc. 1992 Symposium on Nucl. Data, 26-27 Nov. 1992, Tokai.
7) H. Derrien: To be published in J. Nucl. Sci. Technol.
8) L.C. Leal et al.: Nucl. Sci. Eng., 109, 1 (1991).
9) M.C. Moxon et al.: Int. Reactor Phys. Conf., 18-22 Sept. 1988, Jacksonhole, Vol.1, p.281 (1988).
10) H. Derrien: To be published in J. Nucl. Sci. Technol.
11) H. Derrien and G. de Saussure: Nucl. Sci. Eng., 106, 415 (1990).
12) J.A. Wartena et al.: IAEA, Tecdoc 491, 123 (1987).
13) H. Weigmann et al.: Proc. Int. Conf. Nuclear Data for Science and Technol., Jülich, 13-17 May 1991, p.38, Springer-Verlag (1992).
14) Yu.V. Adamchuk et al.: Proc. Int. Conf. Nuclear Data for Science Technol., Antwerp, 6-10 Sept. 1982, p.730, D. Reidel (1983).
15) F. Corvi: Proc. NEANDC/NEACRP Specialist's Meeting on Fast Neutron Capture Cross Sections, April 20-23, 1982, ANL, p.314, ANL-83-4 (1983).
16) L.W. Weston and J.H. Todd: Nucl. Sci. Eng., 88, 567 (1984).
17) T. Ohsawa: Proc. 1991 Symp. Nucler Data, 28-29 Nov. 1991, Tokai. p.82, JAERI-M 92-027 (1992).

18) A.B. Smith et al.: Proc. Int. Conf. Nuclear Data for Science and Technol., Antwerp, 6-10 Sept. 1982, p.39, D. Reidel (1983).
19) M. Baba et al.: Nucl. Sci. Technol., 27, 601 (1990).
20) N.V. Kornilov: Private Communication (1992).
21) S. Cierjaks et al.: "High Resolution Total Neutron Cross Sections between 0.5 and 30 MeV", KfK-1000 (1968).
22) D.C. Larson et al.: "Measurement of the Neutron Total Cross Section of Sodium from 32 keV to 37 MeV", ORNL/TM-5614 (1976).
23) A. Hasegawa: private communication.

Table 1 Items to be revised

DDX

^{6}Li, ^{9}Be, ^{12}C, ^{14}N, ^{19}F, ^{27}Al, Ti, Cr, Co, Zr, Nb, Mo, Sb, Ta, W, Pb, Bi, ^{232}Th, U

Total cross section

Fe, Na, N

Heavy nuclides

χ for ^{233}U, ^{238}U, ^{239}Pu, ^{235}U

ν & η for ^{235}U

Resonance parameters for ^{233}U, ^{235}U, ^{239}Pu, ^{241}Pu

Cross sections for ^{233}U(n,n'), ^{233}U(n,2n), ^{235}U(n,f), ^{235}U(n,γ), ^{238}U(n,n'), ^{237}Np

γ-ray production data

Some nuclides

Table 2 Resolved resonance parameters

Nuclide	JENDL-3.1	JENDL-3.2	ENDF/B-VI
U-233	SLBW 1 ～ 100 eV 159 res	R-M 0 ～ 150 eV 189 res	A-A 0.79 ～ 60 eV 83 res
U-235	SLBW 1 ～ 100 eV 148 res	R-M 0 ～ 500 eV 1029 res	R-M 0 ～ 2.25 keV 3355 res
U-238	MLBW 0 ～ 9.5 keV 841 res	R-M 0 ～ 10 keV 1651 res	R-M 0 ～ 10 keV 1913 res
Pu-239	R-M 0 ～ 1 keV 393 res	R-M 0 ～ 2.5 keV 1070 res	R-M 0 ～ 2 keV 787 res
Pu-241	SLBW 0 ～ 100 eV 92 res	R-M 0 ～ 300 eV 243 res	R-M 0 ～ 300 eV 243 res

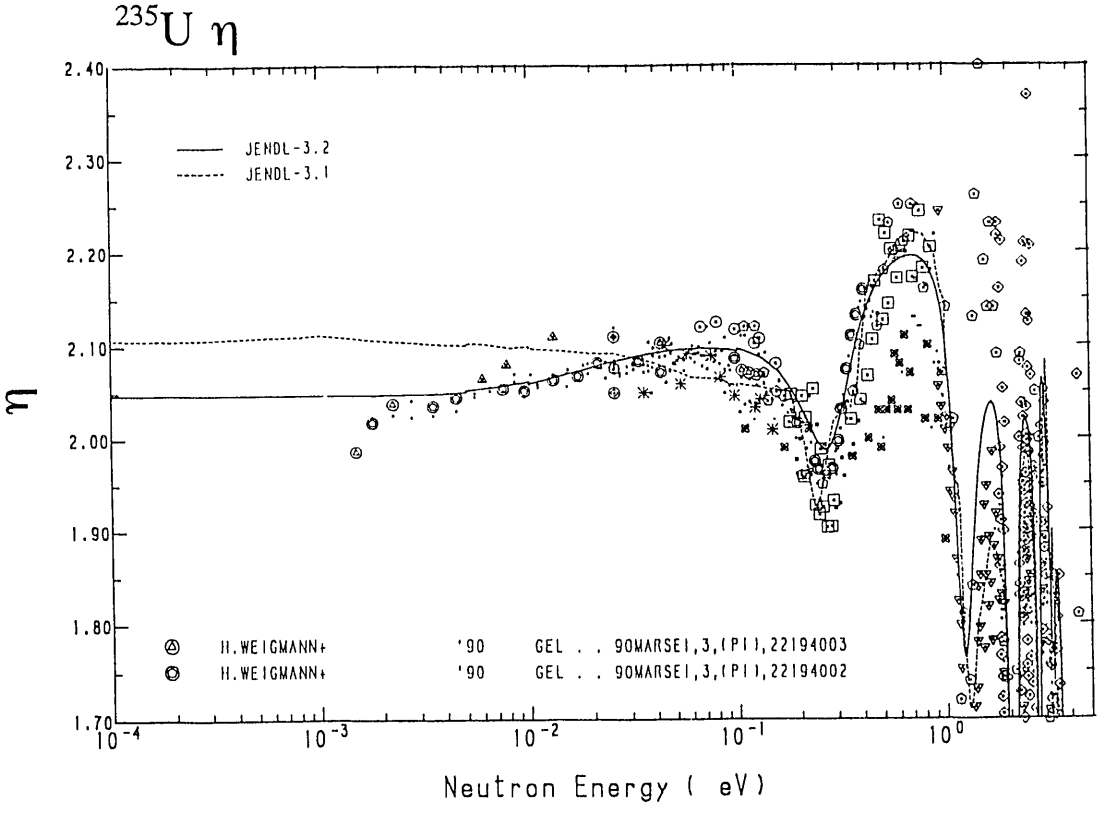

Fig. 1 η-value of ^{235}U.

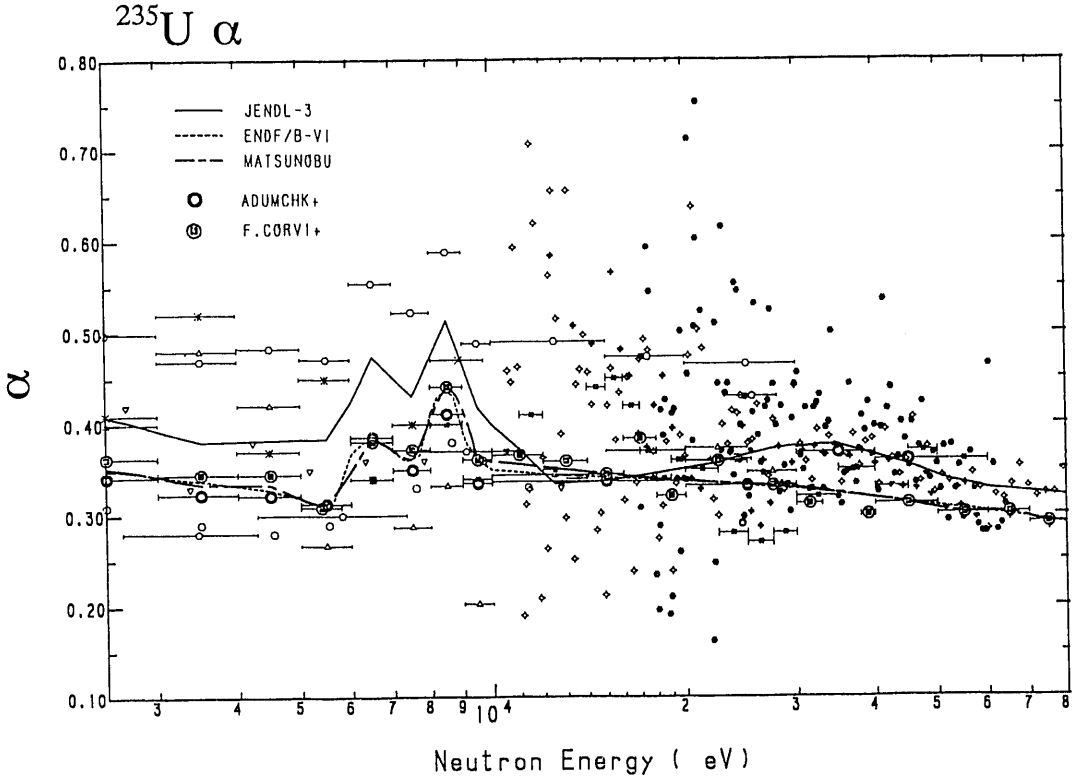

Fig. 2 α-value of ^{235}U. Experimental data shown are those reported after 1970. A one-dotted line (MATSUNOBU) is the preliminary result by Matsunobu.

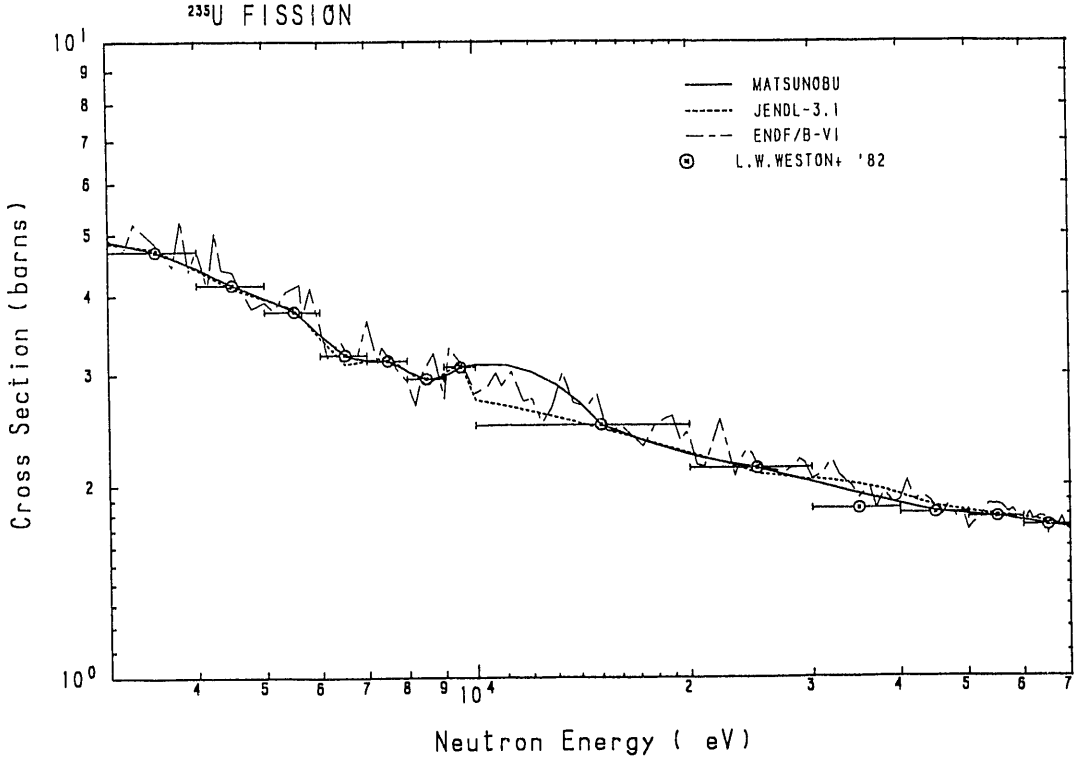

Fig. 3 Fission cross section of ^{235}U. A solid line (MATSUNOBU) is the preliminary result by Matsunobu.

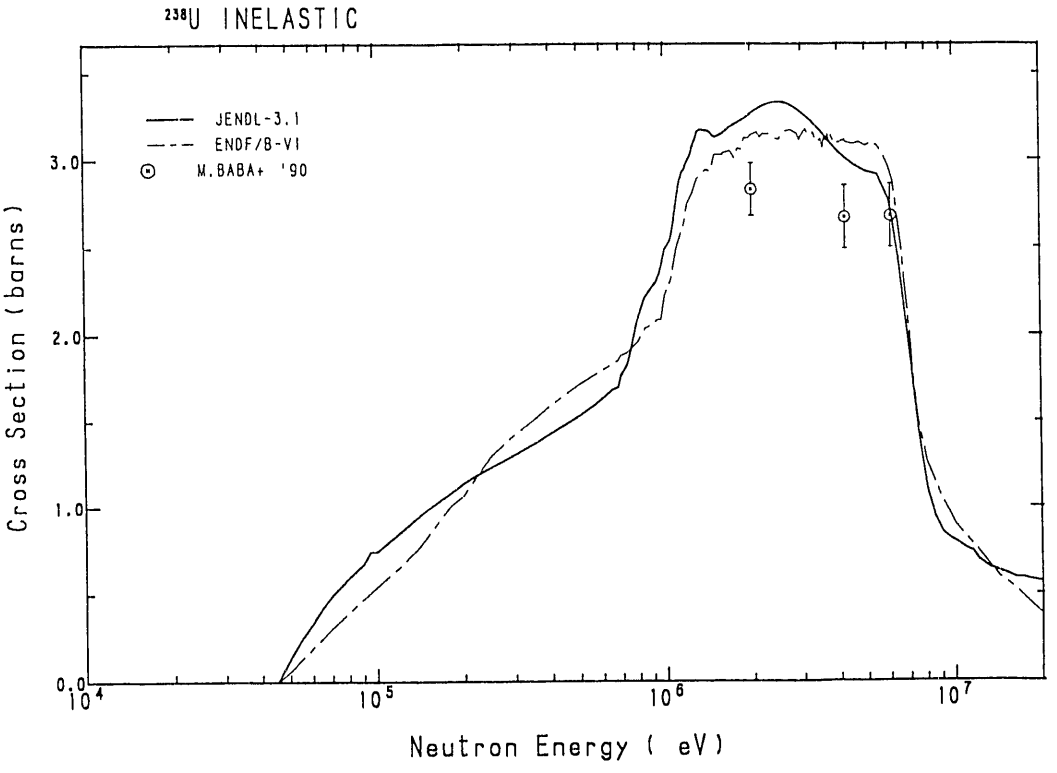

Fig. 4 Inelastic scattering cross section of ^{238}U.

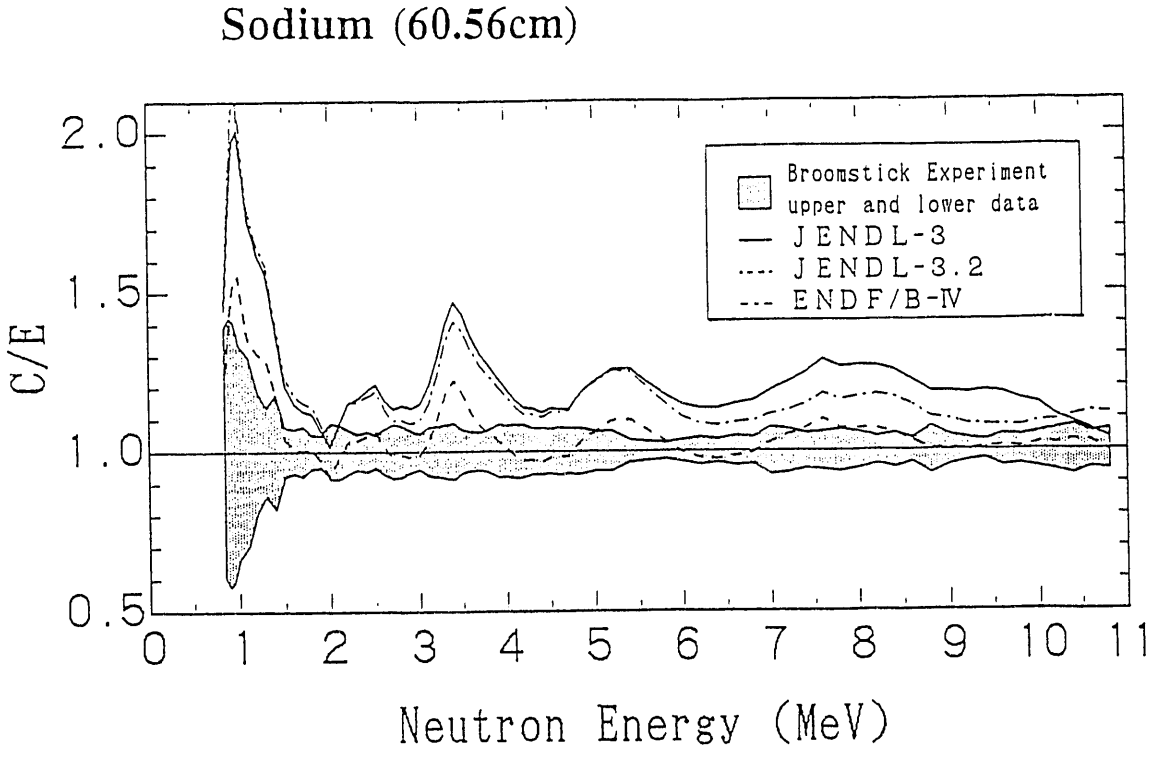

Fig. 5 C/E-values of uncollided flux for sodium broomstick benchmark.

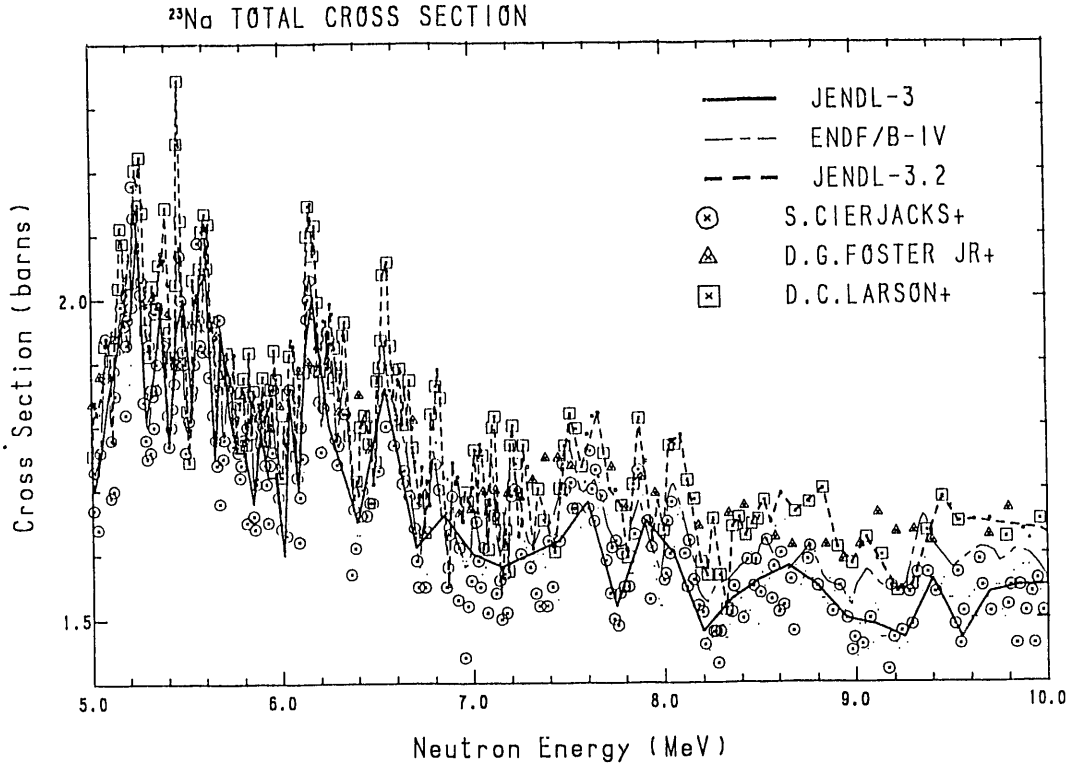

Fig. 6 Total cross sections of sodium.

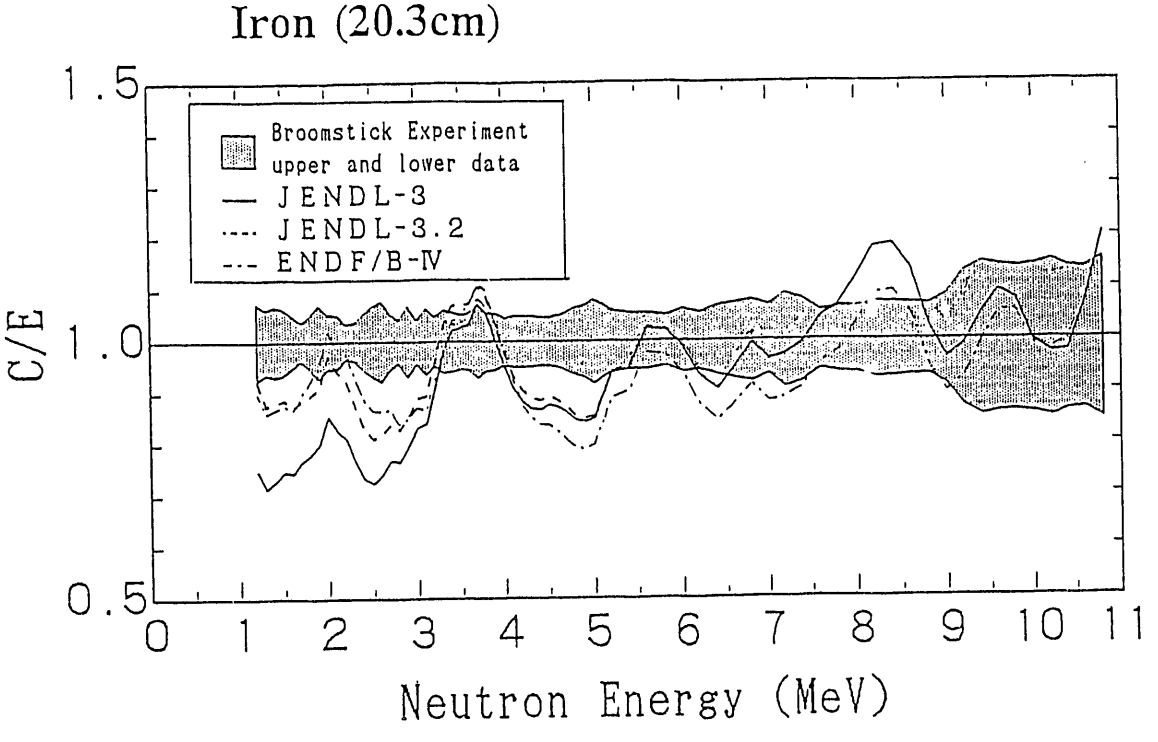

Fig. 7 C/E-values of uncollided flux for iron broomstick benchmark.

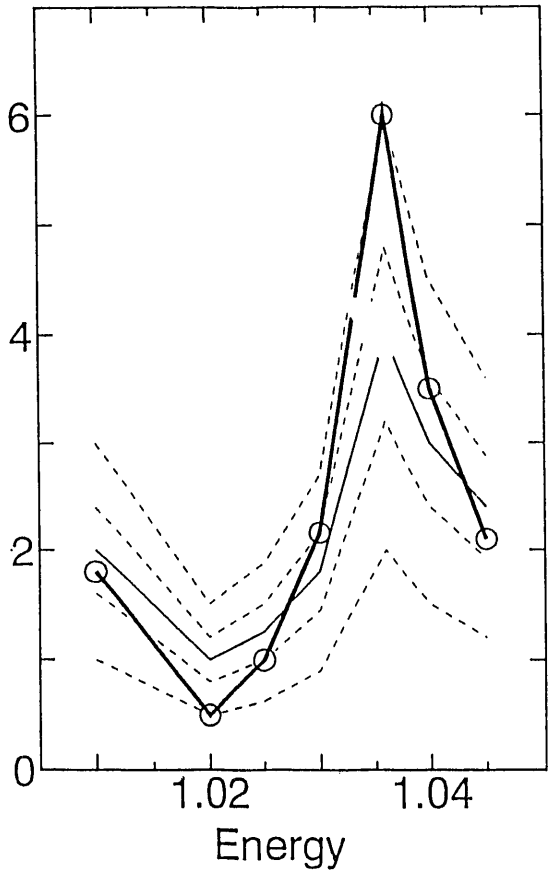

Fig. 8
Unfolding of the resonance structure. A thin solid line represents the data in JENDL-3 based on the experimental data. By using a correction factor calculated from Eq.(1) given in the text, modified values are obtained as a thick solid line with circles. Each dashed curve is renormalized one by the factor at each energy point.

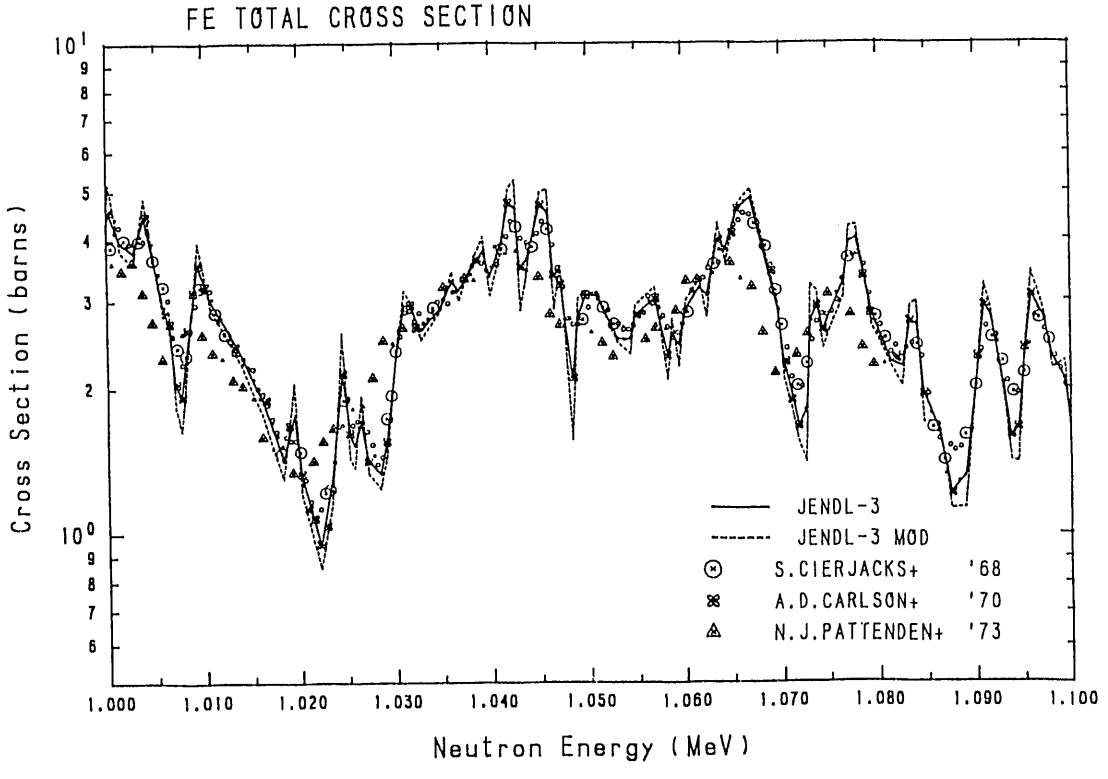

Fig. 9 Total cross sections of iron.

2.2.2 Present Status of JENDL-3 γ-Ray Production Data

S. Igarasi
Nuclear Energy Data Center
Tokai-mura, Naka-gun, Ibaraki-ken 319-11

Status-quo of γ-ray production data of JENDL-3 are reviewed by comparing them with experimental data, examining trends of γ-ray multiplicity, testing energy conservation for thermal neutron capture γ-ray data, etc. Most of the data are very well, but there are some defects in the thermal neutron capture γ-ray data and higher values of spectrum data for some intermediate nuclides in the 4 to 6 MeV γ-ray energy region. In this report, it will be given how to remedy these defects for a revised version of JENDL-3.

1. Introduction

It was the first experience for JNDC members in JENDL-3 work to evaluate γ-ray production data. Since JENDL-3 was released in 1989, many studies using its γ-ray production data have been made, and various valuable results have been gotten, in spite of the immature first version. In some aspects, however, a few critiques to the γ-ray data were reported from the users. They are

(1) JENDL-3 underestimates γ-ray heating compared to the FNS experiments by 50 to 60%,
(2) false results are given in the calculation of γ-ray spectra from spherical bulk system of some nuclides,
(3) questionable data exist in some structural material nuclides,

etc. In order to polish the γ-ray data file, JNDC set up a working-group (WG)* to investigate the data which bring about these defects, and to revise them.

The WG began by reviewing the status-quo of JENDL-3 by comparing them with experimental data, and saw some significant differences in the low energy neutron capture γ-ray data, higher values of γ-ray spectra for some intermediate nuclides in the MeV region, etc. In order to catch further details of the data, non-elastic cross sections and

---

* working group member

T. Asami (Data Eng.), K. Hida (Toshiba), M. Igashira (TIT), H. Kitazawa (TIT), M. Mizumoto (JAERI), S. Igarasi (NEDAC, group leader)

γ-ray production cross sections were compared by plotting the data, and multiplicities of the γ-rays were studied. The γ-ray production cross sections for each reaction were examined by checking numerical data also. Special attention was given to the thermal neutron capture data, because it is easy to see the energy conservation and to check relation between the spectrum-averaged energy and multiplicity, etc.

From these studies, the WG understood that most of the defects came from trivial mistakes. Some serious problems were such as the energy conservation was broken for some nuclides, widths of energy-bin for spectra were rather wide, and energy-points of the incident neutrons were small for reproducing the γ-ray spectra in the energy region including threshold reactions. In particular, spectra for several energy points corresponding to the lowest excited levels of the target nucleus are necessary. Further, transition probability (or line spectrum) data between these levels should be used, instead of fictitious continuous spectra.

In the next Chapter, a survey of evaluation on the JENDL-3 γ-ray data will be given. In Chapter 3, examples of the status-quo of the data will be shown in numerical tables and graphs. In the final Chapter, discussion on remedy of false data will be made in an optimistic tone.

2. Survey of JENDL-3 γ-Ray Data

JENDL-3 has γ-ray production data for 59 nuclides and elements. The data for natural elements are mostly composed of the data of the elemental isotopes. But some elements have main isotopes only. For example, data of Ni are made of those for ^{58}Ni and ^{60}Ni. Evaluation of the data for these isotopes was mainly done by using statistical model calculation and some parts of them were modified with experimental data[1]. The elements and isotopes are shown in Table 1.

Tentative data file of JENDL-3, JENDL-3T, had been tested by Cai et al.[2] They compared JENDL-3T data with ENDF/B-IV and experimental data measured at ORNL[3]. They showed that there were significant differences in the thermal capture γ-ray data between JENDL-3T and ENDF/B-IV, in particular, structure of the γ-ray spectrum. For the fast neutron data, JENDL-3T agreed well with experiments, except for the spectra of some structural materials between 4 and 6 MeV of γ-ray energies.

Cai et al. modified the thermal neutron capture data for 16 nuclides or elements in such a simple way as the shape of the experimental spectrum was reproduced[2]. Using the modified data file, they obtained average γ-ray production cross sections for thermal neutron capture within 20% deviation from the experimental data, and they got quite well agreement with the experiments for the fast neutron data. After these test and modification were over, JENDL-3 was released.

3. Status-Quo of γ-Ray Production Data

As mentioned in Chapter 1, there have been various studies concerning γ-ray

productions using JENDL-3, and several discrepancies between experiments and analyses were reported. In order to make cause of these defects clear, the WG examined the JENDL-3 data by the following way,

(a) comparison between the JENDL-3 data and the experiments,
(b) comparison between the γ-ray production cross sections and non-elestic scattering cross sections,
(c) study on systematic trend of the γ-ray spectra versus neutron energy,
(d) check of energy-bin for the γ-ray spectrum data,
(e) check of the γ-ray data for the thermal neutrons,

etc.

The item (a) showed that most γ-ray production cross sections agreed well with the experimental data, but several spectrum data had disagreement with the experiments. In Fig.1, the γ-ray production cross sections of Ni calculated with the γ-ray energy above 690 keV agree well with the experimental data[4] in which the γ-rays below 690 keV was cut off. This example suggests that the JENDL-3 γ-ray production cross section of Ni may reproduce the experiments, if the measurements were done with full γ-ray energy.

The γ-ray spectra of low neutron energy are apt to disagree with experiments. Figure 2 shows that the JENDL-3 spectrum of Ni is several times higher than the expermental data. The JENDL-3 γ-ray data of Ni consist of those for ^{58}Ni and ^{60}Ni, abundance of which is 95%. Since the first excited level of ^{58}Ni is 1.45 MeV and that of ^{60}Ni is 1.33 MeV, no inelastic scattering γ-ray spectrum is expected for the neutron energy of 1.24 MeV. Hence the peak around 1 MeV in Fig. 2 is questionable for both the experiment and the calculation. This problem will be discussed later again.

Calculated and experimental γ-ray spectra agree well with each other with increasing neutron energy. Figure 3 shows the spectrum of Ni at 9.5 MeV neutron energy, which is an example of good agreement. Significant difficulty, however, still remains in Fe spectrum. To this element or its isotopes, statistical model calculation may not be applicable. Therefore, reevaluation may be proposed to do by tracing the experimental data for this element such as those of Fig. 4.[5]

Adequacy of multiplicity data was examined by the item (b). Most data exhibit reasonable trend, and they give plausible γ-ray production cross sections. A few data, however, show strange behavior. They might happen to do mistakes in filing the data. Correction of these must be easy.

In general, data of γ-ray spectra seem to have more significant problems than production cross sections. Hence, systematic trend of the spectrum data was examined (item (c)) by plotting the data at the neutron energies of 0.0253 eV, 500 keV, 3 MeV, 10 MeV and 14 MeV. Although most data were obtained by using the statistical model calculations, some data were replaced with experimental data. In such case, inconsistent and strange data appear in the plotted graphs. Figure 5 shows unrealistic shape of Zr spectrum data at thermal neutron energy. This might have been replaced with the data

of which γ-rays below 1 MeV were cut off.

The item (d) is concerned with the problem mentioned in Fig. 2. The WG checked whether energy points of neutron and γ-ray were taken reasonably, and saw in some cases that the necessary energy points such as those corresponding to the discrete excited levels and threshold energies of the reactions were lacking. As mentioned above, the γ-ray spectrum of Ni at 1.24 MeV neutron energy should not have inelastic scattering component. The spectrum in Fig. 2 was calculated by interpolation of the spectra at 1.0 and 1.5 MeV neutron energies. As the latter has the inelastic scattering component, this interpolation makes a strange shape of the spectrum. In order to make reasonable shape of the spectrum, new data for interpolation are needed around 1.3 MeV. Spectrum shown in Fig. 6 was calculated by setting a fictitious spectrum at 1.25 MeV. This seems to be more reasonable, in physical sense, than that in Fig. 2.

Caution should be paid also to the width of energy-bin for γ-rays. In some spectra of JENDL-3, there are those with bin-width more than 500 keV. Since the middle value of each bin is taken as reference data, this width may be too large in calculation or interpolation of the data, and plausible bin-width seems to be less than or equal to 250 keV.

Most line spectra were averaged in the corresponding energy bin and mixed with the continuum spectra. This procedure threatens to break the energy conservation. In order to make sure of the energy conservation, transition probabilities between low-lying levels should be used, instead of the fictitious continuous spectra.

For the thermal neutron, it is particularly important to examine whether adequate data are adopted. In JENDL-3, Q-value was taken from the table of Wapstra-Bos[6]. For natural element, it was adopted from the largest value of the component isotopes. From the viewpoint of the energy conservation, it may be better to take an average value of those for component isotopes. Further, there are some nuclei whose Q-values were not equal to the γ-ray energies calculated using their spectrum data. These defects may be removed by revising spectrum or multiplicity data.

4. Concluding Remarks

JENDL-3 has been widely used since it was released, and many studies have been reported including validity of the JENDL-3 data. They showed that JENDL-3 could reproduce most of the experimental data. However, it was pointed out that there were still significant defects in some γ-ray production data of JENDL-3.

In this report, these defects were examined, and their causes were investigated. To remedy them, the following matters should be done;

(a) spectrum data for important intermediate nuclei are revised so as to reproduce experimental data,

(b) spectrum data at neutron energies corresponding to low-lying levels and some reaction threshold are added so that interpolation of γ-ray spectra could be done

reasonably,

(c) at least at thermal energy, spectrum and multiplicity data are revised so that total γ-ray energies calculated using them could be equal to the corresponding Q-values,

(d) in order to make sure of energy conservation, transition probability data between low-lying discrete levels are placed, if possible, instead of fictitious continuum spectra,

(e) appropriate energy bins for neutron and γ-ray energies are taken.

The author is deeply indebted to T. Nakagawa for his kindly help with handling the JENDL-3 γ-ray data.

References

1) Shibata K., Nakagawa T., Asami T., Fukahori T., Narita T., Chiba S., Mizumoto M., Hasegawa A., Kikuchi Y., Nakajima Y. and Igarasi S.: "Japanese Evaluated Nuclear Data Library, Version-3 -- JENDL-3 --", JAERI 1319 (1990).

2) Cai S., Hasegawa A., Nakagawa T. and Kikuchi Y.: J. Nucl. Sci. Technol. **27**, 844 (1990).

3) Maerker R.E. and Muckenthaler F.J.: "γ-Ray Spectra Arising from Fast-Neutron Interactions in Elements Found in Solids, Concretes and Structural Materials", ORNL-4475 (1970).

4) Dickens J.K., Love T.A. and Morgan G.L.: "γ-Ray Production from Neutron Interactions with Nickel for Incident Neutron Energies between 1.0 and 10 MeV: Tabulated Differential Cross Sections", ORNL-TM-4379 (1973).

5) Hasegawa K., Mizumoto M., Chiba S., Sugimoto M., Yamanouti Y., Igashira M. and Kitazawa H.: "γ-Ray Production Cross Section Measurements of Some Structural Materials between 7.8 and 13.0 MeV", Proc. Int. Conf. Nuclear Data for Science and Technology, Juelich (1991), p.329, (Ed. S. Qaim), Springer-Verlag.

6) Wapstra A.H. and Bos K.: Atomic Data and Nuclear Data Tables **19**, No.3 (1977)

Table 1 Fifty-nine nuclieds whose γ-ray data are evaluated in JENDL-3

H-1	Li-6	Li-7	Be-9	B-10
B-11	C-12	N-14	N-15	O-16
Na-23	Mg	Al-27	Si	Si-28
Si-29	Si-30	Ca	Ca-40	Ti
Cr	Mn-55	Fe	Fe-54	Fe-56
Fe-57	Fe-58	Ni	Ni-58	Ni-60
Cu	Cu-63	Cu-65	Zr	Nb-93
Mo	Ag	Ag-107	Ag-109	Cd
Eu	Hf	Hf-174	Hf-176	Hf-177
Hf-178	Hf-179	Hf-180	Ta-181	W
Pb	Pb-204	Pb-206	Pb-207	Pb-208
Bi-209	U-235	U-238	Pu-239	

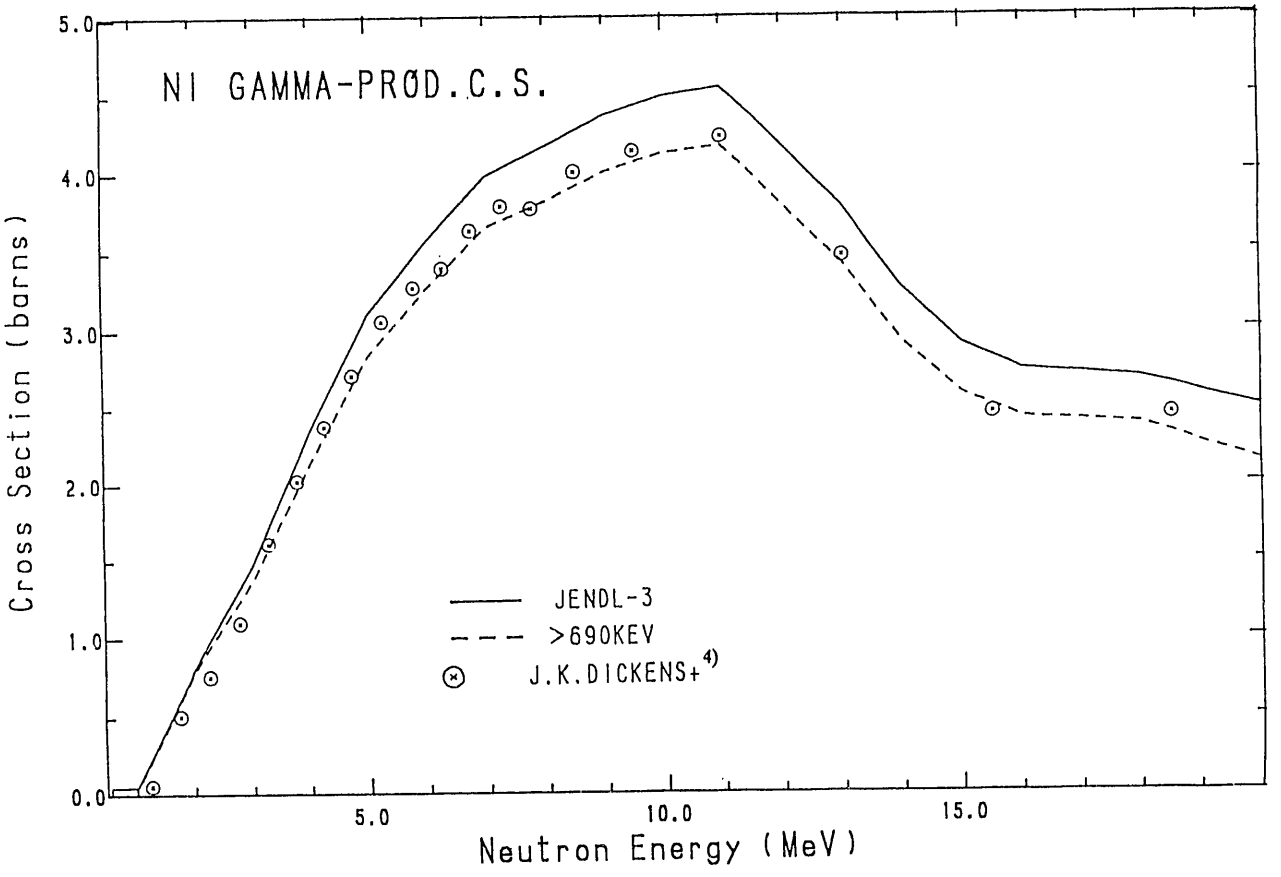

Fig. 1 γ-ray production cross sections of Ni. Solid line is calculated using JENDL-3, and dashed line is done by cutting off the γ-rays below 690 keV. The latter agrees well with the experimental data by Dickens et al.[4)]

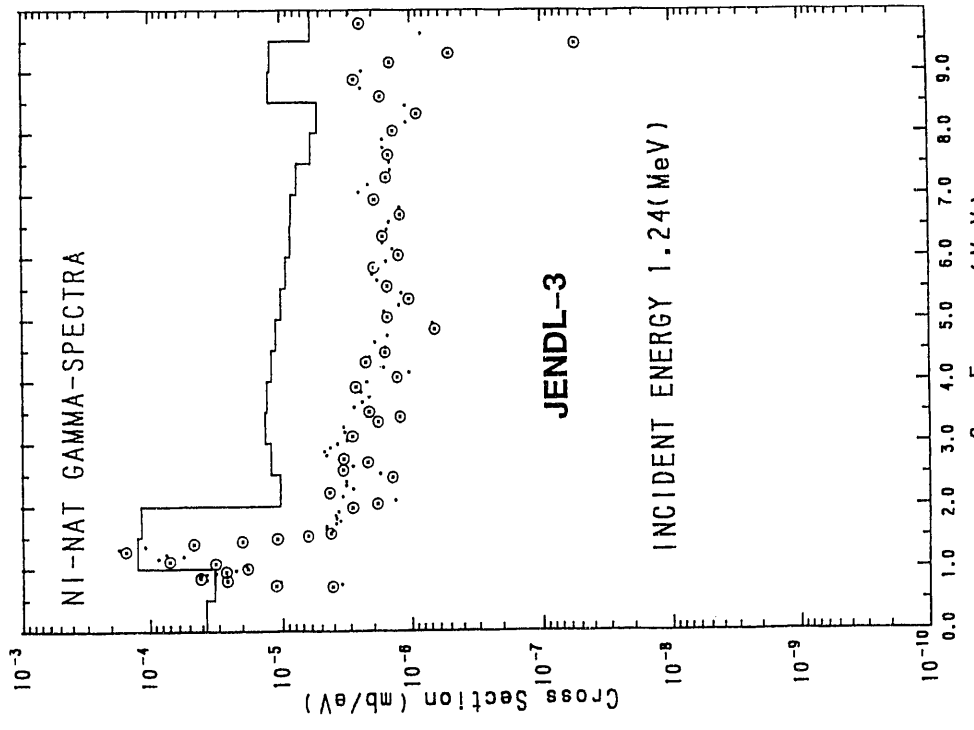

Fig. 2 γ-ray spectrum of Ni at 1.24 MeV neutron energy. No inelastic scattering channel opens at this energy. The spectrum is obtained by interpolation of the data at 1.0 and 1.5 MeV. Significant difference between calculated and experimental data exists, in general, in low energy capture γ-ray spectra.

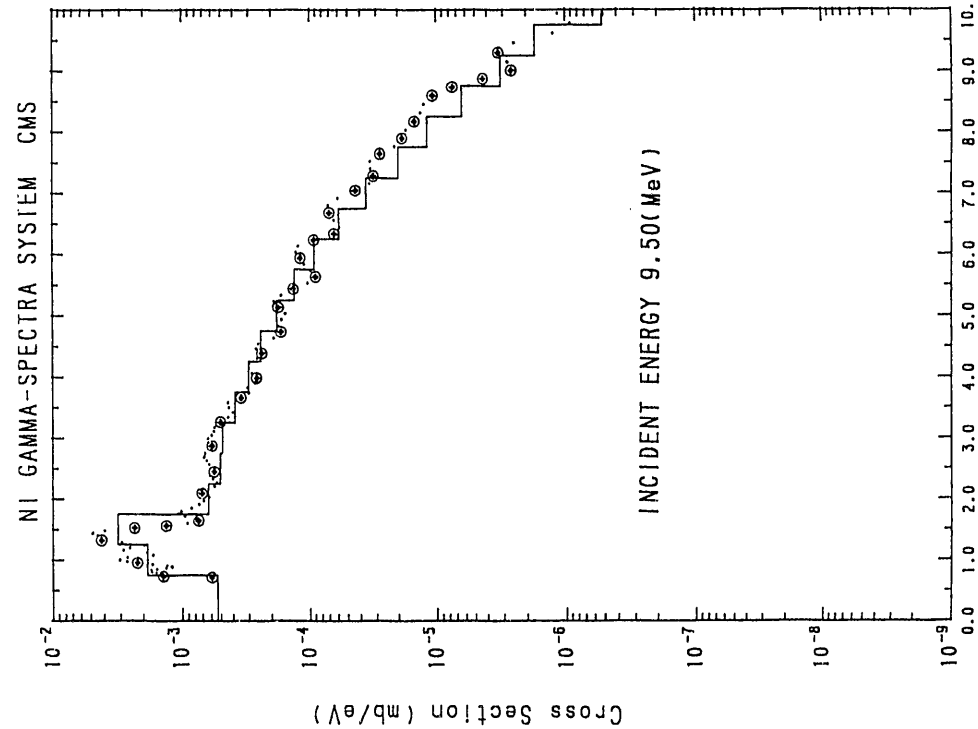

Fig. 3 γ-ray spectrum of Ni at 9.50 MeV neutron energy. Agreement between calculated and experimental data becomes well, in general, with increasing neutron energy.

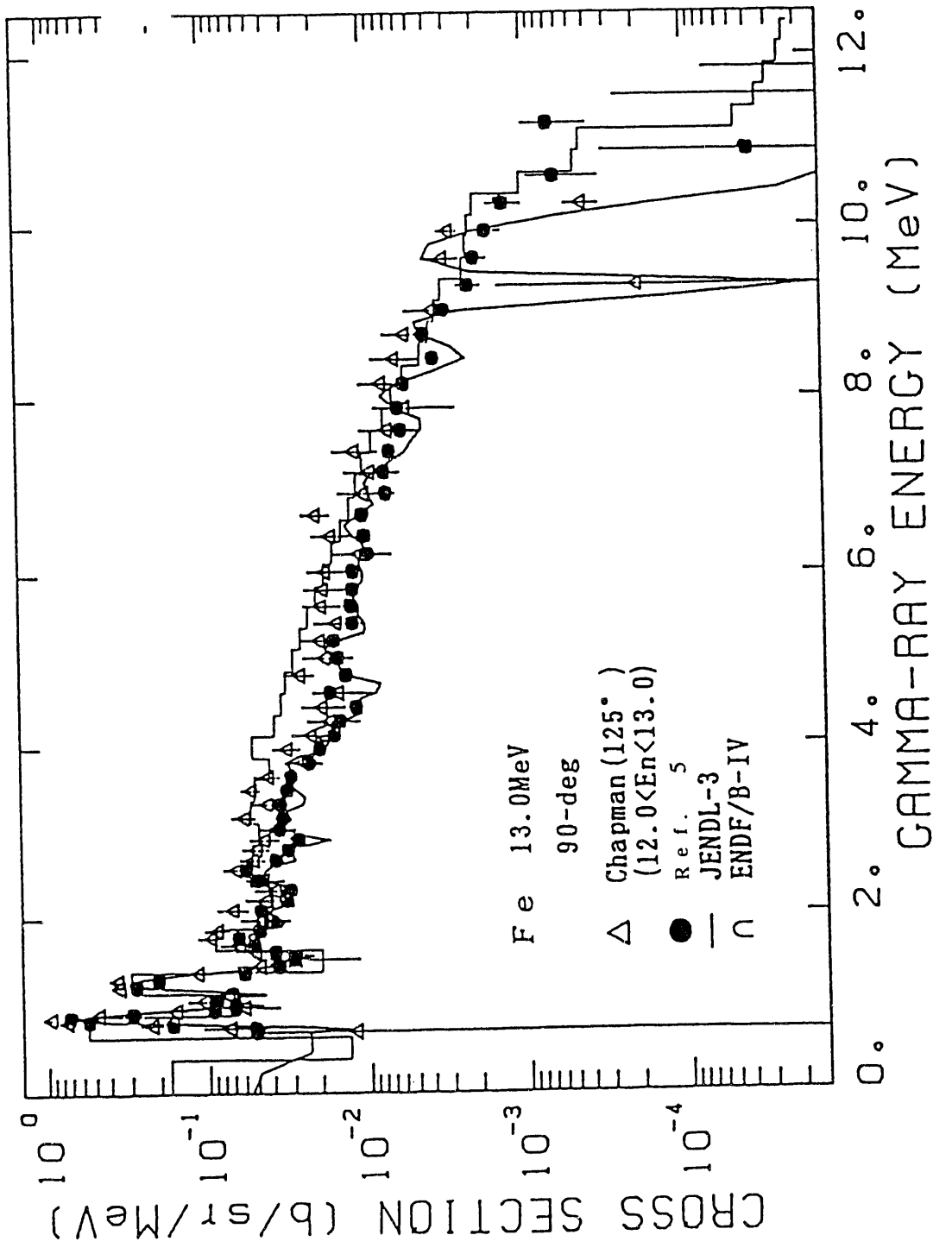

Fig. 4 γ-ray spectrum of Fe at 13.0 MeV neutron energy. JENDL-3 gives higher values than measured data between 2 and 6 MeV.

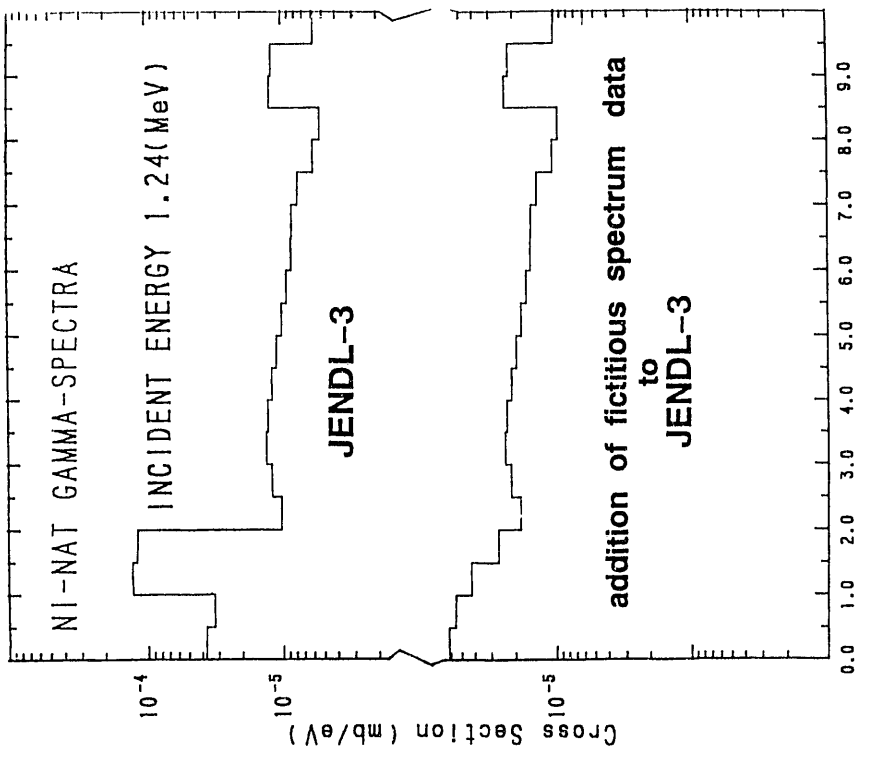

Fig. 6 γ-ray spectra of Ni at 1.24 MeV neutron energy. Upper part is the same spectrum as in Fig. 2, and lower part is made by interpolation of the data at 1.0 and 1.25 MeV. Spectrum at 1.25 MeV is added in JENDL-3 file tentatively.

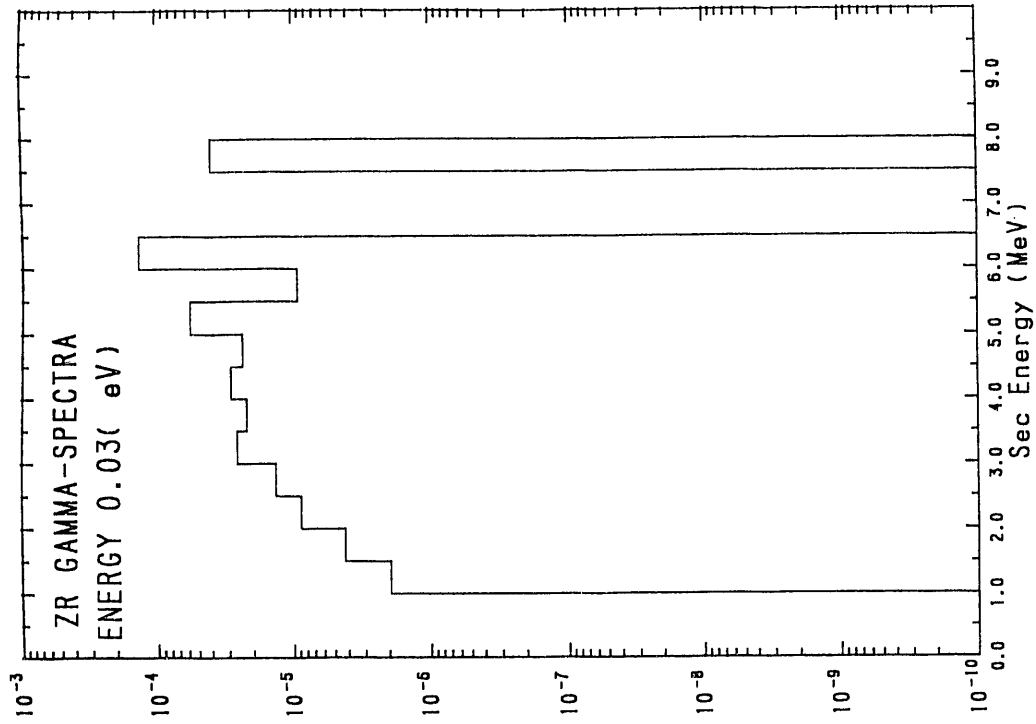

Fig. 5 γ-ray spectrum of Zr at thermal neutron energy. Typical example of wrong data. Evaluated data might be replaced by experimental data partly. Such replacement happens to cause unbalance in the data.

2.3 Adjustment of Group Constants

2.3.1 Development of An Adjusted Group Cross-section Set for Large LMFBR Cores using the JUPITER Analytical Results

Makoto ISHIKAWA*1 Takashi HOSHI*2 Toshio SANDA*3
Takanobu KAMEI*4 Takashi KAWAKITA*5

*1 Power Reactor and Nuclear Fuel Development Corporation (PNC), 4002, Narita-cho, O-arai-machi, Ibaraki-ken 311-13 *2 The Japan Atomic Power Company (JAPC), 1-6-1, Ohtemachi, Chiyoda-ku, Tokyo 100 *3 Hitachi Ltd., 7-2-1, Omika-cho, Hitachi-shi, Ibaraki-ken 319-12 *4 Toshiba Corporation, 8, Shinsugita-cho, Isogo-ku, Yokohama 235 (present : FBR Engineering Co., Ltd.) *5 Mitsubishi Atomic Power Industries, Inc., 4-1, Shibakouen, 2-chome, Minato-ku, Tokyo 105, JAPAN

Abstract

A cross-section adjustment study was performed for three years using the results of the JUPITER experiment and analysis. Analytical tools and a set of data for the cross-section adjustment were established as a consistent system in order to improve the nuclear design method and its accuracy for large FBR cores. The results of JUPITER analysis were effectively utilized in the present study and the adjusted cross-section set developed here was found to possess sufficient reliability and applicability for analyzing large FBR cores.

1. Introduction

In the core design of large liquid-metal fast breeder reactors, it is of importance to improve the prediction accuracy of nuclear characteristics from the viewpoint of both reducing cost and insuring reliability of the plant. JUPITER[1], a cooperative critical experimental program between DOE and PNC, was performed at the ZPPR facility from 1978 till 1988 in this context. By the results of JUPITER study, analytical methods for FBR cores made great progress and important knowledge of reactor physics like spatial dependence of C/E(Calculation/Experiment) values in large FBR cores was obtained. In order to reflect these integral information from critical experiments on the FBR core design, the cross-section adjustment method has been found to be the most efficient way, instead of the E/C bias method which was traditionally used in Japan. Figure 1 shows the flow diagram of FBR core design by the cross-section adjustment method. The primary objective of the present study, preliminary results of which were reported previously[2], is to establish the cross-section adjustment method as an improved nuclear design method for FBR cores with sufficient reliability and applicability. In the present report, the adjustment results are discussed especially from the aspects of nuclear data evaluation.

2. Cross-Section Adjustment Method

The idea of the cross-section adjustment is based on the Bayesian parameter-estimation method, that is, the probability that a cross-section set, T, is true should be maximized under the condition that integral information, Re, is obtained. The equations for the cross-section adjustment were compiled in comprehensive matrix forms by Dragt et al[3]. The fundamental assumptions for the formulation are : (a) all kinds of errors have statistical Gaussian distributions, and (b) integral parameters have linearity to cross-section changes. The cross-section set after adjustment, T', is derived using the least-square technique and expressed by :

$$T' = To + MG^t[GMG^t + Ve + Vm]^{-1}[Re - Rc(To)]$$

The covariance of the adjusted cross-section set, M', is also changed as :

$$M' = M - MG^t[GMG^t + Ve + Vm]^{-1}GM$$

where,

To	:	a basic cross-section set before adjustment
M	:	covariance of To
Re	:	experimental values of integral parameter
Rc	:	analytical values corresponding to Re
Ve	:	experimental errors of integral parameter Re
Vm	:	analytical errors of integral parameter Rc
G	:	sensitivity coefficients defined by $(dR/R)/(d\sigma/\sigma)$

The contributions of cross-section errors to the prediction error of integral parameters are expressed by GMG^t and $GM'G^t$, before and after adjustment, respectively.

These formulas are incorporated in the ABLE code[4] developed by Osaka Univ. These equations indicate several important features of the cross-section adjustment method : (a) cross-sections which have large sensitivity and uncertainty will be mainly changed to make the C/E values close to unity, (b) values of Ve and Vm relative to GMG^t must be small in order to improve accuracy of a cross-section set, and (c) improvement of integral-parameter prediction is obtained from the reduction of cross-section covariance from M to M', and not related to C/E values themselves.

3. Cross-Section Data

The basic cross sections to be adjusted here is a 70-group constant set JFS-3-J2[5] generated from JENDL-2[6], which has been a standard cross-section set for FBR design and reactor physics study in Japan so far. The number of energy groups for the adjustment is 18, which is considered as most effective for FBR analysis in the capacity of current computers. For practical use in reactor analytical systems, the adjusted results were extended to the standard 70-group structure by spline-fitting technique. The nuclear data for the adjustment were selected from the viewpoint of significance in large FBR core analysis. As shown in Table 1, they include infinite cross-sections of 32 reactions from eleven nuclides such as plutonium, uranium and structure materials, fission spectra of two nuclides, and delayed neutron fractions of six nuclides. On the contrary,

matrix components of inelastic cross-sections or self-shielding factors were not adjusted in the present study.

The adjustment procedure needs a full matrix of nuclear-data covariance. JENDL does not provide any covariance files yet, therefore, 18-group covariance data of the above-mentioned reactions were newly evaluated in the present study in cooperation with JAERI nuclear data center. The variances(diagonal terms) of the cross-section errors were basically estimated from the statistical scattering of nuclear experimental values around JENDL-2 as follows :

$$\text{variance} \simeq [\Sigma w(\sigma_{exp}-\sigma_{J2})^2/\sigma_{J2}^2]/\Sigma w$$

where, w : weight (square of experimental error)

σ_{exp} : experimental value

σ_{J2} : JENDL-2 value

The correlation factors(non-diagonal terms) were basically determined by the following policy : (a) classification of energy ranges corresponding to each evaluation method of nuclear data, (b) weak correlations in the region apart from the diagonal, and (c) smoothness between adjacent energy regions. Furthermore, the covariance data were somewhat modified iteratively according to feedback from preliminary adjustment results, so as to make the cross-section changes reasonable from the viewpoint of nuclear-data evaluators. Evaluated covariance data of Pu239 fission reaction are shown in Table 2 as a typical example.

4. Integral Data and Sensitivity Coefficients

Through consideration of physical consistency and plenty of numerical experiments, a set of 82 C/E values of reactor core characteristics was finally selected from the recent JUPITER analysis as the integral data for the adjustment. The features of the ZPPR experimental cores and main C/E values by JFS-3-J2 are summarized in Table 3. The integral experimental data include various kinds of reactor core sizes, control rod positions and nuclear characteristics such as criticality, reaction rate ratio and distribution, control rod worth and sodium void reactivity from a variety of core concepts which include homogeneous, axially and radially heterogeneous ones. The noticeable results of the C/E values by JFS-3-J2 are : (a) criticalities are generally under-estimated and the degrees depend on core concepts, (b) reaction rate ratios of C28/F49(U238 capture/Pu239 fission) are overestimated by 4~6%, (c) reaction rate distributions and control rod worths show large dependence on radial positions in the core region, and (d) sodium void worths are largely overestimated.

The experimental and analytical errors, Ve and Vm, of the integral parameters are shown in Table 4. The experimental errors and their correlations of the integral data were based on the estimation of ANL experimenters. On the other hand, the analytical errors and their correlations were systematically estimated in the present work applying a kind of sensitivity consideration about the influence of analytical modeling methods to the calculational values.

Sensitivity coefficients of each core parameters were calculated by the SAGEP code[7] based on

the generalized perturbation theory. A formula to calculate the sensitivity of the fission spectrum was developed and implemented in the code. Figures 2～4 show a part of sensitivity coefficients, from which we can find some indications for cross-section improvements : (a) large sensitivities come from dominant isotopes in FBR cores like U238, Pu239, O, Fe and Na etc., (b) reduction of U238 capture cross section in 500eV～100keV energy range is effective for reducing C/E radial dependence, as well as improving underestimation of keff and overestimation of C28/F49 reaction rate ratio, (c) reduction of O, Fe and Na elastic cross section in 50～500keV is also effective for reducing C/E radial dependence, and (d) sensitivities of sodium void reactivity are high for U238 capture and Pu239 fission reactions in the energy region of a few keV, which corresponds to the resonance energy of sodium capture cross section.

5. Adjustment Results

The adjustment results for ZPPR-9 core are summarized in Table 5 and Fig.5～6 : (a) C/E values of criticality after the adjustment reached 1.0 very closely and dependence on core concepts almost disappeared as seen in Fig.5, (b) C/E values of reaction rate ratio such as C28/F49 were quite improved, (c) radial dependence of C/E values were almost vanished as shown in Fig.6, and (d) the prediction uncertainties caused by cross-section errors, GM'G^t, were markedly improved through all kinds of the integral characteristics after adjustment.

The main changes of JFS-3-J2 cross-sections by the adjustment are shown in Table 6 and Fig.7～9. The main features of the cross-section changes are : (a) U238 capture cross-section was decreased by 2～6% in the energy range from 100eV to 200keV and well agreed with JENDL-3 above 30keV as shown in Fig.7, (b) Pu239 fission cross-section was decreased by 2～3% in 100keV～1MeV and agreed with JENDL-3 above 2keV as seen in Fig.8, although the large cross-section change of +6～7% around 1keV which was caused by the overestimation of sodium reactivity by JENDL-2, would raise arguments from the standpoint of nuclear data evaluation, (c) U238 inelastic reaction was decreased by 4～8% above 1MeV, which is the opposite direction with JENDL-3 or the recent experiments as found in Fig.9, (d) U235 fission cross-section was decreased by 2～4% in 10keV～1MeV and well agreed with JENDL-3 above 10keV, on the other hand, the adjusted cross-section is larger than JENDL-3 by 5% in 200eV～10keV, (e) fission spectrum of Pu239 was changed toward hardening, and (f) delayed neutron fractions based on Tuttle's and Saphier's data were decreased by 0.5～1.2%.

The correlation matrix of Pu239 fission reaction after adjustment is shown in Table 7. As expected from the equations of adjustment, the correlation factors generally change to negative directions compared with Table 2. The improvement of prediction accuracy after adjustment seems to arise from these negative correlations as well as the reduction of diagonal variances.

Most parts of the cross-section changes were found to be reasonable from the viewpoint of nuclear data evaluation except several points such as the U238 inelastic reaction.

6. Reliability and Applicability of Adjusted Cross Sections

To insure the reliability and applicability of the adjusted cross-section set, several approaches were applied in the present study. First, as partly mentioned above, each of the adjusted cross sections was inspected in detail from the viewpoint of nuclear data and found to have no serious singularity or anomaly exceeding nuclear data uncertainty. Second, the adjusted cross sections were applied to a set of benchmark problems[8] mainly compiled by the Cross Section Evaluation Working Group in BNL. The purpose of the benchmark test is to investigate the applicability to other reactors which were not used as the adjustment data. The performance of the adjusted cross sections was found to be reasonable in the wide range of reactor core volumes as shown in Fig.10~11. Third, to check statistical consistency, the chi-square test was applied to the data group of the adjustment and a value of 0.47 was obtained for the ratio of the chi-square value to degrees of freedom. These adjustment data were judged to be reasonable statistically, although there is a possibility that our error estimation might be a little conservative. Fourth, to verify the linearity assumption of the sensitivity analyses, some ZPPR assemblies were directly analyzed with the adjusted cross sections, and the C/E values were compared with those calculated from the sensitivity coefficients and the cross-section changes. The calculated values of both cases show satisfactory agreements. And finally, a wide range of parametric study was performed concerning the arbitrariness of data used in the adjustment procedure such as the covariance of cross sections or the analytical errors for the adjustment. Tables 8~9 show some results of the parametric study. Overall performance of the adjustment method was found not to be significantly influenced due to the uncertainties of these data.

7. Application to FBR Core Design

The cross-section adjustment method was applied to a 600MWe-class FBR core design and the performance was evaluated. The estimation of design prediction accuracy is based on the formulas derived by Takeda et al.[9] Table 10 compares the resulted accuracy of the FBR core by three methods to reflect the JUPITER integral information. The accuracy of the adjustment method is superior to that of the traditional E/C bias method for predicting all kinds of FBR core characteristics.

8. Conclusions

Analytical tools and a set of data for the cross-section adjustment were established as a consistent system in order to improve the nuclear design method and its accuracy for large FBR cores. The results of JUPITER analysis were effectively utilized in the present study and the adjusted cross-section set developed here possesses sufficient reliability and applicability for large FBR cores. The next steps for further improvement would be : (a) extension of integral experimental data, especially burnup-related information from FBRs like JOYO or MONJU, (b) adoption of a new basic cross-section library, (c) refinement of cross-section covariance data, and

(d) development of an advanced theory, especially to adjust self-shielding factors.

We believe the cross-section adjustment method will play an important role in the LMFBR core design works hereafter.

Acknowledgment

The authors appreciate Toshikazu Takeda, Tsuneo Nakagawa, Yasuyuki Kikuchi, Hideki Takano and Susumu Iijima for their collaborations and useful discussions to the present study. The present paper is based on the results of the cooperative research between PNC and JAPC. (JAPC performed the work under auspices of nine utilities and Electric Power Development Co.)

References

1) Shirakata K., Yamamoto T., Yoshimura A. and Takeda T. : Proc. of Inter. Conf. on Nuclear Data and Science and Technology, Mito, 53 (1988)
2) Sanda T., Kamei T., Kawakita T., Saito M., Sato M., Ishikawa M. and Hayashi H. : JAERI-M 91-032, 425 (1991)
3) Dragt J.B., Deckker J.W.M., Gruppelaar H. and Janssen A.J. :Nucl. Sci. Eng. 62,117 (1977)
4) Takeda T. : private communication
5) Takano H. and Kaneko K. : JAERI-M 89-141 (1989)
6) Nakagawa T. : JAERI-M 84-103 (1984)
7) Hara A., Takeda T. and Kikuchi Y. : JAERI-M 84-027 (1985)
8) Hardie R. W., Schenter R. E. and Wilson R. E. : Nucl. Sci. Eng. 57, 222 (1975)
9) Takeda T., Yoshimura A., Kamei T. and Shirakata K. : Nucl. Sci. Eng. 103, 157 (1989)

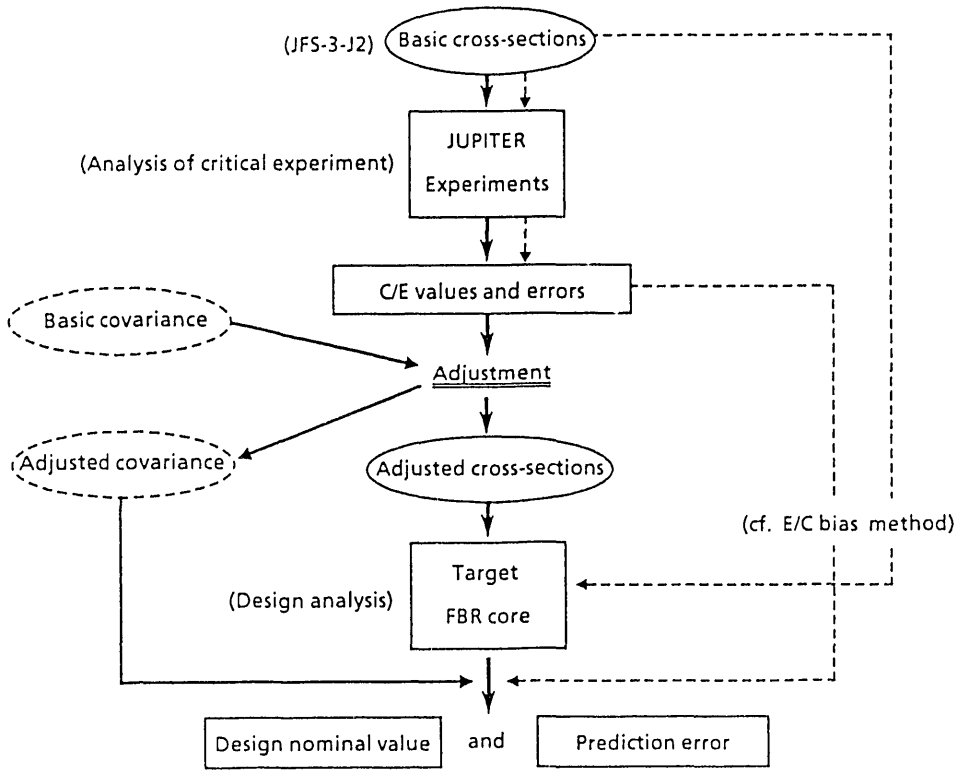

Fig. 1 Flow diagram of FBR core design by cross-section adjustment method.

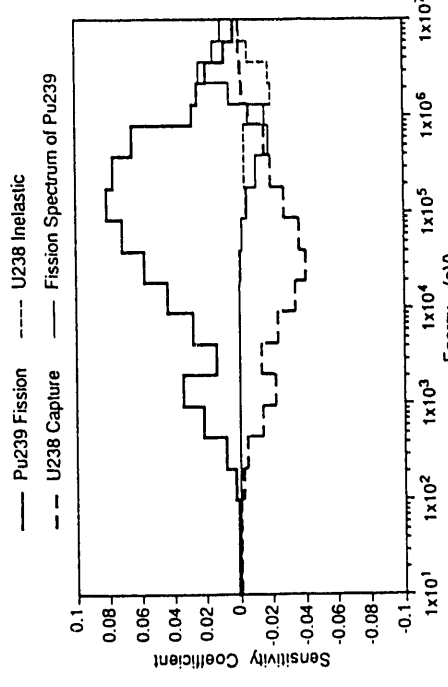

Fig. 2 Sensitivity for criticality (ZPPR-9 Core).

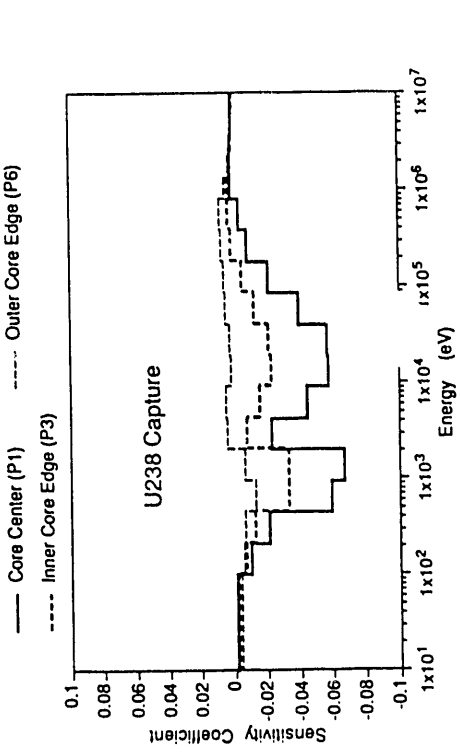

Fig. 3 Sensitivity for control rod worth (ZPPR-9 Core).

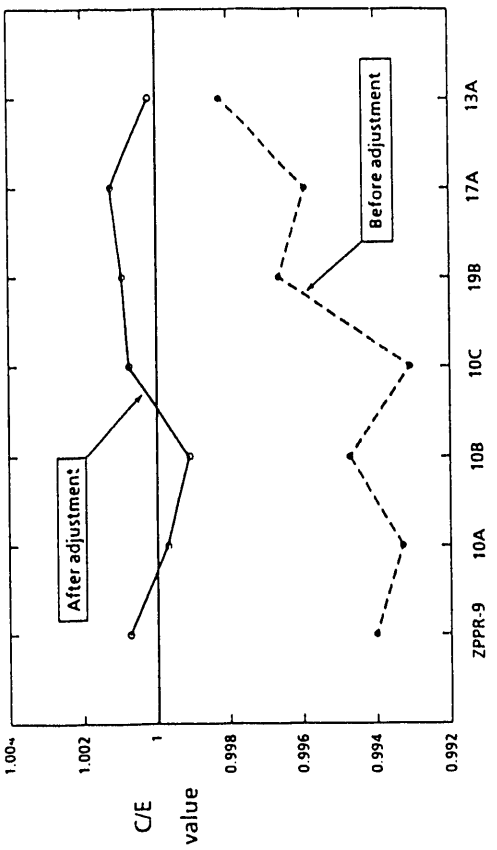

Fig. 5 C/E values before and after adjustment (1) (Criticality).

Fig. 4 Sensitivity for Na void reactivity (ZPPR-9 Core).

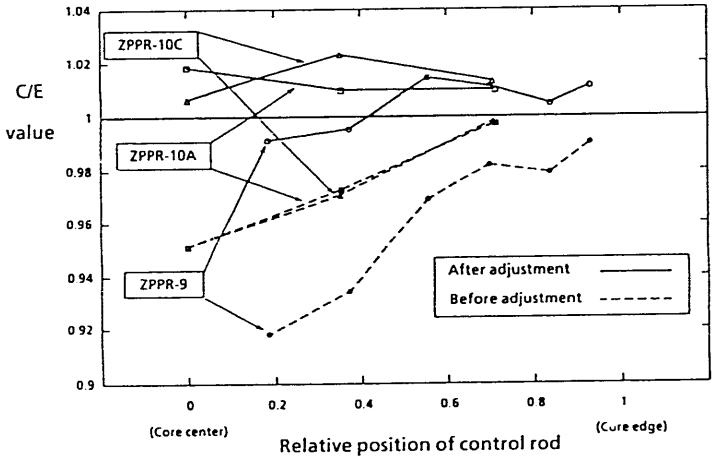

Fig. 6 C/E values before and after adjustment (2) (Control Rod Worth).

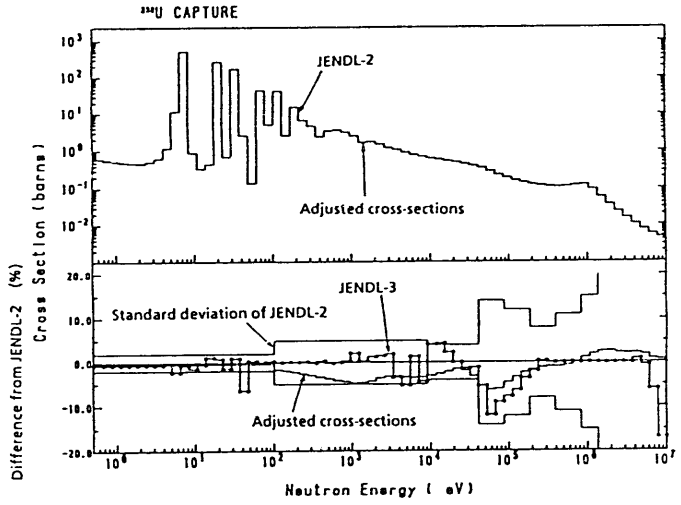

Fig. 7 JFS-3-J2 cross-section changes by adjustment (1) U238 capture (*plotted by JAERI Nuclear Data Center).

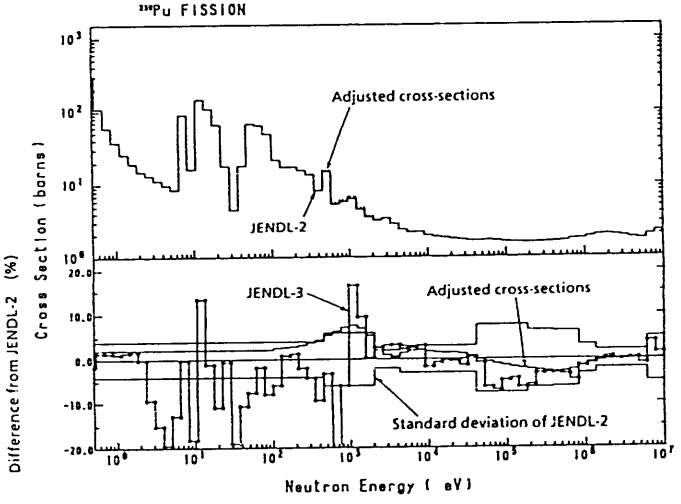

Fig. 8 JFS-3-J2 cross-section changes by adjustment (2) Pu239 fission (*plotted by JAERI Nuclear Data Center).

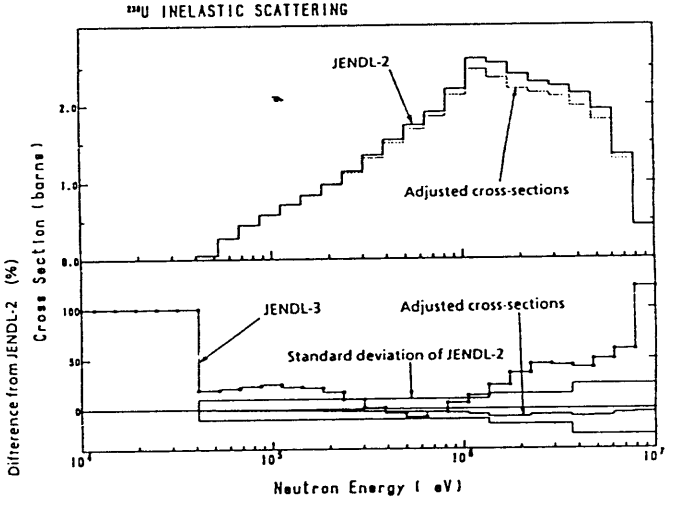

Fig. 9 JFS-3-J2 cross-section changes by adjustment (3) U238 inelastic (*plotted by JAERI Nuclear Data Center).

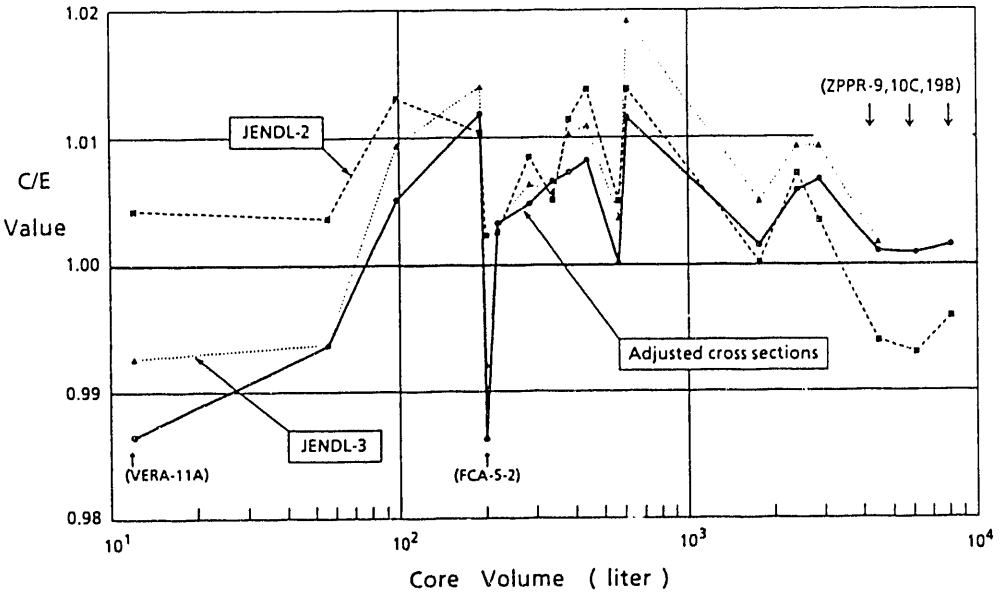

Fig. 10 International Benchmark Test (1)
(Plutonium Core - Criticality)
(*calculated by H. Takano, JAERI).

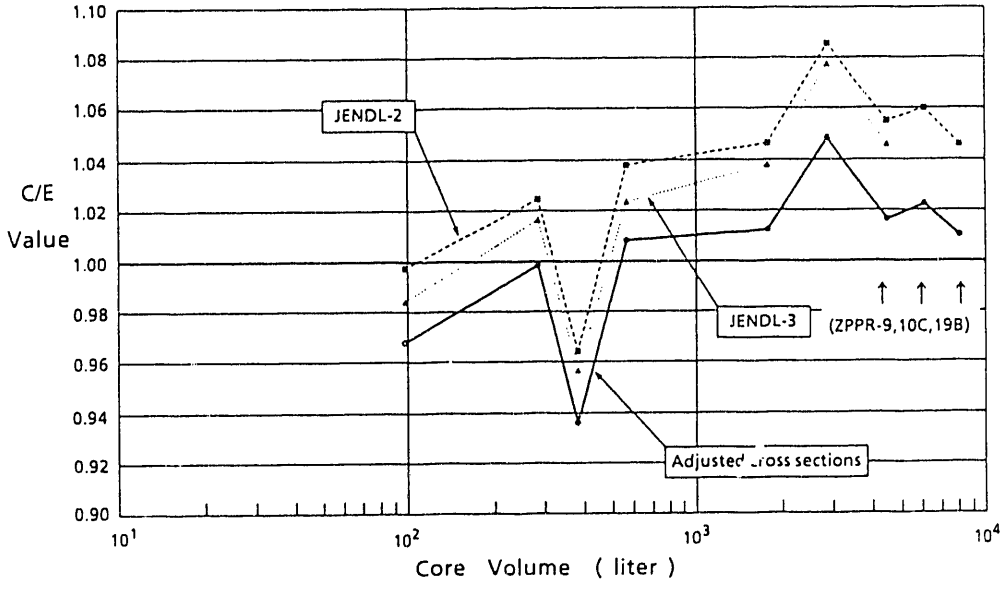

Fig. 11 International Benchmark Test (2)
(Plutonium core - C28/F49)
(*calculated by H. Takano, JAERI).

Table 1 Adjusted nuclides and reactions and prepared covariance data

Nuclide \ Reaction	cap.	fis.	ν	ela.	inela.	μ	χ	β
U235	◎	◎	◎	–	△	–	◎	△
U238	○	◎	◎	◎	◎	○	–	△
Pu239	◎	◎	◎	–	△	○	◎	△
Pu240	○	–	◎	–	–	–	–	△
Pu241	△	○	◎	–	–	–	–	△
Pu242	–	–	–	–	–	–	–	△
C12	△			–	–	–		
O16	–			○	○	○		
Na23	○			○	–	○		
Cr	–			–	–	○		
Fe	○			○	–	○		
Ni	–			–	–	○		

△ : only diagonals ○ : diagonals and correlations between energy groups
◎ : diagonals and correlations with other nuclides or reactions – : not adjusted

Table 2 18-group covariance data (Pu239 fission reaction)

Energy group	1	2	3	4	5	6	7	8	9	10	11	12	13	14	15	16	17	18
1	1.0	0.7	0.65	0.6	0.1	0	0	0	0	0	0	0	0	0	0	0	0	0
2	0.7	1.0	0.75	0.7	0.2	0.1	0	0	0	0	0	0	0	0	0	0	0	0
3	0.65	0.75	1.0	0.75	0.3	0.2	0.1	0.1	0	0	0	0	0	0	0	0	0	0
4	0.6	0.7	0.75	1.0	0.7	0.3	0.2	0.2	0.1	0	0	0	0	0	0	0	0	0
5	0.1	0.2	0.3	0.7	1.0	0.8	0.7	0.6	0.5	0	0	0	0	0	0	0	0	0
6	0	0.1	0.2	0.3	0.8	1.0	0.8	0.7	0.6	0	0	0	0	0	0	0	0	0
7	0	0	0.1	0.2	0.7	0.8	1.0	0.8	0.7	0	0	0	0	0	0	0	0	0
8	0	0	0.1	0.2	0.6	0.7	0.8	1.0	0.8	0.1	0.1	0	0	0	0	0	0	0
9	0	0	0	0.1	0.5	0.6	0.7	0.8	1.0	0.5	0.3	0.1	0	0	0	0	0	0
10	0	0	0	0	0	0	0	0.1	0.5	1.0	0.5	0.3	0.1	0	0	0	0	0
11	0	0	0	0	0	0	0	0.1	0.3	0.5	1.0	0.5	0.3	0.1	0	0	0	0
12	0	0	0	0	0	0	0	0	0.1	0.3	0.5	1.0	0.5	0.3	0.1	0	0	0
13	0	0	0	0	0	0	0	0	0	0.1	0.3	0.5	1.0	0.5	0.3	0.1	0.1	0
14	0	0	0	0	0	0	0	0	0	0	0.1	0.3	0.5	1.0	0.5	0.3	0.2	0.1
15	0	0	0	0	0	0	0	0	0	0	0	0.1	0.3	0.5	1.0	0.5	0.3	0.2
16	0	0	0	0	0	0	0	0	0	0	0	0	0.1	0.3	0.5	1.0	0.5	0.3
17	0	0	0	0	0	0	0	0	0	0	0	0	0.1	0.2	0.3	0.5	1.0	0.5
18	0	0	0	0	0	0	0	0	0	0	0	0	0	0.1	0.2	0.3	0.5	1
Standard deviation(%)	5.0	2.0	2.0	2.0	3.2	6.3	6.5	7.7	7.7	3.0	3.0	3.0	2.0	6.0	6.0	4.0	4.0	4.0

(Smoothed cross-section region) (Un-resolved region) (Resolved region)

Table 3 ZPPR core features and main C/E values of JUPITER by JFS-3-J2

ZPPR core		9	10A	10B	10C	13A	17A	19B
Core size (MWe-class)		600	600	600	800	650	650	1000
Core concept		Homo	Homo	Homo	Homo	R. Hetero	A. Hetero	Homo
Number of CR / CRP		0 / 0	0 / 19	7 / 12	0 / 19	0 / 0	0 / 0	0 / 24
Number of data used for adjustment		19	10	6	9	5	24	9
Main C/E value	Criticality	0.9940	0.9933	0.9947	0.9931	0.9982	0.9966	0.9959
	Reaction rate ratio (C28/F49)	1.055	1.057	1.062	1.060	1.042	1.039	1.046
	Reaction rate distribution (F49)	1.037	1.034	1.029	1.029	–	1.048	1.056
	CR Worth (Innermost ring)	0.918	0.951	–	0.951	–	0.883	0.884
	(Outermost ring)	0.990	0.998	–	0.999	–	–	0.991
	Na Void Reactivity (Core region)	1.21~1.36	–	–	–	–	1.31	–

Table 4 Experimental and analytical error

(1σ level)

Integral parameter	Experimental error	Analytical error
Criticality	0.04%	0.31%
Reaction rate ratio		
C28/F49, F25/F49	2.2%	1.0%
F28/F49	2.5%	2.0%
F41/F25 (B-B chamber)	2.0%	2.0%
Reaction rate distribution		
[Core] F49	1.0%	1.0~2.1%
F28	2.5%	1.4~3.4%
[Blanket] F49	1.0~1.3%	2.5%
F28	4.0~10.0%	5.2%
Control rod worth		
Absolute value	1.2%	2.4%
Relative value	0.6%	1.5%
Na void reactivity	2.0~4.0%	9.0%

Table 5 Changes of C/Es and uncertainties before and after cross-section adjustment

Integral parameters (ZPPR-9 core)	C/E value		Uncertainty due to cross-section error (1σ, %)	
	Before adjustment	After adjustment	Before (GMG^t)	After ($GM'G^t$)
Criticality (keff)	0.994	1.001	2.5	0.3
Reaction rate ratio				
• F25/F49	1.015	0.992	4.9	1.4
• C28/F49	1.055	1.016	5.8	1.4
• F28/F49	0.972	0.981	7.7	2.2
Reaction rate distribution				
• F49, Outer Core Region	1.037	0.987	2.3	0.5
Control rod worth				
• Core center position	0.918	0.991	5.3	1.7
• Core edge position	0.990	1.010	2.5	0.6
Na void reactivity				
• Small region void	1.21	1.13	7.1	3.6
• Large region void	1.36	1.23	8.8	4.3

Table 6 JFS-3-J2 cross-section changes by adjustment

Energy Group	Pu239 χ	Pu239 fission	U238 fission	U238 capture	U238 inelastic	U235 fission	Na elastic
1 (10.0 MeV~)	2.5	-0.1	-0.2	0.8	-4.4	-0.6	-0.0
2 (6.07 MeV~)	1.2	-0.1	-0.2	2.0	-7.8	-0.6	-0.1
3 (3.68 MeV~)	0.5	-0.3	-0.2	2.1	-6.1	-0.6	-0.2
4 (2.23 MeV~)	-0.2	-0.4	-3.2	2.5	-7.9	-1.0	-0.5
5 (1.35 MeV~)	-0.5	-1.3	-4.2	1.4	-4.6	-1.6	-0.8
6 (821 keV~)	-0.7	-2.7	-1.2	-0.5	-3.1	-3.5	-1.2
7 (388 keV~)	-0.9	-2.5	-2.4	-1.3	-2.3	-3.0	-1.5
8 (183 keV~)	-0.9	-1.8	-3.6	-3.5	-1.5	-3.1	-1.7
9 (86.5 keV~)	-0.9	-0.6	-3.4	-5.8	-1.0	-3.1	-2.9
10 (40.9 keV~)	-0.9	1.1	-3.2	-2.1	0.0	-1.7	-1.7
11 (19.3 keV~)	-	1.6	-2.1	-2.6	0.0	-1.5	-0.4
12 (9.12 keV~)	-	1.8	-1.6	-3.4	0.0	-2.2	0.6
13 (4.31 keV~)	-	1.4	-0.2	-3.3	0.0	-1.2	1.2
14 (2.04 keV~)	-	6.8	-3.3	-4.5	0.0	0.6	1.2
15 (961 eV~)	-	6.3	-9.9	-4.1	0.0	1.4	0.6
16 (454 eV~)	-	3.8	-0.0	-2.9	0.0	0.6	0.3
17 (214 eV~)	-	2.8	-0.1	-2.0	0.0	0.2	0.2
18 (101 eV~)	-	2.2	-0.4	-0.4	0.0	-0.1	0.1
βeff (Tuttle, Saphier)	-	-0.5	-1.2	-	-	-1.0	-

Table 7 Covariance data after adjustment (Pu239 fission reaction)

Energy group	1	2	3	4	5	6	7	8	9	10	11	12	13	14	15	16	17	18
1	1.0	0.69	0.65	0.61	0.06	-0.10	-0.10	-0.09	0.06	0.01	0.01	0.01	0.01	0.01	0.01	0.01	0.00	-0.00
2	0.69	1.0	0.74	0.70	0.17	0.01	-0.17	-0.15	-0.10	0.01	0.01	0.01	0.02	0.02	0.02	0.02	0.01	-0.00
3	0.65	0.74	1.0	0.73	0.21	0.05	-0.13	-0.10	-0.23	0.01	0.01	0.02	0.02	0.03	0.03	0.02	0.01	-0.00
4	0.61	0.70	0.73	1.0	0.74	0.04	-0.16	0.12	-0.23	-0.01	0.00	0.02	0.03	0.04	0.04	0.03	0.01	-0.01
5	0.06	0.17	0.21	0.74	1.0	0.47	0.16	-0.08	-0.19	-0.14	-0.09	-0.01	0.04	0.05	0.07	0.05	0.03	0.01
6	0.10	0.01	0.05	0.04	0.47	1.0	0.35	0.06	-0.09	-0.21	-0.15	-0.05	0.01	0.04	0.06	0.06	0.04	0.03
7	0.10	-0.17	-0.13	-0.16	0.16	0.35	1.0	0.29	0.09	-0.28	-0.20	-0.08	-0.01	0.01	0.04	0.04	0.04	0.04
8	-0.09	0.15	0.10	-0.12	0.08	0.06	0.29	1.0	0.37	-0.13	-0.06	-0.13	-0.06	-0.05	-0.01	0.02	0.03	0.07
9	-0.06	0.10	-0.23	-0.23	0.19	-0.09	0.08	0.37	1.0	0.57	0.27	0.02	-0.10	-0.11	-0.06	-0.01	0.02	0.08
10	0.01	0.01	0.01	-0.01	0.14	-0.21	-0.28	-0.13	0.57	1.0	0.44	0.24	0.03	-0.10	-0.08	-0.05	-0.01	0.04
11	0.01	0.01	0.01	0.01	-0.09	-0.15	-0.20	-0.06	0.27	0.44	1.0	0.46	0.24	0.00	-0.09	-0.05	-0.01	0.05
12	0.01	0.01	0.02	0.02	-0.01	-0.05	-0.08	-0.13	0.02	0.24	0.46	1.0	0.46	0.22	0.01	-0.07	-0.02	0.03
13	0.01	0.02	0.02	0.03	0.04	0.01	-0.01	-0.06	-0.10	0.03	0.24	0.46	1.0	0.44	0.22	0.03	0.07	0.02
14	0.01	0.02	0.03	0.04	0.05	0.04	0.01	-0.05	-0.11	-0.10	0.00	0.22	0.44	1.0	0.39	0.19	0.13	0.08
15	0.01	0.02	0.03	0.04	0.07	0.06	0.04	-0.01	-0.06	-0.08	-0.09	0.01	0.22	0.39	1.0	0.41	0.21	0.14
16	0.01	0.02	0.02	0.03	0.05	0.06	0.04	0.02	-0.01	-0.05	-0.05	-0.07	0.03	0.19	0.41	1.0	0.42	0.21
17	0.00	0.01	0.01	0.01	0.03	0.04	0.04	0.03	0.02	-0.01	-0.01	-0.02	0.07	0.13	0.21	0.42	1.0	0.37
18	-0.00	-0.00	-0.00	-0.01	0.01	0.03	0.04	0.07	0.08	0.04	0.05	0.03	0.02	0.08	0.14	0.21	0.37	1.0
Standard deviation(%)	4.96	1.97	1.93	1.85	2.02	3.61	3.37	4.04	4.41	2.82	2.83	2.88	1.90	5.41	5.40	3.64	3.63	3.01

(Smoothed cross-section region) (Un-resolved region) (Resolved region)

Table 8 Parametric study (1) C/Es before and after adjustment

Integral parameters (ZPPR-9 core)	Before adjustment	After adjustment		
		Reference case (83 C/Es)	Cross-section error ×1.6	Analytical error ×2
Criticality (keff)	0.994	1.001	1.001	1.002
Reaction rate ratio				
• F25/F49	1.015	0.992	0.989	0.998
• C28/F49	1.055	1.015	1.013	1.012
• F28/F49	0.972	0.984	0.983	0.980
Reaction rate ristribution				
• F49、Outer Core Region	1.037	0.988	0.986	0.991
Control rod worth				
• Core center position	0.918	0.991	0.993	0.985
• Core edge position	0.990	1.011	1.011	1.011
Na void reactivity				
• Small region void	1.21	1.13	1.11	1.20
• Large region void	1.36	1.24	1.20	1.34

Table 10 Design accuracy of various design methods (600MWe-class FBR core)

1σ value (%)

Nuclear Characteristics	No Information from Integral Experiments	E/C Bias Method (Mock-up core : ZPPR-10A)	Cross-Section Adjustment Method
keff	2.2	0.6	0.4
Burnup reactivity	19.4	–	9.4
Breeding ratio			
• BOEC	5.2	–	2.5
• EOEC	4.0	–	2.0
C28/F49	6.0	2.3	1.5
Control rod worth			
• Ring 1	4.0	4.4	2.8
• Ring 2	5.0	4.6	3.1
• Ring 3	4.3	4.0	2.8
Power distribution			
• Inner core edge	1.8	2.0	1.3
• Outer core center	3.0	2.9	2.3

Table 9 Parametric study (2) JFS-3-J2 changes by adjustment

(Unit : %)

Energy Group	Pu239 fission			U238 capture		
	Reference case (83 C/Es)	Cross-section error ×1.6	Analytical error ×2	Reference case (83 C/Es)	Cross-section error ×1.6	Analytical error ×2
1 (10.0 MeV~)	-0.3	0.1	-0.5	0.4	0.8	0.8
2 (6.07 MeV~)	-0.2	-0.1	-0.3	0.9	1.7	2.1
3 (3.68 MeV~)	-0.4	-0.2	-0.5	0.8	1.8	2.1
4 (2.23 MeV~)	-0.6	-0.4	-0.8	0.4	1.7	2.4
5 (1.35 MeV~)	-1.8	-1.7	-2.3	-0.2	0.8	1.2
6 (821 keV~)	-3.4	-3.1	-4.7	-2.4	-0.8	-1.1
7 (388 keV~)	-3.2	-3.0	-4.6	-2.4	-1.3	-1.8
8 (183 keV~)	-2.6	-2.2	-4.6	-4.8	-3.0	-4.4
9 (86.5 keV~)	-1.1	-0.9	-3.7	-6.5	-4.2	-6.9
10 (40.9 keV~)	1.2	1.3	0.4	-1.9	-1.6	-2.4
11 (19.3 keV~)	1.8	2.2	0.5	-2.3	-2.2	-2.8
12 (9.12 keV~)	2.0	2.6	0.5	-3.0	-3.0	-3.5
13 (4.31 keV~)	1.6	2.1	0.4	-2.9	-3.1	-3.3
14 (2.04 keV~)	7.5	9.8	2.3	-4.4	-5.1	-4.7
15 (961 eV~)	7.2	9.0	2.6	-4.2	-4.9	-4.3
16 (454 eV~)	4.4	5.5	2.0	-3.0	-3.5	-3.0
17 (214 eV~)	3.2	3.9	1.6	-2.0	-2.3	-1.9
18 (101 eV~)	2.4	2.9	1.7	-0.4	-0.4	-0.4
βeff (Tuttle, Saphier)	-0.4	-0.3	-0.1	–	–	–

2.4 Nuclear Data in Medium Energy Region

2.4.1 Study of Nuclear Reaction by Molecular Dynamics Methods

H. Horiuchi

Department of Physics, Kyoto University, Kyoto 606-01, Japan

Recent development of the microscopic study of nuclear reaction by the use of molecular dynamics approaches is reviewed. The characteristic point of the molecular dynamics approach is its capability of describing the *dynamical formation of clusters* which the mean field transport theories like VUU can not treat. We discuss a few typical examples of the analyses with the quantum molecular dynamics which is largely of *classical nature* in spite of its name. Then we explain the antisymmetrized molecular dynamics which has been constructed recently by our Kyoto group as the first microscopic simulation theory of *quantum mechanical nature*.

1. Introduction

In nuclear reactions especially heavy-ion induced reactions around and more than Fermi energy, many kinds of reaction processes appear depending on the incident energy, impact parameter, and the system mass number. One of the main aims of the study of the heavy ion reaction in the intermediate and high incident energy region is the study of nuclear matter at high temperature and high density. For this purpose, we need to know the reaction processes which lead to the formation of the hot and dense nucleus, and also the phenomena and observable quantities which reflect the hot nuclear state. However, since the hot nuclear state formed by the heavy ion reaction is neither isotropic nor static, the time-dependent dynamical description of the reaction process is very desirable. The microscopic simulation calculation of the nuclear reaction makes such dynamiclal description possible. Also the microscopic simulation calculation enables us to describe variety of nuclear reaction mechanisms and their evolution (in energy, impact parameter and mass number) in a single and unified theoretical framework.

The microscopic simulation calculation has been developed starting from the intra-nuclear cascade method and the classical molecular dynamics method up to the VUU / BUU (Vlasov / Boltzmann - Uehling - Uhlenbeck) method.[1] The VUU/BUU method is so constructed as to incorporate the desription of the nuclear mean field into the intra-nuclear cascade method. However, both the intra-nuclear cascade method and the VUU/BUU method cannot describe the dynamical formation process of the fragments (or clusters). This is a serious drawback of these methods since the most of the experimental data are nothing but the data about the fragments produced by reactions.

In order to make it possible to describe the dynamical formation process of fragments, the method named "quantum" molecular dynamics (QMD)[2] has been proposed. The QMD is different from the classical molecular dynamics approach[3] in that nucleons in QMD are described not as point particles but by wave packets and the stochastic two-nucleon collision process is taken into account. These two different points from the classical molecular dynamics are the reason why the name of QMD contains " quantum ". But in spite of its name, this framework of QMD is of classical nature

just like the intra-nuclear cascade method and the VUU/BUU method. The calculational procedure of QMD is very similar to that of VUU/BUU except one important difference; namely in QMD one does not take the average of the events at each time step which is, however, necessary in VUU/BUU in order to calculate the nuclear mean field as accurately as possible. This difference makes the QMD possible to describe the dynamical formation of fragments.

QMD has been extensively and successfully applied to the studies of many phenomena.[2),4)] However, since QMD only describes limited time scale of the nuclear reaction process, it cannot treat the long-time-scale decay process of the fragments which are dynamically produced during the violent reaction process and hence are highly excited with high spin in general. Therefore QMD needs to be combined with the multi-step statistical decay calculation of produced fragments. This kind of calculations have been first performed by the group of the author.[5)]

In spite of its great success, the QMD has unsatisfactory features many of which are due to its insufficient treatment of the Fermi statistics of nucleons. Therefore the anti-symmetrized version of QMD was constructed by the author and his collaborators,[6)] and was given an abbreviated name AMD. In this AMD one describes the time-development of the wave function of the total system. Therefore it is of quantum mechanical nature. AMD is the first quantum mechanical framework of the microscopic simulation of nuclear reactions.

An important characteristic feature of AMD due to this quantum mechanical nature is its capability of describing shell effects. For example, with AMD we have been able for the first time to take into account the enhaced production yield of alpha particles during the dynamical reaction process in addition to the enhaced production yield of alpha particles due to the evaporation process of fragments. Since the data about the alpha particles are very important in many phenomena, this feature of AMD is expected to bring about large progress in theoretical understanding of reaction processes.

In my talk at this JAERI meeting I first discussed the QMD and showed some examples of QMD analyses of heavy-ion reaction data. Then I explained the AMD theory and its application.

2. QMD and its applications

In QMD, a nucleon is described with a Gaussian wave packet whose position parameter $\vec{D}$ and momentum parameter $\vec{K}$ develop in time by obeying the equation of motion and by stochastic two-nucleon collisions. The equation of motion is as follows:

$$
\begin{aligned}
(d/dt)\vec{D}_j &= \partial\mathcal{H}/\partial\vec{K}_j, \quad (d/dt)\vec{K}_j = -\partial\mathcal{H}/\partial\vec{D}_j, \\
\mathcal{H} &= <\Phi|H|\Phi>, \\
H &= \Sigma_j(-\hbar^2)\Delta_j/2m + (1/2)\Sigma_{ij}v_{ij}(1-P_{ij}), \\
\Phi &= \Pi_{j=1}^{A}\phi(j)\chi(j), \\
\phi(j) &= (2\nu/\pi)^{(3/4)}\exp[-\nu(\vec{r}-\vec{D}_j)^2 + i\vec{K}_j\vec{r}/\hbar],
\end{aligned}
\tag{1}
$$

where χ stands for a spin-isospin function of nucleon and P_{ij} for an exchange operator of nucleon i and nucleon j. The two-nucleon collision occurs when positions of two

nucleons, $\vec{D}_1$ and $\vec{D}_2$, become close within a distance $d_{NN}=\sqrt{\sigma_{NN}/\pi}$ where σ_{NN} stands for the nucleon-nucleon scattering cross section in nuclear medium. The two-nucleon collision does not change the positions of the two nucleons but change the momenta of the two nucleons so that the scattering occurs according to the differential cross section of the nucleon-nucleon scattering. However if the new set of position and momentum of the nucleon after the two-nucleon collision is occupied by any other nucleon, this two-nucleon collision is cancelled, namely Pauli-blocked.

QMD is not a mean field theory but it treats n-body dynamics. Thus QMD can describe the dynamical formation of clusters unlike the mean field transport theory like VUU. One of the important results obtained by the QMD calculation is by the Frankfurt group[2] which demonstrated for the first time that the power-law behavior of the inclusive yields of clusters must not be directly related to the phase transition between gas and liquid phases of nuclear matter.

At the JAERI meeting on nuclear data, I showed several results of the QMD analyses of heavy ion reactions made by our Kyoto group. The data analysed by us include the low energy fusion data[4], the mass distribution of fragmentation reactions[5], the energy spectra of light fragments[4], and the spin polarization of the projectile fragments[7]. Here I only show in Fig.1 the comparison of the QMD calculation of the fragment mass distribution with the data in ^{40}Ar + ^{27}Al at the incident energy 44 Mev/nucleon. In this calculation, the multi-step statistical decays of produced fragments are also taken into account.

3. AMD and its application

As explained in section 1, AMD can be regarded as the antisymmetrized version of QMD. We describe the system by the following Slater determinant which has the form obtained just by antisymmetrizing Φ of Eq.(1)of QMD.

$$\Phi = \det\left[\Pi_{j=1}^{A}\phi(j)\chi(j)\right],$$
$$\phi(j) = (2\nu/\pi)^{(3/4)}\exp[-\nu(\vec{r}-\vec{D}_j)^2 + i\vec{K}_j\vec{r}/\hbar]. \qquad (2)$$

The time development of the parameters $\vec{D}_j$, $\vec{K}_j$ (j=1∼A) is determined by the time-dependent variational principle

$$\delta\int_{t_1}^{t_2} dt\,\frac{<\Phi|(i\hbar\frac{d}{dt}-H)|\Phi>}{<\Phi|\Phi>} = 0, \qquad (3)$$

which gives the following equation of motion for the complex parameter coordinates $\vec{Z}_j$ whose real and imaginary parts are $\vec{D}_j$ and $\vec{K}_j$, respectively:

$$i\hbar\sum_{j\tau} C_{i\sigma,j\tau}\dot{Z}_{j\tau} = \frac{\partial\mathcal{H}}{\partial Z^*_{i\sigma}} \qquad \text{and c.c.,}$$

$$\vec{Z}_j = \sqrt{\nu}\vec{D}_j + \frac{i}{2\hbar\sqrt{\nu}}\vec{K}_j. \tag{4}$$

Here $\sigma, \tau = x, y, z$, and $\mathcal{H}$ and $C_{i\sigma,j\tau}$ are given as

$$\begin{aligned} \mathcal{H} &= < \Phi|H|\Phi > / < \Phi|\Phi >, \\ C_{i\sigma,j\tau} &= \frac{\partial^2}{\partial Z^*_{i\sigma}\partial Z_{j\tau}} \log < \Phi|\Phi > . \end{aligned} \tag{5}$$

This framework expressed by Eq.(2)∼ Eq.(5)was first proposed by Feldmeier[8] and was named FMD (fermionic molecular dynamics). However, FMD can not be applied to heavy ion collisions in this form. We have to solve two problems. One is the *initialization problem*, namely the construction of the ground state wave functions of colliding nuclei, and the other is the *incorporation of two-nucleon collisions*. The construction of the ground state wave function means to determine the values of all the coordinate parameters $\{\vec{Z}_j\}$ which minimize $< \Phi(\vec{Z})|H|\Phi(\vec{Z}) > / < \Phi(\vec{Z})|\Phi(\vec{Z}) >$. It is a multi-dimensional variational problem. The incorporation of two-nucleon collisions is not a simple problem because the position parameters $\{\vec{D}_j\}$ do not represent nucleon positions and also the momentum parameters $\{\vec{K}_j\}$ do not represent nucleon momenta. This fact can be easily understood when we consider the following example. Let all $\vec{D}_j$ and $\vec{K}_j$ be vanishingly small in ^{16}O system. The resulting total wave function Φ is almost equal to the harmonic oscillator shell model wave function $\Phi_{c.s.}$ of the double closed shell configuration of $0s$ and $0p$ shells, $(0s)^4(0p)^{12}$. Nucleons of the state $\Phi_{c.s.}$ are neither all located at the space-coodinate origin nor all condensed to zero momentum state in spite of $D_j \approx 0$, $K_j \approx 0$ for all j.

We have solved these two problems and have thus constructed a quantum mechanical method of microscopic simulation of heavy ion collisions. We call this new method AMD (antisymmetrized version of molecular dynamics with inclusion of two-nucleon collisions). Solution of the initialization problem and its development are discussed in detail in Refs.(9) and (10), and we here do not give the explanation of it. The frictional cooling method used for solving the initialization problem has proved to be a very powerful tool not only for the nuclear reaction problems but also for the study of various nuclear structure problems.

The incorporation of two-nucleon collisions[6),11)] is explained below slightly in detail since it is a new theoretical development. The key point is the recognition that the wave function of AMD (or FMD) of Eq.(2)is a special case of the wave function of the time-dependent cluster model[12)] given as follows:

$$\begin{aligned} \Phi &= \det\Big[\Psi_I(\vec{D}_I, \vec{K}_I)\Psi_{II}(\vec{D}_{II}, \vec{K}_{II})\cdots\Big], \\ \Psi_j(\vec{D}_j, \vec{K}_j) &= \textit{Slater determinant} \\ &\propto \exp\left[-A_j\nu\left(\vec{r}_{Gj} - \vec{D}_j\right)^2 + i\frac{\vec{K}_j}{\hbar}\vec{r}_{Gj}\right]\Phi(j), \\ j &= I, II, III, \cdots, \end{aligned}$$

$$
\begin{aligned}
A_j &= mass\ number\ of\ cluster\ j, \\
\vec{r}_{Gj} &= center\ of\ mass\ coordinate\ of\ cluster\ j, \\
\Phi(j) &= internal\ wave\ function\ of\ cluster\ j.
\end{aligned} \tag{6}
$$

An important progress made in the theoretical framework of the time-dependent cluster model was the proposal of the theory of the canonical coordinates of Ref.[13]. Like in AMD, the original coordinates $\{\vec{D}_j\}$ and $\{\vec{K}_j\}$ are neither canonical coordinates nor physical coordinates. In the case of two-cluster system, the authors of Ref.[13] showed how to construct explicitly the exact canonical position and momentum coordinates from the original coordinates $\{\vec{D}_j\}$ and $\{\vec{K}_j\}$. The canonical relative position and momentum coordinates, $\vec{R}_r$ and $\vec{P}_r$, are given as

$$
\begin{aligned}
&\vec{W}_r \equiv \sqrt{Q}\vec{Z}_r, \quad Q \equiv \frac{\partial}{\partial(\vec{Z}_r^* \vec{Z}_r)} \log < \Phi|\Phi >, \\
&\vec{Z}_r = \sqrt{\mu\nu}\vec{D}_r + \frac{i}{2\hbar\sqrt{\mu\nu}}\vec{K}_r, \quad \vec{W}_r = \sqrt{\mu\nu}\vec{R}_r + \frac{i}{2\hbar\sqrt{\mu\nu}}\vec{P}_r, \\
&\vec{D}_r \equiv \vec{D}_1 - \vec{D}_2, \quad \vec{K}_r \equiv \mu(\vec{K}_1/A_1 - \vec{K}_2/A_2), \\
&\mu \equiv A_1 A_2/(A_1 + A_2).
\end{aligned} \tag{7}
$$

An important property of the canonical coordinate $\vec{W}_r$ is that there exists a *Pauli-forbidden region*[13] in the phase space of $\vec{W}_r$. We can easily prove that $\vec{W}_r$ satisfies

$$
\vec{W}_r^* \vec{W}_r = \frac{1}{\hbar\omega}\Big(\frac{\vec{P}_r^2}{2\mu} + \frac{\mu\omega^2}{2}\vec{R}_r^2\Big) \geq N_A, , \tag{8}
$$

where N_A stands for the lowest number of the oscillator quanta which the wave function of the relative motion can have[13),14)]. Hence in other words, $\vec{W}_r$ cannot enter the Pauli-forbidden region defined by $|\vec{W}_r| < N_A$.

Since AMD wave function is a special case of the wave function of the time-dependent cluster model, we have mimicked the theory of the canonical coordinates of the time-dependent cluster model in constructing physical nucleon coordinates.[6),11)] As will be seen below, once we introduce the physical coordinates, the treatment of the Pauli blocking in two-nucleon collisions becomes trivial because there exists the *Pauli-forbidden region* in the phase space of the physical coordinates just like in the case of the time-dependent cluster model.

The physical nucleon coordinates $\{\vec{R}_j, \vec{P}_j, j = 1 \sim A\}$ we use are defined as follows,

$$
\begin{aligned}
\vec{W}_j &= \sqrt{\nu}\vec{R}_j + \frac{i}{2\hbar\sqrt{\nu}}\vec{P}_j \equiv \sum_{k=1}^{A}\Big(\sqrt{Q}\Big)_{jk}\vec{Z}_k, \\
Q_{jk} &\equiv \frac{\partial}{\partial(\vec{Z}_j^* \cdot \vec{Z}_k)} \log < \Phi|\Phi > .
\end{aligned} \tag{9}
$$

In the absence of antisymmetrization we of course have $\vec{W}_j = \vec{Z}_j$. We can easily prove the following relations:

$$
\begin{aligned}
N_{\rm osc} &= <\Phi|\sum_j \vec{a}_j^\dagger \vec{a}_j|\Phi> / <\Phi|\Phi> = \sum_{jk} \vec{Z}_j^* \vec{Z}_k Q_{jk} \\
&= \sum_j \vec{W}_j^* \vec{W}_j = \frac{1}{\hbar\omega}\sum_j (\frac{1}{2m}\vec{P}_j^2 + \frac{m\omega^2}{2}\vec{R}_j^2), \\
<\Phi|\vec{L}|\Phi> &/ <\Phi|\Phi> = (-i\hbar)\sum_{jk} \vec{Z}_j^* \times \vec{Z}_k Q_{jk} \\
&= (-i\hbar)\sum_j \vec{W}_j^* \times \vec{W}_j = \sum_j \vec{R}_j \times \vec{P}_j,
\end{aligned} \tag{10}
$$

where $\vec{a}_j$ stands for the destruction operator of harmonic oscillator quanta of j-th nucleon, $\vec{a}_j = \sqrt{\nu}\vec{r}_j + (i/2\hbar\sqrt{\nu})\vec{p}_j$, and $\vec{L}$ is the total orbital angular momentum operator. Furthermore as for the center-of-mass coordinate we can show

$$
\sum_j \vec{Z}_j = \sum_j \vec{W}_j. \tag{11}
$$

Also there holds the following relation; namely if $\vec{Z}_j$ are simultaneously displaced by $\vec{c}$, $\vec{Z}_j \rightarrow \vec{Z}_j + \vec{c}$, then $\vec{W}_j$ are simultaneously displaced by the same amount $\vec{c}$, $\vec{W}_j \rightarrow \vec{W}_j + \vec{c}$. From these properties of $\{\vec{W}_j\}$, we regard that $\{\vec{W}_j\}$ are physical coordinates.

Once we have physical nucleon coordinates, we can treat two-nucleon collisions just as the two-nucleon collisions in QMD.[2),4),5),7)] When $\vec{R}_j$ and $\vec{R}_k$ come near each other, two nucleons j and k are made to scatter isotropically. Namely initial $\vec{P}_j$ and $\vec{P}_k$ are changed into final $\vec{P}_j'$ and $\vec{P}_k'$ keeping initial $\vec{R}_j$ and $\vec{R}_k$ unchanged. Speaking in terms of complex coordinates $\vec{W}$, initial $\vec{W}_j$ and $\vec{W}_k$ are changed into final $\vec{W}_j'$ and $\vec{W}_k'$. In order to continue the calculation of time development of the system wave function after this two-nucleon collision, we need to back-transform $\{\vec{W}_1, \cdot\cdot, \vec{W}_j', \cdot\cdot, \vec{W}_k', \cdot\cdot, \vec{W}_A\}$ into $\{\vec{Z}_1', \vec{Z}_2', \cdots, \vec{Z}_A'\}$. However, in general, the back-transformation from $\{\vec{W}_j, j = 1 \sim A\}$ to $\{\vec{Z}_j, j = 1 \sim A\}$ does not always exist. When the back-transformation does not exist, we regard that the two-nucleon collision is Pauli-blocked.

The existence of $\{\vec{W}_j, j = 1 \sim A\}$ for which we have no corresponding $\{\vec{Z}_j, j = 1 \sim A\}$ is easily verified by using the relation $N_{\rm osc} = \sum_j \vec{W}_j^* \vec{W}_j$ of Eq.(9). This immediately shows that the coordinate origin $\{\vec{W}_j = 0, j = 1 \sim A\}$ cannot be constructed from any $\{\vec{Z}_j, j = 1 \sim A\}$, because $N_{\rm osc}$ can not be zero if $A > 4$. When we choose the center-of-mass at the coordinate origin, $\sum_j \vec{W}_j = 0$, we have

$$
(N_{\rm osc})_{\rm min} \leq \frac{1}{A}\sum_{i<j} |\vec{W}_i - \vec{W}_j|^2, \tag{12}
$$

from which we get

$$\sqrt{<|\vec{W}_i - \vec{W}_j|^2>_{\text{average}}} = \sqrt{\frac{2(N_{\text{osc}})_{\min}}{A-1}} \geq \sqrt{2}. \tag{13}$$

If the relative distances $|\vec{W}_i - \vec{W}_j|$ are too small as to violate the relation of Eq.(12), such $\{\vec{W}_j, j = 1 \sim A\}$ cannot be back-transformed to any $\{\vec{Z}_j, j = 1 \sim A\}$. $\{\vec{W}_j, j = 1 \sim A\}$ is defined to be in Pauli-forbidden region if it cannot be back-transformed to any $\{\vec{Z}_j, j = 1 \sim A\}$. The notion of the Pauli-forbidden region defined above is obviously an extension of that of the time-dependent cluster model.

We have analysed fragment production in $^{12}C + ^{12}C$ reaction at 28.7 MeV/u by our new microscopic simulation framework AMD. The calculated production cross sections of fragments obtained at 200 fm/c after the contact of two ^{12}C's reproduce the gross feature of the data. Especially the observed large cross section of α particle is reproduced rather well by the theory. It is to be noted that the QMD can never show this kind of shell effect since it is of classical nature.

Produced fragments in AMD framework which are analysed at around 200 fm/c are not in their ground states but are fairly excited. These fragments will decay by evaporating particles in a long time scale. Therefore in order to compare theory with experiments, we need to calculate statistical decay processes of produced fragments. After the inclusion of multi-step statistical decay processes of produced fragments we have found very nice reproduction of the data by theory, which is shown in Fig.2. We have analysed how large the constribution of multi-step statistical decay processes is. We have found that about 1/3 of the α particle yield comes from the dynamical reaction process while large part of the remaining 2/3 of α yield is due to the statistical decay of excited ^{12}C produced in dynamical stage. The yield of intermediate mass fragments has been shown to be supplied by statistical decays of various heavier fragments produced in dynamical stage, while the the dynamically produced intermediate mass fragments have all decayed into lighter fragments. Details of this AMD study of the fragmentation reaction of $^{12}C + ^{12}C$ can be seen in Refs.[6, 11].

4. Summary

The quantum molecular dynamics (QMD) is a very useful microscopic reaction theory since it can successfully describe the cluster (or fragment) production in heavy ion reactions. We explicitly demonstrated it by showing good reproduction of various kinds of reaction data including the low energy fusion data[4], the mass distribution of fragmentation reactions[5], the energy spectra of light fragments[4], and the spin polarization of the projectile fragments[7]. In this report, however, I only showed in Fig.1 the comparison of the QMD calculation of the fragment mass distribution with the data.

The antisymmetrized molecular dynamics (AMD) which our Kyoto group constructed recently is an improved version of QMD. In this AMD one describes the time-development of the wave function of the total system. Therefore it is of quantum mechanical nature. AMD is the first quantum mechanical framework of the microscopic simulation of nuclear reactions. On the contrary, QMD is of classical nature in spite of

its name. An important characteristic feature of AMD due to this quantum mechanical nature is its capability of describing shell effects. For example, with AMD we have been able for the first time to take into account the enhaced production yield of alpha particles during the dynamical reaction process in addition to the enhaced production yield of alpha particles due to the evaporation process of fragments. Since the data about the alpha particles are very important in many phenomena, this feature of AMD is expected to bring about large progress in theoretical understanding of reaction processes.

REFERENCES

1. G. F. Bertsch and S. Das Gupta, Phys. Rep. **160** (1988),189.
2. J. Aichelin and H. Stöcker, Phys. Lett. **176B** (1986), 14; G. Peilert, H. Stöcker, W. Greiner, A. Rosenhauer, A. Bohnet and J. Aichelin, Phys. Rev. **C39** (1989), 1402; J. Aichelin, Phys. Reports **202**(1991), 233.
3. L. Wilet, E. M. Henley, M. Kraft and A. D. MacKellar, Nucl. Phys. **A282** (1977), 341.
4. T. Maruyama, A. Ohnishi, and H. Horiuchi, Phys. Rev. **C42** (1990), 386; **C45** (1992), 2355.
5. T. Maruyama, A. Ono, A. Ohnishi, and H. Horiuchi, Prog. Theor. Phys. **87** (1992), 1367.
6. A. Ono, H. Horiuchi, T. Maruyama, and A. Ohnishi, Phys. Rev. Letters **68** (1992), 2898; Prog. Theor. Phys. **87** (1992), 1185.
7. A. Ohnishi, T. Maruyama, and H. Horiuchi, Prog. Theor. Phys. **87** (1992), 417.
8. H. Feldmeier, Nucl. Phys. **A515** (1990), 147.
9. H. Horiuchi, Nucl. Phys. **A522** (1991), 257c.
10. Horiuchi, T. Maruyama, A. Ohnishi, and S. Yamaguchi, *Proc. Int. Conf. on Nuclear and Atomic Clusters*, Turku (1991), eds. M. Brenner, T. Lönnroth, and F. B. Malik, (Springer, 1992), p.512; *Proc. Int. Symp. on Structure and Reactions of Unstable Nuclei*, Niigata (1991), eds. K. Ikeda and Y. Suzuki, (World Scientific, 1992), p.108.
11. H. Horiuchi, A. Ono, T. Maruyama, and A. Ohnishi, *Proc. Eighth Winter Workshop on Nuclear Dynamics*, Jackson Hole (1992), eds. W. Bauer and B. Back, (World Scientific, 1992), p.213.
12. S. Drożdż, J. Okolowcz, and M. Ploszajczak, Phys. Lett. **109B** (1982), 145; E. Caurier, B. Grammaticos and T. Sami, Phys. Lett. **109B** (1982), 150; W. Bauhoff, E. Caurier, B. Grammaticos and M. Ploszajczak, Phys. Rev. **C32** (1985), 1915.
13. M. Saraceno, P. Kramer, and F. Fernandez, Nucl. Phys. **A405** (1983), 88.
14. H. Horiuchi and K. Ikeda, *Cluster Model of the Nucleus, International Review of Nuclear Physics* **Vol.4**, eds. T. T. S. Kuo, and E. Osnes, (World Scientific, Singapore, 1985), pp.1 $\sim$ 258.

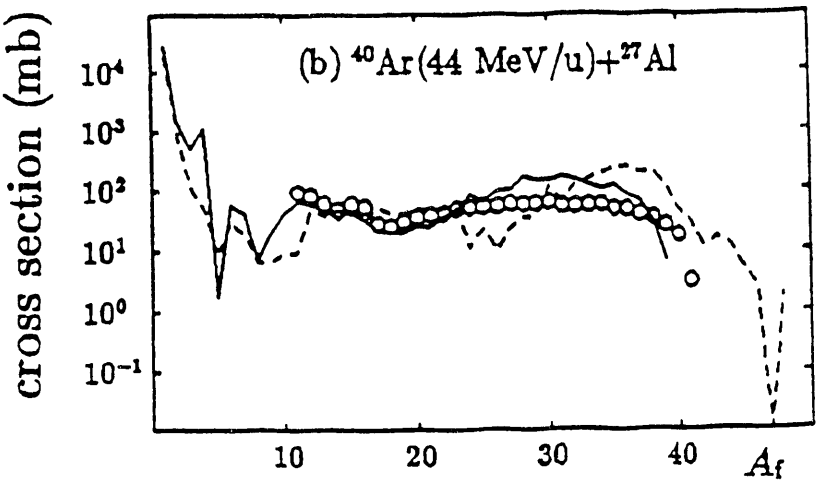

Fig. 1 Fragment mass distribution in the ^{40}Ar + ^{27}Al reaction at the incident energy 44 MeV/necleon. Open circles are data while dashed line shows QMD result and solid line the result after the calculation of the multi-step statistical decays of the QMD fragments. The data are due to R. Dayras, A. Pagano, J. Barrette, B. Berthier, D.M. De Castro Rizzo, E. Chavez, O. Cisse, R. Legrain, M.C. Mermaz, E.C. Pollacco, H. Delagrange, W. Mittig, B. Heusch, R. Coniglione, G. Lanzano, and A. Palmeri, Nucl. Phys. A460 (1986), 299. This figure is due to Ref.(5).

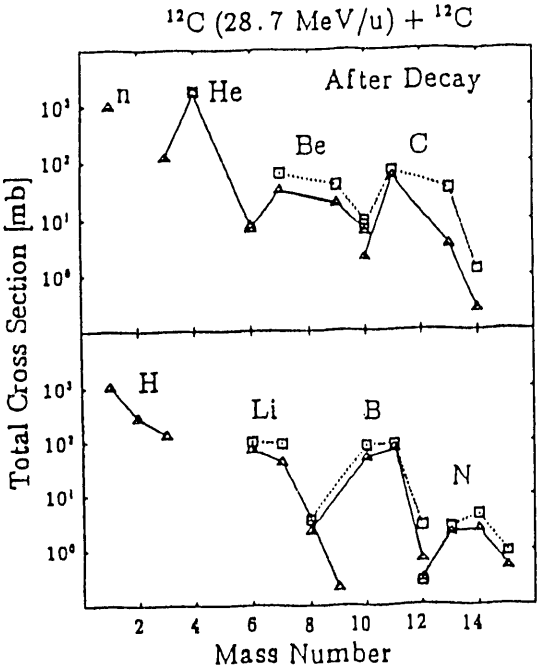

Fig. 2 Isotope distribution of fragmentation products in the ^{12}C + ^{12}C reaction at the incident energy 28.7 MeV/nucleon. Boxes are data while triangles are the calculated cross sections which are obtained after the calculation of multi-step statistical decays applied to the AMD fragments. Lines connect isotopes. The data are due to J. Czudek, L. Jarczyk, B. Kamys, A. Magiera, R. Siudak, A. Strzalkowski, B. Styczen, J. Hebenstreit, W. Oelert, P. von Rossen, H. Seyfarth, A. Budzanow-ski, and A. Szczurek, Phys. Rev. C43 (1991), 1248. This figure is due to Ref.(6).

2.4.2 Benchmark Calculations of Theoretical Calculation Codes for Nuclear Data Evaluation in the Intermediate Energy Region

Tokio FUKAHORI, Satoshi CHIBA,
Nuclear Data Center, Dept. of Physics, Japan Atomic Energy Research Institute, Tokai-mura, Naka-gun, Ibaraki, 319-11 Japan,

Hiroshi TAKADA,
Reactor Physics Experiment Laboratory, Dept. of Reactor Engineering, Japan Atomic Energy Research Institute, Tokai-mura, Naka-gun, Ibaraki, 319-11 Japan,

Norio KISHIDA,
CRC Research Institute, Inc., Makuhari Development Center, 1-3D-16 Nakase, Mihama-ku, Chiba-shi, Chiba, 261-01 Japan,

Yukinobu WATANABE,
Energy Conversion Engineering, Interdisciplinary Graduate School of Engineering and Sciences, Kyushu University, 6-1 Kasuga-kohen, Kasuga-shi, Fukuoka, 818 Japan,

and

Nobuhiro YAMAMURO,
Data Engineering, 60 Kitayasaku-cho, Midori-ku, Yokohama-shi, Kanagawa, 226 Japan.

Theoretical calculation codes, SINCROS-II, ALICE-F, EXIFON, MCEXCITON, HETC-3STEP and NUCLEUS, are applicable for the nuclear data evaluation in the intermediate energy region. This paper introduces their functions and applied theories briefly, and gives the results of benchmark calculations performed by the Theoretical Calculation Code Working Group of the Japanese Nuclear Data Committee. Quantities of the benchmark calculations are isotope production cross sections of manganese and iron induced by neutrons or protons below 50 MeV, and those of aluminum, iron and bismuth by protons above 50 MeV.

1. Introduction

Nuclear data in the intermediate energy region are necessary in a lot of applications such as accelerator shielding calculation, production rate estimation of medical radioactive isotopes and design of TRU incineration targets. Evaluated nuclear data files, however, are not available in this energy region, except for iron[1], and lead and bismuth[2]. Recently, some trial evaluations were reported in an international symposium for the nuclear data evaluation methodology at the Brookhaven National Laboratory[3], and an intercomparison of theoretical calculation codes applicable in the intermediate energy region are being performed by OECD/NEA.

Several theoretical calculation codes are considered to be candidates for the nuclear

data evaluation in the intermediate energy region. However, before performing an intensive evaluation, it is worthwhile to make benchmark calculations in order to check the advantages and limitations of these codes which are based on various different theories, approximations and methods of numerical calculations. As the first trial, benchmark calculations were performed by members of the Theoretical Calculation Code Working Group of the Japanese Nuclear Data Committee without any serious parameter adjustment. Selected codes were SINCROS－II[4], ALICE－F[5], EXIFON[6], MCEXCITON[7], NUCLEUS[8] and HETC－3STEP[9-11]. The first three of these codes employ deterministic methods, while the last three codes are based on the Monte－Carlo method. The basic features of these codes are briefly introduced in Chapter 2. Quantities selected for the benchmark calculations were several isotope production cross sections of manganese and iron in the energy region from 20 to 50 MeV with incident neutrons or protons, and isotope production cross sections for aluminum, iron and bismuth by proton irradiation in the energy region from 50 MeV to 1 GeV. The experimental data to be compared with the calculations are explained in Chapter 3. Results of the benchmark calculations are given in Chapter 4, and some qualitative discussions are made. Chapter 5 gives the concluding remarks.

2. Brief Descriptions of the Codes Considered in this Work

Characteristics of the considered codes are summarized in **Table 1**. In this Chapter, some explanations are made for theories, models, assumptions and parameters which these codes are based on.

2.1 NUCLEUS

This code is based on the intranuclear cascade and evaporation models. Weisskopf－Ewing formula, which does not consider conservation of angular momentum and discrete levels, is adopted for the equilibrium model part calculation. No gamma－ray competition and the preequilibrium process are not taken into account.

The level density is given by the following equation;

$$w(E)=w_0\times\exp[2\sqrt{a(E-\Delta)}]\,, \tag{1}$$

where w_0 is irrelevant in the Monte－Carlo algorithm, a the level density parameter, E the excitation energy of the residual nucleus, and Δ the pairing energy. In the present benchmark calculation, $a = A/8$ was employed, where A is the mass number of the residual nucleus which undergoes particle emission.

In NUCLEUS, the high energy fission process proposed by Nakahara[11] is taken into account as a competitive process with the evaporation. NUCLEUS outputs neither cross sections nor particle spectra in original version. Since the energy and directional cosine of the outgoing particles are calculated in the code, the cross sections can be obtained by the use of a supplementary program.

2.2 HETC－3STEP

This code is based on the intranuclear cascade, preequilibrium and evaporation models with the Monte－Carlo sampling technique. Cross sections, particle spectra (angle－integrated) and angle－energy distributions can be calculated. Spectrum is represented in certain energy bins and, is given by point data. Weisskopf－Ewing formula without considering of conservation of angular momentum and discrete levels is adopted for the equilibrium part

calculation. No gamma-ray competition is included. The preequilibrium process is treated by the exciton closed form as a correction to the statistical model. The Monte-Carlo algorithms formulated by Nakahara and Nishida[11] are employed with the use of the exciton models proposed by Griffin, Kalbach[12] and Gudima et al[13].

The total level density is given by the same equation as NUCLEUS. The particle-hole level density was calculated by the formula which have been derived by Williams[14] and was corrected for the exclusion principle and indistinguishability of identical excitons by Ribansk'y et al.

$$\omega_+(p,h,E)=\frac{1}{2}g\frac{[gE-A(p+1,h+1)]^2}{n+1}\left[\frac{gE-A(p+1,h+1)}{gE-A(p,h)}\right]^{n-1}, \tag{2}$$

$$\omega_0=\frac{1}{2}g\frac{gE-A(p,h)}{n}[p(p-1)+4ph+h(h-1)], \tag{3}$$

$$\omega_-(p,h,E)=\frac{1}{2}gph(n-2), \tag{4}$$

$$A(p,h)=\frac{1}{4}(p^2+h^2+p-h)-\frac{1}{2}h, \tag{5}$$

where p, h and n are numbers of particle, hole and excitons, respectively.

Systematics of Kalbach[15] is adopted to angular distributions in the preequilibrium part. The high energy fission model proposed by Atchison[9] is taken into account in this code.

2.3 MCEXCITON

MCEXCITON is based on the "random-work" exciton + evaporation models. Cross sections and multi-particle emission can be calculated with multiple preequilibrium decay treatment. Total particle production spectra and recoil energy spectra of residual nuclei can be also calculated. There is no restriction for a number of reaction channels. The code does not include a pion production process.

Weisskopf-Ewing formula is adopted for the equilibrium model part calculation. No gamma-ray competition is included. The "random-walk" equation[13,16] is simulated by the Monte-Carlo method. The equilibrium and preequilibrium parts are not separated in the calculation. The equilibrium part is achieved only as a limit of the preequilibrium stage. At the equilibrium part, the internal transition rate of $\lambda^+ = \lambda^-$ is realized. All the preequilibrium calculations are performed under the never-come-back assumption.

For total level density calculation in the equilibrium part, the back-shifted Fermi-gas model is adopted. When $E-B-\Delta \leq 0$ (E is the excitation energy of the parent nucleus, B the binding energy of a emitted particle and Δ the pairing energy), the threshold energy of the reaction is changed. Thus we use

$$\rho(U) \propto \exp(2\sqrt{E-B-\Delta-\varepsilon}) \quad (E-B>\Delta), \tag{6}$$

$$\rho(U) \propto \exp(2\sqrt{(E-B)(1-\Delta/2.5)-\varepsilon}) \quad (E-B\leq\Delta), \tag{7}$$

where $U=E-B-\Delta-\varepsilon$. For the particle-hole level density, Williams state density without an energy shift or a pairing energy correction is adopted. Single particle state density is taken as $g = A/13$ MeV^{-1}.

Machner's method[17] is used to internal transition rate. Inverse reaction cross sections are used instead of transmission coefficients. Spectrum is represented in energy bins with variable width. For angular distribution calculation, a phase-space approach[18] which takes into account the distribution of the linear momenta of excitons are applied. For α-emission, the form factor according to Iwamoto-Harada[19] is taken into account. Form factors for d, t and ^{3}He are also used those by Iwamoto-Harada-Sato[20].

2.4 EXIFON

This code is based on the statistical multistep direct (SMD) and compound (SMC) theory of Kalka[6]. Cross sections, particle spectra (angle-integrated), angle-energy distributions (DDX) and multi-particle emission can be calculated with the multiple preequilibrium decay treatment. Discrete levels can be included in calculations of direct collective excitations. Two low-lying vibrational levels (2+ and 3−) are considered here.

In this model, the equilibrium component is included in a calculation of the SMC process. The SMC cross section for (a,b) reaction has the following form

$$\frac{d\sigma_{a,b}^{SMC}(E_a)}{dE_b}=\sigma_a^{SMC}(E_a)\sum_{N=N_0}^{N'}\frac{\tau_N(E)}{\hbar}\sum_{(\Delta N)}\Gamma_{N,b}^{(\Delta N)}(E,E_b)\uparrow , \tag{8}$$

where $\sigma_a^{SMC}(E_a)$ is the SMC formation cross section, $\Gamma_{N,b}^{(\Delta N)}(E,E_b)\uparrow$ the escape width, and the mean-life time $\tau_N(E)$ satisfy the time-integrated master equation;

$$-\hbar\delta_{NN_0}=\Gamma_{N-2}^{(+)}(E)\downarrow\tau_{n-2}(E)+\Gamma_{N+2}^{(-)}(E)\downarrow\tau_{N+2}(E)-\Gamma_N(E)\tau_N(E) \tag{9}$$

for the exciton number N. The quantity E is the excitation energy of the composite nucleus. This model calculates the preequilibrium part as an incoherent sum of SMD and SMC processes. The SMD cross section is given as a sum over s-step direct processes. As a result, this model can consider the direct transition to low-lying collective states in the SMD process.

The particle-hole level density is defined with distinction between "bound" and "unbound" states. Both state densities are calculated as convolutions of the single particle state density given below. The state density of free ("unbound") particle c is given by

$$\rho(E_c)=4\pi V\mu_c(2\mu_c E_c)^{1/2}/(2\pi\hbar) , \tag{10}$$

where $V=4\pi R^3/3$ is the nuclear volume and μ_c the mass of the particle. The single particle state density of bound particles (at Fermi energy) is defined by

$$g=4\rho(E_F) . \tag{11}$$

The bound state density is derived by using the single particle state- and hole state-densities with restriction due to the finite potential well, and results in the Williams formula[14] with finite-well restrictions. In the calculation, pairing effects are considered by using effective binding energies. In addition, shell structure effects are considered in the SMC processes. The state density is modified by the shell correction energy on the basis of Ignatyuk's idea[21].

The multiple particle emission is calculated in a pure SMC concept. The master equation is solved for each intermediate excitation energy with an initial exciton number independent of the excitation energy. In total γ−emission spectra, the full cascade de−excitation is not included. Since isospin conservation is considered for proton−induced reactions, the SMC cross section is decomposed into two parts distinguished by the isospin,

$$\frac{d\sigma_{a,b}^{SMC}(E_a)}{dE_b} = \frac{d\sigma_{a,b}^{SMC}(T_>; E_a)}{dE_b} + \frac{d\sigma_{a,b}^{SMC}(T_<; E_a)}{dE_b}, \qquad (12)$$

where $T_>=T_0+1/2$ and $T_<=T_0-1/2$, and $T_0=(N-Z)/2$ is the target isospin.

In the present work, the modified version of EXIFON was also used as "EXIFON (modified)", while the normal version is called "EXIFON (standard)". The pairing shift in the level density calculation is improved in this version.

2.5 SINCROS−II

The SINCROS−II consists of three major codes; DWUCKY which is the modified version of DWUCK4[22], EGNASH which is modified version of GNASH[23], and CASTHY2[24], and several auxiliary programs. In the present calculation, DWUCKY and EGNASH were used. Direct inelastic scattering cross sections were calculated by DWUCKY. The collective vibrational model is used as the default option. Cross Sections, particle spectra (angle−integrated), angle−energy distributions of multi−particle emission without multiple preequilibrium decay treatment can be calculated. For the multi−particle emission, up to 40 decaying nuclei and seven outgoing particles (n, p, d, t, ^{3}He, α and γ) can be taken into consideration. Discrete levels are also included in equilibrium calculation.

For the equilibrium part, Hauser−Feshbach theory with j−independent transmission coefficients is employed. Width fluctuation correction of Tepel et al., improved by Hofmann et al.[25], is possible as an option. Kalbach's PRECO−C is included, which is based on the master equation exciton model only in the first particle emission for preequilibrium part without quantum mechanical conservation of angular momentum. Closed form (never come back) approximation is possible as an option. The pickup and stripping (p−s), and knock−out and inelastic scattering (k−i) processes of composite particles are considered as a part of the non−equilibrium reactions.

Gilbert−Cameron's composite formula is employed for the total level density in the equilibrium calculation. Ignatyuk's formula is used above the neutron separation energy if required. Temperature in the constant temperature model is calculated from the information on the given discrete level. For the particle−hole state density required in the pre−equilibrum calculation, Williams' formula with a pairing energy shift is adopted. The state density for the initial p−h configuration is corrected in order to account for variations of the single−particle state density with energy and to account for effects due to the finite depth of the nuclear potential.

The internal transition rates are proportional to the matrix element M^2, which is parameterized as a function of $e = E/n$ as given in Eq. (13), where E is the excited energy, n the number of excitons, and k Kalbach constant.

Particle production spectra can be calculated. Emission spectra are also calculated for every reaction and every outgoing particle. Gamma−ray cascade calculation is possible. Systematics of Kalbach−Mann is adopted for the angular distributions, where the multi−step direct (MSD) part is replaced by the preequilibrium cross sections. The gamma−ray transmission coefficients are calculated by Brink−Axel formula for the giant dipole resonance.

$$
\begin{aligned}
M^2 &= \frac{k}{\sqrt{14A^3}}, && (e < 2\ MeV) \\
&= \frac{k}{A^3 e}\sqrt{\frac{e}{7}}, && (2\ MeV < e < 7\ MeV) \\
&= \frac{k}{A^3 e}, && (7\ MeV < e < 15\ MeV) \\
&= \frac{k}{A^3 e}\sqrt{\frac{15}{e}}, && (15\ MeV < e)
\end{aligned}
\qquad (13)
$$

The calculated capture cross section can be normalized to the experimental average capture cross section at 100 keV.

2.6 ALICE-F

This code is based on the hybrid and geometry-dependent hybrid model (GDH) for the preequilibrium process and the Weisskopf-Ewing evaporation model for the equilibrium process. Cross sections, particle spectra, angle-energy distributions and multi-particle emission with two step preequilibrium decay treatment can be calculated. The multi-particle emission up to 9 protons and 22 neutrons can be considered. Discrete levels are not considered.

The total level density in the equilibrium part is calculated with one of the Fermi-gas model, back-shifted Fermi-gas model, liquid drop model and Ramamurthy's method with shell and pairing correction. As particle-hole level density, Williams state density with an energy shift or pairing energy correction is adopted. Single particle state density is given as $g = A/13\ \mathrm{MeV}^{-1}$ where A is the mass number of the compound nucleus.

Particle production spectra can be calculated. Gamma-ray cascade calculation is possible with Weisskopf formula. Spectrum is represented in energy bins with equal width. For the cluster particles, the form factor of Iwamoto-Harada is used to the preequilibrium part. Inverse cross sections are used instead of transmission coefficients in the equilibrium part.

3. Quantities Used for Benchmark Calculations

The experimental data of isotope production cross sections measured by the Tohoku university CYRIC group[26] were one of the selected data for the neutron incident reaction data, because their wide incident energy range in the 20-50 MeV region. For the proton, mainly data of Michel et al.[27] and Jenkins et al.[28] were selected in this energy region. The calculations of iron were performed for ^{56}Fe.

Above 50 MeV, only the proton induced reactions were chosen for the benchmark calculation, since very few experimental data exist for the neutron incident reactions. Aluminum, iron and bismuth were selected, because they have relatively a lot of experimental data on isotope production cross sections.

4. Results of Benchmark Calculations and Discussions

4.1 Results below 50 MeV

Figure 1 shows the comparison for the calculated cross sections of the $^{55}Mn(n,x)^{54}Mn$ reaction with experimental data. NUCLEUS reproduced the tendency of the experimental results well, although it gave somewhat smaller values than the experimental ones between 20 and 30 MeV. The results of ALICE－F and MCEXCITON are in good agreement with the experimental data above 18 MeV. Two EXIFON calculations, which are identified to be standard and modified, can reproduce them in the near threshold energy, but too rapidly decrease above 22 MeV.

The experimental results indicate that the cross section of the $^{55}Mn(n,x)^{51}Ti$ reaction is around 0.8 mb between 30 and 40 MeV as shown in **Fig.2**. NUCLEUS predicted it about 10 times smaller than the experimental results. MCEXCITON overestimated them above 28 MeV. The result of ALICE－F calculation was in good agreement with the experimental data above 28 MeV. Below 28 MeV, the calculations are much smaller than the experimental data.

The results of the calculation for the $Fe(p,x)^{56}Co$ reaction cross section are given in **Fig.3**. NUCLEUS overestimated the experimental results for the whole energy region. The calculated results were larger than the experimental data by a factor 3 to 4 in the tens of MeV. HETC－3STEP gave the better results than NUCLEUS. In the EXIFON calculation, the cross sections calculated with the pairing shift $\Delta=12.8A^{-1/2}$ MeV (standard) overestimate the experimental data over the whole incident energy region. This situation is improved by a modification of the pairing shift, as the results is much closer to the experimental data than before. MCEXCITON, EXIFON modified and SINCROS－II almost reproduce the experimental data.

In the case of the $Fe(p,x)^{55}Co$ reaction cross section as shown in **Fig.4**, a significant discrepancy was seen between the calculated results of NUCLEUS and ALICE－F, and the experimental data. They overestimated the experimental data by a factor 2 to 3 in the energy region from 20 to 50 MeV. HETC－3STEP reproduced the experimental results fairy well in tens of MeV. In the EXIFON calculation, the modification led to remarkable underestimation while the standard calculation significantly led to overestimation below 28 MeV. The results of MCEXCITON and SINCROS－II had almost the same magnitude with the experimental data, however, their shape was discrepant from each other.

4.2 Results above 50 MeV

In this energy region, ALICE－F, MCEXCITON and NUCLEUS were compared. The cross section of the $^{27}Al(p,x)^{24}Na$ reaction is shown in **Fig.5**. For NUCLEUS, a discrepancy of one order of magnitude was seen near the threshold energy around 40 MeV between the calculated and experimental results. As the incident energy increased, NUCLEUS reproduced better the experimental results. The result calculated by MCEXCITON is similar to NUCLEUS below 60 MeV, but much smaller than the experimental data above 60 MeV. ALICE－F reproduced the experimental data below 150 MeV, and gave smaller results as the incident energy increased.

Figure 6 shows the results of the $^{27}Al(p,x)^{18}F$ reaction cross section. The result calculated by NUCLEUS gradually increased from the threshold energy of 50 MeV and reached to about 10 mb at hundreds of MeV region. The result of MCEXCITON gave much smaller values than the experimental data. The ALICE－F result has same tendency to that

of ^{24}Na production in **Fig.5**. For both of the ^{27}Al+p reactions, the experimental data has a saturation shape. Only NUCLEUS can reproduce this shape.

Figure 7 shows the results for the ^{56}Fe(p,x)^{56}Co reaction cross section. The calculations except that of MCEXCITON overestimated the experimental data below 200 MeV. For the ^{56}Fe(p,x)^{52}Mn reaction cross section shown in **Fig.8**, all calculated the results have the same trend as the experimental data. Below 50 MeV, however, the results of MCEXCITON and NUCLEUS underestimated the experimental data, and the result calculated by HETC-3STEP did not have the two peak shape found in the experimental data.

As shown in **Fig.9**, the ^{209}Bi(p,x)^{206}Po reaction cross section was reproduced by all the calculations. The calculated results of the ^{209}Bi(p,x)^{206}Bi reaction (**Fig.10**) reproduce the tendency of the experimental results. The magnitude of the ALICE-F result agrees best with the experimental data.

5. Concluding Remarks

The present results must be useful to consider which code can be usable to the nuclear data evaluation in the intermediate energy region. The code selection should be done carefully, since each code has specified merits. Combination of two or more codes would give a better result in some cases.

Acknowledgement

The authors wish to thank to the members of the Theoretical Calculation Codes Working Group of the Japanese Nuclear Data Committee for their discussions and suggestions.

References

1) Pearlstein S., J. Astrophys., 346, 1049 (1989).
2) Fukahori T. and Pearlstein S., JAERI-M 91-032, p.106 (1991).
3) Proc. of Symposium on Nucl. Data Evaluation Methodology, Brookhaven National Laboratory, Oct. 12-16, to be published.
4) Yamamuro N., JAERI-M 90-006 (1990).
5) Fukahori T., JAERI-M 92-039, p.114 (1992).
6) Kalka H., Z. Phys. A-Hadron and Nuclei, 341, 289 (1992); Proc. of the XXth Int. Symp. on Nuclear Physics, Nuclear Reaction Mechanisms, Castle Gaussig, Germany, Nov. 12-16, 1990, (Ed. by D. Seeliger and H. Kalka, World Scientific, 1991), pp.87.
7) Kishida N., private communication.
8) Nishida T., Nakahara Y. and Tsutsui T., JAERI-M 86-116 (1986).
9) Atchison F., Jül-Conf-24 (1980).
10) Ishibashi K., JAERI-M 90-025, p.362 (1990).
11) Nakahara Y. and Nishida T., JAERI-M 86-074 (1986).
12) Kalbach C., Z. Physik, A283, 401 (1977).
13) Gudima K.K., Osokov G.A. and Tonneev V.D., Yad. Fiz., 21, 260 (1975); Eng. transl. in: Sov. J. Nucl. Phys., 21, 138 (1975).
14) Williams Jr. F.C., Nucl. Phys., A166, 231 (1971).
15) Kalbach C., Phys. Rev., C37, 2350 (1988).
16) Akkermans J.M. and Gruppelaar H., Z. Phys. A - Atoms and Nuclei, 300, 345 (1981).
17) Machner. M., Z. Phys. A - Atoms and Nuclei, 302, 125 (1981).
18) Niita K., Z. Phys. A - Atoms and Nucl., 316, 309 (1984).
19) Iwamoto A. and Harada K., Phys. Rev., C26, 1821 (1982).
20) Sato K., Iwamoto A. and Harada K., Phys. Rev., C28, 1527 (1983).
21) Ignatyuk A.V., "Statistical Properties of Excited Atomic Nuclei", INDC(CCP)-233/L (1985).
22) Kunz P.D., "Distorted Wave Code DWUCK4", University of Colorad (1974).
23) Young P.G. and Arthur E.D., LA-6947 (1977).
24) Iijima S., Nakagawa T., Kikuchi Y., Kawai M., Matsunobu H., Maki K. and Igarasi S., J. Nucl. Sci. Technol., 14, 161 (1977).
25) see, e.g., Gadioli, E. and Hodgeson P.E. "Pre-Equilibrum Nuclear Reactions", Clarendon Press, Oxford (1992).
26) Nakamura T., Kondo Y., Sugita H. and Uwamino Y., Proc. of Int. Conf. on Nucl. Data for Sci. and Technol., Mito, May 30 - June 3, p1017 (1988).
27) Michel et al., Nucl. Phys., A322, 40 (1979).
28) Jenkins et al., J. Inog. Nucl. Chem., 32, 1419 (1970).

Table 1 Summary of considered codes

	NUCLEUS	HETC-3STEP	MCEXCITON	EXIFON	SINCROS-II	ALICE-F
Method	Monte-Carlo			Analytic		
I.C.M.*	yes	yes	no	no	no	no
Direct Process	no	no	no	yes	yes	no
Preequilibrium	no	Exciton Closed Form	Random Walk Equation	SMD+SMC	Exciton Model	Hybrid Model, GDH
Equilibrium	Weisskopf-Ewing	Weisskopf-Ewing	Weisskopf-Ewing	SMC	Hauser-Feshbach	Weisskopf-Ewing
Total Level Density	$\exp[2\sqrt{a(E-\Delta)}]$	$\exp[2\sqrt{a(E-\Delta)}]$	Back-shifted Fermi Gas	no	Gilbert-Cameron, Ignatyuk	Fermi gas, Ramamurthy, Liquid Drop
p-h Level Density	Williams	Williams	Williams	Williams for bound states	Williams	Williams
Discrete Level	no	no	no	yes	yes	no
Angular Distribution	no	Kalbach-Mann, Kalbach Syst.	Phase-Space Approach	Kalbach-Mann, Kumabe Syst.	Kalbach-Mann Syst.	Pearlstein, Kalbach-Mann, Kalbach Syst.
γ-Emission	no	no	no	yes	yes	yes
Other Functions	Fission Cross Section, Mass Yield	Fission Cross Section, Mass Yield	Recoil Energy Spectra of Residual Nuclei		Isometric State Production Cross Section	Fission Cross Section

* I.C.M. : Intranuclear Cascade Model

JAERI-M 93-046

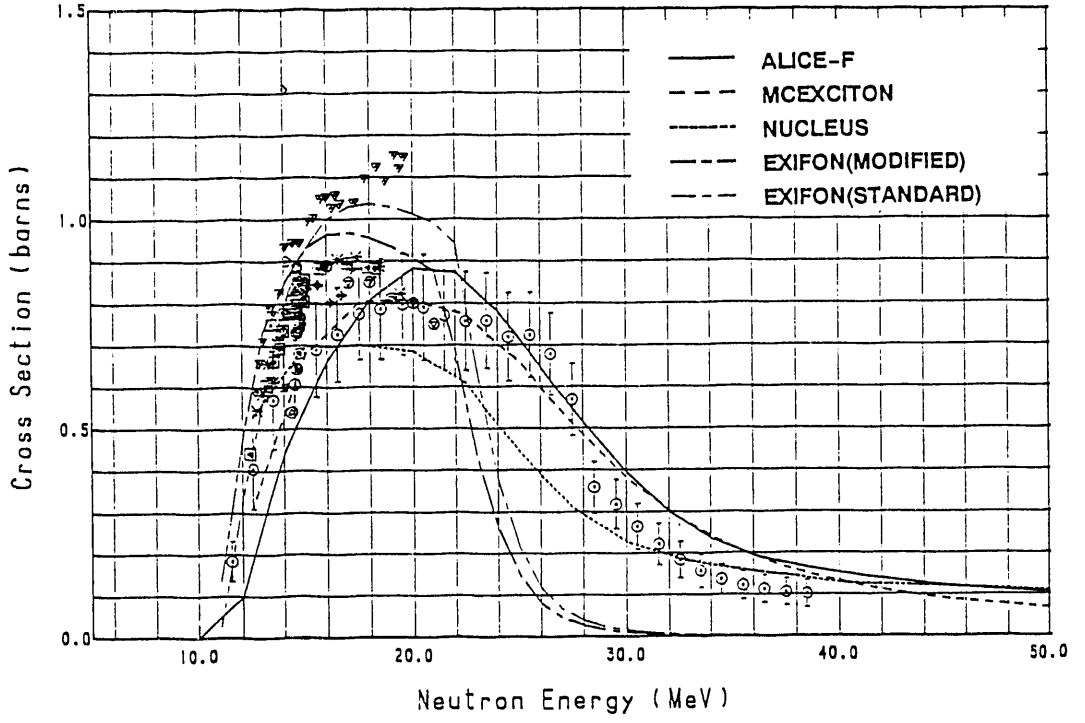

Fig. 1 The cross section of the $^{55}Mn(n,x)^{54}Mn$ reaction.

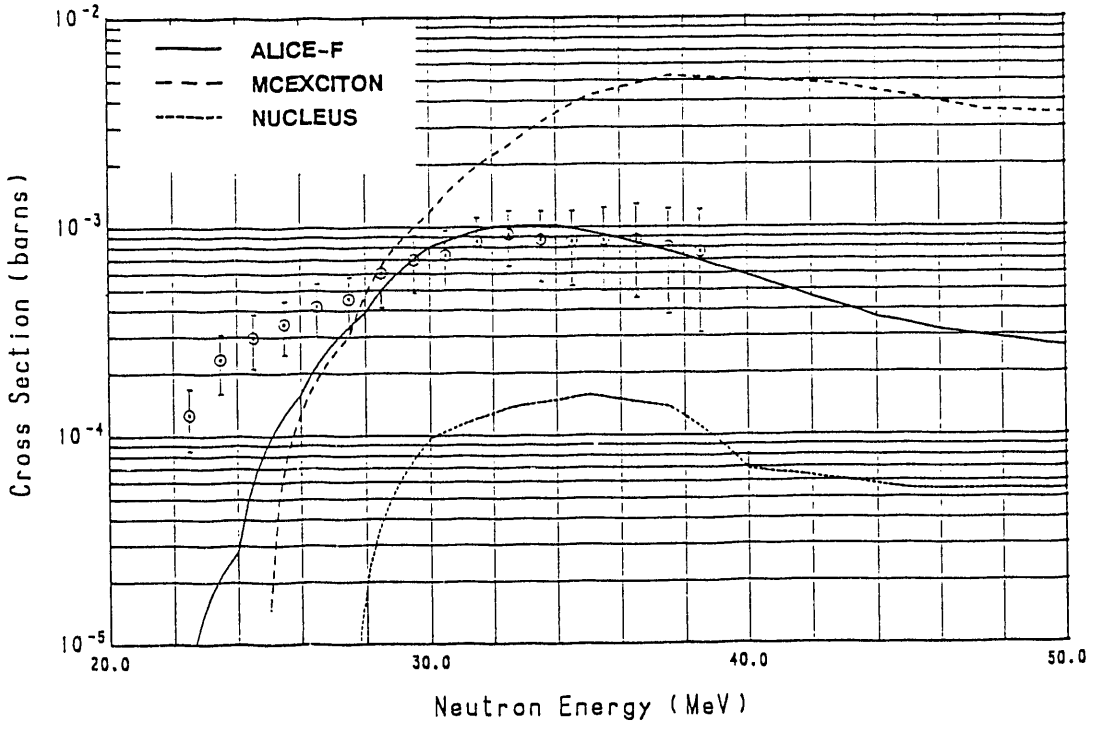

Fig. 2 The cross section of the $^{55}Mn(n,x)^{51}Ti$ reaction.

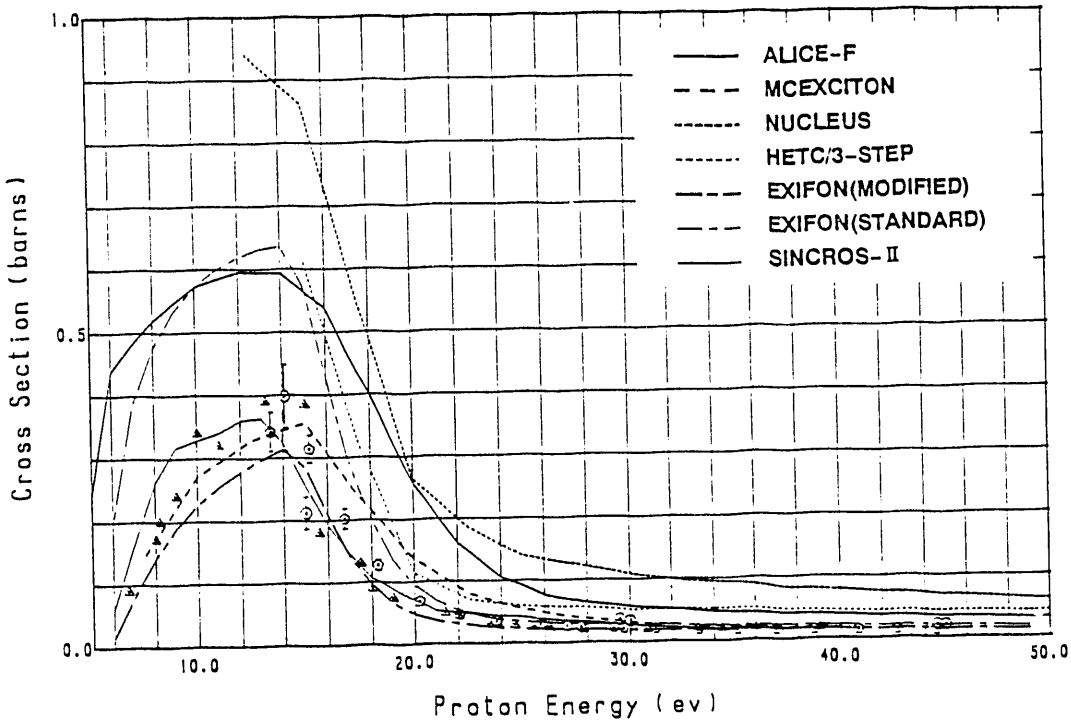

Fig. 3 The cross section of the Fe(p,x)^{56}Co reaction.

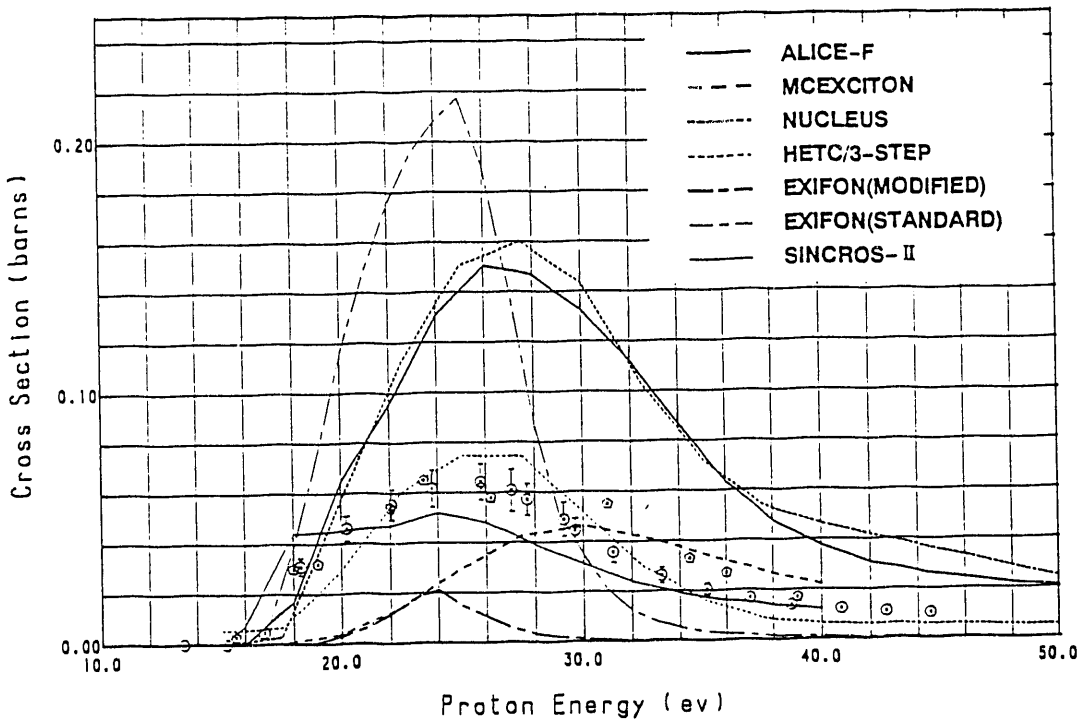

Fig. 4 The cross section of the Fe(p,x)^{55}Co reaction.

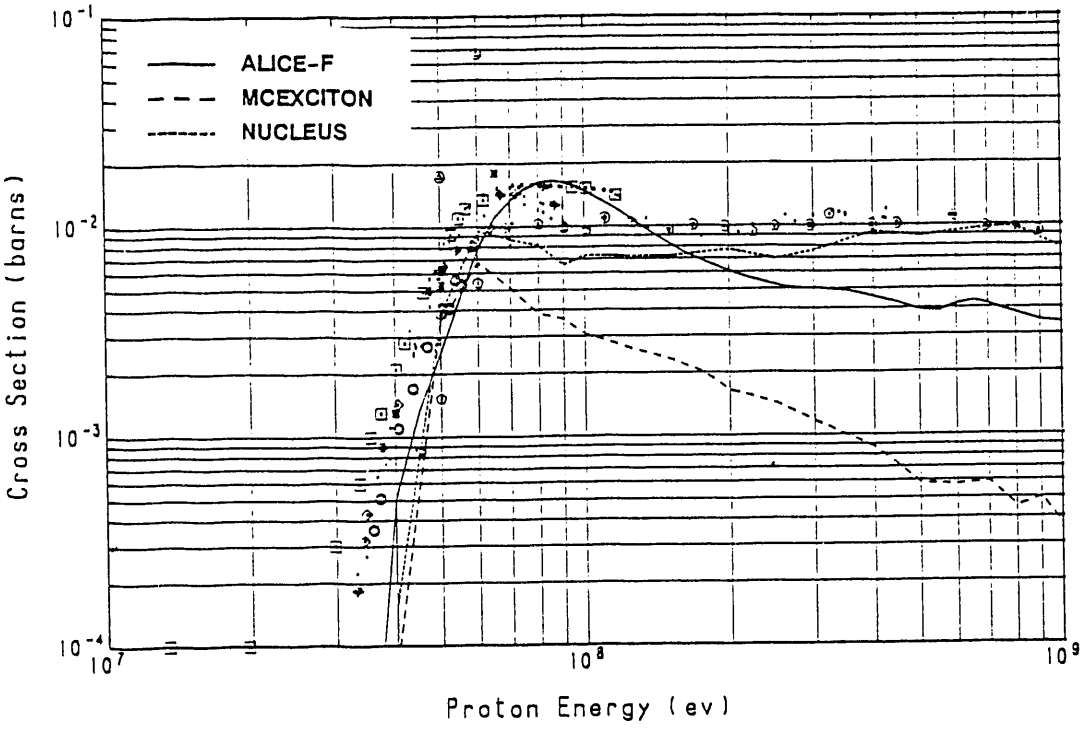

Fig. 5 The cross section of the $^{27}Al(p,x)^{24}Na$ reaction.

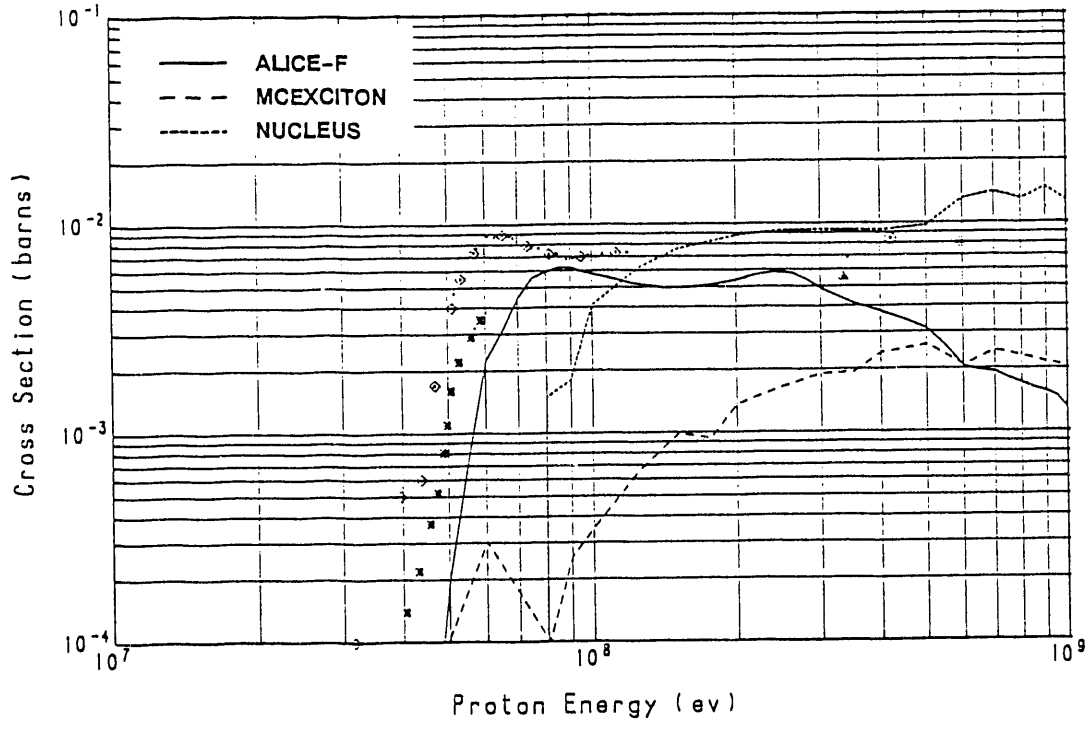

Fig. 6 The cross section of the $^{27}Al(p,x)^{18}F$ reaction.

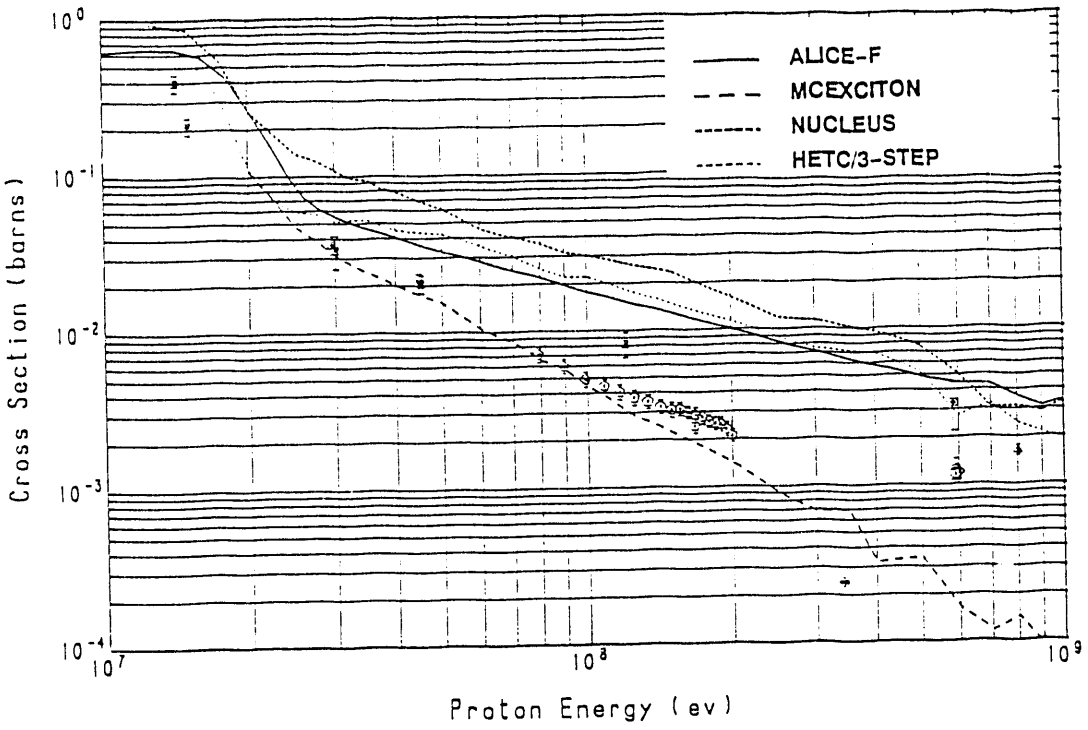

Fig. 7 The cross section of the $^{56}Fe(p,x)^{56}Co$ reaction.

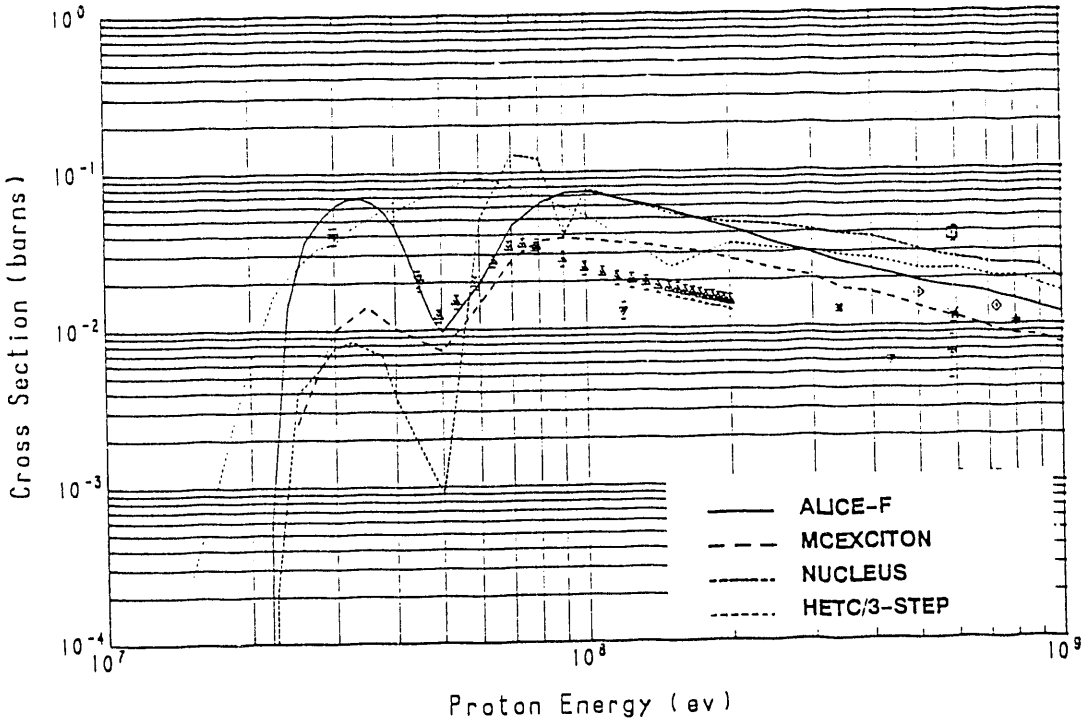

Fig. 8 The cross section of the $^{56}Fe(p,x)^{52}Mn$ reaction.

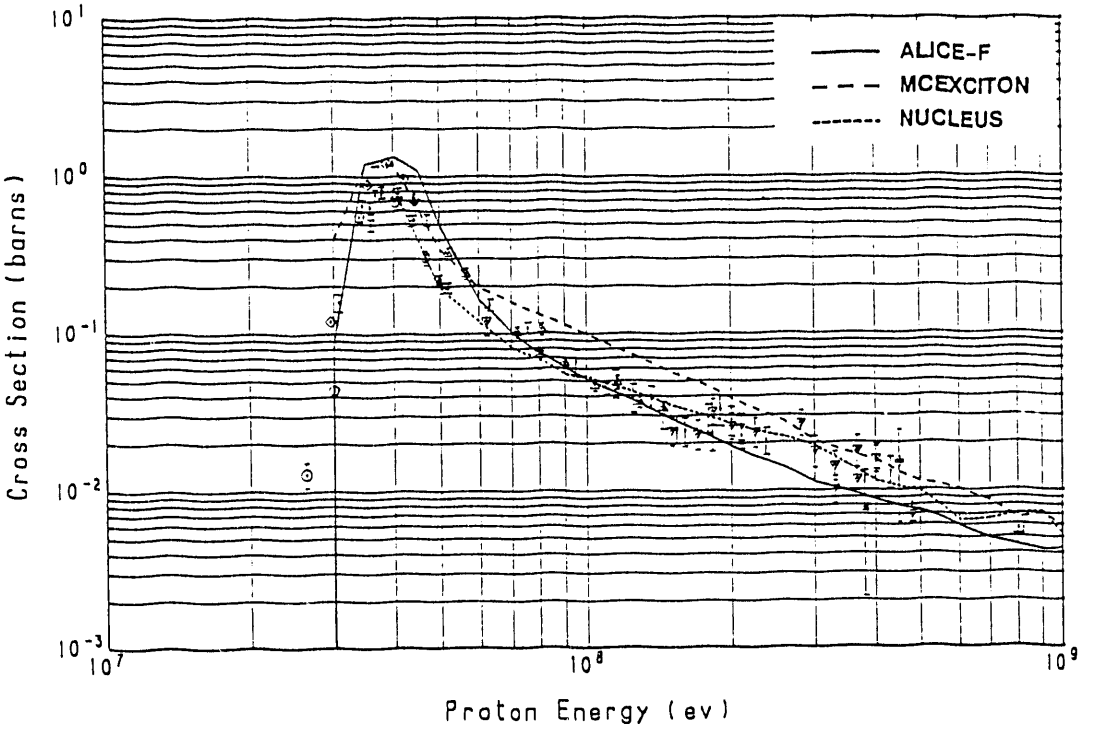

Fig. 9 The cross section of the $^{209}Bi(p,x)^{206}Po$ reaction.

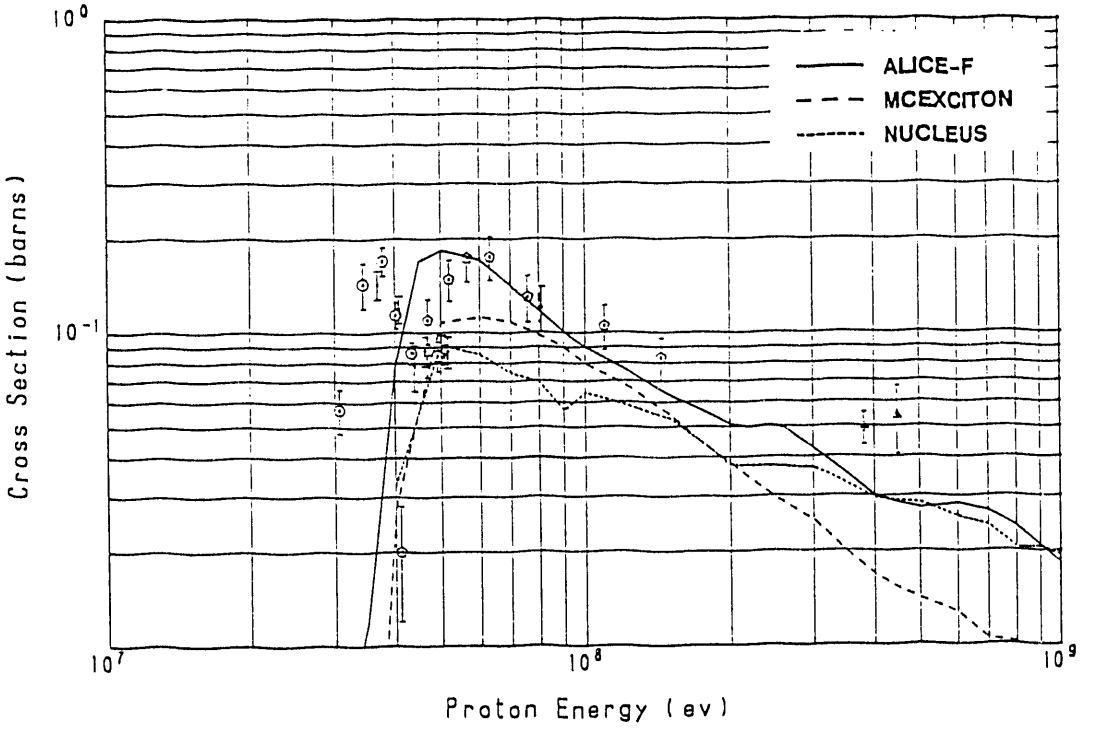

Fig. 10 The cross section of the $^{209}Bi(p,x)^{206}Bi$ reaction.

2.4.3 Integral Spallation Experiment with a Lead Assembly Irradiated with 500 MeV Protons

H.Takada, K.Hasegawa, T.Sasa, S.Meigo and I.Kanno*

Japan Atomic Energy Research Institute
Tokai-mura, Naka-gun, Ibaraki 319-11, Japan

*Department of Nuclear Engineering, Kyoto University
Yoshida-Honcho, Sakyo-ku, Kyoto, 606, Japan

An integral spallation experiment with a lead assembly was performed using 500 MeV protons. Lead and tungsten were employed as target in the assembly. The spatial distribution of the nuclide yields was obtained by the use of the activation method. It was found from the measured data that the number of the high energy neutrons in deep position in the assembly was smaller for tungsten target than for lead target. A calculation was made with the nucleon meson transport code NMTC/JAERI. The calculated results reproduced the spatial distribution of the nuclide yield well except for the one in the deep position on the axis.

1.Introduction

Recently, from the viewpoint of the disposal of the long-lived radioactive waste such as actinide nuclides and fission products, a great interests are taken in the accelerator based transmutation. Some conceptual studies[1-3] were made. In target design study, the codes which based on the intranuclear cascade evaporation model[4] were employed to simulate the spallation reaction and the transport of the high energy particle because there are few available evaluated nuclear data files in the medium energy region of several tens of MeV to several GeV. However, the validity of the simulation codes has not been ensured yet. Because the spallation neutron yield and the power distribution are the important factors to decide the performances of the transmutation system, it is necessary to estimate these quantities as accurate as possible.

In order to investigate the yield of the spallation products and the neutron transport phenomenon dependent on the target material, we performed an integral spallation experiment with a lead assembly using 500 MeV protons. Lead and tungsten were employed as target. The nuclide yields were investigated with the use of various activation

samples. The spatial distribution of the nuclide yields was obtained in the assembly. The calculation was also carried out with the nucleon meson transport code NMTC/JAERI(5). The calculated results were compared with the measured ones.

2. Experimental Procedures

The experiment was performed in the beam dump room of the 500 MeV booster proton synchrotron facility of National Laboratory for High Energy Physics. Figure 1 shows the cross sectional view of the lead assembly. The size of the lead assembly was 60 cm in diameter and 100 cm in length. The proton beam comes perpendicular to the target, which is 16cm in diameter and 30 cm in length, through the beam injection hole of 16 cm in diameter and 20 cm in length.

The following high purity metals were employed: Al(99.999%), Fe(99.99%), Ni(99.9%), Cu(99,99%), Au(99.999%) and Pb(99.99%). The size of the samples was 6 mm in diameter and 10 mm in length, respectively. The samples were packed in the metal capsule of 50cm in length and were inserted into the holes made along the beam axis in the radial position of 0, 3, 6, 10, 15, 20 and 25 cm in the assembly. Seven to eight pieces of Pb samples and others were put per 10 cm in the metal capsule not to make void region.

The intensity of the proton beam was about 1.5×10^{12} ppp. The beam current was monitored by a pick up coil in the beam line and a current integrator which counts the charge injected in the lead assembly. Several runs were done to obtain appropriate activities in the samples for γ–ray counting. The integral current on the lead assembly was between 3×10^{14} and 3×10^{15} protons. The beam profile was also measured by the activation of the aluminum foil which was attached to the top surface of the beam injection hole. The full-width-half-maximum of the profile was 16mm with respect to both horizontally and vertically injected surface.

After cooling of about 30 hours, γ rays from the activation samples were measured with a 100cc Ge-detector (relative efficiency of 20% to 3"x3" NaI scintillation detector).

3.Data Analysis

The measured data were taken on the computer by 4k channels and were analyzed by the program BOB(6). Yield of the nuclide produced in the activation samples was obtained by the following relation,

$$Y_j exp = \frac{\lambda_j I_j}{\varepsilon_j \eta \delta P N (1-e^{-\lambda_j Tr}) e^{-\lambda_j Tc} (1-e^{-\lambda_j Tm})}, \quad (1)$$

where j is jth produced nuclide, λ_j the decay constant, I_j the peak area, P the number of protons, N the number of atoms in an activation sample, ε_j the peak efficiency of the Ge-detector, η the number of photons emitted per decay, δ the self-absorption for photons in an activation sample, Tr the irradiation time, Tc the cooling time and Tm the measuring time.

The peak efficiency ε_j was determined by the calibrated gamma sources of ^{22}Na, ^{60}Co, ^{137}Cs and ^{152}Eu. The self absorption for photons in an activation sample δ was calculated by Monte Carlo method assuming that the photons were produced uniformly in the sample. The uncertainties for the decay constant and the number of photon per decay were not included in this estimation.

4.Calculation

Calculation was made by using NMTC/JAERI for the energy region above 15 MeV. The code simulates the spallation reaction based on the intranuclear cascade evaporation model including the high energy fission model proposed by Y.Nakahara[4]. As the level density parameter, A/8 was employed. Below 15MeV, neutron transport calculation was done by Monte Carlo code MORSE-DD[7].

Nuclide yield was calculated by folding the nuclide production cross section with the nucleon flux:

$$Y_{jcal} = \sum_{i=1}^{2} \int_{Eth}^{500} \sigma^i_j(E)\, \phi^i_j(E)\, dE, \quad (2)$$

where i stands for proton or neutron, $\sigma^i_j(E)$ is the production cross section for the nuclides j, $\phi^i_j(E)$ the flux of nucleon i and Eth the threshold energy. In this calculation, the nuclide yield was calculated by the energy range divided into some groups:

$$Y_{jcal} = \sum_{i=1}^{2} \sum_{g} \sigma_{j,i,g}\, \phi_{j,i,g}, \quad (3)$$

where, g indicates the number of energy group. Because there is few available evaluated nuclear data files for above 20 MeV, calculated nuclide production cross sections with NMTC/JAERI were employed.

5. Results and Discussion

5.1 Spatial Distribution of Nuclide Yield

Figure 2 shows the spatial distribution of the yield of ^{56}Ni produced in Ni samples. The calculated results reproduced well the spatial distribution except for the one on the axis. A significant discrepancy was observed in the deep position on the axis. A streaming effect of the high energy particles along the axis seemed to cause the discrepancy. Due to the calculated results, the nuclear reaction in the range of the incident proton on the axis was induced predominantly by the proton.

Figure 3(a), (b) and 4 show the yields of spallation products for Cu and Fe samples placed at 24 - 25 cm on the axis, respectively. The calculated results agreed with the measured data within factor 2 to 3 of magnitude. Figure 5 and 6 show the comparison with the calculated cross sections and the experimental results for proton induced reactions of ^{56}Fe(p,n)^{56}Co and ^{56}Fe(p,2p3n)^{52}Mn. NUCLEUS[11] is identical with the programme used for spallation reaction analysis in NMTC/JAERI. As is mentioned above, the contribution by the incident proton was predominant around 24 cm on the axis. It is natural that the systematics seen in the Figure 5 was included in the results obtained by this integral experiment. In that sense, more improvements are required for the calculation model adopted in the spallation reaction analysis.

5.2 Target Material Dependence on Nuclide Yield

Figure 7 and 8 show the axial distribution of the yield of ^{57}Ni and ^{52}Mn in Ni samples. Almost the same yields were obtained between 20 and 35 cm in depth. As the depth increases, however, the yields for tungsten target became smaller than the ones for lead target. It was found that the difference of about factor 3 of magnitude was observed in the depth 60 cm between the measured data for the two targets.

The threshold energies of ^{57}Ni and ^{52}Mn production in Ni are 12.7 and 35 MeV, respectively. It can be easily concluded from the measured data that the number of high energy neutrons transported to deep position in the lead assembly was smaller for tungsten than for lead. Figure 9 shows calculated neutron spectrum. The calculated results qualitatively agreed with the difference of the high energy neutron flux between tungsten and lead.

Due to the neutron yield calculation for bare target of 16cm in diameter and 30 cm in length, the number of produced neutron is about 10 for tungsten and lead. The microscopic total cross section is almost the same for both targets. On the other hand, the density of tungsten (18.3 g/cc) is larger than that of lead (11.34g/cc). Consequently, the macroscopic cross section for tungsten becomes about twice or more than for lead. In addition, the range of 500 MeV protons is 12cm for tungsten and 20cm for lead. This leads to the fact that the significant difference of the high energy component seen in Figure 9.

References

(1) E. D. Arthur: Proc. of 6 th Int. Conf. Emerging Nucl. Energy Systems, Fusion Technol., **20**, Part 2, 641(1991)
(2) H. Takahashi: ibid., p657
(3) H. Takada, et al.: ibid., p673
(4) H. W. Bertini: Phys. Rev. **131**, 1801(1963).
(5) For example, Y. Nakahara and T. Tsutsui: JAERI-M 82-198 (1982).
(6) H. Baba: JAERI-M 7017 (1977).
(7) M. Nakagawa and T. Mori: JAERI-M 84-124 (1984).
(8) R. Michel, et al.: Nucl. Phys.**A322** 40 (1979).
(9) R. Michel and R. Stuck.: J. Geophys. Res. **89**, B673 (1984).
(10) K. Ishibashi, el al.: JAERI-M 90-025 p.362 (1990)
(11) T. Nishida, Y.Nakahara and T. Tsutsui : JAERI-M 86-116 (1986)
(12) P.Cloth., et al.: Jul-Spez 196 (1983)

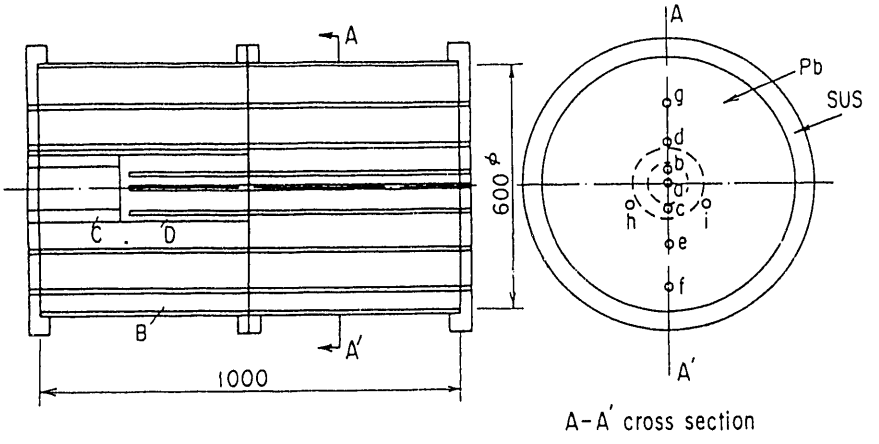

Fig. 1 Cross sectional view of the lead assembly. The small holes (a to i) indicate the places where activation samples are inserted. The capitals B stands for the lead assembly, C the beam entrance hole, D the lead target which can be replaced with different one.

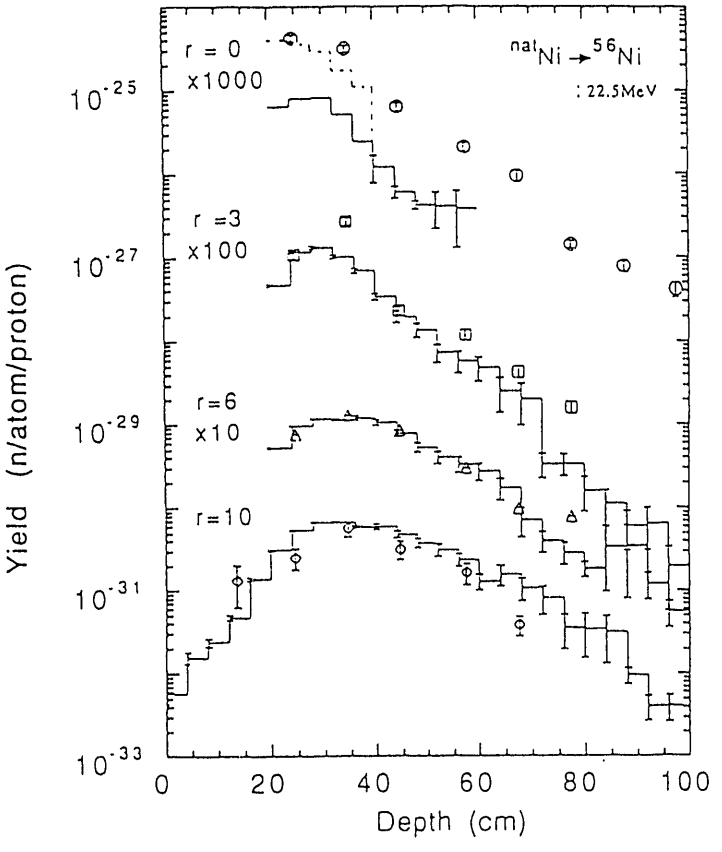

Fig. 2 Spatial distribution of the yield of ^{56}Ni produced in the Ni samples for 500 MeV proton incidence on the lead assembly. The open marks stand for the measured data. The solid lines indicate the calculated nuclide yield induced by neutrons. The dotted line represents the nuclide yield induced by protons and neutrons.

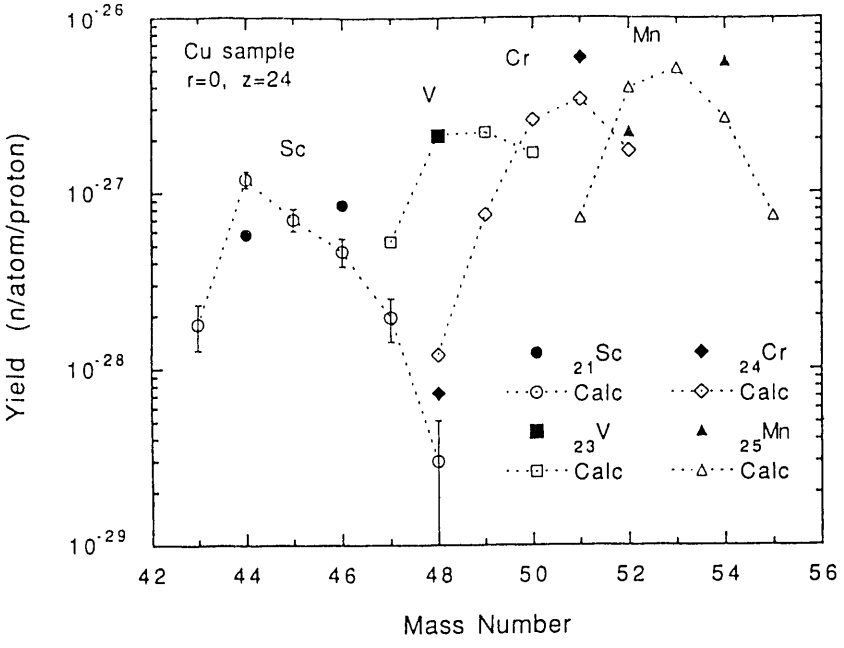

Fig. 3(a) Yield of the nuclides with 21 < Z < 26 produced in the Cu sample placed at 24 cm on the axis. The solid marks stand for the measured data. The open marks indicate the calculated yield with NMTC/JAERI. The lines are for eye guide.

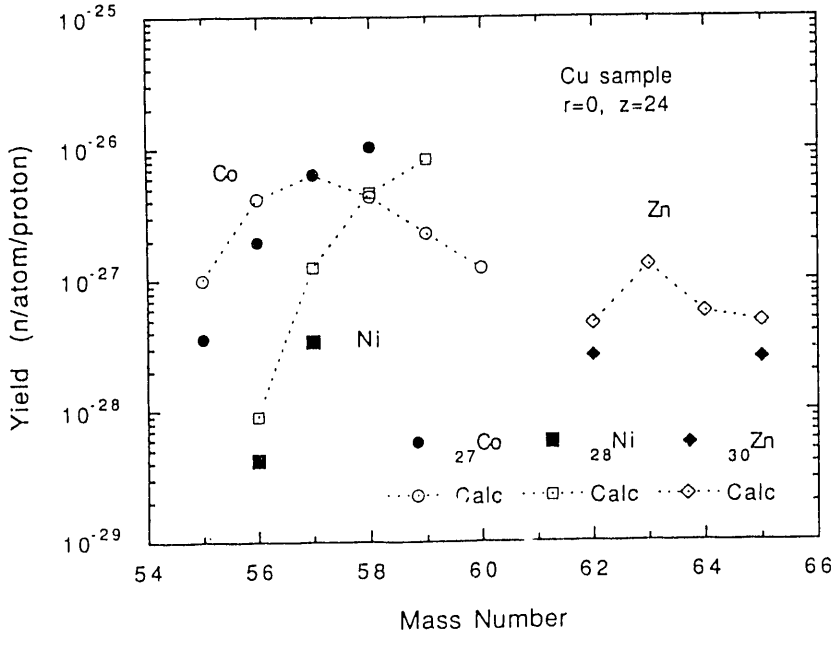

Fig. 3(b) Yield of the nuclides with 27 < Z < 30 produced in the Cu sample placed at 24 cm on the axis. The solid marks stand for the measured data. The open marks indicate the calculated yield with NMTC/JAERI. The lines are for eye guide.

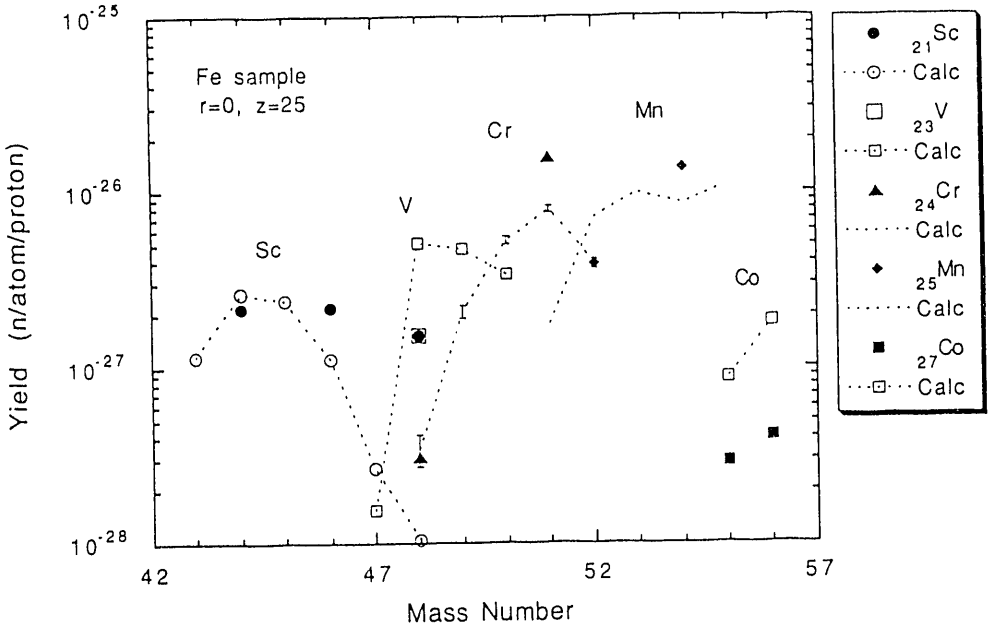

Fig. 4 Yields of the nuclides with 21 < Z < 27 produced in the Fe sample placed at 25 cm on the axis. The solid marks stand for the measured data. The open marks indicate the calculated yield with NMTC/JAERI. The lines are for eye guide.

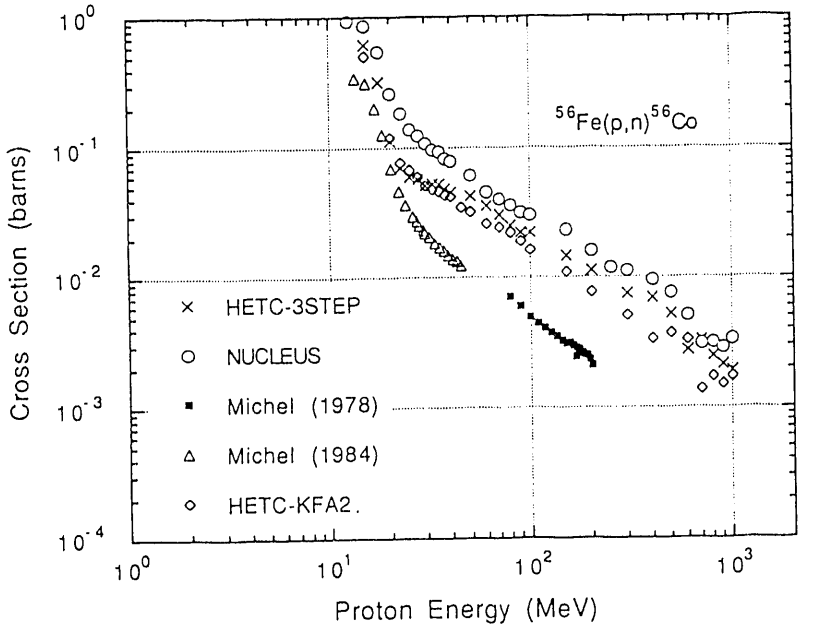

Fig. 5 ^{56}Co production cross section for proton incidence on ^{56}Fe. The triangle and the solid square stand for the experimental data by Michel et al.[8,9] The cross mark, the open circle and the open diamond represent the calculated results with HETC-3STEP[10], NUCLEUS[11] and HETC-KFA2[12], respectively.

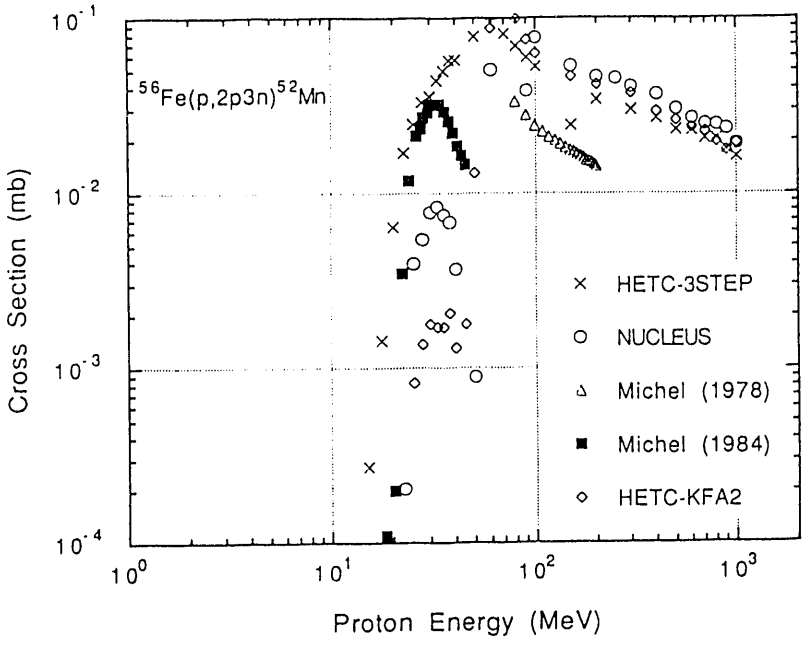

Fig. 6 ^{52}Mn production cross section for proton incidence on ^{56}Fe. The triangle and the solid square stand for the experimental data by Michel et al.[8,9] The cross mark, the open circle and the open diamond represent the calculated results with HETC-3STEP[10], NUCLEUS[11] and HETC-KFA2[12], respectively.

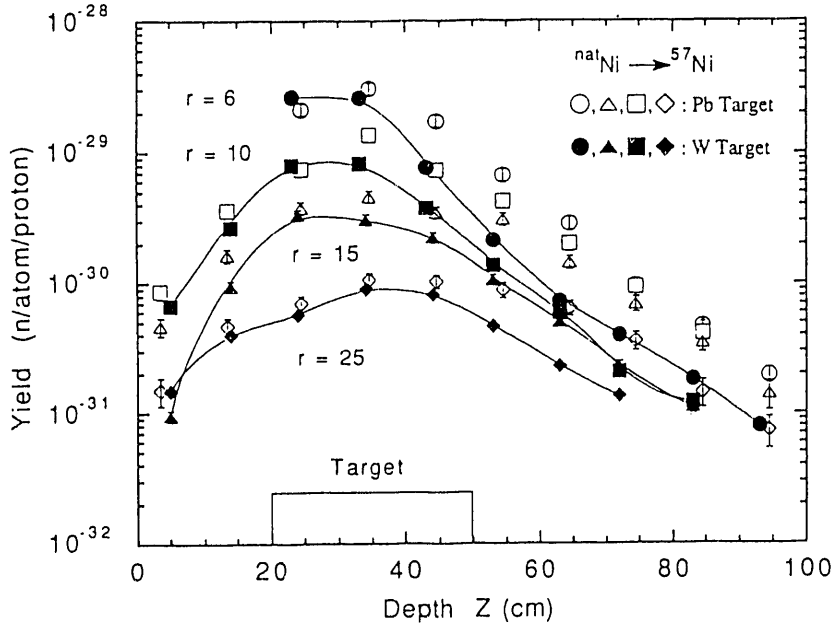

Fig. 7 Yields of ^{57}Ni produced in the Ni samples. The open marks indicate the measured data for the lead target. The solid ones represent the one for tungsten target.

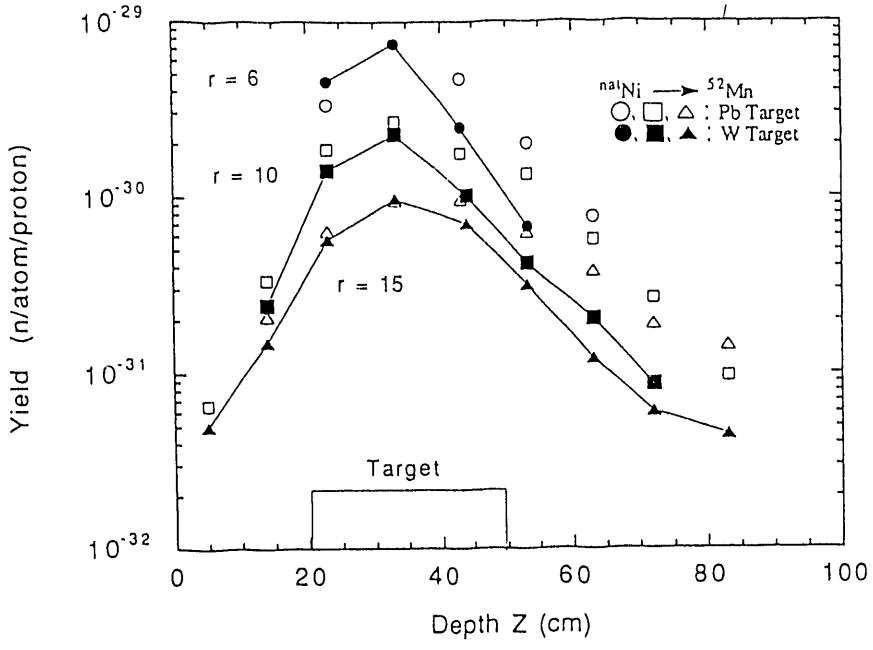

Fig. 8 Yields of ^{52}Mn produced in the Ni samples. The open marks indicate the measured data for the lead target. The solid ones repesent the one for tungsten target.

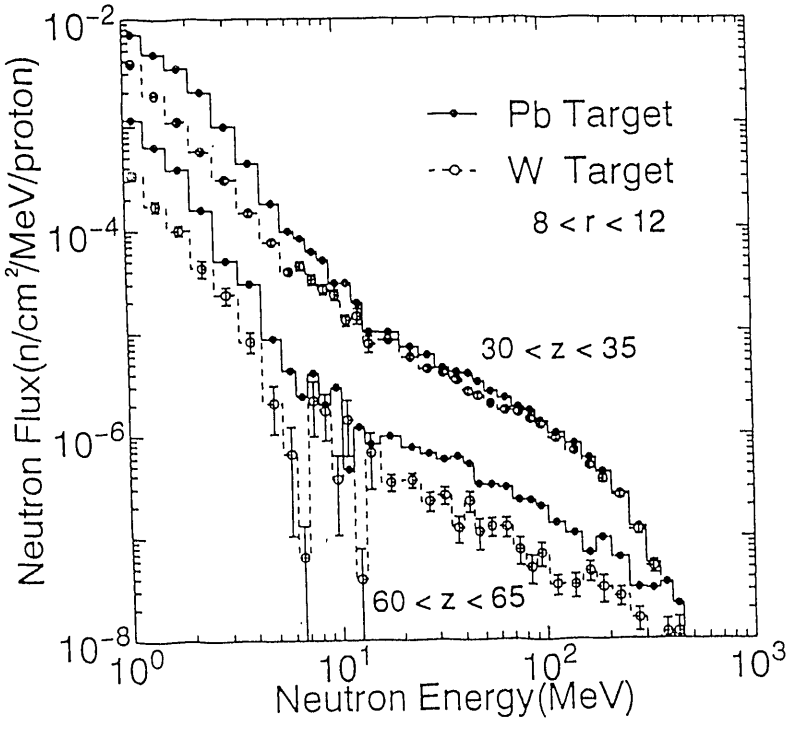

Fig. 9 Calculated neutron flux in the region of 30 < Z < 35 cm and 60 < Z < 65 cm in depth with 8 < r < 12 cm in radial distance. The solid lines are for lead target. The dotted ones are for tungsten ones.

2.4.4 Neutron Measurement for (p, Xn) Reaction with Protons of GeV Range

Kenji ISHIBASHI, Tatsushi. NAKAMOTO, Naruhiro MATSUFUJI, Keisuke MAEHATA, Shouichirou SAKAGUCHI, Yoshihisa WAKUTA, Yukinobu WATANABE*, Hiroshi TAKADA**, Shin-ichiro MEIGO**, Satoshi CHIBA**, Masaharu NUMAJIRI***, Yoshio YOSHIMURA***, Yuzuru MATSUMOTO+ and Takashi NAKAMURA++

Department of Nuclear Engineering, Kyushu University
Hakozaki, Higashi-ku, Fukuoka-shi 812
*Department of Energy Conversion, Kyushu University
Kasugakoen, Kasuga-shi 816
**Japan Atomic Energy Research Institute
Tokai-mura, Naka-gun, Ibaraki-ken 319-11
***National Laboratory for High Energy Physics (KEK)
Oho, Tsukuba-shi 305
+Dep. of Management Information, Kyushu Teikyo Junior College
Shinkattachi-machi, Omuta-shi 836
and
++Cyclotron RI center, Tohoku University
Aramaki, Sendai-shi 980

The neutron-emission cross sections were measured by the time-of-flight method at National Laboratory for High Energy Physics (KEK). The experiment was carried out with targets of C and Pb at incident proton energies of 0.8, 1.5 and 3.0 GeV. The preliminary data analysis was made, and the double differential cross section for Pb at 0.8 GeV was consistent with the data of a different laboratory. The measurement is planned to be continued with targets of Al, Fe and In.

1. Introduction

It is of interest to investigate the neutron-emission cross section for the reaction (p,xn) by incident protons in the medium energy region. The data are useful for studying such facilities as the spallation neutron sources and the accelerator-driven transmutation systems. The experimental data were obtained by the time-of-flight (TOF) method at IUCF[1] with incident proton energies of 120 and 160 MeV, at PSI (SIN)[2] with that of 585 MeV, and at LANL[3-6] with those of 113 to 800 MeV. At higher energies than these, a test measurement[7] was made at National Laboratory for High Energy Physics (KEK). However, systematic data covering many targets have not been taken in the energy region above 800 MeV so far.

With increasing proton energy from 113 to 800 MeV, the experimental

neutron cross section showed a systematic difference[5] from the calculated results in the evaporation and preequilibrium regions. To make clearer the quantitative behaviors of the cross section, we have planned to measure the double differential cross section (DDX) of the spallation neutrons by the TOF method. The incident proton energies were chosen to be 0.8, 1.5 and 3 GeV. Protons were supplied by $\pi 2$ beam line at KEK. The protons are obtained as secondary particles generated by an internal target, which is placed in the accelerator ring of the 12 GeV proton synchrotron.

2. Test measurement

Some test measurements were made at the $\pi 2$ beam line with protons of 1.5 GeV. The scintillator NE213 was chosen for the neutron detection. An early question was whether or not to shield neutron detectors from background neutrons and gamma rays. The results at 90° are plotted in Fig. 1. Open triangular marks show the data taken by a bare neutron detector, while solid square ones indicate those by the detector surrounded with iron blocks of 0.5 to 1 m thick. A large disagreement is seen at a few MeV. The heavy shielding was not appropriate in the experimental circumstances. Neutron detectors were, therefore, determined to be used on the bare condition.

At first, we followed the zero-cross method[8] for the pulse-shape discrimination between neutron and gamma ray. The results by this method ware shown in Fig. 2. The discrimination was worse for high energy events. This is because the saturation effect on the zero-cross time was induced in a pulse-shaping preamplifier, due to the large dynamic range of the incident particles. To eliminate such saturation, a two-gate integration method[9] was tested at a later test run. The photomultiplier signal was branched into two pulses, and they were input into charge ADC's worked by different gate pulses. The fast gate on one ADC covered the initial peak of the photomultiplier signal, whereas the tail gate made another ADC to accept only the slow tail portion thereof. The fast gate had a duration of 30 ns, and the tail gate owned that of 500 ns after a delay of 130 ns. The results are shown in Fig. 3. The discrimination is excellent and no saturation effect is seen. The two-gate integration method was adopted in the measurement thereafter.

The simplest method for background correction is to make two kinds of experiments of target-in and -out measurements: The cross section is obtained by subtracting the latter data from the former ones. However, in this case, the influence from such effects as the floor-scattered (or -generated) neutrons may not be removed. We were afraid that the floor-scattering effect might arise because of the rather short height (1.7 m) between the floor and the beam line. The experimental check was made by inserting a shadow bar of 1m length between target and detector. The TOF flight pass was 1.5 m. The results are shown in Fig. 4, together with the cross section measured. One can see the effect like the floor scattering is negligible in the energy region at the flight pass.

3. Experimental arrangements

The experimental specification is listed in Table 1. The NE213 detectors have two kinds of sizes (φ5"x5" and φ2"x2"). The larger detectors were used for making the neutron-detection efficiency as high as possible, although they produce a rather poor time resolution in the TOF measurement. The smaller ones exhibit good neutron-gamma pulse-shape discrimination even in the neutron energy region below 1 MeV.

The experimental arrangement is illustrated in Fig. 5. The beam intensity of the $\pi 2$ beam was very weak and in a level of 10^5 particles/2.5s because of its generation as a secondary beam. Incident particles were easily counted one by one by plastic scintillators. The protons were identified from pions by a pair of TOF scintillators (Pilot U) located at a separation distance of 20 m. Each Pilot U scintillator was connected on opposite sides with two photomultipliers (Hamamatsu H2431). The particle identification is shown in Fig. 6, for instance, at a beam momentum of 3.83 GeV/c, i.e. proton kinetic energy of 3.0 GeV. The timing was determined by software by averaging the time signals of the two sides. The time resolution was 0.35 ns, and protons are well discerned from pions with a separation time of 1.7 ns. The beam damp was formed by carbon of 0.5x0.5 m^2 in area and 1 m thick. The carbon was surrounded by sufficiently thick iron blocks except at the beam-incident surface. The distance between the target and the beam dump was 8.5 m.

For the neutron TOF measurement, the time standard was taken by the Pilot U scintillator adjacent to the target. The beam-incident target area was defined by a pair of scintillators. Because of the low beam intensity, the flight pass of the neutron TOF was limited to short distances: It was 1 to 1.5 m for the φ5"x5 detectors, and 0.6 to 0.9 m for φ2"x2 ones. The values of flight pass were shorter than the beam-line height 1.7 m from the floor. Veto plastic scintillators were used for finding charged-particle events in the neutron detectors. They were installed in front of all neutron detectors as illustrated in Fig. 5. The picture of the detector system is presented in Fig. 7. The whole frame was made of aluminum alloy.

The block diagram of the measurement circuit is shown in Fig. 8 with simplified drawing. When the incident-beam coincidence took place at all the beam scintillators, the pulse with a typical width of 150 ns was sent to the next coincidence module. Then, the signal of neutron detectors was accepted by this module for 150 ns. The events arising from incident pions were eliminated by tuning a hardware timing in the beam coincidence. The example of the TOF spectrum is shown in Fig. 9. The prompt gamma rays are seen as a sharp peak in the right hand side. The time resolution of the neutron TOF measurement was 0.75 ns for 5" detectors and 0.55 ns for 2" ones. The detection efficiency of the neutron detectors was calculated by the use of the Cecil code[10] of the Kent State University version. The experimental check on the detection efficiency is scheduled in 1993.

Fig. 10 The cross section of the $^{209}Bi(p,x)^{206}Bi$ reaction.

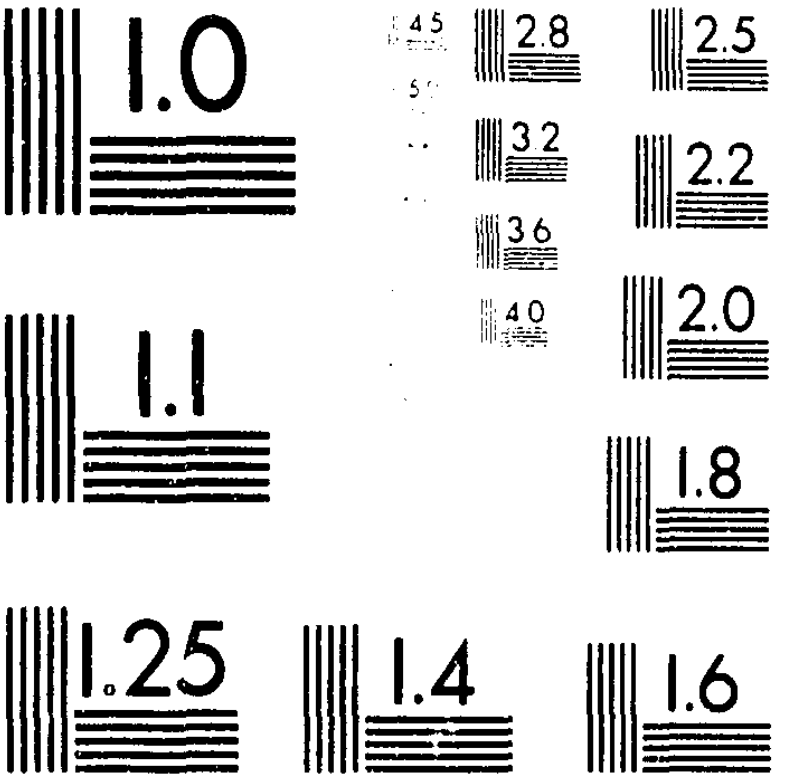

MICROCOPY RESOLUTION TEST CHART
NATIONAL BUREAU OF STANDARDS
STANDARD REFERENCE MATERIAL 1010a
(ANSI and ISO TEST CHART No 2)

4. Results of cross section

The measurement has already been carried out for targets of Pb and C at proton energies of 0.8, 1.5 and 3.0 GeV. At present, however, the data analysis is not completed. The preliminary DDX data of the φ5"x5" detectors are shown in Figs. 10-12 for Pb. The relatively worse time resolution for the short flight pass lead to considerable ambiguity in neutron energies above 200 MeV as listed in Table 2; we are is not concerned about it because our interest is mainly in the preequilibrium and the evaporation neutrons. There may be some problem in the detection efficiency at 120° at several MeV. Calculation results by the cascade-evaporation model (HETC)[11] was shown by lines. The experimental data at 0.8 GeV are compared with those[5,6] of LANL in Fig. 13. The present preliminary DDX agrees with the LANL data within a discrepancy of 10%. Further checks and corrections will be made on such items as the detection efficiency and multiple scattering effects in the target itself. The measurement for other targets is to be performed in 1993.

5. Conclusion

The measurement of (p,xn) reaction at incident proton energies of 0.8, 1.5 and 3.0 GeV was started. The experimental difficulties were overcome through the test measurement. The measurement on the heaviest element of Pb and the lightest C had already been carried out. The DDX for Pb at 0.8 GeV was compared preliminarily with the LANL data, and was confirmed to agree with them in an acceptable manner. Further experiment on the rest of the targets is planned to be completed in 1993.

The authors express their gratitude to Prof. K. Nakai and the beam channel staffs of KEK for his continuous encouragement and their generous support of this experiment, and tender their acknowledgements to Prof. H. Hirabayashi and Prof. N. Watanabe of KEK, and Prof. M. Arai of Kobe University for their useful discussion.

References

1) SCOBEL,W. et al.: Phys. Rev. C 41, 2010 (1990)
2) CIERJACKS,S. et al.: Phys. Rev. C 36, 1976 (1987)
3) MEIER,M. et al.: Radiation Effects 196, 1415 (1987)
4) MEIER,M. et al.: Nucl.Sci.Eng. 104, 339 (1990)
5) AMIAN,W. et al.: Proc. Nucl. Data for Sci. and Technol., p.696 (1991)
6) AMIAN,W. et al.: Nucl.Sci.Eng. 112, 78 (1992)
7) CHIBA,R.: Genshikaku-kenkyu 21, 41 (1985) in Japanese.
8) PLISCHKE,P. et al.: Nucl. Instrum. Meth. 139, 579 (1976)
9) BELL,Z.W. et. al.: Nucl. Instrum. Meth. 188, 105 (1981)
10) CECIL.R.A. et al.: Nucl. Instrum. Meth. 161, 439 (1979)
11) ATCHISON,F.: JUL-CONF-34 (1980)

Table 1 Experimental specification

Proton energy (GeV)	0.8, 1.5, 3.0
Targets (thickness)	C(10cm), Pb(1.2cm)
	Al, Fe, In (planned)
Method	Time of Flight
Neutron detector	NE213, φ2"x2" and φ5"x5
Flight pass (m)	0.6~0.9 for φ2"x2"
	1~1.5 for φ5"x5"
Photomuliplier	H1250 for φ5"x5"
	H1161 for φ2"x2"
	H2431 for Pilot-U
Angle (deg)	15, 30, 60, 90, 120, 150

Table 2 Neutron energy resolution*

Neutron energy (MeV)	Flight time (ns)	Energy resolu. (%)
10	25	13
20	18	15
50	12	19
100	8.6	24
200	6.5	35
300	5.6	45
500	4.9	64

*TOF with a mean flight pass of 1.1m and a time resolution of 0.75ns.

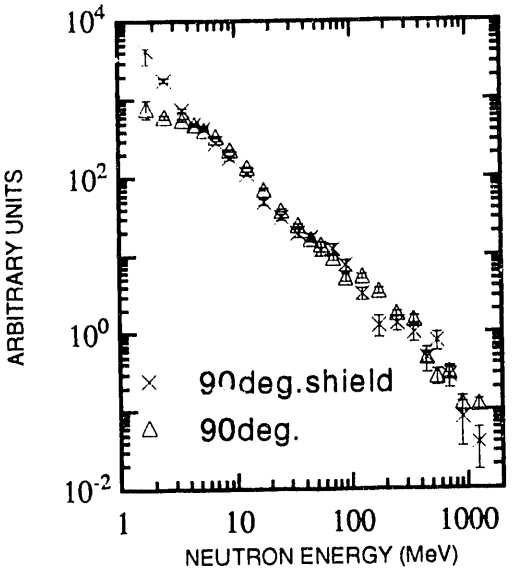

Fig. 1 Neutron spectra at 90° by 1.5 GeV protons with and without iron shielding around a neutron detector. The vertical axis is in a relative scale.

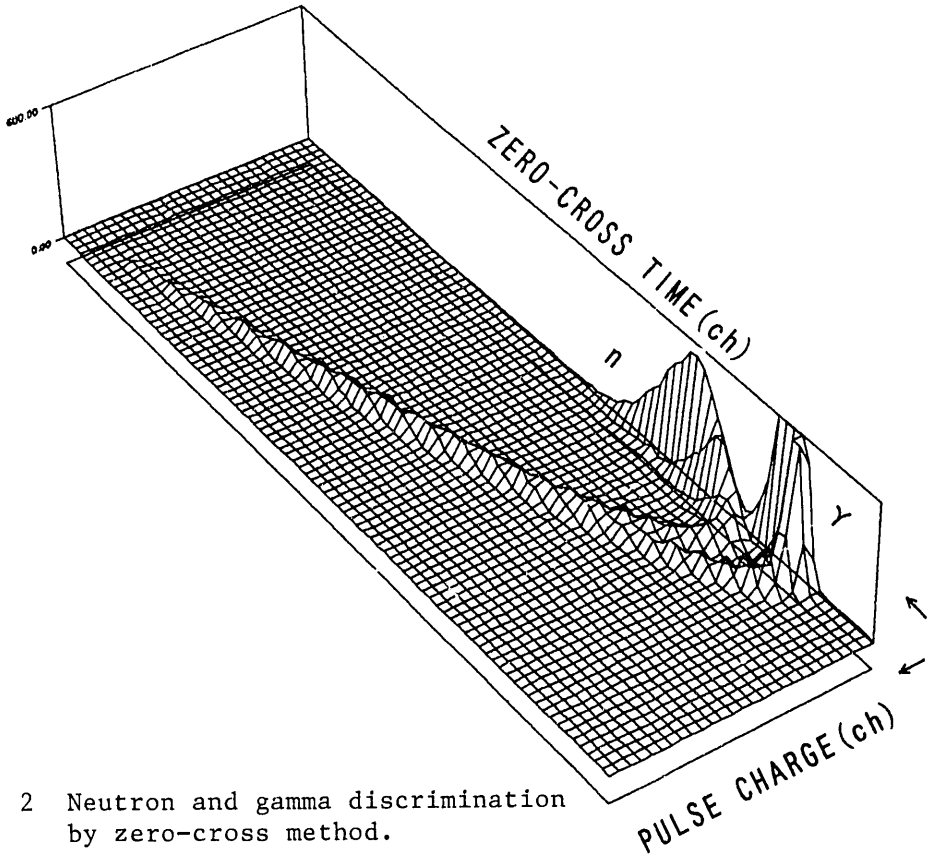

Fig. 2 Neutron and gamma discrimination by zero-cross method.

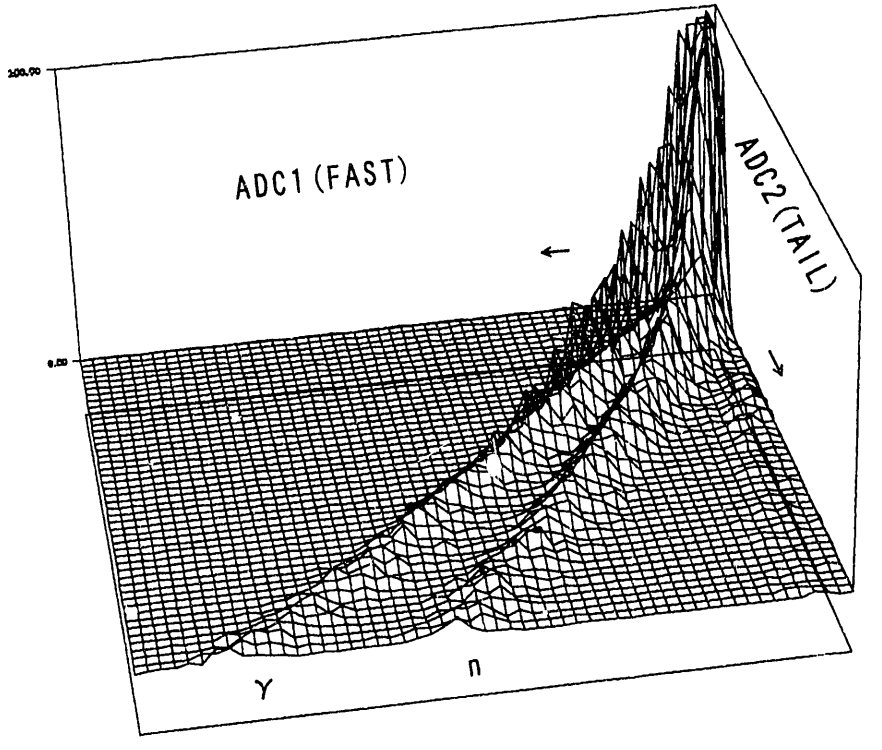

Fig. 3 Neutron and gamma discriminaton by two-gate integration method.

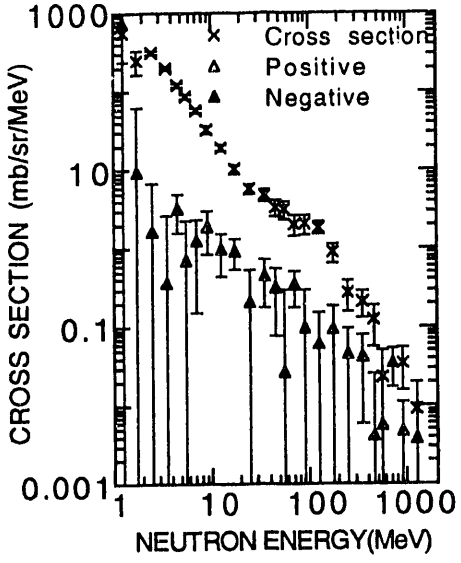

Fig. 4 Results of the shadow bar test. The shadow bar size was $\phi 15 \times 100\ cm^2$ and the flight pass 1.5 m. Test results occasionally showed negative values after background subtraction.

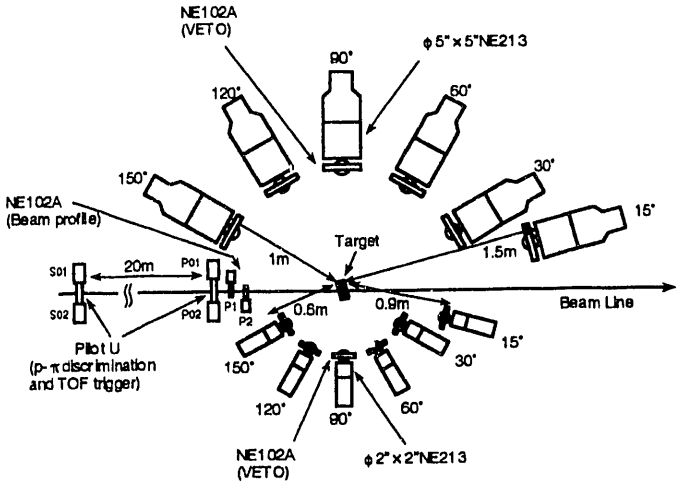

Fig. 5 Illustration of the experimental arrangement.

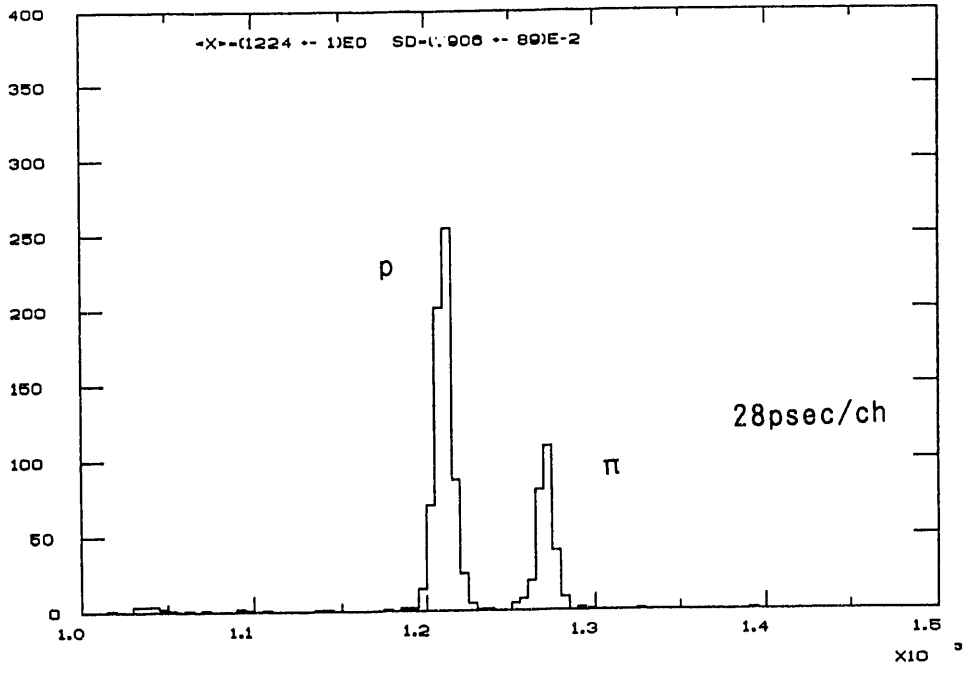

Fig. 6 Proton-pion separation in TOF spectrum for beam of 3.83 GeV/c.

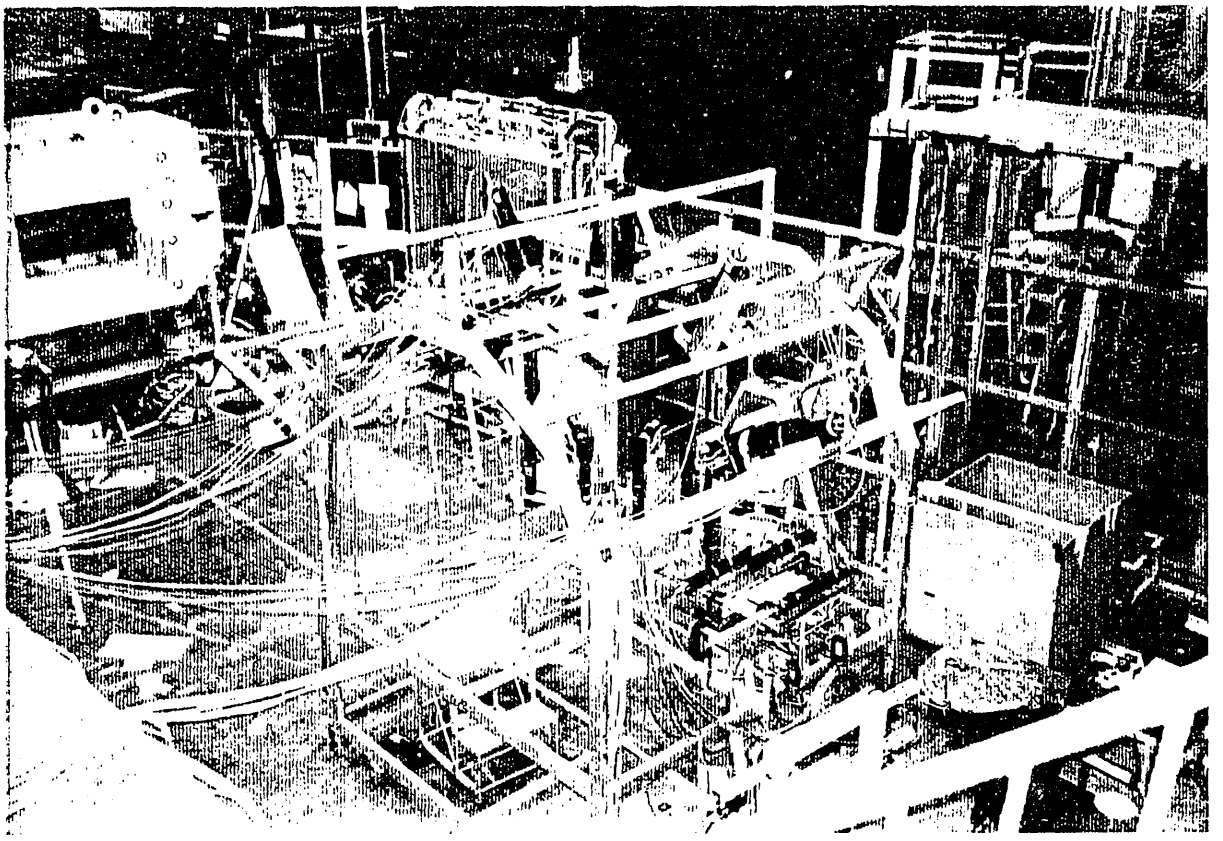

Fig. 7 Picture of the detector system. Incident particles come from the right side.

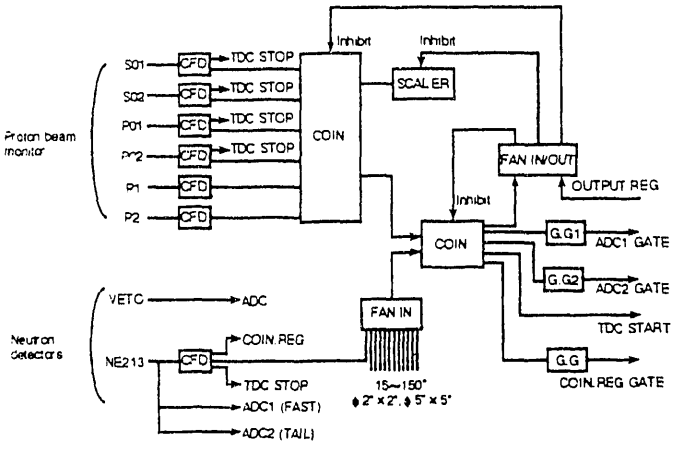

Fig. 8 Block diagram of the electronic system with simplification.

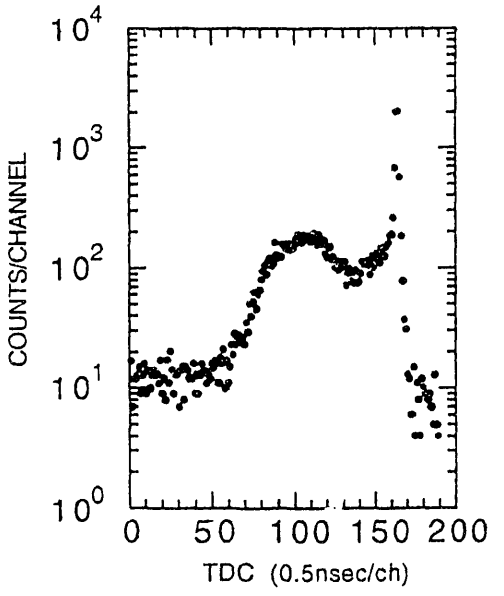

Fig. 9 TOF spectrum at 15° for an incident proton energy of 1.5 GeV.

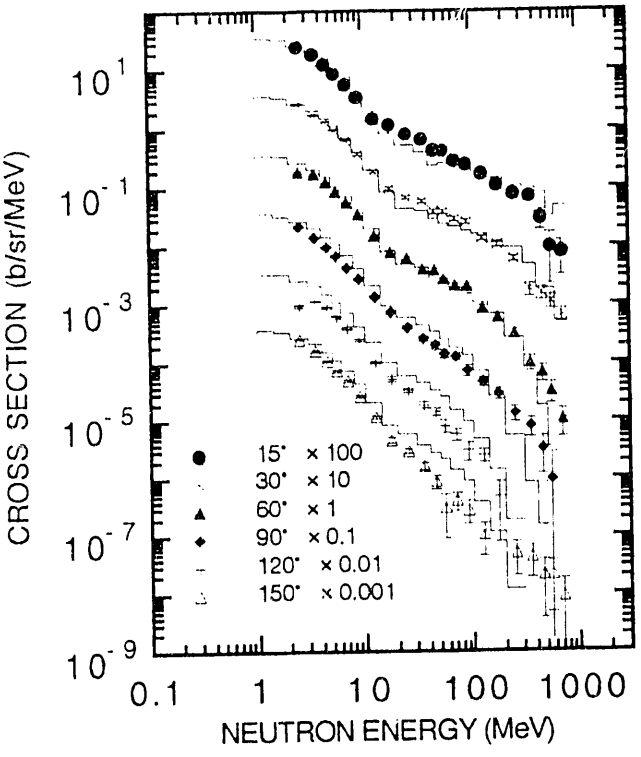

Fig. 10 Double differential cross section at 0.8 GeV for Pb. Lines show calculation results by HETC.

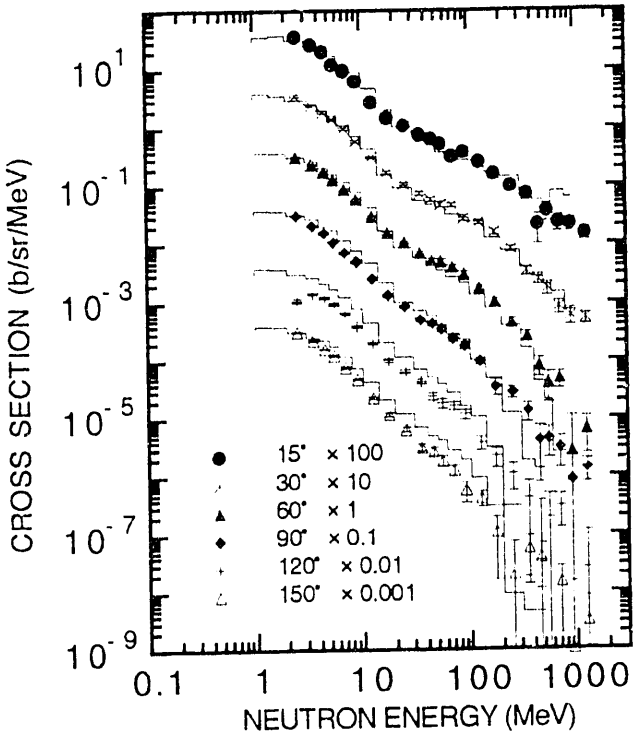

Fig. 11 Double differential cross section at 1.5 GeV for Pb. Lines show calculation results by HETC.

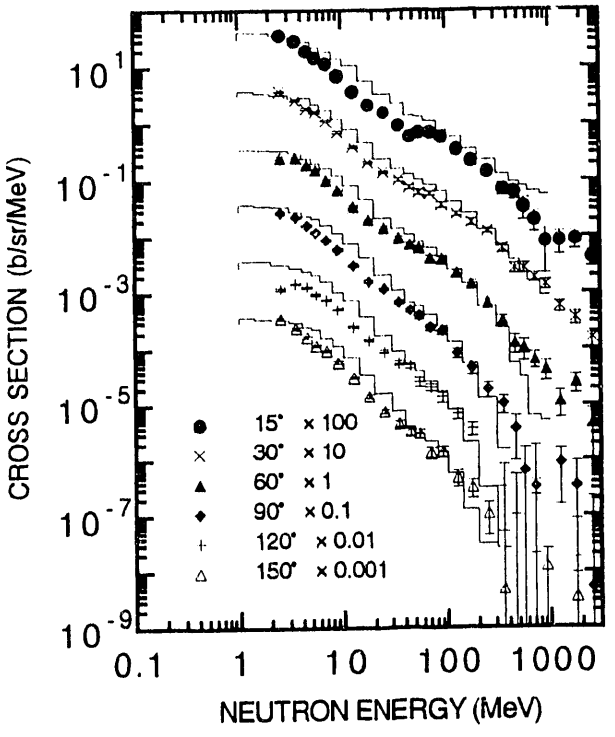

Fig. 12 Double differential cross section at 3.0 GeV for Pb. Lines show calculation results by HETC.

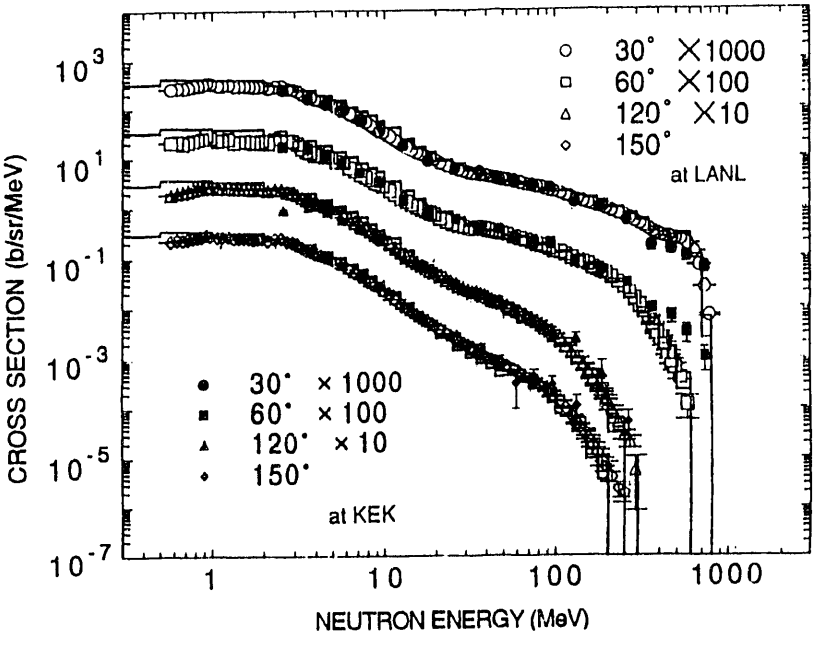

Fig. 13 Double differential cross section at 0.8 GeV for Pb, presented together with the results of LANL.

2.5 Topic 2

2.5.1 Collective Enhancement of Nuclear Level Density in the Frame of the Interacting Boson Model

Alberto Mengoni[1]

Department of Physics, Nuclear Data Center
Japan Atomic Energy Research Institute
319-11 Tokai-mura, Ibaraki-ken, Japan

Abstract. The Interacting Boson Model (IBM) has been applied to the calculation of the collective enhancement of nuclear level density. The problem of including collective excitations into the Fermi-Gas Model is reviewed. The technique for estimating the enhancement due to collective degrees of freedom is applied to the calculation of the level density of ^{238}U.

Introduction

The relations derived from the Fermi Gas Model are widely used for the calculation of the density of nuclear states at excitation energies ranging from a few MeV up to several tenths of MeV. In its simplest formalization, the FGM gives only very rough estimates of nuclear level densities. However, a certain number of improvements of the basic FGM have been proposed to cure it, for instance, for pairing effects and shell inhomogeneities. These effects are present in actual nuclei and it is unquestionably important to introduce them into the FGM description of nuclear states.

The derivation of simple expressions for the description of nuclear level density as a function of excitation energy has been worked out using different methods by many authors in the past (see for instance the textbook by Borh and Mottelson, 1969, and the recent paper by Engelbrecht and Engelbrecht, 1991) and certainly need not to be reported here. We will start our treatment with the basic relation, first derived by H. Bethe in 1936 (Bethe, 1936) which provides the density of states for a gas of non-interacting A nucleons, distributed over a uniform single-particle spectrum with spacing g_f

$$\rho(A,U) = \frac{1}{\sqrt{48}} \frac{1}{U} e^{2(aU)^{1/2}} \tag{1}$$

where

$$a = \frac{\pi^2}{6} g_f \tag{2}$$

is the only parameter to be evaluated and U is the excitation energy. If the gas is supposed to be composed of two species of nucleons, N neutrons and Z protons, the expression 1 becomes slightly

[1]Permanent address: ENEA, Ente per le Nuove tecnologie, l' Energia e l' Ambiente, Nuclear Data and Codes Laboratory, V.le G. B. Ercolani 8, 40138 Bologna, Italy.

more complicated. If, in addition, we want to consider nuclear *levels* instead of nuclear states, i.e. states of given angular momentum J and parity Π, then we have

$$\rho(N,Z,U,J,\Pi) = \frac{\sqrt{\pi}}{24\, a^{1/4}\, U^{5/4}}\, e^{2(aU)^{1/2}}\, \frac{(2J+1)}{\sigma^2\sqrt{2\pi\sigma^2}}\, e^{\frac{-J(J+1)}{2\sigma^2}} \cdot \frac{1}{2} \qquad (3)$$

where the factor 1/2 comes from assuming the same probability for each parity value. σ^2 is a spin cut-off factor whose expression can be given by

$$\sigma^2 = I_{rr}\, T, \qquad \text{with:} \quad I_{rr} = 0.0139 A^{5/3} \quad \text{and} \quad T = \sqrt{U/a}\,. \qquad (4)$$

In equation 4, I_{rr} is the momentum of inertia associated with a rigid-rotor and T is the nuclear temperature.

A rough, but effective estimation of the correction due to pairing correlations can be taken into account simply re-defining the excitation energy of the Fermi-Gas

$$U' = U - \Delta \qquad \text{with} \quad \Delta = \begin{cases} 2\times 12/\sqrt{A} & \text{for even nuclei} \\ 12/\sqrt{A} & \text{for odd-mass nuclei} \end{cases} \qquad (5)$$

and $\Delta = 0$ for odd Z - odd N nuclei.

Shell inhomogeneities can be introduced taking into account the bouncing of the single-particle spectrum on which the intrinsic states of the FGM are built. This procedure leads to an expression for the parameter a which depends on the excitation energy (Ignatyuk, 1975)

$$a(U) = a(*)\left[1 + \frac{\delta E_{sh}}{U}\left(1 - e^{-\gamma U}\right)\right] \qquad (6)$$

where δE_{sh} is the shell correction energy to the liquid-drop model for the mass-formula

$$\delta E_{sh} = M_{exp} - M_{ld} \qquad (7)$$

and γ a dumping parameter which can take that values $\gamma = 0.40 / A^{1/3}$ MeV^{-1} (Ignatyuk et al., 1979).

When applying this procedure, a systematic behavior of the parameter a as a function of the mass number can be derived.

We have used the experimental values of the level spacings of s-wave resonances, compiled by Mughabghab (Mughabghab, 1984) to evaluate the l.h.s. of equation 3. From that, at an excitation energy corresponding to the neutron binding, the parameter a can be derived for each nucleus. In figure 1 we show the systematics of the parameter $a(*)$ as defined in equation 6. As can be seen, this parameter does not exhibit the shell fluctuations, typically observed in the a-systematics. In other words, $a(*)$ represent a level density parameter opportunely corrected for shell effects.

An alternative procedure to treat shell effects has been proposed by Kataria, Ramamurthy and Kapoor (Kataria, Ramamurthy and Kapoor, 1978). The results obtained using that technique are altogether equivalent to the recipe of Ignatyuk.

Collective excitations

Collective degrees of freedom can be introduced into the FGM description making the following assumptions

i) the intrinsic (non-collective) degrees of freedom are decoupled from the collective excitation

modes

ii) every intrinsic state can be thought as a band-head of a discrete collective spectrum, similar to that of the ground state.

Within these assumptions, the density of states at excitation U can be written as (Maino, Mengoni and Ventura, 1990)

$$\rho(U) = \rho_i(U)\ Z_{coll}(\beta) \tag{8}$$

where

$$Z_{coll}(\beta) = \sum_c e^{-\beta E_c}\ , \qquad \text{with} \quad \beta = 1/T \tag{9}$$

is the definition of the collective enhancement factor, equal to the canonical partition function for the collective degrees of f dom of the system. In equation 8, ρ_i is the *intrinsic* level density that can be calculated, for instanc q the expression of equation 3.

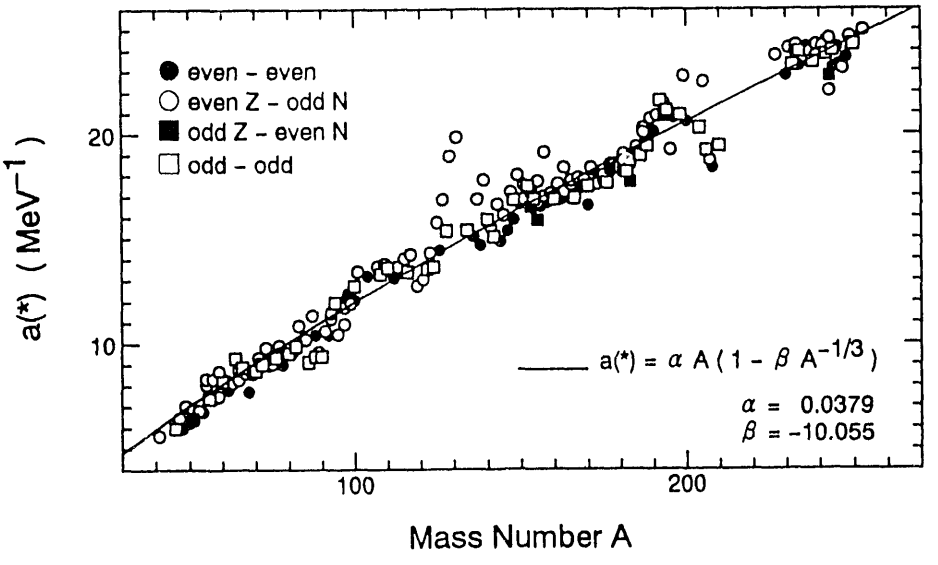

Fig. 1 Level density parameter a(*) versus the mass number A.

A first estimate of the collective enhancement factor can be made using *geometrical* models for the collective excitations (Ignatyuk, 1979, Rastopchin et al. 1988)

$$Z_{vib} = \exp\{1.7\,[\frac{\rho_0\, A^2}{\hbar^2\ \sigma_0}]^{2/3}\ r_0^{\,2}\ T^{4/3}\} \tag{10}$$

and

$$Z_{rot} = \begin{cases} 1 & \text{for spherical nuclei} \\ \sigma_\perp^2 & \text{for axi-symmetric deformed nuclei} \end{cases} \tag{11}$$

(see Rastopchin et al., 1990, for the definition of the parameters). Then,

$$Z_{coll}(U) = Z_{vib}(U) \cdot Z_{rot}(U) \tag{12}$$

However, using these prescriptions, some basic question remains unanswered. For instance, it is not clear what model has to be applied for transitional nuclei.

A possible way to answer to this question is to use the Interacting Boson Model (IBM) of Arima and Iachello. IBM describes the properties of even-even deformed medium-mass and heavy nuclei using algebraic methods, based on boson realizations of Lie algebras. A complete description of IBM is given by Iachello and Arima (Iachello and Arima, 1987). Using this model, a more realistic estimation of Z_{coll} can be derived.

IBM predictions for Z_{coll} : the ^{238}U case

Recently, we have applied the IBM for estimating the enhancement of the level densities due to collective excitations. We have, at first, studied the temperature dependence of Z_{coll} for the three dynamical symmetries of IBM (Maino, Mengoni and Ventura, 1990). Those correspond to the geometrical configurations, spherical vibrations: U(5) dynamical symmetry, axi-symmetric rotations: SU(3) dynamical symmetry and γ-unstable deformations: O(6) dynamical symmetry.

Successively, we have studied two transitional classes, for mass A ~ 150 and for mass A ~ 190 (Mengoni and Maino, 1992).

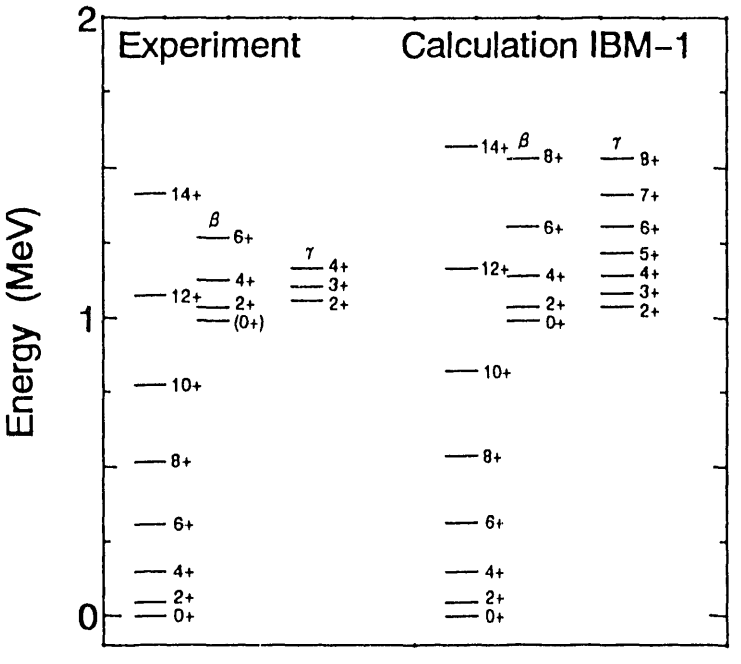

Fig. 2 Experimental and calculated spectrum of ^{238}U.

Here we would like to concentrate on a particular case: that of ^{238}U. This nucleus has collective properties that can be described by the SU(3) dynamical symmetry limit of IBM. Using this model, the IBM Hamiltonian can be written as

$$H = E_0 + \delta C^2_{SU(3)} + \gamma C^2_{O(3)} \qquad (13)$$

where E_0, δ and γ are constants and the C^2 are the Casimir invariants of the SU(3) and O(3) Lie groups respectively.

The energy spectrum generated by the Hamiltonian 13 can be calculated analytically using the expression

$$E(\lambda,\mu\ ;J\ ) = E_0 + \frac{2}{3}\delta\,(\lambda^2+\mu^2+\lambda\mu+3\lambda+3\mu\ ) + 2\gamma J(J+1) \qquad (14)$$

where the two quantum numbers λ,μ take values related to the total number of bosons N for the given nucleus under consideration. Since the parameter E_0 serves only to fix the ground-state energy position, there are essentially only two parameters to be determined from the experimental spectrum.

For ^{238}U we have: N=12 with δ = −10.79 KeV and γ = 3.74 KeV.

The calculated spectrum, as compared with the experimental one (Shurshikov , 1988) is given in figure 2.

As can be seen, the band structure is quite well reproduced. Only the low energy part of the whole spectrum is reproduced in figure 2. The collective states calculated using the IBM extends up to about 5 MeV.

The neutron binding energy of ^{238}U is S_n = 6.153 MeV, corresponding to a nuclear temperature T = 0.446 MeV. Using the expression

$$Z_{coll}(U) = \sum_c (2J+1)e^{-\frac{E_c}{T}} \qquad (15)$$

where c runs over all the collective states of the spectrum, we can estimate the collective enhancement to the nuclear level density. We have obtained

$$Z_{coll} = 43.1 \qquad (16)$$

including all the states.

We can compare the result obtained using the IBM with that obtained using the geometrical model, i.e. a rigid-rotor model. In this case we have that

$$Z_{coll} = \sigma_\perp^2 = I\cdot T = \begin{cases} 61.8\ (a) \\ 29.8\ (b) \end{cases} \qquad (17)$$

The two values, labelled a and b, are obtained as follows:

a) using I = 138.5 (in MeV^{-1} units) as from the relation $I = I_{rr}\ (1+1/3\,\varepsilon)$ where ε is the nuclear deformation of ^{238}U

b) using I = 66.8 (in units of MeV^{-1}) derived from the ground-state rotational band expression $E_{rot} = J(J+1)\ /\ 2I$.

It can be seen that IBM predicts a collective enhancement which is higher than the one calculated as in (b). This is to be expected because the band structure of the ^{238}U spectrum is much richer than the simple ground-state band (see figure 2). However, the magnitude of the collective enhancement factors for the total level density is comparable whether calculated with the geometrical models or with the IBM.

In order to see the dependence of Z_{coll} on the upper part of the collective spectrum, we can *cut* the spectrum at a given excitation energy, say E^*. The result of this procedure is shown in figure 3. It can be seen that, for 2 MeV ≤ E^* ≤ 5 MeV, the value of Z_{coll} remains practically constant.

We can also explore the effect of collective excitations on the nuclear level density at the neutron binding for selected values of the total angular momentum. In fact, at the neutron binding we have an experimental determination of the density of nuclear states of fixed spin and parity

$$<D_{exp}>^{l=0} = \frac{1}{\rho(U, J=I_0-1/2) + \rho(U, J=I_0+1/2)} = \frac{1}{\rho(U, J=0) + \rho(U, J=1)} \quad (18)$$

where I_0 = 1/2. Now, if we assume that $\rho(U,J) \sim (2J+1) \cdot \rho_0(U)$, we have that

$$<D_{th}>^{l=0} = \frac{1}{\rho_0 + 3\rho_0} \quad (19)$$

and, including collective effects

$$<D_{th}>^{l=0} = \frac{1}{Z_{coll}(J=0)\ \rho_0 + Z_{coll}(J=1)\ 3\rho_0} . \quad (20)$$

Using IBM we have that $Z_{coll}(J=1) = 1$. In fact, no J=1 states are present in the IBM−1, which is the model we have using all throughout the present analysis.

On the other hand, $Z_{coll}(J=0) = 1.14$ and therefore

$$<D_{th}>^{l=0} = \frac{1}{1.14\rho_0 + 3\rho_0} = 3.38\ eV. \quad (21)$$

This value has to be compared with the experimental value of 3.5 ± 0.8 eV (Mughabghab, 1984). Under the present circumstances, it is therefore impossible to detect the effect of enhancement due to collective degrees of freedom on states selected by $l=0$ neutrons (s-wave resonances).

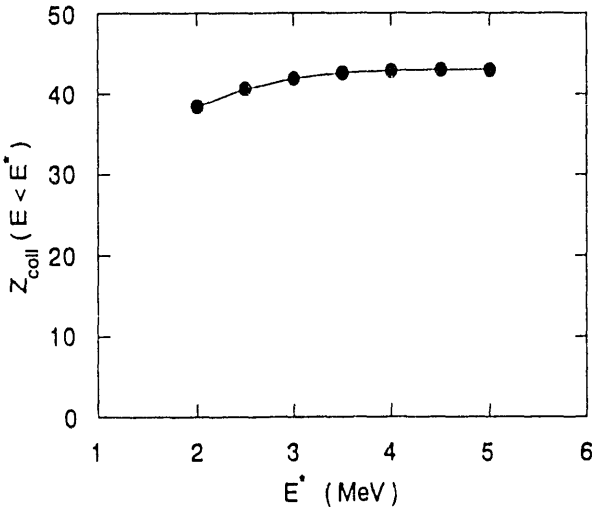

Fig. 3 Z_{coll} behavior with a cut-off energy E^*. See text for explanations.

For ^{238}U we have also studied the temperature dependence of the collective enhancement factor, calculated using different prescriptions. In figure 4, three sets of calculations are shown. The first one (empty dots in the figure), represents the calculation made using equation 15, including only the ground rotational band of the spectrum. The second set of calculations (triangles), has been made using the full IBM spectrum, with the parameters of the Hamiltonian 13, kept constant with the temperature. Finally, the third set (full dots) represents the calculations made allowing the number of bosons to change with the temperature (Maino, Mengoni and Ventura, 1990). The latter is the most

realistic technique, since it is clear that as the excitation energy increases, the chances of breaking nucleon-pairs (bosons) increases correspondingly and the number of bosons, N, decreases.

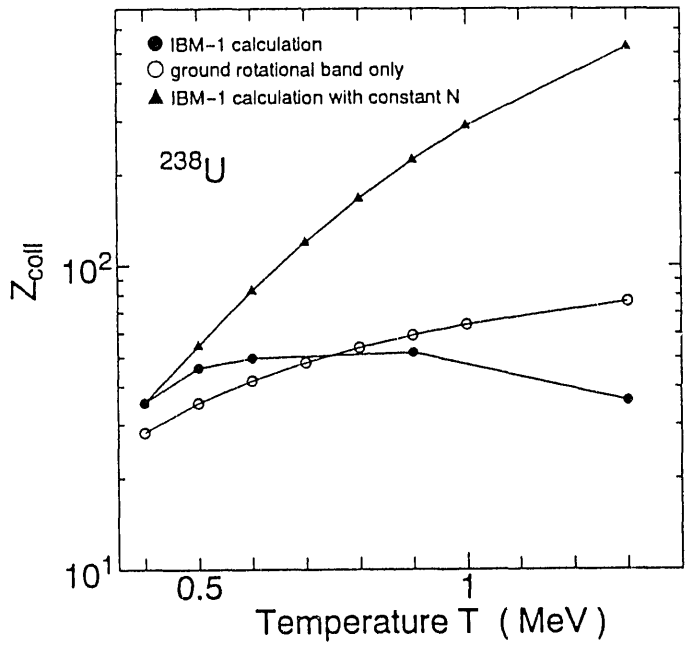

Fig. 4 Temperature dependence of the collective ehhancement factor Z_{coll}. See the text for explanations of the entries.

Discussion and conclusions

From the present analysis we can conclude that the enhancement of the nuclear level density due to collective excitations is considerable. Our calculations made using the IBM represent an improvement respec. to those made using conventional geometrical models. However, the order of magnitude of the calculations performed using IBM are comparable with those made using other models. From the analysis of the level density at excitation energies corresponding to the neutron separation energy, it is not possible to derive directly any conclusion on the entity of the collective enhancement. This is mainly due to the fact that the available experimental quantity is determined for selected values of the total angular momentum, J, whereas the calculations predict a strong enhancement on the *total* level density. An alternative way to check the validity of the theoretical calculations would be to make the analysis for nuclei whose parent target-isotope has a high spin. In fact, in this case the contribution due to collective excitations should be much more consistent, possibly leading to a clear separation between intrinsic and collective contributions. This kind of analysis is presently going on for the other Uranium isotopes that fulfill the mentioned requirements.

Acknowledgments

This work has been supported by the Commission of the European Communities, under the Science and Technology Fellowship Programme in Japan (EC-STFP 6). The hospitality offered by Japan Atomic Energy Research Institute, Nuclear Data Center is highly acknowledged.

References

Bethe, H., 1936, Phys. Rev. **50**, pag. 332.
Bohr, A., and Mottelson, B. R., 1969, *Nuclear Structure, Vol. I*, Benjiamin, New York.
Engelbrecht, C. A., and Engelbrecht, J. R., 1991, Ann. Phys. **207**, pag. 1.
Iachello, F. and Arima, A., 1987, *The Interacting Boson Model*, Cambridge University Press, Cambridge.
Ignatyuk, A. V., Istekov, K. K., and Smirenkin, G. N., 1979, Sov. J. Nucl. Phys. **24**, pag. 450.
Ignatyuk, A. V., Smirenkin, G. N.,and Tishin, A. S., 1975, Sov. J. Nucl. Phys. **21**, pag. 255.
Kataria, S. K., Ramamurthy, V. S., and Kapoor, S. S., 1978, Phys. Rev. **C18**, pag. 549.
Maino, G., Mengoni, A., and Ventura, A., 1990, Phys. Rev. **C42**, pag. 988.
Mengoni, A., and Maino, G., 1992 (in press), *Specialists' meeting on nuclear level densities*, Tokai-mura, Japan. Proceedings to be published by OECD.
Mughabghab, S. F., 1984, *Neutron Cross Sections*, Vol. 1-2, Academic Press, New York.
Rastopchin, E. M., Svirin, M. I., and Smirenkin, G. N., 1991, Sov. J. Nucl. Phys. **52**, pag. 799.
Shurshikov, E. N., 1988, Nuclear Data Sheets **53**, pag. 601

2.6 Nuclear Data Evaluation Methods

2.6.1 Integrated Nuclear Data Evaluation System: INDES

Tsuneo Nakagawa and Tokio Fukahori

Japan Atomic Energy Research Institute
Tokai-mura, Naka-gun, Ibaraki-ken 319-11

An Integrated Nuclear Data Evaluation System (INDES) is being developed. This system gives useful information on nuclear data to nuclear data evaluators, makes JCL and input data of theoretical calculation codes, recommends the most suitable set of codes for evaluation of certain nuclide, and processes output of the theoretical calculation codes. INDES consists of many interactive FORTRAN programs, and works on the JAEPI large computer system.

1. Introduction

The third version of Japanese evaluated nuclear data library, JENDL-3[1,2], was released in 1989 and its first revision in 1991. The evaluation of the nuclear data has been made for more than 300 nuclei. In this evaluation work, a lot of experiences on nuclear data evaluation were accumulated. For new evaluation work, these experiences will be quite useful. The Integrated Nuclear Data Evaluation System (INDES) is being developed in a large computer system at Japan Atomic Energy Research Institute (JAERI) in order to store such experiences of the evaluation and to support new evaluation work.

INDES consists of many interactive programs written in FORTRAN77. Each program in INDES is called as a segment. Parameters used for theoretical calculations for JENDL-3 are stored in a data file named "Evaluation Data File (EVLDF)". By using the information on EVLDF, input data for theoretical calculation codes can be set-up. Because of a long CPU time, theoretical calculations are suitable for batch jobs for a large computer. The input data made by INDES are written on a disk file with JCL and submitted to a main frame computer. Furthermore, INDES supplies useful information for nuclear data evaluation to the evaluators.

2. Structure of INDES

Figure 1 shows conceptional structure of a current version of INDES. The ROOT segment always stays in a core memory. Conversation between the evaluator and INDES is carried outthrough a character display terminal. A screen of the terminal is designed by using IPF which is a subroutine package for interactive programs. The screen design data (menu) are stored in a MENU file. Each segment selected by the evaluator is loaded from the INDES

load module file by a TSS command issued at the ROOT segment. Such commands are stored in procedure files.

In each segment, the evaluator can ask for meaning of input parameters. A HELP file stores answers to the questions from the evaluators. EVLDF provides parameters used in the theoretical calculation codes. Knowledge-bases are used in an evaluation guidance segment, ET[3]. They are a rule-base with rules for code selection, a frame which stores characteristics of the codes and two example-bases which store names of codes and energy ranges where the code was used for the post evaluation work.

Each user has to have a private information file named as INDES.INF which stores the user ID, names of a tentative parameter file, a JCL file, an ET work file, etc.

3. Evaluation Data File

The Evaluation Data File (EVLDF) stores the following parameters for theoretical calculation codes:

- Optical model parameters
- Level density Parameters
- Level scheme
- Deformation parameters
- Nuclide information such as mass excess, half-life, spin and parity of ground and meta-stable states

The format of EVLDF is similar to EXFOR. Figure 2 shows an example of level density parameters stored in EVLDF. Storing parameters used for the JENDL-3 evaluation is now in progress in Working Group on Databases for Nuclear Data Evaluation. Code names and energy ranges where the code was used are also stored. Therefore, the experiences of JENDL-3 can be accumulated in EVLDF. On the basis of EVLDF, an example-base of the evaluation is created and used as one of the knowledge-bases for ET.

4. Functions of INDES

Current functions installed in INDES are listed in Table 1. They are classified into information retrieval, parameter evaluation, code selection, JCL and input data set-up for theoretical calculation codes and post processing of results of the theoretical calculations. Segments developed so far are mainly for the information retrieval, code selection and JCL/input data set-up. Segments for other functions will be gradually completed.

4.1 Information Retrieval

(1) Evaluated Data

Many evaluated data such as JENDL, ENDF/B and JEF are stored in the JAERI computer system. Since they are stored in many separate files, an index file has been created

to store Z, A, and MAT numbers, library name, file name, etc. INDES shows the index data on a nuclide requested by the evaluator and makes a data retrievals.

(2) Experimental Data

Data in EXFOR are obtained from the NEA Data Bank and are stored in Neutron Data Storage and Retrieval System (NESTOR-2) after converting their format. The data are stored in index, numerical and comment files. The evaluator can get information on the existing data in NESTOR-2, and retrieve the data to a tentative data file.

(3) CINDA

By specifying some of atomic and mass numbers, quantity, laboratory, range of publication year, corresponding CINDA entries are shown on the screen. Figure 3 is an example of CINDA retrieval. The screen can be scrolled up and down by function keys.

(4) Level scheme

Evaluated Nuclear Structure Data File (ENSDF) can be treated in the LEVEL segment. Usually "ADOPTED LEVEL" sections are retrieved in the ENSDF format or numerical formats by specifying atomic and mass numbers. One of the numerical formats is the same as that of EVLDF. After small modification, they can be saved in the tentative parameter file and be used for input data of the theoretical calculation codes.

(5) Information on nuclei

The NUCLIDE segment shows mass-excess, abundance, half-life and particle separation energies.

(6) Q-values

The QVAL segment gives a list of reaction Q-values calculated from mass-excess data in EVLDF.

(7) Parameters in EVLDF

EVLDF stores several sets of certain parameter for certain nuclide. Therefore, the evaluator has to select one set of the parameters by using parameter retrieval segment GET. After the selection, the parameters are written on the tentative parameter file defined on INDES.INF, and any modification for the parameters is possible with a powerful EDIT function of the large computer.

4.2 Code Selection

The segment of ET (Evaluation Tutor)[3] is a guidance system for nuclear data evaluation. Knowledge engineering technology is adapted in the ET segment. First, the evaluator makes input on a target nuclide, an incident particle and an energy range. Then an inference engine

of ET makes a few questions to the evaluator according to a rule-base. On the basis of the answers to the questions and information in a frame and example-bases, the inference engine calculates certainty factors of recommendation for each code. Last of all, the ET segment recommends the code having the largest certainty factor for each reaction processes such as direct and compound processes.

The recommendations of the ET segment are displayed on the screen as shown in Figure 4. The parameters to be retrieved from EVLDF are listed in the first part of the screen. Segments for setting-up JCL and input data of the theoretical codes are listed below. If any character is given at the left-hand side of one of the recommendations, the GET segment or corresponding INDES segment is executed. In the usual use, the evaluator should execute the segments from the top to the bottom. Since auxiliary programs have not yet been provided enough at present, however, the flow of evaluation is not perfect.

4.3 JCL and Input Data Set-up

By specifying segment name on the ROOT segment screen or the output screen of the ET segment, a segment for JCL and input data set-up is started. The parameters needed to the theoretical code have to be retrieved and stored in the tentative parameter file defined in INDES.INF.

Figure 5 is an example of JCL and input data set-up for CASTHY[4] which calculates the total, elastic and inelastic scattering, and capture cross sections of neutron-induced reactions, and angular distributions of neutrons, and γ-ray production cross sections and spectra. Figure 5(a) is the first panel and in this example the evaluator specified only TITLE, NEN (number of energies), ENORML and SIGCAP (energy and capture cross section for normalization), COMPETING-SIG FILE (name of file for competing cross sections and its MAT and MT numbers) and OUTPUT FILE (name of output file and MAT number). Such parts are underlined in the figure. On the energy, the CASTHY segment has standard energy tables. In this example, the evaluator gave NEN=-1, then 46 standard energy points were displayed. After pushing an ENTER key of the terminal, all the data for input data are ready to output.

By pushing a function key of 9 or 21, the screen is changed to other panels. Figures 5(b), 5(c) and 5(d) show optical potential parameters, level density parameters and level scheme, respectively. These parameters were taken from the parameter files listed on the last line of each panel. In these panels, the evaluator can replace values of parameters or name of the parameter files.

If the evaluator gives a command of EXEC on the command line at any panels, JCL and input data are written on the JCL file defined in INDES.INF, and are shown in the screen by using EDIT of PFD (Programming Facility for Display user). The evaluator can submit the batch job by SUBMIT command to a main frame computer.

So far, segments have been provided are CASTHY, DWUCKY[5] which is a modified

version of DWUCK4[6], EGNASH2[5] which is a modified version of GNASH[7], and PEGASUS[8] which is a preequilibrium and multi-step evaporation code for threshold reactions. In the case of PEGASUS, since its CPU time is quite short, it is executed in interactive mode.

5. Conclusion

INDES is very useful to get information for nuclear data evaluation, and to make JCL and input data for theoretical calculation codes for nuclear data. However, INDES is just under development. Much more functions will be added to INDES.

We have to make more segments for JCL and input data set-up. Post-processing of calculated results is absolutely weak in the current version. The functions of format conversion of output to the ENDF format will be put as soon as possible for every theoretical calculation codes.

In future, we want to make graphs on the screen. If graphs are available, segments for parameter evaluation will be developed. By seeing the calculated results, the evaluator can make quick feed back to the calculation, and the results will be more reliable. Multi-window is also interesting function for INDES.

Acknowledgement

The authors would like to thank all the members of Working Group on Databases for Nuclear Data Evaluation for their helpful discussion on INDES.

References

1) Shibata K., Nakagawa T., Asami T., Fukahori T., Narita T., Chiba S., Mizumoto M., Hasegawa A., Kikuchi Y., Nakajima Y., and Igarasi S.: "Japanese Evaluated Nuclear Data Library, Version-3", JAERI 1319 (1990).
2) Kawai M., Iijima S., Nakagawa T., Nakajima Y., Sugi T., Watanabe T., Matsunobu H., Sasaki M., and Zukeran A.: J. Nucl. Sci. Technol., **29**, 195 (1992).
3) Fukahori T., and Nakagawa T.: "Prototype of Evaluation Guidance System in Integrated Nuclear Data Evaluation System", JAERI-M 92-027, p.214 (1992).
4) Igarasi S., and Fukahori T.: "Program CASTHY - Statistical Model Calculation for Neutron Cross Sections and Gamma Ray Spectrum", JAERI 1321 (1991).
5) Yamamuro N.: "A Nuclear Cross Section Calculation System with Simplified Input-format Version II (SINCROS-II)", JAERI-M 90-006 (1990).
6) Kunz P.D.: Univ. Colorado (1974).
7) Young P.G., and Auther E.D.: "GNASH: A Preequilibrium, Statistical Nuclear-Model Code for Calculation of Cross Sections and Emission Spectra", LA-6947 (1977).
8) Iijima S., Sugi T., Nakagawa T., and T. Nishigori: "Program PEGASUS, A Precompound and Multi-step Evaporation Theory Code for Neutron Threshold Cross Section Calculation", JAERI-M 87-025, p.337 (1987).

Table 1 Functions of current INDES

(1992 Dec. 18)

Segment	Functions
General	
SET	sets a private information file INDES.INF.
Information retrieval	
CINDA	lists CINDA entries.
EVLINF	shows information on evaluated data stored in JAERI large computer system. Retrieval of data is also possible.
EXPINF	shows the index file of NESTOR-2 (Neutron Data Storage and Retrieval System). The experimental data can be retrieved to a tentative data file.
GET	makes a tentative parameter file from EVLDF.
LEVEL	makes retrieval of data in ENSDF (Evaluated Nuclear Structure Data File).
NUCLIDE	gives information of nuclei (mass-excess, half-life, spin-parity, etc.)
QVAL	shows reaction Q-values.
Evaluation guidance system	
ET	recommends the most suitable set of theoretical calculation codes for certain nuclide and energy range.
JCL and input data set-up	
CASTHY	makes JCL and input data for CASTHY.
DWUCKY	makes JCL and input data for DWUCKY.
EGNASH	makes JCL and input data for EGNASH2.
PEGASUS	makes input data for PEGASUS, and execute PEGASUS in interactive mode.
Parameter evaluation	
ASREP	makes JCL and input data for ASREP which determines the unresolved resonance parameters so as to reproduce the given total, capture and fission cross sections.
LDP	an evaluation tool of level density parameters. The parameters for Gilbert-Cameron formula are determined on the basis of cumulative number of excited levels.
Post processing	
EVLCHK	checks evaluated data in the ENDF format. FIZCON, PSYCHE, CHECKR, etc. are executed in interactive mode.

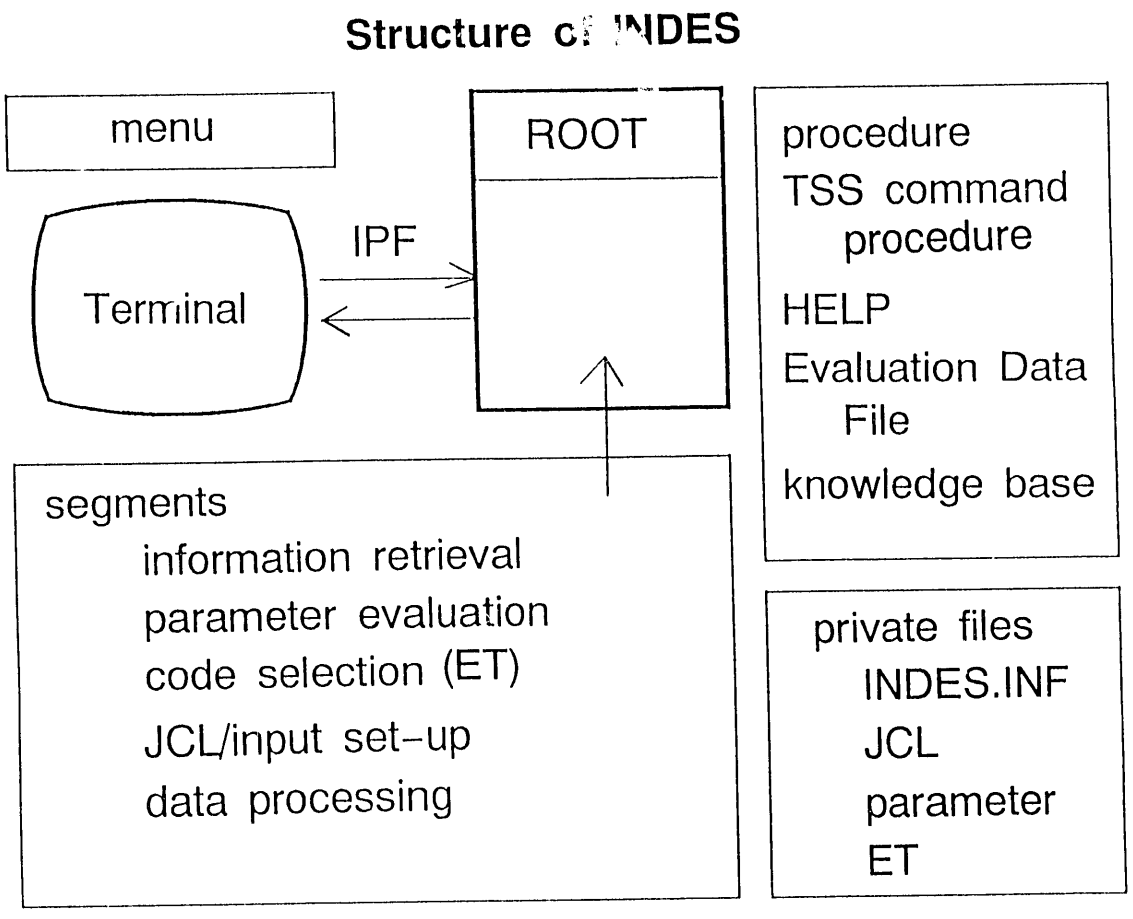

Fig. 1 Structure of INDES.

```
LDP
SET         J3FPLDP; FOR JENDL-3 FP NUCLEAR DATA
COMMENT     MAIN PART OF THIS LDP SET WAS DETERMINED BY JNDC FP NUCLEAR
            DATA WG FOR EVALUATION WORK OF JENDL-3 FP NUCLEAR DATA LIB.
            DATA FOR LIGHTER AND HEAVIER NUCLIDES THAN FP MASS REGION WERE
            ADDED.
            HISTORY
             1991-02 DATA WERE CONVERTED FROM PARAMETER FILE OF JOBSETTER.
FORMULA     GILBERT-CAMERON
SCOEF       0.142
DATA        A, T, PAIR, EX, SCF
0420910      1.1680E+01, 7.8200E-01, 1.2800E+00, 5.7702E+00, 5.0000E+00
0420920      1.0640E+01, 7.7700E-01, 2.2100E+00, 5.9383E+00, 1.3125E+01
0420930      1.1250E+01, 7.8000E-01, 1.2800E+00, 5.4568E+00, 5.0000E+00
0420940      1.3010E+01, 6.8500E-01, 2.0000E+00, 5.7695E+00, 7.7614E+00
0420950      1.3600E+01, 7.1500E-01, 1.2800E+00, 5.8351E+00, 6.1842E+00
0420960      1.4030E+01, 7.4100E-01, 2.4000E+00, 7.6451E+00, 7.6964E+00
0420970      1.5170E+01, 6.8000E-01, 1.2800E+00, 6.0358E+00, 7.0750E+00
0420980      1.5940E+01, 6.9000E-01, 2.5700E+00, 7.8876E+00, 5.2917E+00
0420990      1.7740E+01, 6.2000E-01, 1.2800E+00, 6.0582E+00, 2.8750E+00
ENDDATA
ENDSET
ENDLDP
```

Fig. 2 Example of EVLDF. This example shows a part of level density parameters used for the evaluation of data of fission product nuclei.

```
.......................... < C I N D A > ..............................
118 ENTRIES FOUND.
ATOMIC NUMBER => TC          ENERGY RANGE(EV) =>
MASS NUMBER ===> 99          YEAR RANGE =======>
QUANTITY   ====> NG          FIRST AUTHOR =====>
LABORATORY ====>

NUCLIDE = TC- 99   QUANTITY = (N,GAMMA)
  ENERGY    LAB  TYPE    REFERENCE     YR    AUTHOR AND COMMENT
---------------------- ------------------------------------------------------
FAST         RCN REVW-R ECN-176         85 JANSSEN¦ COMPARISON OF INTEG VALUES
5.013 1.015 ORL EXPT-J AJ   313   808 87 WINTERS¦ TBL. MAXW. AVG. SIG.
2.713 2.016          J NSE   81 4 520 82 MACKLIN. TBL, GRPH CFD EVALS.
NDG                  R DOE-NDC-43 144 87 WINTERS¦ASTRON. ASTROPHYS. TBP.
5.013 1.015          R DOE-NDC-38 140 86 WINTERS¦ CS(30KEV)=782¦-39MB.
2.713 2.016          P DOE-NDC-27 110 82 MACKLIN. AGREES ENDF ABOVE 900 KEV.
NDG                  R ORNL-5787  176 81 MACKLIN¦ TBD
NDG                  P DOE-NDC-24 120 81 MACKLIN. CAPT CS MEAS TBD. NDG.
3.013 1.914          4 EXFOR12753.002 82 .31 PTS.  AV SIGMA.
1.013 1.016 FEI EVAL-J YK  1987 1   3 87 IGNATYUK¦ SIG(E), EXPTS, EVAL, GRPH, CFD
2.5-2       IAE EVAL-B OKAMOTO    199 87 GRYNTAKIS¦. ACTIV. TBL:2200 M/S SIG
1.014 5.014 KFK EVAL-J AND   36   411 87 BAO¦ GRPH, TBL. 30 KEV MAXW. AVG. SIG.
2.5-2       JAE REVW-S IAEA-491    94 89 ISHIGURO¦. DISCREP:TBL DATA FILES CFD
  PF1, PF18 = 'UP', PF2, PF21 = 'DOWN', PF3, PF15 = 'STOP'
```

Fig. 3 Example of CINDA retrieval.

```
                <<CODE SELECTION ACCORDING TO E.T.>>

COMMAND ==>

S      CODE      PURPOSE   CERTAINTY FACTOR, ETC.                    STATUS
-      --------  --------- ----------------------------------------- ------
       GET       NUCLIDE      430990    431000
       GET       LDP          430990    431000
       GET       LEVEL        410000    430990
       GET       OMP          430990    430990
       GET       DEFORM       430990    430990
       DWUCKY    DIRECT      0.52901
       PEGASUS   PRECOMP     0.81306
       CASTHY2   COMPOUND    0.99012
       CTOB      COMPILE
       ELIESE3   #PEGASUS

  ENTER ANY CHARACTER AT LEFT SIDE OF CODE NAME
```

Fig. 4 Output of the evaluation guidance system ET.

```
                    << CASTHY PANEL-1 >>
                                          PF9/PF21 : CHANGE SCREEN
COMMAND ===>
TARGET ==== 43099        TITLE = TC-99 CASTHY RUN
NEN= 46          OUTPUT OPTION = 11
EN =  1.00-6 3.00-6 1.00-5 3.00-5 1.00-4 3.00-4 1.00-3 2.00-3 3.00-3 5.00-3
   =  8.00-3 1.00-2  0.015  0.020  0.025  0.030  0.050  0.080  0.100  0.150
   =    0.200  0.250  0.300  0.500  0.700  0.800  0.900  1.000  1.250  1.500
   =    1.750  2.000  3.000  4.000  5.000  6.000  7.000  8.000  9.000 10.000
   =   12.000 14 000 15.000 16.000 18.000 20.000
NFLCR = -110
ENORML= 1.00000-1 SIGCAP= 3.8000012 ERROR  =  1.00000-2
T-GAM =  0.0      D-OBS =  0.0       G-WIDTH=  0.0
NPROF = 1
P11   =  0.0      P12   =  0.0
ER    =  0.0      WIDTH =  0.0       EXCHNG =  0.400000
ER2   =  0.0      WIDTH2=  0.0       SIGBM1 =  0.0       SIGBM2=  0.0
COMPETING-SIG FILE = J2608.J3TC099.DATA(PEGOUT)      MAT= 4399  MT= 999
MASS EXCESS FILE === J2608.PP.DATA(NUCLIDE)
OMP FILE =========== J2608.PP.DATA(OMP)
LDP FILE =========== J2608.PP.DATA(LDP)
LEVEL SCHEME ======= J2608.PP.DATA(LEVEL)
OUTPUT FILE ======== J2608.OUT1.DATA                 MAT= 4399
JCL FILE =========== J2608.JCLFILE.CNTL
```

Fig. 5(a) The first panel of the CASTHY segment.

```
                    << CASTHY PANEL-2(OMP) >>
                                          PF9/PF21 : CHANGE SCREEN
 COMMAND ===>

 TARGET   = 43099

<POTENTIAL DEPTH>
              CONTS.       E          E*2         SYMMETRIC
  REAL TERM =  4.7500011   0.0         0.0          0.0
  VOLUME    =  0.0         0.0         0.0
  SURFACE   =  9.740000    0.0         0.0         SQRT TERM=  0.0
  SPIN-ORBIT=  7.000000    0.0         0.0
  IM.(S-O)  =  0.0         0.0         0.0

<FORM FACTOR>
              RADIUS     DIFFUSENESS    TYPE
  REAL TERM =  1.291010    0.620000     WS
  VOLUME    =  0.0         0.0          NO          DWS: DER.WOOD-SAXON
  SURFACE   =  1.425445    0.350000     DWS         WS : WOOD-SAXON
  SPIN-ORBIT=  1.290513    0.620000                 G  : GAUSS

 OMP FILE =========== J2608.PP.DATA(OMP)
```

Fig. 5(b) The second panel of the CASTHY segment.
Optical model parameters are listed.

```
                    << CASTHY PANEL-3(LDP) >>
                                        PF9/PF21 : CHANGE SCREEN
 COMMAND ===>

 TARGET    = 43099

                          TARGET          COMPOUND
              A PARAMETES =  1.6000011      1.6370011
  SPIN CUT-OFF PARAMETER =  0.0             0.0
         PAIRING ENERGY  =  1.290000        0.0
                      C0 =  0.0             0.0
            JOINT ENERGY =  5.983700        3.635400
             TEMPERATURE =  0.655000        0.585000
                CONSTANT =  2.973426        1.1893911
     SPIN CUT-OFF FACTOR =  7.900000        5.000000
     FORM OF TEMPERATURE =     1               1
    FORM OF SPIN CUT-OFF =     2               2

 LDP FILE ========== J2608.PP.DATA(LDP)
```

Fig. 5(c) The third panel of the CASTHY segment. Level density parameters.

```
                  << CASTHY PANEL-4(LEVEL SCHEME) >>
                                        PF9/PF21 : CHANGE SCREEN
 COMMAND ===>
 TARGET    = 43099

NO  ENERGY    SPIN-PRTY  NO  ENERGY    SPIN-PRTY  NO  ENERGY    SPIN-PRTY
GS  0.0         4.5  1   15                        30
 1  0.140508    3.5  1   16                        31
 2  0.142630    0.5 -1   17                        32
 3  0.181070    2.5  1   18                        33
 4  0.509100    1.5 -1   19                        34
 5  0.534300    2.5 -1   20                        35
 6  0.625400    3.5  1   21                        36
 7  0.671500    2.5 -1   22                        37
 8  0.726300    5.5  1   23                        38
 9  0.761600    2.5  1   24                        39
10  0.762000    6.5  1   25                        40
11  0.900000   -1.0  0   26                        41
12                       27                        42
13                       28                        43
14                       29                        44

 LEVEL DATA FILE ==== J2608.PP.DATA(LEVEL)
```

Fig. 5(d) The fourth panel of the CASTHY segment. Level scheme.

2.6.2 Methods of Covariance Generation for Nuclear Data

Y. Kanda

Department of Energy Conversion Engineering,
Kyushu University,
Kasuga, Fukuoka, 816, Japan

Abstract, Covariances for evaluated cross sections are generated with the methods based on the uncertainties of experimental data or estimated by combining experimental and theoretical information. The former methods are in principle preferred but are limited in application because of lack of experimental information. The latter methods are available in many cases. However, they have been generated with the procedures which are adopted by individual evaluators as to adapt to their understanding for covariances. The values of the estimated covariances which decisively depend on the adopted procedures are too different at every evaluation to be agree by other evaluators and be accepted by users of them. In order to arrive at an agreement about the definitive understanding of the covariance generation we must discuss on this problem. It is another problem to solve the one mentioned above that the method to visualize the covariance must be developed to quantitatively compare it with the other.

Covariance matrices for evaluated nuclear data are inevitably required to give information on uncertainties or reliabilities of the evaluated data. As primarily the nuclear data are the physical constants the measured and evaluated values for them should finally converge to the true values. They, however, can not be known by us but be expressed as some ones inferred from measurements, which naturally involve experimental uncertainties. These are the origin of errors for measurements and then covariances for evaluated data. The uncertainties estimated in experiments strongly depend on their conditions i.e. used methods, techniques, apparatuses, data procedure, correction, and even experimentalists

themselves. Although the values measured as the nuclear data similarly depend on them, they are determined from acquired data recording nuclear events. If the experiment was not mistake it would give a reasonable outcome apart from the amount of the uncertainty. Even if the experimental results are reasonable in the procedures there are no guarantee that they are right. Experimenters thoroughly understand it and always make corrections and estimate uncertainties for the data. Their dependencies on the experimental condition, however, are not clear. If they are clear the experimenters can improve them in their procedures. Therefore, they can correct their data and estimate the uncertainties for them on the assumptions about the experimental conditions. The correction factors are usually not so large that they are outside in our discussion, though the measurements having too large correction factors are not reasonable and reliable. The uncertainties presented for the experimental data play a main role in our discussion.

The covariance generation for nuclear data is desired in their application field but it has not been filled by the evaluation group. There is a few reasons. One of the most possible one is that a useful method to generate covariances is not available. A few methods has been developed and reveral covariances have been produced for many nuclear data. The covariances generated from various method for the same nuclear data are too different to discuss the dependency on the method.

A problem in development of the method for the covariance generation is that there is no method to visualize and compare quantitatively them. Evaluated cross sections can be visualized to draw curves and compare quantitatively their values at the same energy. The covariance is usually visualized with a bird's-eye view. Comparison of two bird's-eye views can not give us any quantitative information. Such a situation hinder the development of the covariance generation method and then the covariance evaluation for nuclear data.

The Covariances for nuclear data are generated from experimental uncertainties which are ambiguous as mentioned above. The estimated covariances depend on the evaluator's understanding for the uncertainties. If there is a sufficient set of measurements for the nuclear data to be evaluated the results which are not so different by the evaluators are expected. However, it is not sure because individual evaluators possibly postulate different correlation factors for components of experimental uncertainties. It may be avoided if the

experimental himself gives the correlation factors for his data. Even for this case, the different covariance can be produced by the evaluator who does not agree with the experimenter's understanding for the correlation.

When the evaluation is performed with theoretical calculation the covariances strongly depend on the evaluators. It was reviewed and discussed in detail in two papers presented at NEANSC Specialists' meeting [1] and Symposium on Nuclear Data Methodology [2] in the last October. As the description will be duplicate with them they are not presented here.

In order to develop usable and reliable methods to generate the evaluated covariances, the evaluators must discuss and then reach the agreement on the understanding of the experimental uncertainties and their treatment. At present, mathematical formulation on the covariance is developed enough to calculate it without ambiguity if the input data mentioned above are prepared on the basis of the physically agreeable understand. The mathematical method has been too ahead of the handling of the experimental uncertainty. The evaluators has been disturbed with this situation. Another reason for it is impossibility of the quantitative comparison for the evaluated covariances.

The values of the estimated covariances which decisively depend on the adopted procedures are too different at every evaluation to be agree by other evaluators and be accepted by users of them. In order to arrive at an agreement about the definitive understanding of the covariance generation we must discuss on this problem. It is another problem to solve the one mentioned above that the method to visualize the covariance must be developed to quantitatively compare it with the other.

References

1. Y.Kanda, "Generation of Covariance Data from Combined Experimental and Theoretical Data", *NEANSC Specialists' Meeting on Evaluation and processing of Covariance Data*, 7-9 Oct. 1992, Oak Ridge, USA.
2. Y.Kanda, "Determination of Covariance of Calculated Cross Sections", in Symposium on Nuclear Data Evaluation Methodology 12-16 Oct. 1992, Brookhaven National Laboratory, Upton, New York, USA.

2.7 Topic 3

2.7.1 Symmetry Violations under Space Reflection and Time Reversal and Neutron Spin

Y. Masuda

National Laboratory for High Energy Physics, 1-1 Oho Tsukuba-shi, 305 Japan

P- and *T*-violation effects in polarized neutron transmission through a polarized nuclear target are discussed. Namely, *P*-violating neutron-spin rotation due to a $\sigma \cdot \boldsymbol{k}$ correlation and *T*-violating neutron-spin-flip process due to a $\sigma \cdot (\boldsymbol{I} \times \boldsymbol{k})$ correlation are discussed. The measurements of these effects are conducted at KEK. The polarization of ^{3}He nuclear spin was developed as a neutron-spin analyzer for these measurements. An apparatus to convert the spin-rotation angle to the projection angle on the magnetic field was developed by using the Meissner effect. This apparatus is found to be quite useful for the neutron-spin control in the *T*-violation experiment as well as the measurement of the *P*-violating neutron-spin rotation.

I. Introduction

The particle spin has been used as a probe to detect symmetry violation under space reflection and time reversal in fundamental interactions, since the spin has different transformation under these operations than the position vector and the linear momentum. The neutron spin plays an important role in a symmetry-violation test on the neutron-nucleus interaction.

The neutron propagates through matter quite easily due to its chargeless property. The interaction with matter, namely strong and weak interactions with nuclei as well as magnetic interactions in some medium, results in the phase shift of a transmitted neutron plane-wave. The phase shift is described in terms of the forward scattering amplitude, $f(0)$, atomic number density, ρ and neutron propagation length, l as

$$\delta = \lambda \rho l f(0), \qquad (1)$$

where, λ is the neutron wavelength.[1] The forward scattering amplitude is represented in terms of scalar products between the spin and the linear momentum, which are invariant under space rotation. If the target nuclear spin, $\boldsymbol{I}$ is in the x axis and the neutron momentum, $\boldsymbol{k}$ in the z axis, then the vector product, $\boldsymbol{k} \times \boldsymbol{I}$ is in the y axis. In general, the forward scattering amplitude of a spin 1/2 particle is represented in terms of Pauli spin matrices as[2]

$$f(0) = F_0 + F_1 \sigma_x + F_2 \sigma_y + F_3 \sigma_z$$
$$= F_0 + F_1 \sigma \cdot \hat{I} + F_2 \sigma \cdot (\hat{k} \times \hat{I}) + F_3 \sigma \cdot \hat{k}. \quad (2)$$

F_0 is well-known coherent scattering amplitude. F_1 is spin-incoherent scattering amplitude, which is due to the spin dependence of the nuclear force. The real part of F_1 induces neutron-spin rotation around the nuclear spin. The rotation is known as "pseudomagnetic precession". The imaginary part induces the neutron-spin dependence of the capture cross-section, which is known as the "polarization cross-section". If the nuclear spin is polarized in the direction of the static magnetic field, Larmor precession is also included in the real part of F_1. F_3 is a P-odd term. In low energy neutron-transmission, a dominant contribution to the F_3 term comes from parity mixing between the p- and s-wave resonances of the neutron-nucleus reaction. In recent experiments, a very large enhancement was found in the neutron-helicity dependence of the p-wave resonance cross-section.[3,4,5,6] The largest enhancement was found in the p-wave resonance of ^{139}La. The value is large as 10^6. The helicity dependence is induced by the imaginary part of F_3. The real part induces neutron-spin rotation around the neutron momentum. Although an experiment was carried out in cold-neutron region,[7] no experiment was conducted in the resonance region. F_2 is the P- and T-violation term which is due to the imaginary part of the parity-mixing matrix-element between the p - and s-wave resonances. The F_2 term induces asymmetry in spin-flip probabilities in time-reversed processes. The asymmetry is defined as being a spin detailed-balance, A_{spin}. The F_2 term also induces asymmetry in transmission for parallel and antiparallel neutron spins with respect to the $\boldsymbol{k} \times \boldsymbol{I}$ direction and neutron polarization in the $\boldsymbol{k} \times \boldsymbol{I}$ direction during transmission.

Here, we discuss a method to detect the F_2 and F_3 terms. The measurement of the F_2 term has three prominent features as the T-violation experiment. Firstly, the experiment is free from final-state interactions, since the final state of the neutron is represented by the same plane-wave as the initial state in neutron transmission. Secondly, the ratio of F_2 and F_3 terms is free from the uncertainty of the nuclear wave-function.[8] Thirdly, a large enhancement is expected. Among the three effects of the F_2 term, we discuss the spin detailed-balance. We also discuss a method to measure the real part of the F_3 term in the p-wave resonance which is indispensable for the theoretical explanation of the very large P-violation effect in the p-wave resonance and in the estimation of the spin detailed-balance.

II. Spin detailed-balance and P-violating neutron-spin rotation

The value of the spin detailed-balance is described in terms of the phase shift δ. The incident neutron plane-wave, ψ_i transforms after transmission as

$$\psi_f = exp(\delta)\ \psi_i. \quad (3)$$

The spin-flip probabilities are obtained as

$$\sigma(\uparrow - \downarrow) = \mathrm{Tr}(F \cdot (1 + \sigma_z)/2 \cdot F^{+} \cdot (1 - \sigma_z)/2) \quad (4)$$

and

$$\sigma(\downarrow-\uparrow) = \mathrm{Tr}(F \cdot (1 - \sigma_z)/2 \cdot F^{+} \cdot (1 + \sigma_z)/2). \quad (5)$$

Here, F is

$$F = exp(\delta), \quad (6)$$

$\sigma(\uparrow-\downarrow)$ and $\sigma(\downarrow-\uparrow)$ are the spin-flip probabilities for up to down and down to up in the direction of the beam, respectively. After a simple calculation, the spin detailed-balance is obtained as

$$\begin{aligned} A_{spin} &= \{\sigma(\uparrow-\downarrow) - \sigma(\downarrow-\uparrow)\} / \{\sigma(\uparrow-\downarrow) + \sigma(\downarrow-\uparrow)\}. \\ &= 2(\mathrm{Im}(\lambda\rho l \cdot F_1) \cdot \mathrm{Re}(\lambda\rho l \cdot F_2) - \mathrm{Re}(\lambda\rho l \cdot F_1) \cdot \mathrm{Im}(\lambda\rho l \cdot F_2)) \\ &\quad / |\lambda\rho l \cdot F_1|^2. \end{aligned} \quad (7)$$

The spin detailed-balance is proportional to the T-odd term. $|\lambda\rho l \cdot F_1|^2$ is the T-invariant spin-flip probability. The value of the T-invariant spin-flip probability can be reduced by adjusting the magnetic field strength so that the pseudomagnetic and the Larmor precessions are canceled by each other. If the value of $|\lambda\rho l \cdot F_1|^2$ is reduced to 1% by the cancellation of the Larmor and pseudomagnetic precessions, the value of A_{spin} is obtained as

$$A_{spin} \sim 0.2\eta \cdot P_I \quad (8)$$

around the p-wave resonance of ^{139}La after a simple calculation; η is the ratio of F_2 to F_3 term; P_I is the nuclear polarization.[9] The value of $\lambda\rho l$ is assumed to be 2.4 x 10^{14} cm^{-1}. For the cancellation, we need to measure neutron-spin rotation precisely.

In the derivation of the value of A_{spin} , we assume the F_2 term is proportional to the F_3 term[7] and use the value of F_3 in the p-wave resonance. We have the experimental value of the imaginary part of the F_3 term in the p-wave resonance. For the real part, however, we have experimental value only at λ = 7 A. We used a theoretical extrapolation for the real part in the p-wave resonance.

The value of F_3 is obtained by a measurement of the neutron-spin rotation around the momentum axis. The rotation angle, θ_W, is represented in terms of helicity dependent phase shifts as the following.

$$\begin{aligned} \theta_W &= \delta(+) - \delta(-) \\ &= 2\lambda\rho l \cdot \mathrm{Re}(F_3) . \end{aligned} \quad (9)$$

Here, $\delta(+)$ and $\delta(-)$ are phase shifts for positive and negative neutron-helicity states, respectively.

III. Measurement of neutron-spin rotation

We developed a method to measure the neutron-spin rotation in the target region by using a polarized ^{3}He filter. The experimental arrangement is shown in Fig. 1. The neutron spin is polarized upon passage through the polarized proton filter. The neutron polarization is guided to a superconducting box following an adiabatic passage.[10] For the adiabatic passage, we used a magnet system, which

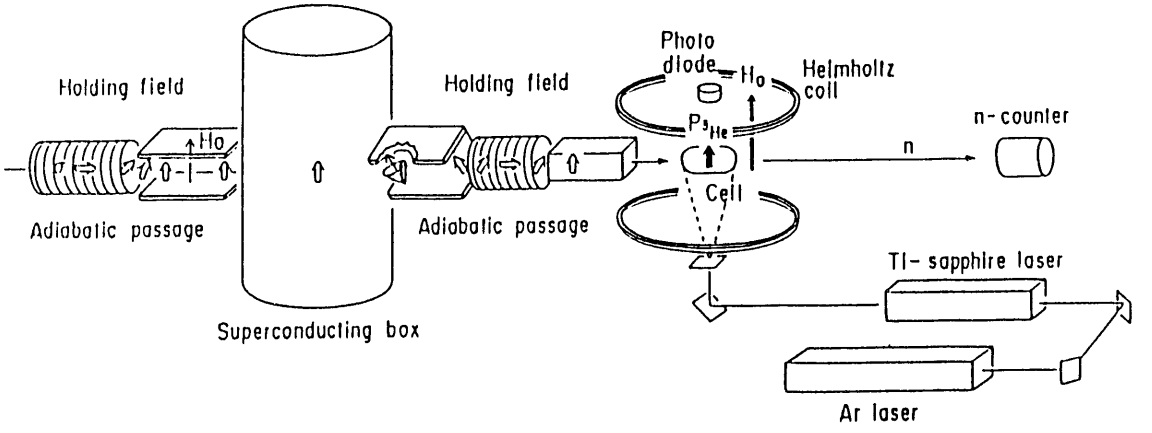

Fig. 1 Measurement of the neutron spin direction.

comprised a solenoid and a transverse dipole magnet for neutron-spin folding. The magnetic field direction is rotated from the longitudinal to transverse direction before entering into the superconducting box. The magnetic field in the superconducting box is separated from the outside. The neutron spin passes through a superconducting sheet non-adiabatically, namely the neutron spin enters into the box without any change in its direction. If the magnetic field inside the box is zero, the neutron spin travels without rotation. After traveling through the box, the neutron spin enters into another transverse magnet set downstream. If the downstream magnetic field is rotated with respect to the upstream magnetic field by θ, the projection angle of the neutron spin is θ, since the neuron spin passes through the superconducting sheet non-adiabatically. As a result, the $\cos\theta$ component of the incident neutron polarization is held and guided to the polarized ^{3}He filter following an adiabatic passage.

The ^{3}He spin was polarized by an optical pumping, which is also shown in Fig. 1. An alminosilicate glass cell was filled with 3-atm ^{3}He gas, 100-torr nitrogen gas and a small amount of rubidium droplet. The ^{3}He cell was mounted in a 40-G Helmholtz coil. Inhomogeneity of the magnetic field was less than 10^{-3} in the ^{3}He cell. The cell was heated up to 180^o in order to obtain a rubidium atomic number density of 4×10^{14}/cm^3. The value is suitable for the optical pumping.[11,12] The linear polarization of light from a 4-W Ti-Sapphire laser system was transformed into circular polarization by placing a $1/4\lambda$ plate in the laser beamline. The wavelength of the laser beam was 795 nm, which correspond to the D1 resonant light of the rubidium atom. The photon spin polarization is transferred to the rubidium atomic spin upon absorption of the D1 resonant light. As a result the rubidium atom is polarized. The rubidium atomic polarization is transferred to the ^{3}He nuclear spin by a spin-exchange hyperfine interaction during an atomic collision. The spin exchange rate (γ_{se}) is ~1/10 hour^{-1} at 180^{o}c.

^{3}He polarization was obtained by using a polarized neutron transmission. The ^{3}He nucleus has a large capture-cross-section for the neutron. For example, the value of the cross section is σ = 1000 b at E_n = 0.7 eV. The capture process is a resonance reaction of ^{3}He(n,p)t at E_0 = -518 keV with a resonance width of Γ = 1158 keV. The spin of the resonance state is J = 0.[13] In the resonance, the neutron spin

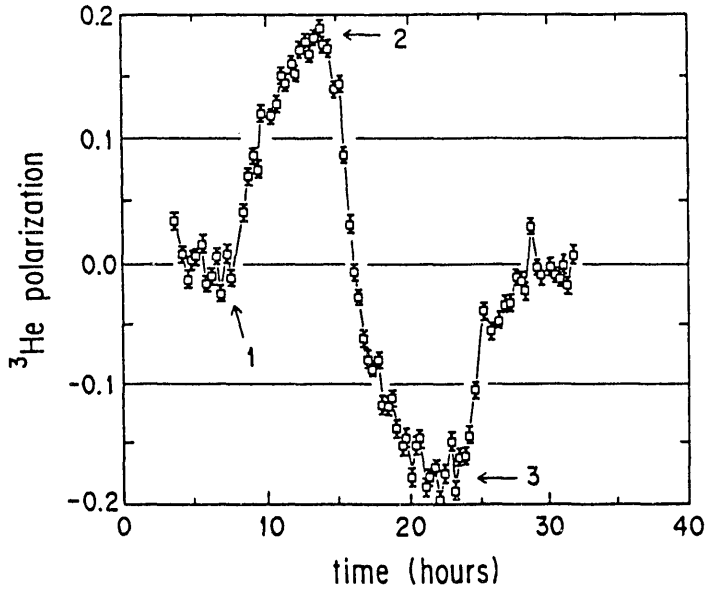

Fig. 2 ^{3}He nuclear polarization.

couples with the ^{3}He spin antiparallel. Neutrons of the same spin direction as the ^{3}He spin are not absorbed. As a result, the neutron transmittance is given by

$$T_n(\pm) = exp(-N\sigma t(1 \mp P_{^3He})). \quad (9)$$

The upper and lower signs refer to the transmittances for neutrons in parallel and antiparallel spin states, respectively. N is the atomic number density of ^{3}He and t the thickness of the polarized ^{3}He filter. $P_{^3He}$ is the ^{3}He polarization.

We set the rotation angle of the downstream transverse-magnet at $\theta = 0^o$. The neutron spin propagated through the superconducting box without changing the projection component on the magnetic field and entered the transverse magnetic field of the Helmholtz coil. Transmitted neutrons through the polarized ^{3}He filter were detected by a ^{10}B-loaded liquid scintillator. A typical result of the neutron transmission is shown in Fig. 2. At point 1, the laser beam was switched on and ^{3}He nuclei were polarized in the same direction as the incident neutron polarization. The transmittance of the ^{3}He filter increased as the ^{3}He polarization built up. The time constant of the polarization evolution is determined by the spin-exchange rate, γ_{se} as well as the ^{3}He-polarization relaxation rate. At point 2, the circular polarization was reversed and the ^{3}He-polarization built up in the opposite direction. As a result, the ^{3}He transmittance decreased. At point 3, the laser power was switched off, then the ^{3}He-polarization relaxation was observed. The relaxation rate is almost determined by a collision with a paramagnetic center on the glass wall. A typical value of the relaxation rate was Γ_w = 1/14 hour^{-1}. We obtained the ^{3}He polarization by the results of the neutron transmission. The value of the polarization is written on the vertical axis in Fig. 2. The present maximum ^{3}He polarization was 50% at a ^{3}He pressure of 3 atm. The cell size was 25 mm in diameter and 40 mm in length.

Now we can use the polarized ^{3}He filter as a neutron-spin analyzer. We

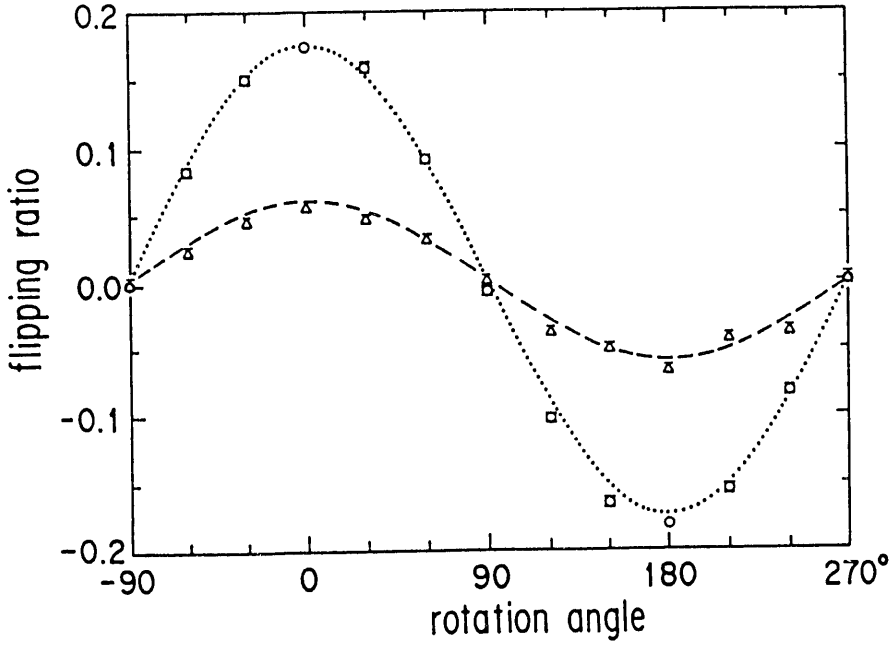

Fig. 3 Result of the neutron spin direction measurement.

measured the neutron transmission through the polarized ^{3}He filter as a function of the rotation angle, θ. In the measurement, the incident neutron polarization was flipped every 4 sec. A flipping ratio, which is defined as

$$R = (T_+ - T_-) / (T_+ + T_-) = P_n \cos\theta \tanh(N\sigma t P_{^3He}) \quad (10)$$

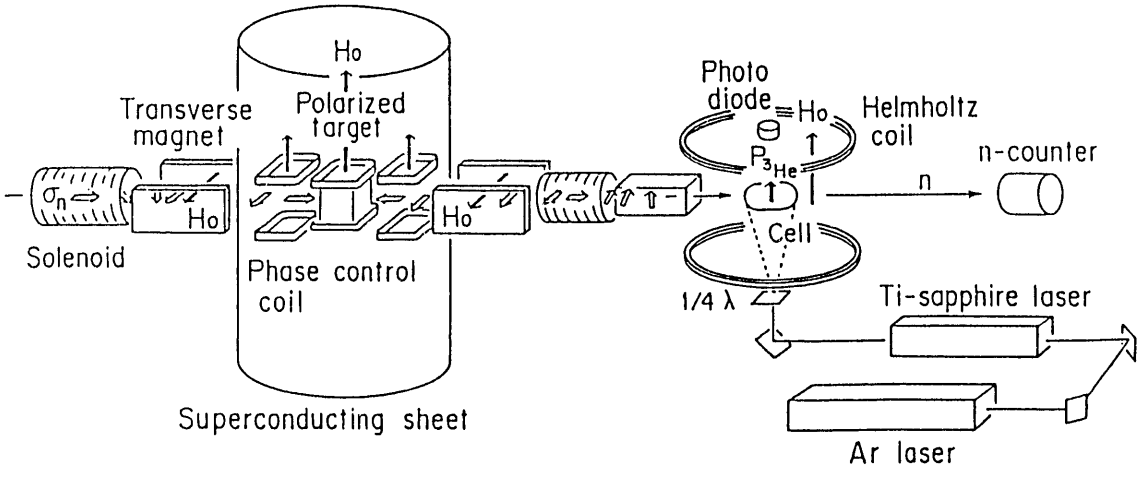

Fig. 4 Experimental set-up for the measurement of the spin detailed balance.

was obtained. Here, T_+ and T_- are the neutron transmissions for non-flipped and flipped states, respectively. The result is shown in Fig. 3. In the figure, a clear $\cos\theta$ distribution can be seen in the flipping ratio. The result shows we can measure accurately the direction of the neutron spin in the target region.

In the P-violating neutron spin rotation experiment, a target is placed in the superconducting box. The rotation upon propagation through the target is measured at $\theta = 90^o$. In the T-violation experiment, a magnetic field and a pseudomagnetic field exist in the superconducting box. The neutron spin rotations due to these fields can be measured by using the present method. This is quite important in the neutron spin control for the T-violation experiment. The experimental scheme is shown in Fig. 4. The last problem is to polarize the target nuclear spin. The apparatus for the polarization of the target is now under development. [14]

The authors would like to thank Prof. H. Sugawara, Prof. N. Watanabe, Prof. K. Nakai and Prof. Y. Yamaguchi for their warm encouragement. We also thank Dr. V.P. Gudkov for his useful discussion.

[1] I.I. Gurevich and L.V. Tarasov, "Low-Energy Neutron Physics" North-Holland (1968)
[2] L. Stodolsky, Nucl. Phys. B197(1982)213; Phys. Lett. 172B(1986)5.
[3] V.P. Alfimenkov et al., Nucl. Phys. A398(1983)93.
[4] Y. Masuda et al., Hyp. Int. 34(1987)143; Nucl. Phys. A478(1988)737c; Nucl Phys. A504(1989)269.
[5] S.A. Biryukov et al., Sov. J. Nucl. Phys. 45(1987)937.
[6] C.D. Bowman et al., Phys. Rev. C39(1989)1721.
[7] M. Forte et al., Phys. Rev. Lett. 45(1980)2088.
[8] V.P. Gudkov, Phys. Rep. 212(1992)79.
[9] Y. Masuda et al., Hyperfine Interactions 74(1992)149.
[10] Y. Masuda et al., Nucl. Inst. Meth. A264(1988)169.
[11] K.P. Coulter et al., Nucl. Inst. Meth. A270(1988)90.
[12] B. Larson et al., Phys. Rev. A44(1991)3108.
[13] S.F. Mughabghab et al., "Neutron Cross Section" Academic Press, New York, (1981).
[14] Y. Masuda et al., Proc. 18th INS Int. Symp., World Scientific, (1991)293.

2.7.2 Atomic and Nuclear Data for Development of Soft X-ray and Gamma-ray Lasers

Hideo KITAZAWA, Masazumi TEZUKA, Hirobumi TAKAKUWA,
and Koichi SHIMIZU

Tokyo Institute of Technology
2-12-1 O-okayama, Meguro-ku, Tokyo 152, Japan

and

Osamu SAGANO, Osamu NOZAWA, and Shousuke KARASHIMA

Science University of Tokyo
1-3 Kagurazaka, Shinjuku-ku, Tokyo 162, Japan

The recent progress of soft X-ray laser researches is briefly reviewed. In addition, the hydrodynamical behavior of a laser-produced, highly ionized magnesium dense plasma in the recombination phase is simulated for an approach to soft X-ray lasers in the "water window" spectral region. The results demonstrate lasing for the Balmer-α transition (λ=45.6 Å) of hydrogen-like magnesium ions. The paper also discusses the possibility of gamma-ray lasers, placing a special stress upon the underlying basic science and technology different from those of soft X-ray lasers.

1. Prelude to soft X-ray laser research

The emerging technology of soft X-ray lasers (3-300 Å) has novel applications to microscopy, lithography, and other fields. In particular, an X-ray laser operating in wavelengths between the K edge of carbon at 44 Å and that of oxygen at 25 Å would be optimal in terms of penetration, contrast, and resolution for microscopy of biological specimens. In this biological "water window" spectral region, the X-ray scattering cross sections of the carbon-rich condensed structures can be high, while the X-ray penetrability through the aqueous environment of a cell is also relatively high.[1)]

Highly ionized, laser-produced plasmas with high electron density seem to be the most promising sources of soft X-ray lasers at the high intensity required

for laser action (see Fig. 1). In those plasmas, various atomic processes preferentially fill the upper ion levels, which leads to a population-density inversion between excited levels. For many years, a variety of atomic excitation schemes were proposed to create a population inversion and subsequent gain in the X-ray region. However, recent studies have concentrated on recombination and collisional excitation schemes.

In one of the experiments, done at Princeton University, recombination lasing at 182 Å has been observed in a plasma formed by focusing a 300-joule, 50-nsec CO_2 laser pulse onto a solid carbon target.[2] As the fully stripped carbon atoms recombined with electrons in the magnetically confined, cooling plasma, a population inversion with a gain-length product of 6.5 was generated between the principal quantum number n=3 and n=2 states of hydrogen-like carbon.

At the same time, researchers at Lawrence Livermore National Laboratory were experimenting with collisionally excited, highly stripped selenium atoms in a laser-produced hot, dense plasma.[3] In this case, half-nanosecond pulses of 5320 Å visible light from a frequency-doubled, high power neodymium-doped-glass laser illuminated a thin selenium film. A population inversion was established between the 3p and 3s states of neon-like selenium, resulting in significant amplification of the 206 and 209 Å lines with a gain-length product of 6-7.

In further experiments involving collisional excitation, the Livermore researchers have observed a lasing line at 44.83 Å which corresponds to the 4d-4p transition in nickel-like tantalum.[4]

There is now such an enhanced interest in X-ray lasers in the biological "water window" spectral region.

2. Population inversion schemes for multicharged plasma

2.1. Recombination scheme

In the recombination scheme, a powerful, pulsed laser is focused onto a solid target, creating a large population of plasma ions in an ionization stage above the one in which a population inversion between excited levels is desired, that is, of fully stripped ions for a population inversion in hydrogen(H)-like ions or of helium(He)-like ions for a population inversion in lithium(Li)-like ions. After the laser pulse illumination, the plasma is dominantly cooled by the adiabatic expansion and to a certain extent cooled by the radiation losses. At a relatively low electron temperature and high electron density, three-body recombination

followed by cascading processes dominates collisional ionization and excitation processes, putting into upper excited levels a high population which decays downward by collisional radiative cascade.

In H-like ions, the level n=2 decays rapidly to the ground level by its strong radiative transition due to the large overlap of the radial wave functions of those levels, and a population inversion is built up between the levels n=3 and n=2 (see Fig.2). The same approach works in Li-like ions also. In this case the 3-2 transition has a high radiative decay rate, and gain can be generated on the 4-3 and 5-3 transitions. The Li-like sequence has the advantage of a shorter wavelength lasing transition for ions of similar ionization potential, that is, a better quantum efficiency.

On the other hand, the speed of recombination depends strongly on the electron temperature of plasma. Above a threshold temperature which is determined from a species of ion and the electron density, the speed is not so large. However, the recombination proceeds rapidly below the threshold. In other words, a large population of bare ions or He-like ions in the ground state is preserved to a sufficiently low electron temperature, playing a role of the source of lasant ions. Therefore, the rapid cooling of electron temperature realizes a large population inversion, making rapid progress of the efficiency for a recombination-plasma X-ray laser.

2.2. Collisional excitation scheme

For the collisional excitation scheme (see Fig.3), the closed shell ions are chosen to produce a population inversion. In the neon(Ne)-like plasma, a large population of ions is collisionally excited to the 3p level. It involves $2p \rightarrow 3p$ valence-electron excitation, where the 2p level is the ground state in a $1s^2 2s^2 2p^6$ configuration. The 3p level is quite metastable against direct spontaneous dipole decay to the ground state. However, the 2p-3p monopole excitation rate is comparable to that for $2p \rightarrow 3s$ or $2p \rightarrow 3d$ dipole excitation. The 3s level has a relatively low population since it has a fast radiative transition to the ground state, and a population inversion is built up between the 3p and 3s levels. Namely, lasing then takes place on a $\Delta n=0$ transition, so that heavy ions of much higher charge state are required to achieve the same lasing wavelengths as for hydrogenic $\Delta n=1$ transitions.

Since in this pumping scheme the gain for a soft X-ray laser is maintained when the plasma is kept at high temperature, it is principally possible to drive the laser in a steady state.

3. Approach to X-ray lasers in the "water window" spectral region

For the development of a soft X-ray laser in the "water window" spectral region, we have simulated the behavior of a laser-produced H-like magnesium plasma in the recombination phase, using a hydrodynamic model for compressible fluid.[5] In the calculation, a cylindrically symmetric plasma was assumed, and its dynamic behavior was described by the hydrodynamic equations for mass, momentum, and energy conservation.

The continuity equation for mass conservation is given by

$$\frac{\partial n_i}{\partial t} + \frac{1}{r}\frac{\partial}{\partial r}(m_i v) = \delta_i \quad (i=0,1,2,\ldots,12), \tag{3.1}$$

where n_i is the population density of the ground state of ions in the ith charge state, v is the mean fluid velocity, and δ_i is given by

$$\delta_i = -n_e n_i R_i - n_e n_i S_i + n_e n_{i+1} R_{i+1} + n_e n_{i-1} S_{i-1} \ . \tag{3.2}$$

Here, R and S are the rate coefficients for recombination and ionization, respectively, and n_e is the electron density, $n_e = \Sigma_{i=0}^{i=12} i n_i$. The recombination coefficient includes the contributions from radiative and three-body recombination.

The equation for the momentum conservation is

$$Mn\left(\frac{\partial v}{\partial t} + v\frac{\partial v}{\partial t}\right) = -\frac{\partial}{\partial r}[k(n_e T_e + nT_i) + Q] \ , \tag{3.3}$$

where M is the ion mass, n is the total ion density, $n=\Sigma_i n_i$, k is the Boltzmann constant, and T_e and T_i are electron and ion temperature, respectively. The Neumann-Rychtmyer artificial viscosity term, Q, is introduced to remove the numerical instabilities, which take place because of the propagation of a shock wave.

A high power, ultra-short pulse laser illuminates a thin magnesium foil in a elongated line focus (see Fig.1). Then it can be pictured that the laser radiation is absorbed by electrons, and that a highly ionized plasma is formed in the steady state. After the pulse illumination, the plasma expands adiabatically, when the electrons exchange their energy with ions at the classical equipartition rate and the shock wave heats ions only. In this picture, the electron temperature, T_e, is given by

$$\frac{\partial T_e}{\partial t} + v\frac{\partial T_e}{\partial r} = -\frac{2}{3} T_e \frac{1}{r}\frac{\partial}{\partial r}(rv) + \frac{2}{3}\frac{1}{n_e}\frac{1}{r}\frac{\partial}{\partial r}(\kappa_e r \frac{\partial T_e}{\partial r})$$

$$-\frac{T_e - T_i}{\tau_{eq}} - \frac{2}{3} P_{rad} , \qquad (3.4)$$

where κ_e is the electron thermal conductivity divided by the Boltzmann constant, τ_{eq} is the equipartition time, and P_{rad} is the total radiation energy loss power from the plasma.

The ion temperature, Ti, is governed by

$$\frac{\partial T_i}{\partial t} + v\frac{\partial T_i}{\partial r} = -\frac{2}{3}(T_i + \frac{Q}{n\,k})\frac{1}{r}\frac{\partial}{\partial r}(rv)$$

$$+\frac{2}{3}\frac{1}{n}\frac{\partial}{\partial r}(\kappa_i r \frac{\partial T_i}{\partial r}) + \frac{T_e - T_i}{\tau_{eq}} . \qquad (3.5)$$

The first term on the right-hand side includes the shock-wave heating. The quantity, κ_i, is the ion thermal conductivity divided by the Boltamann constant.

A Lagrangian scheme was adopted to solve Eqs.(3.1)-(3.5). In this scheme Eq.(3.3) is treated explicitly, and Eqs.(3.1), (3.4) and (3.5) are treated implicitly. The boundary conditions are

$$\frac{\partial n_i}{\partial r}=0,\quad v=0,\quad \frac{\partial T_e}{\partial r}=0,\quad \frac{\partial T_i}{\partial r}=0 \quad \text{at } r=0,$$

and

$$\frac{\partial n_i}{\partial r}=0,\quad \frac{\partial v}{\partial r}=0,\quad \frac{\partial T_e}{\partial r}=0,\quad \frac{\partial T_i}{\partial r}=0 \quad \text{at r=outer radius.}$$

The initial electron and ion temperature profiles are set to be Gaussian, as shown in Figs. 5(a) and 5(b). The electron temperature at the center of the plasma is taken to be 1000 eV. In the recombination soft X-ray laser scheme for

hydrogenic ions, plenty of fully stripped ions is assumed initially. Figure 4 shows the large fraction of fully stripped magnesium ions at this temperature. The profiles of total ion density, steady state ionization balance, and electron density are determined from the local pressure balance.

Using the initial conditions mentioned above, the hydrodynamic code calculates, at each time step, various hydrodynamic parameters, that is, temperature, density and ground-state population of each ion (see Figs. 6(a) and 6(b)). The population densities of excited levels of hydrogenic ions are calculated at each time step, using a quasi-equilibrium model. Then, the gain coefficient, G, is given by

$$G = N_u \sigma_{stim} \left(1 - \frac{N_l g_u}{N_u g_l}\right), \qquad (3.6)$$

where N_u and N_l are the upper and lower laser state population densities, respectively, and g_u and g_l are the corresponding statistical weights. The stimulated cross section, σ_{stim}, is written by the frequency ν, line width $\Delta\nu$, and A-coefficient A_{ul} for the laser line:

$$\sigma_{stim} = \frac{C^2}{8\pi\nu^2} \frac{1}{\Delta\nu} A_{ul} . \qquad (3.7)$$

Figure 7 shows the gain coeffcient for the Balmer-α (3p-2s) transition of M_g^{11+} at each time step. As seen from the figure, the lasing begins at 100 ps after laser-pulse illumination, and culminates at a time between 150 and 200 ps, when the maximum gain coefficient at r=12.5 μm is ~6 cm^{-1}. Also, the electron temperarure and density for the maximum gain are ~350 eV and ~$1\times10^{21} cm^{-3}$, respectively. Using those parameters, it is found that the "collision limit" quantum number, n', then exists between n=3 and n=2 (see Fig.8).

For quantum states higher than n', collisional excitation is equally or more likely than radiative decay to take place. For those states lower than n', radiative decay dominates. Hence, a population density inversion can be generally produced between the upper level n=3 and the lower level n=2.

In the present calculation, the Lyman-α trapping is not taken into account. But, this trapping may lead to a considerable decrease of the gain coefficient. Therefore, more efficient electron cooling should be devised to obtain a saturated gain coefficient > 10 cm^{-1}. We also emphasize the necessity of reliable atomic data

for the three-body recombination, collisional excitation or deexcitation, and radiative recombination processes in highly ionized dense plasma.

4. Possibility of gamma-ray lasers

4.1. Scale differences between soft X-ray and gamma-ray lasers[6)]

Can a gamma-ray laser (graser) be situated on an extension of the soft X-ray laser development? The answer is presumably "no", because nuclear gamma radiation does not have many of the properties taken for granted in atomic or molecular radiation and necessary for lasers. Therefore, the basic science and technology underlying those differences must be properly understood in discussion on feasibility of gamma-ray lasers.

The nuclear gamma-ray transitions involve more complex physics, not existent in the longer wavelength conventional laser systems. Normal intution from optical transitions may break down for gamma-ray transitions. Let R denote the size of the radiating system, e.g., nucleus, atom or molecule, D denote the distance between neighbouring radiators (lattice constant in a crystal), x denote the amplitude of zero-point or thermal oscillations of the radiator, k denote the wave number of the radiation. Then for normal optical laser transitions,

$$kx \ll kR \sim kD \ll 1 \quad . \tag{4.1}$$

For nuclear gamma-ray radiation,

$$kR \ll kx \sim 1 \ll kD \quad . \tag{4.2}$$

In both cases kR«1, indicating the validity of a long wave approximation and multipole expansion. But, the fact that kD»1 for gamma-ray case and kx is of order unity causes phase incoherence in the emitted radiation. The large kD value means that considerable effort is needed to control the phase in order to maintain coherence. Also, the reduction in the coherent intensity due to thermal and zero-point motion is geven by the Debye-Waller factor $\exp(-k^2\langle x^2\rangle)$. In a gamma-ray laser, therefore, the host solid including lasant nuclei would be refrigerated to decrease the amplitude of thermal oscillations of a radiating nucleus.

Additional differences are that the energy of optical radiation E_{opt} is much less than atomic ionization energies E_I, while the energy of nuclear gamma rays E_γ is much greater:

$$E_{opt} \ll E_I \ll E_\gamma . \tag{4.3}$$

This allows the gamma-ray energy to be non-resonantly lost in the host by photoelectric ionization processes absent in conventional optical lasers. The large photoelectric loss of gamma rays makes it difficult to pull a laser beam out of the host and to demonstrate the feasibility of gamma-ray lasers. In this point of view, existing feasibility evaluations which do not take into account the energy loss would be too optimistic. However, the use of coherent effects like the Borrmann effect[7] in a nearly perfect crystal may lead to a considerable decrease of the energy loss.

Also, in the optical case the kinetic energy of the recoil of an atom due to photon emission is much less than the natural line width of the radiative transition. In the gamma-ray case the recoil energy is very much larger than the natural line width Γ and is of the same order as the thermal energy or the Debye temperature of the crystal, $k_B\theta_D$:

$$\Gamma \ll \frac{(h\,k)^2}{2M} \sim k_B\theta_D , \tag{4.4}$$

where M is the nuclear mass and k_B is the Boltzmann constant. Therefore, the emitted radiation cannot induce another transitions in neighbouring radiators. This difficulty could be overcome by using the Mössbauer effect, according to circumstances, in a cool solid.

4.2. Population inversion and stimulated emmision cross section[8]

For amplification of radiation by stimulated emmision from the upper level 2 to the lower level 1, the photons must be added by transitions between the two levels into a limited number of modes of the radiation field more rapidly than they are removed:

$$(N_2 - \omega N_1)\,\sigma_s \geq N_i\sigma_i \tag{4.5}$$

with

$$\omega = g_2/g_1 , \tag{4.6}$$

where N_1, g_1 and N_2, g_2 are the population densities and degeneracy factors for the lower and upper levels, respectively. The stimulated emission cross section for interaction of monochromatic photons with a resonant system at exact resonance is

$$\sigma_S = (\lambda^2/2\pi)(\Gamma_\gamma/\Gamma) , \qquad (4.7)$$

where λ is the wavelength, and Γ_γ and Γ are the radiative and total linewidths of the energy levels, respectively.

In the gamma-ray region of interest, photons are lost mainly by photo-electric absorption, with the cross section

$$\sigma_i = C_i\, Z_i^{9/2}\lambda^3(1-\varepsilon) \qquad (4.8)$$

dependent on the atomic number Z and wavelength λ. The coeffcient C_i depends on the particular electron shell involved in absorption.

The factor ε accounts for the Borrmann effect. In a perfect crystal, photons can channel between the lattice planes if the Bragg condition is satisfied by interfering direct and scattered waves. Since it is demonstrated by the Mössbauer effect that matter is sufficiently transparent for a pumped medium to amplify recoilless gamma radiation, the Borrmann effect gives more latitude for satisfying the requirement of photon balance inequality Eq.(4.5).

For lasing action the ratio of the inversion density, $N^*=N_2-\omega N_1$, to the total atmic density, N_i, must exceed the ratio of the cross section for non-resonant photon removal, σ_i, to the resonant stimulated cross section σ_S:

$$N^*/N_i \geq \sigma_i/\sigma_S . \qquad (4.9)$$

Here, the right hand side of Eq.(4.9) is the order of 10^{-3}, except for the Borrmann factor. Thus, it is easily understood that extremely strong pumping would be required in the graser development.

So far, various pumping schemes have been proposed to generate a population inversion between two nuclear levels of which upper level is an isomer. Those schemes include radiative pumping, ion-beam pumping, neutron pumping, two-stage pumping, separate pumping, and hybrid pumping. However, a promising graser scheme which satisfies the photon balance inequality Eq.(4.5)

is not found yet. Here, it should be noted that in the graser development, simple generation of a population inversion would not be essential.

5. Summary

In the recent progress of soft X-ray lasers, wavelengths are coming into the "water window" spectral region. A variety of applications of those lasers will be performed in the near future, including applications to holographic experiments in the imaging of biological species.

On the graser, however, it is still difficult to discuss the feasibility. Probably, the key to graser development comes from advances in nuclear spectroscopy which may reveal a new pumping scheme with a specified nucleus, from advances in techniques in Mössbauer spectroscopy, from the isomer-separation approach, and from investigations of the Borrmann effect. In particular, considerable basic research will be strongly needed to establish whether the Borrmann effect exists and has the desired properties relevant to grasers.

This work has been performed as one of the projects of Tokyo Electric Power Company's Endorsed Chair of Highly Sophisticated Energy System at the Department of Electrical and Electronic Engineering in the Tokyo Institute of Technology.

References

1) Elton R.C. : X-ray Lasers, Academic, New York (1990).
2) Suckewer S. *et al.* : Phys. Rev. Lett., **55**, 1753 (1985).
3) Matthews D.L. *et al.* : Phys. Rev. Lett., **54**, 110 (1985).
4) MackGowan B.J. *et al.* : X-ray Lasers 1990, Adam Hilger, Bristol (1990).
5) Kim D. *et al*, : J. Opt. Soc. Am. B, **6**, 115 (1989).
6) Lipkin H.J. : X-ray Lasers 1987, American Institute of Physics, New York (1987).
7) Hannon J.P. and Trammell G.T. : Opt. Comm., **15**, 330 (1975).
8) Baldwin G.C. : Phys. Rep., **87**, 1 (1982)

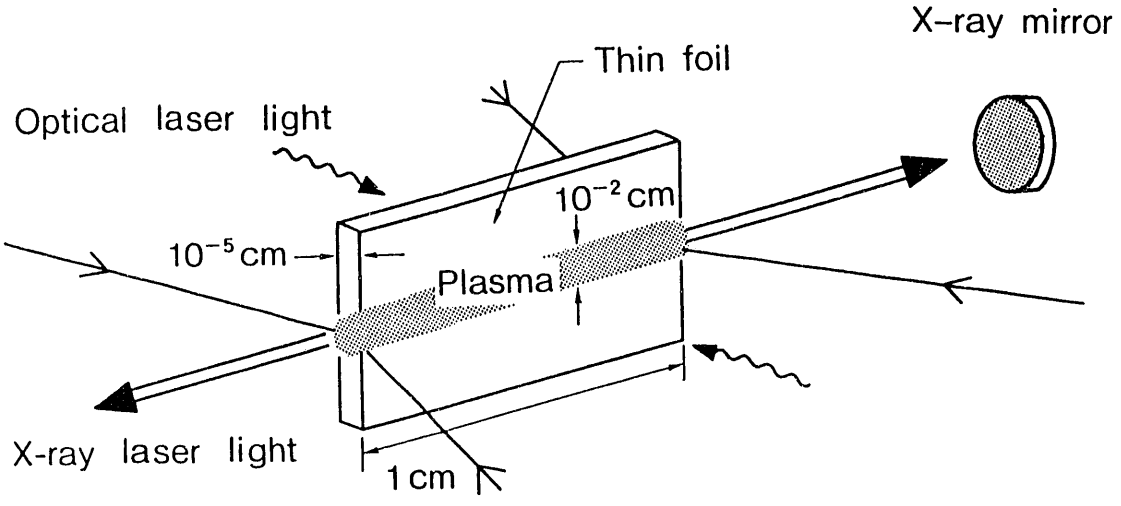

Fig. 1 Exploding-foil X-ray laser.

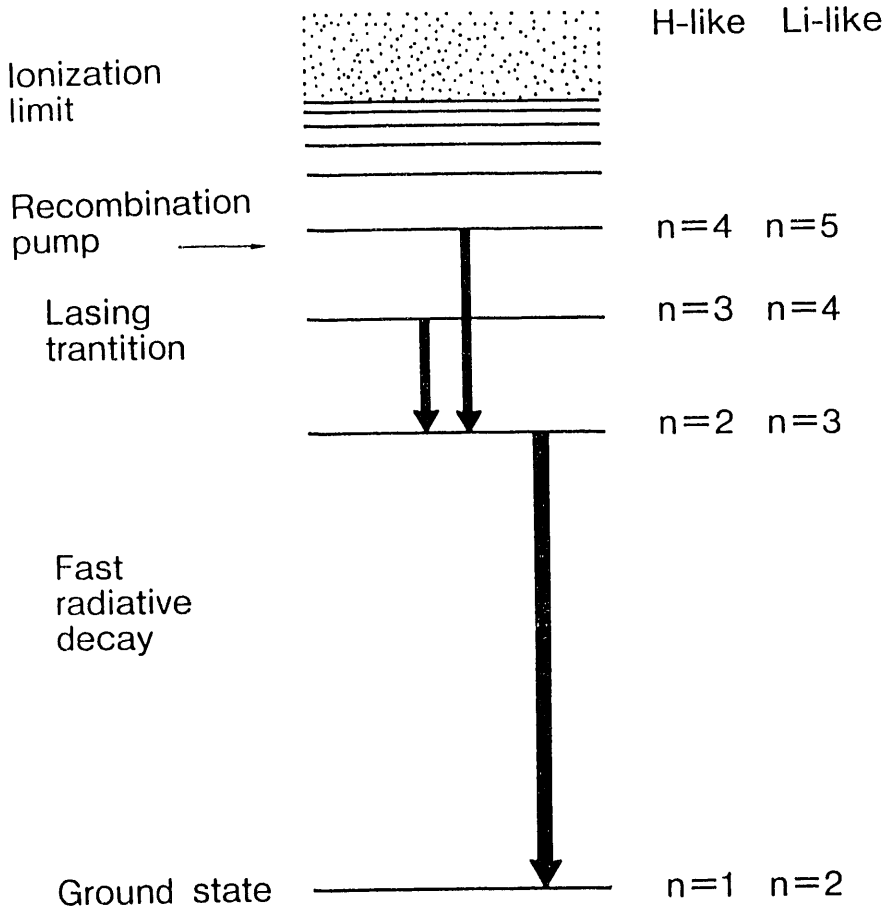

Fig. 2 Partial energy diagram of hydrogen-like and lithium-like recombination X-ray laser scheme.

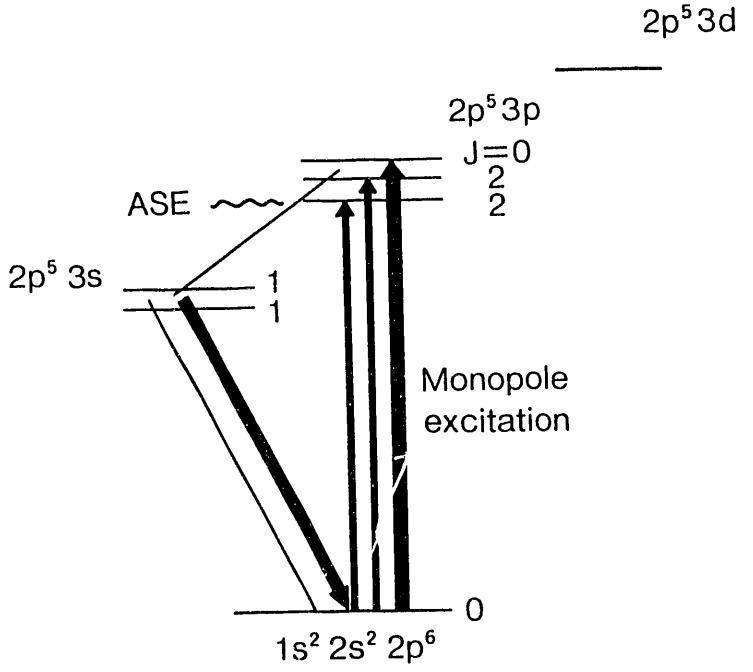

Fig. 3 Partial energy diagram of neon-like collisional excitation X-ray laser scheme.

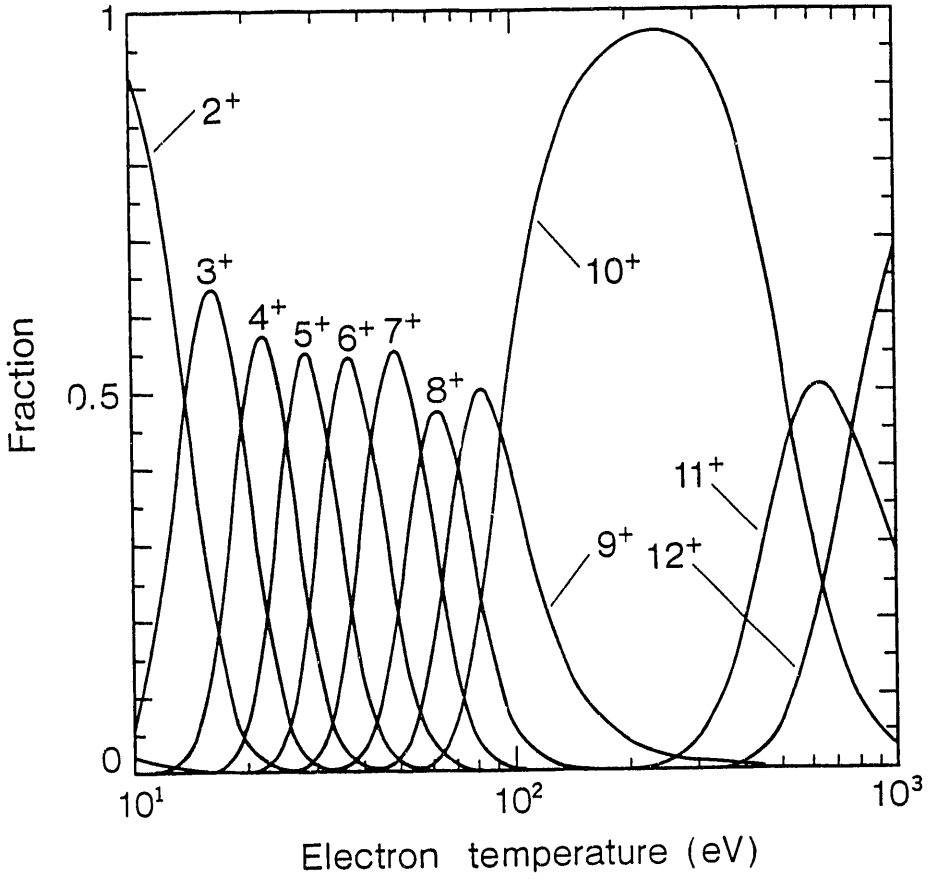

Fig. 4 Fractional ion abundances calculated for a dense magnesium plasma versus electron temperature.

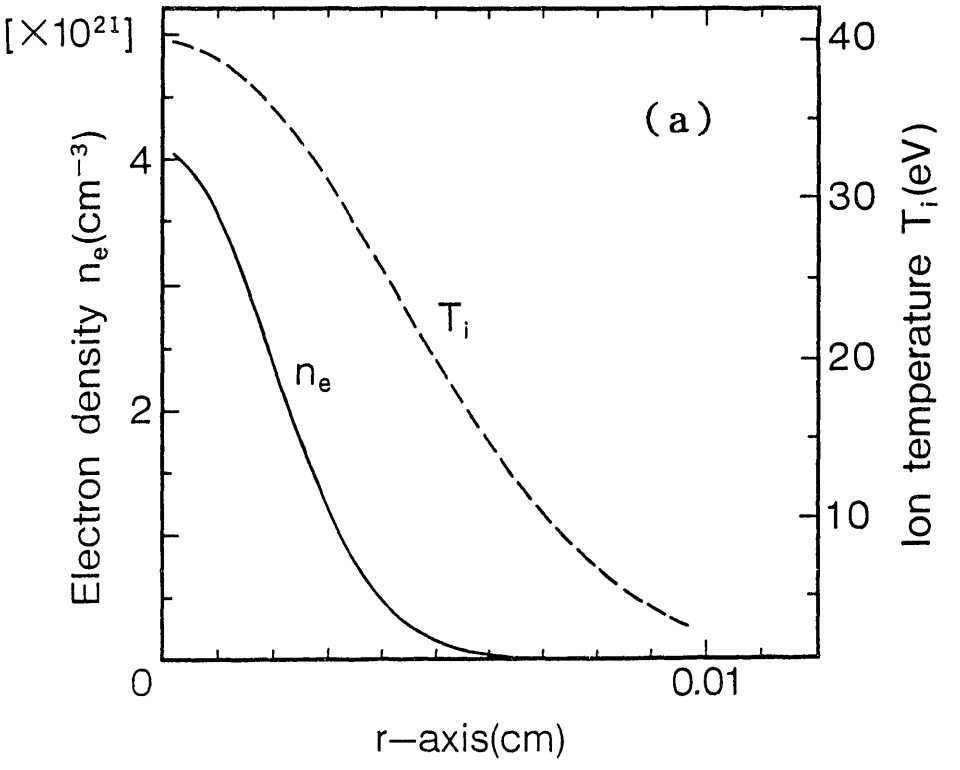

Fig. 5(a) Initial profiles of electron density and ion temperature.

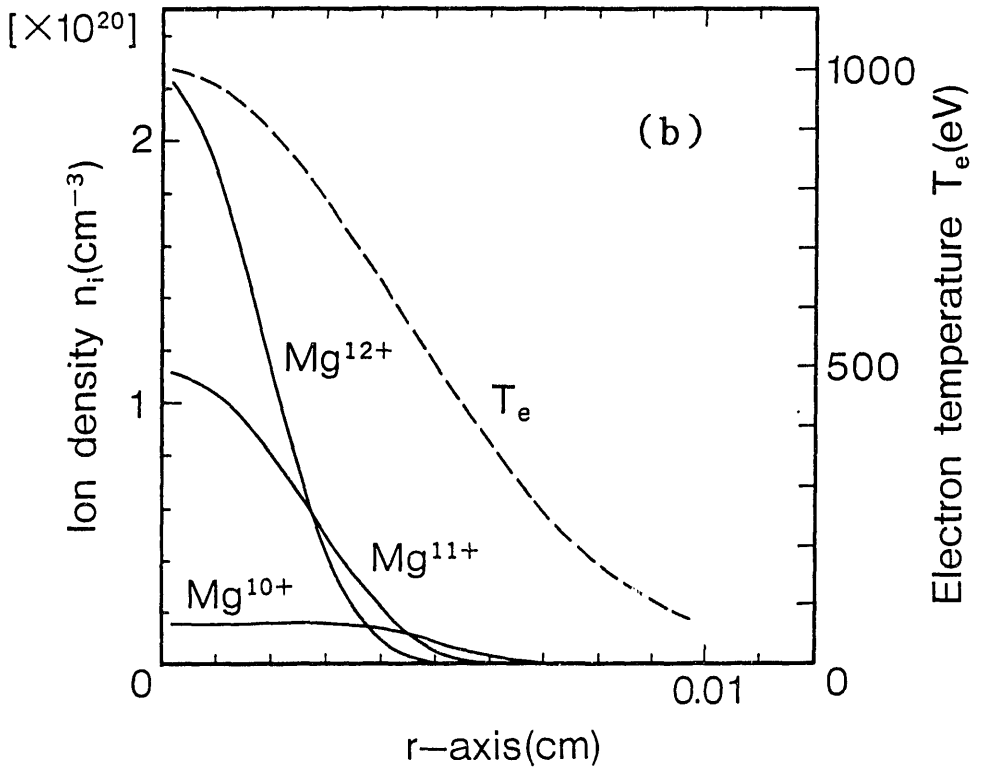

Fig. 5(b) Initial profiles of ion density and electron temperature.

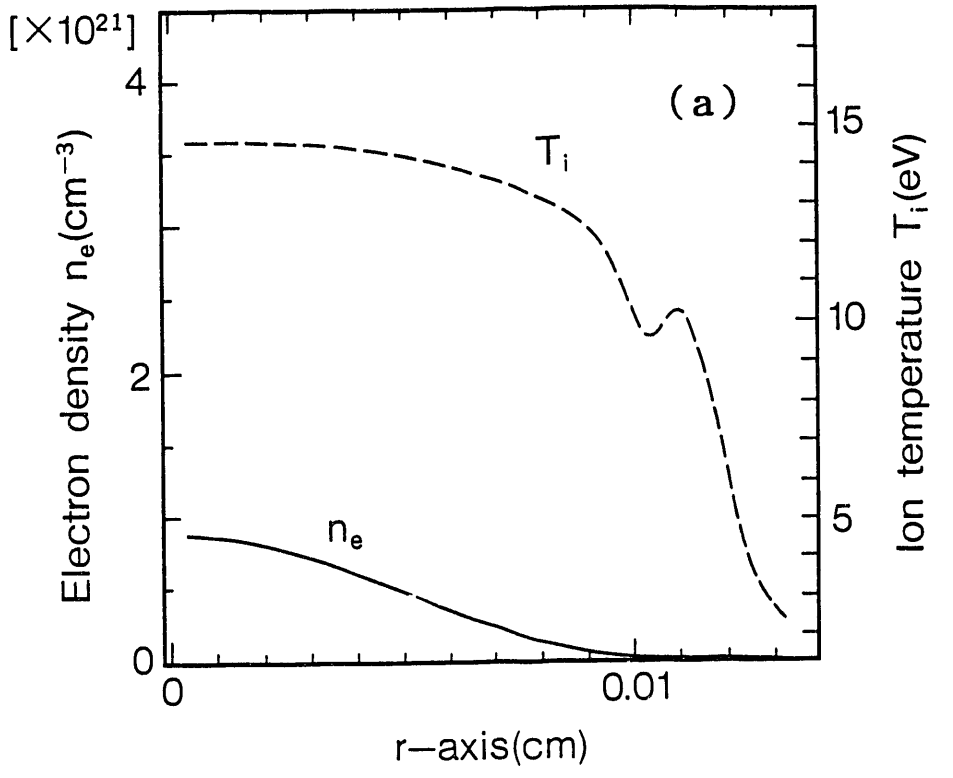

Fig. 6(a) Profiles of electron density and ion temperature at t=150 ps after laser-pulse illumination.

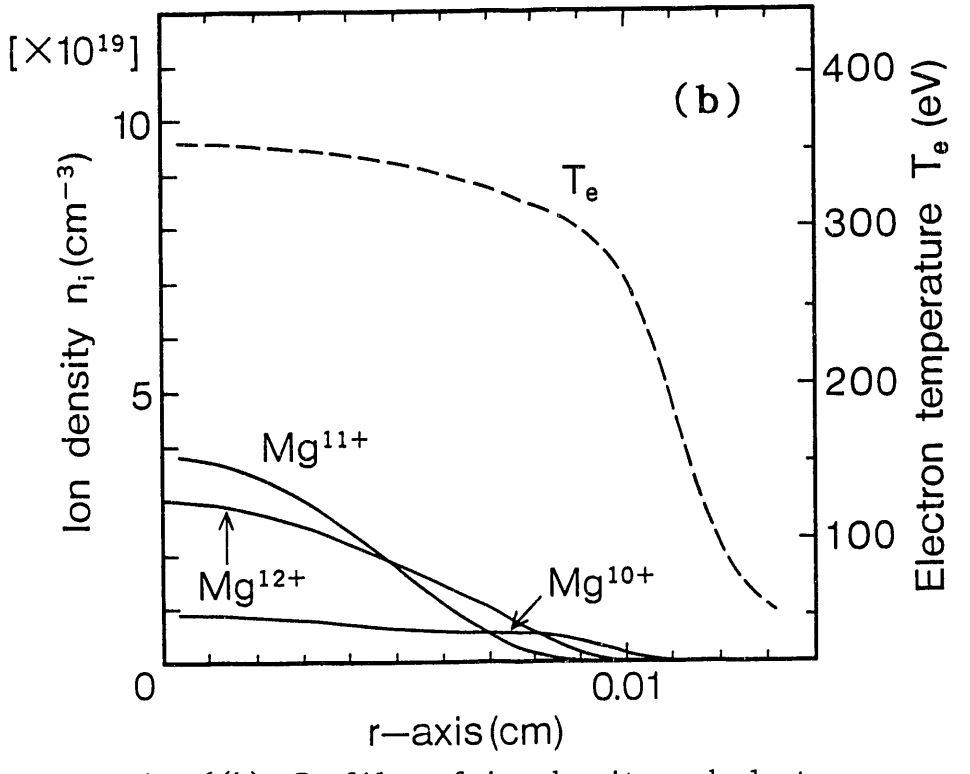

Fig. 6(b) Profiles of ion density and electron temperature at t=150 ps after laser-pulse illumination.

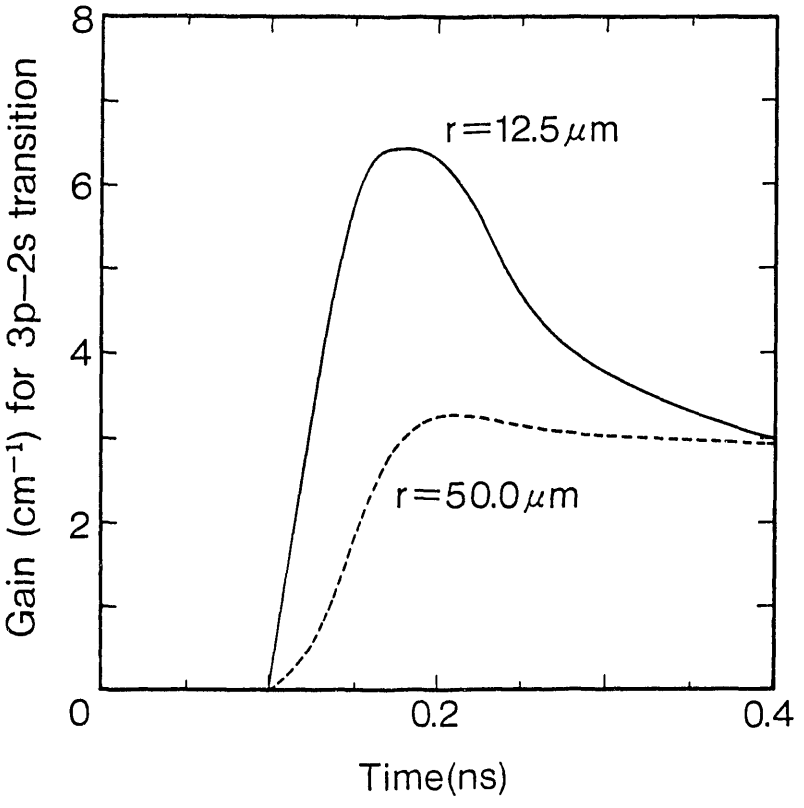

Fig. 7 Gain coefficients for the 3p-2s transition of hydrogen-like magnesium ions in a recombining plasma versus plasma-expansion time. Those values are calculated at r=12.5 μm and r=50.0 μm.

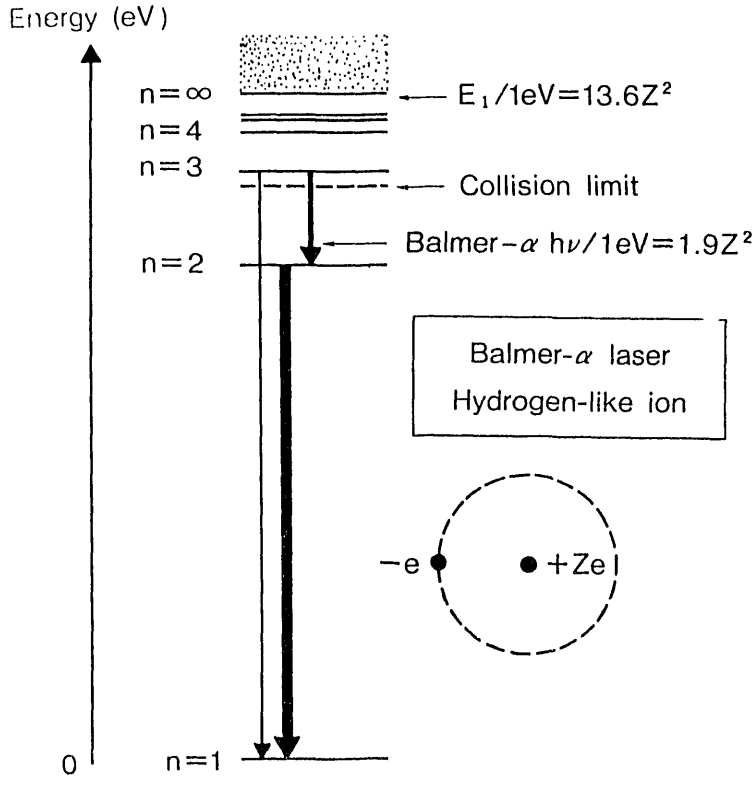

Fig. 8 Energy levels of a hydrogen-like ion of nuclear charge +Ze.

2.8 Integral Data Analyses

2.8.1 Measurement of Doppler Effect up to 2000℃ at FCA

Shigeaki OKAJIMA, Hiroyuki OIGAWA, Takehiko MUKAIYAMA

Japan Atomic Energy Research Institute
Tokai-mura, Naka-gun, Ibaraki-ken 319-11

For the improvement of the Doppler effect calculation accuracy in high temperature range, new experimental devices were developed to measure Doppler effect up to 2000℃ and measurements were carried out at Fast Critical Assembly of JAERI. For the measurements, two methods were used: the one is a sample reactivity measurement and the other is a foil activation measurement with laser heating. In the analyzing the experimental data, a new cell calculation code of ultra-fine groups, PEACO-X, was used to generate effective cross sections of the Doppler sample, which took into account the resonance overlapping effect between the ^{238}U of the Doppler sample and the tungsten structural material of experimental devices. The calculation of the Doppler effect underestimated the measured Doppler reactivity worths for the sample reactivity method, while it showed a good agreement with the measured *Doppler ratio* for the foil activation method.

1. Introduction

Most of Doppler effect measurements so far have been carried out in the temperature range from 20 to 800℃ at various fast critical facilities around the world. The Doppler effect at higher temperature plays an important role for the transient behavior of the FBR.

In order to improve the accuracy of the Doppler effect calculation in high temperature range, new devices were developed to measure Doppler effect to 2000℃ and measurements were carried out at Fast Critical Assembly (FCA) of JAERI.

2. Measurement of the high temperature Doppler effect

2.1 Measurement techniques

Two methods were combined to extend the temperature range of Doppler measurement to higher temperatures. The first method involves sample reactivity measurements and is used for temperatures to 1500℃. The other method uses foil activation measurements with laser heating and is useful for temperatures to 2000℃.

(a) Sample reactivity measurement

A UO_2 Doppler sample is placed in the core center and kept at a desired high temperature for a certain period. The Doppler effect is derived from the difference between the reactivities measured for the unheated Doppler sample and the heated sample placed at the core

center by turns. The reactivity difference is determined by the position difference of a fine control rod which maintains the reactor at a constant power level.

Figure 1 shows the schematic view of experimental device on the sample reactivity measurement. The depleted UO_2 Doppler sample is 20 mm in diameter, 150 mm in length and contains 390 g of uranium. The sample is contained in a tungsten holder which is surrounded by a tungsten electric heater. The sample and heater, in turn, are surrounded by several layers of tungsten thermal-reflector. This assembly is placed in an evacuated stainless steel inner tube. This tube is positioned inside a stainless steel outer tube. Cooling air flows through the space between the inner and outer tubes. This removes heat escaping from the heated Doppler sample and prevents an increase in temperature of adjacent core materials, which induces a reactivity drift in the core.

To compensate the reactivity drift effect of the core which is caused by the slight temperature rise of the core materials, the reactivity measurements are performed for both of a reference sample and the Doppler sample at the core center by turns. Both samples are loaded in a 5 cm square drawer, and the drawer is repetitively oscillated in and out so that one of samples is at the core center while the other is out of the core .[1),2)] The accuracy of the reactivity measurement is $\pm 3 \times 10^{-7}$ Δ k/k.

(b) Foil activation measurement

The sample reactivity measurement is impractical for temperature range above 1500℃ because the limited space does not allow adequate thermal insulation for a massive Doppler sample at higher temperatures. A foil activation method is used to measure the Doppler effect in the temperature range to 2000℃.

A UO_2 foil placed at the core center is kept at a given high temperature (up to 2000℃) by exposure of Nd-YAG laser beam. After several hours of irradiation, the irradiated foil is removed from the core and the γ rays (106, 210 and 277 keV) from ^{239}Np which is neutron capture products of ^{238}U are counted. The experimental Doppler effect is expressed as the *Doppler ratio*, the ratio of the increase in foil activity caused by the temperature rise compared to the activity of the unheated foil:

$$\textit{Doppler ratio} \equiv \frac{R(T) - R(T_0)}{R(T_0)} .$$

where $R(T)$: γ ray count rate of a foil irradiated at temperature T

T_0 : room temperature

A schematic view of the experimental device on this method is also shown in Figure 1. A depleted UO_2 foil 12.7 mm in diameter and 0.5 mm thick is wrapped in tungsten cover. These elements are suspended in the center of a vacuum capsule which has silica glass windows at both ends along the longitudinal direction of the drawer. One side of the foil is exposed to a Nd-YAG laser beam. The laser beam, transmitted by an optical fiber cable from a

laser oscillator, enters the capsule through one window. The temperature of the other side of the foil is monitored, through the other window, with a monochromatic radiation thermometer. The thermal insulation for this device is similar to the device described previously.

2.2 Measurement

The Doppler effect measurement to 2000℃ was made in the FCA assembly XVII-1, which is a mock-up core for a prototype oxide-fueled FBR. Figure 2 shows the experimental results obtained by both measurement techniques.

3. Analysis of the higher temperature Doppler effect measurement

3.1 Calculation method

From the standpoint of neutron cross section, tungsten has a lot of resonance peaks. Figure 3 shows capture cross sections of ^{238}U and tungsten at temperature of 300K between 900 eV and 1 keV. In this figure, some of the resonance peaks are overlapped. It is, therefore, important to evaluate the resonance overlapping effect between the ^{238}U of the Doppler sample and the tungsten structural material in the devices. For the analysis of this resonance overlapping effect, a new collision probability code, PEACO-X[3], was used. The code calculates the regional neutron flux with ultra-fine group structure ($\Delta u = 0.25 \sim 4 \times 10^{-4}$) based on the RABBLE method[4] and generates effective cross sections with the JFS-3 type group structure ($\Delta u = 0.25$)[5].

The Doppler reactivity worth was calculated by a first order perturbation theory. The effective cross section of the Doppler sample was obtained from PEACO-X. The real and adjoint fluxes were obtained from a two-dimensional diffusion calculation. The calculated *Doppler ratio* in the foil activation method was obtained from the combination of PEACO-X results in the energy range below 100 keV and the conventional cell code's results above 100 keV. In these calculations, the JENDL-3 data[6] was used.

3.2 Calculated results

The calculated resonance overlapping effect between the ^{238}U of the Doppler sample and the tungsten structural material contributed only 1.0% to the Doppler reactivity measured, and 2.1% to the *Doppler ratio* in the foil activation measurement.

The calculated results are also shown in Figure 2. The ratios of the calculated value to the experimental one (C/E values) are 0.86 for the Doppler reactivity worth for the temperature change from 20℃ to 1500℃ and 1.06 for the *Doppler ratio* at 2000℃.

4. Conclusion

The Doppler effect was measured up to 2000℃ at FCA using newly developed experimental devices. The cell calculation code with ultra-fine groups was developed and used

for the analysis of the resonance overlapping effect between the ^{238}U of the Doppler sample and the tungsten structural material of the experimental devices. The calculation showed relatively small overlapping effect. The calculation of the Doppler effect was 15-20% lower than the measured values for sample reactivity method, and was in good agreement with the results of foil activation method.

The measurements are performed in various cores at FCA to obtain the neutron spectrum dependence of the very high temperature Doppler effect.

References

1) Okajima S. and Mukaiyama T.: "Doppler effect measurement in FCA assembly X-3 and XI-1," JAERI-M 84-086 (1984).

2) Mukaiyama T. and Okajima S.: J. Nucl. Sci. and Technol., 22, 243 (1985).

3) Okajima S., Oigawa H. and Mukaiyama T.: "Measurement of Doppler Effect up to 2000℃ at FCA (3) - Development of a cell Code, PEACO-X, with Ultra-fine Group Structure - ," JAERI-M 92-185 (1992).

4) Kier P.H. and Robba A.A.: "RABBLE, A Program for Computation of Resonance Absorption in Multiregion Reactor Cells," ANL-7326 (1967).

5) Takano H. and Ishiguro Y.: "Production and Benchmark Test of Fast Reactor Group Constant Set JFS-3-J2," JAERI-M 82-135 (1982).

6) Shibata K., et al., "Japanese Evaluated Nuclear Data Library, Version-3 - JENDL-3 -," JAERI-1319 (1990).

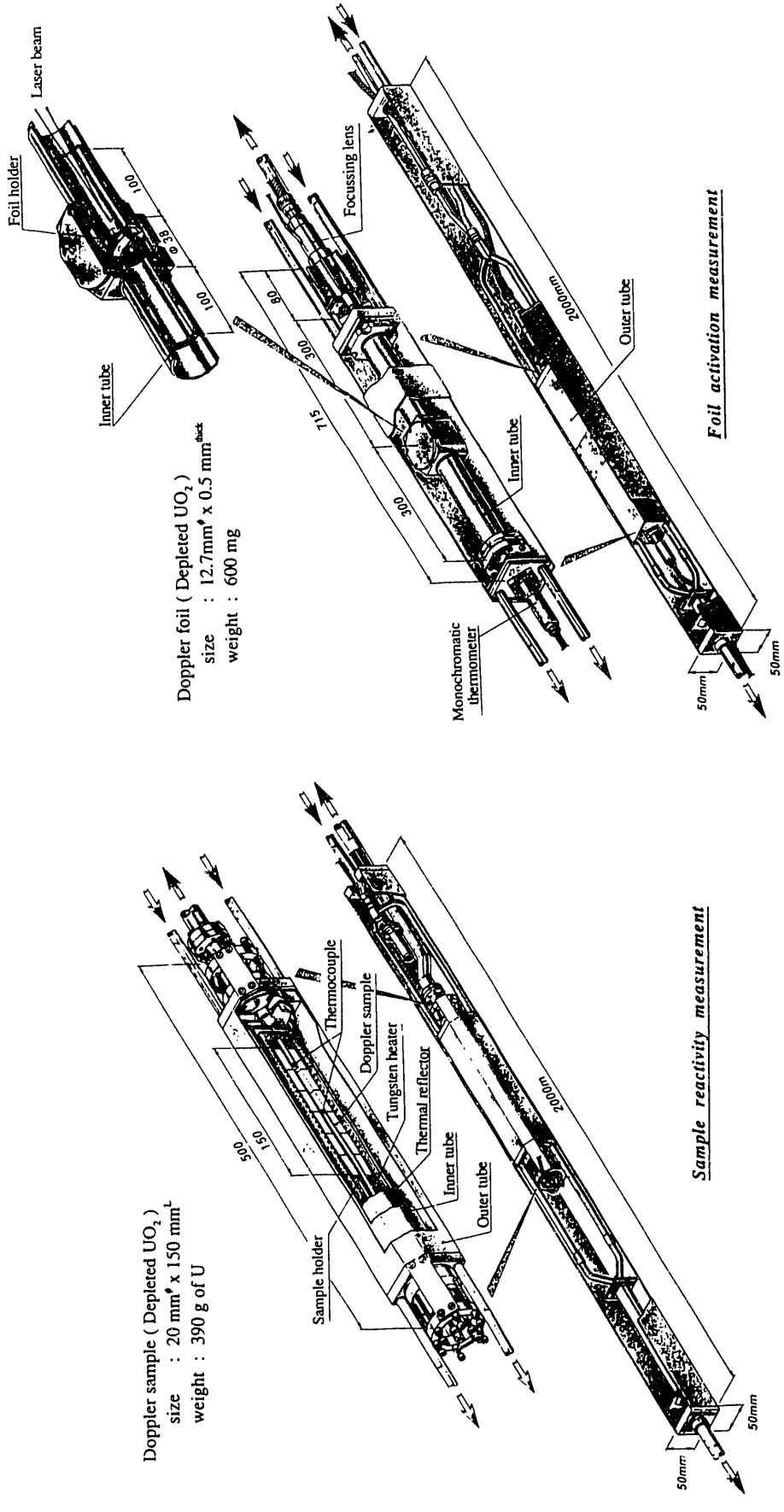

Fig. 1 Schematic view of experimental devices used in FCA Doppler effect experiment.

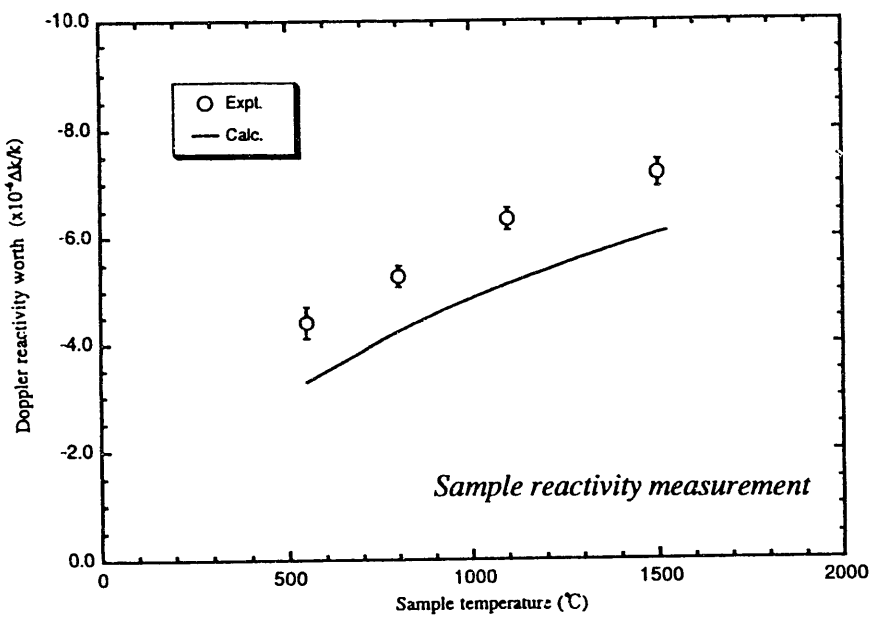

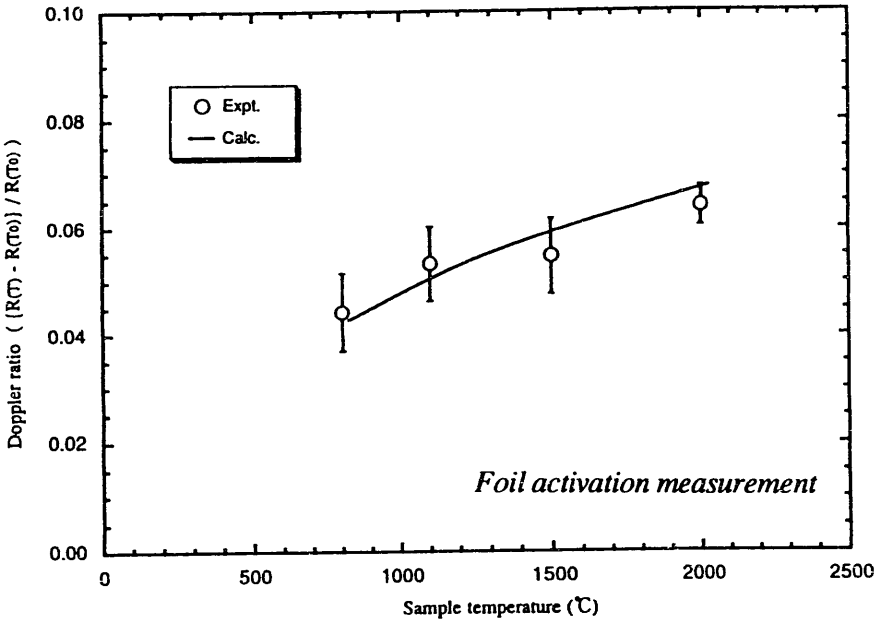

Fig. 2 Experimental and calculated results of ^{238}U Doppler effect measured in mock-up core of MOX-fueled FBR at FCA (Left side: Sample reactivity measurement, Right side: Foil activation measurement).

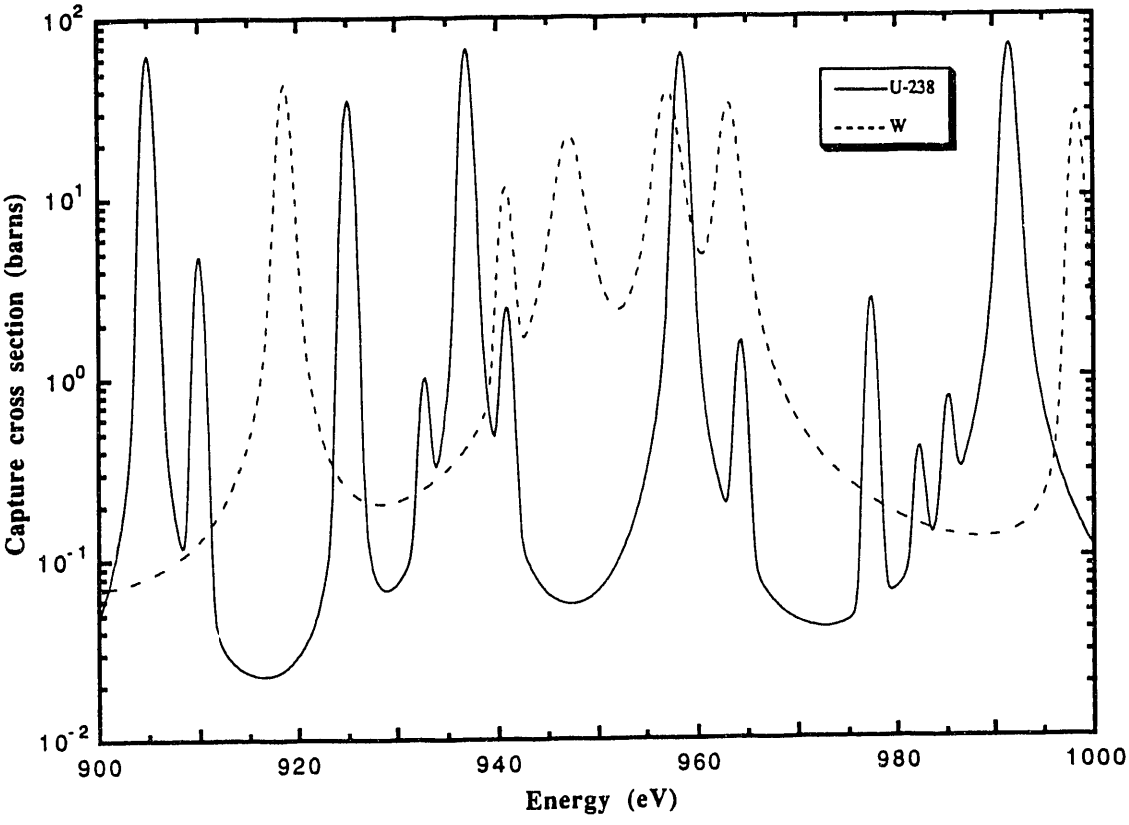

Fig. 3 Capture cross sections of ^{238}U and Tungsten (T=300K).

2.8.2 Benchmark Tests of JENDL-3 and ENDF/B-VI

Kaoru KOBAYASHI and Atsushi ZUKERAN

Energy Research Laboratory, Hitachi, Ltd.
2-1, Omika-cho, 7-chome, Hitachi-shi, Ibaraki-ken, 319-12

Benchmark tests for fast and thermal reactor cores were carried out with the MCNP-3B code. Differences between measured and calculated k_{eff}'s (unit: $\%\Delta k$) were 0.13 (GODIVA; uranium fast core), -0.30 (JEZEBEL; plutonium fast core), -0.32 (PNL-1; plutonium thermal core) and 0.68 (PNL-2) based on the JENDL-3 file, and -0.14, -0.55, -0.20 and 0.38, respectively, based on the ENDF/B-VI file. Calculated leakage spectra of GODIVA, based on both files, give underpredicted values in the energy range of leakage neutrons from 2 to 5 MeV, while those of JEZEBEL agreed well with experimental values. Calculated lattice parameters of k_{∞}'s, ρ^{28}'s, δ^{25}'s and δ^{28}'s of TRX cores were predicted with the same accuracy for both files.

1. INTRODUCTION

The latest versions of JENDL-3 and ENDF/B-VI nuclear data files were released in 1989 and 1990, respectively. Since, then many JENDL-3 benchmark tests of FBR and LWR cores have been made by JNDC Working Groups, and applicability of JENDL-3 for typical nuclear properties of fast and thermal reactor cores has been evaluated[1,2]. A few benchmark tests for ENDF/B-VI have been performed for thermal reactors of uranium cores[3,4], no tests for fast or plutonium fueled thermal reactor cores have been made.

In this study, benchmark tests which emphasize ENDF/B-VI were carried out with the continuous energy Monte Carlo code MCNP-3B[5] which has high applicabilities to arbitrary geometries and can give accurate neutron fluxes.

2. NUCLEAR DATA

Important differences between JENDL-3 and ENDF/B-VI are in formulae for resonance parameters, correlation functions between the angle and energy of secon-

dary neutrons, and numbers of points for interpolating ν-values. More specifically, these differences are as follows.

(1) Resonance formulae are compared for most important nuclides ^{235}U and ^{238}U in Table 1. In particular the ^{235}U resolved resonance region in ENDF/B-Ⅵ is increased by about 20 times that in JENDL-3 as shown in figure 1. By contrast, both files have a similar formula, a single level Breit-Wigner, in the unresolved resonance region.

(2) In JENDL-3, angle and energy distribution parameters of secondary neutrons are separately given in files 4 and 5 for angle and energy, respectively, while those in ENDF/B-Ⅵ are compiled in file 6 for both energy and angle descriptions by Legendre coefficients or systematical formula by Kalbach and Mann which are formulae for double differential cross sections. Those formulae can accurately describe the angle and energy distributions of secondary neutrons. For instance, ^{235}U in JENDL-3 has files 4 and 5 including elastic, fission, inelastic, (n,2n), (n,3n) and (n,4n) reactions, while ^{235}U in ENDF/B-Ⅵ has file 6 including (n,2n), (n,3n) and (n,4n) reactions, and also files 4 and 5 for other reactions.

(3) The numbers of interpolation points for ^{235}U and ^{239}Pu ν-values in ENDF/B-Ⅵ are greater than those in JENDL-3. Figure 2 compares ^{235}U ν-values. The authors recommend that the numbers of those points for ^{235}U and ^{239}Pu in JENDL-3 should be increased.

3. BENCHMARK CORES

Benchmark tests were performed for typical fast and thermal reactors, as shown in Table 2. The core types and measured quantities are summarized below.

(1) GODIVA - a fast reactor with a bare spherical core of 94% enriched uranium metal[6]. K_{eff} and leakage spectrum were calculated for the benchmark tests.

(2) JEZEBEL - a fast reactor with a bare spherical core of plutonium metal[6]. The benchmark tests were performed for the same items as in GODIVA.

(3) PNL-1 and PNL-2 - thermal reactors with unreflected spherical cores of plutonium nitrate solutions, where ratios of ^{1}H to ^{239}Pu atoms are 700 and 131, respectively[7]. The calculated k_{eff}'s were compared with the experimental values (k_{eff}'s=1.0). In these cores, atom densities of ^{14}N were missed, because they were negligibly small.

(4) TRX-1 through TRX-4 - light water moderated thermal reactors with slightly enriched uranium lattices. Their lattice parameters of k_{∞}'s, ρ^{28}'s, δ^{25}'s and δ^{28}'s were measured[8] and compared with their calculated values.

4. CALCULATIONAL METHOD

The cross section processing code NJOY91.13[9] was used for the present work as shown in figure 3. It treats the cross section libraries of MCNP-3B, based on JENDL-3 and ENDF/B-Ⅵ files, which were modified by 'Format conversion code'. The original ACER module in NJOY91.13 converts parameters of files 4 and 5 to numerical values accepted by the MCNP-3B library formats, but it does not accept the file 6 of the ENDF/B-Ⅵ. Therefore, it was necessary to develop the 'Format conversion code'. Conversion processes are described as follows.

$$F_E(\mu,E) = \int f(\mu,E,E')dE' \tag{1}$$

$$F_\mu(E,E') = \int f(\mu,E,E')d\mu \tag{2}$$

where

μ : cosine of scattered angle,
E : incident energy,
E' : secondary energy,
$F_E(\mu,E)$: angular distributions in file 4,
$F_\mu(E,E')$: energy distributions in file 5,
$f(\mu,E,E')$: energy-angular distributions in file 6.

Equations (1) and (2) are calculated by using a trapezoidal formula, and numbers of divisions of μ and E' variables are determined to satisfy the following condition.

$$\left|\int f(\mu,E,E')d\mu dE' - 1.0\right| \leq 0.001 \tag{3}$$

In calculation of equation (3), the number of divisions of E' is variable, but the number for μ is constant and is 32 equiprobable cosine bin the same as the MCNP-3B library format has. Figure 4 shows the relation between number of divisions of E' and integral value with the (n,2n) reaction. The integral values converge to 1.0 as the number of divisions of E' increases. Then the parameters of the energy-angle distributions in file 6 are accurately converted to separated parameters in files 4 and 5. Meanwhile, point-wise cross sections of total, absorption, elastic and fission reactions contained in both libraries have a 0.5% reconstruction tolerance. Therefore, MCNP-3B libraries prepared from JENDL-3 and ENDF/B-Ⅵ have enough accuracy

for the present analyses.

Core calculations were performed by MCNP-3B using both libraries. The number of neutrons in Monte Carlo calculations are 200,000 for k_{eff}'s of the GODIVA, JEZEBEL and PNL cores, and are 100,000 for k_{∞}'s of the TRX cores. K_{eff}'s and k_{∞}'s uncertainties are typically around 0.2 and 0.1%Δk, respectively.

5. FAST REACTOR BENCHMARK TESTS

The GODIVA and JEZEBEL cores have much harder spectra than those of large FBR cores, because these two cores have small radii of 8.7 and 6.4 cm, respectively. Figure 5 shows averaged neutron spectra of both cores calculated by MCNP-3B using libraries based on ENDF/B-VI. Then, benchmark tests, using both files, were performed for integral properties of the high energy region from 10^5 to 10^7 eV; in particular fission, capture, elastic, inelastic and (n,2n) cross sections were focused on. Table 3 gives a summary of calculated k_{eff}'s for GODIVA and JEZEBEL cores, respectively. The k_{eff}'s of the GODIVA core, based on both files, agree well with experimental values, but those of the JEZEBEL core are underestimated about 0.5%Δk. Then, the difference in the k_{eff}'s based on both files is about 0.3%Δk.

Respective leakage spectra of the GODIVA and JEZEBEL cores have been measured by Frye, et al.[10] and Stewart[11]. Calculated leakage spectra were estimated by counting the number of neutrons passing through core surfaces by the newly provided surface tally from MCNP-3B. The number of neutrons to be compared with the experimental data can be obtained from integration of the following equation.

$$N_L(E) = -\int_{Eh}^{E} N(E')dE \qquad (4)$$

where

$N_L(E)$: integrated neutron leakage in the energy range from the highest energy E_h (about 10MeV) to E,

$N(E')$: number of neutrons which leak above neutron energy E'.

Figure 6 compares measured and calculated leakage spectra of the GODIVA and JEZEBEL cores. The calculated leakage spectra of the GODIVA core agree with experimental ones, except from 2 to 5 MeV. It seems that the ^{235}U fission spectra of both files is underestimated in this energy region. On the other hand, the calculated leakage spectra of the Pu-fueled JEZEBEL core agree well with experimental values.

Concerning fast reactors of uranium and plutonium metal cores with very hard

spectra, calculated k_{eff}'s based on both files agree with experimental values within 0.5% Δk. Calculated leakage spectra of the uranium metal core are underpredicted in the energy range of leakage neutrons from 2 to 5 MeV in both files, while spectra for the plutonium metal core show no significant difference with experimental data.

6. THERMAL REACTOR BENCHMARK TESTS

Benchmark tests of thermal reactor cores have been performed for PNL-1, -2 and TRX-1 through TRX-4 cores.

(1) PNL-1 and -2 cores

Neutrons in the PNL-1 core are well moderated by hydrogen, while those of the PNL-2 core are undermoderated. The spectrum of the latter is close to that of high conversion light water reactors as shown in figure 7. Table 4 gives the calculated k_{eff}'s for the PNL-1 and -2 cores. The k_{eff} of the PNL-2 core based on JENDL-3 tends to be overpredicted about 0.7% Δk, while that of the PNL-1 core agrees well. Meanwhile, calculated k_{eff}'s by JENDL-3 and ENDF/B-Ⅵ files are almost the same values within the Monte Carlo statistical errors of about 0.2% Δk. The the calculated k_{eff}'s are dominated by thermal cross sections which have almost comparable values in both files, since the cores have thermal fission reactions below 0.625 eV of about 96% and 84%, respectively, according to investigations of calculated neutron balances.

For thermal reactors of plutonium nitrate solutions, differences in calculated and measured k_{eff}'s are within 0.7% Δk.

(2) TRX-1 through TRX-4 cores

Spectra of TRX-1 through TRX-4 cores are similar to light water reactors as shown in figure 8. Table 5 gives the calculated k_{∞}'s of all TRX cores. Predicted k_{∞}'s by both files are nearly the same within the Monte Carlo statistical errors of about 0.2% Δk. According to investigations of neutron balances, neutron absorption rates of ^{235}U based on ENDF/B-Ⅵ decrease in comparison with those of JENDL-3 for decreasing volume ratio to harder neutron spectra, while those of ^{238}U indicate an opposite trend, as indicated in figure 8. Thus absorption rates of ^{235}U and ^{238}U are canceled by each other for calculated k_{∞}'s. Then the causes of different absorption rates in both files are discussed from the viewpoint of ^{235}U fission and capture cross sections, since differences in absorption rates of ^{235}U are larger than those of ^{238}U.

Figure 10 shows effective fission cross sections in a 190-group structure con-

densed from fission cross sections with continuous energy, and their ratios for ENDF/B-Ⅵ to JENDL-3. Differences of fission cross sections from JENDL-3's in each energy group are large, but they are canceled by an energy integral to obtain all energy contributions, so as a result ^{235}U fission contributions to the absorption rates in both files are nearly equal to each other. Figure 11 shows effective capture cross sections and their ratios for ENDF/B-Ⅵ to JENDL-3. The capture cross sections of ENDF/B-Ⅵ tend to be smaller than JENDL-3's in the resonance region from 1 to 1.5 $\times 10^5$ eV. Then capture differences in absorption rates are enlarged by decreasing the volume ratio, i.e. increasing neutron absorption on the resonance region.

Table 6 gives lattice parameters of ρ^{28}'s, δ^{25}'s, δ^{28}'s and their C/E values for TRX-1 and TRX-2. The C/E values based on both files are very close.

For slightly enriched uranium fueled thermal reactors, calculated lattice parameters of k_∞'s, ρ^{28}'s, δ^{25}'s and δ^{28}'s have nearly the same C/E-values for both files. Significant differences in ^{235}U absorption rates calculated by both files were found in cores with large ^{235}U capture contributions, because the ^{235}U capture cross section in ENDF/B-Ⅵ is smaller than the one in JENDL-3 by about 15% in the resonance region.

7. CONCLUSIONS

JENDL-3 and ENDF/B-Ⅵ files were tested for typical fast and thermal reactors, namely GODIVA, JEZEBEL, TRX-1 through TRX-4, PNL-1 and -2 by using the continuous energy Monte Carlo code MCNP-3B. In this analysis, in order to generate the MCNP-3B library, energy-angle distributions of secondary neutrons, described by Legendre coefficients or Kalbach-Mann systematics in ENDF/B-Ⅵ, were decomposed to angle and energy distributions respectively, and an adaptive method was employed in order to reduce interpolation errors.

(1) Regarding fast reactors of uranium and plutonium metal cores (GODIVA and JEZEBEL, respectively) with very hard spectra, calculated k_{eff}'s based on both files agreed with experimental values within 0.5% Δk.

(2) Calculated leakage spectra of the uranium metal core (GODIVA) were underpredicted in the energy range of leakage neutrons from 2 to 5 MeV in both files, while spectra of the plutonium metal core (JEZEBEL) had no significant difference with experimental data.

(3) For thermal reactors of plutonium nitrate solutions (PNL-1 and -2), differences in calculated and measured k_{eff}'s were within 0.7% Δk.

(4) For slightly enriched uranium fueled thermal reactors (TRX-1 through TRX-4), calculated lattice parameters of k_∞'s, ρ^{28}'s, δ^{25}'s and δ^{28}'s had nearly the same C/E-values between both files. Significant difference of ^{235}U absorption rates calculated by both files were found in cores with large ^{235}U capture contributions, because the ^{235}U capture cross section in ENDF/B-VI is smaller than the one in JENDL-3 by about 15% in the resonance region.

REFERENCES

(1) S. Iijima: JAERI-M 90-025, p5 (1990)
(2) Y. Kikuchi: ibid, p29 (1990)
(3) J. Hardy, Jr. and A. C. Kahler: Advances in Mathematics, Computations, and Reactor Physics, VOL 4, International Topical Meeting, April 28 - May 2, 1991, Pittsburgh, PA, USA, 19.1 1-1 (1991)
(4) J. Kim and C. Gil: JAERI-M 92-027, p394 (1992)
(5) Documentation for CCC-200/MCNP, Version 3B Code Package (1989)
(6) G. E. Hansen and H. C. Paxton, LA-4208 (1969)
(7) R. C. Lloyd, et al.: Nuclear Science and Engineering, 25, 165 (1966)
(8) J. Hardy, Jr, et al.: Nuclear Science and Engineering, 40, 101 (1970)
(9) Documentation for PSR-171/NJOY91.13 Code Package (1991)
(10) G. M. Frye, Jr., et al.: Los Alamos scientific Laboratory, TID-10073 (1954)
(11) L. Stewart: Nuclear Science and Engineering, 8, p595 (1960)

Table 1 Comparisons of resonance formulae and resonance regions for ^{235}U and ^{238}U

Data files		ENDF/B-VI		JENDL-3	
Nuclides		^{235}U	^{238}U	^{235}U	^{238}U
Resolved resonance region	Formula	Reich-Moore	Reich-Moore	SLBW[1]	MLBW[2]
	Region (keV)	0.0 - 2.25	0.0 - 10.0	0.001 - 0.1	0.0 - 9.5
Unresolved resonance region	Formula	SLBW	SLBW	SLBW	SLBW
	Region	2.25 - 25.0	10.0 - 149.0	0.1 - 30.0	9.5 - 50.0

1) SLBW: Single-level Breit-Wigner

2) MLBW: Multi-level Breit-Wigner

Table 2 Core types and measured quantities

Cores		Measurements
Fast reactors	GODIVA (uranium) JEZEBEL (plutonium)	k_{eff}'s Leakage spectra
Thermal reactors	TRX-1 to -4 (uranium)	Lattice parameters
	PNL-1, PNL-2 (plutonium)	k_{eff}'s

Table 3 Calculated k_{eff}'s of the GODIVA and JEZEBEL cores

core	JENDL-3	ENDF/B-VI	Diff.[1]
GODIVA	1.0013±0.0013[2]	0.9986±0.0013	0.0027
JEZEBEL	0.9970±0.0014	0.9945±0.0014	0.0025

1) Diff.=JENDL-3 - ENDF/B-VI

2) Statistical error in Monte Carlo calculation of 200,000 histories

Table 4 Calculated k_{eff}'s of PNL-1 and PNL-2

Core	JENDL-3	ENDF/B-Ⅵ	Diff.[1]
PNL-1	0.9968±0.0019[2]	0.9980±0.0019	-0.0012
PNL-2	1.0068±0.0022	1.0038±0.0022	0.0030

1) Diff.=JENDL-3 - ENDF/B-Ⅵ

2) Statistical error in Monte Carlo calculation of 200,000 histories

Table 5 Calculated k_∞'s of benchmark cores

Core	Volume ratio	JENDL-3	ENDF/B-Ⅵ	Diff.[1]
TRX-1	2.35	1.1827 ±0.0013[2]	1.1836 ±0.0010	-0.0009
TRX-2	4.02	1.1667 ±0.0013	1.1661 ±0.0010	0.0006
TRX-3	1.00	1.0652 ±0.0014	1.0673 ±0.0016	-0.0021
TRX-4	8.11	1.0213 ±0.0009	1.0225 ±0.0012	-0.0012

1) Diff.=JENDL-3 - ENDF/B-Ⅵ

2) Statistical error in Monte Carlo calculation of 100,000 histories

Table 6 Experimental lattice parameters and their C/E values of TRX-1 and TRX-2

	Exp.	C/E value	
		JENDL-3	ENDF/B-Ⅵ
TRX-1			
ρ^{28}	1.320 ±0.021	0.982	0.987
δ^{25}	0.0987±0.0010	0.960	0.972
δ^{28}	0.0946±0.0041	0.992	0.964
TRX-2			
ρ^{28}	0.837 ±0.016	0.969	0.971
δ^{25}	0.0614±0.0008	0.954	0.965
δ^{28}	0.0693±0.0035	0.977	0.956

ρ^{28}: cadmium ratio of ^{238}U capture

δ^{25}: cadmium ratio of ^{235}U fission

δ^{28}: ratio of ^{238}U fission to ^{235}U fission

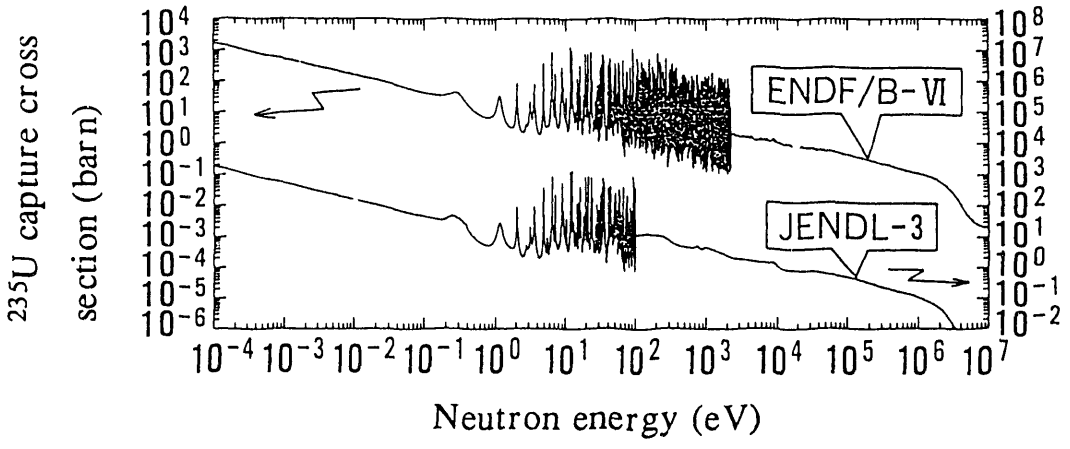

Fig. 1 Comparison of ^{235}U capture cross sections between JENDL-3 and ENDF/B-VI.

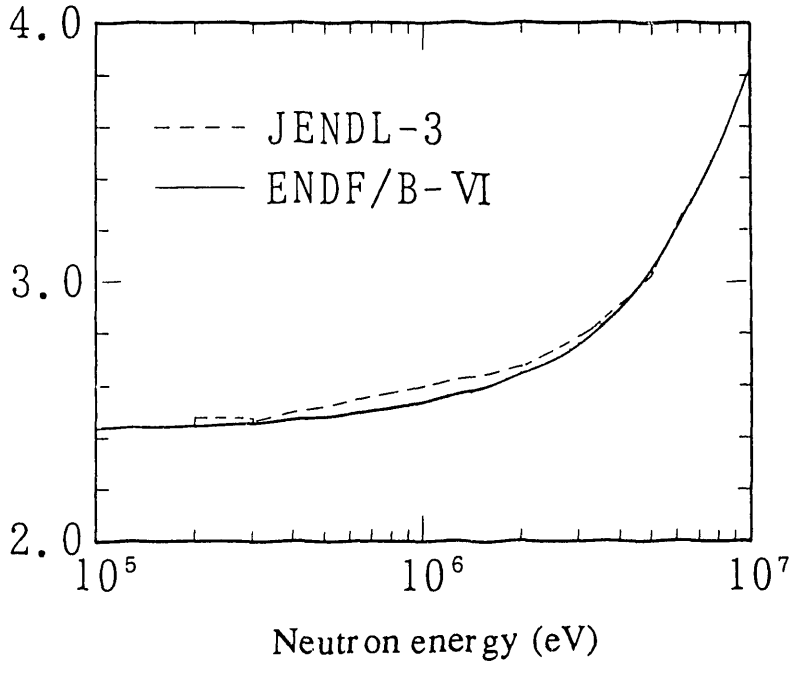

Fig. 2 Comparison of ^{235}U ν-values between JENDL-3 and ENDF/B-VI.

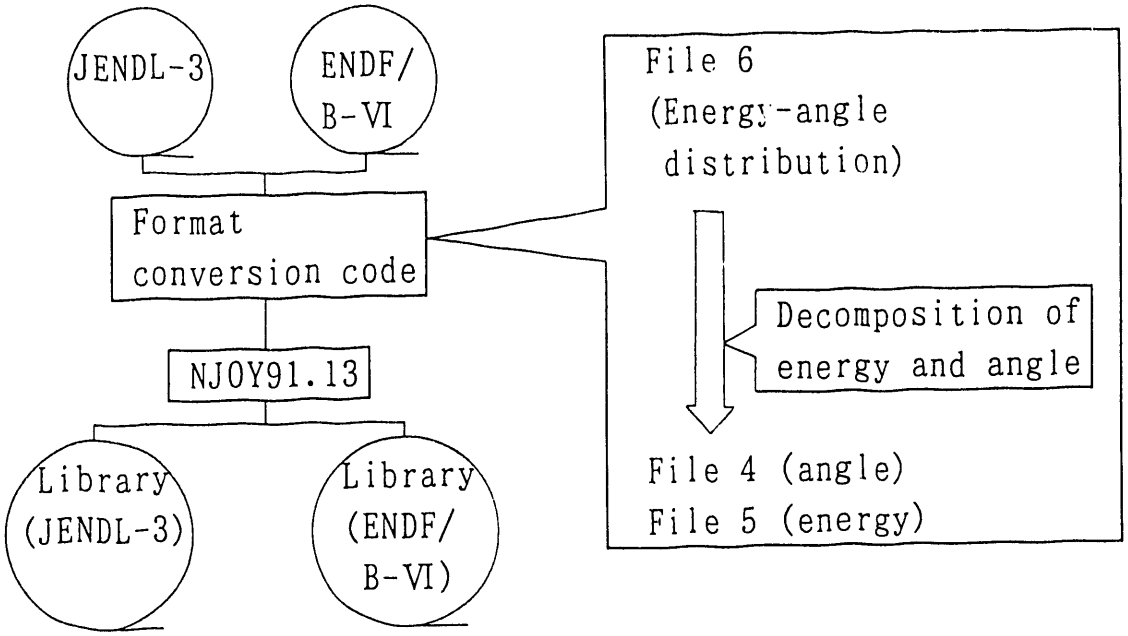

Fig. 3 Calculational flow of MCNP-3B libraries based on JENDL-3 and ENDF/B-VI.

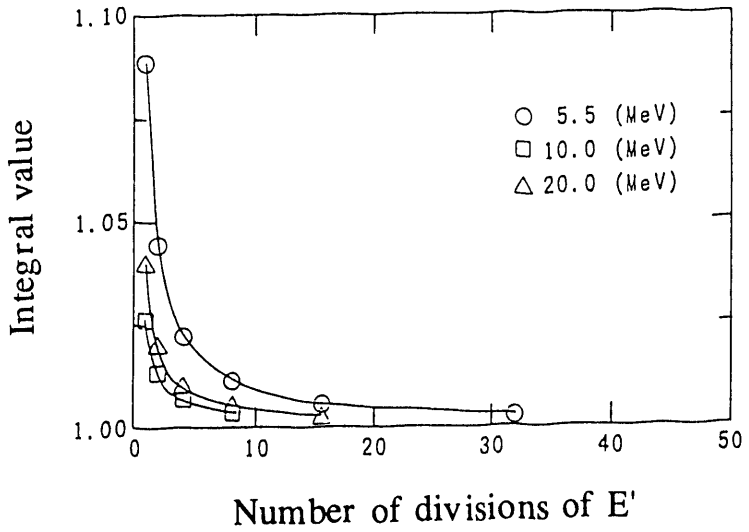

Fig. 4 Relation between number of divisions of E' and integral value with (n,2n) reaction.

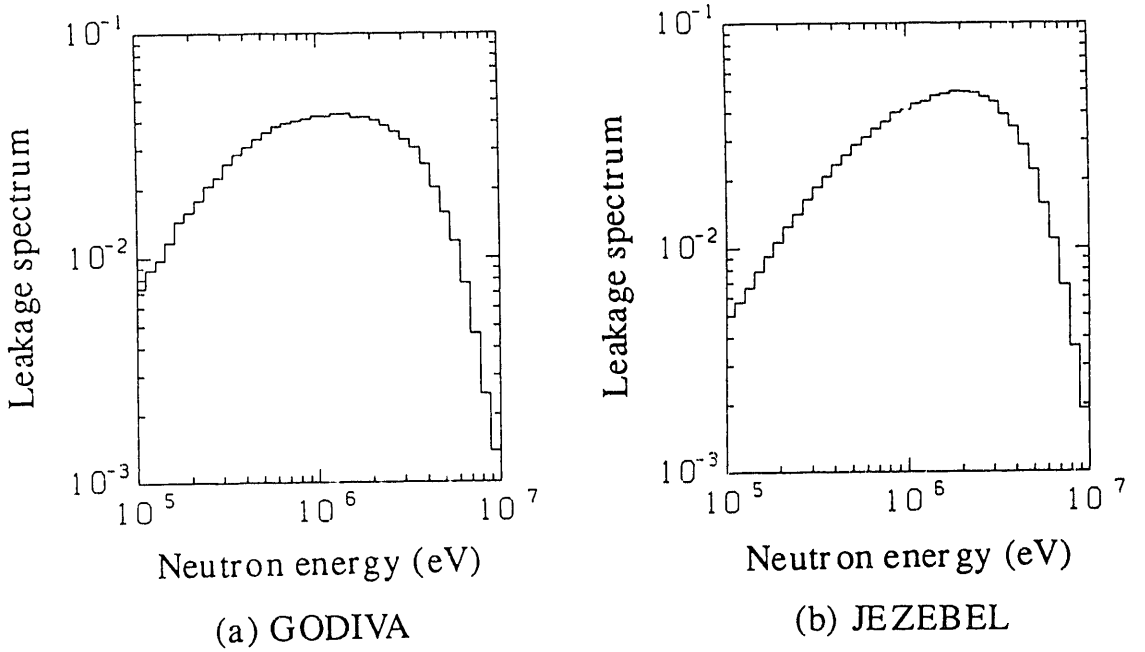

Fig. 5 Averaged neutron spectra of GODIVA and JEZEBEL cores. The spectra were calculated by MCNP-3B using libraries based on ENDF/B-VI.

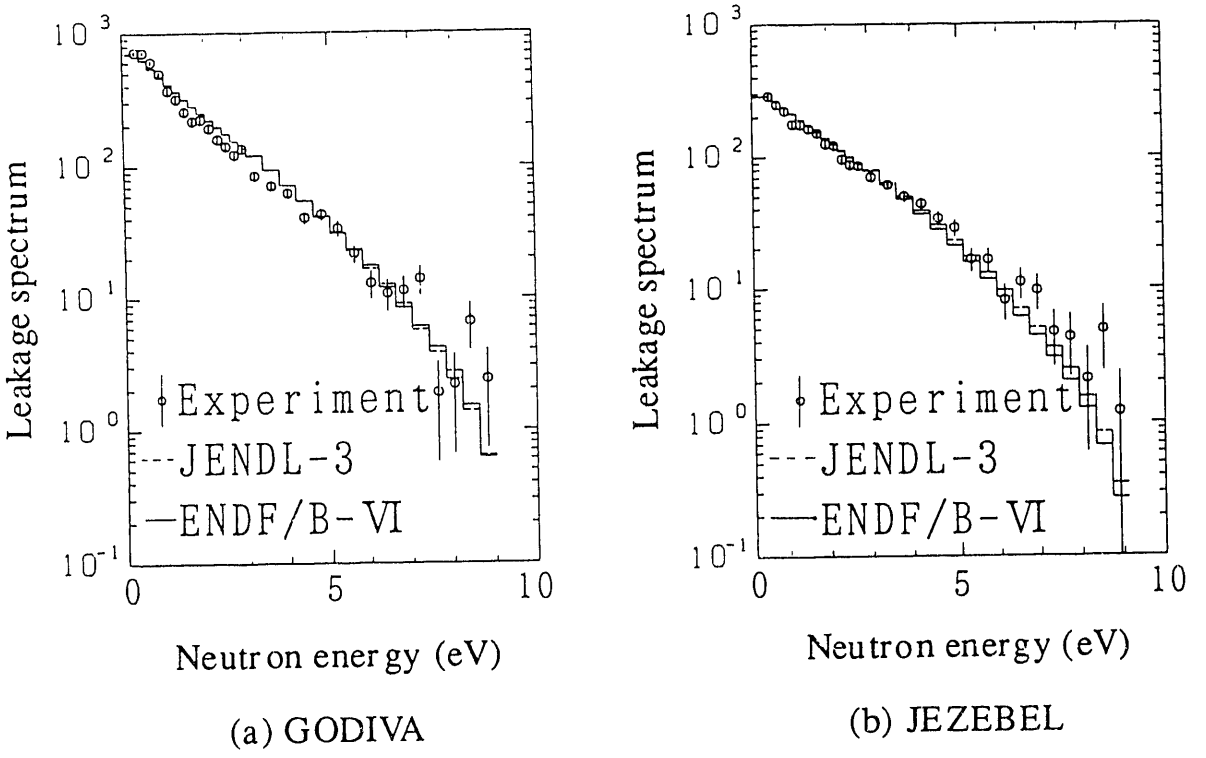

Fig. 6 Comparisons of measured and calculated leakage spectra of GODIVA and JEZEBEL cores.

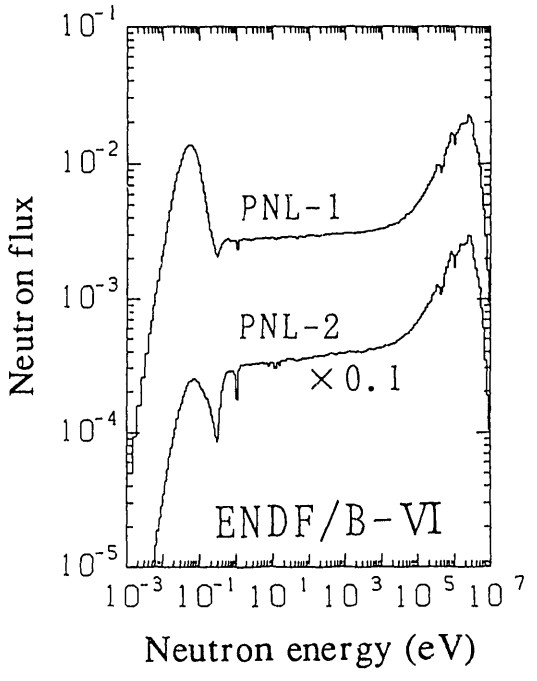

Fig. 7 Averaged neutron spectra of PNL-1 and PNL-2 cores.

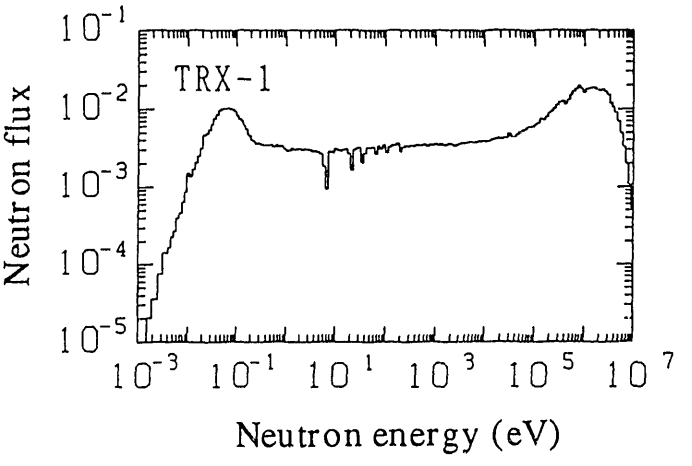

Fig. 8 Spectrum in the fuel region of TRX-1 core.

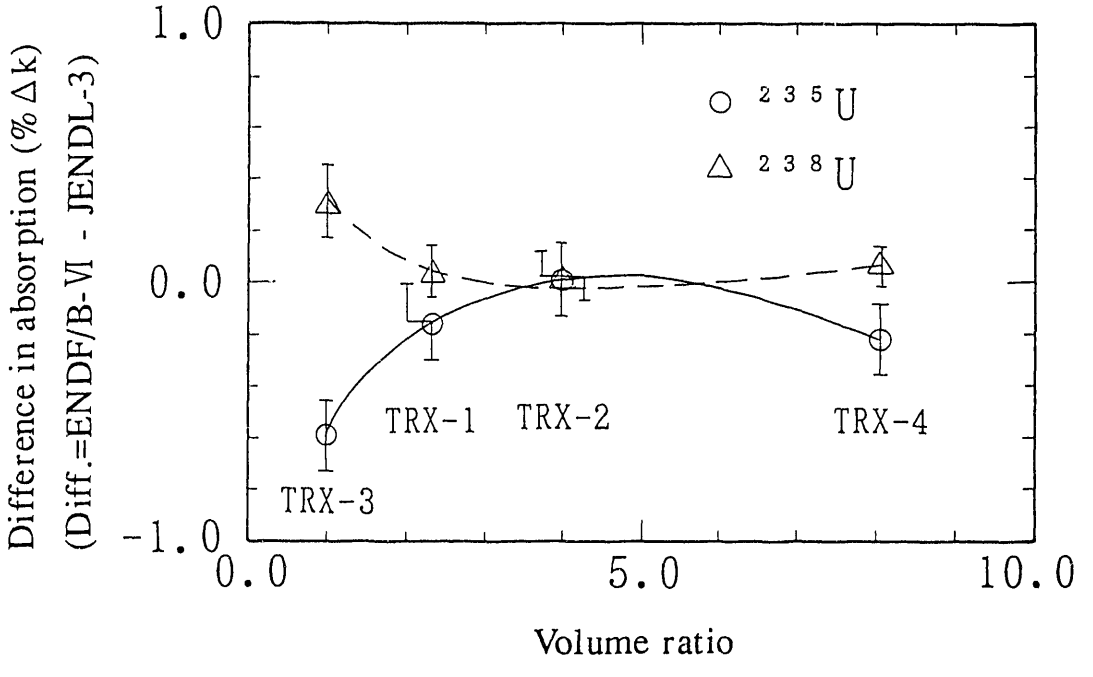

Fig. 9 Differences in ^{235}U and ^{238}U neutron absorptions.

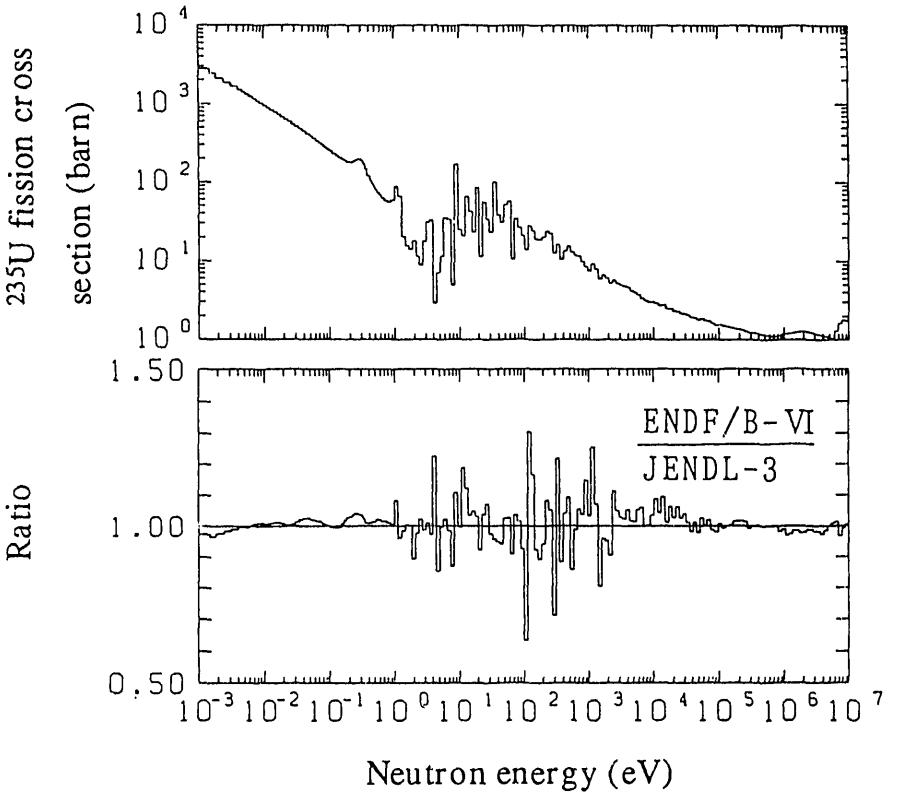

Fig. 10 Comparison of ^{235}U fission cross sections.

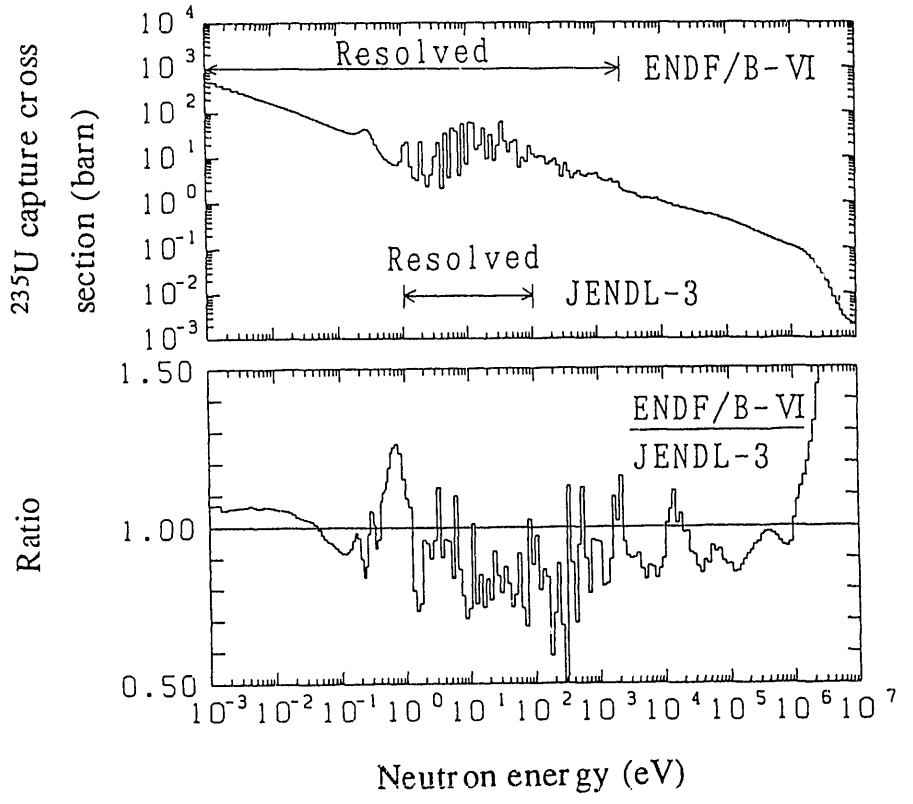

Fig. 11 Comparison of ^{235}U capture cross sections.

3. Papers Presented at Poster Session

3.1 Comparison of Nuclear Data Files in PWR-type Core Geometries

Y. Imamura, T. Jigami and K. Ikeda

Nuclear Fuel Department, Shikoku Electric Power Co., Inc.
Takamatsu, Kagawa 760-91, Japan

Bondarenko-type multi-group constants files are assembled from the latest versions of the evaluated nuclear data files JENDL-3.1 and ENDF/B-VI. And benchmark calculations to examine characteristics of both files for PWR-type core application are executed, based upon experimental results of JAERI TCA geometry and B & W critical facility.

1. Introduction

For electric power companies, optimization of core management is indispensable not only for reactor safety but for fuel procurement strategy. So, we developed core management code system, SENTAS(SEPCO Nuclear and Thermo-hydraulics Analysis System), over ten years ago, and recently, its improvement task has been accomplished[1]. In this system, nuclear data for most of important nuclides such as uranium, plutonium species were from ENDF/B-IV, and those of a few TRU nuclides(americium, curium, etc.) and FP species were from a part of ENDF/B-V and JENDL-2 as supplements. But, lately, the latest versions of the evaluated nuclear data files JENDL-3.1 and ENDF/B-VI were released. So, before incorporating these files into SENTAS, we must examine characteristics of both files for LWR design applications.

Our objects in this study are to do comparative study on multi-group constants between ENDF/B-VI and JENDL-3.1, and to examine characteristics of both files by benchmark calculations. We selected experiments executed at Japan Atomic Energy Research Institute(JAERI) TCA geometry[2] and Babcock & Wilcox(B & W) critical facility[3], and we also adopted these files to

commercial PWR-type core geometry.

2. Production of Multi-group Constants

2.1 Nuclear Data Processing

Fig.1 shows the flow scheme for evaluated nuclear data processing. Evaluated nuclear data are interpolated linear-linear by LINEAR code[4], and resonance parameters are treated by RECENT code[5] and smooth data are added to FILE3. Doppler broadening effect is treated by SIGMA1 code[6]. For moderators, such as hydrogen, GASKET[7] calculates scattering law $S(\alpha, \beta)$ and write them into FILE7, and MODY code, reformed from PIXSE code[8], calculates scattering cross sections. Lately, nuclear data points are generated at arbitrary energy points and scattering angles of incident neutrons in each temperature points of the nucleus.

Number of nuclides treated by this system are shown in Table I.

2.2 Multi-group Constants Calculations

Multi-group constants for important nuclides, such as uranium, plutonium are calculated by RABBLE code[9], for the fast and resonance regions, and by THERMOS code[10] for the thermal region. For not so important nuclides, such as minor FP species, GROUPIE code[11] is used and NR approximation is applied. Fig.2 shows a flow sheet of multi-group constants calculations.

In advance of transport equation calculations, in order to optimize energy points, we developed Automatic Energy Mesh Generating Method, where the energy meshes are generated in two steps:

(1) The basic energy mesh structure is selected from the boundary energy points of the multi-group constants and the resonance peak points of the nuclides of interest.

(2) The superfine mesh structure is generated by dividing the basic mesh into an equivalent lethargy width for the fast and resonance energy regions and an equivalent neutron velocity for the thermal energy region. This procedure guarantees that the relative errors of summation of the mesh-stripped cross sec-

tions to the one directly integrated from the nuclear data curve are less than the permitted criteria, which were determined to ensure ≤ 1% error of each multi-group constant for each reaction type:0.1% for relative error judgment and 0.1barn for absolute error judgment.

Condensed multi-group constants have fifty six energy groups, twenty two groups for the fast and resonance regions and thirty four groups for the thermal region. Fig.3 shows microscopic effective absorption cross section of ^{238}U, and are compared with ENDF/B-IV,VI and JENDL-3.1. Here, in resonance region, ENDF/B-VI and JENDL-3.1 have similar values. This effect in effective cross section would be derived by original data and extended resolved resonance region in both files. Fig.4 shows the microscopic effective cross section of ^{235}U. As shown here, JENDL-3.1 has larger values than that of ENDF/B-VI.

As for capture cross sections, effective resonance integral value in the fast and resonance regions of JENDL-3 is about 0.2% larger for ^{238}U and about 17% larger for ^{235}U than those of ENDF/B-VI.

2.3 Production of Bondarenko-type Multi-group Constants Library

After transport equation calculation, group constants are assembled in Bondarenko-type file. Here, Bondarenko-type means that multi-group constants can be interpolated using self-shielding factors, mutual shielding factors and infinite dilution values.

We evaluate self-shielding effect in following steps. First, we rewrite neutron flux calculated from transport equation into the form of NR approximation.

$$\phi(E)=\frac{1}{\Sigma_t(E)}\phi_s(E) \tag{1}$$

$\phi_s(E)$ is the standard spectrum and is composed of fission spectrum, 1/E curve and Maxwell distribution. Contribution of resonance to self-shielding effect is evaluated by next equation.

$$\sigma_o^i(E)=\frac{\mathrm{SUM}_{j\neq i}\ N^j\,\sigma_t^j(E)}{N^i} \tag{2}$$

Here, N^j is number density of species j. Suppose that background cross section $\sigma^l_{0,g}$ is constant in an energy region, flux can be written as

$$\phi(E)=\frac{\phi_s(E)}{N^l(^l\sigma_t(E)+\sigma^l_{0,g})} \quad (Eg-\ell \leq E \leq Eg-u) \tag{3}$$

Accordingly, self-shielding cross section can be expressed as

$$\sigma^i_{x,g}=\frac{\int_{Eg-\ell}^{Eg-u}\frac{\sigma^l_x(E)\cdot\phi_s(E)}{\sigma^l_t(E)+\sigma^l_{0,g}}dE}{\int_{Eg-\ell}^{Eg-u}\frac{\phi_s(E)}{\sigma^l_t(E)+\sigma^l_{0,g}}dE} \tag{4}$$

and, lately, self-shielding factor is defined as

$$F^l_{x,g}(\sigma^l_{0,g})=\frac{\sigma^l_{x,g}(\sigma^l_{0,g})}{\sigma^l_{x,\infty}} \tag{5}$$

and are tabulated. Here, $\sigma^l_{x,\infty}$ is infinite dilution microscopic cross section.

On the other hand, ^{238}U has the overwhelming majority in fuel pellet, and flux concerning mutual shielding effect of ^{238}U can be written as

$$\phi(E)=\frac{\phi s(E)}{N^l\{\sigma^l_t(E)+Ri\sigma^{238}_t(E)+\sigma^{*l}_0(E)\}}\ , \tag{6}$$

Here, Ri is the ratio of number density between species i and ^{238}U. $\sigma^{*l}_0(E)$ is background cross section and is defined as

$$\sigma^{*l}_0(E)=\frac{1}{N^l}\{SUM_{j\neq i,238}\ N^l\ \sigma^l_t(E)\}=\sigma^{*l}_{0,g}=\text{const.} \tag{7}$$

Defining $\overline{\sigma}^l_{x,g}$ as multi-group constant not concerning mutual shielding effect, mutual shielding factor can be defined as

$$M^l_{x,g}(\sigma^{*l}_{0,g},Ri,T)=\frac{\sigma^l_{x,g}(\sigma^{*l}_{0,g},Ri,T)}{\overline{\sigma}^l_{x,g}(\sigma^l_{0,g},T)}\ . \tag{8}$$

Then, using Bondarenko-type multi-group constants file, microscopic and macroscopic effective cross section can be derived by infinite dilution cross section, self-shielding factors and mutual shielding factors, corresponding with number density, temperature, background cross section for nuclides of interest.

$$\begin{aligned}\sigma^l_{x,g}(\sigma^{*l}_{0,g},T,Ri)=&\sigma^l_{x,g}(\sigma^l_{x,\infty},300^\circ K,0)\\ &\times F^l_{x,g}(\sigma^l_{0,g},T,0)\\ &\times M^l_{x,g}(\sigma^{*l}_{0,g},300^\circ K,Ri)\end{aligned} \tag{9}$$

$$\sigma_{0,g}^{l} = \sigma_{0,g}^{*l} + Ri \cdot \sigma_{l,g}^{238} \quad (10)$$

$$\sigma_{0}^{*l} = \frac{1}{N^{l}} \left(\sum_{j \neq i,238} N^{l} \sigma_{l} + \frac{aG}{\ell} \right) \quad (11)$$

ℓ : Mean Cord Length
G : Dancoff Factor
a : Bell's Factor

Here, geometrical heterogeneity is considered by Dancoff factor.

This Bondarenko-type multi-group constants file(BMGF) is used with multi-group fission spectrum file(GFSF) and multi-group scattering matrix file(GSMF) for reactor constants calculations. We prepared each multi-group constants file corresponding to JENDL-3.1 and ENDF/B-VI, respectively.

3. Benchmark Calculations

In the first place, we examined characteristics of both files by benchmark calculations of TCA geometry and B & W critical facility, in use of Monte Carlo code KENO[12]. Among a lot of TCA experiments, we selected forty cases, including gadolinia-uranium dioxide fuel rods 21X21 lattice systems(twenty four cases), M X N lattice systems(eight cases), iron reflector systems(two cases) and control rod arranged 15X15 lattice systems(six cases).

Neutron history conditions for KENO calculation are below:

Neutrons per generation : 3000
Number of generations : 200

Errors of eigenvalues and pin power error distributions(for relative power ≥ 1), calculated from each nuclear data file, are compared in Table II. As shown here, ENDF/B-VI yields higher eigenvalues than those of JENDL-3.1. Analysis of multi-group constants profile revealed that, generally, each file has similar energy dependence of cross section, but that absorption cross sections of ^{238}U and ^{235}U of JENDL-3.1 are larger than those of ENDF/B-VI. The main reason of tendency on eigenvalues would be derived from this effects. On the other hand, there is almost no systematic feature on pin-wise power error distributions as shown in Fig.5.

Secondly, we executed PWR-type core characteristics calculations, using Advanced Nodal Method. In this case, assembly-wise reactor constants are produced by collision probability method and diffusion method, in place of Monte Carlo method. Fig.6 shows error distributions of assembly average power at movable detector positions(for relative power $\geq$ 1) and that they have almost normal distribution profile.

4. Conclusions

Bondarenko-type multi-group constants files are assembled from the latest versions of ENDF/B and JENDL, and their benchmark calculations are executed. As for eigenvalues, ENDF/B-VI yields higher values than those of JENDL-3.1. But, generally, nuclear data in each file have similar energy dependency against those of ENDF/B-IV, and both files have almost no systematic feature on pin-wise and assembly-wise power error distributions. Further verifications of these nuclear data files for PWR-type core application are now in progress.

References

1) Imamura,Y.,et al.:Proc.15th Biennial Mtg. on Reactor Operating Experience,Bellevue,WA,(1991).
2) Matsuura,S. et al.:JAERI-M 9844,(1981).
3) Green,I.D.:NPG-TM-179,(1972).
4) Cullen,D.E.:UCRL-50400,vol.17,Part A,Rev.2.
5) Cullen,D.E.:UCRL-50400,vol.17,Part C,Rev.2.
6) Cullen,D.E.:UCRL-50400,vol.17,Part B,Rev.2.
7) Koppel,J.U.,et al.:GA-7417,(1966).
8) Macdougall,J.:AEEW-M318,(1963).
9) Kier,P.H.,et al.:ANL-7326,(1967).
10) Honeck,H.C.:BNL-5826,(1961).
11) Cullen,D.E.:UCRL-50400,vol.17,Part D,Rev.2.
12) Whitesides,G.E.:Proc.Livermore Array Symp.,CONF-680909(1968).

Table I Number of nuclides treated by SENTAS

	ENDF/B-VI	JENDL-3.1
HEAVY NUCLIDES (Z=90-94)	14	13
TRU NUCLIDES (Z=95-100)	9	9
STRUCTURAL MATERIAL NUCLIDES	17	32
FP NUCLIDES	181	157

Table II Statistical analysis of benchmark calculations

CRITICAL FACILITY	NUCLEAR DATA FILES	ERRORS OF k_{eff} (%)		ERRORS OF PIN POWER <R.P.≧1> (%)	
		Avg.	S.D.	Avg.	S.D.
TCA (40 CASES)	ENDF/B-VI	0.05	0.23	0.17	2.74
	JENDL-3.1	-0.94	0.31	-0.16	2.87
B&W (15 CASES)	ENDF/B-VI	0.33	0.15	-0.02	1.90
	JENDL-3.1	0.13	0.14	0.01	1.68

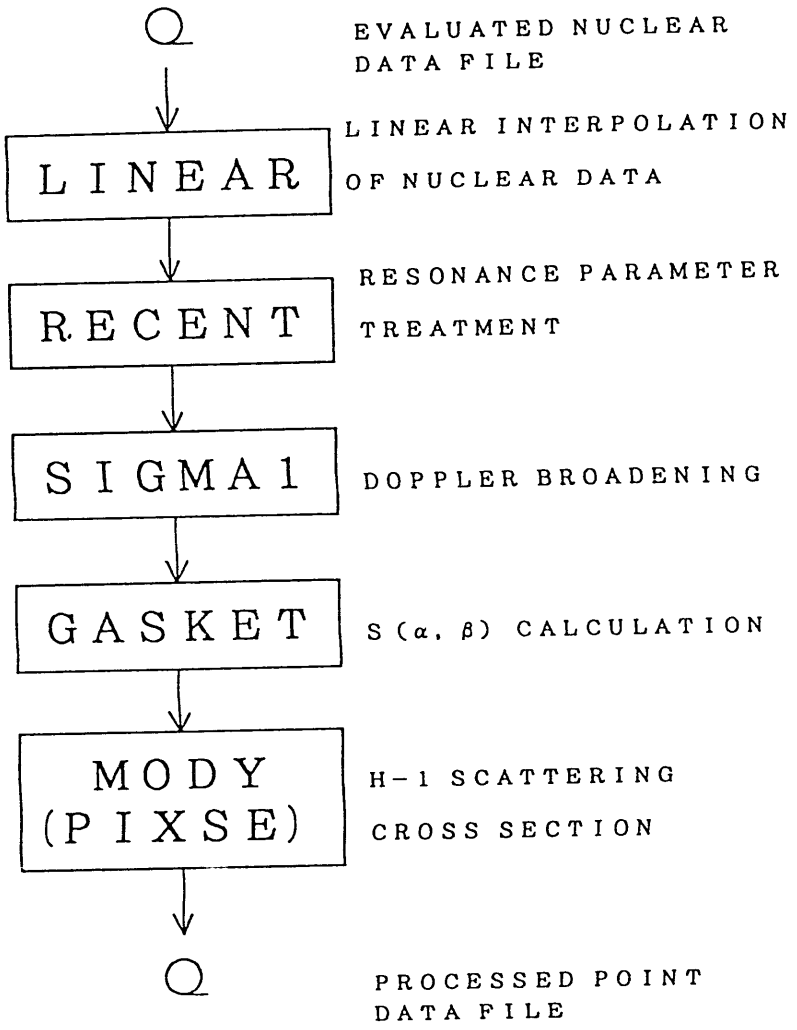

Fig. 1 Flow scheme for nuclear data processing.

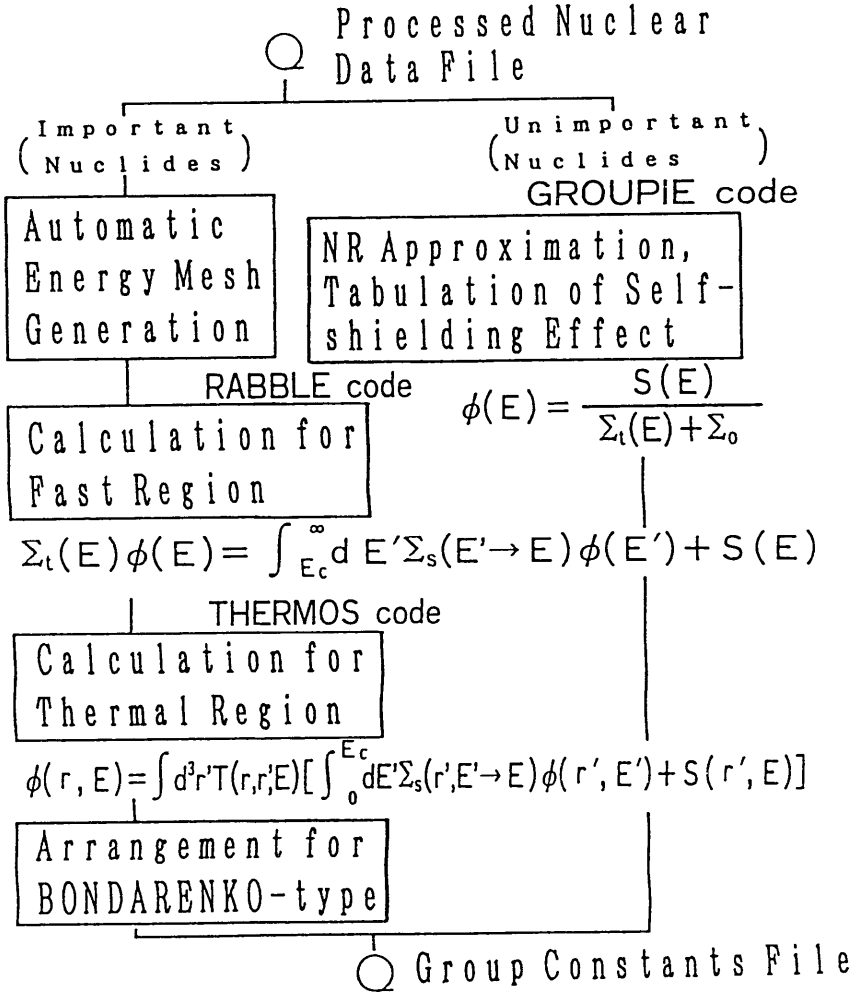

Fig. 2 System flow of multi-group constants calculations.

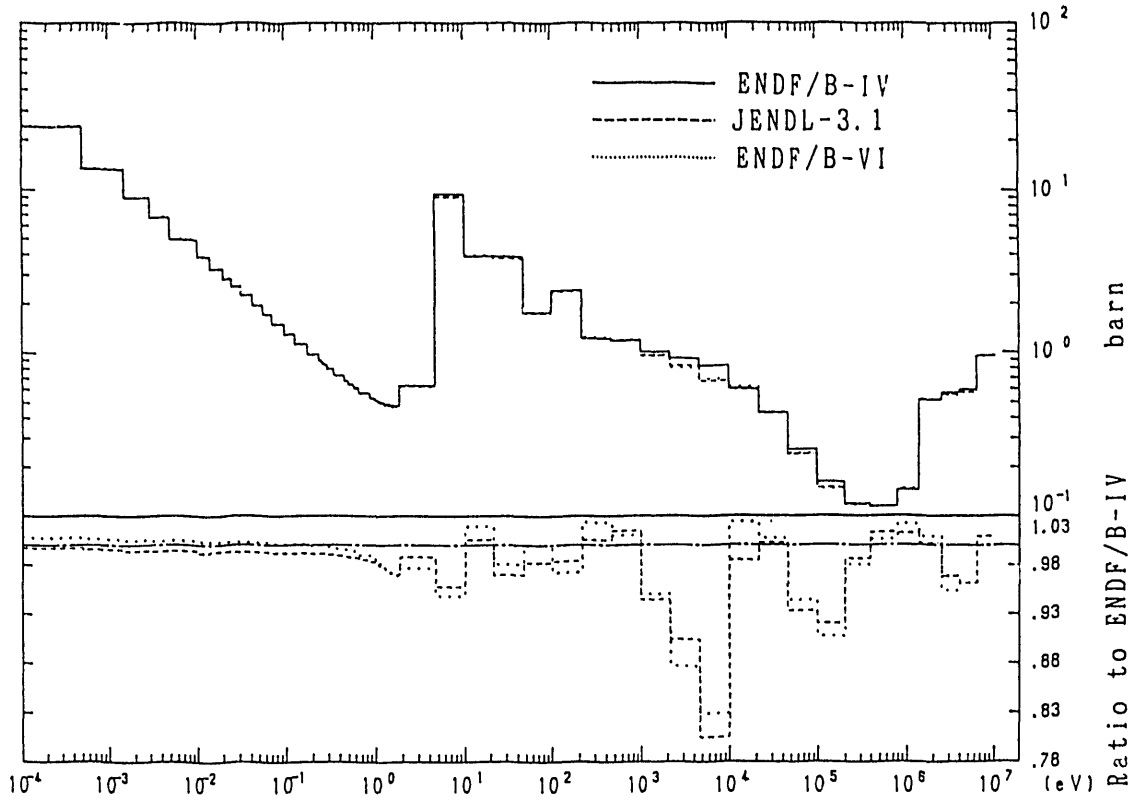

Fig. 3 Microscopic effective cross section (σ_a of ^{238}U).

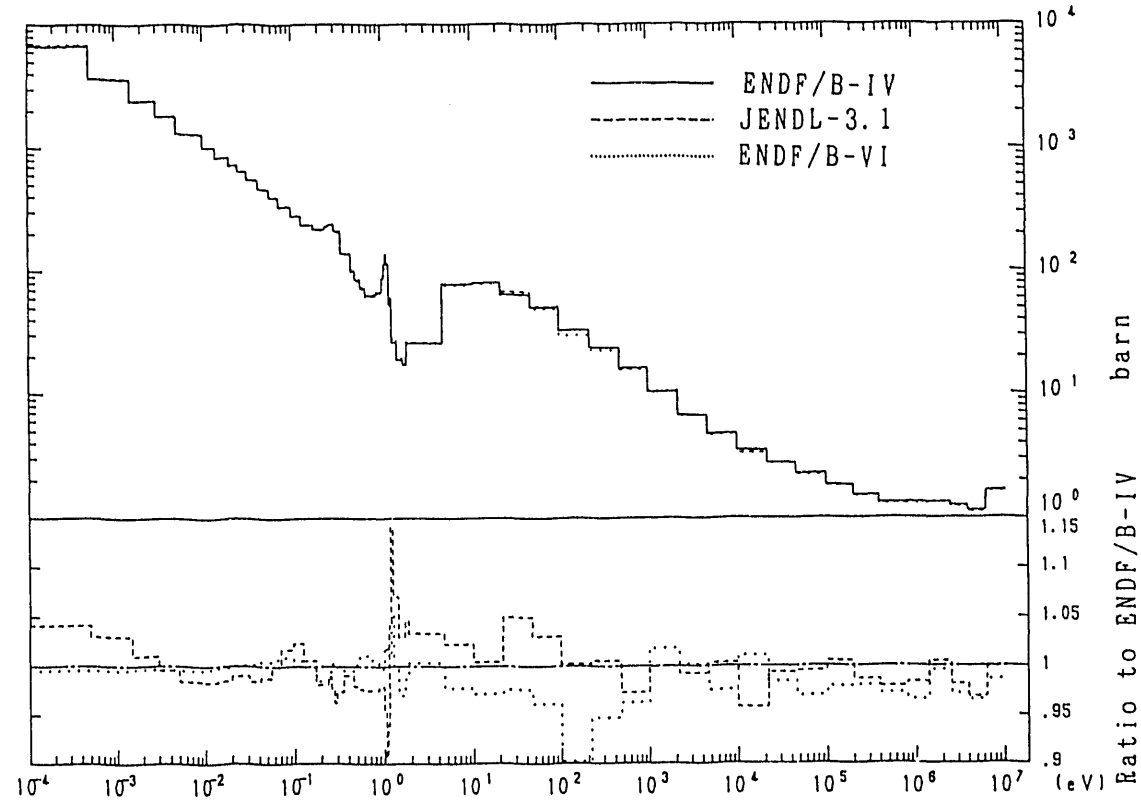

Fig. 4 Microscopic effective cross section (σ_a of ^{235}U).

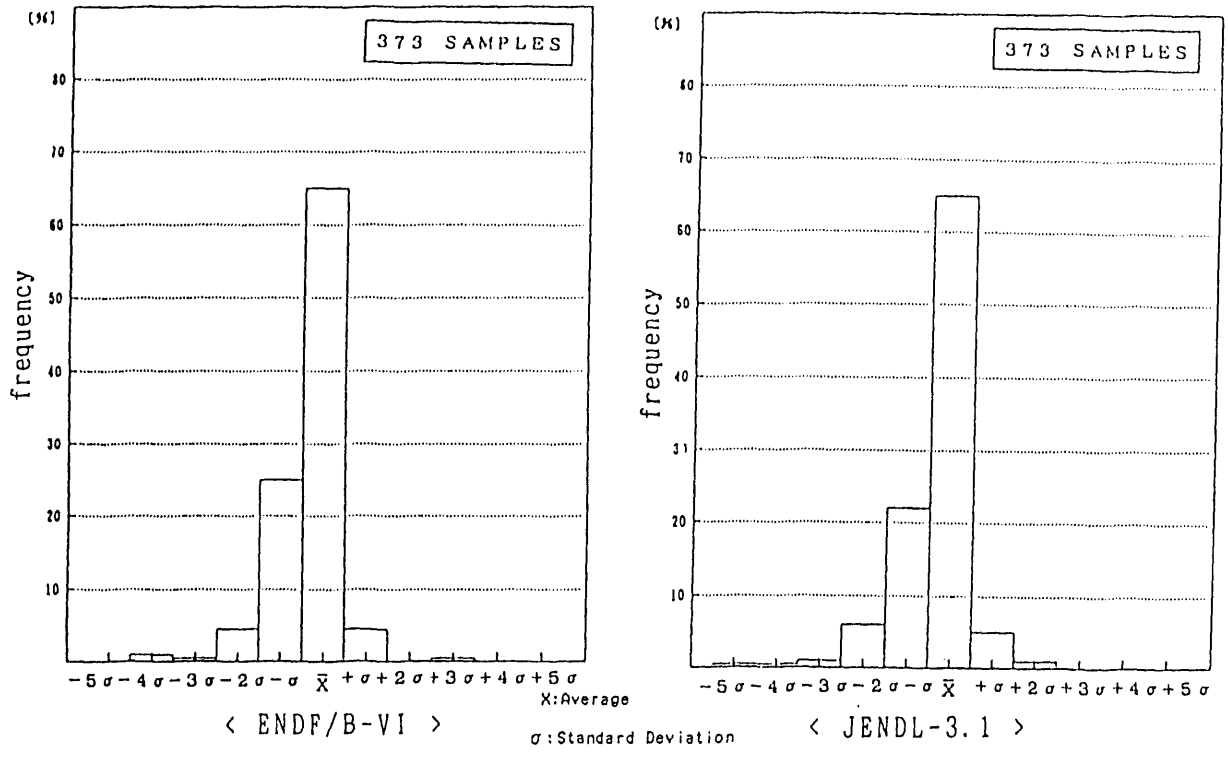

Fig. 5 Error distributions of pin power (R.P. > 1)

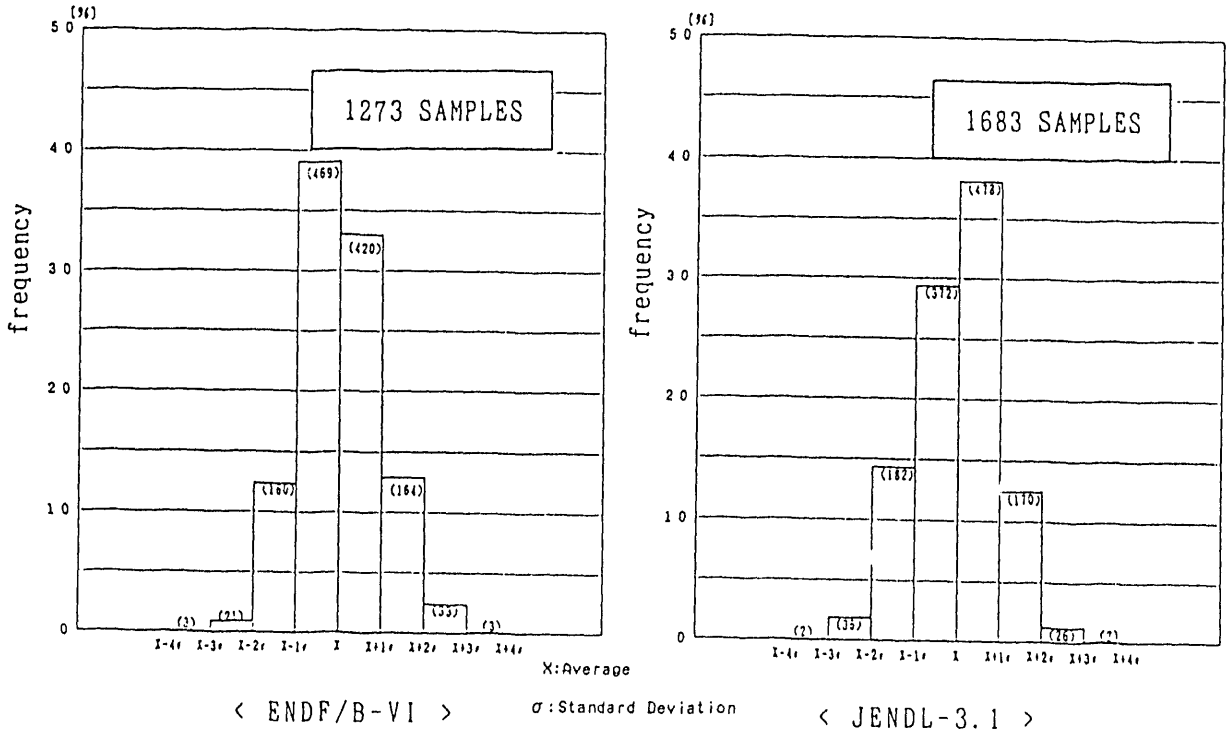

Fig. 6 Error distributions of assembly average power (R.P. > 1)

3.2 Thermal Reactor Benchmark Calculations for MCNP on JENDL-3

Yuji UENOHARA and Yoshihira ANDO
NUCLEAR ENGINEERING LAB., TOSHIBA CORPORATION,
4-1,UKISHIMA-CHO, KAWASKI-KU, KAWASAKI 210, JAPAN

The benchmark calculations for MCNP were performed for the infinite cell models of two types of UO_2 cores, TRX-1 and TRX-2, and four types of MOX core TCA. The authors evaluated k-∞s, flux averaged cross sections, and neutron spectra with an accuracy of 0.1-5 %. It was necessary to modify slightly NJOY.89 code for these calculations. The ACER module in NJOY.89 evaluates infinitely diluted cross sections in unresolved resonance regions. However, the calculated reactor parameters are almost consistent with those of the VIM calculations presented in the thermal reactor benchmark calculations for JENDL-3, performed by LWR-Integral-Data-Testing-WG.

1. Introduction

Nuclear data potentially plays an important role in neutronic calculation. Deterministic methods for neutronic calculations, however, are still ambiguous. Most researchers and engineers are interested in modifications of the computational models and aware of confusion brought from the changes of nuclear data. They recognize nuclear data to be significant but have little incentive to improve it. It is necessary to process evaluated nuclear data in order to change data libraries. Nuclear data processing is very difficult and requires many special techniques. If the methods were free from ambiguity of computation models and the simple processing techniques were supplied, many potential users would have access to nuclear data.

The continuous energy Monte Carlo method is free from the ambiguity of computational models. Nuclear data processing is very simple. It, however, requires tremendous computing resources. Most users cannot easily use Monte Carlo codes. The current progress of computer technology is making the Monte Carlo method familiar. This progress comprises two trends: Downsizing and parallelism. Downsizing realized powerful engineering workstations and Personal Computers. Downsizing has enabled many users to become familiar with heavy computations which were gigantic about ten years ago. Parallel processing enables users to approach astronomical scale of problems, which are still

considered insoluble. Parallelism will change the impossible to the possible. Downsizing represents the main stream of the current computing environment. Parallel processing is likely to be the main technique of supercomputing in the future. Downsizing makes the Monte Carlo method user friendly while parallel processing makes it competitive with deterministic methods.

The subject of the present work is the testing of the thermal reactor benchmark calculations reported in reference/1/. In this report, several calculation codes based on deterministic methods and three Monte Carlo codes are tested. Only one VIM code was referred to the continuous energy Monte Carlo code. The nuclear data processing system for VIM code is closed to us. The authors, therefore, cannot produce the libraries for VIM from JENDL-3.

The MCNP/2/ is a continuous energy Monte Carlo code. Its libraries can be produced with the ACER module in nuclear data processing system NJOY.89/3/. These codes are completely open. Everyone can easily obtain the detailed information. The authors used the open computation systems, too. The processing and benchmark calculations were performed on the EWS-AS-4000 series, which are designed on the open architecture and open UNIX operating systems. The authors tried to test the JENDL-3 by using this open information only. Everyone, therefore, can test our results even if huge computing systems and special information are unavailable.

The benchmark tests were performed for the infinite cell models of two types of UO_2 cores TRX-1 and TRX-2, and four types of MOX core TCA. The authors evaluated k-∞s, flux averaged cross sections, and neutron spectra with an accuracy of 0.1-5 %. It was necessary to modify slightly NJOY.89 code for these calculations. The ACER module in NJOY.89 evaluates infinitely diluted cross sections in unresolved resonance regions. However, the calculated reactor parameters are consistent with those of the VIM calculations except for $^{238}U(n,\gamma)$ cross section in fast neutron energy region.

2. Benchmark Calculation Models

The MCNP.V3B was employed in the present benchmark calculations. The MCNP is a general-purpose Monte Carlo code for neutron and photon transport simulations. It was developed at Los Alamos National Laboratory. The MCNP code is famous for being one of the most powerful applications for source problems such as fusion neutronics. It can be applied to eigenvalue problems such as fission reactor analysis. The MCNP is an open code. Every user can

obtain its detailed information. The cross section libraries for MCNP can be produced using the ACER module in the NJOY code.

3. Nuclear Data Processing

The nuclear data processing system, NJOY.89, is employed in the present work. The ACER module in NJOY.89 produces a nuclear data library for MCNP. Fig. 1 shows the procedures for the production of MCNP libraries. The RECONR module in NJOY.89 reconstructs excitation curves from resonance parameters and interpolation schemes using the method of RESEND. The BROADR module reads the reconstructed cross sections and Doppler-broadens them using the method of SIGMA1. The ACER module produces MCNP library using the Doppler-broadened cross sections and angular distribution: MF=4, energy distribution: MF=5, and double differential cross sections: MF=6 files in JENDL-3 file.

Only one linear-linear interpolation scheme(INT=2), in the tabulated MF=5 file(LF=1), is available for the ACER module. The MF=5 files in JENDL-3 have almost all been specified by log-linear interpolation scheme(INT=4). The ACER module, therefore, cannot process them. The authors changed the log-linear interpolation scheme of MF=5 files in JENDL-3 to linear-linear schemes. The authors describe the procedures, briefly. The MF=5 files were reconstructed by inserting new energy grid points between the original data points. Two types of values at the inserted energy point are evaluated with log-linear and linear-linear interpolation schemes. If their difference is greater than the criterion given, the data point evaluated with log-linear interpolation scheme is inserted into the MF=5 files.

The ACER module in NJOY.89 can evaluate only infinitely diluted cross sections in unresolved resonance regions. The MCNP accompanied with the present cross section libraries overestimates unresolved resonance cross sections.

4. Comparisons of the MCNP Calculations

4.1 TRX Critical Cores

Fig. 2 shows the specifications of TRX-1 and TRX-2 cores. In this chapter, multiplication factors of these cores and averaged cross sections of ^{235}U and ^{238}U are discussed.

4.1.1 Multiplication Factors

Figs. 3 and 4 show the k-∞s calculated for TRX-1 and TRX-2. The k-s calculated with MCNP are consistent with those of VIM within their standard deviations.

4.1.2 Averaged Cross Sections

Group cross sections averaged over fast(9.1keV-10MeV), resonance(5eV-9.1keV), and thermal(below 5eV) energy regions are compared for ^{235}U, and ^{238}U in Figs. 5-8.

The present results are consistent with those calculated by VIM, except for only $^{238}U(n,\gamma)$ averaged cross sections in the fast neutron energy region. The difference is about ten times larger than the estimated standard deviations. The ACER module in NJOY.89 gives infinitely diluted cross sections in unresolved resonance regions. Since the ^{238}U atom abounds in this fuel, the overestimation of unresolved resonance absorption was observed. The other deterministic analyses resulted in similar effects, quantitatively.

4.2 TCA Critical Cores

There are scarce water-moderated lattice experiments with plutonium fuels. The accurate experiments with 3.0 w% PuO_2-natural UO_2 fuel rods of TCA cores were selected. The water-fuel volume ratios cover from 2.42 to 5.55. Fig. 9 shows the specifications of TCA MOX cores. In this section, multiplication factors of these cores and averaged cross sections of ^{238}U, ^{239}Pu, and ^{240}Pu are discussed.

4.2.1 Multiplication Factor

The k-s calculated are shown in Figs. 10-13. As for k-s, the results calculated with MCNP are consistent with the VIM's results within their standard deviations except for the case of Pitch=2.474cm.

4.2.2 Averaged Cross Sections

Group cross sections averaged over fast(9.1keV-10MeV), resonance(5eV-9.1keV), and thermal(below 5eV) energy regions are compared for ^{238}U, ^{239}Pu, and ^{240}Pu in Figs. 14-18. These cross sections are consistent with the VIM results within the estimated standard deviation. The overestimation of

$^{238}U(n,\gamma)$ averaged cross sections in the fast neutron energy region was not observed.

5. Results and Discussions

Processes of evaluated nuclear data and neutronic calculations can be performed using only open codes(NJOY.89 and MCNP) and using open computer systems(EWS-SUN4:AS-4000 Series). It takes several hours of CPU time to solve an infinite-cell problem.

The differences between VIM and MCNP results are almost always caused by the statistical fluctuations. The authors, therefore, conclude that MCNP is consistent with VIM with an accuracy of 0.1%. Although NJOY.89 still has many programming bugs except for the incomplete modules such as the unresolved resonance treatments, the effects of these bugs, however, have not appeared in the present work. Many larger histories are necessary to verify NJOY.89 and MCNP more precisely.

Processes of unresolved resonances will be improved in the next version of NJOY.91. The authors, however, regard the concept of unresolved resonance as temporal. The extension of resolved resonance regions is a simple and an ideal solution. It requires a great deal of computing resources in current computing environments. The progress of computer technology,however, will make it feasible.

References

/1/ TAKANO, H, et al.: Thermal Reactor Benchmark Calculations for JENDL-3, JAERI-M 92-027

/2/ BRIESMEISTER, J.F., et al.: MCNP: A General Monte Carlo Code for Neutron and Photon Transport, LA-7396-M, Rev.2, 1986

/3/ MacFARLANE,R.E., et al.: The NJOY: Nuclear Data Processing System, :User's Manual LA-9303-M, Vol.I-III, 1982

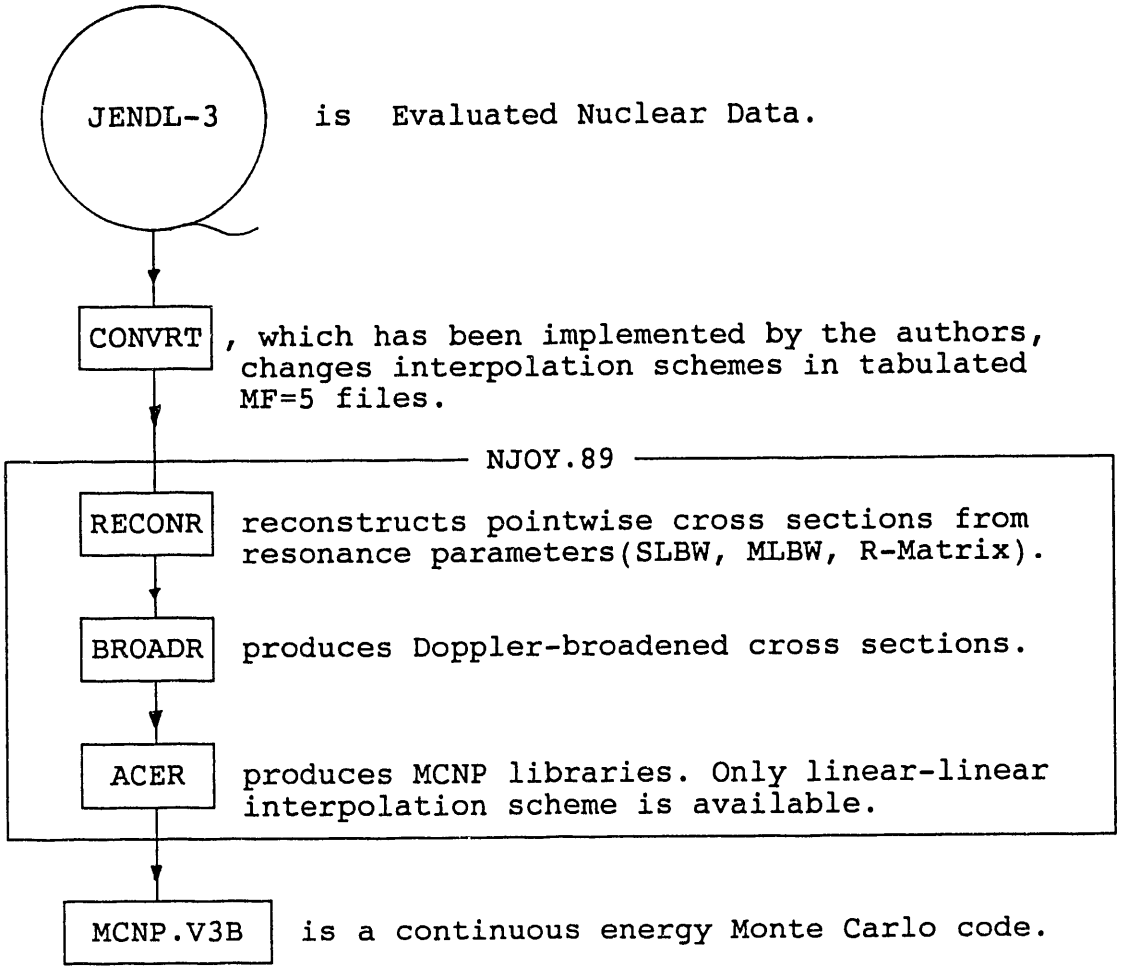

Fig. 1 Block diagram of procedure for MCNP library production.

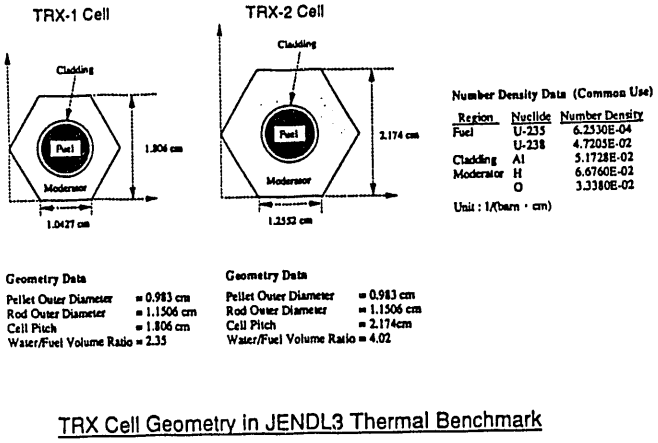

TRX Cell Geometry in JENDL3 Thermal Benchmark

Fig. 2 Specifications of TRX UO_2 cores.

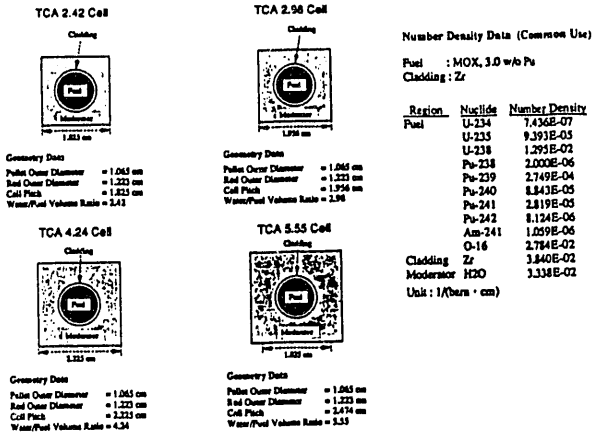

TCA Cell Geometry in JENDL3 Thermal Benchmark

Fig. 3 Specifications of TCA-MOX cores.

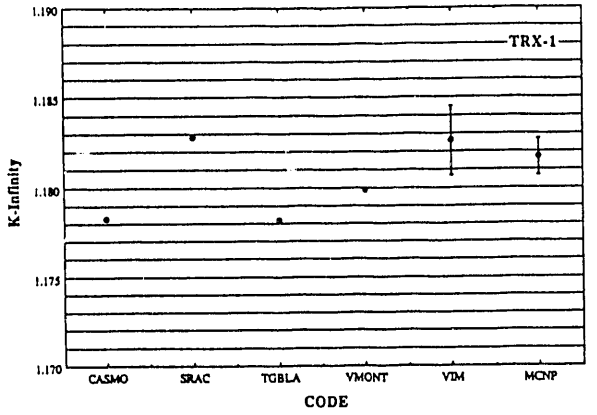

Fig. 4 Comparisons of k-∞s for TRX-1 core with the present MCNP calculations. The error bars in the figure denote the standard deviations evaluated by the Monte Carlo calculation.

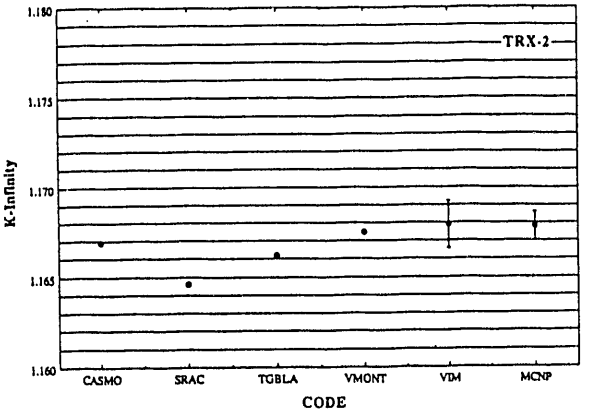

Fig. 5 Comparisons of k-∞s for TRX-2 core.

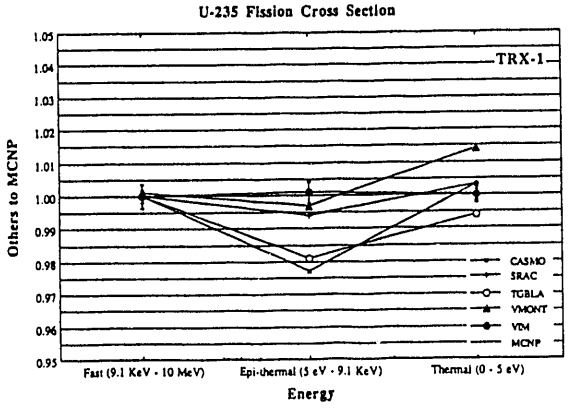

Fig. 6 Comparisons of $^{235}U(n,f)$ cross sections in the fuel region of TRX-1 infinite lattice. The error bars in the figure denote the standard deviations evaluated by the Monte Carlo calculation.

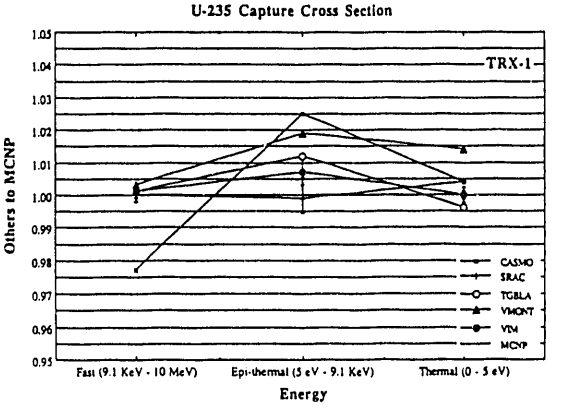

Fig. 7 Comparisons of $^{235}U(n,\gamma)$ cross sections in the fuel region of TRX-1 infinite lattice.

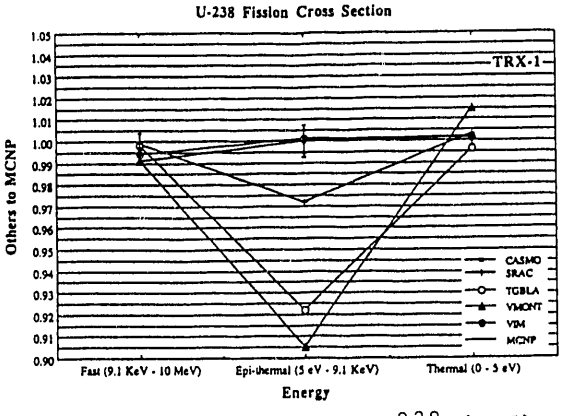

Fig. 8 Comparisons of $^{238}U(n,f)$ cross sections in the fuel region of TRX-1 infinite lattice.

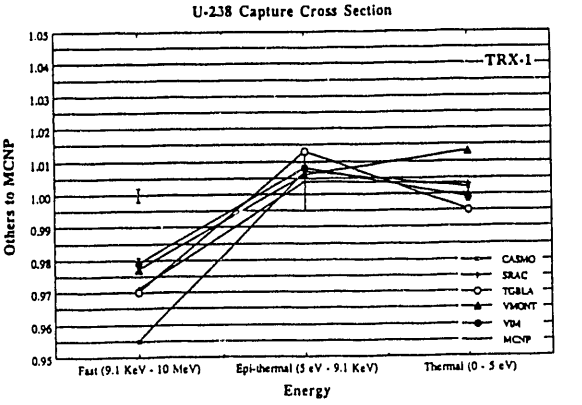

Fig. 9 Comparisons of $^{238}U(n,\gamma)$ cross sections in the fuel region of TRX-1 inifinite lattice.

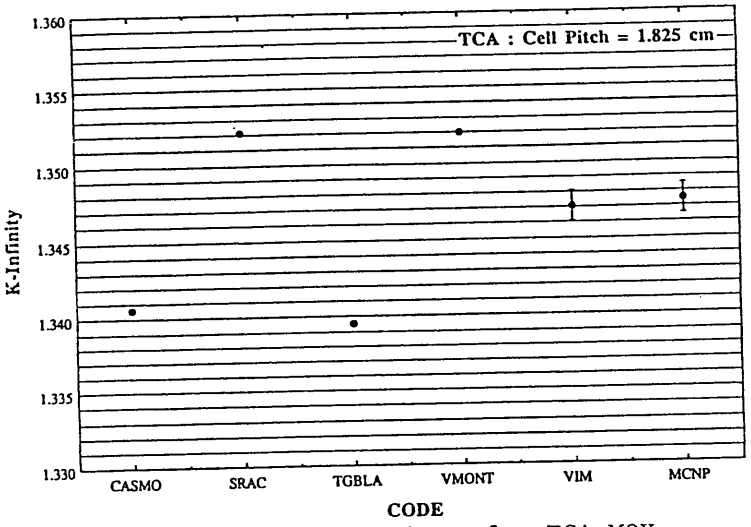

Fig. 10 Comparisons of k-∞s for TCA-MOX core (Pitch=1.825cm). The error bars in the figure denote the standard deviations evaluated by the Monte Carlo calculation.

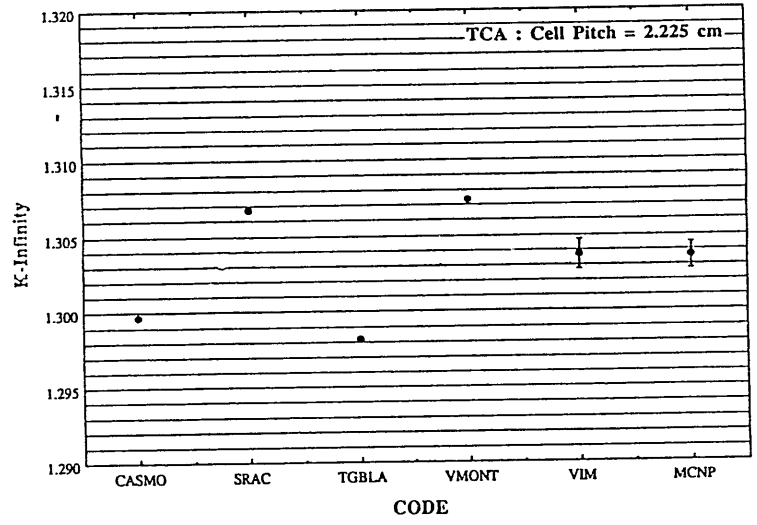

Fig. 12 Comparisons of k-∞s for TCA-MOX core (Pitch=2.225cm).

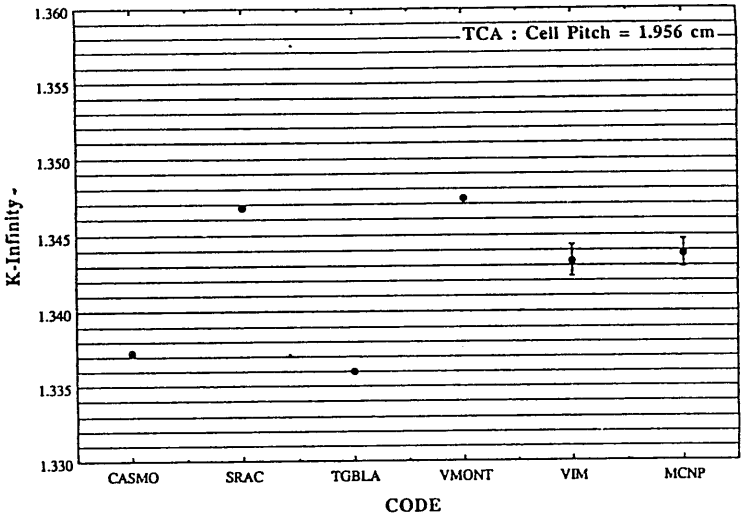

Fig. 11 Comparisons of k-∞s for TCA-MOX core (Pitch=1.956cm).

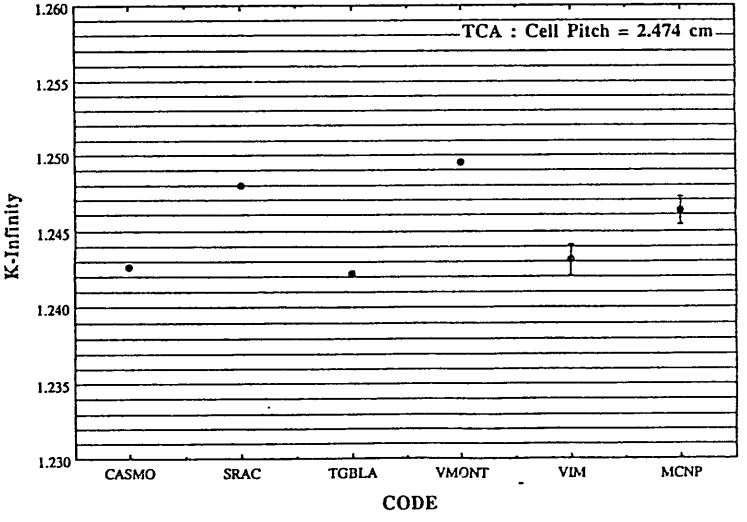

Fig. 13 Comparisons of k-∞s for TCA-MOX core (Pitch=2.474cm).

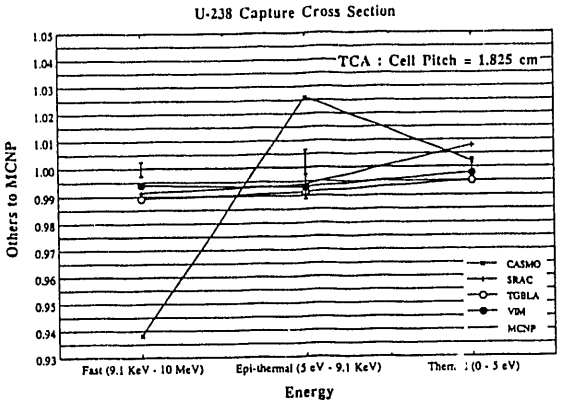

Fig. 14 Comparisons of $^{238}U(n,\gamma)$ cross sections in the fuel region of TCA-MOX infinite lattice (Pitch=1.825cm). The error bars in the figure denote the standard deviations evaluated by the Monte Carlo calculation.

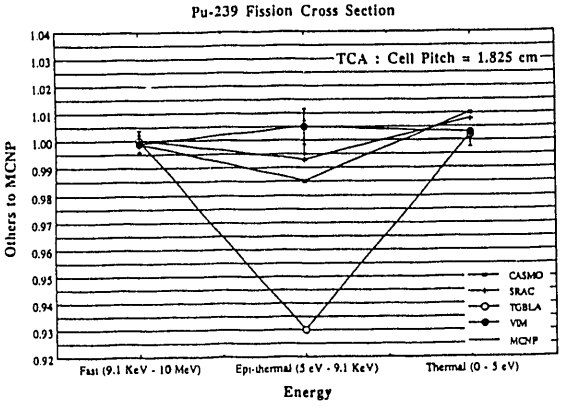

Fig. 15 Comparisons of $^{239}Pu(n,f)$ cross sections in the fuel region of TCA-MOX infinite lattice (Pitch=1.825cm).

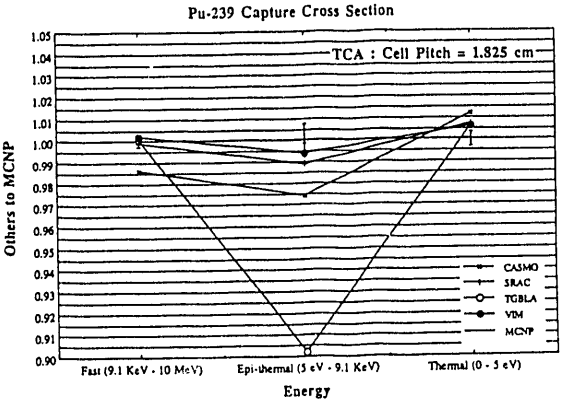

Fig. 16 Comparisons of $^{239}Pu(n,\gamma)$ cross sections in the fuel region of TCA-MOX infinite lattice (Pitch=1.825cm).

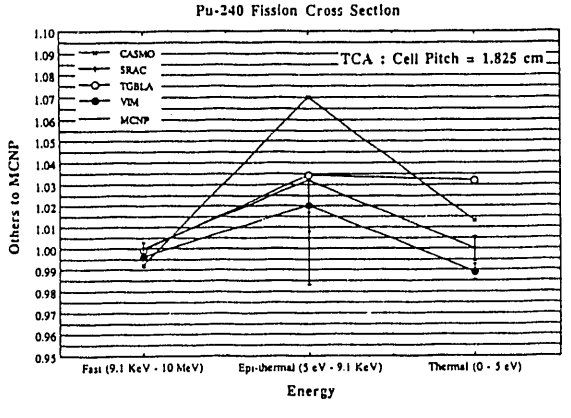

Fig. 17 Comparisons of $^{240}Pu(n,f)$ cross sections in the fuel region of TCA-MOX infinite lattice (Pitch=1.825cm).

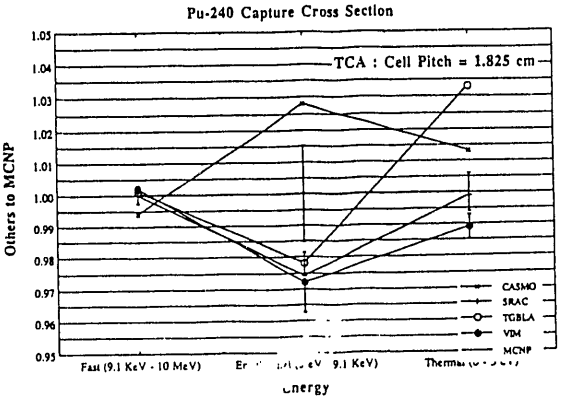

Fig. 18 Comparisons of $^{240}Pu(n,\gamma)$ cross sections in the fuel region of TCA-MOX infinite lattice (Pitch=1.825cm).

3.3 Nuclear Data Requirements for Fast and Perfect Transmutation of Actinide Wastes using A-Burner

Tomohiko Iwasaki and Naohiro Hirakawa

Department of Nuclear Engineering, Tohoku University
Aoba, Aramaki, Aoba-ku, Sendai-shi, Japan 980

A reactor-base facility "A-Burner" with the total flux of 1. $0x10^{16}$ n/cm^2/sec is proposed for the transmutation of the actinide wastes. It consists of a small core and a large D_2O reflector. The reflector and the central region of the core have the optimized spectra for transmutation of the lower and higher actinides, respectively. First, the lower actinides are transmuted in the reflector with the well-thermalized spectrum. For ^{237}Np, the transmutation half-life becomes 9 days and the transmuted amount is 37 kg/y. The byproduct, which is accumulated on the first step, is transmuted in the central region of the A-Burner with the slightly hard spectrum. The transmutation half-life of ^{248}Cm is 70 days. By irradiating 1000 days, the amount of actinides reduces to 10^{-4}. Furthermore, ^{250}Cm with the spontaneous fission probability of 100% is mainly produced as the final byproduct. The A-Burner has the possibility of the fast and perfect transmutation of the actinide wastes. However, the performance strongly depends on the nuclear data of actinides. We require the addition of the nuclear data to JENDL-3 for ^{238}Np, ^{243}Pu, ^{244}Pu, ^{253}Cf and ^{253}Es. The resonances data are also required for ^{249}Cm, ^{250}Cm, ^{254}Cf, ^{254}Es and ^{255}Es. The decay data are needed for ^{250}Cm.

I. Introduction

The question for the management of the high-level long-lived radioactive waste is one of the difficult issues associated with the fission energy. The aim of the transmutation of those is to reduce the time required for the waste management for the long-lived nuclides. Actinides, which include many nuclides with the half-lives over a million years, are the main object of the transmutation. There is no stable nuclide in actinides. The short-lived actinides generate the long-lived actinides due to the alpha-decay chain. To shorten the lives, those must be fissioned to escape from the chain.

The researches for the transmutation of the actinides have been performed at various research laboratories. Many laboratories have been proposed the neutron-base concepts using thermal rectors, fast reactors and accelerated sppallation sources. The thermal reactors are not enough to transmute the wastes in a period of time comparable with a human life since the neutron fluxes of the reactors is too poor. The fast reactors are available to obtain higher flux. However, the effective reaction cross sections are too small. Huge inventories of the actinides must be loaded in the cores to make transmutation worthy. Both the large effective cross section of the thermal rectors and the high fluxes of the fast reactors are needed to achieve effec-

tive transmutation.

A facility to realize the both conditions have been designed in Oak Ridge National Laboratory. The facility /1/, which is named Advanced Neutron Source (ANS), is developed to obtain the thermal flux of $1.0x10^{16}$ n/cm^2/s and to supply neutrons for the research for condensed matter physics, material science, isotope production and fundamental physics. The ANS core can meet the conditions mentioned above. We propose a reactor facility "A-Burner" for transmutation of the actinide wastes based on ANS /1/. The A-Burner also has the total flux of $1.0x10^{16}$ n/cm^2/s. The A-Burner core is slightly modified from the ANS core to involve two regions optimized for the transmutation of the lower actinides such as ^{237}Np and the higher actinides such as ^{246}Cm and ^{248}Cm. It is expected that the A-Burner transmutes the actinides with high speed by small inventory.

Furthermore, we must mention one more issue of transmutation that is a problem of the byproduct of the transmutation. A transmutation concept using an accelerator-base neutron source has been proposed by Los Alamos National Laboratory /2,3/. The transmutation is performed in a thermal field with the thermal flux over $1.0x10^{16}$ n/cm^2/s. The approach of transmutation is quite similar to that of our study. It is also expected that the transmutation could be possible with the speed same as the A-Burner or more. However, they do not mention about the higher actinides accumulated as the byproduct of transmutation. Since the generation of the higher actinides could not avoided, this problem is quite important to reduce the time for the waste management.

We study the transmutation of those considering re-irradiation of the accumulated actinides as the second step of transmutation in another region of the A-Burner. Investigating the nuclear characteristics of the higher actinides, it is found that there are many nuclides with the high fission cross section or the spontaneous fission probability of 100%. We expect that the transmutation of those is not so difficult. Furthermore, if the nuclide with the spontaneous fission probability of 100% remains as the final byproduct, the perfect transmutation could be possible. In this paper, we describe about the system and the transmutation concept using the A-Burner with calculation results. The nuclear data needed for our study is summarized.

II. System and Transmutation Scheme

The A-burner consists of a small hollow core (100 cm high and 50 cm in diameter) and a large D_2O reflector (400 cm high and 400 cm in diameter), as shown in Fig.1. The core contains the 93%-enriched ^{235}U, produces the thermal power of 360 MW for about 14 days, and achieves the total neutron flux over $1x10^{16}$ n/m^2/sec. Although the ANS core consists of two core-assemblies, three core-assemblies in the A-Burner are arranged in barrel shape in order to yield higher epithermal flux at the central region of the core. The core assemblies have the

similar dimensions to the ANS core assemblies. The volumes of the reflector and the central region are about 20000 and 50 liter, respectively.

The fuel elements contain totally about 15 kg 93%-enriched ^{235}U. The loading of ^{235}U is varied continuously axially and radially to flatten the power distribution. The fuel plates are about 1.27-mm thick with the aluminum clad of 0.25-mm-thick. In the coolant gap of 1.27-mm, heavy water flow up with the velocity of about 20 to 30 m/s. Due to many fuel plates, high velocity and short heated length, the safety removal of the fission power is available.

On the first step of the transmutation, the lower actinides are transmuted in the reflector. The actinide wastes are directly diluted into D_2O and the solution is reprocessed to remove plutonium and fission products between the refueling interval. The D_2O moderator generates the very soft spectrum that enhances the reactions of the nuclides with large thermal cross section such as ^{237}Np. By the high flux of $1.0x10^{16}$ n/cm^2/sec and the spectrum, the transmutation advances rapidly.

Continuing the transmutation, ^{246}Cm and ^{248}Cm with low thermal cross section are accumulated in the reflector as the byproducts. The accumulated curium is transmuted in the central region of the A-Burner on the second step of the transmutation. The curium is packed into the pins and loaded in that region. The curium isotopes are transmuted to the higher actinides and fissioned at the nuclides with the large fission cross section (^{247}Cm, ^{251}Cf, ^{252}Cf and ^{253}Cf) and the spontaneous fission probability of 100% (^{254}Cf and ^{250}Cm). It is expected that the total actinide weight rapidly decreases.

III. Analysis and Result

The analysis flow is given in Fig.2. The nuclear data for the nuclides appeared in the burn-up chain were fulfilled by combining JENDL-3 and ENDF/B-VI. RESEND-D and CRECTJ codes were used to prepare the 107-group cross sections of 42 nuclides above ^{235}U. The one dimensional cell calculation by SRAC /4/ produced the 107-group spectrum and the 5-group library for CITATION. The 5-group cross sections for each material were collapsed from the 107-group cross sections using the 107-group spectra. The two-dimensional core calculation was performed by CITATION. The 1-group cross sections for ORIGEN-2 were obtained for 15 subregions of the A-Burner based on the 5-group cross sections and the 5-group spectra from CITATION.

In Fig.3, the neutron spectra are shown in the central region, the fuel region, the reflector region and the whole core. The reflector region has the well-thermalized spectrum and the central region has the slightly hard spectrum. The 1-group cross sections of ^{237}Np and ^{248}Cm dependent on the radial position are the core is presented in Fig.4. The cross sections of ^{237}Np and ^{246}Cm show maxima at the reflector and the central region, respectively.

The characteristics of the core with the various actinide concentrations are calculated. The k-eff variation of the ANS core is presented in Fig.5 for the case that ^{237}Np with the concentration of 1 g/l is initially loaded in the reflector. The cycle length is maintained to be 14 days. Figure 6 shows the total flux distribution in the A-Burner. It is indicated that the total flux is about 1.0×10^{16} n/cm^2/s in the reflector and the central region. The actinides of about 200 kg can be loaded in the reflector at 1 g/l.

At each subregion of the reflector, the diluted actinides are transmuted as shown in Table 1 and Fig.7. It should be paid attention that all the data in Table 1 are the values for the half core except for the two lines from the bottom. The weights of neptunium and plutonium are also given in Table 1 at the end of cycle. The solid line in Fig.7 indicates the variation in the whole reflector. The half-life of transmutation is about 9 days since the transmutation of ^{237}Np is accelerated due to the high fission cross section of ^{238}Np. The amount of ^{237}Np of 0.7 kg is transmuted by fission in one cycle. The plutonium of 1.1 kg is produced. Considering the reprocess of the plutonium, the transmuted weight is about 1.8 kg per cycle and about 37 kg per year. The residual actinides are continued to transmute in the reflector. After the long-term transmutation, ^{246}Cm and ^{248}Cm are accumulated in the reflector, as shown in Fig.8.

As the second step of the transmutation, the accumulated curium is transmuted in the central region of the A-Burner. The variation of the amount of the total nuclides is presented in Fig. 9 when only ^{248}Cm is loaded. The total actinide weight rapidly decreases without saturation. At 1000 days, the actinide weight reduces to the fraction of 10^{-4}. The half-life of transmutation is about 70 days. At 1500 days, i. e., 4 years, it is found that the main byproduct of the transmutation is ^{250}Cm that has the probability of the spontaneous fission of 100%. Since it may be unusual case that only ^{248}Cm is loaded, this result would not be guaranteed for other nuclide compositions. The A-Burner, however, has the possibility that all the actinides could be burned perfectly. We will continue the study of perfect transmutation by investigating irradiation methods or nuclide compositions.

IV. Nuclear Data Requirement

As mentioned above, the fast and perfect transmutation might be possible using the A-Burner. However, this situation strongly depends on the nuclear data of actinides. Recently, the nuclear data are quite improved for actinides. Table 2 shows the contents of the nuclear data libraries of ENDF/B and JENDL. It is found that the recent libraries have enlarged to involve many higher nuclides. Comparing the two libraries, JENDL-3 includes more nuclides; especially over curium. However, even JENDL-3 is not enough for this study. In the high flux condition, the very higher actinides up to ^{255}Fm or the unusual nuclides such as ^{244}Pu appear in the burn-up chain. We require that the evaluated data for ^{238}Np, ^{243}Pu, ^{244}Pu, ^{253}Cf and ^{253}Es

Fig. 6 Error distributions of assembly average power (R.P. > 1)

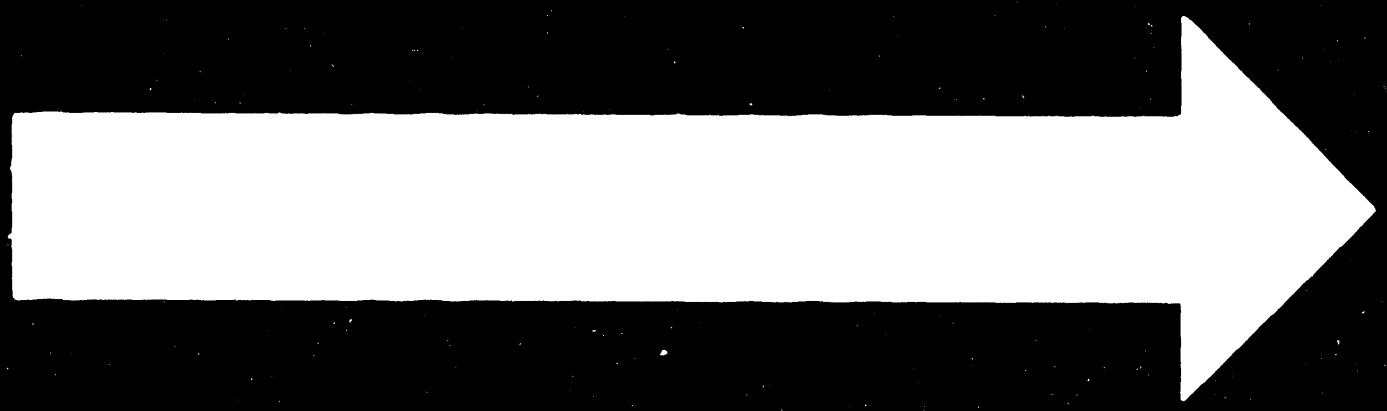

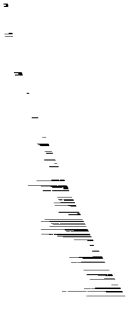

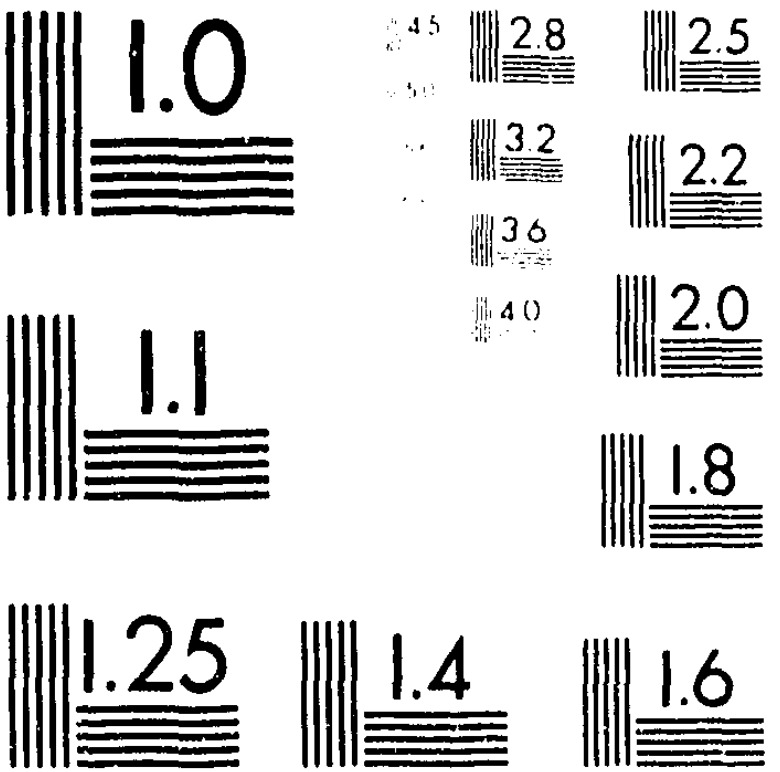

are added to JENDL-3. Furthermore, the resonances data are also required for the following nuclides; ^{249}Cm, ^{250}Cm, ^{254}Cf, ^{254}Es and ^{255}Es. We prepared the nuclear data needed in this study by combining JENDL-3 and ENDF/B-VI. The complete and consistent library is important for our study.

Furthermore, We need the decay data of the very higher actinides. Especially, the half-life of ^{250}Cm, which is very important for this study, does not fix yet. In Table of Isotopes (7th Ed.), two half lives are presented; 11300 years and 17400 years. On the other hand, 6900 years is given in another reference /5/. More decay data for the very higher actinides are also required.

Reference

1. "Reactor Design of Advanced Neutron Source", J. M. Rsykamp et.al., Nuclear Technology, 93 (1991) 330-349
2. "A New Concept for Accelerator Driven Transmutation of Nuclear Wastes ", E. D. Arthur, Fusion Technology, 20(1991) 641-647
3. "Nuclear Energy Generation and Waste Transmutation using An Accelerator driven Intense Thermal Neutron Source", C. D. Bowman et. al., Nuclear Instruments and Methods, A320(1992)
4. "Revised SRAC Code System ", K. Tuchihashi et. al., JAERI-1302 (1986)
5. "Chart of the Nuclides ", Compiled by Y. Yoshizawa et. al., published by Japanese Nuclear Data Committee (1988)

Table 1 Transmutation of ^{237}Np in the reflector of A-Burner

	Half Core Initial		Region ave.	Residuals after 1-cycle		
Reg	Vol(l)	Np (g)	Flux(n/cm2/s)	Np(g)	Pu(g)	Total
1	19.16	19.16	9.016E+15	9.076	4.012	13.86
2	61.14	61.14	7.243E+15	26.15	12.32	40.68
3	127.0	127.0	6.346E+15	52.32	24.49	81.09
4	335.8	335.8	3.823E+15	189.9	43.71	245.2
5	919.7	919.7	2.056E+15	674.3	125.2	827.5
6	2160.	2160.	8.375E+14	1902.	165.5	2109.
7	3850.	3850.	3.401E+14	3656.	139.7	3833.
8	2796.	2796.	1.410E+14	2737.	44.94	2794.
Total		10268		9246.	559.8	9944.
(Dif)				(1022.)		(324.4)
Fissioned Weight/cycle						648.9
Produced Weight /cycle					1119.	

Table 2 Contents in evaluated nuclear data files for actinide

Isotope	JENDL-2	JENDL-3	ENDF/B-IV	ENDF/B-V	ENDF/B-VI
Am-240	—	—	—	□	—
241	○	○	○	○	○
242	○	○	—	○	•
242m	○	○	—	○	•
243	○	○	○	○	○
244	—	○	—	□	—
244m	—	○	—	□	—
Cm-241	—	○	—	○	•
242	○	○	—	○	•
243	○	○	—	○	•
244	○	○	○	○	•
245	○	○	—	○	•
246	—	○	—	○	•
247	—	○	—	○	•
248	—	○	—	○	•
249	—	○	—	□	—
250	—	○	—	—	—
Bk-249	—	○	—	○	○
250	—	○	—	□	—
Cf-249	—	○	—	○	○
250	—	○	—	○	•
251	—	○	—	○	•
252	—	○	—	○	•
253	—	—	—	○	•
254	—	○	—		—
Es-253	—	—	—	○	•
254	—	○	—	—	—
255	—	—	—	—	—
Fm-255	—	○	—	—	—

○ - All data is stored
□ - Decay data only
† - Not open
• - In ENDF/B-VI , not re-evaluated.only format conversion from ENDF/B-V

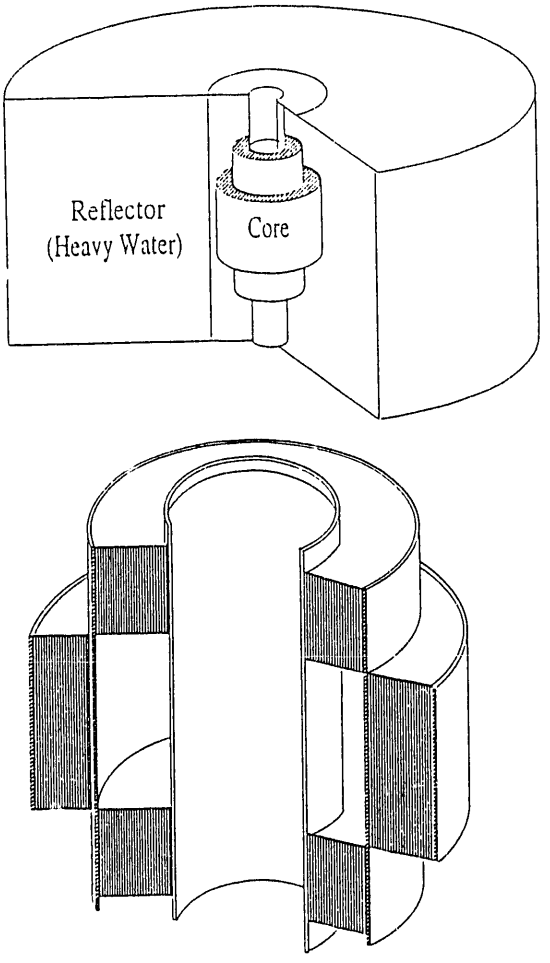

Fig. 1 Schematic view of A-Burner.

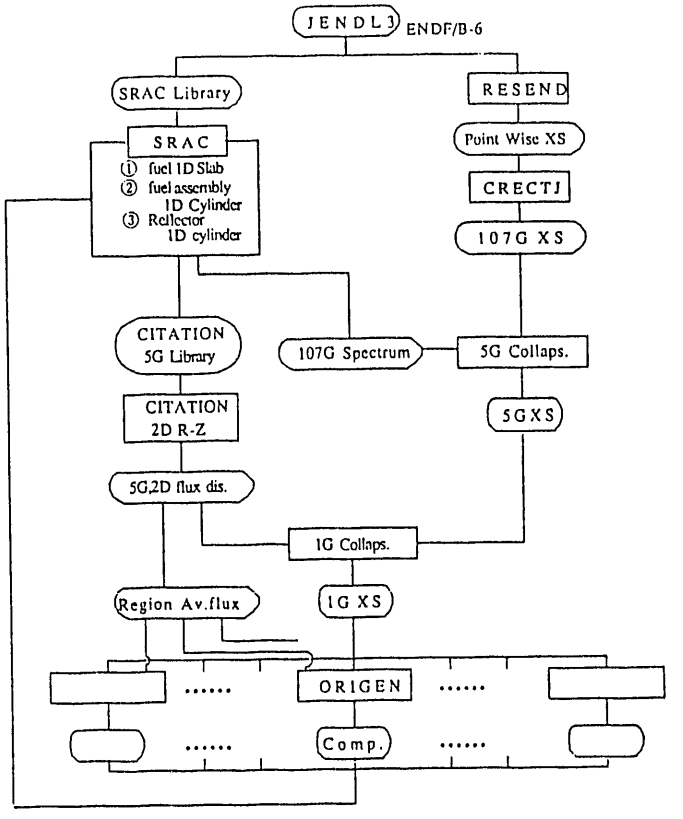

Fig. 2 Analysis flow chart for transmutation of A-Burner.

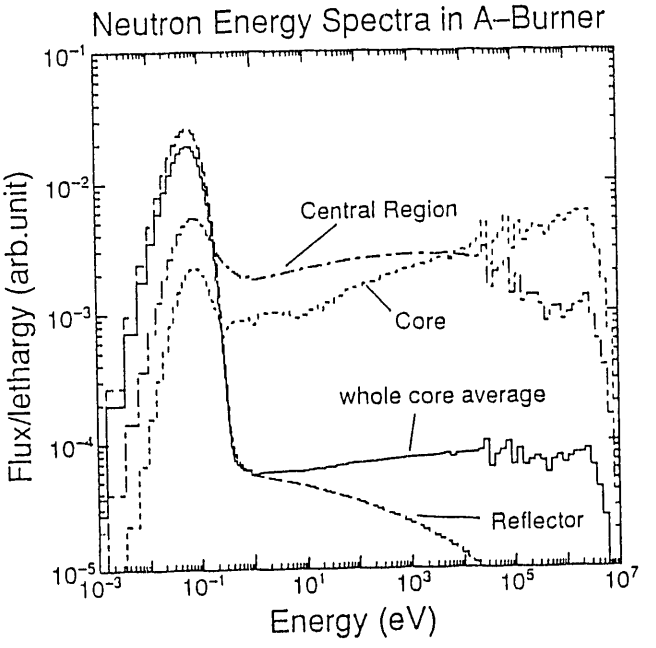

Fig. 3 Neutron spectra in various region of A-Burner.

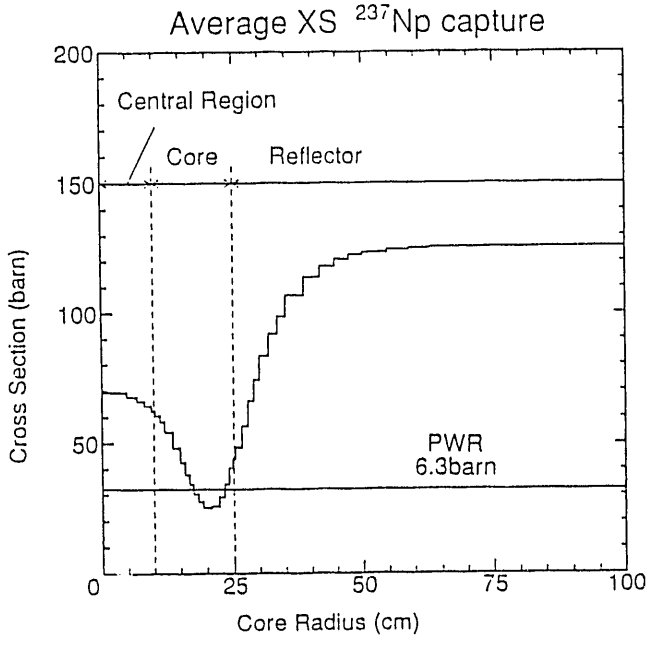

Fig. 4(1) One group cross section of ^{237}Np in A-Burner.

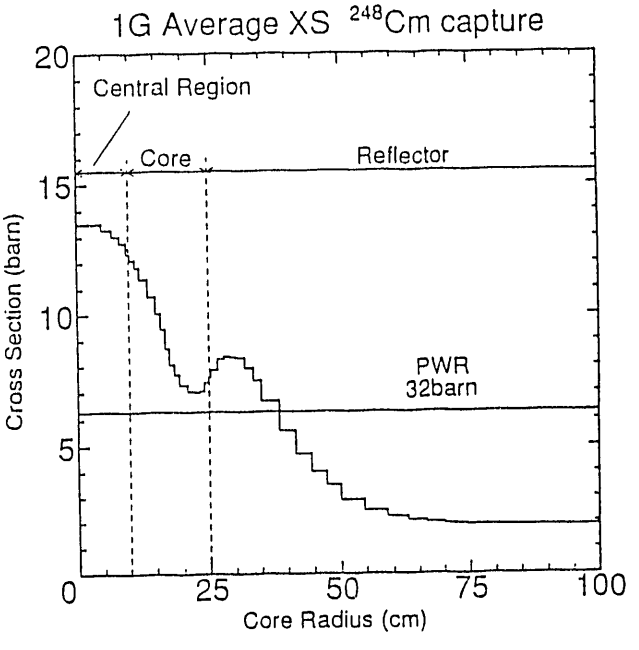

Fig. 4(2) One group cross section of ^{248}Cm in A-Burner.

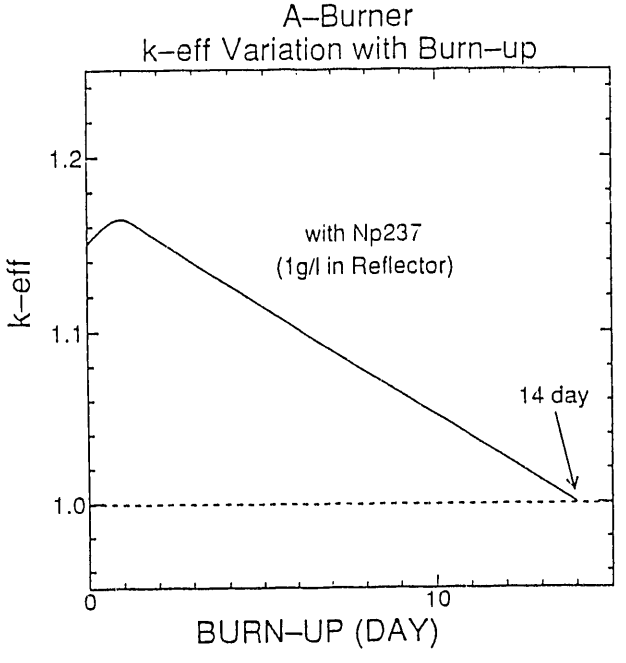

Fig. 5 Variation of k-eff of A-Burner.

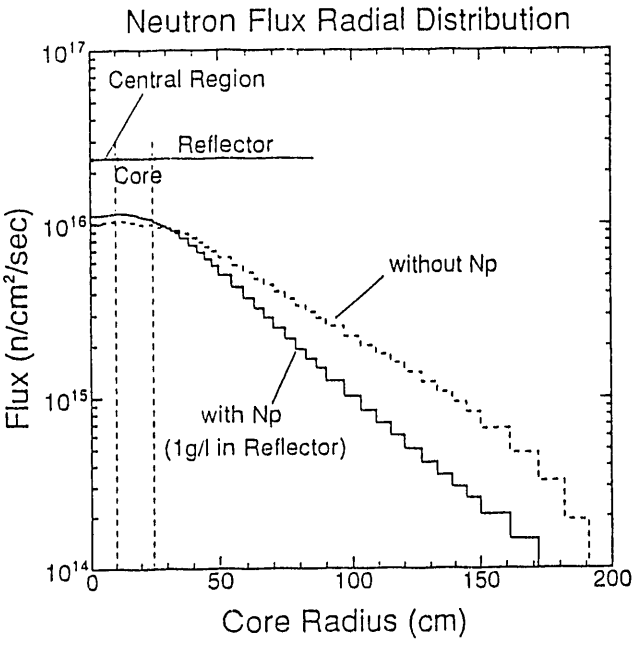

Fig. 6 Total flux distribution in A-Burner.

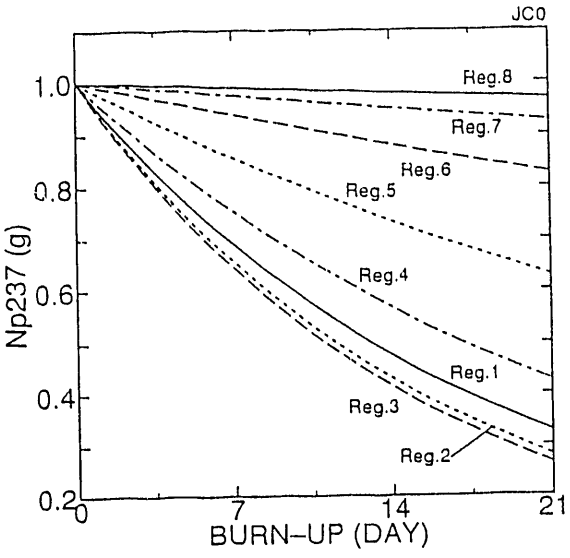

Fig. 7 Burn-up variation of nuclides at each region of reflector.

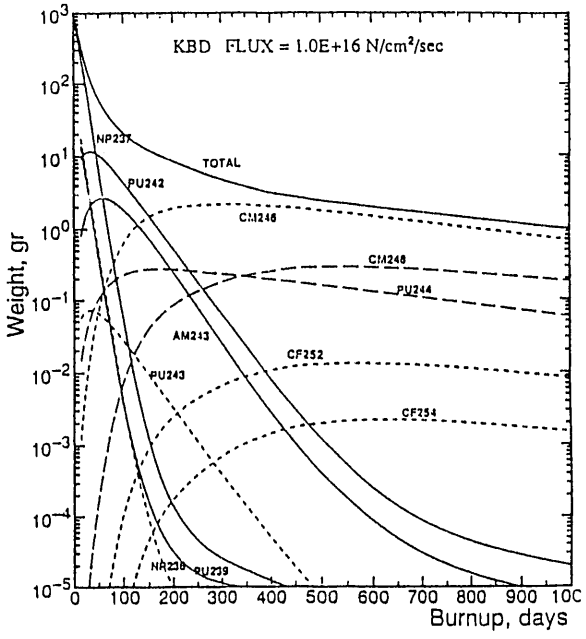

Fig. 8 Burn-up variation of nuclides for long-term transmutation in reflector.

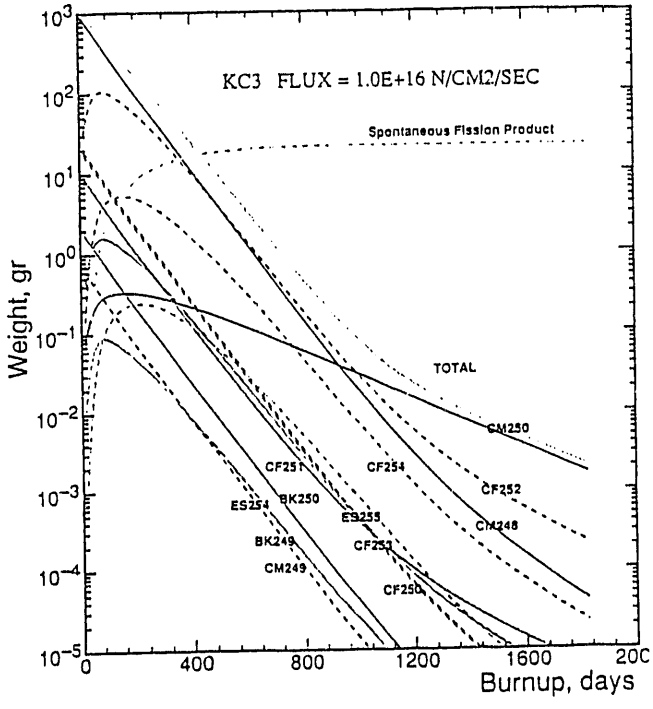

Fig. 9 Burn-up variation of nuclides in central region of A-Burner.

3.4 Present Status and Future Problems of NRDF

K. Katō, M. Chiba*) and H. Yoshida
Department of Physics, Hokkaido University, Sapporo 060
and
*)Sapporo Gakuin University, Bunkyodai-11, Ebetsu, Hokkaido 069

Abstract

From a utilization view of point, we report the present status of the charged particle nuclear reaction database NRDF (Nuclear Reaction Data File). The amount of domestic data in NRDF is 42.5 % but many data remain to be stored. We discuss several problems in NRDF, which should be solved in future.

1. Introduction

Since 1980, we have been compiling charged particle nuclear reaction data (CPND) in the NRDF system. The amount of data which have been stored up to March 1992 reached into 54.26 MB (18,889 Records). The NRDF has become one of the largest database of CPND in the world. Recently, CPND have received much attention of utilization from many fields of experimental nuclear physics, nuclear engineering, nuclear medicine and so on. From a view-point of utilization, we here report the present status of NRDF.

On the basis of data exchange with EXFOR which is organized by IAEA, we have been compiling the charged particle nuclear reaction data produced in Japan. However, the amount of domestic data in NRDF is 42.5 % at the end of March in 1991 and many data still remain to be stored. We analyzed the compiled data produced in every institute of accelerators. Based on the results, we planed a system to accumulate completely domestic data. Furthermore, we found that it is very important to compile new data of unstable nuclear beams and high energy nuclear reactions, whose data are rapidly increasing. We have studied

new coding formats and key terms for the data of unstable nuclear beams and high energy nuclear reactions. We here report the results of analysis of the domestic data stored in NRDF.

We also introduce the recent utilization status of NRDF and have several comments on future problems.

2.Present status of NRDF

At the end of March 1992, total amount of compiled data in NRDF reached into 54.26 MB (18,889 Records) and amounts of compiled data in every year from 1977 to 1991 are shown in Table I. Recently, especially in the last year, compiled data decreased. The main reason is considered due to replacement of accelerator in Research Center of Nuclear Physics (RCNP) of Osaka University. Domestic data stored in NRDF account for a large part of the data from RCNP and Institute of Nuclear Study (INS) in University of Tokyo. Thus, amount of NRDF data depends on cooperation of these institutes. To keep constant data amount in compilation, however, it is very important to accumulate experimental data from all institutes in Japan.

Table I Amount of data compiled with NRDF format

	Data compiled in a yaer		Accumulated data	
year	Number of record	Amount	Number of record	Amount
1980	2,144 (rec.)	5.96 (MB)	2,144 (rec.)	5.96 (MB)
1981	1,824	6.81	3,968	12.78
1982	1,801	6.52	5,769	19.30
1983	2,252	6.53	8,021	25.83
1984	1,703	5.03	9,724	30.86
1985	2,170	5.50	11,894	36.36
1986	962	3.14	12,856	39.50
1987	1,364	3.16	14,220	42.66
1988	1,384	3.30	15,604	45.96
1989	1,224	3.20	16,828	49.16
1990	1,282	2.90	18,100	52.06
1991	789	2.20	18,889	54.26

In Table II, we summarize NRDF data amounts obtained from every institutes of accelerators. We should note that this

result does not mean the activity of the institutes but our activity does not cover all of it. The experimental data of many institutes remain still to be stored. In order to input them into NRDF, we have started to accumulate the experimental data reported in annual reports of every institutes. Furthermore, we have requested experimentalists to send their new data to us.

Table II NRDF data from every institute

Ins.	Number of documents	percentage of data
INS	77	21.3
IPC	21	5.8
JAE	12	3.3
JCL	7	1.9
KEK	15	4.1
KTO	8	2.2
KYU	23	6.4
OSA	12	3.3
RCN	110	30.4
TKY	5	1.4
TIT	15	4.1
TOH	23	6.4
TSU	34	9.4

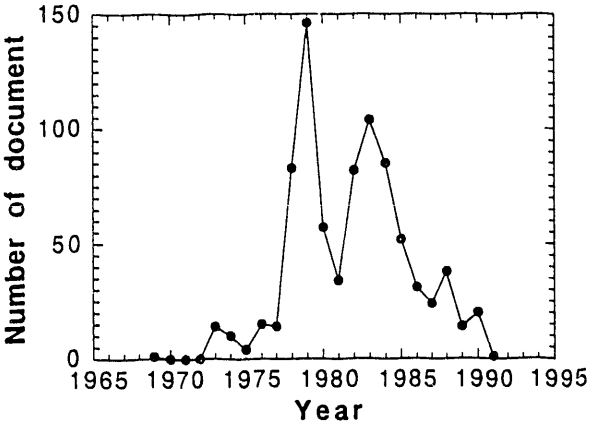

Fig. 1 The number of documents which can be retrieved.

The total number of documents which are available to be retrieved by the NRDF retrieval system is 829. In Fig.1, we show their items and observe two peaks at 1979 and 1983. The former consists mostly of proton induced data which also include foreign data, as we have accumulated all proton induced data before 1980. The latter is considered to consist of domestic data which include all kinds of charged particle reaction data.

Recently, we have received many requests of CPND. Most of them are about existence of the data. We retrieve them and can easily answer. However, unfortunately, we don't know whether requesters satisfied with them or not. Since it is available to retrieve NRDF by using an on-line system connected with the Hokkaido University Computing Center, we hope that many people utilize the NRDF system directly. It is very easy to use the

NRDF system. A guide for the retrieval is given in the NRDF Annual Report 87 (March, 1988).

3.Future problems in NRDF

We here discuss three problems of NRDF which should be solved in near future.

One of them is a problem on compilation of new data. As presented in the previous section, our compilation activity does not cover data from all institutes. In particular, it has been pointed out that many experimental data from KEK and RIKEN cannot be compiled in the present NRDF format. Most of data from those institutes are unstable-beam and K-on beam nuclear reaction data. The observed quantities by those reactions are new types which are not prepared in the NRDF key-codes. In order to accumulate those data, it is necessary to introduce new codes and to make format for compilation. We have investigated this problem of hyper-nucleus data and reported the results in the NRDF Annual Report 91 (March, 1992) by Noto, Nojiri and Tezuka. Based on those discussions, we have tentatively tried to accumulate experimental data of hyper-nuclei which have been produced from KEK. Final form of coding sheets and key-codes will be decided in very near future.

The second is a problem of utilization of NRDF. From utilization point of view, unfortunately, NRDF data may be not satisfactory, because they are dominantly proton induced data from 1980 to 1985 and domestic charged particle data from 1980. Many users might want to retrieve from a larger number of data. Most of them want to know whether a specific kind of data exists or not. A possible way to answer such requests is to make a new retrieval system of the index data which are reconstructed not only from NRDF data but also from EXFOR data. In the international meeting which was held at Vienna in the last autumn, it was admitted to use the EXFOR data to make a new index database. We have a plan to implant the new database into the National Center for Science Information System.

The final problem is to construct an evaluation system on the basis of NRDF. The evaluation system of the neutron reaction data has been established and played a very important role in practical use of database. On the other hand, it is rather difficult to construct an evaluation system of charged particle reaction data due to very wide varieties of physical quantities. For instance, even if we specify a target nucleus, there are many possibilities of choices of incident particles and many kinds of observation of physical quantities. Therefore, to construct an evaluation system of CPND we must focus our purpose and objects. Furthermore, for the purpose, it is necessary to examine whether data of the present NRDF are suitable to be evaluated or not.

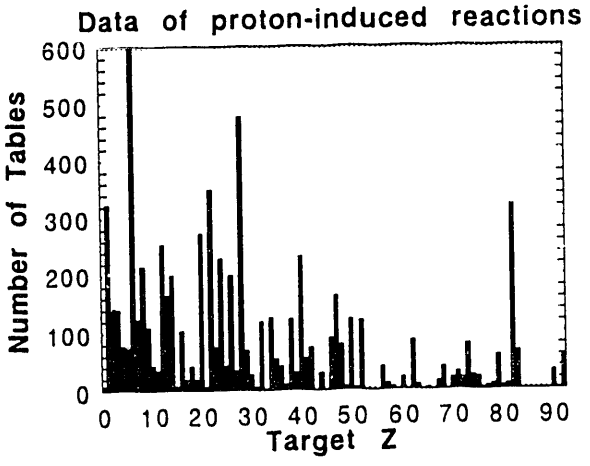

Fig. 2 Data tables of proton induced reactions.

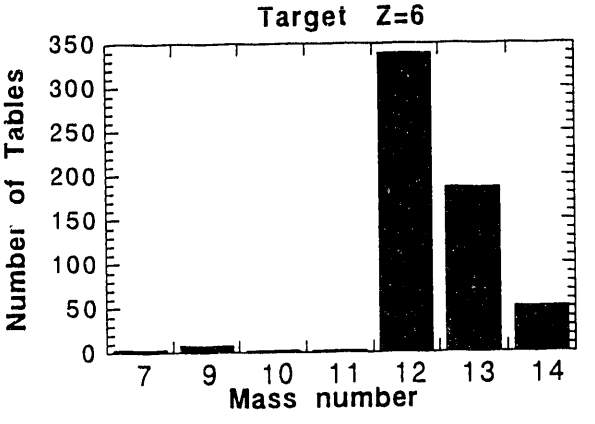

Fig. 3 Data tables of proton-induced carbon-target reactions.

We have investigated those problems by focussing the purpose on the total cross sections of proton induced reactions. In data of NRDF, there are 6,941 data tables of proton induced reactions whose items are shown Fig.2. A number of the most data tables is 597 of the carbon (Z=6) target. Fig.3 shows the number of data tables for carbon-isotope targets. We can see that the ^{12}C-target reaction data are the most in NRDF data. However, unfortunately, we found only one data table of the total cross section in the ^{12}C-target reaction data. This means that it is

impossible to discuss evaluation of data for the total cross section of the $^{12}C+p$ reactions on the basis of NRDF data. Most of data in NRDF are data of other quantities rather than the total cross sections. Therefore, if we construct a evaluation system base on NRDF, we must have other evaluation quantities. For those problems, further studies will be needed.

4.Conclusion

Until now, we have been engaged mainly in accumulation of data to increase the amount of data. At present, the total amount of data in NRDF exceeded 50 MB and the number of documents which are available for retrieval is going to reach into 1,000. Furthermore, recently, much attention is brought to CPND.

Under such situation, our activity should be also directed to utilization of the database. For this purpose, we have to take up several subjects. One of them is improvement of circumstances for utilization. Another is advertisement.

References:

(1) NRDF Annual Report 88 (in Japanese), (March 1989).
(2) NRDF Annual Report 91 (in Japanese), (March 1992).
(3) M. Chiba, JAERI-M 90-025 (1990), 169.
(4) M. Chiba, JAERI-M 92-039 (1992), 88.

3.5 Depth Dose Distribution of Heavy Ion Beam

T.Kanai and L.Sihver

Division of Accelerator Research,
National Institute of Radiological Sciences
4-9-1, Anagawa, Inage-ku, Chiba-shi, CHIBA 263 JAPAN

A computer code to calculate depth dose distributions of heavy ion beams has been developed. Dose contributions from secondary and tertiary fragments produced by nuclear collisions with a target material were taken into account in the calculation. Fluence and LET distributions were calculated besides the depth dose distribution. The results were compared with experimental results of 670 MeV/u Ne beam in water.

1. INTRODUCTION

Radiation therapy with heavy ions is expected to be superior to conventional radiation therapies using photons or electrons because of their excellent dose localization and high LET effects of the biological responses. It is very important to calculate dose and LET distributions of the heavy ion beams in human body for estimating therapeutic gain of the beams.

When heavy ions penetrate in human body, fluence of a primary beam decrease and fluence of lighter ions increase by nuclear interaction with target nucleus. In this report, a method for the calculation of the depth dose and LET distributions is presented based on a semi-empirical formula of a total nuclear reaction cross section and a partial nucleus-nucleus reaction cross section[1,2].

2. CROSS SECTIONS

Semiempirical formula have been developed for reaction cross sections and partial nucleus-nucleus cross sections. Details on the semiempirical cross sections is discussed by *L.Sihver et al.* in ref. [1,2].

reaction cross section

Different formula of the total reaction cross section, σ_r, were used for the case of proton-nucleus and of nucleus-nucleus reactions.

proton-nucleus reaction

For the incident energy of protons below 200 MeV, the reaction cross section was

expressed by a function depending on the proton energy. And for the energy over 200 MeV, the reaction cross section was expressed by a function independent on the proton energy.
$\sigma_r(E < 200\ MeV)$ = exponential law energy function
$\sigma_r(E > 200\ MeV) = \pi r_0^2[1 + A_t^{1/3} - b_0(1 + A_t^{-1/3})]^2$

where r_0=1.36fm, A_t is mass number of the target nucleus and parameter b_0 is obtained as follows;
$b_0 = 2.247 - 0.915(1+A_t^{-1/3})$

nucleus－nucleus reaction

An energy independent function for the nucleus－nucleus reaction cross section were developed. The function is similar to the cross section of the case of high energy proton－nucleus reaction.
$\sigma_r = \pi r_0^2[A_p^{1/3} + A_t^{1/3} - b_0(A_p^{-1/3} + A_t^{-1/3})]^2$
where b_0 is a different function from that for the proton－nucleus case and is given as follows;
$b_0 = 1.581 - 0.876(A_p^{-1/3} + A_t^{-1/3})$

Mean free path of 400 MeV/u Ne ions in water was calculated and compared with a experimental result at GSI[3]. The measured mean free path was 163 ±8 mm. The calculated value for the mean free path was 163 mm, i.e. in total agreement with the experimental value.

partial cross section of nucleus－nucleus reaction

The projectile fragmentation cross sections are calculated using a scaling factor, S_c, which is calculated from the reaction cross sections as follows;
$\sigma(E_i,A_i,A_j) = S_c*\varepsilon_\Delta*\varepsilon_L*\varepsilon_1*\sigma(E_p,A_i,p)$
where the meaning of the cross sections $\sigma(E_i,A_i,A_j)$ and $\sigma(E_p,A_i,p)$ are

$\sigma(E_i,A_i,A_j)$ the partial cross section for the breakup of nucleus (Z_i,A_i), colliding with (Z_j,A_j).

$\sigma(E_p,A_i,p)$ the partial cross section for the breakup of nucleus (Z_i,A_i), colliding with protons.

and $\varepsilon_\Delta,\varepsilon_L,\varepsilon_1$ are a correction factor for the case of large change of mass number, a correction factor for the lightest products, and enhancement factor for the case of single－nucleon stripping. The scaling parameter S_c is obtained square root of the ration of the reaction cross section of nucleus－nucleus and proton－nucleus reactions.

$S_c = \sqrt{\sigma^r(E_i,A_i,A_j) / \sigma^r(E_p,A_i,p)}$

where

$\sigma^r(E_i,A_i,A_j)$ the total reaction cross section for the reaction of (Z_i,A_i), colliding with (Z_j,A_j),

$\sigma^r(E_p,A_i,p)$ the total reaction cross section for the reaction of (Z_i,A_i),

Figures 1 and 2 show typical results of the calculation of the cross sections for productions of high Z and low Z fragments in reaction of 600MeV/u ^{40}Ar ions on ^{12}C, respectively.

3. DEPTH DOSE DISTRIBUTION

The depth dose distribution was calculated using the above semiempirical formula for the nuclear cross sections, the Bethe formula for stopping power, and energy loss straggling. Fluence of the primary beam decrease with a mean free path calculated from the total nuclear reaction cross section. Average energy of the primary ions decrease with a rate of the stopping power in penetrating in human body. Energy spread around the average energy is calculated from the range straggling theory developed by Payne[4].

Secondary fragments are produced by nuclear collision of the primary ions with a target nucleus. In the calculation of the dose contribution from the secondary fragments, range straggling of the secondaries in penetrating the human body is neglected. Fluence of the secondary fragments decrease again with a rate of the mean free path calculated from the semiempirical nuclear reaction cross section.

Tertiary fragments produced by nuclear collision of the secondary fragments with a target nucleus are taken into account in the calculation of the depth dose distribution. Fluence decrease of the tertiary fragments due to nuclear reaction cross section, and contribution from the forth and more generation fragments are neglected.

Figure 3 illustrates the method of the calculation of the depth dose distribution.

4. RESULTS

Figure 4 shows a typical result of the depth dose distribution for Ne 670 MeV/u beam in water. Solid line in the figure shows total dose. The top of the dashed curve shows dose contributed from fragments of Z=1－9, next dashed curve shows that of Z= 1－8, and so on.

Figure 5 shows a fluence distribution of the primary ions and fragments when the 670 MeV/u Ne beam penetrate in water. Solid line in the figure shows fluence of Z=10 particles. The top of the dashed curve shows the fluence of Z=1 particles, next one shows Z=2 particles and so on.

Marks in the figure represent the experimental result of the fluence distribution by J.Llacer et al.[5]. Triangles, closed circle, closed rectangular, closed diamonds, open circle and open rectangulars show the fluence of Z = 10, 9, 8, 7, 6, and Z = 1 to 5 particles, respectively. The calculations agree with the experimental results as a whole. More detailed experiments are desired for the comparison.

References

1) Sihver,L., and Kanai,T., NIRS report NIRS-M-87, HIMAC002, July 1992.
2) Sihver,L., et al., Phys. Rev. C (in press).
3) Schall,I., et al., GSI Scientific report 1991, p.306.
4) Payne,M.G., Phys. Rev. 185 (1969) 611.
5) Llacer,J., et al., Med. Physics 11 (1984) 266
6) Webber,W.R., Kish,J.C., and Scrier,D.A., Phys. Rev. 41, 547 (1990).

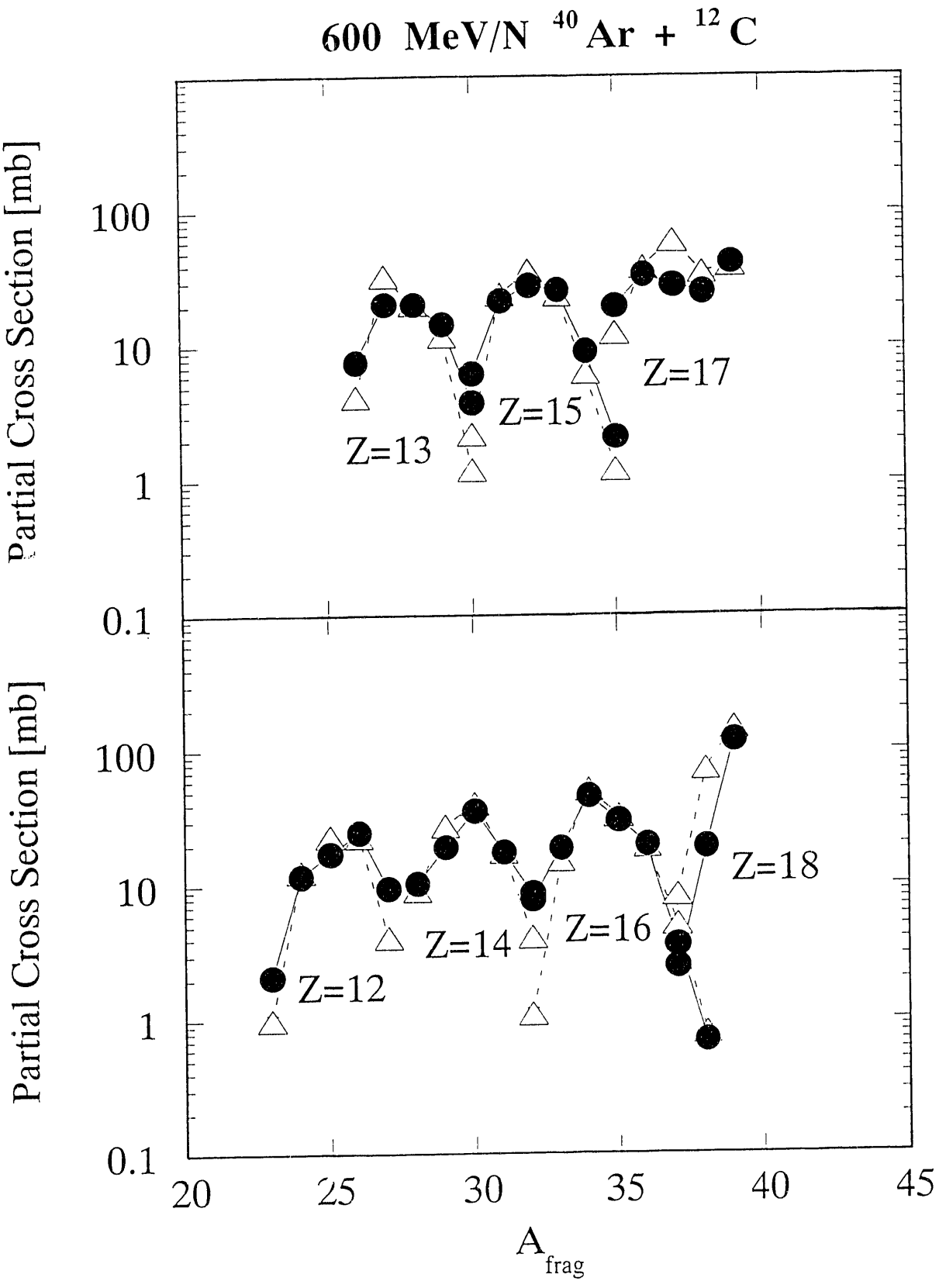

Fig. 1 Partial cross sections for productions of high Z fragments in reaction of 600 MeV/u ^{40}Ar ions on ^{12}C. Closed circles and open triangles show the results of the semiempirical calculation and experimental results measured by W.R. Webber et al.[6], respectively.

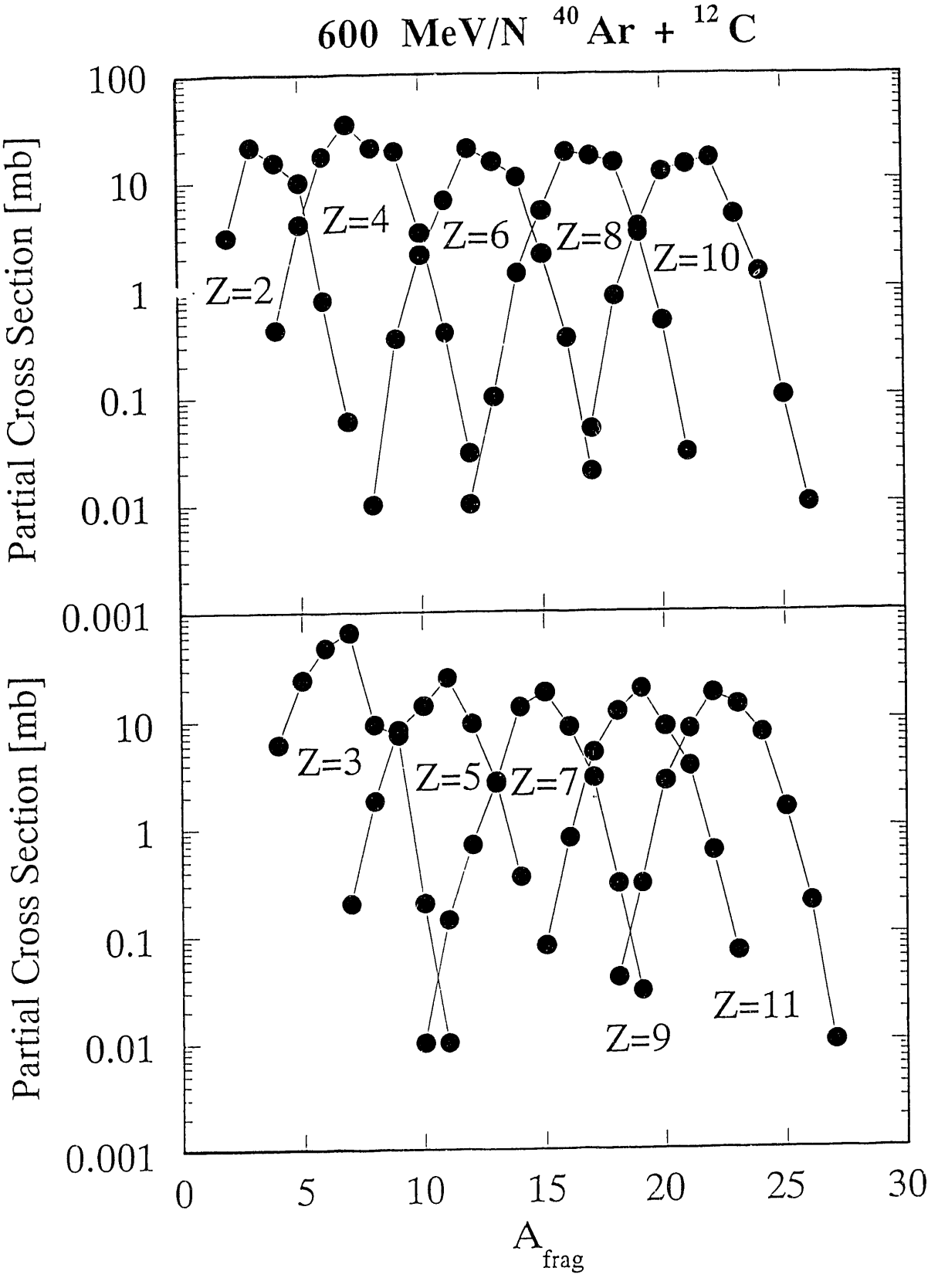

Fig. 2 Partial cross section for productions of low Z fragments in reaction of 600 ^{40}Ar ions on ^{12}C. Closed circles represent the results of the semiempirical calculation.

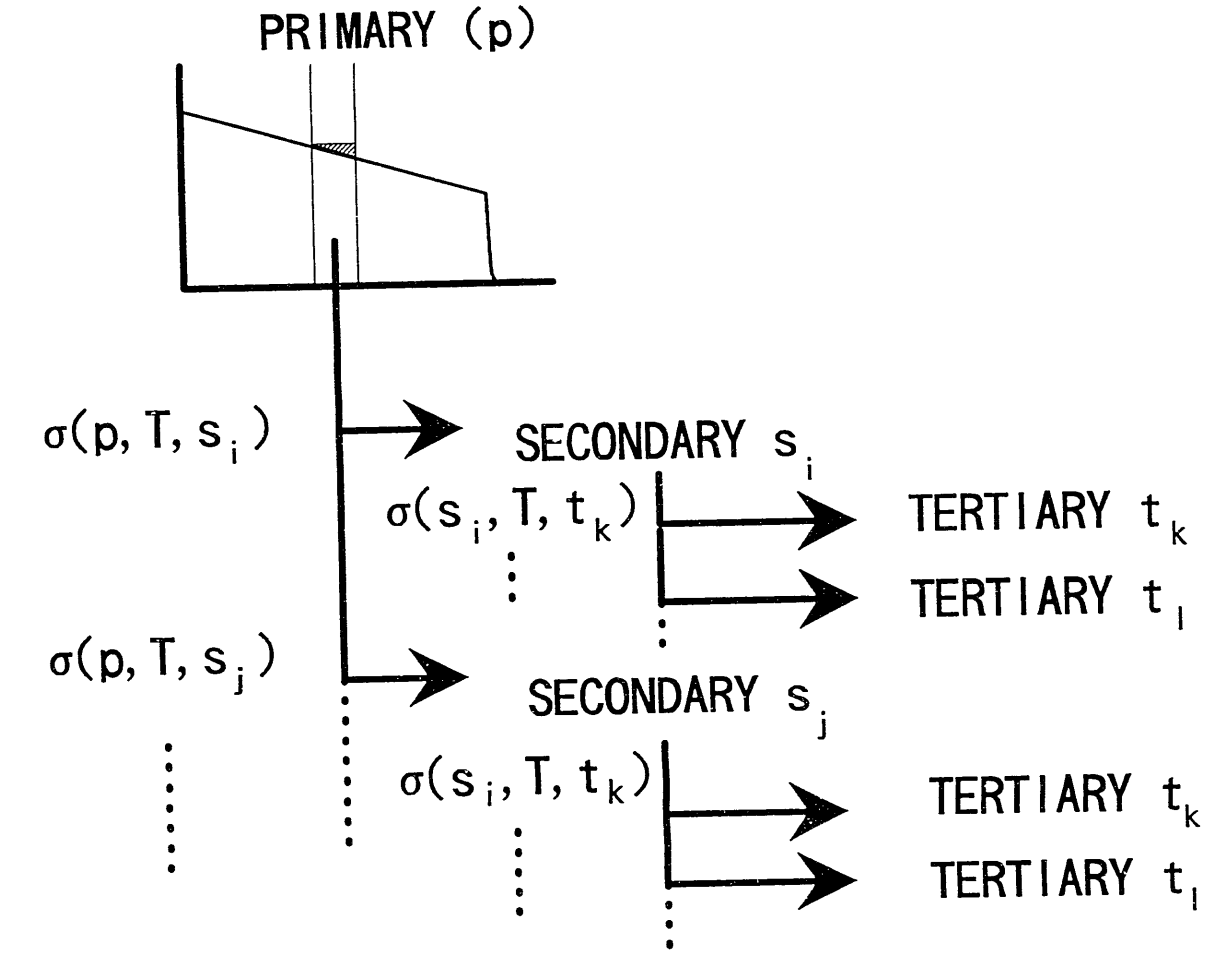

Fig. 3 An illustration of the method of the calculation of the depth dose distributions.

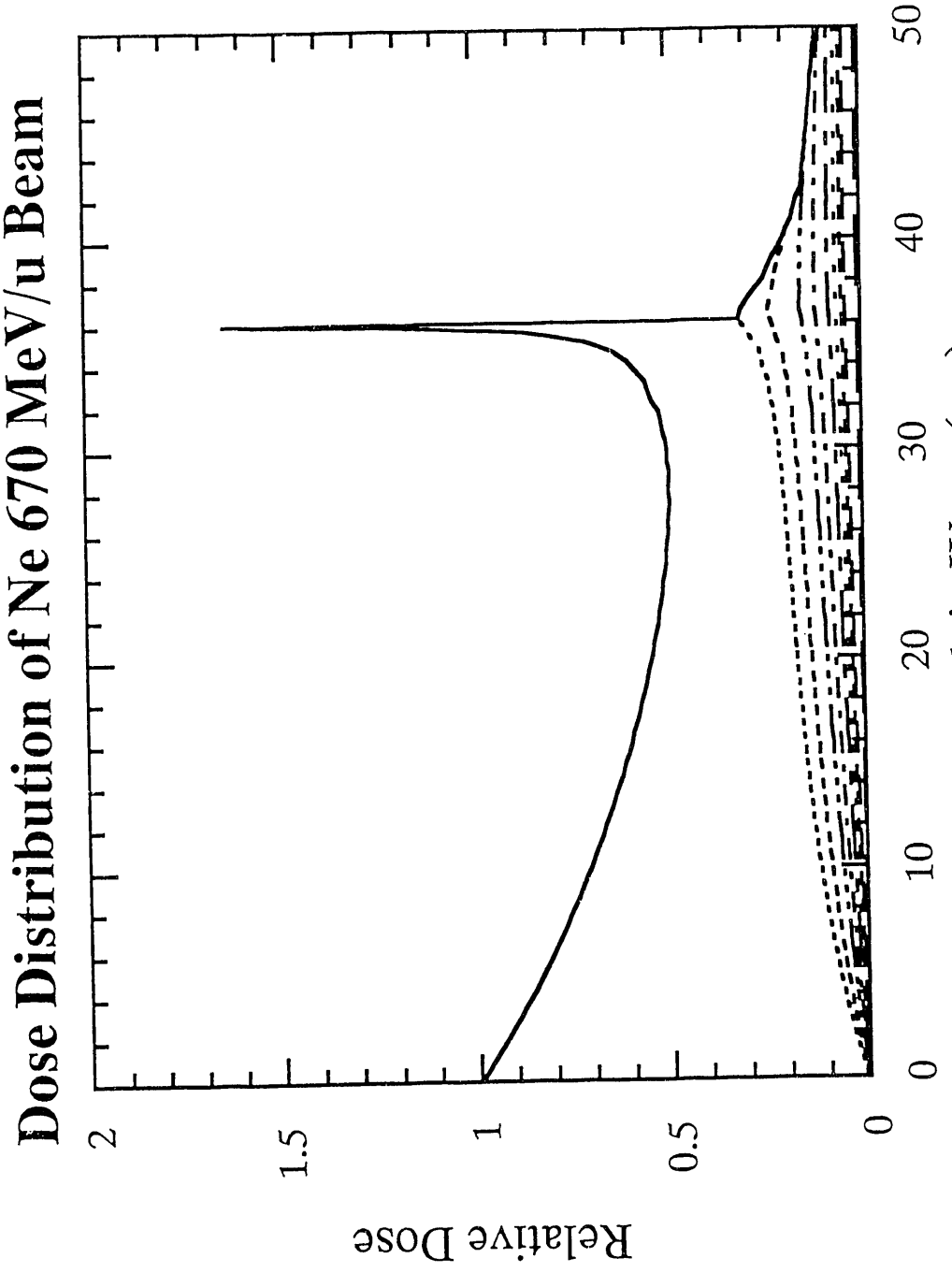

Fig. 4 The result of the calculation of the depth dose distribution in water for 670 MeV/u neon beam. Solid line and dashed lines show the total doze distribution and the sum of the dose contributions from Z=1 to some Z particles, respectively. From the top to bottom dashed line, they correspond the summed dose from Z=1 to Z=9, to=8, and so on.

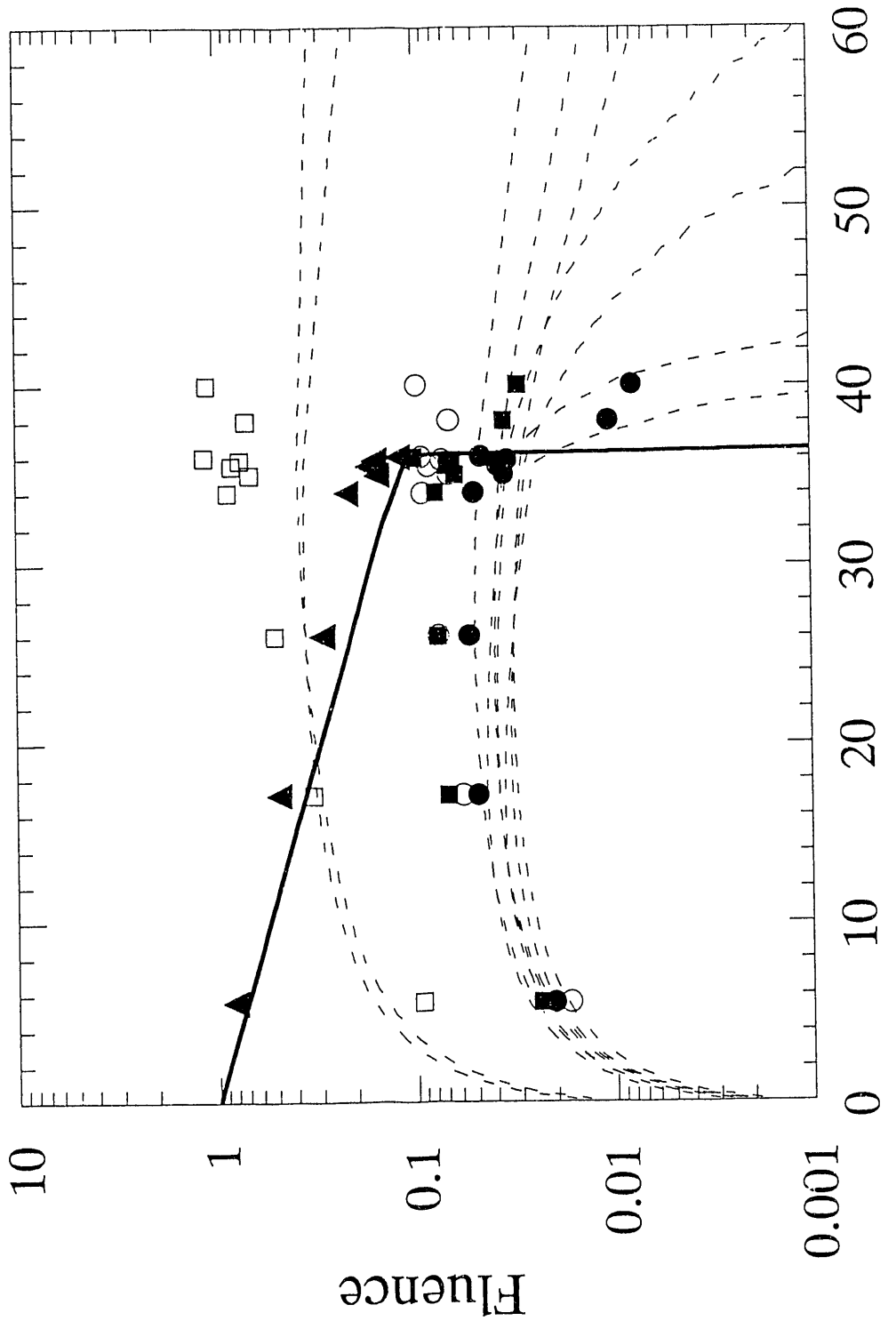

Fig. 5 The result of the calculation of the fluence distribution when 670 MeV/u neon beam penetrates in water. The solid line shows the fluence of Z=10 ions. The dashed lines correspond the fluence of Z=9, Z=8, and so on from the bottom. Triangles and other marks are the experimental results measured by L. Llacer et al.[5].

3.6 Consideration on the Possibility of a Laser-induced Gamma-ray Laser

Kenichi ISHIKAWA, Tetsuo IGUCHI, and Masaharu NAKAZAWA

Department of Nuclear Engineering, Faculty of Engineering, University of Tokyo
7-3-1 Hongo, Bunkyo-ku, Tokyo, 113 Japan

The feasibility of a gamma-ray laser using laser-induced nuclear transitions between isomeric states was studied. First, laser energy flux required to obtain population inversion was estimated with the transition probability between isomeric states, taking laser linewidths into account. Second, the candidate nuclei for a laser-induced gamma-ray laser were searched for in terms of the laser intensity requirement. $^{73}_{34}Se$ was turned out to be only one hopeful nucleus at the present stage, while an uncertainty existed in the estimation.

1. Introduction

The laser has revolutionized optics. Many fields of science and technology, previously unrelated, have benefited from the use of coherent radiation. The development of lasers that would generate coherent gamma radiation, can likewise be expected to lead to a vast array of new scientific and technological developments.

In the past three decades, plenty of proposals and suggestions have been put forward so as to develop such a laser.[1] A common impression is that the future stimulated emission devices with photon energy more than 5keV would be based on transitions between stationary states of nuclear isomers using the Mössbauer effect.

Up to now, however, no attempt to develop a gamma-ray laser (graser) has not been successful. The main difficulties encountered may be summarized as follows.[7] The long-lived isomers with lifetimes of more than a few hours can, in principle, be prepared with presently available technology, e.g. pumped by neutron radiative capture reactions and separated as well as concentrated by radio- or photochemical means to reach population inversion. However, the Mössbauer effect is presently not observable in such long-lived isomers (by conventional methods) but only in transition of lifetime shorter than 10μs, because nuclei are perturbed by locally varying internal fields in solids, so that the resonance of the longer-lived transitions are randomly displaced by more than their natural linewidths. A given subset of modes of the radiation field then can interact with only a small fraction of the isomer population. In short, the inhomogeneous line broadening severely reduces the cross section for stimulated emission and makes amplification impossible. On the other hand, the shorter-lived isomers with lifetime less than 10^{-5}s are available to observe the Mössbauer effect and possess sufficiently high amplification,

but the intense pumping needed to invert isomers must be increased as the fourth power of laser photon energy, consequently overheating or even destroying the solid hosts that support the recoilless emission.

There is a proposal[2-6] that may overcome those obstacles. In that proposal, long-lived isomers are transformed into shorter-lived species with the help of optical laser radiation as follows.

Suppose that there exists a nuclide which has two isomeric states 1 and 2 with almost the same energies but with very different lifetimes, as shown in **Fig. 1**. In this figure, T_i is lifetime of level i (i = 1, 2), γ_i is the spontaneous decay rate, E_i is the excitation energy, $\Gamma_i = \hbar\gamma_i$ is the total level width and **b** represents all low lying levels accessible from level 1 and 2. Assuming the shorter-lived level to be the higher one, it follows:

$$E_2 - E_1 << E_2 , \tag{1}$$

$$T_1 >> T_2 . \tag{2}$$

Let the long-lived isomer be prepared, radio- or photochemically, in the form of a transparent crystal-line filament, and be irradiated suddenly by an intense laser light with the wavelength corresponding to the energy separation of the two levels, so as to induce transitions between them. If the induced transition probability from state 1 to 2, W_{12} , can be made sufficiently high, then this transition will saturate before the population of state **b** has accumulated appreciably, and nearly half of the initial population of long-lived states will be transformed into a full population inversion of the shorter-lived transition. If the latter has a recoilless line, not too greatly broadened, and its other nuclear parameters are favorable, it can lase.

The smartness of this proposal is that, instead of supplying the full excitation energy of level 2 at once, all we have to do is to supply the much smaller energy difference $E_{21} = E_2 - E_1$ within a time interval of an order of T_2.

The objective of the present paper is to recognize the possibility that this approach would enable a gamma-ray laser to be developed, and to search for the candidate nuclei for this type of gamma-ray laser.

In sect. 2, we estimate the incident laser intensity required to reach inversion in the short-lived isomeric state, taking the laser linewidth into account, with the help of the laser-induced transition probability between isomeric states calculated in literatures. In terms of the calculated laser power requirement, it is shown that the laser-induced gamma-ray laser would be feasible if favorable arrangements of nuclear levels are found to exist. In sect. 3, the results of the search for the candidate nuclei for the laser-induced gamma-ray laser are shown and discussed. In sect. 4, conclusions are given.

2. Laser-induced Isomeric Transitions

2.1 Transition Probability

The probability per unit time for laser-stimulated resonant transition between two closely spaced isomeric states is written as follows:

$$W_{12}(E) = F(E)\sigma_{12}(E), \tag{3}$$

where $F(E)$ is the flux of photons of energy E per unit area, and $\sigma_{12}(E)$ is the cross section of the transition from level 1 to 2 induced by photons of energy E and of wavelength λ.

According to ref. 1), $\sigma_{12}(E)$ can be written as follows:

$$\sigma_{12}(E) = \frac{g_2}{g_1}\frac{\lambda^2}{8\pi}\frac{\Gamma\Gamma_{21}}{(E - E_{21})^2 + \frac{1}{4}\Gamma^2}, \tag{4}$$

where Γ_{12} is the spontaneous partial radiative width between the states 1 and 2, $\Gamma = \Gamma_1 + \Gamma_2$, $g_i = 2J_i + 1$ is the statistical weight factor, and J_i is the level spin(i=1, 2).

On the other hand, according to ref. 7), $\sigma_{12}(E)$ can be calculated by means of a parametrization approach as follows:

$$\sigma_{12}(E) = \frac{g_2}{g_1}\frac{\lambda_{21}^3}{8\pi\lambda}\frac{\Gamma\Gamma_{21}}{(E - E_{21})^2 + \frac{1}{4}\Gamma^2}, \tag{5}$$

where $\lambda_{21} = hc/E_{21}$ is the wavelength corresponding to the energy difference.

If the following condition:

$$|E - E_{21}| << E_{21} \quad \text{i.e.} \quad \lambda \cong \lambda_{21}, \tag{6}$$

is satisfied, the equations (4) and (5) give almost the same value. In this paper we, therefore, adopt the following expression of $\sigma_{12}(E)$ by assuming eq. (6) is satisfied,

$$\sigma_{12}(E) = \frac{g_2}{g_1}\frac{\lambda_{21}^2}{8\pi}\frac{\Gamma\Gamma_{21}}{(E - E_{21})^2 + \frac{1}{4}\Gamma^2}. \tag{7}$$

Probably some modification will be necessary in the case that eq. (6) is not satisfied.[5]

If the incident radiation is at exact resonance with the transition, i.e. $E = E_{21}$, it follows:

$$\sigma_{12}(E = E_{21}) = \frac{g_2}{g_1}\frac{\lambda_{21}^2}{2\pi}\frac{\Gamma_{21}}{\Gamma}. \tag{8}$$

2.2 Effect of Laser Linewidth[7]

It is a common case that the laser linewidth is larger than the radiative width of an isomeric state. The former is of the order of 10MHz for a high-power pulsed laser, whereas the

latter is about 10 kHz for isomeric states with lifetime 10^{-4}s. Thus the effect of the laser linewidth must be taken into account.

In this case, the effective transition probability is

$$\overline{W}_{12} = \int W_{12}(E) R_L(E) dE , \tag{9}$$

where $R_L(E)$ is the laser line shape function.

Assuming $R_L(E)$ can be described by a normalized Lorenzian function:

$$R_{(L)}(E) = \frac{1}{2\pi} \frac{\Gamma_L}{(E - E_L)^2 + \frac{1}{4}\Gamma_L^2} , \tag{10}$$

where Γ_L denotes the laser linewidth, and E_L is the centric energy, the effective transition probability is,

$$\overline{W}_{12} = \frac{g_2}{g_1} \frac{\lambda_{21}^2}{8\pi} \frac{(\Gamma + \Gamma_L)\Gamma_{21}}{(E_L - E_{21})^2 + \frac{1}{4}(\Gamma + \Gamma_L)^2} F . \tag{11}$$

In the case of $E_L = E_{21}$, it follows:

$$\overline{W}_{12}(E_L = E_{21}) = \frac{g_2}{g_1} \frac{\lambda_{21}^2}{2\pi} \frac{\Gamma_{21}}{\Gamma + \Gamma_L} F . \tag{12}$$

Thus the transition probability is reduced by a factor of $(\Gamma_L + \Gamma)/\Gamma$ compared with the case that the laser has no linewidth.

2.3. Laser Power Requirement

According to the eq. (19) of ref. 7), the critical transition probability to hold the population inversion between the level 2 and the ground state level **b** for each nucleus can be obtained by,

$$\frac{\overline{W}_{12}}{g_2} = \gamma_2 . \tag{13}$$

Using eqs. (12) and (13), the threshold photon flux F_{th} in the case of $E_L = E_{21}$ is,

$$F_{th} = \frac{2\pi}{\lambda_{21}^2} g_1 \gamma_2 \frac{\Gamma + \Gamma_L}{\Gamma_{21}} . \tag{14}$$

Using eq. (14), the threshold laser energy flux defined as $P_{th} = E_{21} F_{th}$ is written as,

$$P_{th} = \frac{E_{21}^3}{2\pi(ch)^2} g_1 \gamma_2 \frac{\Gamma + \Gamma_L}{\Gamma_{21}} . \tag{15}$$

The important quantity is the ratio $(\Gamma + \Gamma_L)/\Gamma_{21}$, which can be rearranged as follows:

$$\frac{\Gamma+\Gamma_L}{\Gamma_{21}} = \frac{\Gamma}{\Gamma_{21}}\left(1+\frac{\Gamma_L}{\Gamma}\right). \tag{16}$$

As stated earlier, Γ_L/Γ is usually by far larger than unity. Γ/Γ_{21} is the ratio of the total linewidth to the partial radiative width.

2.4 Estimation of the Threshold Laser Energy Flux

Let us make a numerical estimation of the threshold by assuming $T_1 = 10^4$s (long-lived radiochemically producible isomer), $T_2 = 10^{-5}$s (upper limit of the Mossbauer effect), $E_L = E_{21} =$ 1eV, $g_1 = g_2 = 1$, $\Gamma_L/\Gamma = 10^3$. We evaluate the crucial quantity Γ_{21} in terms of the E1 Weisskopf unit.[8] (see **Table 1**) Assuming the nucleon number, A is equal to 100, one gets $\Gamma_{21}^{(E1)} = 2.3\times10^{-37}$Joule and, therefore,

$$P_{th} = 3.0\times10^5 \quad \mathrm{W/cm^2}.^* \tag{17}$$

This laser energy flux could be obtained using the current or near future technology. It is, therefore, meaningful to search for candidate nuclides for a laser induced gamma-ray laser.

3. The Search for the Candidate Nuclei

3.1 The Requirements for the Candidate Nuclei

Let us pick up the conditions the candidate nuclei should satisfy:

(1) They should have an isomer level 1 with relatively long lifetime. The time required to activate, separate, concentrate and crystallize an appreciable number of isomeric nuclei is at least a few seconds; commonly it requires several hours. Level 1, therefore, should have a longer lifetime than one hour as least.

(2) They should have an isomer level 2 with a shorter lifetime just above the level 1. Its lifetime is required to be shorter than 10^{-5} seconds, since, as noted earlier, the Mössbauer effect is presently observable only in transition of lifetime shorter than 10^{-5} seconds.

(3) It is desirable that the energy difference between the two levels is less than 1 keV (a few eV if possible).

(4) They should be easily produced by some nuclear reactions such as (n, γ) reaction.

---

* Ho and Pan estimated P_{th} on the basis of the same assumption, but got very difficult results from ours.[7] They may have made some mistakes in calculation.

3.2 Method of the Search of the Candidate Nuclei

Taking the above conditions into account, the search for the candidate nuclei was carried out by the following method:

(1) first, to pick up the nuclei with an excited level 1 with longer lifetime than one hour using ref. 9).

(2) second, for nuclei picked up in procedure (1), to check up the existence of a short-lived level 2 within 1 keV above the long-lived level 1 with the help of refs. 10) and 11).

(3) last, to estimate the threshold laser energy flux P_{th} required to develop a gamma-ray laser using each of the nuclei surviving after two preceding procedures, with the help of the following equation derived from eq. (15):

$$P_{th} = 3.318\times10^{-36}E_{21}^3(\text{in keV})g_1\left(\frac{1}{\tau_2}\right)^2\frac{\chi}{\Gamma_{21}} \quad \text{W/cm}^2 , \tag{18}$$

where τ_2 is the half-life of the level 2, and χ is defined as $\chi = (\Gamma+\Gamma_L)/\Gamma > 1$.

3.3 Results and Discussion

In the ref. 9), a hundred and fifteen nuclei have been found to have an excited level with longer half-life than one hour. According to the ref. 10), only two of these nuclei, $^{152}_{63}$Eu[12] and $^{179}_{72}$Hf[13] have a short-lived level within 1keV above the long-lived level.

We calculated the laser intensity required in the case of these two nuclei. The results are summarized in **Table 2**, which shows that for each of these nuclei ,especially $^{179}_{72}$Hf, the value of P_{th}/χ is extremely high and that it is very difficult to obtain by the current laser technology.

We found, however, an attractive nucleus, $^{73}_{34}$Se[14], which has the levels as displayed in **Fig. 2**. The half-life and parity of 26.33keV level are unknown; Let us estimate the laser intensity requirement by assuming that it has spin-parity of 5/2-.

Noting that E_{21}=0.62keV and that 26.33keV level is supposed to decay into the ground level, the half-life of the level, τ_2, is calculated in terms of E2 Weisskopf unit[8] as 2.5ms, which is too long for Mössbauer effect to be observed. But in the most favorable case it can be as short as 8.2μs, since the recommended upper limit for γ-ray strength (the ratio of the actual radiative width to the Weisskopf single-particle estimate) for A=73 and E2-transition is 300.[15] On the other hand, Γ_{21} is evaluated in terms of E1 Weisskopf unit[8] as 4.5×10^{-29}Joule. The laser energy flux required, therefore, is estimated as following:

$$P_{th} = 1.04\times10^3\chi \quad \text{W/cm}^2 . \tag{19}$$

Assuming $\chi = 10^3$, it follows:

$$P_{th} = 1.04\times10^6 \quad \text{W/cm}^2 . \tag{20}$$

This laser intensity could be obtained by the near future technology, and the development of the gamma-ray laser using $^{73}_{34}$Se might be possible.

It is necessary, however, to note that there are four reasons from which an uncertainty exists in estimating the feasibility of the gamma-ray laser using $^{73}_{34}$Se, which may lead to different estimations:

(1) The half-life of 26.33keV level, τ_2, is unknown; the Mössbauer effect between 26.33keV level and the ground state level is observable only in the most favorable case as above. If τ_2 were lengthened even by a factor of 10, the Mössbauer effect would not be observed and the development of the gamma-ray laser using $^{73}_{34}$Se would be impossible.

(2) Since the electrical dipole radiative strength is commonly exhausted by the electrical giant dipole resonance at high excitation energy ($\approx 80A^{-1/3}$ MeV), the experimentally observed inhibition factor for E1-transitions is on the average of an order of 10^{-3}~10^{-5} in Weisskopf units.[16] Because of that, a factor of 10^3~10^5 in transition rate might be lost. Correspondingly, the laser thresholds would be enhanced by this factor.

(3) While $^{73}_{34}$Se can be produced by ^{70}Ge(α, n), ^{72}Ge(α, $3n$), ^{74}Se(γ, n), ^{75}As(p, $3n$) and ^{74}Se(n, $2n$) reactions,[9] the half-life of 25.71keV level, τ_1, is rather short (39.8min). Thus it is essential for the development of the gamma-ray laser using $^{73}_{34}$Se to establish the method to activate, separate, concentrate and crystallize an appreciable number of isomers of 25.71keV level.

(4) All present calculations were made by assuming that the nuclei are bare, without shielding action of an outside electron shell.[17] At the present stage, there is no convincing theoretical study on this subject.

$^{73}_{34}$Se is, nevertheless, a hopeful candidate nucleus and we believe that it is worth while to make efforts to develop the laser-induced gamma-ray laser using $^{73}_{34}$Se. (The appreciable lifetime reduction of 25.71keV level might be observed if population inversion were not reached.)

4. Conclusion

It is concluded that there is only one nucleus $^{73}_{34}$Se, if any, that could be used for the laser-induced gamma-ray laser of the type proposed by Baklanov, Chebotaev and some other authors.[2-6] We expect that the development of the gamma-ray laser using $^{73}_{34}$Se will be studied by many workers.

On the other hand, it is necessary to try some other methods to produce coherent gamma radiation. For example, a new method[1, 18] using nuclear excitation by electron transition

(NEET) , where a population inversion may be realized by NEET. There are some experimental and theoretical studies on NEET.[19-25]

In addition, it is still meaningful to search for ideal candidate nuclei, for example, through the improvement of the accuracy of experimental data, data base analyses concentrated in specific regions of the periodic table, theoretical effort to provide missing level information, and so on.

Acknowledgments

The authors would like to thank Professor Yu-Kun Ho of Fudan University for his valuable advice and sustained encouragement.

References

1) BOLDWIN, G. C. and SOLEM, J. C. : *Rev. Mod. Phys.*, **53**(4), 687(1981)
2) BAKLANOV, E. V. and CHEVOTAEV, V. P. : *JETP Lett. (Sov. Phys.)*, **21**(5), 131(1975)
3) RIVLIN, L. A. : *Sov. J. Quantum Electron.*, **7**(3), 380(1977)
4) ARAP, B., ELIEZER, S. and PAISS, Y. : *Phys. Lett.*, **A74**(6), 395(1979)
5) BECKER, W., SCHLICHER, R. R. and SCULLY, M. O. : *ibid.*, **A106**(9), 441(1984)
6) COLLINS, C. B. et al. : *J. Appl. Phys.*, **53**(7), 4645(1982)
7) HO, Y. K. and PAN, Z. Y. : *Nucl. Phys.*, **A486**(2), 271(1988)
8) WONG, S. S. M. : "*Introductory Nuclear Physics*", (1990), Prentice-Hall
9) BROWNE, E. and FIRESTONE, R. B. : "*Table of Radioactive Isotopes*", (1986), John Wiley & Sons
10) United States National Nuclear Data Center : *Nuclear Data Sheets*, Academic Press
11) United States National Nuclear Data Center : "*Evaluated Nuclear Structure Data File*", (1987)
12) PEKER, L. K. : *Nucl. Data Sheets*, **58**(1), 93(1989)
13) BROWNE, E., : *ibid.*, **55**(4), 483(1988)
14) KING, M. M., : *ibid.*, **51**(1), 161(1987)
15) see, e.g., *ibid.*, **62**(1), ix(1991)
16) ENDT, P. M. : *At. Data Nucl. Data Tables*, **23**(1), 3(1979); *ibid.*, **23**(6), 547(1979); *ibid.*, **26**(1), 47(1981)
17) ZARETSKII, D. F. and LOMONOSOV, V. V. : *Sov. J. Nucl. Phys.*, **41**, 417(1985)
18) GOL'DANSKII, V. I. and NAMIOT, V. A. : *Phys. Lett.*, **B62**(4), 393(1976)
19) MORITA, M. : *Prog. Theor. Phys.*, **49**(5), 1574(1973)
20) OTOZAI, K., ARAKAWA, R. and SAITO, T. : *Nucl. Phys.*, **A297**(1), 97(1978)
21) FUJIOKA, H., URA, K., SHINOHARA, A., SAITO, T. and OTOZAI, K. : *Z. Phys.*, **A315**, 121(1984)

22) SAITO, T., SHINOHARA, A. and OTOZAI, K. : *Phys. Lett.*, **92B**(3, 4), 293(1980)
23) HO, Y. K., ZHANG, B. H. and YUAN, Z. S. : *Phys. Rev.*, **C44**, 1910(1991)
24) OTOZAI, K., ARAKAWA, R. and MORITA, M : *Prog. Theor. Phys.*, **50**(5), 1771(1973)
25) ARAKAWA, R., SAITO, T. and OTOZAI, K. : *Nucl. Instr.*, **131**, 369(1975)

Table 1 Weisskopf single-particle estimates for E_L- and M_L-transition widths

Multipole L	E_L-transition width Γ(Joule)	M_L-transition width Γ(Joule)
1	$1.08\times10^{-29}A^{2/3}E_\gamma^3$	$3.32\times10^{-30}E_\gamma^3$
2	$7.69\times10^{-42}A^{4/3}E_\gamma^5$	$2.35\times10^{-42}A^{2/3}E_\gamma^5$
3	$3.57\times10^{-54}A^{2}E_\gamma^7$	$1.10\times10^{-54}A^{4/3}E_\gamma^7$
4	$1.12\times10^{-66}A^{8/3}E_\gamma^9$	$3.46\times10^{-67}A^{2}E_\gamma^9$
5	$2.53\times10^{-79}A^{10/3}E_\gamma^{11}$	$7.75\times10^{-80}A^{8/3}E_\gamma^{11}$

E_γ is transition energy in keV. A is uncleon number.

Table 2 Thresholds of laser intensity for $^{152}_{63}$Eu and $^{179}_{72}$Hf

nuclide	E_1(keV)	E_2(keV)	$J\pi_1$	$J\pi_2$	τ_1	τ_2	E_{21}(keV)	P_{th}/χ(W/cm^2)
$^{152}_{63}$Eu	147.81	148.7364	8-	6+	96min	330ps*	0.9264	9.0×10^{24}
$^{179}_{72}$Hf	1105.63	1105.91	25/2-	7/2+	25.1d	<10μs**	0.28	3.6×10^{101}

$J\pi_i$: the spin and parity of the level i (i = 1, 2)
τ_i : the half-life of the level i
Γ_{21}'s in P_{th} are estimated in the terms of the Weisskopf units.
* estimated in the terms of the Weisskopf unit by assuming that level 2 decays into the level of energy 108.1148keV and spin-parity 5+.
** most optimistically assumed as 10μs (upper limit of the Mossbauer effect)

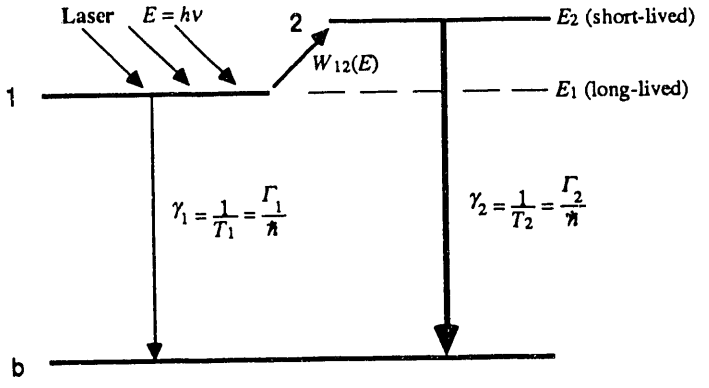

Fig. 1 Schematic structure of isomer states 1 and 2.

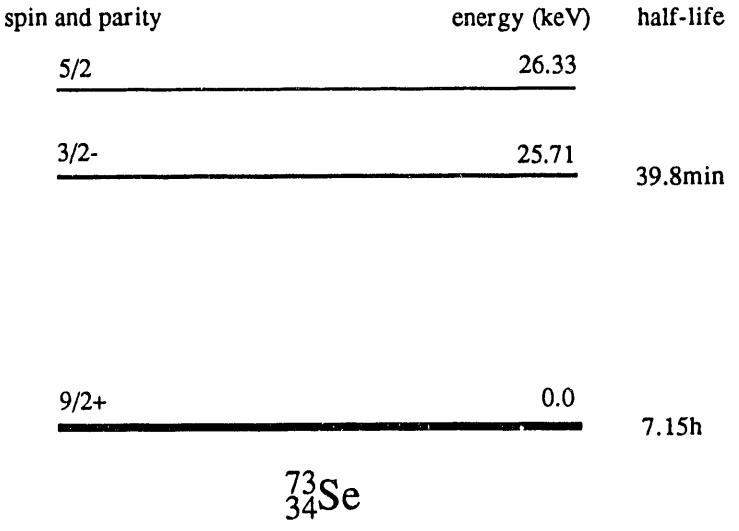

Fig. 2 Nuclear levels in $^{73}_{34}Se$.

3.7 Clustering of Experimental Data and Its Applications to Nuclear Data Evaluation

S. Iwasaki

Department of Nuclear Engineering, Tohoku University
Aramaki-Aza-Aoba, Aoba-Ku, Sendai 980, Japan

Abstract

A semi-automatic pre-processing technique is proposed to classify the experimental data for a reaction into one or a small number of large data groups, called main cluster(s), and to eliminate some data which deviate from the main body of the data. The classifying method is based on a technique like pattern clustering in the information processing domain. Test of the data clustering formed reasonable main cluster(s) for three activation cross sections. This technique will be helpful tool in the neutron cross section evaluation.

1. Introduction

The first and important task of the evaluator of the neutron nuclear data is to gain a set of reliable and mutual consistent experimental data which cover a certain energy range of the incident neutrons, e.g., an excitation function of a reaction from threshold energy to 20 MeV, and to eliminate improper, inconsistent data from the set. This kind of task needs an elaborate work and skilled experience, so is very time-consuming. Among the experimental data of a reaction, there exist a number of data which systematically deviate very much beyond their estimated errors from the main body of the cross section data, sometimes by a factor of two or three. One possible reason of this deviation would be partly due to the old, wrong standard or reference nuclear data used in the cross section data analysis,

which were revised after that. However, it is impossible to attribute such large deviation to the old nuclear data alone.

A semi-automatic method for the pre-processing the experimental data is proposed in this paper: classifying the experimental data using a technique like pattern clustering in the information processing domain. This approach is to classify the experimental data into a small number of large clusters: group of experimental data in which the data sets are highly similar with each other, meaning the mutual consistency; in the first and ideal case, to classify them into one main cluster and extra inconsistent data group; or into a small number of main clusters: a few data groups which may contradict with each other, in the other cases. In both cases, each group can be a candidate of the objective data group of the statistical evaluation or fitting by the theoretical calculation.

2. CLUSTERING METHOD

2.1 Basic Data Cluster

In the method we first consider a unit of group of experimental data to deal with. It is natural to choose a group of data for one reaction in which one or more data are contained; they have been measured and reported by one author group in literature. We call the group "basic (data) cluster".

2.2 Joining of Basic Data Clusters

In order to join the basic data clusters to form larger data clusters, we define a rule, "if majority of the n(n-1)/2-linkage relation is established among n basic data clusters, then they can be joined". A linkage of two basic clusters in question is established when a degree of similarity between them satisfies a criterion; an abstract distance defined between the clusters is smaller than the predetermined values. This means the consistency between the two data clusters. In Fig. 1, the n(n-1)/2-linkage relations between n basic data clusters are shown schematically for n=2,3,4 and 7.

Two kinds of distance are provided in accordance with the cases whether the energy overlapping between the clusters exists or not. In the first case, the distance between i- and j-clusters is defined as follows;

$$D_{ij}=\Sigma_{k=1,\ldots,Nk}[(\sigma_i(E_k)-\sigma_j(E_k))^2/(\delta\sigma_i(E_k)\delta\sigma_j(E_k)],$$

where $\sigma_i(E_k)$ and $\delta\sigma_i(E_k)$ are the cross section and its error at the energy E_k where the cross section has been measured in i- or j-cluster, and N_k is the number of energy points E_k. When the cross section is actually measured at this energy E_k in i-cluster, but not in j-cluster, $\sigma_j(E_k)$ and $\delta\sigma_j(E_k)$ is estimated by the linear interpolation from the measured values at the adjacent energies, E^j_m and E^j_{m+1}, where $E^j_m < E_k < E^j_{m+1}$, and vice versa. The predetermined values are chosen as 1, 2, 3 and 4 times of N_k. If the distance is less than $1*N_k$, two clusters are very close (degree of similarity class C=4); less than $2*N_k$, good (C=3), less than $3*N_k$, average (C=2); less than $4*N_k$, not very far (C=1); more than $4*N_k$, not good (C=0). Examples are shown in Fig. 2.

Even when the energy ranges of the two cluster data are not overlapped (in the second case), extrapolation of one cluster data is allowed at most by a half length of the cluster to the side of another cluster in the average direction determined by the former cluster unless the cluster is not bent so much. An extended distance between the clusters is also defined by similar formula as above, and the similarity grade is classified as good (C=5) if the distance is less than or equal to 2 (see also example of this case in Fig. 2).

In this method, a symmetric matrix with a dimension of the total number of clusters considered is formed, called 'linkage class matrix' whose ij element is the link class value from 0 to 5 corresponding to above mentioned similarity classes between the i and j- clusters. Using the matrix, the multi-link relation can be evaluated, as shown later.

Practically, weaker rule is necessary to form a small

number of main clusters, because the condition of "majority" in the original rule is sometimes too strict, and many basic clusters particularly located in the border region would be rejected. The condition part of the weak rule then become "if two or more linkages of n(n-1)/2-relation are established".

We often encounter the energetically isolated data sets far from the majority out of the range of the extrapolation. There is no way to join such data clusters, and one should join them one by one seeing the plotted data base. One should also be careful to treat the 14-MeV region data, because this energy region is very important from the application respects, and there are many cross section data. In some cases, we should limit the energy region of the distance calculation to the near 14 MeV, as shown in the following examples.

3. CLUSTERING TEST

Present method was actually applied to three dosimetry cross section data of $^{58}Ni(n,2n)^{57}Ni$, $^{59}Co(n,\alpha)^{56}Mn$ and $^{93}Nb(n,2n)^{92m}Nb$ reactions[1].

3.1 $^{58}Ni(n,2n)^{57}Ni$ cross section

This reaction is very typical one whose cross sections divide into two group of basic data clusters. At a glance of plotted data (Fig. 3), at least two groups clearly deviate from each other in the energy region above 15 MeV. In the evaluation of the IRDF-85[2], the lower group was adopted, whereas the higher group was adopted in recent dosimetry files, IRDF-90[3], ENDF/B-VI[4] and JENDL Dosimetry File[5].

In Table 1, the link class matrix is shown. From the matrix, one can easily find a main cluster which consists of the following basic data clusters: No.1, 3, 4, 5, 8, 9, 12, 13, and 14 among which the above rule is satisfied (Fig.4 (left)). Among the rest of the basic clusters, the rule in not satisfied, but, the weak rule is satisfied. Thus, in this case, another main cluster having large cross sections is formed (Fig.4 (right)).

3.2 $^{59}Co(n,\alpha)^{56}Mn$ Cross Sections

All basic data clusters of this reaction are shown in Fig. 5 (left), indicating that there might be no extra cluster to be rejected from the main group. When the rule is applied to them, however, at first one data cluster No.1 is picked up due to the odd behavior from others as shown in Fig. 5 (right); the cluster is crossing the other ones. Closely looking at the clusters around the 14 MeV and applying the additional rule which limits the similarity calculation region between 13 and 15 MeV reveal that there are two main groups; the larger cross section group consists of three clusters (Fig. 6 (left)); the smaller cross section group consists of the other five basic clusters, which distribute from threshold energy to 20 MeV (Fig. 6 (right)). The final result will be fairly dependent on which group is chosen in the evaluation. The smaller cross section group was adopted in the evaluation of ENDF/B-VI[4], and as the objective data in theoretical model calculations by authors[6]. The evaluated curve for JENDL Dosimetry File[5] follows the larger cross section group.

3.3 $^{93}Nb(n,2n)^{92m}Nb$ Cross Sections

The third example is a typical cross section set in which a main group is accompanied by several extra basic clusters. Fig. 7 (left) shows all nineteen basic data clusters to be manipulated. After applying the weak rule, three basic data clusters shown in Fig. 7 (right) are suggested to be rejected by the rule. Data cluster No.16 is actually located at the border region; this data are finally rejected with the human judgment because the error of the data are too large. Final main cluster is shown in Fig. 8 (left), which is quite natural being compared with the newly evaluated data IRDF-90[7].

Fig. 8 (right) shows the basic data clusters which were adopted for the evaluation of dosimetry cross sections (IRDF-90U) by the IRK group[7] through a detailed and careful inspection of the experiment and method described in the original papers one

by one. From the two figures of 8 we can see that the results of the two methods are consistent with each other except for the No. 16 cluster which was adopted by IRK. It is not important for the final result of the evaluation of this reaction cross section whether this cluster is included or not due to the large errors and small weight of the cluster.

4. DISCUSSION

Basically the main clusters are successfuly formed by the proposed method with the aide of human judgment for the joining some clusters which located on the border between main clusters.

Primary purpose of the data clustering is to form one main cluster of the data in which the each basic cluster is consistent with each other, and not to form two or more main clusters for the cross sections of one reaction. However, such multiple clusters were unavoidably formed in some reaction cross sections as shown above, and true cross section curve is expected to pass along with such a cluster.

No one can state that a cluster is definitely correct among the clusters for a reaction only by reviewing of the experimental data and reports; one can only express that a cluster is more reliable than the others. Reliable and possibly 'true' cross sections have been established through the processes of cyclic interactions among the measurements of differential cross sections, evaluation of the cross sections and validation of cross sections by integral experiments. The theoretical model calculation provide an useful information to such processes, too.

References

1. Iwasaki, S and Sugiyama, K.: Ann. M. J Atom En. Soc. (1992).
2. Cullen, D.E., et al.: IAEA-NDS-41/R, (1982), rev.(1985).
3. Kocherov, N.P., and McLaughlin, P.K.: IAEA-NDS-141 (1990).
4. BNL/National Nuclear Data Center: ENDF/B-VI (1990).
5. Nakazawa, M., et al.: JAERI 1325 (1992).
6. Odano, N. et al.: to be published in Jour. Nucl. Sci. Tech.
7. M. Wagner, et al.: INDC(AUS)-014, IAEA (1991).

Table 1 Link class matrix of basic data clusters obtained for $^{58}Ni(n,2n)^{57}Ni$ cross sections.

i[a]	j[a]	1	2	3	4	5	6	7	8	9	10	11	12	13	14
1		9[b]	0	0	0	4	0	0	4	1	0	0	0	3	2
2		0	9	0	0	0	0	4	0	0	2	0	0	0	0
3		0	0	9	0	3	0	0	4	1	0	0	4	2	0
4		0	0	0	9	1	0	0	0	0	0	1	0	3	0
5		4	0	3	1	9	0	0	3	2	0	0	1	3	5
6		0	0	0	0	0	9	3	0	1	2	3	0	0	0
7		0	4	0	0	0	3	9	0	0	0	0	0	0	0
8		4	0	4	0	3	0	0	9	3	0	0	3	1	0
9		1	0	1	0	2	1	0	3	9	0	0	4	2	0
10		0	2	0	0	0	2	0	0	0	9	2	0	0	0
11		0	0	0	1	0	3	0	0	0	2	9	0	0	1
12		0	0	4	0	1	0	0	3	4	0	0	9	0	0
13		3	0	2	3	3	0	0	1	2	0	0	0	9	0
14		2	0	0	0	5	0	0	0	0	0	1	0	0	9

a) i,j: basic data cluster number.

b) 9: the distance is not defined.

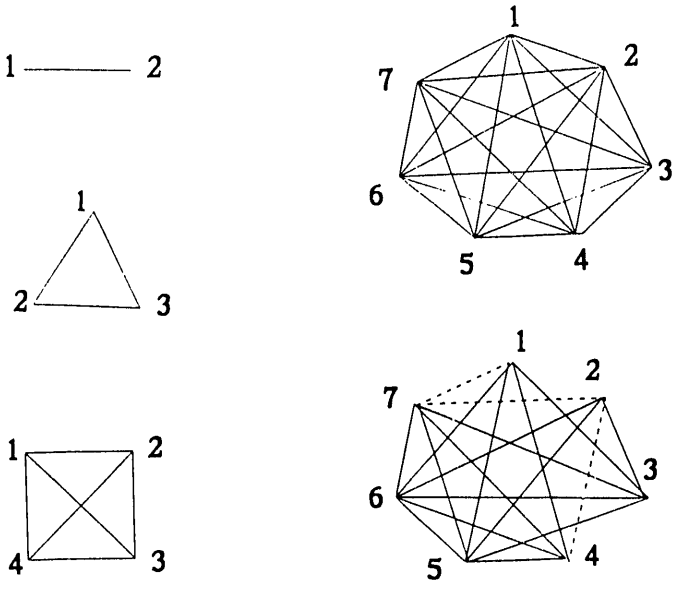

Fig. 1 n(n-1)/2-linkage relation between n-basic clusters. Complete relations for n=2,3,4, and 7. Incomplete one for n=7.

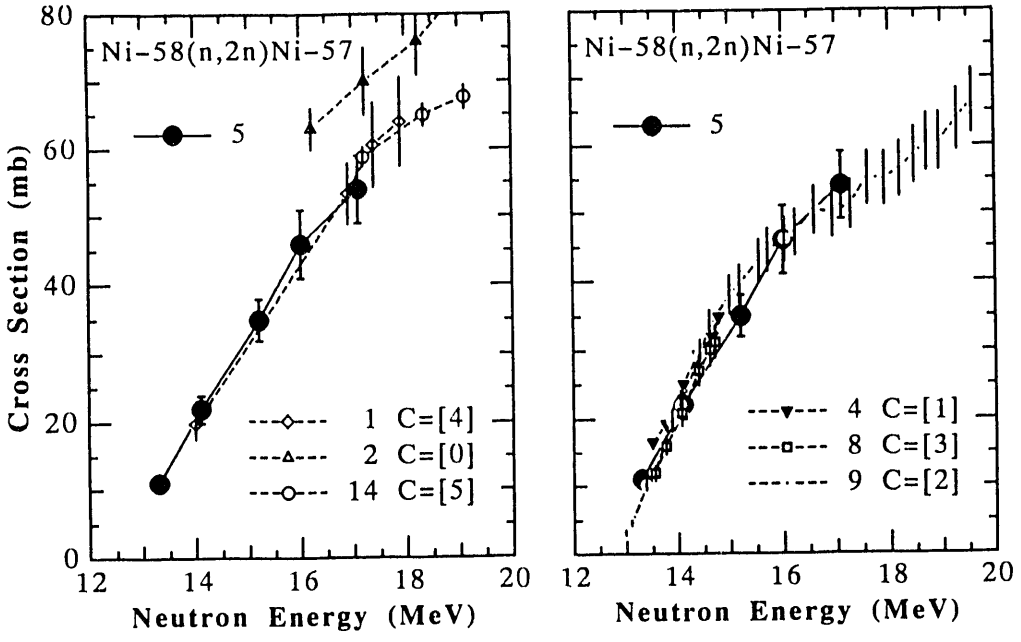

Fig. 2 Examples of the degree of similarity class between actual basic data clusters: ^{58}Ni(n,2n) cross sections (see Fig. 3 & Table 1). Note the symbols of the data are not the same as Fig. 3.

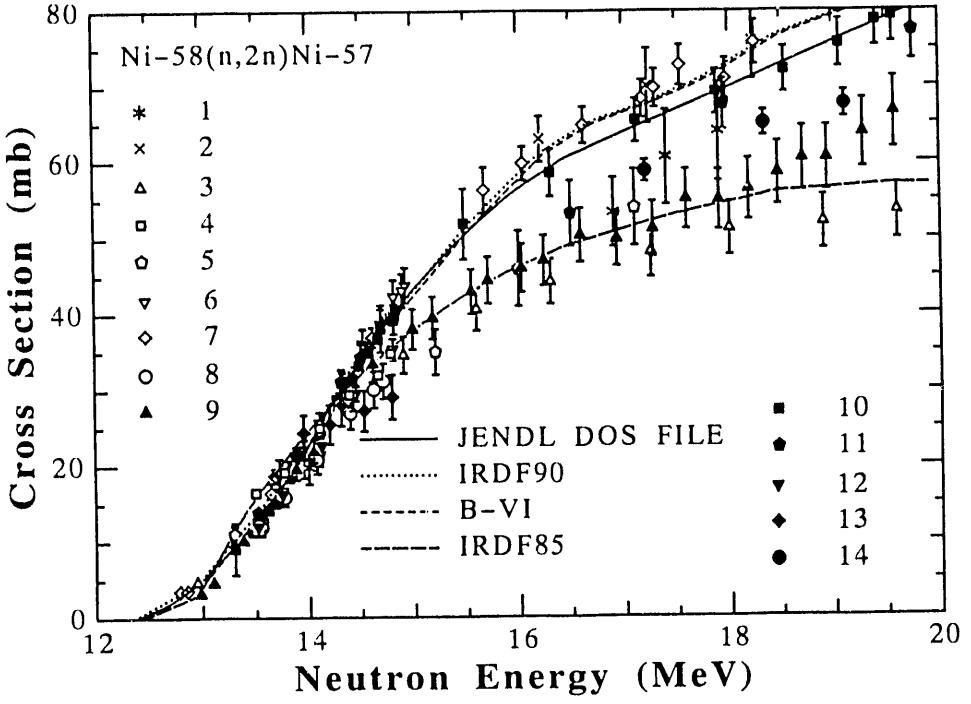

Fig. 3 The basic data clusters of ^{58}Ni(n,2n) reaction.

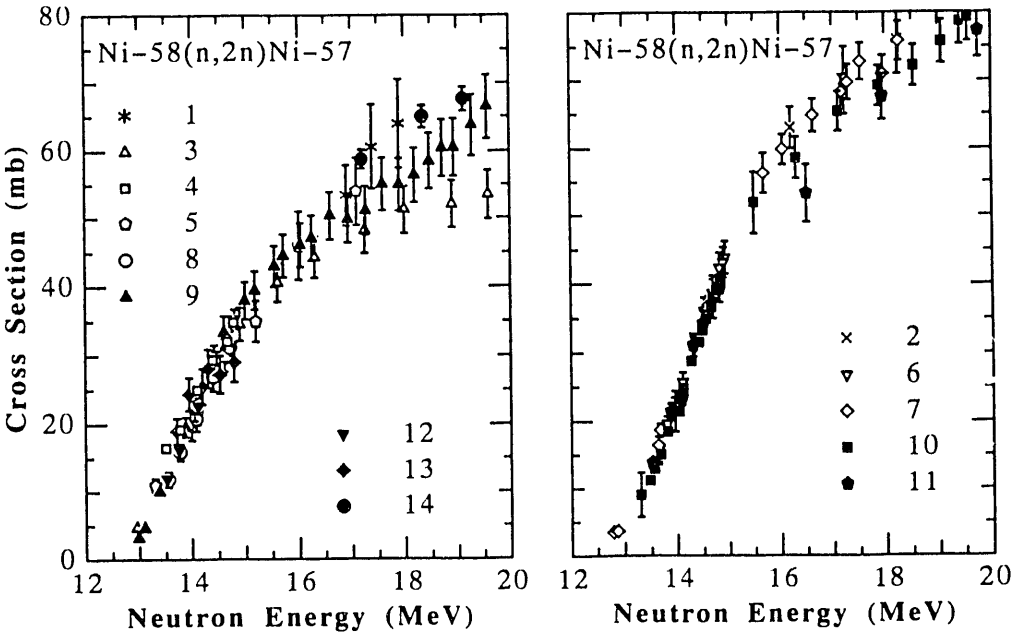

Fig. 4 Smaller cross section group (left) and larger cross section group (right) for ^{58}Ni(n,2n) reaction cross sections.

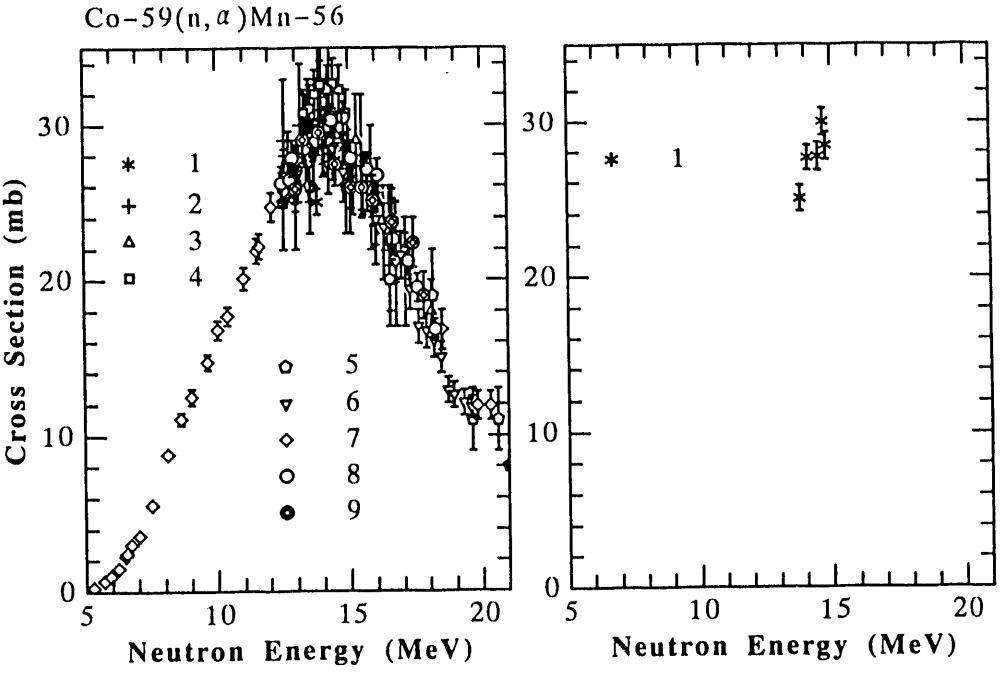

Fig. 5 All basic data clusters (left) and one rejected data cluster for ^{59}Co(n,2n) cross sections.

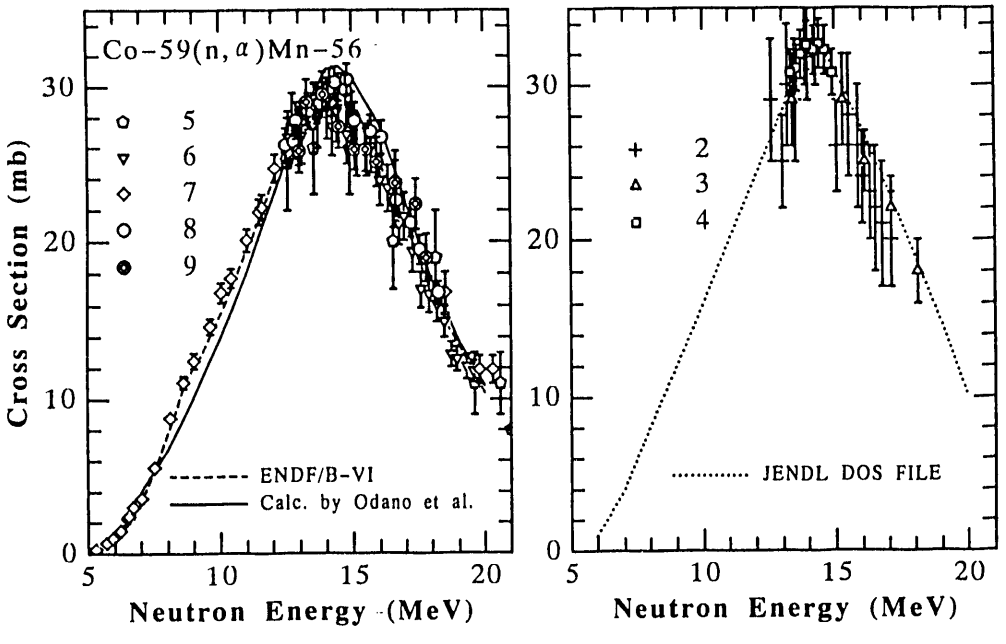

Fig. 6 Main cluster having smaller cross sections (left) and large cross sections (right) for ^{59}Co(n,2n) reaction.

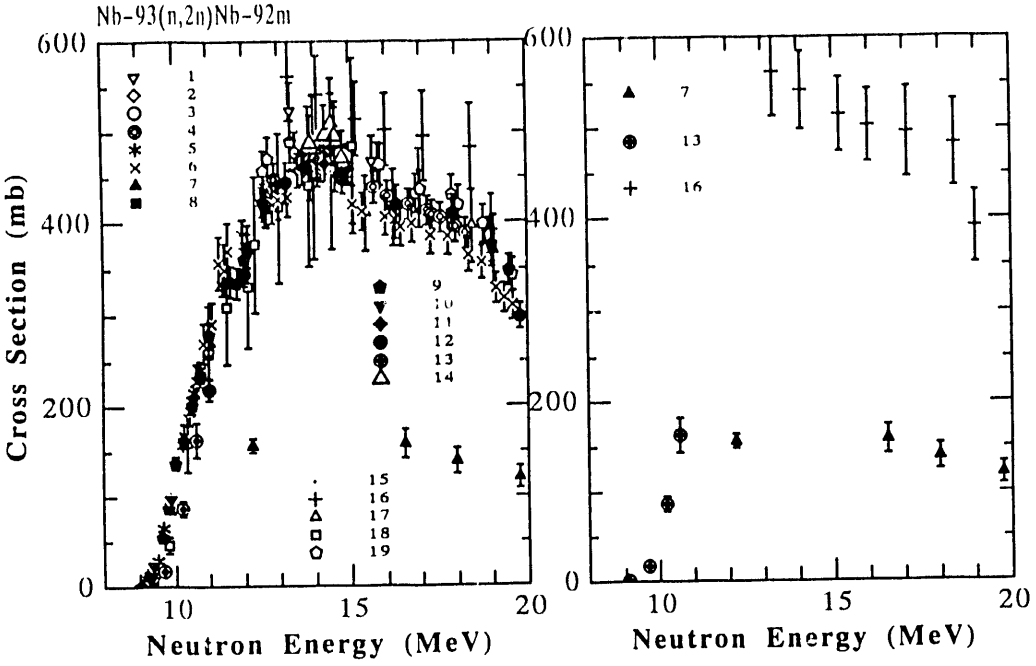

Fig. 7 All basic data clusters (left) and three rejected data clusters (right) of ^{93}Nb(n,2n) cross sections.

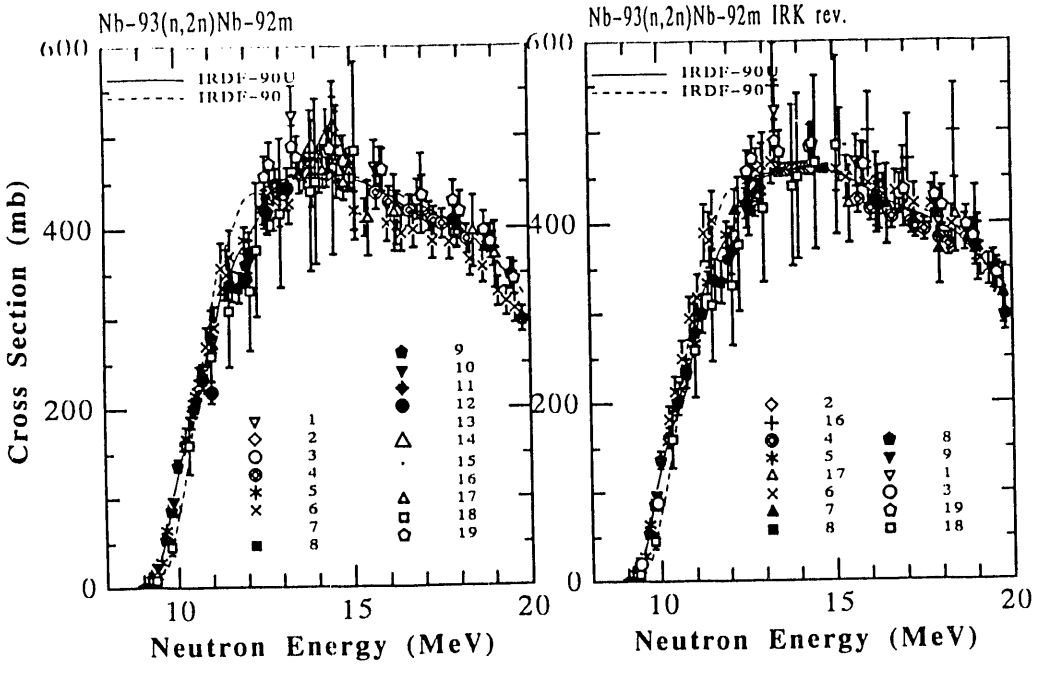

Fig. 8 Obtained data cluster (left), and revised and adopted data clusters by IRK group for IRDF-90 (right) of ^{93}Nb(n,2n) cross sections.

3.8 Energy Dependence of the Optical Potential Parameters for ^{209}Bi in Low Energy Region and Dispersion Relation

T. Kawano, K. Kamitsubo, T. Iwamoto, N. Fujikawa and Y. Kanda

Department of Energy Conversion Engineering,
Kyushu University, Kasuga, Fukuoka 816, Japan

ABSTRACT : When a dispersion relation between real and imaginary potential is considered, the contribution of the volume type imaginary potential is embedded in the real potential while the surface peaked potential causes the surface peaked component in the real potential. We attempt to estimate this surface peaked real potential of ^{209}Bi. In addition, we fit a Brown-Rho parametrization to the imaginary potential in a conventional optical model analysis, and we estimate the energy dependencies of the optical potential parameters due to the dispersion relation.

1. INTRODUCTION

Optical potential with Woods-Saxon form is characterized by its depth, radius, and diffuseness. These geometrical parameters (radius and diffuseness parameters) sometimes show energy dependencies in low energy region ($E_n \leq 10$MeV). This phenomenon is often attributed to an existence of surface peaked component in the real potential.

The imaginary part of the optical potential is consisted of both volume (W_v) and surface (W_s) absorption types. When a dispersion relation between real and imaginary potential is considered, the contribution of the volume type imaginary potential is embedded in the real potential while the surface peaked imaginary potential causes the surface peaked component in the real potential, and the addition of the real surface component makes the geometrical parameters energy dependent in the low energy region. Because of this effect, we often face a difficulty in analyses of an elastic scattering and a total cross section data using the conventional optical model .

There are some approaches to investigate the dispersive optical potential. The one of them is to determine the strength of the surface peaked component directly[1,2], and the other is a radial moment method[3,4]. First, we show the energy dependencies of the optical potential parameters of ^{209}Bi using the conventional parametrization, and secondly, above approaches are adopted to interpret the results.

The target atom ^{209}Bi is regarded as a spherical nucleus then the analysis by the

optical model is simple, and an accurate experimental data is available in the low energy region.

2. Conventional Optical Potential

When incident particles are low energy neutrons the Coulomb electrostatic potential V_C vanishes and the volume type imaginary potential W_v can be neglected, then the optical potential is expressed as

$$U(r) = -Vf(x_V) + i4W_s\frac{df(x_{W_s})}{dx_{W_s}} - \left(\frac{\hbar}{m_\pi c}\right)^2 V_{SO}(\boldsymbol{l}\cdot\boldsymbol{s})\left(\frac{1}{r}\right)\frac{df(x_{SO})}{dx_{SO}}. \quad (1)$$

The form factor $f(x_i)$ has the Woods-Saxon form $f(x_i) = \{1+\exp(x_i)\}^{-1}$, where $x_i = (r - r_i A^{1/3})/a_i$. The parameters to be searched are depths (V, W_s), radii (r_V, r_{W_s}), and diffuseness parameters (a_V, a_{W_s}). The strength of spin-orbit interaction is taken from Ref.2. Since an optical model parameter estimation method was described in Ref.5, a brief outline is given here.

First, a six-parameter fitting are made at the highest energy ($E_n = 9.99$MeV) where an ambiguities among the parameters are regarded to be less. The obtained parameters are used as prior parameters at the neighboring energy point where differential elastic scattering data is available, and we estimate posterior parameters by a Bayes parameter estimation method. Successively, the posterior parameters are used as the prior ones at the neighboring energy. The process is continued toward the lowest energy.

When neutron energies are lower than 6 MeV, compound elastic scattering cross sections are calculated using Hauser-Feshbach theory with width fluctuation correction by Moldauer[6]. Discrete states are included when $E_n \leq 3.12$MeV. Above this energy, the levels are assumed to be overlapped, and Gibert and Cameron's formulas[7] are used to calculate the level density in the continuum region. The adopted level density parameters are, $a = 8.52$ and $\Delta_Z + \Delta_N = 0.55$ for a Fermi gas model, $T = 0.833$, $E_0 = 0.583$ and $\sigma = 3.87$ for a constant temperature model, and a matching energy $E_x = 3.42$. The Moldauer's width fluctuation correction is also taken into account in the continuum region.

The obtained real and imaginary optical potential strengths, expressed as a volume integral per nucleon $J_i = (4\pi/A)\int V_i(r)r^2dr$, are shpwn in Fig.1, and the geometrical parameters r_V, r_W, a_V and a_W, are shown in Fig.2, as functions of neutron incident energy. In Figs.1 and 2, the light solid curves (for real part) and the light dotted curves (for imaginary part) are least-square fitting curves by polynomial functions, the symbols o and Δ are derived real and imaginary potential parameters, respectively. The calculated differential elastic scattering cross sections using these curves are shown in

Fig.3, and the light solid line in Fig.4 is the calculated total cross section. Since there are large number of experimental total cross section data, they are smoothed by a spline function. In Fig.4, symbols are the spline knots and they represent experimental data. As seen in these figures, the calculated cross sections agree with the experimental data.

Apparent energy dependencies of the parameters are demonstrated especially for r_V and a_W in Fig.2. In the 1.5 to 4MeV range, the obtained r_V is larger and a_W is smaller than the Walter and Guss' global potential parameters($r_V = 1.219$ and $a_W = 0.512$)[8]. Similar tendencies were reported by Finlay *et al.*[9] and Annand *et al*[10]. These obtained r_V and a_W approach to the global parameters as the incident energy increases. On the other hand, a_V and r_W seem almost independent to the energy.

The volume inetgral per nucleon of the real potential J_V decreases as the energy increase when $E_n \geq$4MeV, while J_V is almost constant below 4MeV. Theoretical arguments about dispersion relation indicate that the strength of the potential is symmetric about a Fermi energy, and the strength J_V once decreases in the negative energy region. This is consistent with the present results.

3. Surface Peaked Real Potential

The surface peaked imaginary potential causes the surface peaked term in the real potential through the dispersion relation:

$$V(r;E) = V_{\rm HF}(r;E) + \frac{\rm P}{\pi}\int_{-\infty}^{\infty}\frac{W(r;E')}{E'-E}dE', \tag{2}$$

where P stands for a principal-value integral.

The surface peaked imaginary potential dominates at low energies, then there is a possibility of improvement of analyses when a small surface peaked component are added to the real potential in the low energy region. We rewrite the optical potential as,

$$\begin{aligned} U(r) = &- Vf(x_V) + 4V_s\frac{df(x_{V_s})}{dx_{V_s}} + i\,4W_s\frac{df(x_{W_s})}{dx_{W_s}} \\ &- \left(\frac{\hbar}{m_\pi c}\right)^2 V_{\rm SO}(\boldsymbol{l}\cdot\boldsymbol{s})\left(\frac{1}{r}\right)\frac{df(x_{\rm SO})}{dx_{\rm SO}}, \end{aligned} \tag{3}$$

where V_s is the strength of the surface peaked component. We assume that the geometrical parameters for V_s and W_s are the same, and the surface peaked component has the derivative Woods-Saxon form. The other parameters are identical to the values used in the conventional analysis, then searches are made for seven parameters. It is expected that V_s decreases as the energy increase, and that V_s is more insensitive to the calculation than the other parameters because the small V_s is obscure in the dominant real central potential. Therefore parameter estimation is started at the lowest energy,

and the process is continued in the energy increment direction. In addition, we give a larger uncertainty on V_s at each estimation.

The obtained surface peaked components are shown in Fig.5. Above about 6MeV, no evidence of existence of V_s is found. Below 6MeV, the parameters except for V_s are slightly different to the conventional analysis in the previous section, however the anomalous energy dependencies in the geometrical parameters still remain.

In order to confirm the strength of the surface peaked real potential, we adopt the integral of the dispersion relation to the imaginary part. It is convenient to determine the magnitude of the surface peaked component by the volume integral of surface peaked imaginary potential $J_W(E)$, as[1]

$$V_s(E) = \frac{W_s(E)}{J_W(E)} \left(\frac{\mathrm{P}}{\pi} \int_{-\infty}^{+\infty} \frac{J_W(E')\, dE'}{E' - E} \right). \tag{4}$$

In order to calculated Eq.(4), we must know J_W for all energies. We assume that $J_W(E)$ is symmetric about the Fermi energy (taken to be $E_F = -5.65\mathrm{MeV}$)[2]. (i) For $0 \leq E \leq 11$, $J_W(E)$ is given by the searched parameters, and this is $J_W(E) = 29.83 + 1.261E$. (ii) For $E_F \leq E \leq 0$, we assume that $J_W(E)$ is proportional to $(E - E_F)^2$, then it becomes $J_W(E) = 0.935(E - E_F)^2$. (iii) For $11 \leq E \leq 50$, $J_W(E) = 56.14 - 1.130E$ is taken from Walter and Guss's global potential[8]. The calculated V_s is represented by the solid curve in Fig.5. As seen in Fig.5, the magnitude of V_s is almost consistent between the searched values and the prediction of the dispersion relation. It is, However, difficult to conclude that the obtained surface peaked component is reliable, because the obtained V_s includes relatively large uncertainty and the calculated V_s strongly depends on the assumption in the negative energy region.

4. Radial Moments of Potentials

In the framework of the dispersion relation approach of Refs. 3 and 4, the energy dependencies of the Woods-Saxon parameters are determined by three different radial moments

$$\langle r(E)^q \rangle_V = \frac{4\pi}{A} \int_0^{\infty} V(r; E) r^q \, dr. \tag{5}$$

The dispersion relation holds for the radial moment of the potential, that is,

$$\langle r(E)^q \rangle_V = \langle r(E)^q \rangle_{\mathrm{HF}} + \frac{\mathrm{P}}{\pi} \int_{-\infty}^{+\infty} \frac{\langle r(E')^q \rangle_W}{E' - E} \, dE'. \tag{6}$$

The radial moment of the Hartree-Fock component is expressed by $\langle r(E)^q \rangle_{\mathrm{HF}} = A_q + B_q E$, since it is expected to be smooth function of the energy. When a Brown and Rho parametrization[11] is assumed for the $\langle r(E)^q \rangle_W$, an analytic expression of the various

radial moment of the dispersive contribution can be obtained,

$$\langle r(E)^q \rangle_W = \frac{C_q (E - E_F)^2}{(E - E_F)^2 + D_q^2}, \tag{7}$$

$$\langle r(E)^q \rangle_V = A_q + B_q E + \frac{C_q D_q (E - E_F)}{(E - E_F)^2 + D_q^2}. \tag{8}$$

The obtained optical potential parameters in the conventional analysis are used to calculate $\langle r(E)^q \rangle_V$ and $\langle r(E)^q \rangle_W$ when q = 0.8, 2.0, and 4.0, and the values of the parameters A_q, B_q, C_q, and D_q are determined for the three q-values by a least-square fitting. Note that $\langle r(E)^2 \rangle$ is the familiar volume integral per nucleon $J_{V,W}$. The heavy solid curve and the dashed curve in Fig.1 are the calculated values of $\langle r(E)^2 \rangle_V$ and $\langle r(E)^2 \rangle_{\mathrm{HF}}$, respectively. The heavy dotted curve in Fig.1 is $\langle r(E)^2 \rangle_W$. The calculated $\langle r(E)^2 \rangle_V$ is expected to decrease when one extrapolates the energies from positive to negative. The turning point seems to be around 0 MeV from the conventional analysis. The calculated A_2, B_2, C_2, and D_2 values, however, indicates that the turning point is about −3.4MeV. Since no additional data – such as experimental single particle energies or optical potential parameters above 10MeV – are included in this calculation, the calculated curves in Fig.1 may have some uncertainties. The global optical potential parameters by Walter and Guss[8] give somewhat larger $\langle r(E)^q \rangle_W$ values in the 20 to 40 MeV range compared with the present results. When the Walter and Guss parameters are added in the calculation, gradient of the calculated $\langle r(E)^q \rangle_V$ becomes gentler.

When the parameters A_q, B_q, C_q, and D_q are determined for the three q-values, one can calculate the Woods-Saxon parameters for the real potential and the derivative Woods-Saxon parameters for the imaginary potential. The calculated geometrical parameters are displayed by the heavy solid curves in Fig.2. The energy dependencies of the geometrical parameters are similar to the conventional analysis as indicated in Fig.2.

The heavy solid curve in Fig.4 is the calculated total cross sections with these parameters. Reproducibility of the experimental data in the energy range 2.5 to 5.5 MeV is worsened, but it is improved below 2.5MeV. We gave the phenomenological energy variations of the parameters by linear functions below about 2MeV in the conventional analysis because of the limit of the elastic scattering data, then the discrepancy between the data and the calculation grows below 2MeV (light solid curve in Fig.4). Moreover, we used the polynomial functions for the fit to the derived values, then there are no guarantees for the outside of the 1.5 to 10MeV energy range. Since the radial moment method connects the optical potential in the positive energy region to the shell model potential in the negative region, this method is considered to give a good extrapolation of the parameters for $E \rightarrow 0$ and above 10MeV. Consequently the extrapolated parameters solve the discrepancy in the total cross section below 2MeV.

5. CONCLUSION

Energy dependencies of optical potential parameters of ^{209}Bi were estimated by its total cross sections and differential elastic scattering cross sections. The real radius parameter tends to increase and the imaginary diffuseness parameter tends to decrease as the energy approach to zero. The volume integral per nucleon of the real potential was almost constant below 4MeV, though it decreased as the energy above 4MeV.

A strength of a surface peaked real potential due to the dispersion relation was included in the parameter search. The obtained strength was ascertained by the principal-value integral of the surface peaked imaginary potential. The anomalous energy dependencies in the geometrical parameters still remain despite the surface peaked real potential was treated explicitly.

We fitted a Brown-Rho parametrization to the imaginary potential, and we estimated the energy dependencies of the Woods-Saxon parameters by a radial moment method. The tendencies of the obtained parameters were similar to the conventional analysis. These parameters gave good description of the experimental total cross section below 2MeV.

REFERENCES

[1] R.D.Lawson, P.T.Guenther, and A.B.Smith : Phys. Rev., **C34**, 1599(1986).
[2] R.D.Lawson, P.T.Guenther, and A.B.Smith : Phys. Rev., **C36**, 1298(1987).
[3] C.Mahaux and R.Sartor : Phys. Rev. Lett., **57**, 3015(1986).
[4] C.Mahaux and R.Sartor : Phys. Rev., **C36**, 1777(1987).
[5] T.Kawano and Y.Kanda : J. Nucl. Sci. and Technol., **28**,156(1991).
[6] P.A.Moldauer : Nucl. Phys., **A344**, 185(1980).
[7] A.Gilbert and A.C.W.Cameron : Can. J. Phys., **43**, 1446 (1965).
[8] R.L.Walter and P.P.Guss : Proc. Int. Conf. Nucl.
Data for Basic and Applied Science, 1985, Santa Fe, p.1079.
[9] R.W.Finlay, *et al.* : Phys. Rev., **C30**, 796(1984).
[10] J.R.M.Annand, R.W.Finlay and F.S.Dietrich : Nucl. Phys., **A433**, 249(1985).
[11] G.E.Brown and M.Rho : Nucl. Phys., **A372**, 397(1981).

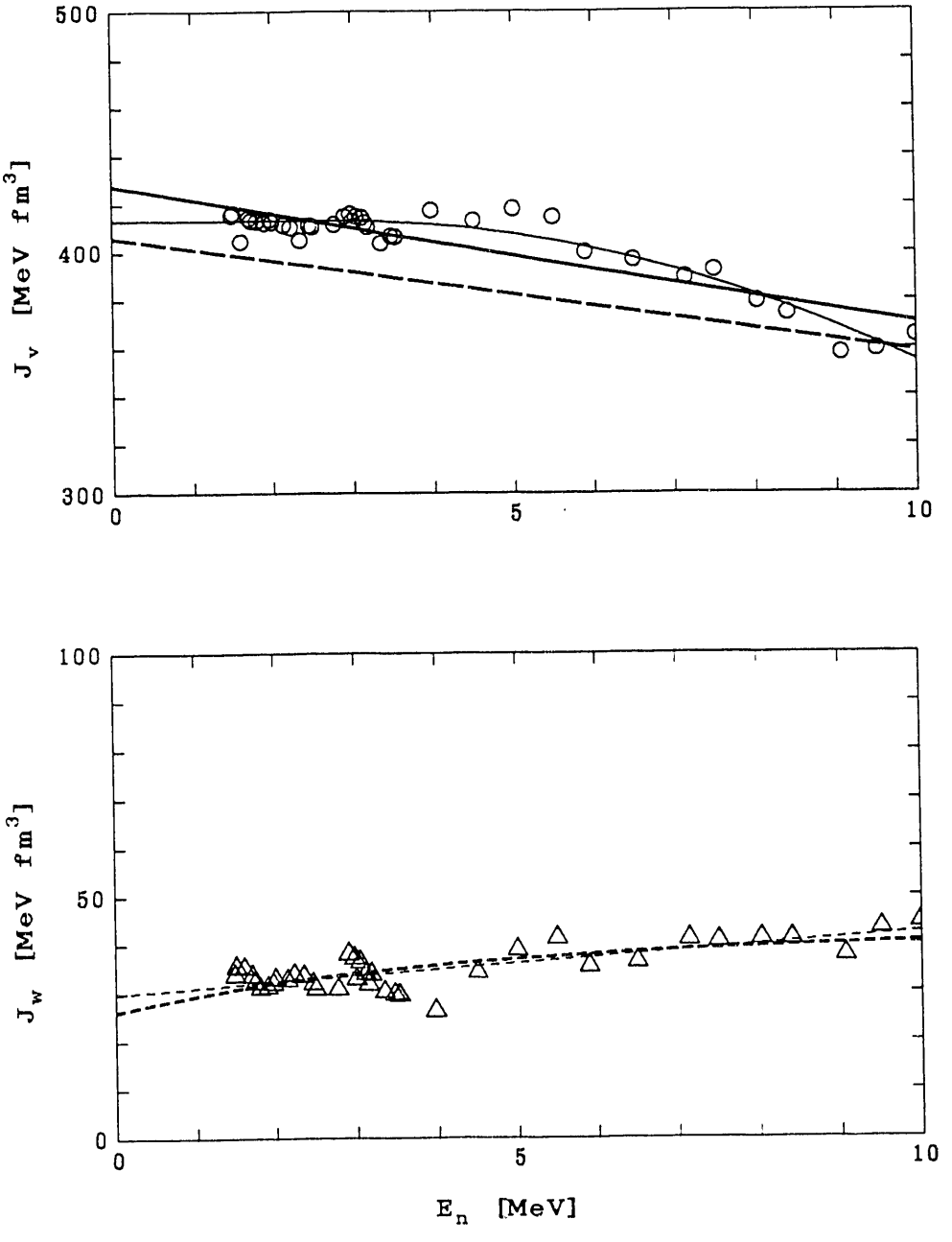

Fig. 1 Volume integrals of the optical potential parameters for ^{209}Bi. The symbols indicate the values derived from the experimental data. The light curves represent the fit to these values. The heavy curves are obtained by the radial moment method. (the solid curves for the real potential and dotted curves for the imaginary potential).

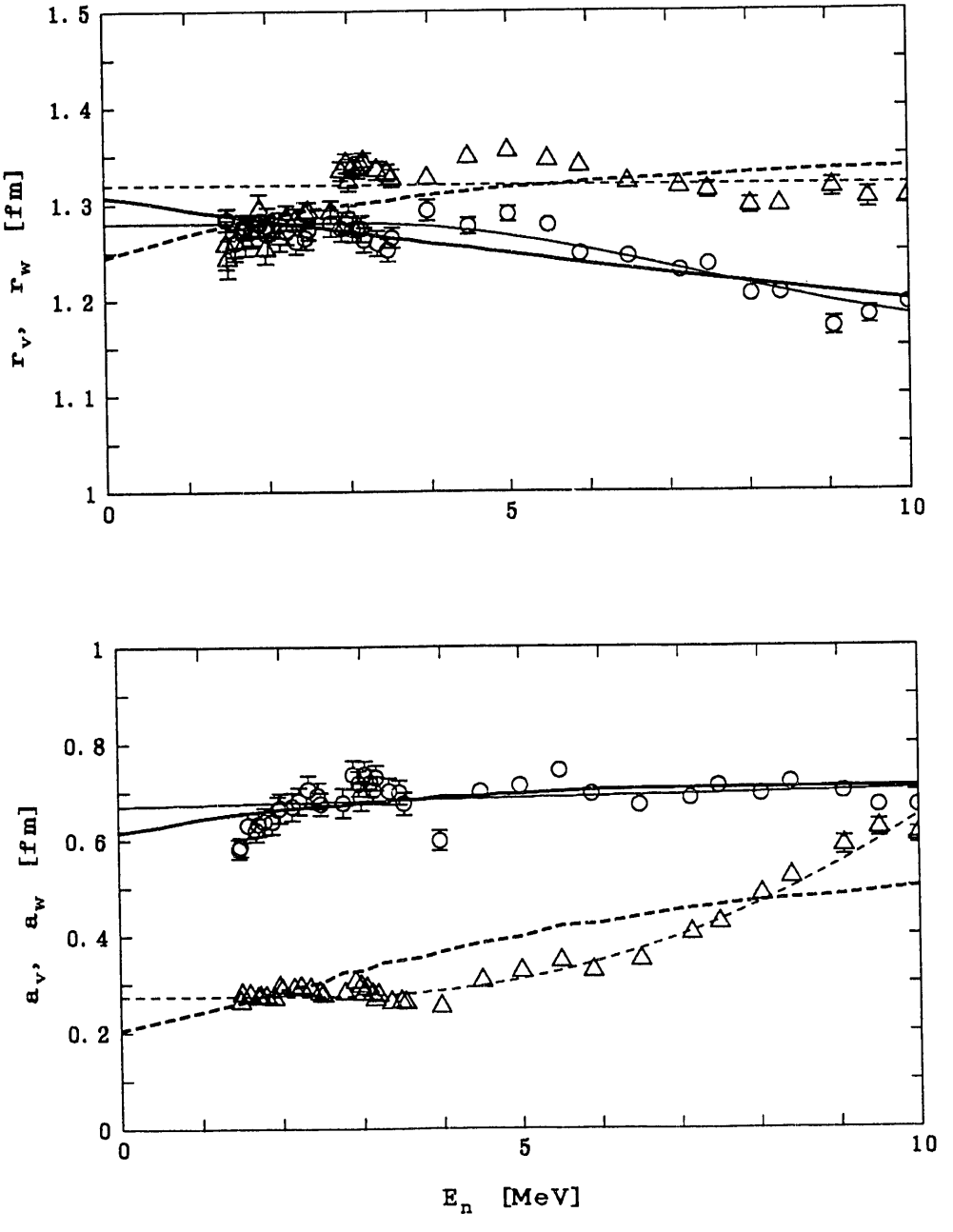

Fig. 2 Radius and diffuseness parameters of ^{209}Bi. The symbols indicate the values derived from the experimental data. The light curves represent the fit to these values. The heavy curves are obtained by the radial moment method. (the solid curves for the real potential and dotted curves for the imaginary potential).

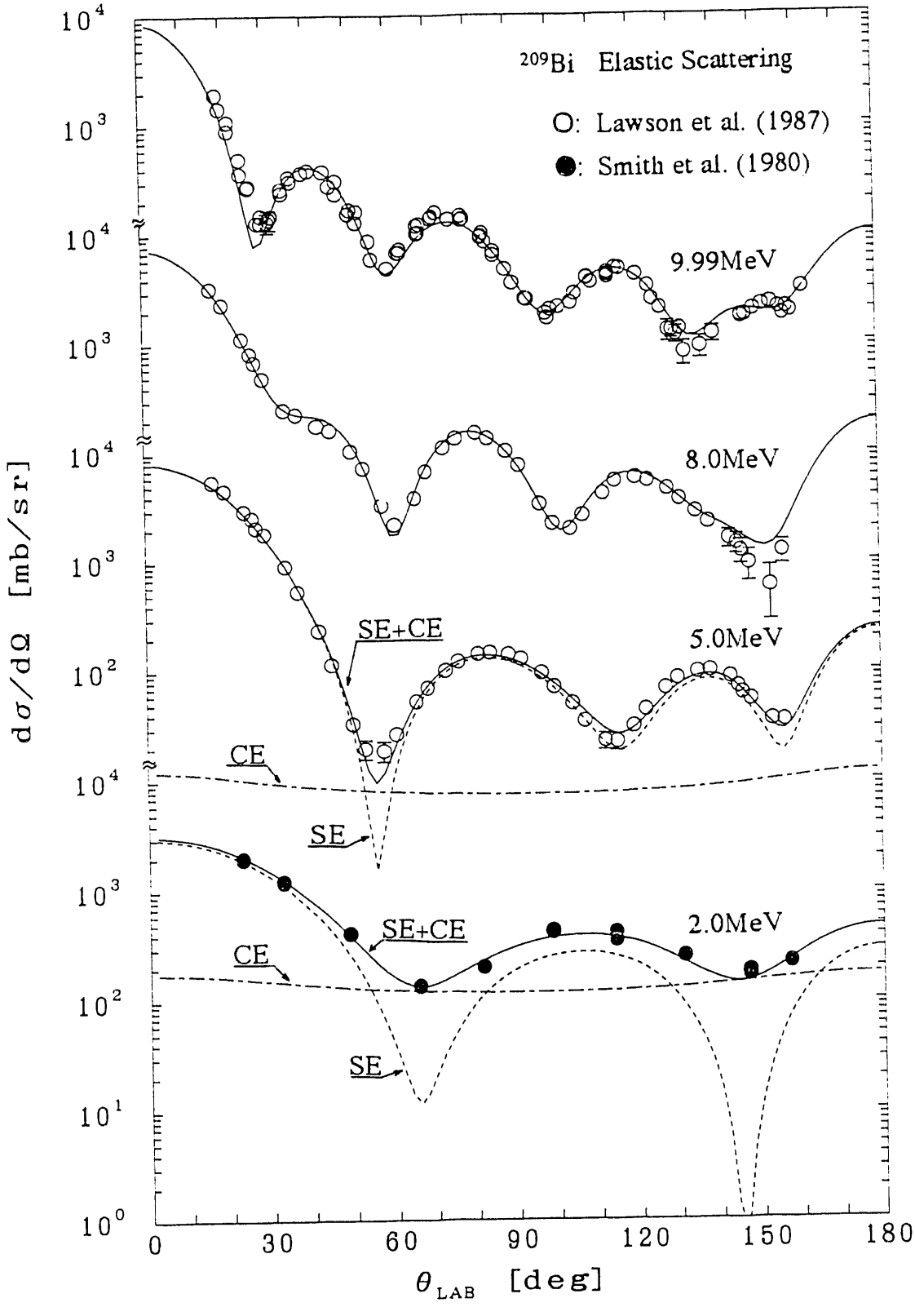

Fig. 3 Comparison of calculated and measured differential elastic scattering cross sections. The solid curves are the results calculated from the conventional optical potential.

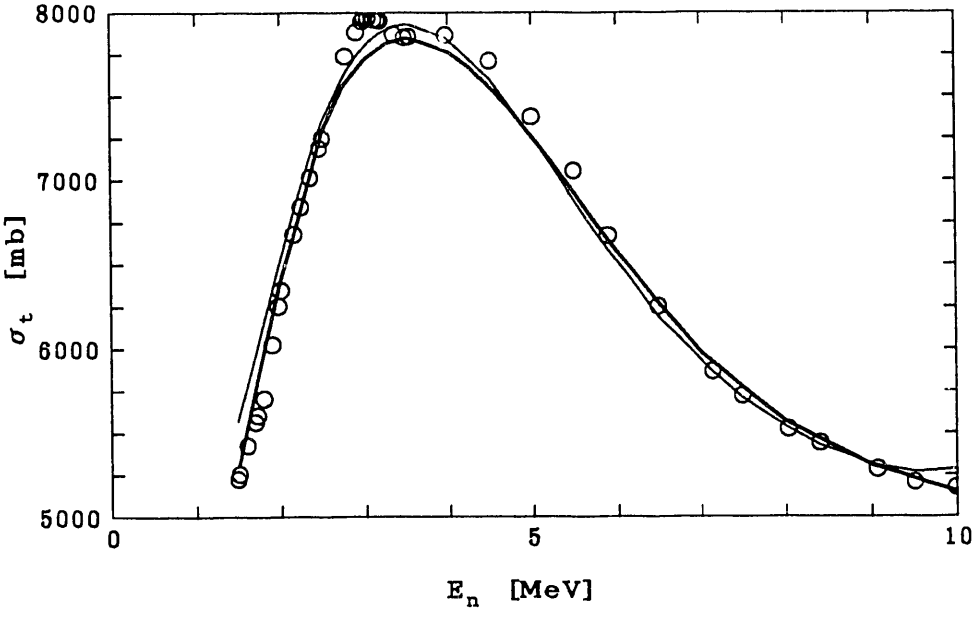

Fig. 4 Comparison of total cross sections. The symbols represent smoothed experimental data. The light curve is the result calculated from the conventional optical potential. The heavy solid curve is calculated with the parameters derived by the radial moment method.

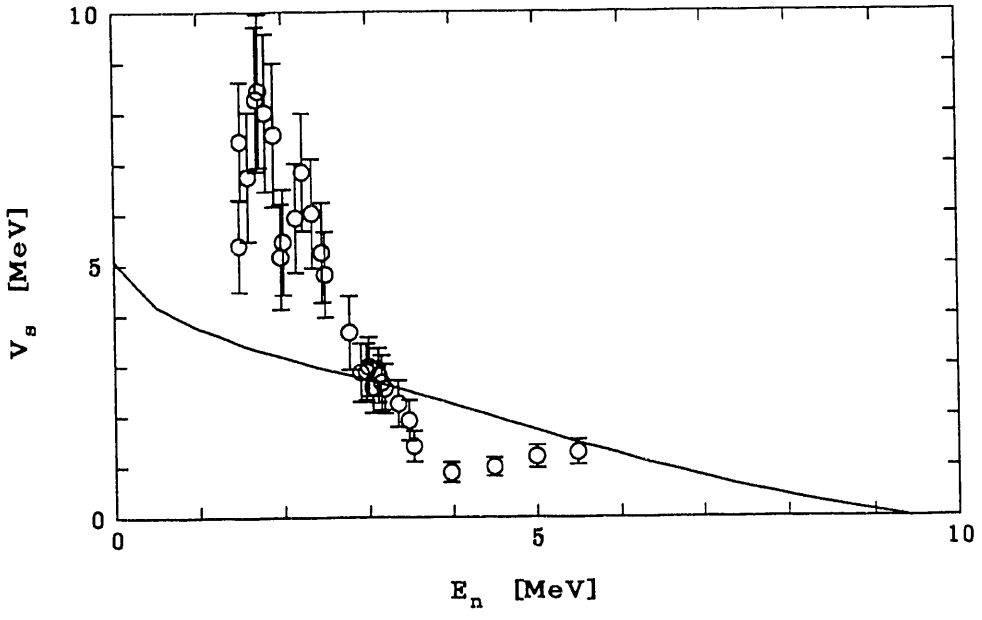

Fig. 5 Estimated strength of surface peaked real potential. Symbols are the estimated values. The solid curve is a calculated dispersive contribution from the surface peaked imaginary potential.

3.9 Evaluation of Photo-reaction Cross Sections for Light Nuclei

TORU MURATA

Isogo Engineering Center, Toshiba Corporation
8 Shin-Sugita, Isogo-ku, Yokohama, 235, Japan

Photo-reaction cross sections have been analyzed and evaluated for natural elements of C, N and O in the photon energy range between 10 MeV and 140 MeV. In the giant dipole resonance region below several tens MeV, experimental cross sections were analyzed with a resonance formula. The quasi-deuteron model was adopted to reproduce the cross sections in the higher energy region. Evaluated cross sections were obtained with the analyses and with theoretical inferences, for the photon-absorption and the emission of neutron, proton, deuteron, triton, He-3 and alpha particle.

1. Introduction

Photo-reaction nuclear data are necessary in the fields of particle accelarator design, medical radio-therapy, radio-isotope production and so on. Japan Nuclear Data Committee decided to provide a photo-reaction data file and a working group for the evaluation was started in 1989, and is now completing the first phase evaluation, which includes 21 elements from C to U. The present work was performed as a part of the evaluation work.

2. Methods of Analysis

Measured cross sections, such as photo-absorption and neutron emission cross sections show the giant resonance composed with many peaks in the energy region below about 30 MeV. In the region, experimental cross sections were analyzed with the following resonance fomula plus small contribution term of the quasi-deuteron model described below,

Photo-absorption (Total) cross section:

$$\sigma_T(E) = 2\pi\lambda^2 \sum_k \frac{2I_k+1}{2I_0+1} \beta_{k0} \frac{(E\Gamma_k)^2}{(E_k^2-E^2)^2+(E\Gamma_k)^2}$$

Particle-i emission cross section:

$$\sigma_i(E) = 2\pi\lambda^2 \sum_k \frac{2I_k+1}{2I_0+1} \beta_{ki}\beta_{k0} \frac{(E\Gamma_k)^2}{(E_k^2-E^2)^2+(E\Gamma_k)^2}$$

where B_{k0} and B_{ki} are the branching ratios of the resonance level k to the ground state gamma-transition and the particle-i emission, respectively. Other notations follow ordinary nomenclature.

Dipole photo-absorption was assumed to analyze the cross sections. Resonance energies and total widths were determined mainly by analyzing the experimental cross sections of photo-absorption and neutron emission. Energy dependence of particle emission branching ratios were taken into account with the potential barrier penetration factor averaged over various orbital angular

momentum with the weight of the corresponding nuclear volume determined by the classical impact parameters.

Above the giant dipole resonance region, observed cross sections show rather smooth features, which can be reproduced with the quasi-deuteron model /1/. The model explains the process of photo-absorption as caused by correlated neutron-proton pairs, so called quasi-deuterons in the nucleus. The quasi-deuteron model gives the photo-absorption cross section as

$$\sigma(E\gamma)=\text{const.}\cdot\sigma_d(E\gamma)\cdot P(E\gamma)$$

$$\sigma_d(E\gamma)\propto (E\gamma-Eb)^{(3/2)}\ E\gamma^{-3}$$

where σ_d is deuteron photo-absorption cross section and $P(E\gamma)$ is the Pauli-blocking factor /2/. The constant is determined, in the present analysis, by normalizing to experimental cross sections above 60 MeV. Particle emission cross sections were assumed to be obtained by multipling branching ratios to the photo-absorption cross section. The branching ratios were determined to reproduce the experimental cross section if available. If not available,the branching ratio in the resonance region was extrapolated with the energy dependence of the statistical model calculated with the transmission coefficients.

3.Results of the evaluation

Figure 1(A), (B) and (C) show the comparison of the present evaluated results and experimental cross sections.

(1)Carbon

In the giant resonance region,experimental cross sections were reproduced with 20 resonances, for the photo-absorption /3/, neutron emission /4/ and alpha particle emission /5/. For proton emission,only cross section to the ground state of B-11 was measured /6/. It is reported that more than 90% of protons were emitted to the ground state at lower energy region of the giant resonance. So,the proton emission cross section was evaluated by reproducing the ground state data below about 25 MeV, and in higher energy region, proton emission branching ratio was determined by subtracting other branching ratios. For other reactions, though experimental cross sections are not given directly, but deduced from the inverse reaction cross section /7/, reaction ratio data /8/ and bremsstrahlung spectrum averaged yield data /9/, in some energy region. With these deduced cross sections, the evaluations were made by normalizing the calculated cross sections with the statistical model.

In the quasi-deuteron model region,only available experimental cross section is that of photo-absorption.Particle emission cross sections were evaluated with the method described in the preceding section.

(2)Nitrogen

Experimental cross sections are available only in the giant resonance region below about 30 MeV. Resonance analysis were made mainly for photo-absorption /10/ and neutron emission /4/ cross sections. At low energy part, however, measured absorption cross section shows abnormal trend down to negative values, so, in this region, main resonance parameters were determined only with the neutron emission cross section. For proton emission, experimental

cross sections are reported on protons to the ground state and 2nd excited state. Referring these data, proton emission cross section was evaluated with the same method described in (1).Large difference between evaluated value and the measured cross section of the ground plus 2nd excited states will be ascribed to the large (γ,pn) cross section/11/. Other experimental cross sections are available for emission of deuteron /12/, alpha particle /13/ and that of He-3 to the ground state deduced from the inverse cross section /14/. With 13 resonances, these cross sections were reproduced.

Above 30 MeV, the absorption cross section were inferred from the cross sections of C and O, with the systematics: absorption cross section is propotional to NZ/A, where N is neutron number,Z, proton number and A,mass number of target nucleus.

(3)Oxygen

Experimental cross sections are available in all energy range for photo-absorption /3/ and neutron emission /15/. With 22 resonances, these cross sections were reproduced including proton and other particle emission cross sections. For proton emission,cross section of protons to the ground, 1st plus 2nd and 3rd, and also protons of energy from 3.4-30 MeV are reported /16/. Experimental triton and alpha particle /18/ emission cross sections are available and also reproduced with the resonance analysis.For deuteron and He-3 emission, cross sections to the ground states were deduced from the inverse cross sections /19/ just above the threshold energy, and extrapolated with the statistical model branching ratios.

References

/1/ J.S.Levinger,Phys.Rev.84(1951)43
K.G.Dedrick,Phys.Rev.100(1955)58
/2/ M.B.Chadwick et al.,Phys.Rev.C44(1991)814
/3/ J.Ahrens et al.,Nucl.Phys.A251(1975)479
/4/ B.L.Berman,Atomic Data and Nuclear Data Tables 15(1975)1
/5/ F.K.Goward,J.J.Wilkins,Proc.Royal Soc.A217(1953)357
/6/ R.Carchon et al.,Phys.Rev.C14(1976)456
/7/ H.D.Shay et al.,Phys.Rev.C9(1974)76
/8/ V.P.Chizhov et al.,Nucl.Phys.34(1962)562
/9/ K.Kraemer et al.,Z.Physik 207(1967)1
/10/N.Bezic et al.,Nucl.Phys.A128(1969)426
/11/A.P.Komar et al.,Nucl.Phys.34(1962)551
/12/H.Taneichi et al.,Proc.of Int.Conf.on Nuclear Structure (Tokyo,1977),p.141
/13/M.E.Toms,Nucl.Phys.54(1964)625
/14/J.L.Black et al.,Nucl.Phys.A153(1970)233
/15/B.L.Berman,Atomic Data and Nuclear Data Tables 15(1975)1,
R.L.Bramblett et al.,Phys.Rev.133(1964)B869,
P.Carlos et al.,Nucl.Phys.A378(1982)317
/16/V.P.Denisov et al.,Nucl.Phys.A113(1968)289
/17/A.Goldmann et al.,Z.Physik 192(1966)282
/18/M.E.Toms,Nucl.Phys.54(1964)625,
F.K.Goward,J.J.Wilkins,Proc.Phys.Soc.65A(1952)671
/19/M.Suffert,Nucl.Phys.75(1966)226,
H.D.Shay et al.,Phys.Rev.C9(1974)76

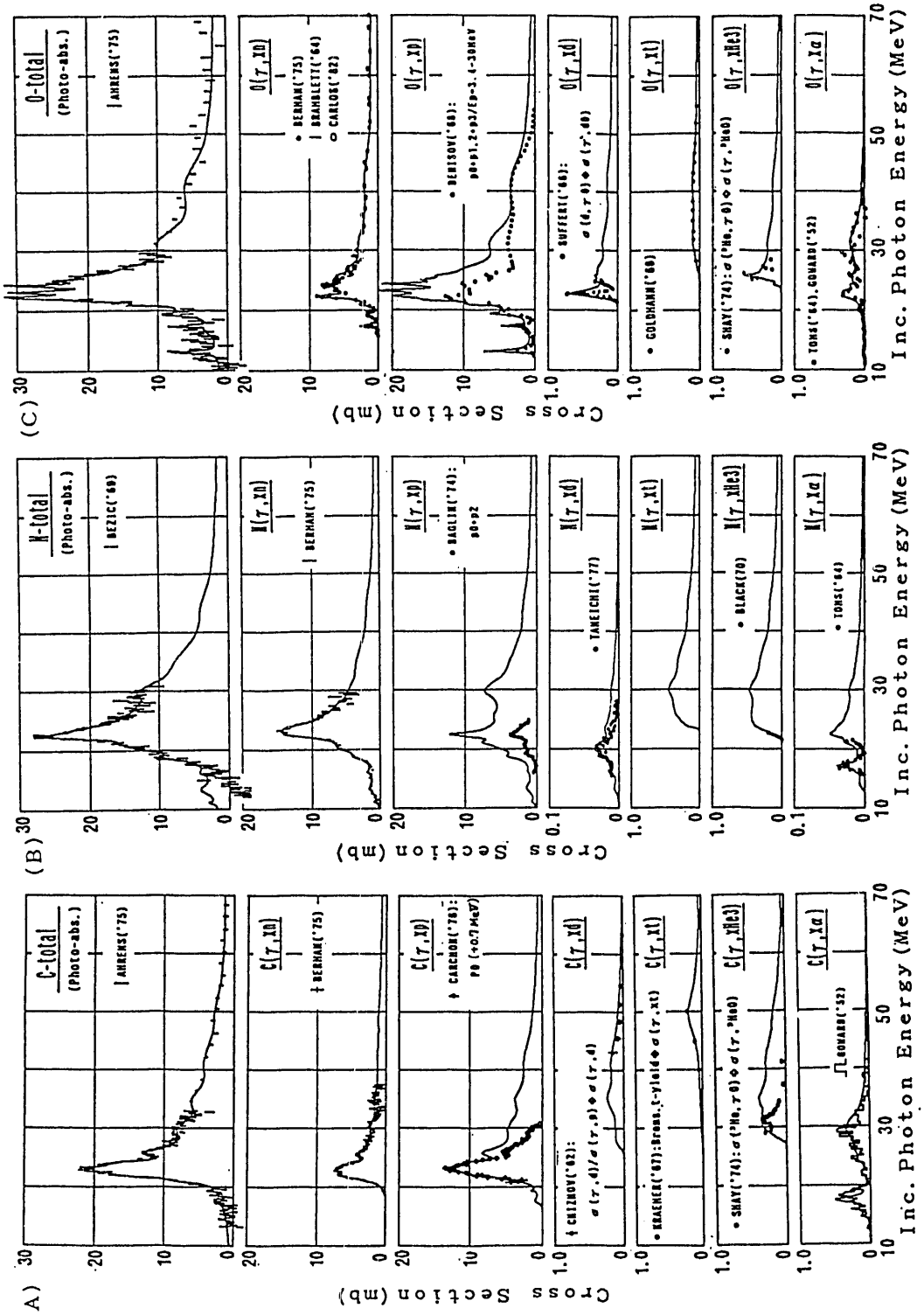

Fig. 1 Comparison of the evaluated cross sections (solid lines) with experimental cross sections: (A) Carbon, (B) Nitrogen, (C) Oxygen. Note that some of the experimental cross sections for charged particle emission are partial, and do not correspond to the evaluated cross sections.

3.10 Semi-gross Theory of Nuclear β-Decay

Takahiro TACHIBANA, Masami YAMADA and Hidehiko NAKATA
Science and Engineering Research Laboratory, Waseda University,
3-4-1 Okubo, Shinjuku-ku, Tokyo 169, Japan

The gross theory of nuclear β-decay is refined so as to include shell effects of parent nuclei. The new-theory has the following features:
(1) Discrete and non-uniform one-particle levels are assumed for the parent nucleus.
(2) The one-particle strength function depends on the orbital and total angular momenta of the one-particle state of the decaying nucleon.
Some preliminary results are given and discussed.

1. Introduction

The gross theory of nuclear β-decay [1-3] was constructed so as to describe the average properties of β-decay strength functions. In this theory, the strength function is given by the following formula:

$$|M_\Omega(E,\varepsilon)|=\int_{\varepsilon_{min}}^{\varepsilon_{max}} D_\Omega(E,\varepsilon)\, W(E,\varepsilon)\, \frac{dn_1}{d\varepsilon} d\varepsilon\,, \qquad (1)$$

where Ω denotes the type of β-decay, ε is the one-neutron (proton) energy for β^--decay (β^+-decay and electron capture), $dn_1/d\varepsilon$ is its distribution, $W(E,\varepsilon)$ is a weight function to take into account the Pauli principle, and $D_\Omega(E,\varepsilon)$ is the one-particle strength function.

In the version of Ref.3), the one-particle strength function of the Gamow-Teller transition $D_{GT}(E,\varepsilon)$ is assumed to be a superposition of two parts, $D^n_{GT}(E,\varepsilon)$ and $D^w_{GT}(E,\varepsilon)$:

$$D_{GT}(E,\varepsilon) = 0.6 D^n_{GT}(E,\varepsilon) + 0.4 D^w_{GT}(E,\varepsilon) \qquad (2)$$

where $D^{n}_{GT}(E,\varepsilon)$ has a large peak near the isobaric analogue state (IAS) corresponding to the giant resonance in the (p,n) reaction and $D^{w}_{GT}(E,\varepsilon)$ distributes in a wide range making a long tail of $D_{GT}(E,\varepsilon)$. These two functions $D^{n}_{GT}(E,\varepsilon)$ and $D^{w}_{GT}(E,\varepsilon)$ are normalized separately.

In the gross theory, the shell effects are taken into account only through the Q_{β}-values which are the input data of the theory. In the present modification, we include shell effects also in $dn_1/d\varepsilon$ and $D_{\Omega}(E,\varepsilon)$. This modification is made without changing the first assumption of the gross theory, *i.e.* Eq. (1). The shell effects included in the present model is those of the parent nuclei, whereas the daughter nuclei are still treated statistically. Therefore, this theory is called semi-gross theory of β-decay.

2. One-particle energy distribution $dn_1/d\varepsilon$

In order to obtain the one-particle energy distribution, we basically follow the method given in Ref.4). Here, we take the proton group as an example, and give an outline of the method. In this model, we assume one-particle levels of degeneracy two. If there were no shell effects, the energy of the j-th level would approximately be given by the Fermi gas model. The energy levels thus obtained are referred to as standard levels ε^{st}_{j}. An actual j-th proton level is shifted from the standard level and this shift is denoted by a_j. The last odd proton has this shift of energy, and it is assumed that each of the paired protons also has this energy shift if they lie sufficiently far below the Fermi surface. An additional energy shift b_j due to the pairing energy is considered for each of the last paired protons just below the Fermi surface. Then, in the case of $Z=2\mu$ (μ : integer), the energy of a proton in the j-th level is given by

$$\varepsilon^{(\mu)}_{j}=\min.\begin{bmatrix}\varepsilon^{st}_{\mu}+a_{\mu}-b_{\mu}\\ \varepsilon^{st}_{j}+a_{j}\end{bmatrix}. \qquad (3)$$

These a_j 's and b_j 's are estimated with use of the nuclear masses, for which we used either experimental or theoretical values.

The function $dn_1/d\varepsilon$ thus obtained is a distribution on discrete levels which are doubly degenerate and non-uniformly spaced. Then, we assign to each level an angular momentum set (l,j) (for single occupancy) or a mixture of sets (l,j) (for double occupancy). These angular momentum sets are obtained from single-particle model calculations with Woods-Saxon-type potentials.

3. One-particle strength function $D_{\Omega}(E,\varepsilon)$

The one-particle strength function for the Gamow-Teller (G-T) transition depends on the set (l,j) owing to the effect of spin-orbit interaction. The function $D^{n}_{GT}(E,\varepsilon)$ which appears in Eq.(2) is taken to be a superposition of two functions. In the case of the transition from the state with $j=l+1/2$ $[j=l-1/2]$ $(l\neq 0)$, one function corresponds to the transition $j=l+1/2\rightarrow j=l+1/2$ $[j=l-1/2\rightarrow j=l-1/2]$ and has a peak at the IAS, and the other function corresponds to the transition $j=l+1/2\rightarrow j=l-1/2$ $[j=l-1/2\rightarrow j=l+1/2]$ and has a peak at a somewhat higher [lower] excitation energy than IAS. Each function is normalized to the strength of the single-particle model. In the case of $l=4$, the narrow-one-particle strength function $D^{n}_{GT}(E,\varepsilon)$ is shown in Fig,1.

4. Some results and discussion

So far, we have only studied the G-T transition. In Fig.2 we compare the G-T strength functions of the gross and semi-gross theories for ^{133}Te and ^{135}Te. Note that the neutron numbers of ^{133}Te and ^{135}Te are just before and after the magic number $N=82$, respectively. Owing to the energy gap at the magic number, the dominant peak of the strength function of the semi-gross theory for ^{133}Te (^{135}Te) shifts to a lower (higher) excitation energy in comparison with that of the gross theory.

We also compare in Fig.3 the half-lives calculated by these two theories with use of the parameter values corresponding to case 2b of Ref.3). In Fig.3, the half-lives T_{sg} are obtained from the partial half-lives of the G-T transitions calculated by the semi-gross theory and those of the first-forbidden transitions by the gross theory. Therefore, T_{sg} does not mean the exact result of the semi-gross theory.

Effects of non-uniform one-particle energy distribution are relatively large and clearly seen in Figs. 2 and 3. On the contrary, effects of the (l,j) dependence of one-particle strength function are very weak, much weaker than experimental data suggest. In order to remedy it, we must incorporate an (l,j) dependence also in the wider part of the one-particle strength function $D^{w}_{GT}(E,\varepsilon)$. A similar consideration will also be required to the first-forbidden transitions caused by the axial-vector β-decay interaction.

References

(1) Takahashi K. Yamada M. and Kondoh T.: Atomic Data and Nuclear Data Tables **12**, 101 (1973).

(2) Kondoh T., Tachibana T. and Yamada M.: Prog. Theor. Phys. **74**, 708 (1985).

(3) Tachibana T., Yamada M. and Yoshida Y.: Prog. Theor. Phys. **84**, 641 (1990).

(4) Kondoh T. and Yamada M.: Prog. Theor. Phys. Suppl. No.60, 136 (1976).

(5) Nuclear Data Sheets **49**, 639 (1986), and **52**, 205 (1987).

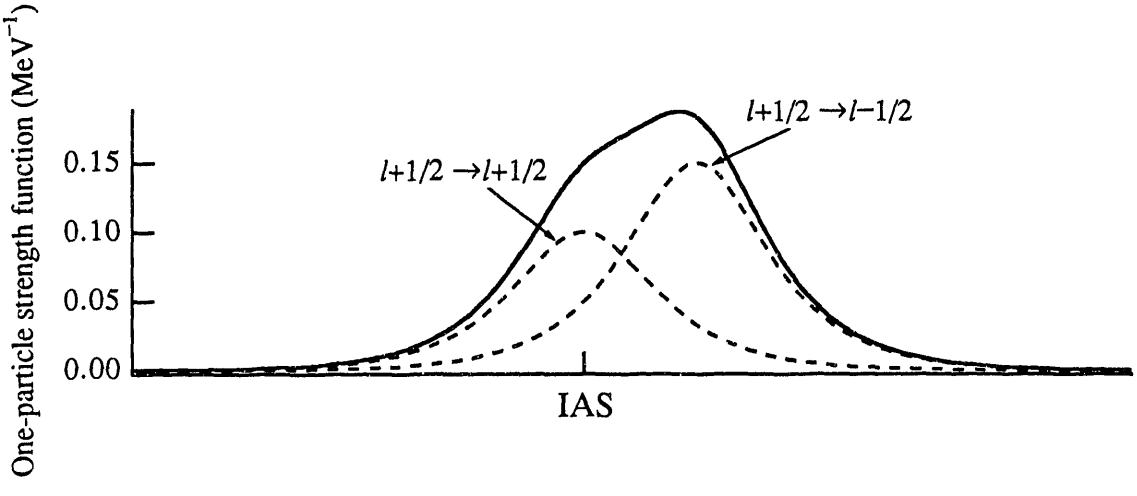

Fig. 1 Example of the narrow part of the one-particle strength function $D^{n}_{GT}(E,\varepsilon)$(solid line), which is a superposition of two functions (dashed line) corresponding to the transitions j=ℓ+1/2→j=ℓ+1/2, and j=ℓ+1/2→j=ℓ-1/2. The case of ℓ=4 and A=90 is shown.

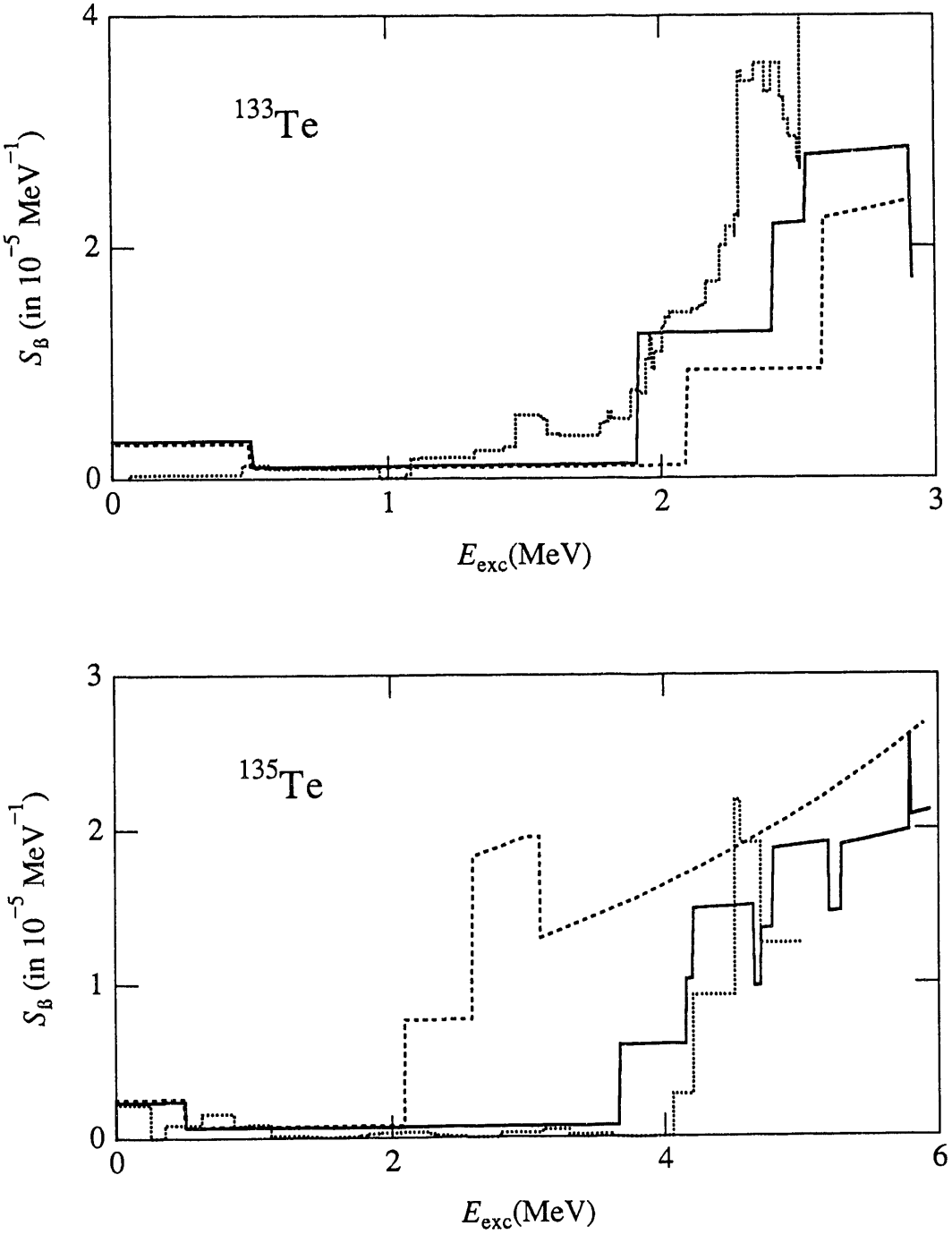

Fig. 2 The Gamow-Teller strength functions for ^{133}Te and ^{135}Te by the semi-gross theory (solid line), and the gross theory (dashed line). The total experimental strength functions are also shown by dotted lines.[5] (The experimental strengths of ^{133}Te are very large in the high-excitation region; we take the smallest values within the uncertainties.) In the theoretical strength functions, δ-functions are drawn with half-width of 0.5 MeV. The experimental strengths are drawn with half-width of 0.25 MeV for each transition.

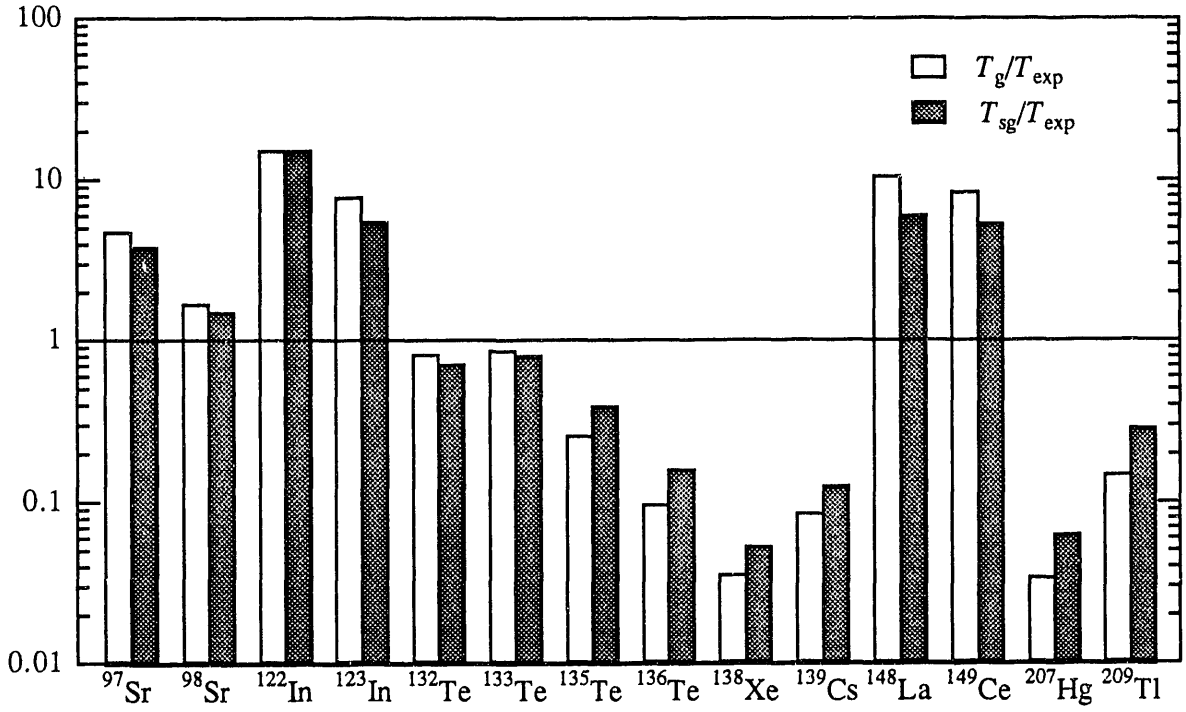

Fig. 3 Calculated half-lives for some nuclei. The open columns represent the ratios of half-lives between the gross theory (T_g) and the experiment (T_{exp}), and the filled columns those between the semi-gross theory (T_{sg}) and the experiment (T_{exp}). See also the text.

3.11 Measurement of (n,Xγ) Cross Sections of Iron for Neutrons up to 33 MeV

Eiji Tanabe, Kazuo Shin and Takashi Nakamura*

Department of Nuclear Engineering, Kyoto University.

** Cyclotron Radio Isotope Center, Tohoku University.*

Neutron-induced gamma ray production cross sections of iron were measured at incident neutron energies 3－33 MeV. The gamma-ray spectra were measured with a BGO spectrometer using the cyclotron at CYRIC, Tohoku university and the Be(p,n) reaction as the neutron source. The resulting spectra were unfolded and corrections were applied for neutron and gamma-ray attenuation.

1 Introduction

There are increasing number of applications of accelerators to variety of fields such as medical therapy, radioactive waste incinerations, spallation radiation sources, and so on. In these facilities, energies of induced and applied radiations are rather higher than those in fission and fusion reactors. Among these radiations, neutrons play important roles. However, measured data of neutron cross sections are rare at the energies above fusion energy.

In this report, measurement of gamma-ray production cross sections of iron was made for neutrons up to 33 MeV.

2 Experimental Method

The experimental layout is shown in Fig.1. An AVF cyclotron at CYRIC, Tohoku university was used in the experiment. White neutrons were produced by (p,n) reactions with a 20-mm thick Be target, which was bombarded by 35-MeV proton beam from the cyclotron. And an iron sample of 2-cm thickness and 20-cm×20-cm cross section area was in the neutron beam. Neutron spectrum at the sample position was obtained by the time of flight method using a 3-inch diameter by 3-inch length NE-213 scintillator at the place of iron sample. Gamma rays produced in the iron sample by neutrons were observed by a 2-inch diameter by 1-inch length BGO scintillator.

3 Data Analysis

3.1 Response Function of the BGO Scintillator

Response functions of the BGO scintillator were calculated by the Monte Carlo method by the EGS4 code. Calculations were made at intervals of 0.25 MeV at energies below 2 MeV, 0.5 MeV at 2 MeV to 10 MeV, 1.0 MeV at 10 MeV to 30 MeV, and 2.0 MeV at 30 MeV to 50 MeV. These intervals are determined by considering the resolution of the scintillator and electronics system. Calculated result was arranged into a 54×54 square matrix.

3.2 Analysis of Neutron Spectrum

Neutron data of the NE-213 were obtained by discriminating against gamma-ray data based on the difference in the rise time, using contour plots of pulse height vs. rise time like one in Fig.2. Right part to the solid line in the figure, corresponds to neutrons which have slower rise time than gamma-rays. Neutron flight-time signals which were tagged by the rise-time discrimination were converted to neutron energy spectrum using the detector efficiency. Thus obtained spectrum is shown in Fig.3.

3.3 Analysis of Gamma-ray Spectrum

Neutron time spectrum was bunched into bins, for each of which gamma-ray pulse height distributions were obtained by the BGO scintillator. The neutron energy bin width is 3 MeV which is enough to eliminate statistical errors. Using the response matrix previously described, the pulse height data were unfolded with the FERDO code to gamma-ray spectra, where the pulse height distribution was calibrated by gamma-rays from Am-Be and ^{137}Cs sources.

3.4 Gamma-ray Production Cross Sections

Using neutron spectrum $\Phi(E)$, and corresponding gamma-ray spectrum $\phi(E')$ obtained above, gamma-ray production cross section $\sigma(E, E')$ is described by Eq.(1),

$$\sigma(E, E') = \Phi(E)\eta_n\eta_\gamma NV/\phi(E'), \tag{1}$$

where N is the atomic density, V is the volume of iron sample, and η_n, η_γ are corrections for neutron and gamma-ray attenuation in the iron sample, respectively.

When a gamma ray is generated in the sample at depth x, attenuation of gamma ray is described as $e^{-\mu x}$ with linear attenuation coefficient μ. Then η_γ is given by Eq.(2),

$$\eta_\gamma = \frac{1}{l}\int_0^l e^{-\mu x}\mathrm{d}x, \tag{2}$$

where $l = l_0/\cos\theta$,l_0 is the thickness of the sample, and θ is the angle of the BGO scintillator with respect to the neutron beam axis.

Attenuation of neutron was assumed to be caused only by non-elastic scattering. When $\phi_n(x)$ is neutron flux in the sample at depth x, $\phi_n(x)$ is described as $\phi_n(x) = \phi_n(0)e^{-Nx\sigma_{non}}$, where σ_{non} is non-elastic scattering cross section. Then η_n is given by Eq.(3),

$$\eta_n = \frac{1}{l_0}\frac{1}{N\sigma_{non}}\left(1 - e^{Nl_0\sigma_{non}}\right). \tag{3}$$

4 Results

Typical examples of the measured differential gamma-ray production cross sections are shown in Figs.4 and 5, and integrated gamma-ray yield above $E_\gamma = 1.5$ MeV in Fig.6. At lower neutron energies, where other data exist, our results give good agreement within statistical errors to those of Dickens et al.[1] and Chapman et al.[2]. Also these data agreed fairly well with calculated data by Young[3] at energies up to 33 MeV.

References:

1)Dickens et al., *NSE 50*, 311-336(1973)

2)Chapman et al., *ORNL-TM-5416*, ORNL(1976)

3)P.Young, private communication

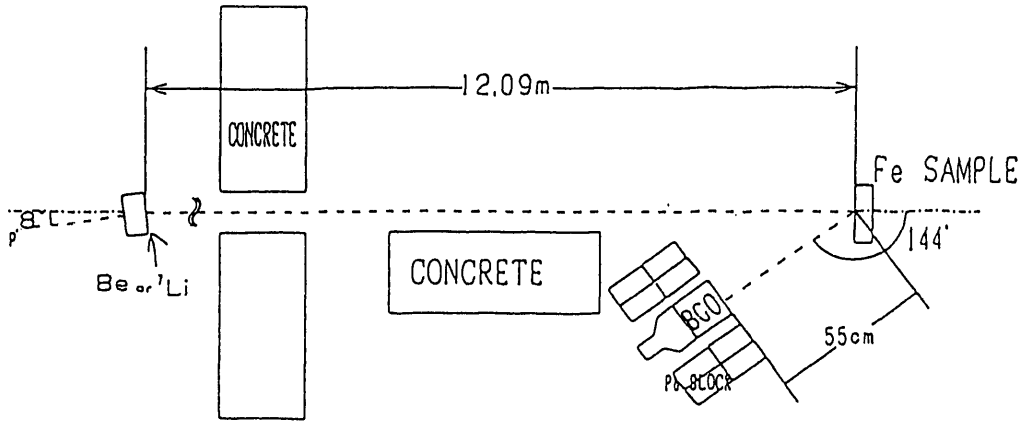

Fig. 1 Experimental arrangement for measuring neutron induced gamma-ray from iron sample by BGO spectrometer.

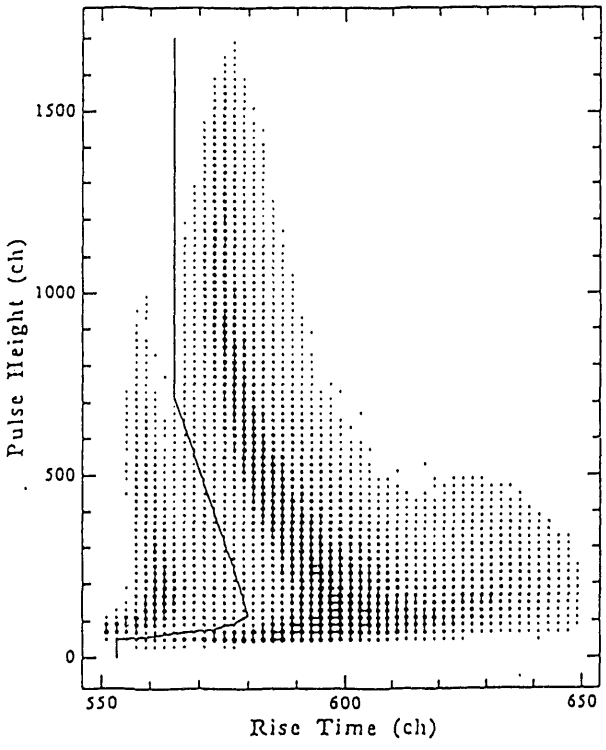

Fig. 2 Two dimensional plot of pulse height vs. rise time in NE-213 bombarded by neutrons from 20 mm thick Be target.

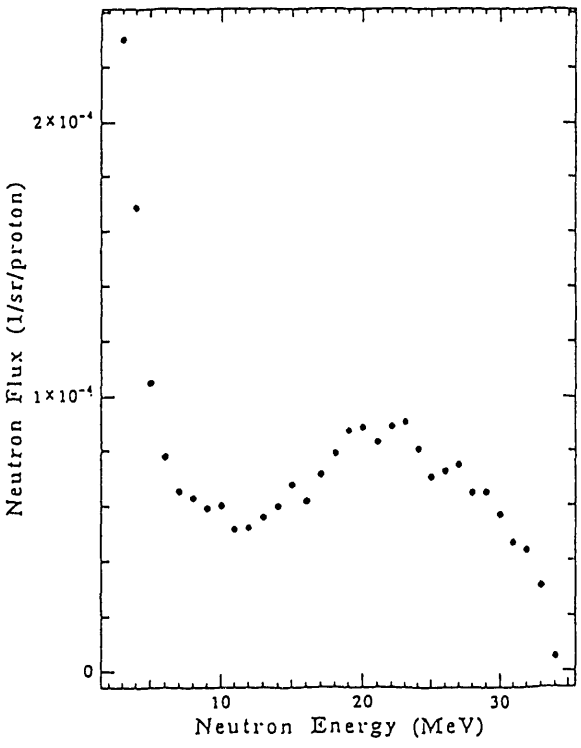

Fig. 3 Emitted neutron spectrum from 20 mm thick Be target bombarded by 35 MeV proton.

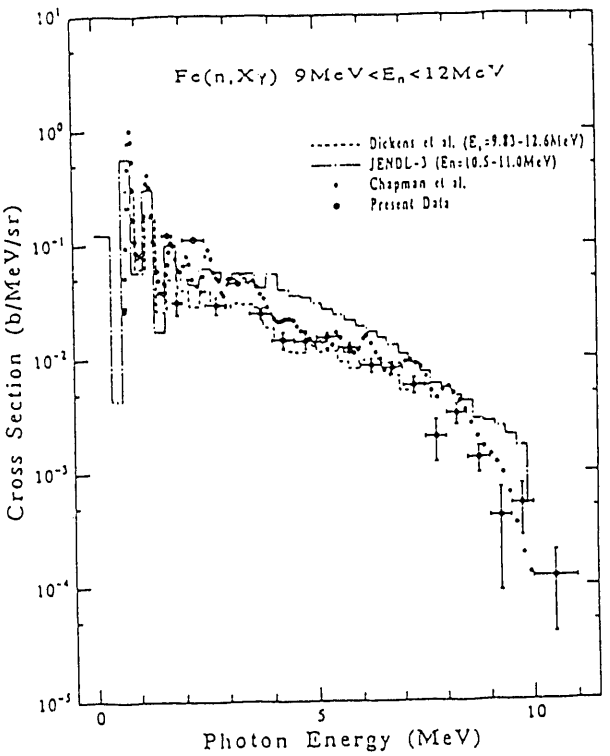

Fig. 4 Differential cross section for neutron energy between 9 and 12 MeV.

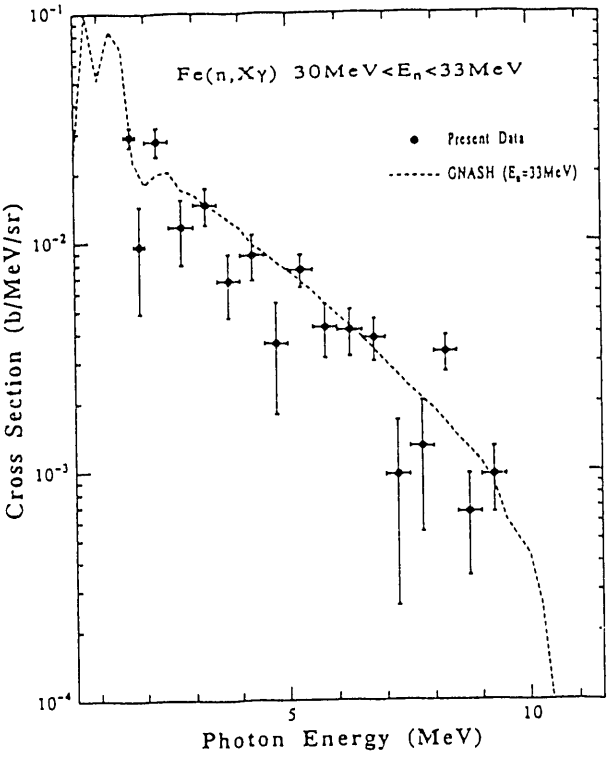

Fig. 5 Differential cross section for neutron energy between 30 and 33 MeV.

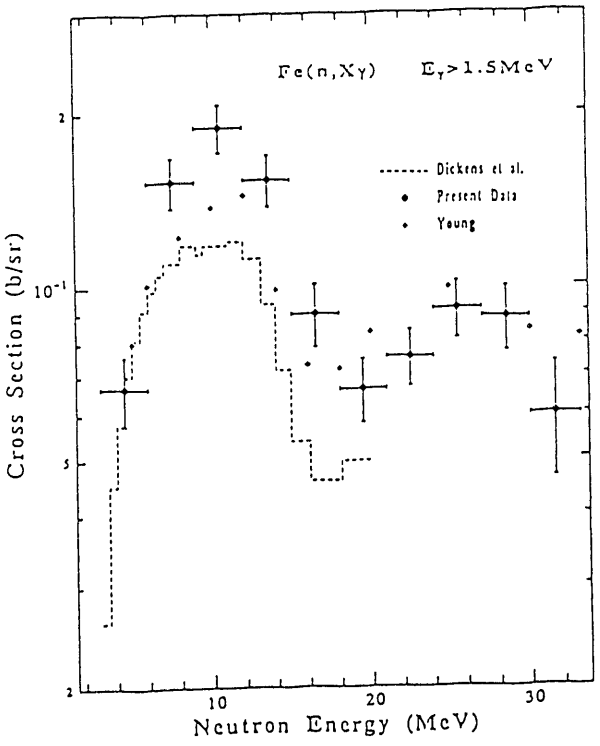

Fig. 6 Total gamma-ray production cross section for gamma ray energy above 1.5 MeV.

3.12 Measurement of Neutron Activation Cross Sections between 15 and 40 MeV

Y. Uno, Y. Uwamino*, T. S. Soewarsono and T. Nakamura

Tohoku University, Cyclotron and Radioisotope Center

Aoba, Aramaki, Aoba-ku, Sendai 980 Japan

**University of Tokyo, Institute for Nuclear Study*

3-2-1, Midori-cho, Tanashi, Tokyo 188 Japan

Abstract

The monoenergetic neutron fields were developed by using a ^{7}Li target bombarded by protons of 20, 25, 30, 35 and 40 MeV. Natural samples of C, Au, Na, and enriched isotope samples of ^{58}Ni, and ^{48}Ti were irradiated in these fields. Absolute neutron fluences at the irradiation point were determined from the measured amount of ^{7}Be($T_{1/2}$=53.4d) induced in the Li target. Neutron activation cross sections of 6 reactions of ^{12}C(n,2n)^{11}C, ^{197}Au(n,2n)^{196}Au, ^{197}Au(n,4n)^{194}Au, ^{23}Na(n,2n)^{22}Na, ^{58}Ni(n,2n)^{57}Ni and ^{48}Ti(n,np)^{47}Sc in the energy range from 15 to 40 MeV were obtained by activation method.

1 Introduction

Neutron activation cross sections in high energy region are needed for neutron dosimetry, radiation safety and material damage studies, and for nuclear physics. However, experimental data of neutron cross sections in the energy region above 15 MeV is still very poor.

An intense semimonoenergetic neutron field using a ^{9}Be target bombarded by protons has previously been developed, and neutron activation cross sections up to 40 MeV have been measured[1]. Since the energy spectrum of neutrons produced by ^{9}Be(p,n)^{9}B reaction has a rather broad peak, the unfolding technique was applied to obtain the excitation

functions from measured reaction rates of irradiated samples. The obtained results therefore include inevitable uncertainties coming from unfolding.

We further measured the neutron activation cross sections without unfolding by means of a neutron field using the ^{7}Li(p,n)^{7}Be reaction, which has a sharp monoenergetic neutron peak due to ground-state and first-exited-state(0.429MeV) of ^{7}Be. This enabled us to obtain the cross sections directly without unfolding.

2 Experiment

2.1 ^{7}Li(p,n) neutron field

The irradiation experiments were carried out in the neutron field using the ^{7}Li(p,n)^{7}Be reaction developed at the SF-cyclotron of the Institute of Nuclear Study(INS), University of Tokyo. The proton beams of energy 20, 25, 30, 35, and 40 MeV bombarded 99.98% enriched ^{7}Li target with 2-mm-thickness and 22-mm-diameter, which were backed by 12-mm-thick graphite to stop protons passing through the target and cooled by air. The samples were irradiated at 0 degree and 10 cm behind from the target.

The energy spectra of neutrons produced from the target in the direction of 0 degree for each proton energy were measured by the TOF method at the TOF facility of the Cyclotron and Radioisotope Center(CYRIC), Tohoku University. A 127-mm-diam × 127-mm-long NE213 scintillation detector was placed at the distance of about 10 m away from the ^{7}Li target. A monoenergetic peak is produced by the ^{7}Li(p,n)^{7}Be reaction to the ground-state and first-excited-state(0.429MeV) of ^{7}Be, as shown in Fig. 1. There can be seen a low-energy neutron tail corresponding to the higher excited states of ^{7}Be and the neutrons coming from the graphite proton beam stopper in Fig. 1. We repeated the TOF measurement of neutron spectrum only from the graphite beam stopper to investigate the neutrons produced from graphite and found that the contribution to the peak neutrons was negligible for all proton energies.

The absolute neutron fluence at an sample irradiation point at INS was determined

by activation technique[2]. The total fluence of peak neutrons due to ^{7}Li(p,n)^{7}Be(0.0 + 0.429 MeV) reaction can be obtained from the number of ^{7}Be induced in the ^{7}Li target, since the 2nd and the higher exited states of ^{7}Be decay with particle emission and do not keep ^{7}Be. The number of ^{7}Be nuclei produced is determined by the measurement of the 0.478MeV gamma-rays from ^{7}Be after irradiation experiment, and the peak neutron fluence ϕ_{peak} at an irradiation point is obtained as follows;

$$\phi_{peak} = \frac{N_7 \left(\frac{d\sigma}{d\Omega}\right)_{\theta=0^\circ}}{d^2 \int_{4\pi} \frac{d\sigma}{d\Omega} d\Omega}, \tag{1}$$

where N_7 is the number of ^{7}Be, $\frac{d\sigma}{d\Omega}$ is the angular differential cross section of combined reaction of ^{7}Li(p,n)^{7}Be(0.0 + 0.429 MeV), and d is the distance between sample and target, respectively. Estimation of $\left(\frac{d\sigma}{d\Omega}\right)_{\theta=0^\circ} / \int_{4\pi} \frac{d\sigma}{d\Omega} d\Omega$ is described in Ref. [3]. The absolute whole spectrum $\Phi(E)$ is determined by normalizing relative whole spectrum $\Phi'(E)$ measured at CYRIC as follows;

$$\Phi(E) = \Phi'(E) \frac{\phi_{peak}}{\phi'_{peak}} \tag{2}$$

where ϕ'_{peak} is the integrated value of peak region of $\Phi'(E)$.

The neutron spectra obtained at the irradiation point for incident proton energy of 20, 25, 30, 35, and 40 MeV are shown in Fig. 1, and characteristics of the neutron fields are listed in Table 1.

2.2 Experimental procedure and calculation of activation rate

The samples were irradiated in the p-^{7}Li neutron fields mentioned above for proton energy of 20, 25, 30, 35, and 40 MeV. The properties of samples for irradiation are listed in Table 2. The samples were irradiated for 1 hour, except carbon irradiated for 10 minutes. As a monitor of neutron flux and its fluctuation in time the proton beam current during irradiation was recorded by the current integrater connected to the multi-channel-scaler.

After irradiation, the gamma-rays from the samples were measured by high-purity Ge detectors(18% and 13%). The observed gamma-ray spectra were analyzed by the KEI-11EF program[4] and full energy peak areas were calculated. The peak detection effi-

ciencies were calibrated using the mixed standard gamma-ray source, and the obtained efficiencies were fitted to the efficiency curves. The activation rates were calculated considering the following corrections.

- Fluctuation of neutron flux during irradiation

  The correction factors were calculated from the data of flux monitor recorded by MCS.

- Self-absorption of γ-ray in the sample

  The self-absorption factors were calculated by the Monte Carlo code PEAK[5].

- Coincidence-summing effect

  The correction factors of coincidence-summing effect were calculated from decay schemes by means of the SUMECC code[6]. Total detection efficiencies, which are necessary for the SUMECC code, were calculated by the PEAK code.

2.3 Calculation of cross section

The cross section σ was calculated from the activation rate A obtained with subtracting the contribution from low-energy neutron tail as follows;

$$\sigma = \frac{A - \int_{E_{th}}^{E_l} \sigma_{ref}\phi(E)dE}{\phi_{peak}} \tag{3}$$

where E_{th} is the threshold energy of the relevant reaction, E_l is the lowest energy of peak neutrons, σ_{ref} is the evaluated or other experimental data of the reaction, $\phi(E)$ is the neutron flux, and ϕ_{peak} is the neutrons flux in peak energy region.

The estimated error components are listed in Table 3.

3 Results and discussion

The obtained cross sections of ^{12}C(n,2n)^{11}C, ^{197}Au(n,2n)^{196}Au, ^{197}Au(n,4n)^{194}Au, ^{23}Na(n,2n)^{22}Na, ^{58}Ni(n,2n)^{57}Ni and ^{48}Ti(n,np)^{47}Sc are shown in Figs. 2-7.

- $^{12}C(n,2n)^{11}C$

  Our present data agree with the data by Brill et al. in BNL-325[8].

- $^{197}Au(n,2n)^{196}Au$

  Our present result and our previous result[1] obtained by using the NEUPAC unfolding code[7] are both lower than the other experimental data in BNL-325 and evaluated data of ENDF/B-VI.

- $^{197}Au(n,4n)^{194}Au$

  There is no other experimental data above 30 MeV. Our present value at 27.6 MeV shows good agreement with the data by Bayhurst et al. . The estimation by Greenwood[9] gives about 30% overestimation.

- $^{23}Na(n,2n)^{22}Na$

  The result in this work agrees well with our previous unfolded result. Other experimental data split into three groups in Fig. 5 and our results are close to the middle data of Menlove et al. in BNL-325 below 18MeV.

- $^{58}Ni(n,2n)^{57}Ni$

  Our present value at 17.6 MeV shows good agreement with the data measured by Iwasaki et al. of Tohoku Univ. . The data by Bayhurst et al. are about 25% large.

- $^{48}Ti(n,np)^{47}Sc$

  No experimental data exists above 16 MeV. Our data is the first one.

4 Summary

An intense monoenergetic neutron field for activation experiment using $^{7}Li(p,n)^{7}Be$ reaction was developed. The neutron activation cross sections of $^{12}C(n,2n)^{11}C$, $^{197}Au(n,2n)^{196}Au$, $^{197}Au(n,4n)^{194}Au$, $^{23}Na(n,2n)^{22}Na$, $^{58}Ni(n,2n)^{57}Ni$ and $^{48}Ti(n,np)^{47}Sc$ from 15 to 40 MeV were obtained using this neutron field.

The cross section data obtained are limited to the reactions of threshold energy above about 10 MeV, since the subtraction of activation from low energy neutron components in Eq. 3 causes large uncertainty of activation rate.

References

[1] Y. Uwamino, H. Sugita, Y. Kondo and T. Nakamura,*Nucl. Sci. Eng.*, **111**, 391-403 (1992)

[2] S. D. Schery, L. E. Young, R. R. Doering, Sam M. Austin and R. K. Bhowmik, *Nucl. Inst. Meth.*, **147**, 399-404 (1977)

[3] T. S. Soewarsono, Y. Uwamino and T. Nakamura, JAERI-M 92-027, 354-363 (1992)

[4] K. Komura, INS-TCH-9, Institute for Nuclear Study, University of Tokyo (1974)

[5] T. Nakamura and T. Suzuki, *Nucl. Inst. Meth.*, **205**, 211 (1983)

[6] A. Torii, Y.Uwamino and T. Nakamura, INS-T-468, Institute for Nuclear Study, University of Tokyo (1987)

[7] T. Taniguchi, N. Ueda, M. Nakazawa and A. Sekiguchi, NEUT Research Report 83-10, University of Tokyo, Department of Nulear Engineering (1984)

[8] V. McLane, C. L. Dunford and P. F. Rose, *"Neutron Cross Sections", Vol.2, Neutron Cross Section Curves*, Academic Press, New York (1988)

[9] L. R. Greenwood, ANL/FPP/TM-115, Argonne National Laboratory (1978)

Table 1 Characteristics of neutron fields for irradiation

Proton energy [MeV]	Effective neutron energy [MeV]	FWHM [MeV]	Neutron flux of peak energy [# cm^{-2} $coulomb^{-1}$]	Total neutron flux [# cm^{-2} $coulomb^{-1}$]
20	17.6	2.3	8.4×10^{12}	1.9×10^{13}
25	21.8	1.9	1.2×10^{13}	2.5×10^{13}
30	27.6	1.7	1.4×10^{13}	3.5×10^{13}
35	32.8	1.5	1.5×10^{13}	4.4×10^{13}
40	38.3	1.4	1.6×10^{13}	6.4×10^{13}

Table 2 Properties of samples for irradiation

Sample	Chemical form	Isotopic abundance	Weight
Natural samples			
Carbon	Graphite	98.9%	1.6g
^{197}Au	Metal	100.0%	0.1g
^{23}Na	Na_2CO_3	100.0%	0.4g
Enriched isotope samples			
^{58}Ni	Metal powder	99.66%	40mg
^{48}Ti	TiO_2	99.81%	65mg

Table 3 Components of uncertainty

Component		Uncertainty(%)
Counting statistics of γ-rays	:	1.0 - 30.0
Peak detection efficiency of Hp-Ge detector	:	3.0
Neutron flux	:	5.0 - 10.0
Uncertainty of reference cross section	:	3.0 - 30.0

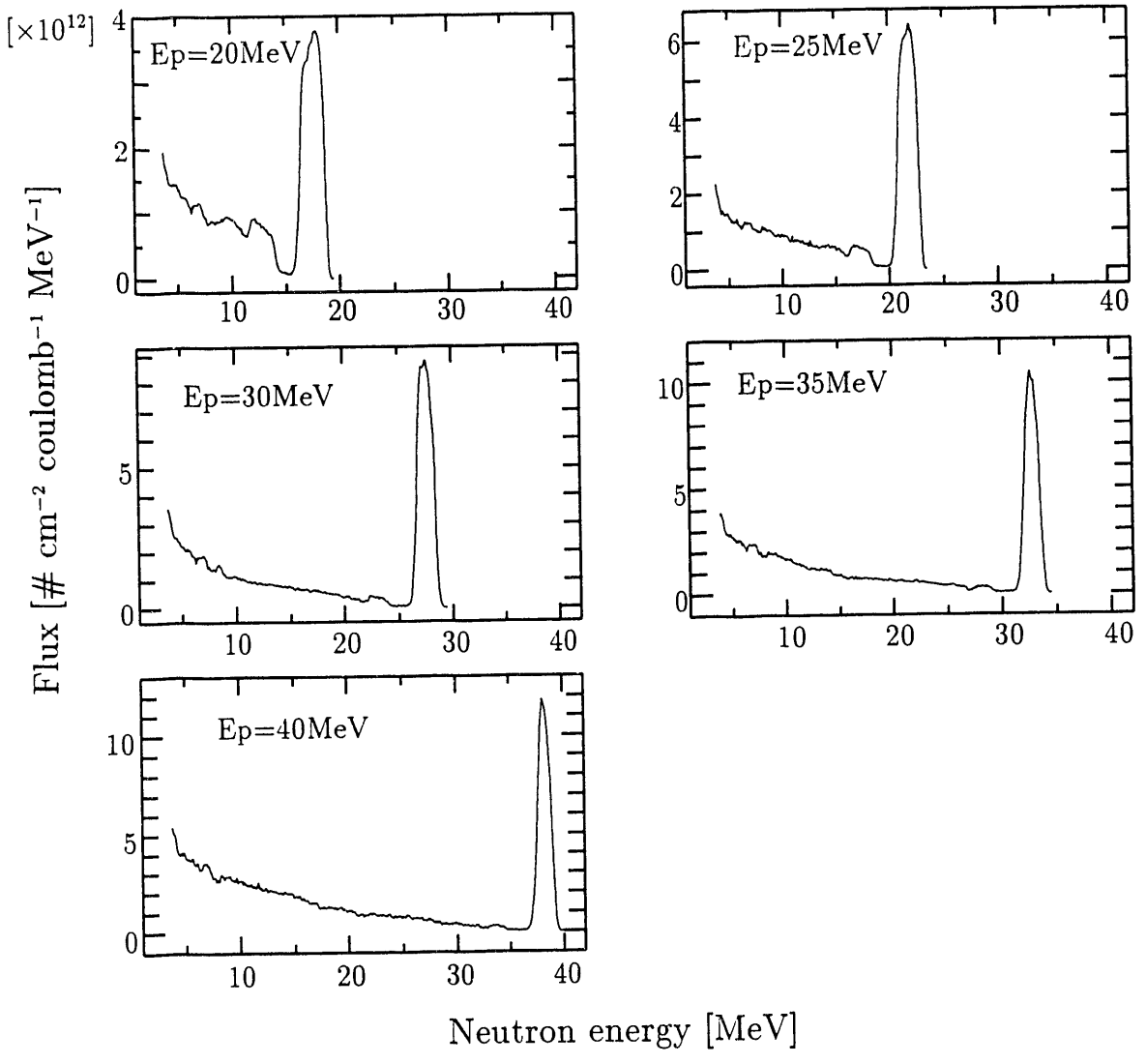

Fig. 1 Spectra of neutron fields for irradiation.

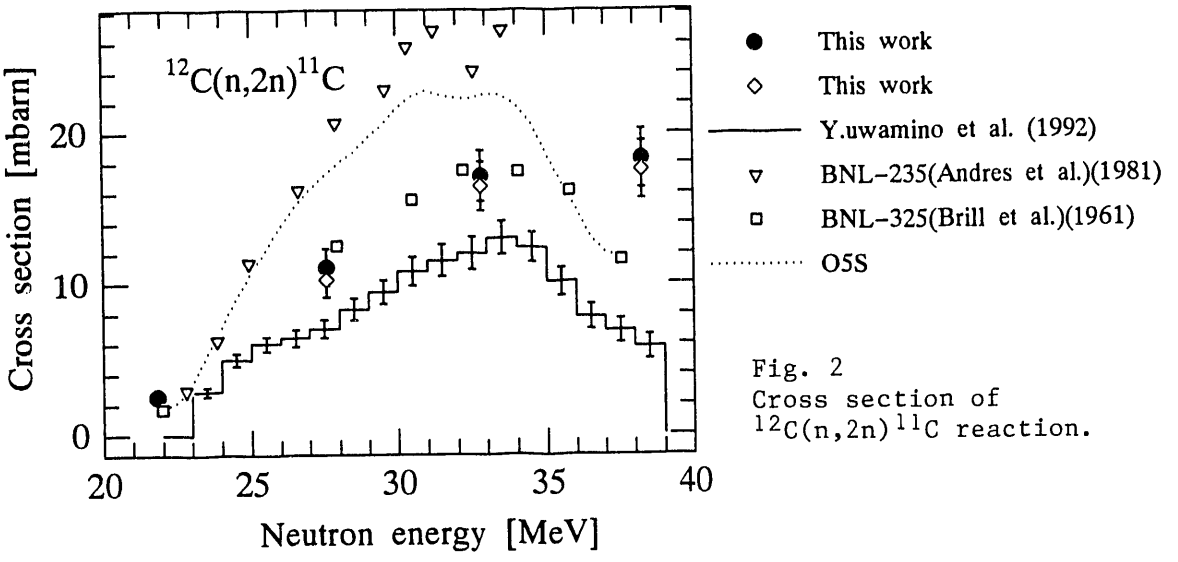

Fig. 2
Cross section of
$^{12}C(n,2n)^{11}C$ reaction.

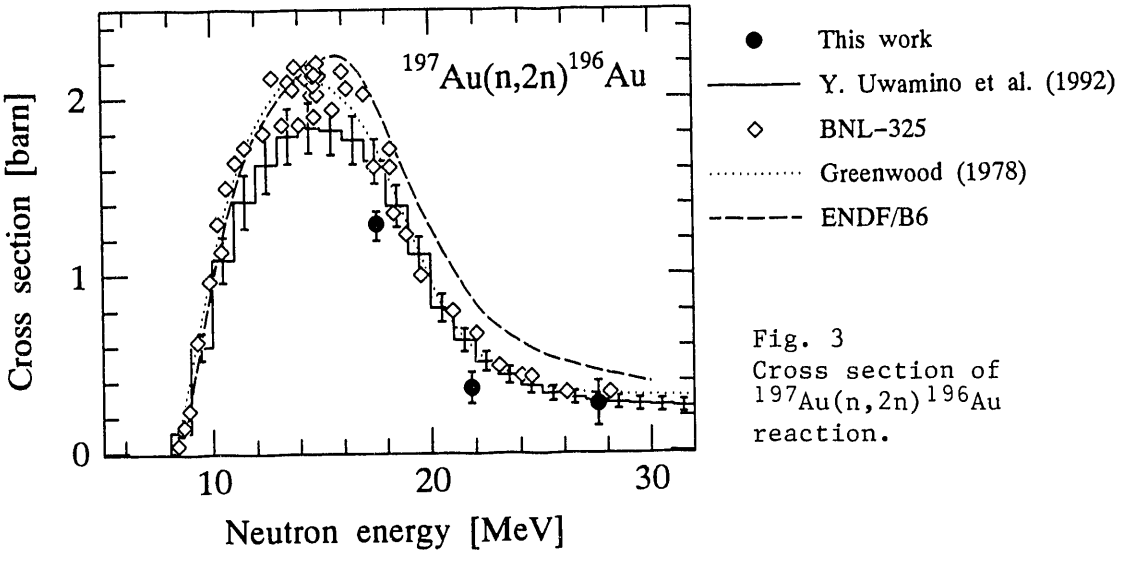

Fig. 3
Cross section of
$^{197}Au(n,2n)^{196}Au$
reaction.

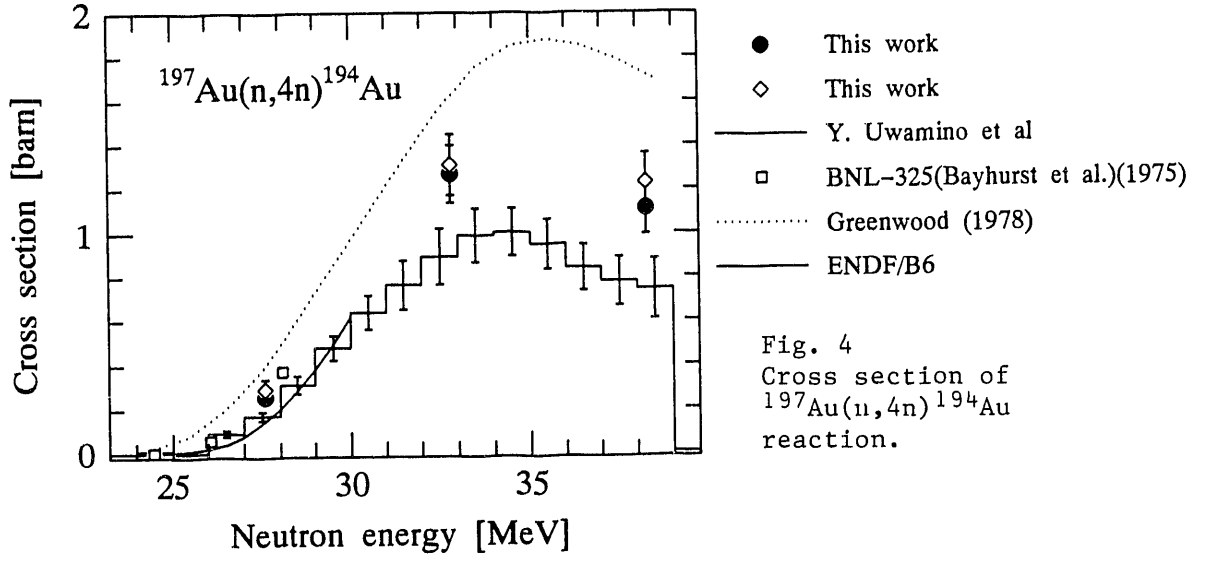

Fig. 4
Cross section of
$^{197}Au(n,4n)^{194}Au$
reaction.

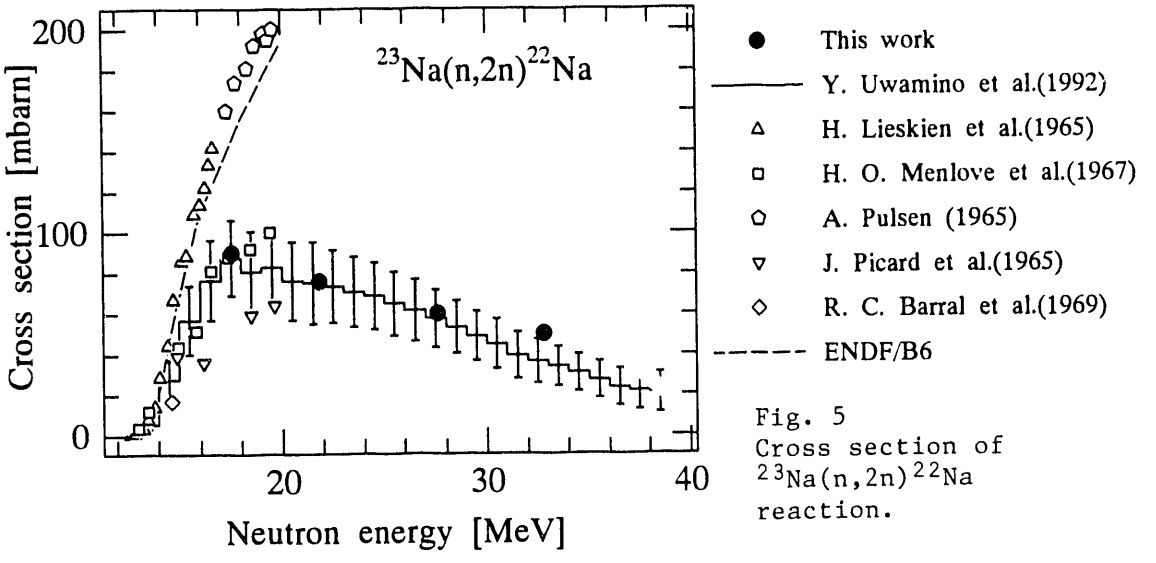

Fig. 5
Cross section of
^{23}Na(n,2n)^{22}Na
reaction.

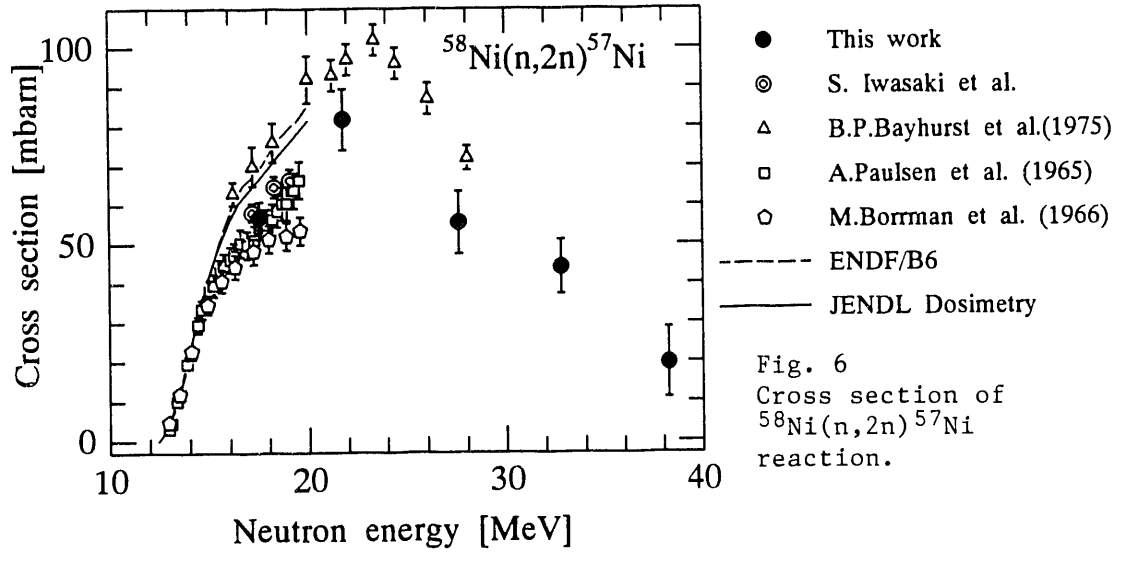

Fig. 6
Cross section of
^{58}Ni(n,2n)^{57}Ni
reaction.

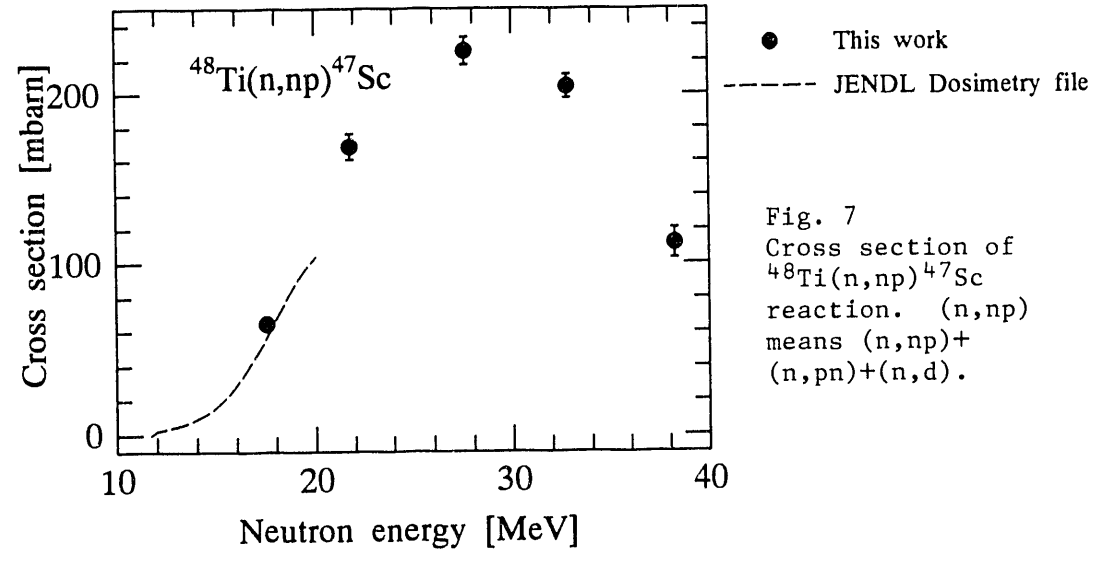

Fig. 7
Cross section of
^{48}Ti(n,np)^{47}Sc
reaction. (n,np)
means (n,np)+
(n,pn)+(n,d).

3.13 Cross Section Measurement for the Neutron Induced Reactions on Ni and Au above 17 MeV by Activation Technique

S. Iwasaki, M. Sakuma, K. Sugiyama

Department of Nuclear Engineering
Tohoku University
Aramaki-Aza-Aoba, Aobaku, Sendai 980 Japan

and

N. Odano

Tokai Branch, Ship Research Institute
Ministry of Transport
Tokai, Nakagun, Ibaraki 919-11, Japan

Abstract

Cross sections of the following four neutron dosimetry reactions on nickel and gold have been measured by the activation technique using the T+d neutron source at Dynamitron Facility of Tohoku University; $^{58}Ni(n,p)^{58}Co$, $^{58}Ni(n,np+pn+d)^{57}Co$, $^{60}Ni(n,p)^{60}Co$, and $^{197}Au(n,3n)^{195}Au$ reactions between 17 and 20 MeV; and also $^{197}Au(n,2n)^{196}Au$ cross sections between 12 and 20 MeV have been derived from the previously obtained ratio data. Besides above, new activation reaction of $^{58}Ni(n,p\alpha)^{54}Mn$ has been found.

1. Introduction

Precise cross section data above 15 MeV are sparse although these are important for the high energy dosimetry, and estimation of damage rates and/or activation levels of structural materials tested or used in the proposed high energy accelerator based neutron fields[1]. Such cross sections also provide indis-

pensable information to establish the nuclear model calculation method for the higher energy applications.

In the present study, residual long-lived activities of the irradiated samples of gold and nickel in the past experiments have been measured, and cross sections for several reactions above 17 MeV have been derived. These samples were irradiated in the two series of the activation experiments which were reported previously[2]: the first one was for $^{93}Nb(n,2n)^{92m}Nb$ and $^{197}Au(n,2n)^{196}Au$ cross section validation of evaluated files[2,3], and the second one for the cross section measurement of $^{23}Na(n,2n)^{22}Na$, $^{55}Mn(n,2n)^{54}Mn$, and $^{58}Ni(n,2n)^{57}Ni$ relative to $^{93}Nb(n,2n)^{92m}Nb$ reactions[2].

2. Experimental and Data Analysis

2.1 Irradiation

Sample irradiations were done using the T+d neutrons which distributed in the energy range from 20 to 12 MeV corresponding to emission angles from forward to backward at the incident deuteron energies of 3.26 MeV and 2.85 MeV in the first experiment and second one, respectively.

2.2 Activity Measurement

Measurement of the residual activities of the samples was performed at about 1 year cooling time after the irradiations using a 80 cc high purity germanium detector at a normal distance of 100 mm and at a short distance of 20 mm for weak activities from the end cap of the detector. Measured gamma rays from the activities are listed in Table 1. It is interesting to note that

834-keV gamma-rays from nickel samples, which could not be detected in activation experiment around 14 MeV, were clearly observed. We concluded that these gamma-rays were emitted associated with the decay of ^{54}Mn as discussed later.

2.3 Data Analysis

Derivation of the reaction rates of each sample from the measured gamma-ray spectra has been done in the usual way. The following four effects have been corrected: (1) contribution of the D+d neutrons due to the built-up deuterium in the target to the reactions having low threshold energies, such as ^{58}Ni(n,p) and ^{60}Ni(n,p); (2) contribution of the interference reactions which produced the same activities to be observed due to various impurities in the nickel samples, e.g. Co, Mn, Fe and Cu and other reactions on nickel; these impurity elements may contribute to the activities of ^{58}Co by ^{59}Co(n,2n), ^{60}Co by ^{63}Cu(n,α) and ^{54}Mn by ^{54}Fe(n,p) and ^{55}Mn(n,2n) reactions, respectively; (3) coincidence summing loss effects and (4) self-absorption effect in the sample in particular for the gold gamma rays.

Corrections for the item (1) have been done using the observed TOF data of the source neutron angular distribution giving relative intensities of the D+d to the T+d neutrons, and the evaluated cross sections given in the files, i.e., JENDL Dosimetry File[4].

As for the (2) effect, the irradiated nickel samples were not of ultra-high purity, and the impurity content was only known to be less than 0.2% for Mn, Co, less than 0.1% for Fe, and less than 0.05% for Cu. The main impurity contributions to the cross section derivation were due to Co and Mn because of both large

(n,2n) cross sections (900 mb) at these energies and the abundances of the target nuclei of 100 %, correction factors for these reactions turned out to be about few % and 10%, respectively. Other contributions were so small and neglected.

Besides above impurity effects, in the case of ^{57}Co, the contribution from the decay of ^{57}Ni by the reaction ^{58}Ni(n,2n)^{57}Ni should be taken into account. The half life of ^{57}Ni is very short (36h), and the total ^{57}Ni activity added to that of ^{57}Co at the measurement time. Thus correction of this effect was so simple; the subtraction of the (n,2n) cross section from the total one. In the present case, we adopted the cross section values obtained by ourselves[2] for this reaction.

The 98.9keV gamma-rays of gold are easily absorbed in the high Z element sample themselves. The thickness of the gold samples (0.2 mm) was optimized for the measurement of the (n,2n) cross section, and whereby was too thick for the 98.9-keV gamma ray measurement. The self-absorption rate was estimated by a simple calculation in the slab geometry approximation.

3. Result and Discussion

3.1 ^{197}Au(n,2n)^{196}Au and ^{197}Au(n,3n)^{195}Au reactions

In Fig. 1, the cross section data obtained in the present study for both reactions are compared with the previously reported data and data taken from three evaluated data, ENDF/B-VI[5], and JENDL Dosimetry File. For the (n,2n), the cross section data were derived from the ratio data[2,3] relative to the ^{27}Al(n,α) cross section given by the IRDF-90[6] data. The (n,2n) data sup-

port the IRDF-90 curve, but not ENDF/B-VI one which was based on a theoretical calculation. Whereas a very new experimental data set by Uwamino et al.[7] shows a relatively lower trend in the energy region below 18 MeV.

The present data for the (n,3n) reaction give smaller cross sections than the other experiments and the evaluation by ENDF/B-VI, but are not considered to be inconsistent because of their large uncertainties due to the large corrections applied. It is necessary to perform another new experiment which will be optimized to this reaction.

3.2 $^{58}Ni(n,np)^{57}Co$ and $^{58}Ni(n,2n)^{57}Ni$ reactions

As shown in Fig. 2 (b), the our results[2] for the (n,2n) reaction are belong to the lower group and inconsistent wit.. the recent evaluations for JENDL Dosimetry File, IRDF-90 and ENDF/B-VI. In contrast. the present data for the (n,np) reaction (Fig.2 (a)) are quite consistent with the newest experimental data by Pavlik et al.[8], etc., and the evaluation of ENDF/B-VI. These two reaction data have been obtained from the activity measurements of the same nickel samples as stated before, and thus based on the same flux values. The derivation of the cross sections of the former reaction could be reliable because no large correction was necessary. This suggests the reliability of the lower cross sections of the (n,2n) reaction, too. However, another experiment for the confirmation of these cross sections is planned.

3.3 $^{58}Ni(n,p)^{58}Co$ and $^{60}Ni(n,p)^{60}Co$ reactions

As shown in Fig. 3, present data for the former reaction are consistent with the evaluated one for JENDL Dosimetry File and ENDF/B-VI except for the highest energy one. The latter reac-

tion's data are relatively larger than the other previously reported data, as shown in Fig. 4. The present data are still tentative and more detailed analysis should be done to reach final results.

3.4 $^{58}Ni(n,p\alpha)^{54}Mn$ reaction

As stated before, this reaction has not been observed nor evaluated until now. Therefore, we first estimated the cross section values roughly by a model calculation using the SINCROS-II[9] with the default model parameter set given in the system. The reaction has relatively lower threshold energy of about 10 MeV than expected one for the reaction of such double charged-particle emission. The theoretical curve rises gradually around 16 MeV, and reaches an appreciable cross section value of a few ten mb below 20 MeV, and is very consistent with the present experimental data, as shown in Fig. 5.

4. Summary

In the present study, we have measured the cross sections of five activation reactions on gold and nickel elements, i.e., $^{197}Au(n,3n)$, $^{58}Ni(n,np)$, $^{58}Ni(n,p)$, $^{60}Ni(n,p)$, and $^{58}Ni(n,p\alpha)$ at the incident neutron energies between 17 and 20 MeV using the activation technique. The cross sections for the $^{197}Au(n,3n)$ and two (n,p) reactions on Ni deviated from the evaluated cross sections, partly due to unknown errors in the large corrections applied for various effects. As for the $^{58}Ni(n,np)$ reaction, the present data are quite consistent with those of the newest measurement, and this indicates indirectly the reliability of the

previously reported cross sections for the $^{58}Ni(n,2n)$ reaction.

Relatively large cross sections for the new reaction $^{58}Ni(n,p\alpha)^{54}Mn$ indicates that it is important to take into accout the multiple charged-particle emmission reactions to evaluate more correctly the inventory of activities and damage (gas production) rates in structural materials in the environment of high energy neutrons.

Present experiment provides valuable data base to improve the dosimetry and activation data file, but the data are still preliminary state. It is planned to perform further detailed analysis and also to carry out another carefully designed experiment to confirm the present results.

References

1). Workshop 1 report, Nuclear Data for Rad. Damage Asses. and Related Safety Aspects 1989, IAEA-TECDOC-**572**, IAEA (1990).

2). Sakuma, M., et. al., Proc. of the 1991 Symposium on Nuclear Data, p278, JAERI-M **92-027** (1992).

3). Iwasaki, S., et. al., to be published in Prog. in Nucl. En. vol.**26**, No.3.

4). Nakazawa, M., et al. "JENDL Dosimetry File", JAERI **1325**, JAERI (1992).

5). BNL/National Nuclear Data Cenrter: ENDF/B-VI (1990).

6). Kochelov, N.P., and McLaughlin, P.K.: "The International Reactor Dosimetry File (IRDF-90)", IAEA-NDS-**141** (1990).

7). Uwamino, Y., et al.: Nucl. Sci. and Eng., **111**, 391 (1992).

8). Pavlik, A., et al.: Nucl. Sci. and Eng., **90**, 186 (1985).

9). Yamamuro, N. : JAERI-M **90-006**, JAERI (1990).

Table 1 List of measured activities and their gamma-rays*)

residual nuclide	reaction	half life (d)	abun-dance (%)	gamma-rays energy (keV)	emiss. prob. (%)
[Nickel]					
^{58}Co	^{58}Ni(n,p)^{58}Co	70.82	68.3	810.8	99.44
^{57}Co	^{58}Ni(n,np)^{57}Co	271.7	68.3	122.1	85.63
	^{58}Ni(n,2n)^{57}Ni(35.9h) ->^{57}Co			136.5	10.62
^{54}Mn	^{58}Ni(n,pa)^{54}Mn	312.14	68.3	834.8	99.975
^{60}Co	^{60}Ni(n,p)^{60}Co	5.271a	26.1	1173.2	99.890
				1332.5	99.983
[Gold]					
^{195}Au	^{197}Au(n,3n)^{195}Au	183	100.0	98.9	10.9

* numerical data are taken from "Nuclear Data Guide for Reactor Neutron Metrology", by J.H. Baard et al., except for the abundance data taken from "Table of Isotopes 7th. Ed.", edited by C.M. Lederer et al.

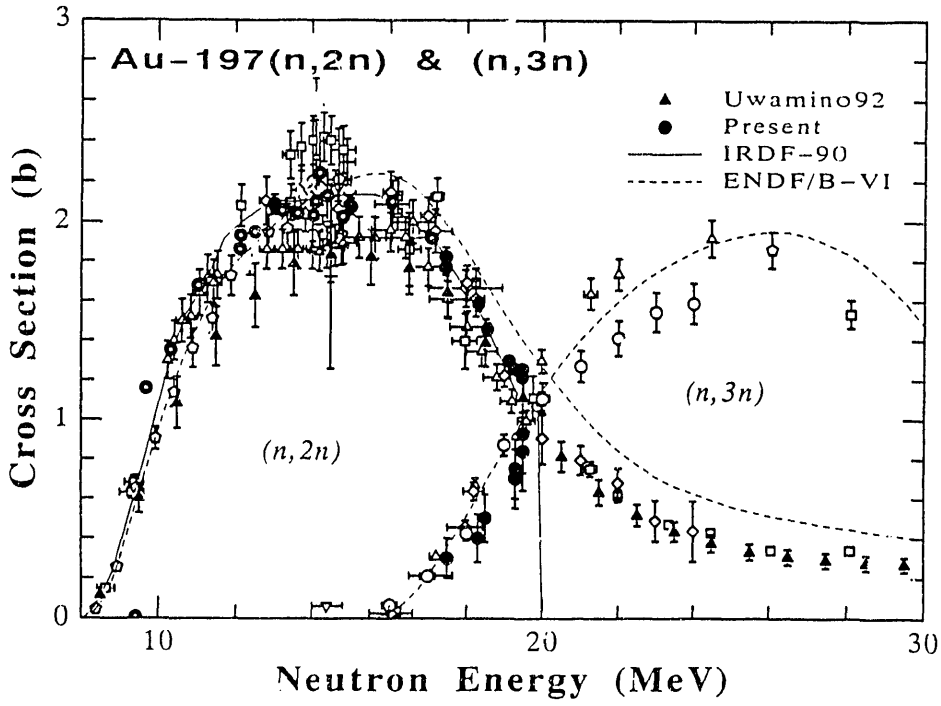

Fig. 1 ^{197}Au(n,2n) and (n,3n) cross sections.

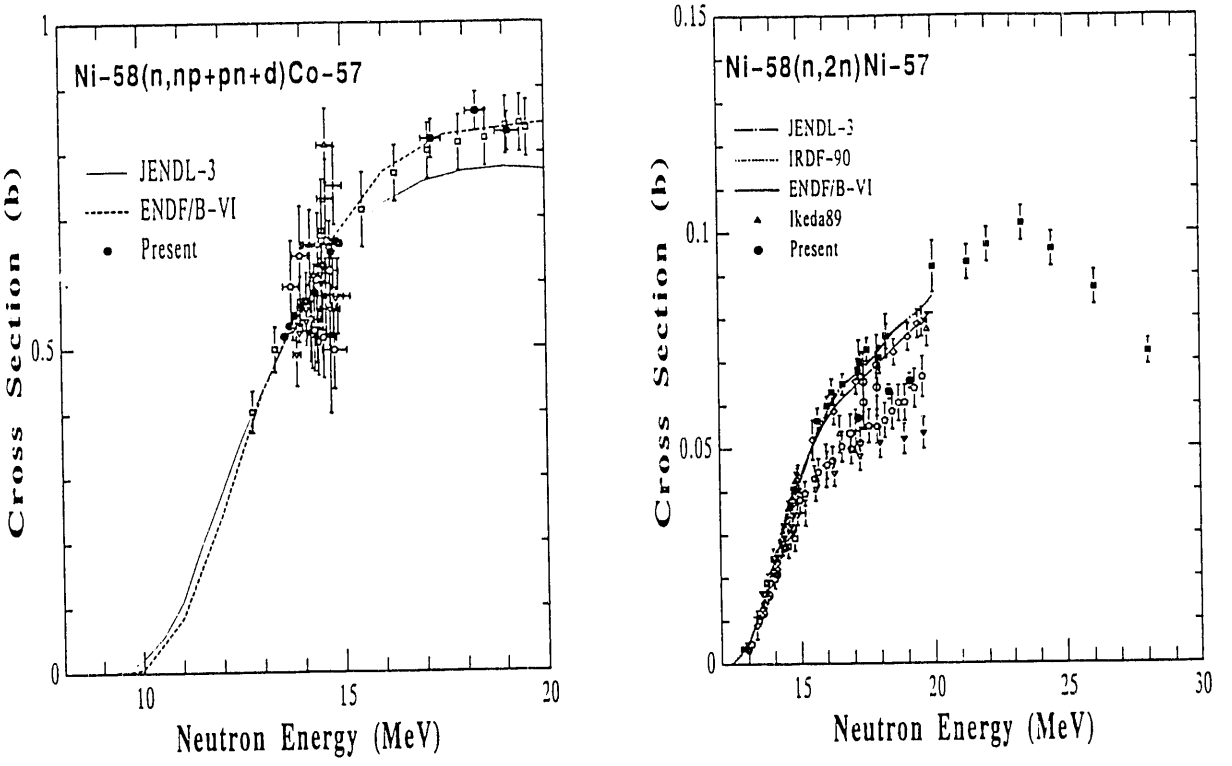

Fig. 2 $^{58}Ni(n,np)^{57}Co$ and $^{58}Ni(n,2n)^{57}Ni$ reactions.

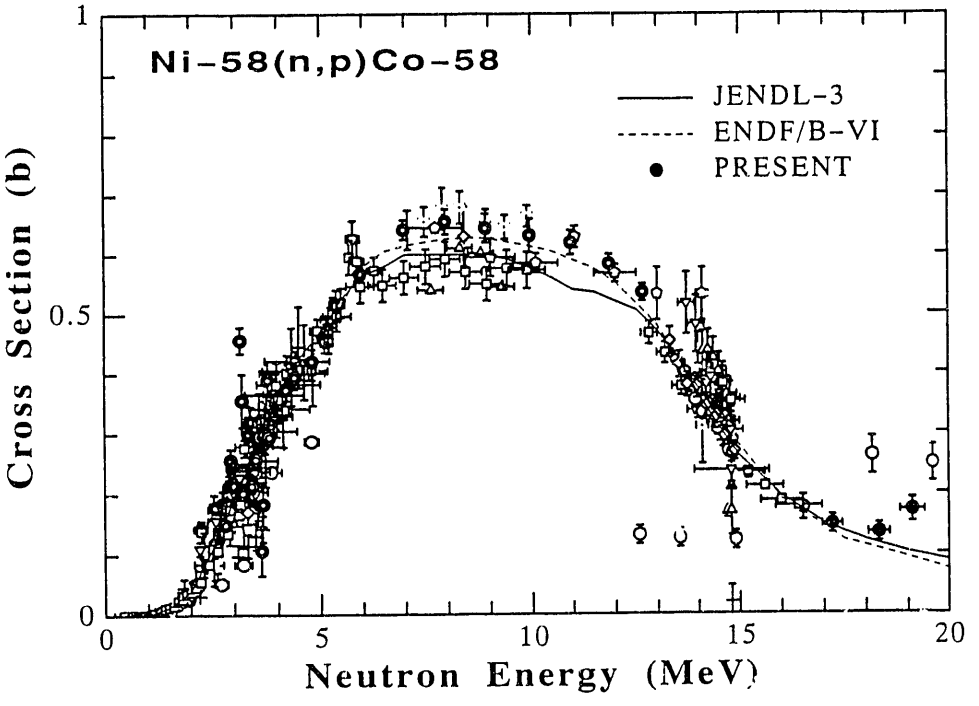

Fig. 3 $^{58}Ni(n,p)^{58}Co$ cross sections.

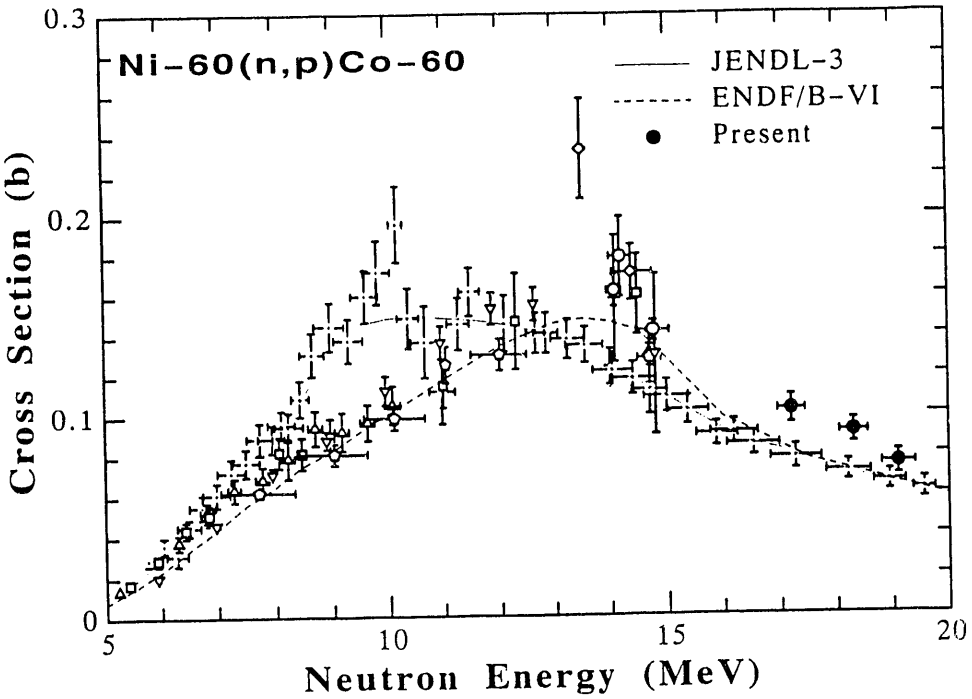

Fig. 4 $^{60}Ni(n,p)^{60}Co$ cross sections.

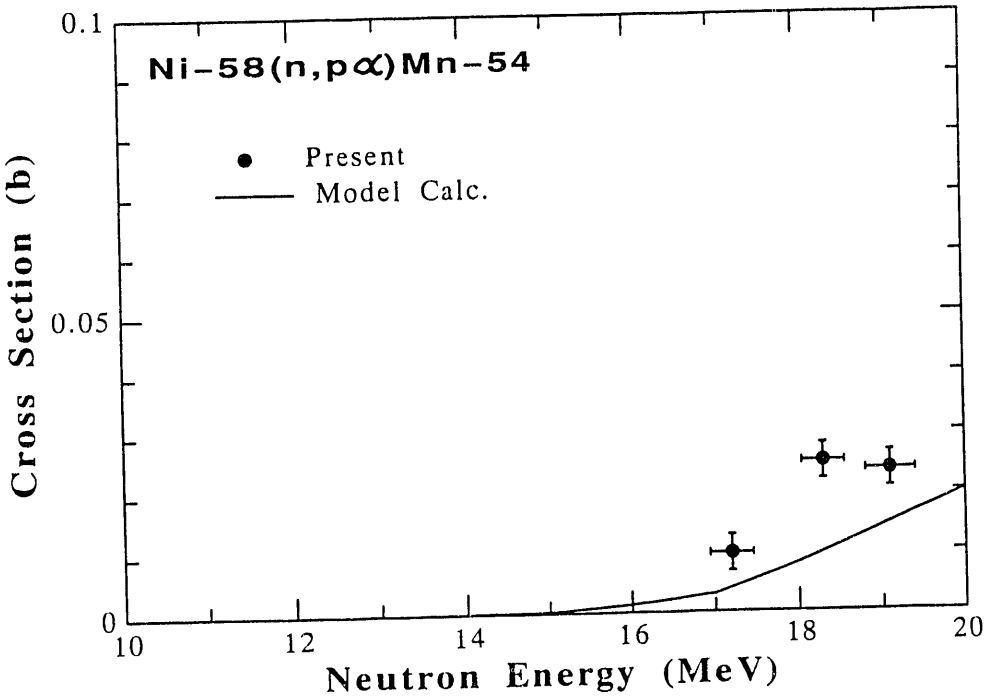

Fig. 5 $^{58}Ni(n,p\alpha)^{54}Mn$ cross sections.

3.14 Beta Half-lives of ^{102m,g}Rh

Akihiko Tanaka, Masato Asai, Hiroshi Yamamoto,
Yujiro Ikeda*, Hiroshi Maekawa* and Kiyoshi Kawade

Department of Nuclear Engineering, Nagoya University
Furo-cho, Chikusa-ku, Nagoya 464-01, Japan
**Japan Atomic Energy Research Institute*
Tokai-mura, Naka-gun, Ibaraki-ken 319-11, Japan

Abstract

Beta half-lives of ^{102m,g}Rh have been measured by following the change of the gamma-ray intensities with an HPGe detector. The values have been determined to be (3.76 ± 0.10) y and (206 ± 3) d, respectively. Two new gamma-rays of 865.5 and 1493.6 keV were found by gamma singles and gamma-gamma coincidence measurements with HPGe detectors.

1. Introduction

The previous values of the half-lives of ^{102m,g}Rh were ~2.9 y and (207 ± 3) d, respectively[1]. There were few measurements of the half-life of ^{102m}Rh and no evaluation of uncertainty was done. These values were measured with GM counters, scintillation counters and beta-ray spectrometer. In this work, we followed the change of the gamma-ray intensities in the decay of ^{102m,g}Rh with an HPGe detector to determine the precise half-lives. In addition, gamma singles and gamma-gamma coincidence measurements were performed with HPGe detectors in order to propose a more detailed decay scheme. In gamma singles measurement, a 115% Ge detector was used to obtain high detection efficiency.

2. Experiments

2−1 Source preparation

A natural Rh foil of 50 μm thickness was irradiated for 32 hours with d-T neutrons at the FNS facility in JAERI to produce ^{102m,g}Rh by a ^{103}Rh(n,2n) reaction.

No chemical separation was performed. The measurements were started after a cooling time of six months, so that the contribution of short-lived components was negligible. The sample was divided into two and each sample was used for half-life measurement and gamma-gamma coincidence measurement, respectively.

2－2 Measurements

2－2a Half-life measurement

The sample was fixed between acrylic plates together with Al foil which had ^{133}Ba on its surface. Fig.1 shows the expanded view of the sample holder. The ^{133}Ba source was used for the check of the possible change in source-to-detector distance for the long experiment period. Gamma-ray spectrum was measured with a 20% Ge detector for 24 hours every one month. The arrangement of the detector and the sample is shown in Fig.2. The source in the acrylic holder was attached to the acrylic spacer at 5cm from the detector. After the measurement was done, the source was removed every time. In this case, it is very important to ensure that the sample is attached at the same position. In this work, a gamma-ray of 356.0 keV from ^{133}Ba source was used for the correction of the distance.

2－2b Gamma singles and gamma-gamma coincidence measurements

Gamma singles measurements were performed with 20% and 115% Ge detectors. In the case of 115% Ge detector, a Pb plate of 2.5 cm thickness was placed between the source and the detector to detect high energy gamma-rays effectively and to reduce sum coincidence effects. The gamma-gamma coincidence measurement was performed with 20% and 23% Ge detectors and a LEPS (low energy photon spectrometer, crystal size of 50 mm$^{\phi}$ × 10 mm^{t}).

3. Results

3－1 Half-life measurement

Fig.3 shows the decay curves of the gamma-rays from ^{102m,g}Rh after correction with ^{133}Ba. The half-lives of ^{102m,g}Rh have been determined to be

$$T_{1/2}(^{102m}\mathrm{Rh}) = (3.76 \pm 0.10)\ [\mathrm{y}]\ \text{and}$$
$$T_{1/2}(^{102g}\mathrm{Rh}) = (206 \pm 3)\ [\mathrm{d}],$$

respectively, which are weighted mean values of two or four gamma-rays in each curve. Present values are compared with previous ones in Fig.4. There is a good

agreement with the previous values of (210 ± 6) d [2], (206 ± 3) d [3] and (205 ± 10) d [4] in the case of ^{102g}Rh, while the present value indicates a longer half-life compared with the previous ones of 1057 d [5] and (2.1 ± 0.9) y [6] in the case of ^{102m}Rh.

3－2 Gamma singles and gamma-gamma coincidence measurements

Fig.5 shows gamma-ray spectrum from ^{102m,g}Rh with a 20% Ge detector. Two new gamma-rays of 865.5 and 1493.6 keV are seen. The 865.5 keV gamma-ray was observed in coincidence with the gamma-rays of 631.3 and 1103.2 keV, but the 1493.6 keV gamma-ray was observed only in singles measurements with 20% and 115% Ge detectors as shown in Figs.5 and 6. A proposed decay scheme is shown in Fig.7.

4. Conclusion

The half-lives of ^{102m,g}Rh have been determined to be

$$T_{1/2}(^{102m}\mathrm{Rh}) = (3.76 \pm 0.10)\ [\mathrm{y}]\ \text{and}$$
$$T_{1/2}(^{102g}\mathrm{Rh}) = (206 \pm 3)\ [\mathrm{d}],$$

respectively. There is a good agreement with the previous values in the case of ^{102g}Rh, while the present value indicates a longer half-life compared with the previous ones in the case of ^{102m}Rh.

From the gamma singles and gamma-gamma coincidence measurements, two new gamma-rays of 865.5 and 1493.6 keV were found, which de-excite the 1968.7 keV level of ^{102}Ru.

References

[1] D. de Frenne and E. Jacobs: Nuclear Data Sheets 63, 373 (1991).
[2] O. Minakawa: Phys. Rev. 60, 689 (1941).
[3] K. Hisatake: J. Phys. Soc. Japan 16, 1280 (1961).
[4] F. K. McGowan and P. H. Stelson: Phys. Rev. 123, 2131 (1961).
[5] P. Born, A. Veefkind, W. H. Elsenaar and J. Blok: Physica 29, 535 (1963).
[6] K. Hisatake, S. Matsuo and H. Kawakami: J. Phys. Soc. Japan 20, 1107 (1965).

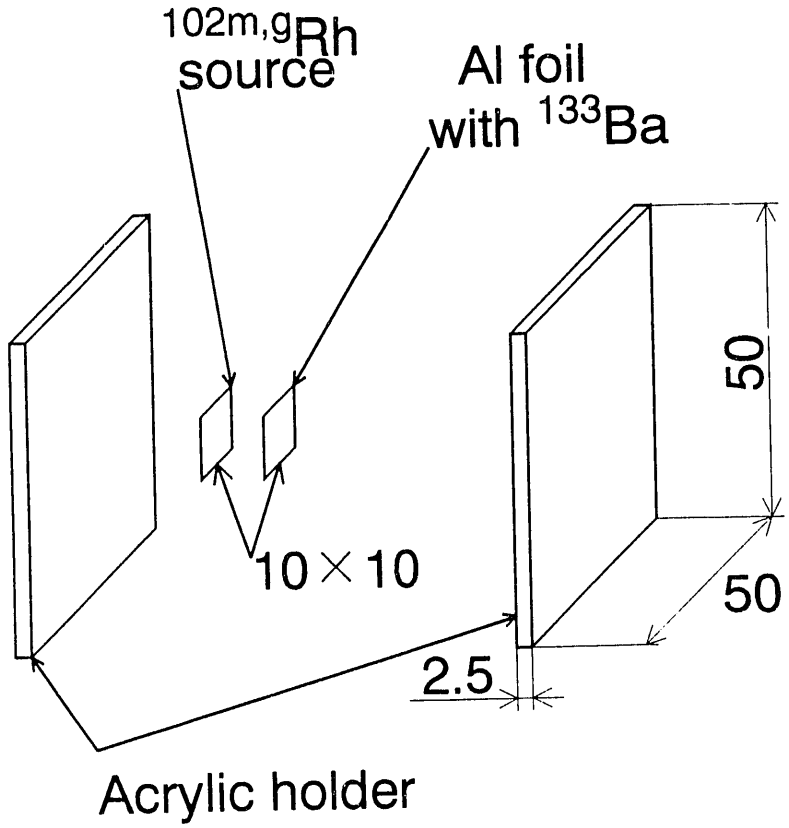

Fig. 1 Expanded view of the sample holder.

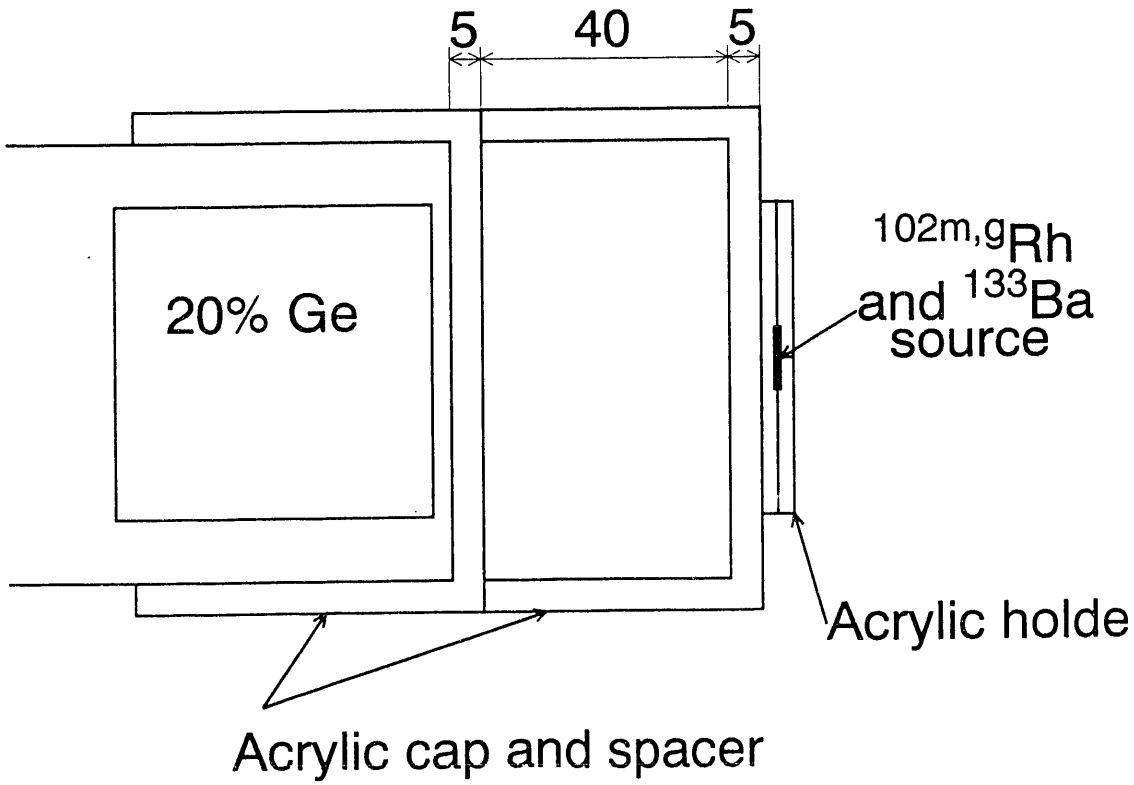

Fig. 2 Source and detector arrangement in half-life measurement. The sample was attached to the spacer with a tape in each measurement.

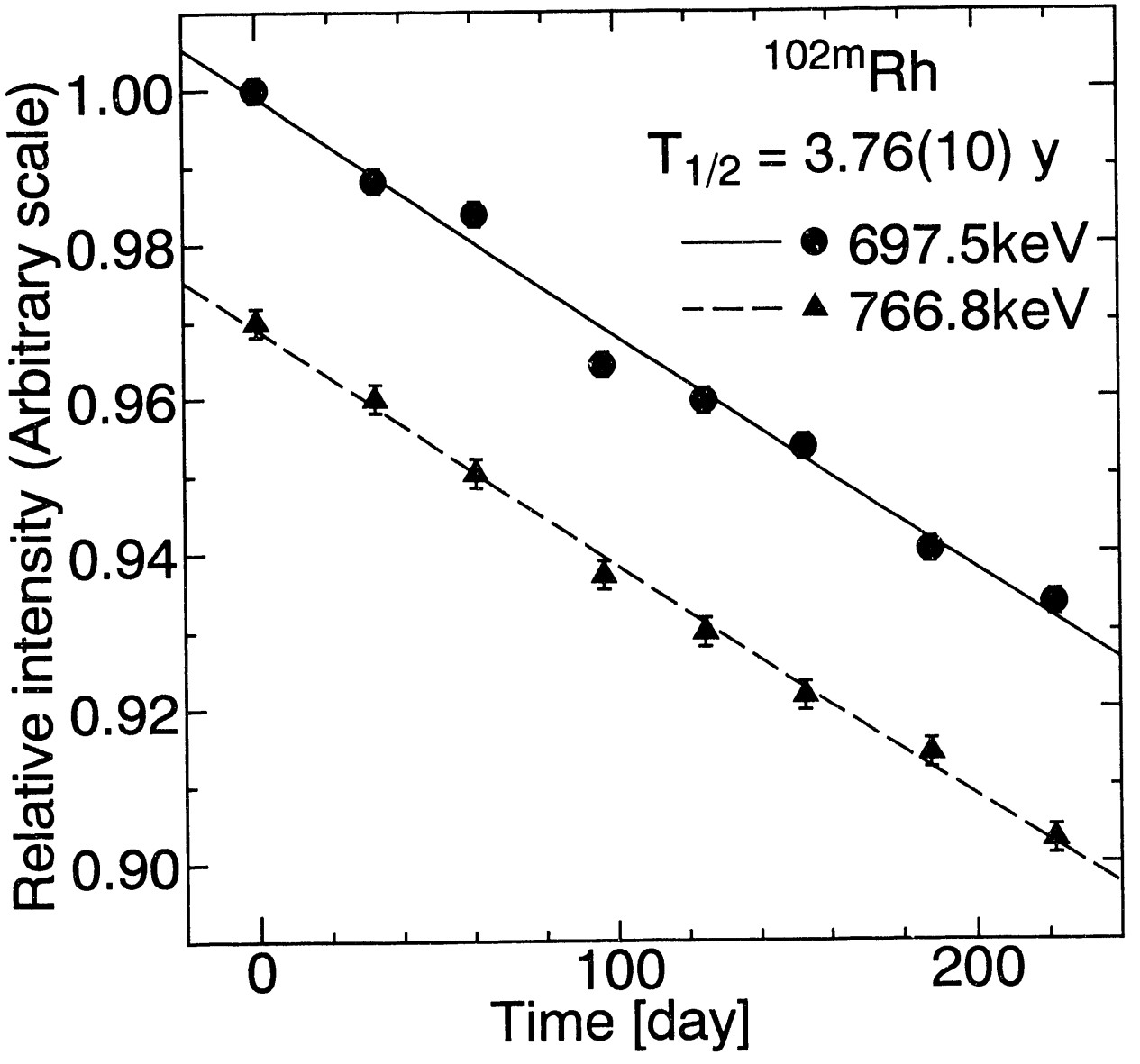

Fig. 3 Decay curves of the gamma-rays from ^{102m,g}Rh after correction with ^{133}Ba.

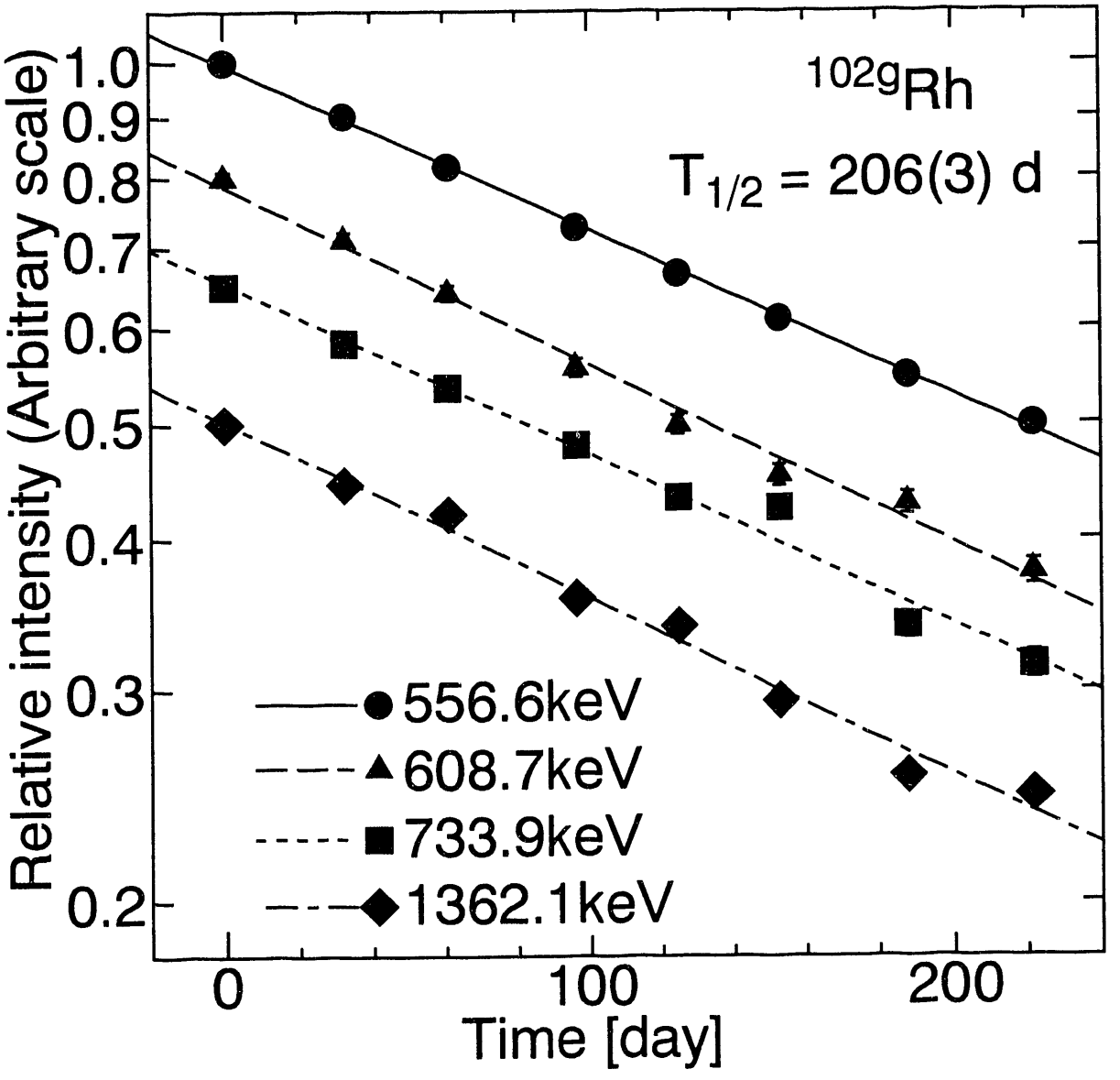

Fig. 3 (Continued)

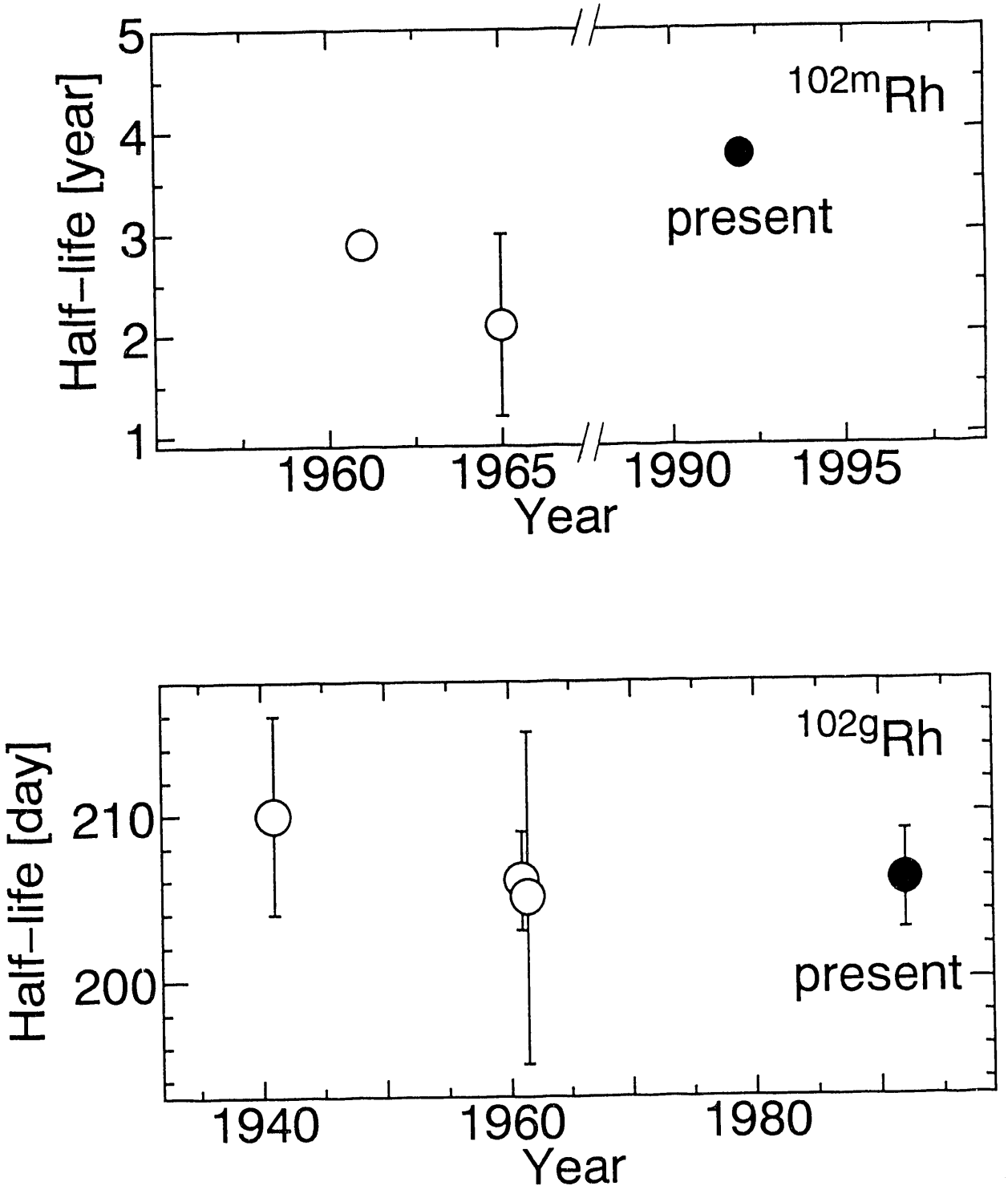

Fig. 4 Comparison of half-lives with previous values.

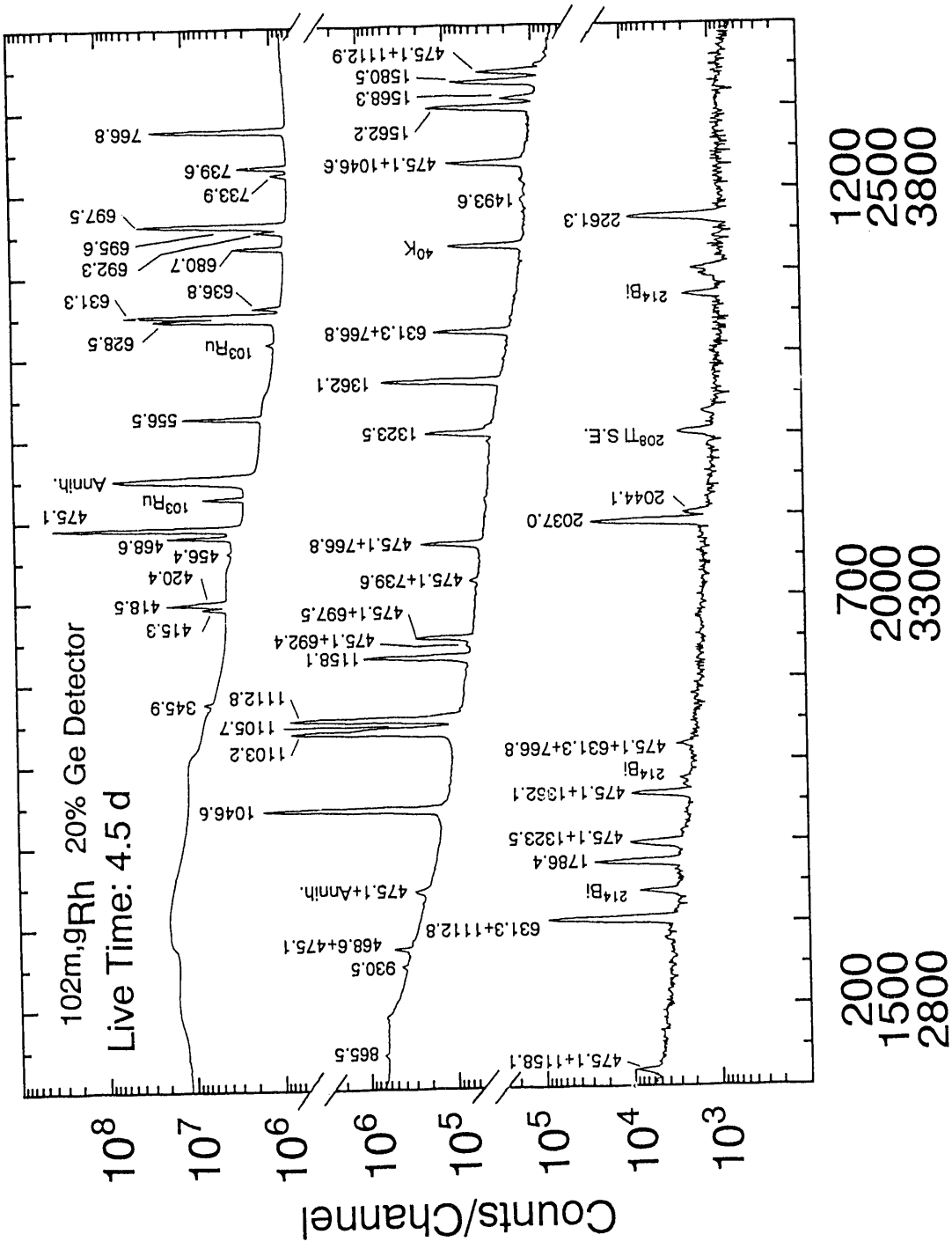

Fig. 5 Gamma-ray singles spectrum from ^{102m,g}Rh with a 20% detector.

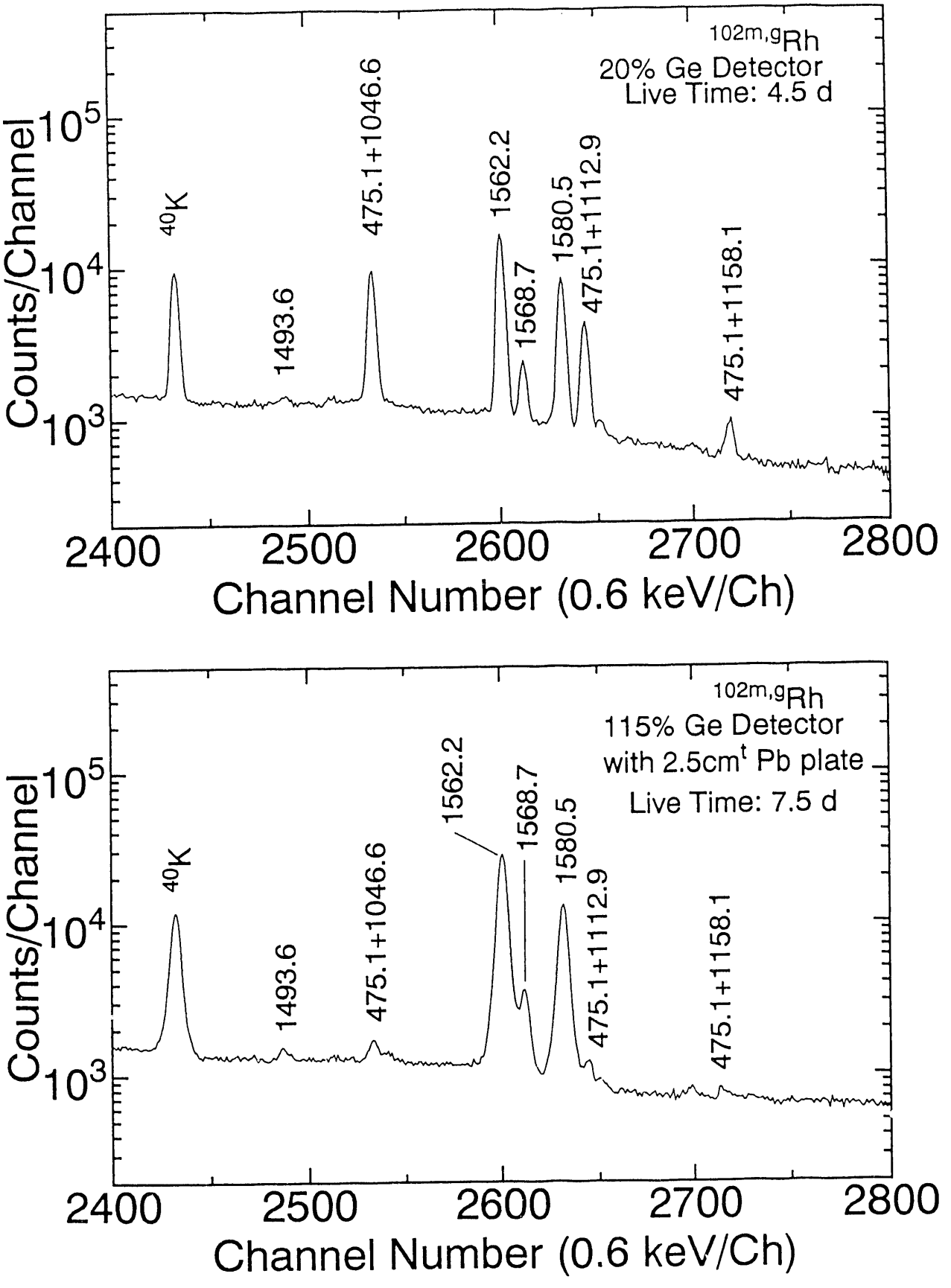

Fig. 6 Part of the gamma-ray singles spectra from ^{102m,g}Rh with 20% and 115% detectors. A new gamma-ray of 1493.6 keV is seen.

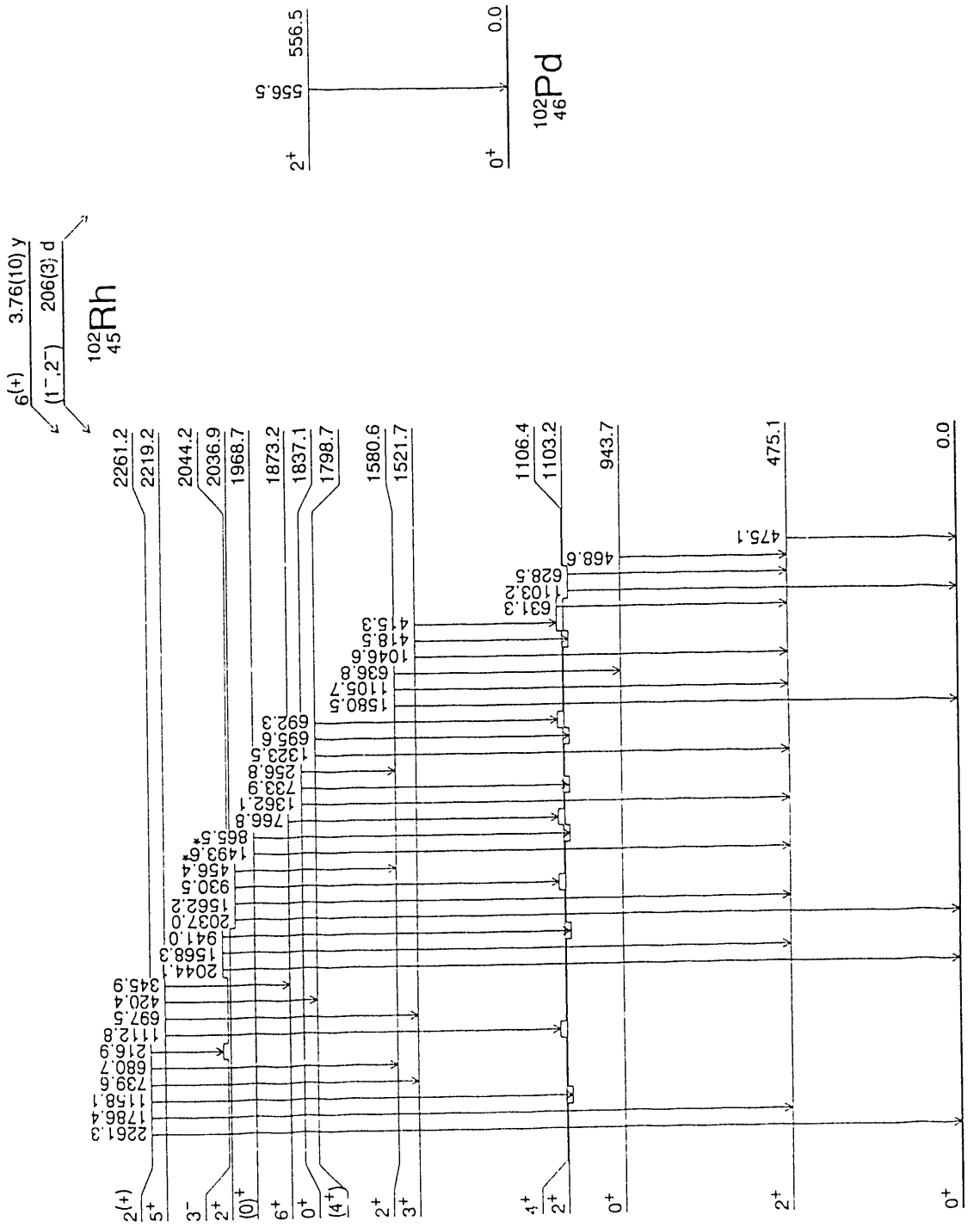

Fig. 7 A proposed decay scheme of 102m,gRh. Gamma-rays indicated by an * were newly observed.

9). Yamamuro, N. : JAERI-M 90-006, JAERI (1990).

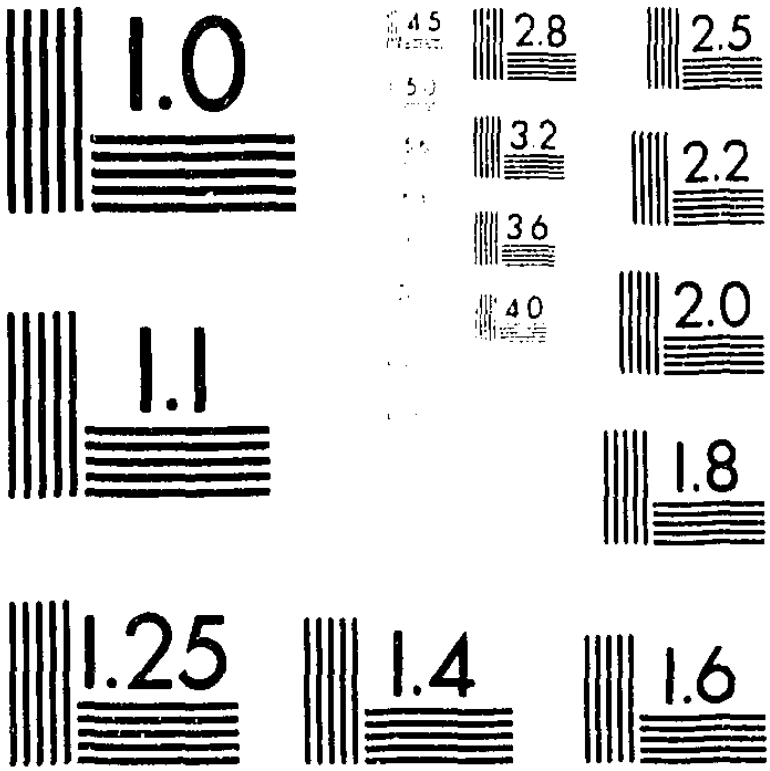

3.15 Measurement of Activation Cross Sections on Ta, W for 14 MeV Neutrons

Y. Kasugai, H. Yamamoto, A. Takahashi*, T. Iida* and K. Kawade

Department of Nuclear Engineering, Nagoya University
**Department of Nuclear Engineering, Osaka University*

Abstract: Neutron activation cross sections producing the nuclei with half-lives between 10 min and 42 d were measured at neutron energy of 13.4 to 14.9 MeV by activation method. Measured reactions were ^{181}Ta(n,p), (n,α)^{m}, (n,np)^{m}, (n,2n)^{g}, ^{182}W(n,p)^{m}, ^{184}W(n,p), (n,α), ^{186}W(n,p), (n,α). A formula which represents the systematic trends of (n,p) reaction cross sections is given.

1. Introduction

Neutron activation cross section data around 14 MeV have become important from the viewpoint of fusion reactor technology, especially for calculations on radiation damage, nuclear transmutation, induced activity and so on.

In this work 9 reaction cross sections producing the nuclei with half-lives between 10 min and 75 d were measured for Ta and W by activation method. Measured reactions are listed in Table 1. A discussion is also given on the systematic trends of (n,p) reaction cross sections based on our data and ref. [1].

2. Experiment

Experiments were performed at the Intense 14-MeV-Neutron Source Facility (OKTAVIAN) of Osaka University. For the activation of samples, pneumatic tube were set at 6 directions. The angles of the irradiation position to the d^+ beam were 0°, 50°, 75°, 105°, 125° and 155°. The distance between the T-target and irradiation points was 15cm. The induced activities were measured with three Ge detectors (21%, 12% and 16%) at an equivalent distance of 5cm. The effective neutron energies were determined by the Zr/Nb method [2]. The errors are estimated to be about 50 keV.

For the measurement of activities with half-lives longer than 30 min, the neutron flux at the irradiation points was monitored by using two niobium foils (purity: 99.9%, 1 cm x1 cm, 0.1 mm^{t}). The reference reaction was ^{93}Nb(n,2n)^{92m}Nb ($T_{1/2}$= 10.5 d).

For the short-lived activity measurements, the neutron flux at the irradiation

points was monitored by using two aluminum foils (purity: 99.2%, 1 cm x1 cm, 0.2 mm[t]). The reference reaction for the flux measurement was $^{27}Al(n,p)^{27}Mg$ ($T_{1/2}$=9.48 min). The cross section of $^{27}Al(n,p)^{27}Mg$ was determined by referring to the standard $^{27}Al(n,\alpha)^{24}Na$ reaction (ENDEF/B-V) [3]. The neutron flux at the irradiation points was about $1x10^8$ n $cm^{-2}\cdot s^{-1}$.

Samples of separated isotopes or natural elements were used for irradiation. Powder samples were wrapped in powder papers about 70 mg in weight (each sample size: 1 cm x 1 cm). Foil samples were rectangular-shaped 1 cm x 1 cm and 0.1 – 0.2 mm thick.

In Table.1, measured reactions and associated data [4] of the half-life ($T_{1/2}$), the γ-ray energy (Eγ) and the absolute intensity in photons per disintegration (Iγ) are listed together with the Q-value.

Corrections were made for time fluctuation of neutron flux, thickness of samples, self absorption of γ-ray, sum-peak effect of γ-ray and contribution of low energy neutrons below 10 MeV. The details of the correction are described elsewhere [5,6].

The total errors (δt) were described by combining the experimental errors (δe) and the errors of nuclear data (δr) in quadratic:

$$\delta t^2 = \delta e^2 + \delta r^2.$$

Estimated major sources of the errors are listed in Table 2. Accuracy of the obtained cross sections were around 3.5% in case of good statistics.

3. Results

Numerical data tables of the cross sections are given in Table 3 and graphs are given in Fig. 1 together with data reported previously. As shown in figures, the present data cover the wider energy range than previous values.

4. Discussion on the systematics of (n,p) reaction.

To study the systematics of the cross sections of (n,p) reactions at 14.9 MeV, our cross section data and the data in ref. [1] were used. In Fig.1, the data at 14.9 MeV are plotted as a function of (N-Z)/A, where N, Z and A are neutron, proton and mass number of the target nuclei, respectively. It is evident that the cross sections depend on the (N-Z)/A and A. The systematics was expressed by the formula given by

$$\sigma_{n,p}(mb)=(6.0x10^{-4})A^{5.7}(0.585)^{(\ln A)^2}\exp\{-33(N-Z)/A\}. \quad (1)$$

Ratios of experimental to estimated cross sections by using the formula (1) are

plotted as a function of mass number of the target nuclei in Fig.3. In the figure, even-odd effect is clearly seen among three kinds of target nuclei (even Z-even N, even Z-odd N and odd Z-even N).

Taking the even-odd effect into account, the following formula is obtained,

$$\sigma_{n,p}(mb)=(6.0\times10^{-4})A^{5.7}(0.585)(\ln A)^{2}\exp\{-33(N-Z)/A+\delta\} \quad (2)$$

$$\delta = \begin{cases} 0 & (e\text{-}e \text{ nucleus}) \\ +0.15 & (e\text{-}o) \\ -0.15 & (o\text{-}e). \end{cases}$$

Ratios of experimental to estimated cross sections by using the formula (2) are plotted in Fig.4. Our estimated values agree with the experimental values within 30%.

5. Summary

Cross sections for 9 reactions of (n,p), (n,α), (n,np), (n,2n) were measured.

Using our data and the data in ref.[1], systematics of (n,p) reaction cross sections at 14.9 MeV was expressed by the simple formula. The estimated values obtained from equation (2) agree with the experimental values within 30%.

References

[1] Y. Ikeda, C. Konno, K. Oishi, T. Nakamura, H. Miyade, K. Kawde, H. Yamamoto, and T. Katoh: JAERI 1312 (1988).

[2] V.E. Lewis and K.J. Zieba : Nucl. Instrum. Methods 174, 141 (1980).

[3] "Evaluated Neutron Data File, ENDF/B-V", ENDF/B Summary Documentation, compiled by R. Kinsey, ENDF-201, 3rd edition, Brookhaven Laboratory (1979).

[4] E. Browne, R.B. Firestone and V.S. Shirley: "Table of Radioactive Isotopes", John Wiley & Sons, New York (1986).

[5] T. Katoh, K. Kawade and H. Yamamoto: JAERI-M 89-083 (1989) (in Japanese).

[6] K. Kawade, H. Yamamoto, T. Yamada, T. Katoh, T. Iida and A. Takahashi: JAERI-M 90-171 (1990).

Table 1 Reactions and decay parameters

Reaction[a]	$T_{1/2}$	Eγ(keV)	Iγ(%)	Q(MeV)
$^{181}Ta(n,p)^{181}Hf$	42.39(6) d	482.0	80.6(6)	-0.25
$^{182}W(n,p)^{182m}Ta$	15.84(10) min	171.6	45.9(43)	-1.55
$^{184}W(n,p)^{184}Ta$	8.7(1) h	414.0	73.9(9)	-2.08
$^{186}W(n,p)^{186}Ta$	10.5(5) min	198.1	59(10)	-3.11
$^{181}Ta(n,\alpha)^{178m}Lu$	23.1(4) min	426.3	97.4(19)	7.24
$^{184}W(n,\alpha)^{181}Hf$	42.39(6) d	482.0	80.6(6)	7.35
$^{186}W(n,\alpha)^{183}Hf$	1.067(17) h	783.8	65(7)	6.42
$^{181}Ta(n,np)^{180m}Hf$	5.519(4) h	332.3	94.4(24)	-5.94
$^{181}Ta(n,2n)^{180g}Ta$	8.152(6) h	93.3	5	-7.58

a) (n,np) means (n,d) + (n,n'p) + (n,pn).

b) Q(n,np) is given here, Q(n,d)=Q(n,n'p)+2.225 MeV.

Table 2 Principle sources of uncertainty in the measured cross sections

Experimental error (δ_e) Source of error	Uncertainty(%)
Counting Statistics	0.5 - 20
Samples mass including purity	0.1
Neutron flux fluctuation	< 0.1 (20% of correction)
Gamma-peak area evaluation	0.5
Detector efficiency	1.5 ($E\gamma$ > 300keV)
	3 (300-80 keV)
	5 ($E\gamma$ < 80 keV)
Efficiency Calibration at 0.5 and 5 cm	2.0
Correction for	
true coincidence sum	< 0.5
random coincidence sum	< 0.4
sample thickness	0.2-0.6 (20% of correction)
self-absorption of γ-rays	0-0.5 (20% of correction)
low energy neutrons	0-5 (30-40% of correction)
Secondary reference cross section for $^{27}Al(n,p)^{27}Mg$	0.5(Only statistics)

Error of nuclear data(δ_r) Source of error	Uncertainty(%)
Reference cross section	
$^{27}Al(n,\alpha)^{24}Na$ (ENDF/B-V)	3.0
$^{93}Nb(n,2n)^{92m}Nb$	4.2
Absolute γ-ray intensity	0-20
Half-life	0-5

Table 3 Digital cross section data measured

En(MeV)	$^{181}Ta(n,p)^{181}Hf$	$^{182}W(n,p)^{182m}Ta$	$^{184}W(n,p)^{184}Ta$
14.87	4.16(24) mb	0.25(8) mb	3.72(17) mb
14.58	3.92(45)	0.22(5)	
14.28	3.19(21)	0.13(4)	2.91(13)
13.88	2.81(18)	0.088(28)	2.33(12)
13.65	2.34(15)		2.16(10)
13.40	2.17(14)	0.080(34)	2.08(10)

En(MeV)	$^{186}W(n,p)^{186}Ta$	$^{181}Ta(n,\alpha)^{178m}Lu$	$^{184}W(n,\alpha)^{181}Hf$
14.87	1.90(40) mb	0.341(29) mb	0.91(13) mb
14.58	1.73(34)	0.301(26)	0.87(11)
14.28		0.240(36)	0.79(10)
13.88	1.08(24)	0.233(20)	0.67(9)
13.65	0.97(21)	0.213(18)	0.56(9)
13.40	0.84(22)	0.192(18)	0.56(9)

En(MeV)	$^{186}W(n,\alpha)^{183}Hf$	$^{181}Ta(n,np)^{180m}Hf$	$^{181}W(n,2n)^{180g}Ta$
14.87	0.71(9) mb	0.151(11) mb	1.24(9) b
14.58	0.56(8)	0.134(11)	1.23(9)
14.28	0.51(7)	0.091(11)	1.25(9)
13.88	0.41(6)	0.066(5)	1.21(8)
13.65	0.38(5)	0.042(5)	1.25(9)
13.40	0.24(8)	0.030(4)	1.24(9)

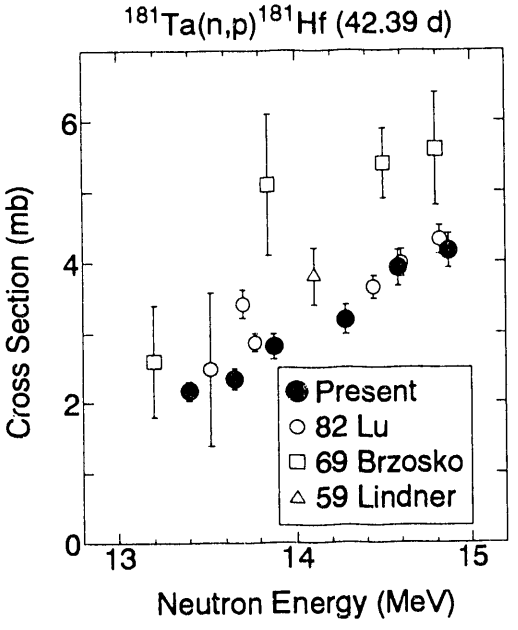

Fig. 1.1 Cross section of $^{181}Ta(n,p)^{181}Hf$.

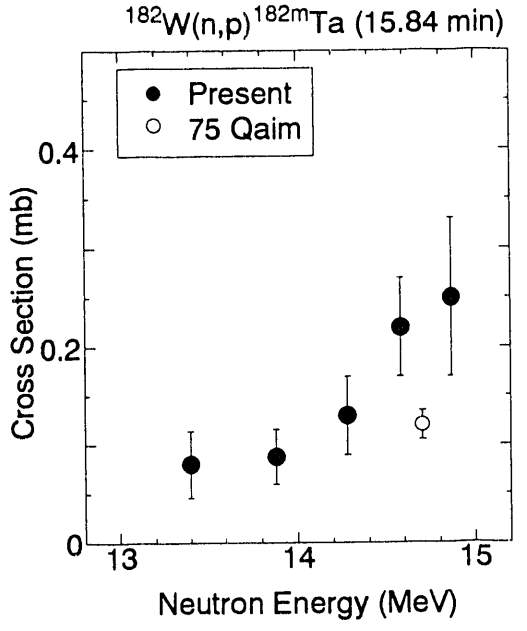

Fig. 1.2 Cross section of $^{182}W(n,p)^{182m}Ta$.

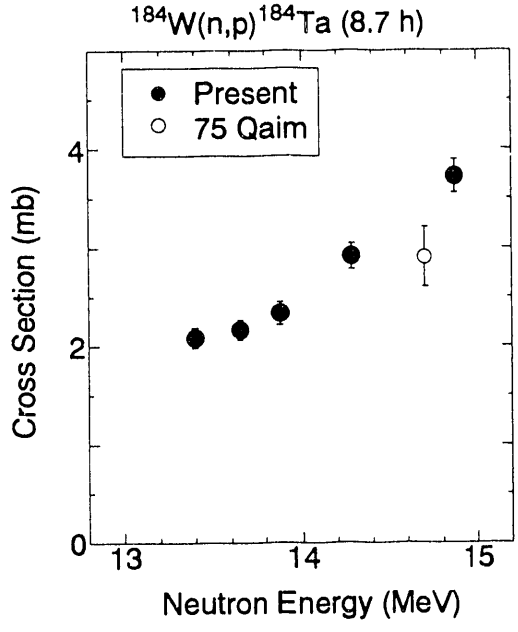

Fig. 1.3 Cross section of $^{184}W(n,p)^{184}Ta$.

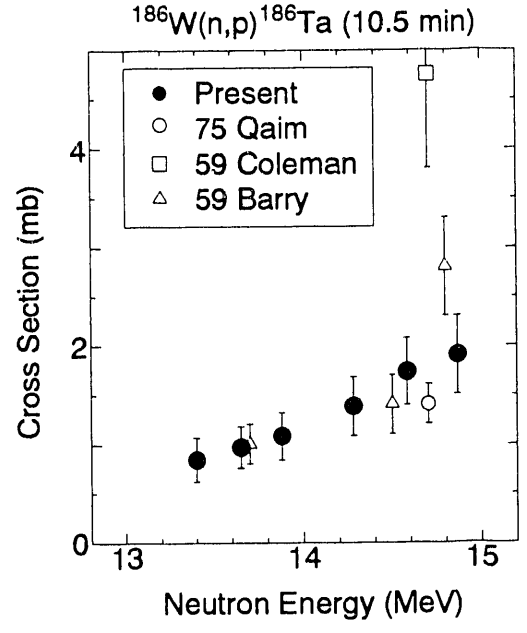

Fig. 1.4 Cross section of $^{186}W(n,p)^{186}Ta$.

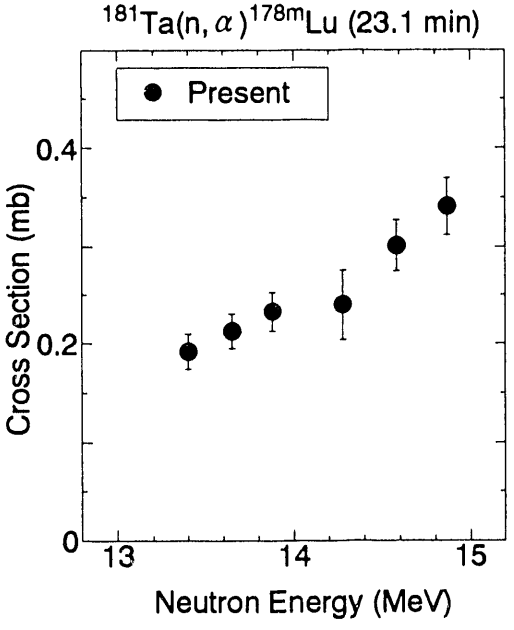

Fig. 1.5 Cross section of $^{181}Ta(n,\alpha)^{178m}Lu$.

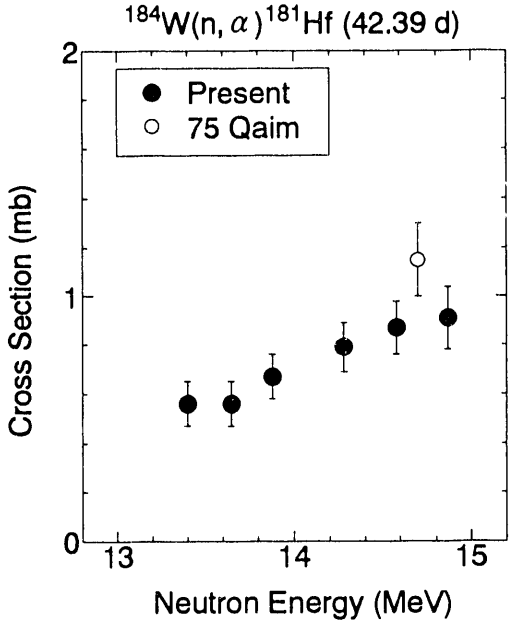

Fig. 1.6 Cross section of $^{184}W(n,\alpha)^{181}Hf$.

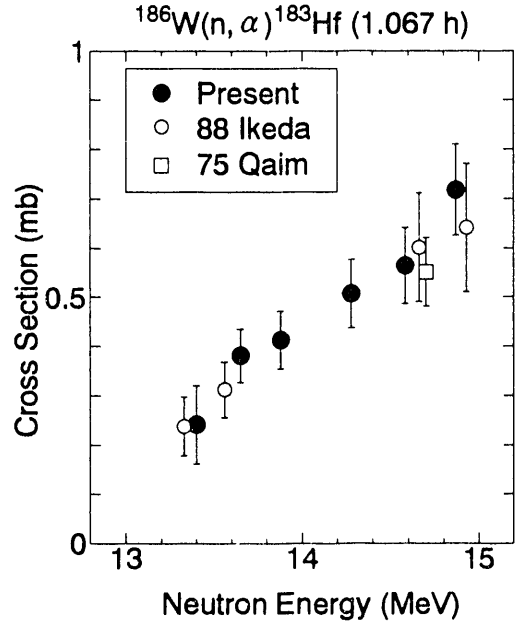

Fig. 1.7 Cross section of $^{186}W(n,\alpha)^{183}Hf$.

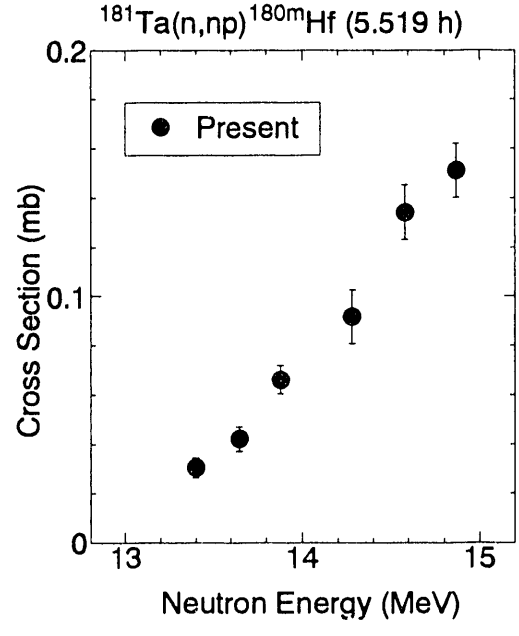

Fig. 1.8 Cross section of $^{181}Ta(n,np)^{180m}Hf$.

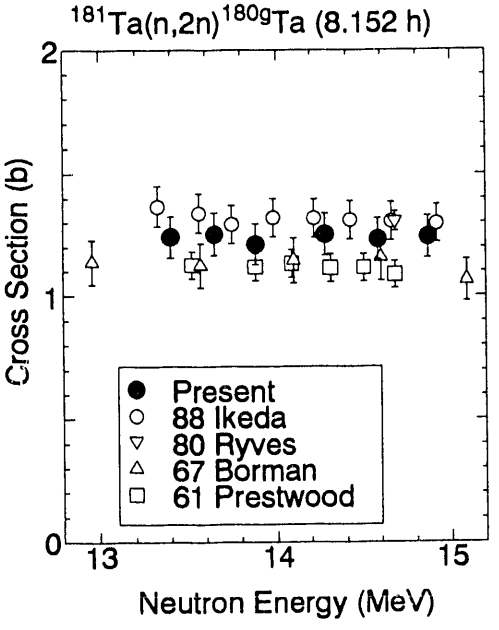

Fig. 1.9 Cross section of $^{181}Ta(n,2n)^{180g}Ta$.

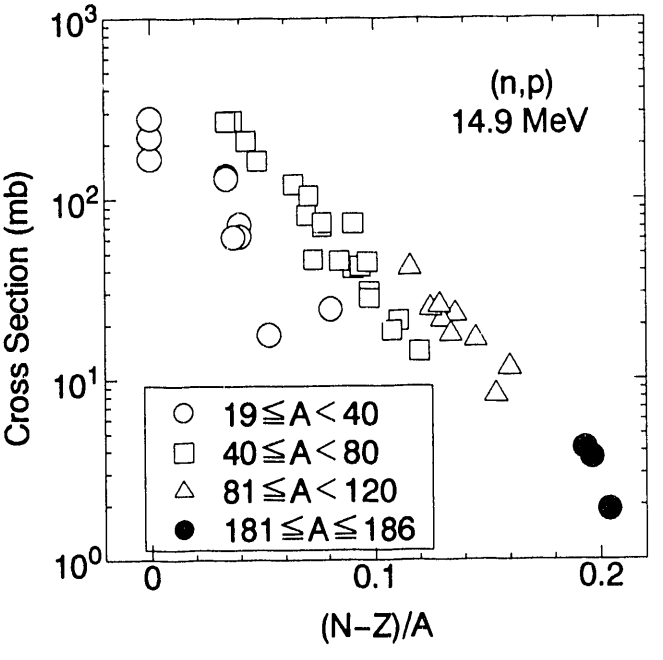

Fig. 2 Systematics of (n,p) reaction cross sections.

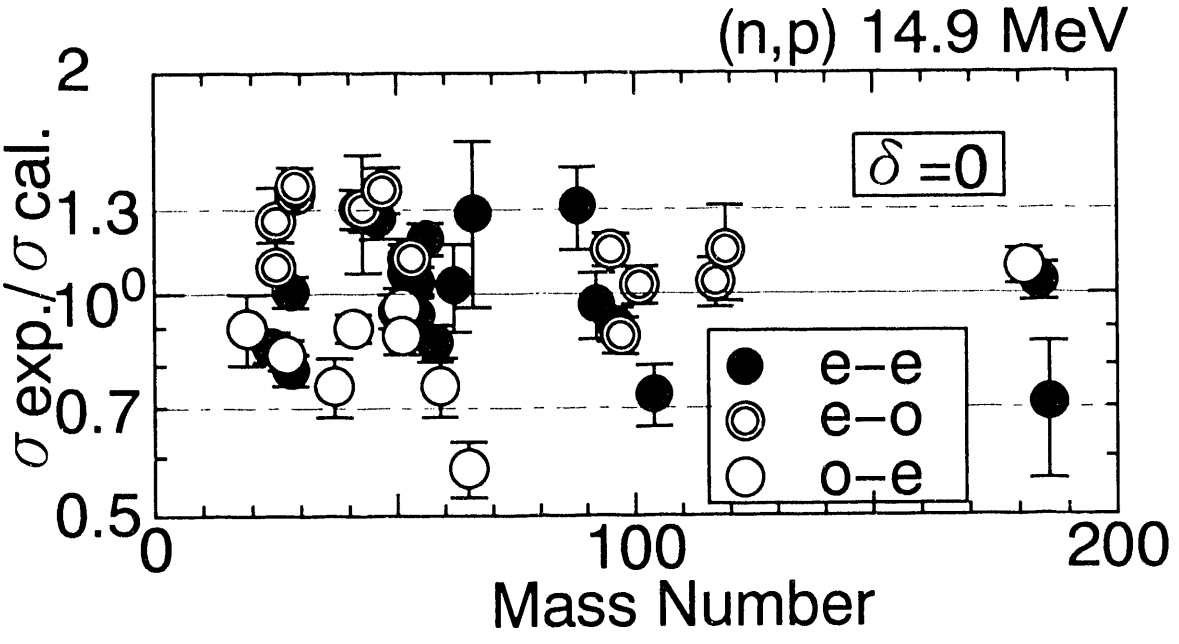

Fig. 3 Ratios of experimental to estimated cross sections by using the formula (1). The even-odd effect is clearly seen.

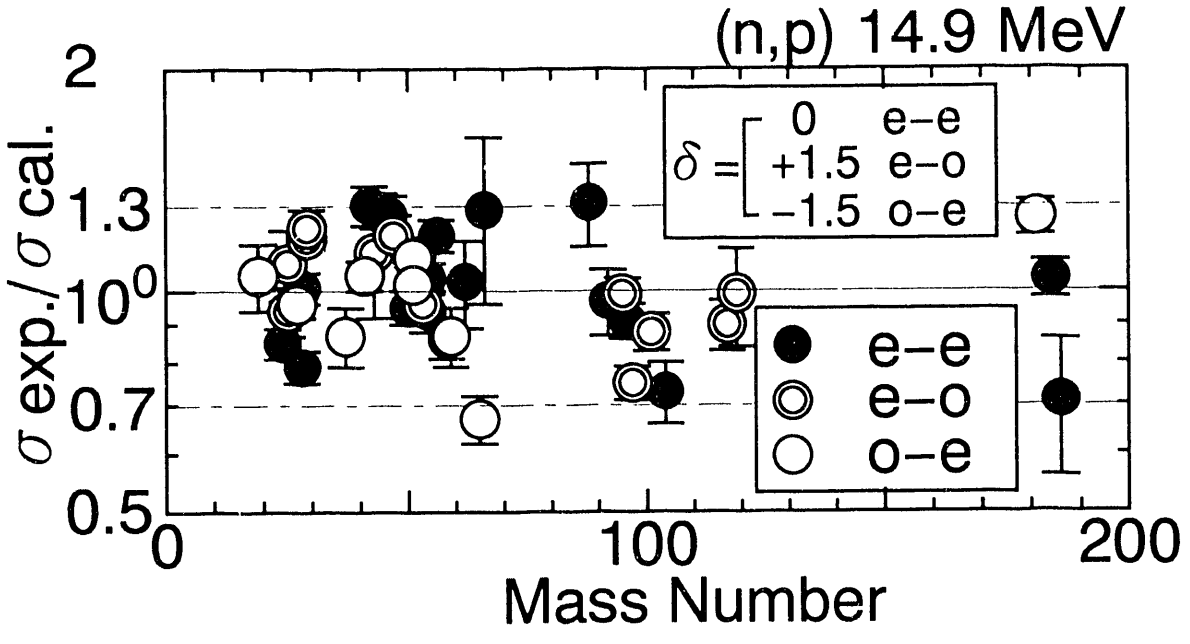

Fig. 4 Ratios of experimental to estimated cross sections by using the formula (2) which depends on the even-odd effect. The estimated values agree with the experimental values within 30%.

3.16 Study of ^{12}C Breakup Processes and Carbon Kerma Factors

H. Kashimoto, Y. Watanabe, Y. Koyama, H. Shinohara,
and
S. Chiba*

Department of Energy Conversion Engineering, Kyushu University,
Kasuga, Fukuoka 816, Japan
** Japan Atomic Energy Research Institute, Tokai-mura, Ibaraki, 319-11, Japan*

Recent studies of ^{12}C breakup processes in nucleon-induced reactions are reported with the following subjects: (i) analyses of spectra of protons and α-particles emitted from proton-induced reactions at 14, 16 and 26 MeV, (ii) development of a Monte Carlo computer code to simulate successive sequential breakup decay from reactions with ^{12}C induced by nucleons, and (iii) application of the results to calculations of carbon kerma factors at incident energies ranging from 10 to 20 MeV.

1. Introduction

Neutron nuclear data on carbon are required for estimation of radiation damage and neutron shielding in fusion reactor design, evaluation of kerma factors for high energy neutron radiotherapy, and calculations of the efficiency of organic scintillators. In reactions on ^{12}C induced by fast neutrons with energies more than 10 MeV, the $^{12}C(n,n')3\alpha$ process (the four-body breakup process) is known to become dominant. In general, the mechanism of such multiparticle breakup processes can be understood in terms of (i) successive sequential decay process via intermediate states and (ii) n-body simultaneous breakup process.[1] The aim of the present work is to investigate the ^{12}C breakup mechanism and to apply the result to calculation of carbon kerma factors.

For the past few years, we have been studying the $^{12}C(p,p')3\alpha$ reaction analogous to the $^{12}C(n,n')3\alpha$ reaction in order to establish a reliable model for the ^{12}C breakup processes.[2,3] In these studies, energy spectra of emitted protons and α particles have been measured at several angles for incident energies of 14 and 16 MeV[2] and 26 MeV[3]. In Sec. 2, we report the analysis of the experimental data using a phase space model based on the kinematics of four body simultaneous breakup (4BSB) process and address the limitation to apply the model. A computer code based on the Monte Carlo technique is being developed by our group, in order to simulate more complicated sequential decay processes in the ^{12}C breakup

reaction. We present the preliminary result for neutron-induced reactions at 14 and 18 MeV in Sec. 3. We also report the result of carbon kerma factors calculated with three evaluated nuclear data files JENDL-3[4], ENDF/B-V[5] and VI[6], comparing with the experimental data in Sec. 4.

2. Analyses of proton induced reactions on ^{12}C at 14, 16 and 26 MeV

Figure 1 shows experimental double differential proton and α emission cross sections into 80° at 14, 16 MeV[2] and 26 MeV[3] by histograms. A distinct continuum underlying peaks is observed in both proton and α spectra. The solid lines indicate the spectra calculated using the phase space model[2] of the 4BSB process. Both the proton and α spectra for 14 and 16 MeV are in good agreement with the experimental ones in the continuum region. On the basis of this result, two (Y.W. and H. K.)[2] of the present authors have pointed out the applicability of the 4BSB model to nucleon-induced reactions on ^{12}C. However, it has been found that the agreement is worse at higher incident energy of 26 MeV although the calculated α spectrum shows good agreement with the experimental one. This may suggest that such sequential decay processes as listed in Fig.2. and/or the sequential decay process involving the three body simultaneous breakup (3BSB) process p + α + ^{8}Be are also concerned in the ^{12}C breakup processes. We, therefore, intend to consider such successive sequential decay processes via intermediate states and analyze these experimental data using an analytical expression based on the Beynon model[7] or a Monte Carlo simulation technique as described in the following section.

There is another evidence which shows the importance of sequential decay processes. That is a large proton yield observed in the low outgoing energy region of the experimental proton spectrum for 26 MeV in Fig.1. There is no such observation in the proton spectrum for 14 and 16 MeV. This component may be interpreted as the sequential proton decay from excited states of ^{12}N following the $^{12}C(p,n)$ reaction (Q = - 18.12 MeV), because the energy of a rise near 6 MeV is reproduced by a reaction kinematics calculation. Further analysis is now in progress.

3. Development of a Monte Carlo simulation code and analyses

To study such sequential decay mode as listed in Fig.2, we have been developing a Monte Carlo based computer code with a code SCINFUL[8] to determine a scintillator full energy response to neutron detection for energies between 0.1 and 80 MeV. Using the Monte Carlo code, we have analyzed neutron-induced breakup processes at 14 and 18 MeV.

The result for neutron emission is shown by solid histograms in Fig.3; the calculated spectra are smoothed using a Gaussian function with an FWHM of 1 MeV. The experimental spectra for 30°, 60°, and 120° are reproduced quite well by the model taking into account all the

sequential decay processes listed in Fig.2. The dotted histograms represent the contribution from the sequential decay following $^{12}C(n,\alpha)^{9}Be$ reaction. Similar result is obtained for an incident energy of 18 MeV.

Next, inclusive α emission spectra measured by Haight et al.[9] are compared with the calculated ones in Fig.4. Solid lines represent the calculated spectra of total α emission and dashed lines the component of the sequential decay via $^{12}C^*$ excited by inelastic scattering. The calculated result provides overall good agreement with the experimental values, although there is a systematic difference in the position of the peaks denoted by α_1; the reason is not clear at present because of disagreement between the position calculated using the reaction kinematics and the experimental values. The continuum underlying those peaks is explained well by the the sequential decay via $^{12}C^*$. At emission energies below 2 MeV, the calculated α spectra show large yields due to the sequential decay of ^{8}Be following the decay $^{9}B \rightarrow n + {}^{8}Be$ after $^{12}C(n,\alpha)^{9}Be$ reaction. On the other hand, no large experimental yield is exhibited because of the threshold (1 MeV) to detect α particles with low energy. Haight et al.[9] have obtained the total α emission cross section of 402 mb by extrapolation to zero energy shown in Fig.4. The value is about a half of those obtained in the present work (853mb) and the others[9]. The present simulation obviously indicates that the large difference is due to the extrapolation in which the influence from the sequential decay is neglected. Therefore, the experiment to measure α particles emitted with as low energies as possible should be performed to investigate the effect of sequential decay processes in the ^{12}C breakup reaction.

Application of the present code to the proton-induced reaction is now in progress.

4. Application - carbon kerma factors -

Evaluation of kerma factors is one of application of nuclear data on ^{12}C. We have calculated the kerma factors at incident energies ranging from 10 to 20 MeV using nuclear data file JENDL-3[4]. The result is compared with several experimental values[9-14] and calculated results using the other files ENDF/B-V[5] and VI[6] in Fig.5. The details have been reported elsewhere[15].

As shown in Fig.5, the kerma factors calculated with ENDF/B-VI are in better agreement with the experimental values than those with JENDL-3 and ENDF/B-V. Both the results with the latter files overestimate the experimental values at incident energies ranging from 14 MeV to 18 MeV. The overestimation is due to the evaluated cross sections of $(n,n')3\alpha$ process as mentioned in the following discussion. Fig.6 shows that the relative fraction of $(n,n')3\alpha$ process to the total kerma factors increases with increasing incident energy and the process becomes most dominant at energies more than 14 MeV. Comparison of the $(n,n')3\alpha$ breakup cross sections between JENDL-3 and ENDF/B-VI indicates that the former is much larger than the latter near 16 MeV of our interest in Fig.7. Another difference lies in the

relative fraction of so-called evaporation component to the total (n,n')3α cross section. ENDF/B-VI has a smaller fraction of the component than JENDL-3. This gives rather large contribution from sequential decay from the excited levels of ^{12}C by inelastic scattering.

In the kerma factor calculations[15] with JENDL-3, the evaporation component of (n,n')3α cross sections was reduced to two sets of double differential cross sections based on the evaporation model and the 4BSB phase space model, respectively. As a result, the calculated kerma factors with the latter model (a dotted-dashed line) are in better agreement with the experimental values than those with the former model (a solid line) at incident energies over 18 MeV as shown in Fig.5. Therefore, the treatment of multiparticle breakup processes is important for evaluation of kerma factors.

Carbon kerma factors calculated with newly evaluated nuclear data have recently been reported by Axton[16]. The result is similar to that of the present work with ENDF/B-VI.

5. Summary

From investigation of the incident energy dependence of the 3α breakup process in the ^{12}C(p,p')3α reaction, it was found that four body simultaneous breakup process alone is not enough to explain the proton spectra observed at the high incident energy of 26 MeV. A Monte Calro based code has been developed to calculate the sequential decay processes in ^{12}C(n,n')3α reactions . The DDXs calculated using the code are in good agreement with experimental ones for 14 and 18 MeV (n,n'x). The result of kerma factor calculations using three evaluated nuclear data, JENDL-3, ENDF/B-V and VI, showed that the 3α breakup process was important at energies over 14 MeV. Better agreement with experimental data has been obtained using ENDF/B-VI. Kerma factor calculations with the Monte Calro code would be necessary for further comparison with the present results based on the evaluated nuclear data files

In future, we intend to apply the present code and results to evaluation of neutron nuclear data on ^{12}C in the incident energy range extending up to 50 MeV for fusion energy development.

References

1) See for instance, B. Antolkovic' et al., Nucl. Scien. Eng., **107**, 1 (1991)

2) Y. Watanabe et al., *Proc. Int. Conf. on Nuclear Data for Science and Technology, Jülich, Germany, May 13-17, 1991, pp.1002*

3) Y. Watanabe et al., *to be published in Proc. of the 1992 Symp. on Nuclear Data, JAERI, Nov. 26-27, 1992*

4) K. Shibata et al., "Japanese Evaluated Nuclear Data Library, Version -3, JENDL-3", JAERI-1319 (1990)

5) "Evaluated Nuclear Data File, ENDF/B-V", Brookheaven National laboratory (1979)

6) "Evaluated Nuclear Data File, ENDF/B-VI", Brookheaven National laboratory
7) T.D. Beynon and A.J. Oastler, Ann. nuclear Energy, **6**, 537 (1979); T.D. Beynon and B.S. Sim, *ibid.*, **15**, 27 (1988)
8) J.K. Dickens, ORNL-6462, Oak Ridge National laboratory (1988)
9) C.R. Haight et al., Nucl. Scie. Eng., **87**, 41 (1984)
10) P.M. Deluca et al., Radiat. Res., **100**, 78 (1984)
11) P.M. Deluca et al., Proc. 5th Symp. Neutron Dosimetry, Munich/Neuherberg, FRG, EUR-9762, p. 193, Commission of the European Communities, Luxembourg (1985)
12) G. Bühler et al., *ibid.*, p.309
13) P.M. Deluca et al., Nucl. Scie. Eng., **94**, 192 (1986)
14) J.C. McDonald, Radiat. Res. **109**, 28 (1987)
15) H. Shinohara et al., Engineering Sciences Reports, Kyushu University, Vol. **14**, 205 (1992)
16) E.J. Axton, NISTIR-4838, National Institute of Standards and Technology (1992)

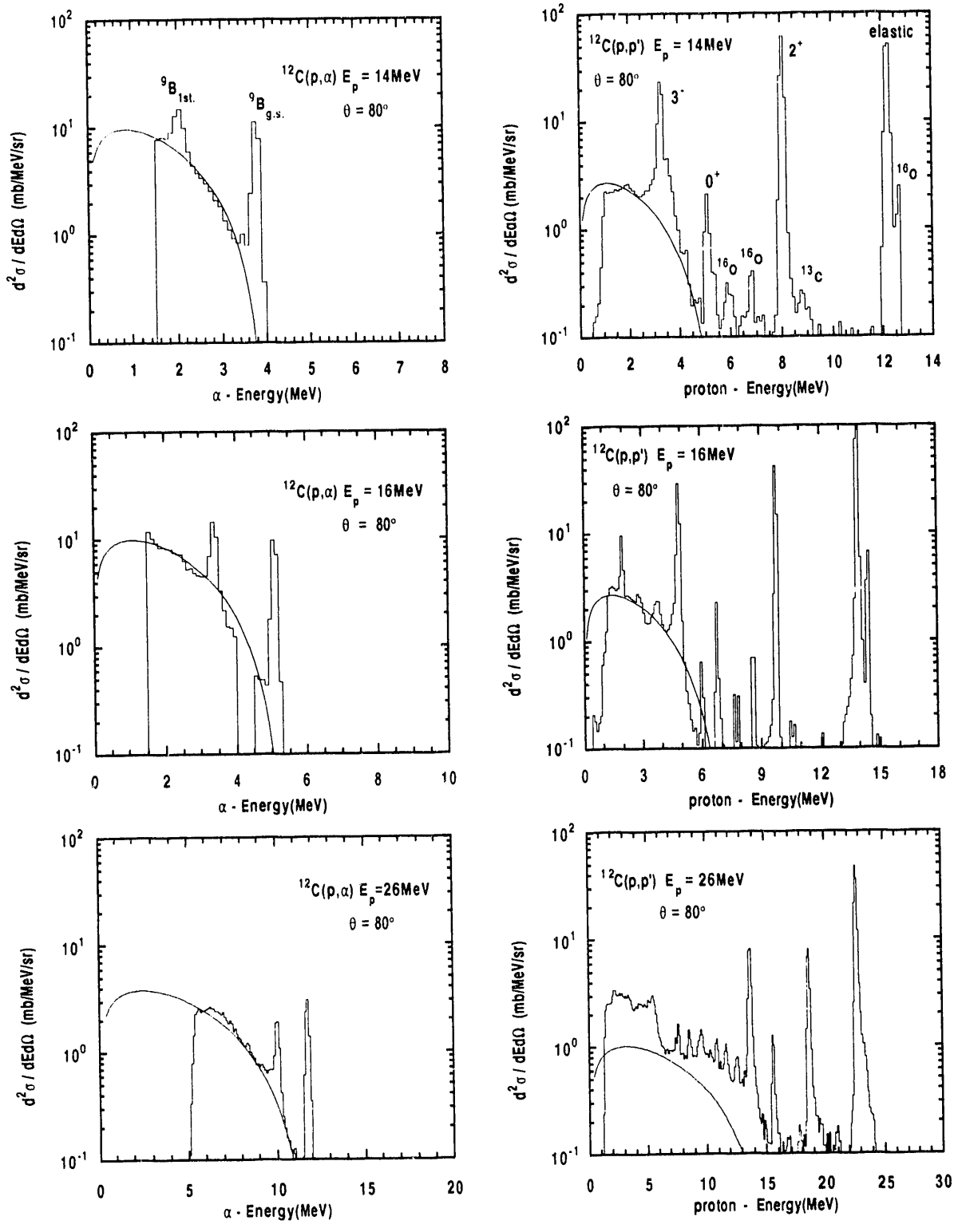

Fig. 1 Double differential cross sections of α particles and protons emitted from proton-induced reactions on ^{12}C into 80° at 14, 16 and 26 MeV. Histograms and solid lines are the experimental data[2,3] and the calculated 4BSB spectra, respectively.

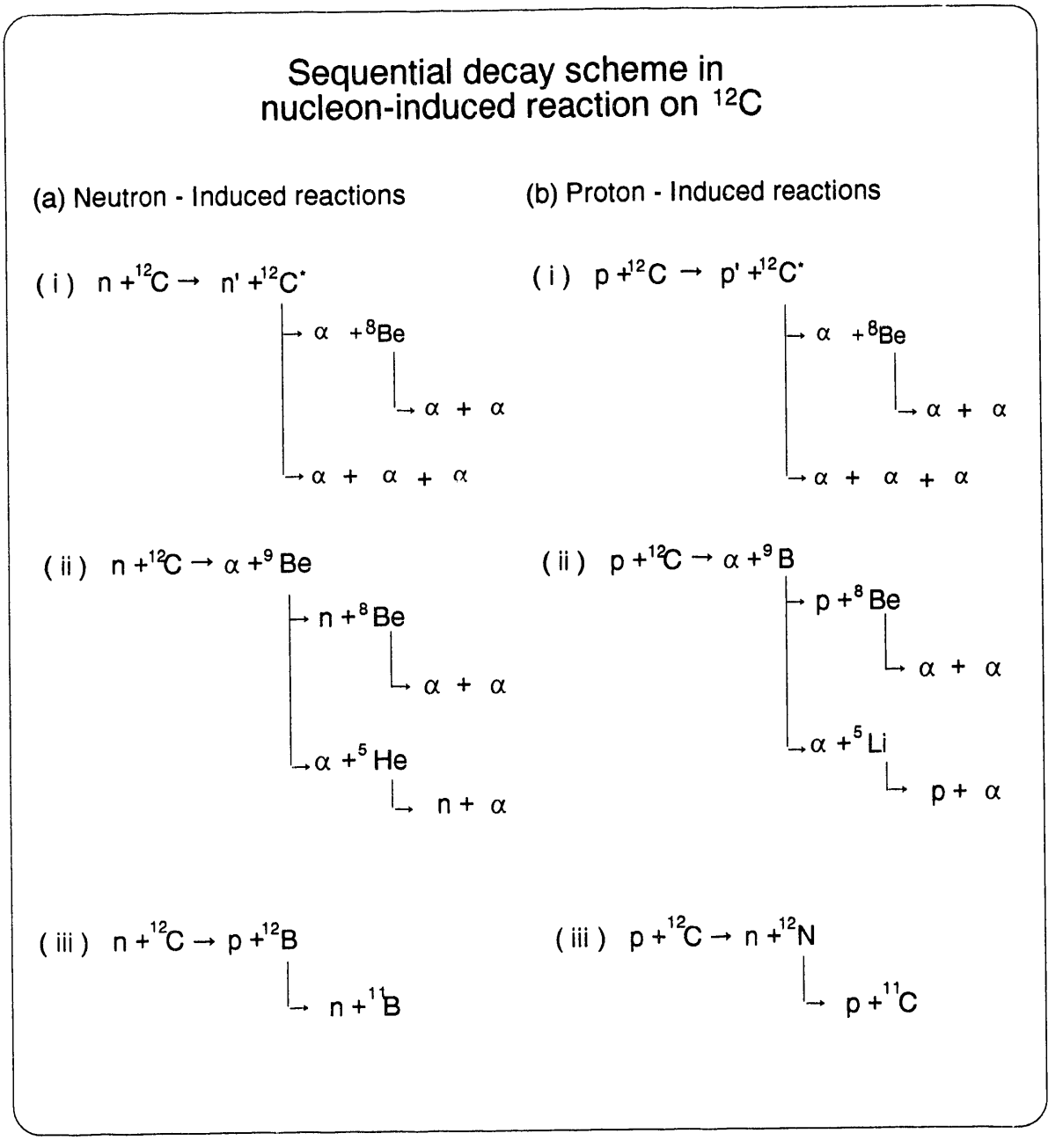

Fig. 2 A scheme of sequential decay processes in nucleon-induced reactions on ^{12}C. These processes can occur mainly at incident energies ranging from 10 MeV to 20 MeV.

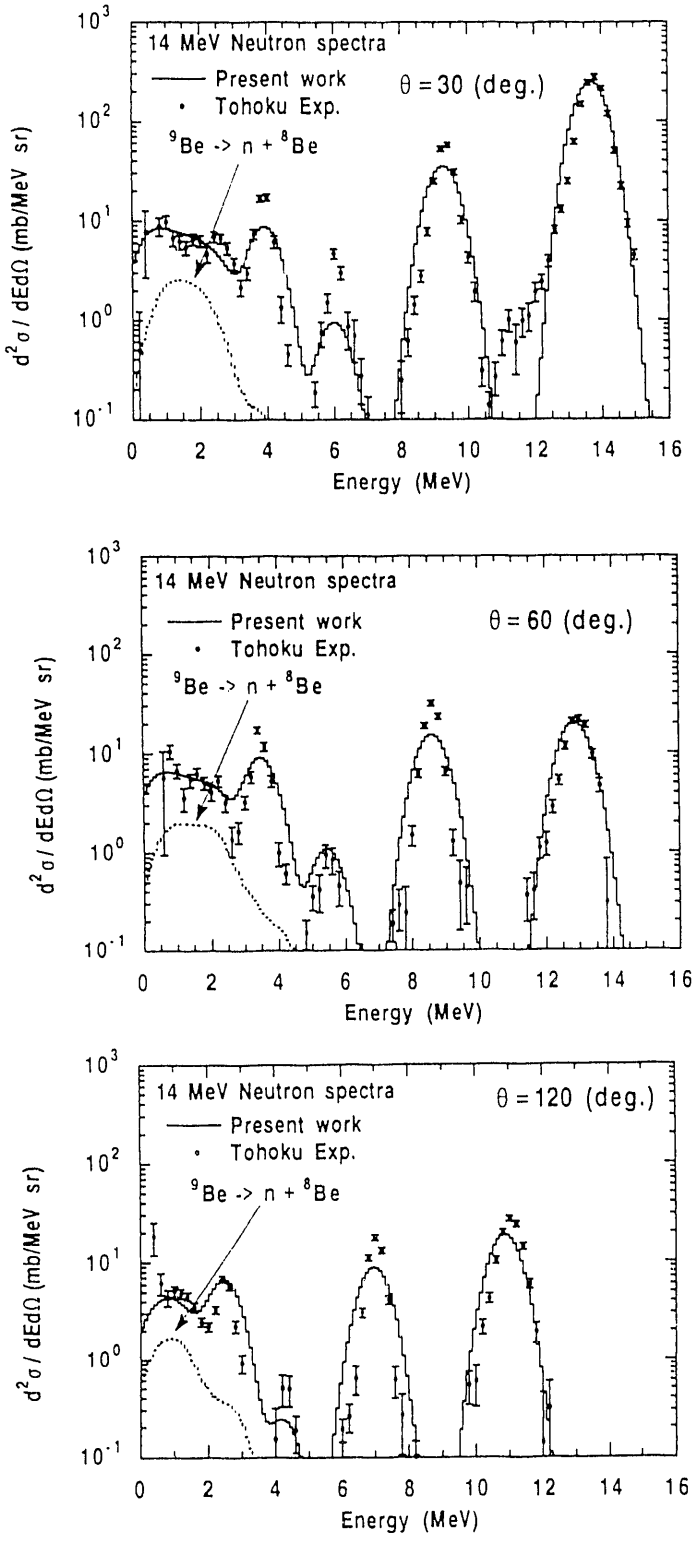

Fig. 3 Comparison between the experimental double differential neutron emission cross sections for reactions on ^{12}C with 14 MeV neutrons (closed circles) and those calculated by the Monte Carlo code (solid histograms). Dotted histograms represent neutron emission from the sequential decay via ^{9}Be.

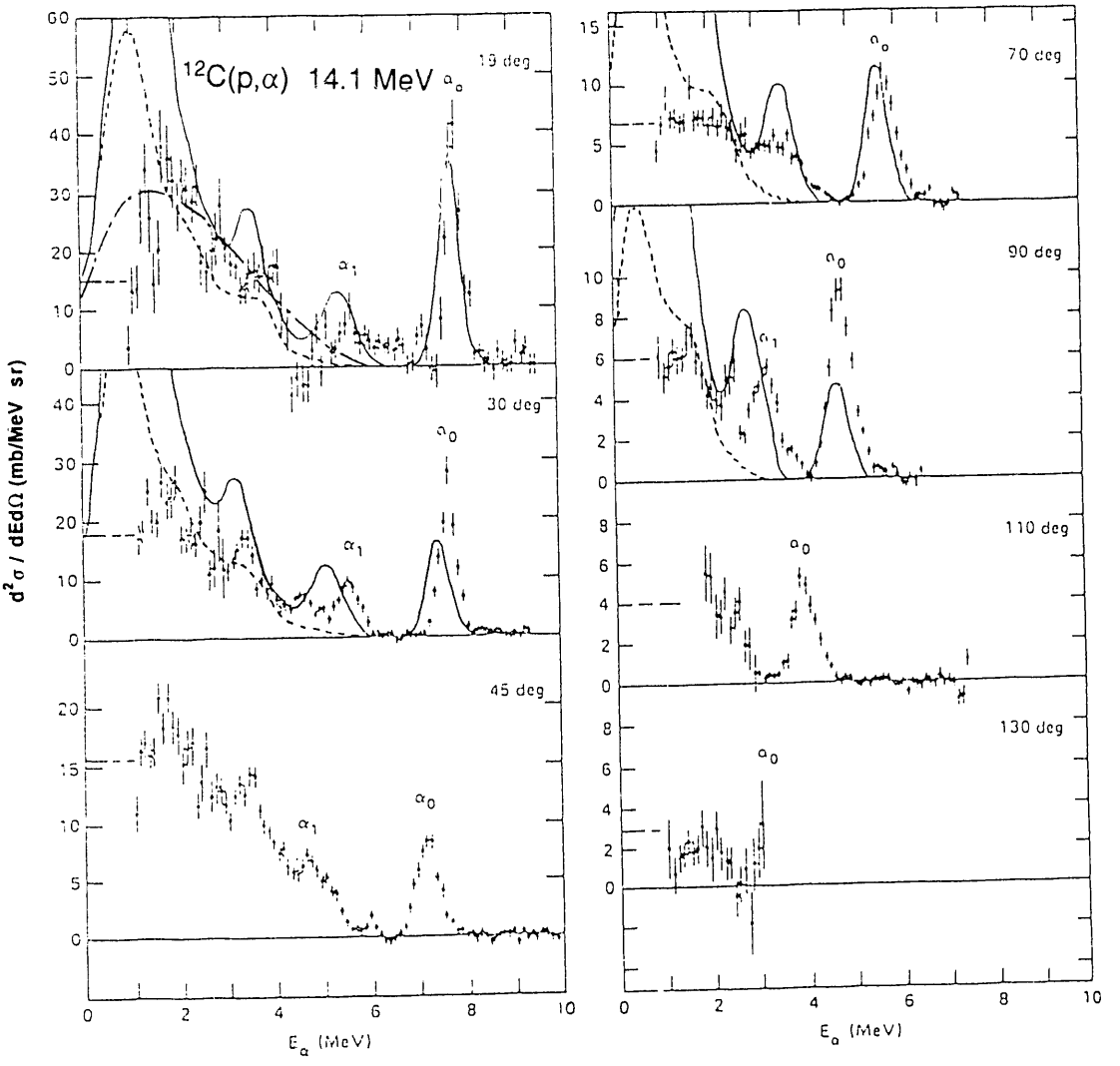

Fig. 4 Comparison between the experimental double differential cross sections of α particles emitted from ^{12}C induced by 14 MeV neutrons (solid circles) and those calculated by the Monte Carlo simulation code. Solid lines are the calculated spectra of total α emission. Dashed lines represent α emission from the sequential decay via ^{12}C. A dotted-dashed line for 19 deg is the 4BSB spectrum calculated with the phase space model. See the details in text.

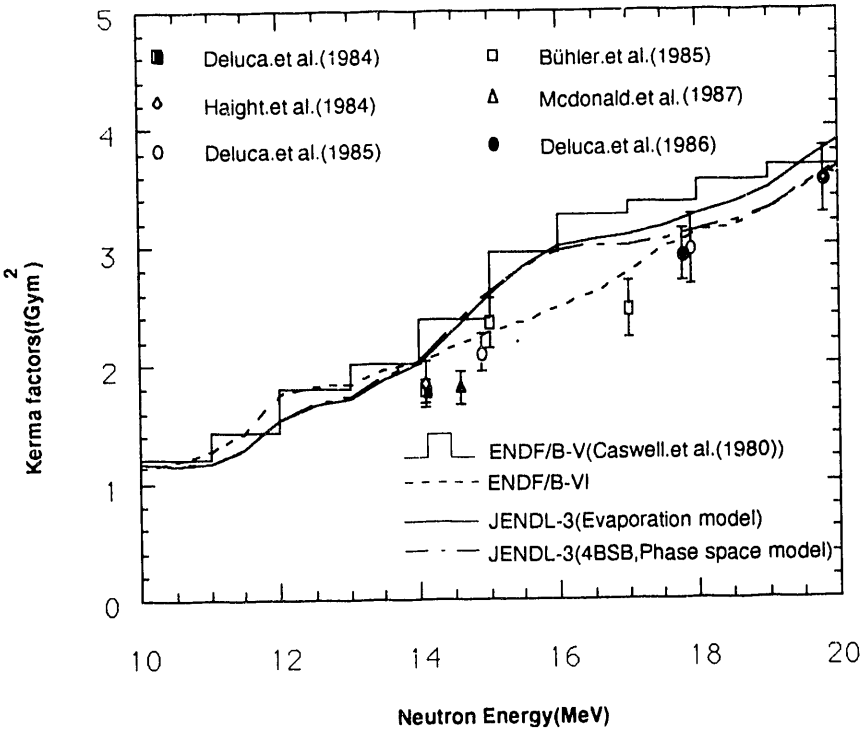

Fig. 5 Comparisons between the calculated kerma factors and the measured ones. See the details in text.

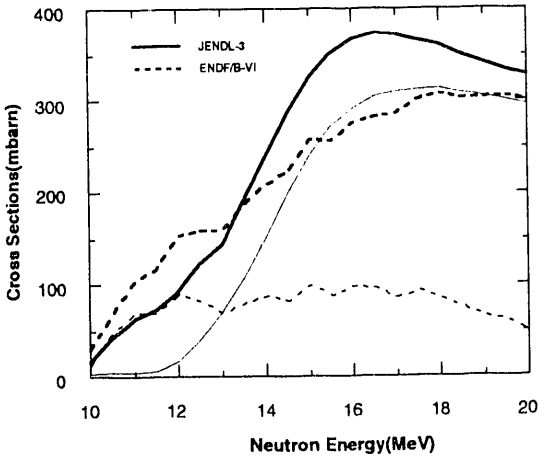

Fig. 6 The $^{12}C(n,n')3\alpha$ breakup cross sections obtained with the evaluated nuclear data files JENDL-3 (solid lines) and ENDF/B-VI (dashed lines). Thick and thin lines represent the total $^{12}C(n,n')3\alpha$ cross sections and the evaporation components of them, respectively.

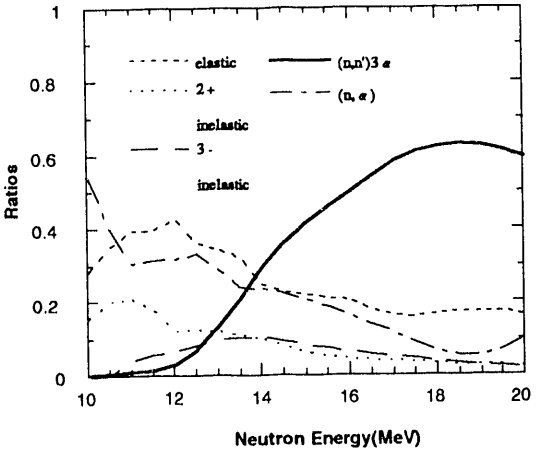

Fig. 7 Fraction of the partial kerma factors for each reaction process to the total kerma factor. The cross section data are taken from JENDL-3.

3.17 Measurement of Double Differential Charged-particle Emission Cross Sections for Reactions Induced by 20–40 MeV Protons (II)

Y. Watanabe, A. Aoto, H. Kashimoto, H. Hane, H. Sakaki, Y. Koyama, N. Koori,*
Y. Yamanouti**, M. Sugimoto**, S. Chiba**, T. Fukahori**,
K. Hasegawa**, and M. Mizumoto**

Department of Energy Conversion Engineering, Kyushu University,
Kasuga, Fukuoka 816, Japan
**College of General Education, The University of Tokushima, Tokushima 770, Japan*
***Japan Atomic Energy Research Institute, Tokai-mura, Ibaraki, 319-11 Japan*

Double differential charged-particle emission cross sections have been measured for proton-induced reactions on C, Si, ^{98}Mo, and ^{106}Pd at 25.6 MeV or 26 MeV, in order to investigate preequilibrium process and multiparticle breakup process. Dependence of continuum angular distributions on incident energy, target mass number and the kind of emitted particles is investigated to examine the applicability of systematics derived by Kalbach-Mann or Kumabe et al. The measured (p,xp) and (p,α) energy spectra are compared with those calculated using a code EXIFON based on the statistical multistep direct and compound (SMD/SMC) model.

1. Introduction

For the last few years, we have been carrying out measurements of double differential cross sections of charged-particles emitted from reactions on several nuclei with 20 - 40 MeV protons using the JAERI tandem accelerator.[1] This work was planned as an extension of the measurements performed in 10- 20 MeV region using the Kyushu University tandem accelerator.[2] The main purpose is to investigate the preequilibrium process in nucleon-induced reactions with medium-heavy nuclei and the multiparticle breakup process in those with light nuclei, and to apply the results to nuclear data evaluation in the intermediate energy range more than 20 MeV.

So far we have performed the experiments for C, Si, ^{98}Mo and ^{106}Pd at 25.6 MeV or 26 MeV. The experimental results and analyses for Si, ^{98}Mo and ^{106}Pd are described in this report; the result for C has been mentioned briefly elesewhere[3]. In the analysis, some systematic trends of continuum angular distribution are investigated, such as dependence on the incident energy, the target mass number and the kind of emitted particles, and the result is compared with the systematics derived by Kalbach-Mann[4] and Kumabe et al.[5] The

experimental (p,xp) and (p,α) spectra are also analyzed using a code EXIFON based on the SMD-SMC model[6], together with the (p,xn) spectra measured by other group[7].

2. Experimental Procedure

The experiments were performed using a 25.6 MeV or 26 MeV proton beam from the JAERI tandem accelerator. The details of the experimental procedure and the data processing have been reported elsewhere[1].

The proton beam was transported in a 50 cm ϕ scattering chamber which was installed in the N1 beam line; its current varied from about 50 nA to 300 nA, depending on the experimental condition. The following targets were chosen: ^{98}Mo (0.45 mg/cm^2), ^{nat}Si (0.2 mg/cm^2), ^{106}Pd (1.02 mg/cm^2) and ^{nat}C (0.1 mg/cm^2). All of them were self-supporting foils with their thickness given in the above parenthesis. A charged particle detecting system consisted of a ΔE-E counter telescope having two or three silicon surface barrier detectors. The electronic equipments used were commercially available standard NIM modules. A particle identification (PI) module was employed to separate signals corresponding to each emitted particle (protons, deuterons, tritons and α particles). Two output signals from the module, ΔE+E and PI, were stored as two-dimensional data using the Canberra MPA/PC Multiparameter system. Energy spectra of emitted charged particles were measured at intervals of 10° between 30° and 150°.

3. Experimental results

In Figs.1 and 2(a), the measured double differential cross sections of protons emitted into 40°, 90°, and 150° are shown by closed circles for Si, ^{98}Mo and ^{106}Pd. It should be noted that protons emitted with energies below about 7 MeV were not detected because they stopped completely in the ΔE detector. The spectrum at 40° for ^{106}Pd shows a broad elastic peak with quite poor resolution due to deterioration of the E-detector during the measurement. It is, however, confirmed that there is no problem with respect to the spectral shape and the magnitude at outgoing proton energies below 20 MeV of interest.

In the proton spectra shown in Figs. 1 and 2(a), one can see some differences depending on the target mass number. Both the spectra for ^{98}Mo and ^{106}Pd have the continuum region between 10 and 20 MeV and the angular distributions are peaked forward. For Si shown in Fig.1(a), however, many inelastic peaks are observed at energies above 14 MeV and the continuum below 13 MeV shows weaker forward peaked angular distributions than for ^{98}Mo and ^{106}Pd. The difference between ^{98}Mo and Si seems to depend on the relative fraction of compound process, as will be mentioned later.

Figure 2(b) shows the experimental energy spectra of α particles emitted into 40°, 90°, and 150° for ^{106}Pd by closed circles. Compared with the proton spectra in Fig.2(a), the α spectra have larger contribution from compound process that is seen as an appreciable

evaporation peak around 12 MeV. The preequilibrium region with forward peaked angular distributions is also observed at energies above 17 MeV.

4. Analyses and discussion

We have investigated some systematic trends of the experimental continuum angular distributions. The angular distribution in each energy bin of 1 MeV is fitted with the following Legendre polynomials up to $l_{max} = 4$:

$$\frac{d^2\sigma}{d\varepsilon d\Omega} = a_0(\varepsilon) \sum_{l=0}^{l_{max}} b_l(\varepsilon) P_l(\cos\theta)$$

and the polynomial coefficients $b_l(\varepsilon)$ are obtained, where the angle-integrated spectra $d\sigma/d\varepsilon$ are equal to $4\pi a_0(\varepsilon)$.

The coefficients $b_1(\varepsilon)$ of each emitted particles - p, n, d, and t - for ^{98}Mo are plotted as a function of the outgoing energy in Fig.3; the experimental data for the (p,n) reaction are taken from ref.[7]. There is an obvious difference between nucleon emission and complex particle emission; the values of $b_1(\varepsilon)$ for d and t are larger than those for p and n over the whole outgoing energy range. This indicates that the influence of direct process such as pickup process in deuteron and triton emission is large compared to nucleon emission. To investigate the incident energy dependence of $b_1(\varepsilon)$, the values obtained from 12-18 MeV (p,p') data[8] for ^{98}Mo are also plotted together with the present data in Fig.4. There is no appreciable dependence although the values are somewhat scattered at low outgoing energies. This result supports the systematics by Kalbach and Mann[4]. In addition, the values of $b_1(\varepsilon)$ are compared between Si and ^{98}Mo to investigate target mass number dependence of (p,p') continuum angular distributions in Fig.5. Those for ^{98}Mo are larger than for Si at outgoing energies between 10 and 18 MeV. This is presumably because compound component in the (p,p') reaction on Si is relatively larger than that on Mo.

In Fig.6, the experimental values $b_1(\varepsilon)$ for ^{98}Mo(p,p') are compared with those calculated using each systematics by Kalbach-Mann[4] and Kumabe et al.[5]. The distinction between SMD and SMC components was determined using the code EXIFON[6] described later. The calculated $b_1(\varepsilon)$ with the latter systematics are in better agreement with those with the former systematics at high outgoing proton energies over 15 MeV, where multistep direct process is dominant. Figures 7 (a) and (b) show the calculated angular distributions at two typical outgoing energies, 7.5 MeV and 18.5 MeV. To make comparison of the shape of angular distribution easy, the angle-integrated values are normalized to the experimental values. Both calculations reproduce well the shape of the experimental angular distributions except at backward angles more than 120° at 7.5 MeV. One the other hand, the shape is largely different between both the calculations at forward and backward angles at 18.5 MeV. The (p,p') angular distribution calculated using the systematics by Kumabe et al.[5] is in better agreement with the experimental one at intermediate angles.

The SMD/SMC model, one of quantum-mechanical models, was applied to calculations of double differential cross sections of protons, neutrons and α particles. The code EXIFON, which was modified in part so as to include the correction of recoil energy, was employed. The angular distributions were calculated using the systematics of Kumabe et al.[5] as one of the options in the code calculation. The strength of effective nucleon-nucleon interaction was fixed to be the recommended value of 27.5 MeV. Other input parameters were set to the default values, except a pairing energy and a phonon width; only the pairing energy of a residual nucleus was set to zero in the calculation of SMD process of (p,p') scattering and the phonon width was taken as 0.3 MeV, corresponding to the experimental resolution.

Some calculated results are shown by solid lines in Figs. 1 and 2(a) for the (p,xp) reactions and in Fig.2(b) for the (p,α) reaction. The calculated (p,xp) spectra are in overall good agreement with the experimental one for Si, ^{98}Mo and ^{106}Pd. However, underestimation of a few tens of percents is seen at low outgoing energies below 15 MeV for ^{98}Mo and ^{106}Pd (p,xp) spectra. This may be due to underprediction of the SMD component leading to forward peaked angular distribution, because the experimental angular distributions are still forward peaked as can be seen in Fig.7(a). On the other hand, the result of Si gives overestimation in low outgoing energy region as shown in Fig.1(a), although the agreement is rather good in high outgoing energy region. A measurement of energy spectra of protons with lower energies is desirable for further discussion on Si.

Compared to the (p,xp) spectra, the calculated (p,α) spectra do not reproduce the experimental ones quite well in shape and in magnitude as shown in Fig.4. Similar results were obtained in comparison between the experimental[9] and calculated spectra for 15 and 18 MeV (p,α) reactions on ^{106}Pd. The reason is still open at present.

In the analysis with the code EXIFON, we have investigated the sensitivity of proton optical model parameters (OMPs) to the (p,xp) and (p,xn) spectra. The result is shown in Fig.8; the proton OMPs used in the comparison are the global ones derived by Perey[10], Becchetti-Greenlees[11], and Menet et al.[12] The calculated (p,xp) spectra depend strongly upon the proton OMPs; the difference among them becomes more than 30% at maximum. On the other hand, the effect on the (p,xn) spectra is small. Therefore, suitable choice of the OMP seems to be essential in the calculation of charged-particle emission spectra.

5. Summary

We have performed the experiments to measure the double differential cross sections of emitted charged-particles from proton-induced reactions on C, Si, ^{98}Mo and ^{106}Pd at 25.6 MeV or 26 MeV. The experimental continuum angular distributions were fitted to the Legendre polynomials up to the 4th order and systematic trends of the obtained Legendre coefficients were investigated, i.e., the dependence on incident energy, target mass number, and the kind of emitted particles. Consequently, the usefulness of the systematics of Kumabe

et al.[5] has been found in the case of nucleon emission. The EXFION calculations with their systematics showed overall good agreement with the experimental (p,xp) spectra, although the calculated (p,α) spectra for ^{106}Pd were not in agreement with the experimental ones in both shape and magnitude. Further study will be necessary to resolve the disagreement.

In future, we intend to perform similar experiments of proton-induced reactions over the wide mass range in order to investigate the preequilibrium process for medium-heavy nuclei and the multiparticle breakup process for light nuclei in more details.

Acknowledgements

The authors wish to thank the members of the accelerator division of JAERI for their kind help during the experiment. One of the authors (Y.W) is also indebted to Dr. H. Kalka for the use of his code EXFION. This work was supported in part by the Grant-in-Aid of the Japanese Ministry of Education, Science and Culture.

References

1) A. Aoto et al., *Proceedings of the 1991 Seminar on Nuclear Data*, JAERI-M 92-027, pp. 330 (1992).
2) See for instance, Y. Watanabe et al., *Proceedings of the XX th Int. Symp. on Nuclear Physics, Nuclear Reaction Mechanism*, Germany, Nov. 12-16, 1990, pp. 151.
3) H. Kashimoto et al., To be published in *Proceedings of the 1992 Seminar on Nuclear Data*, Nov. 26-27, 1992, JAERI, Tokai, Japan.
4) C. Kalbach and F.M. Mann, Phys. Rev. C **23**, 112 (1981).
5) I. Kumabe et al., Nucl. Scie. & Eng. **104**, 280 (1990).
6) H. Kalka, Z. Phys. **A341**, 289 (1992).
7) E. Mordhorst et al., Phys. Rev. C **34**, 103 (1986).
8) Y. Watanabe et al., Z. Phys. **A 336**, 63 (1990).
9) I. Kumabe et al., Phys. Rev. **C 35**, 467 (1987).
10) F.G. Perey, Phys. Rev. **131**, 745 (1963).
11) F.D. Becchetti and G. W. Greenlees, Phys. Rev. **182**, 1190 (1969).
12) J.J.H. Menet et al., Phys. Rev. C **4**, 1114 (1971).

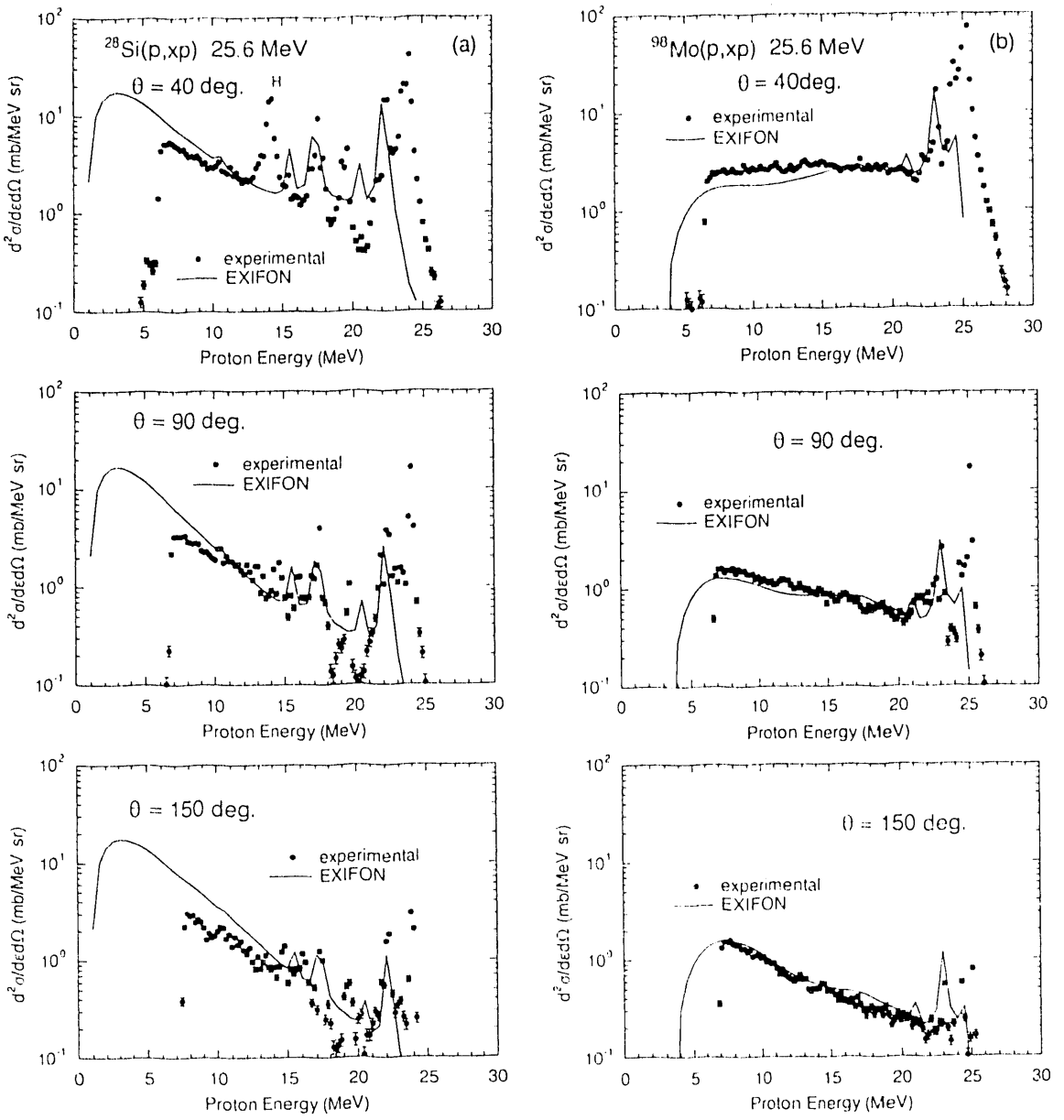

Fig. 1 Experimental double differential proton emission cross sections of (a) Si(p,xp) reaction and (b) ^{98}Mo(p,xp) reaction at 25.6 MeV and those calculated using the code EXIFON.

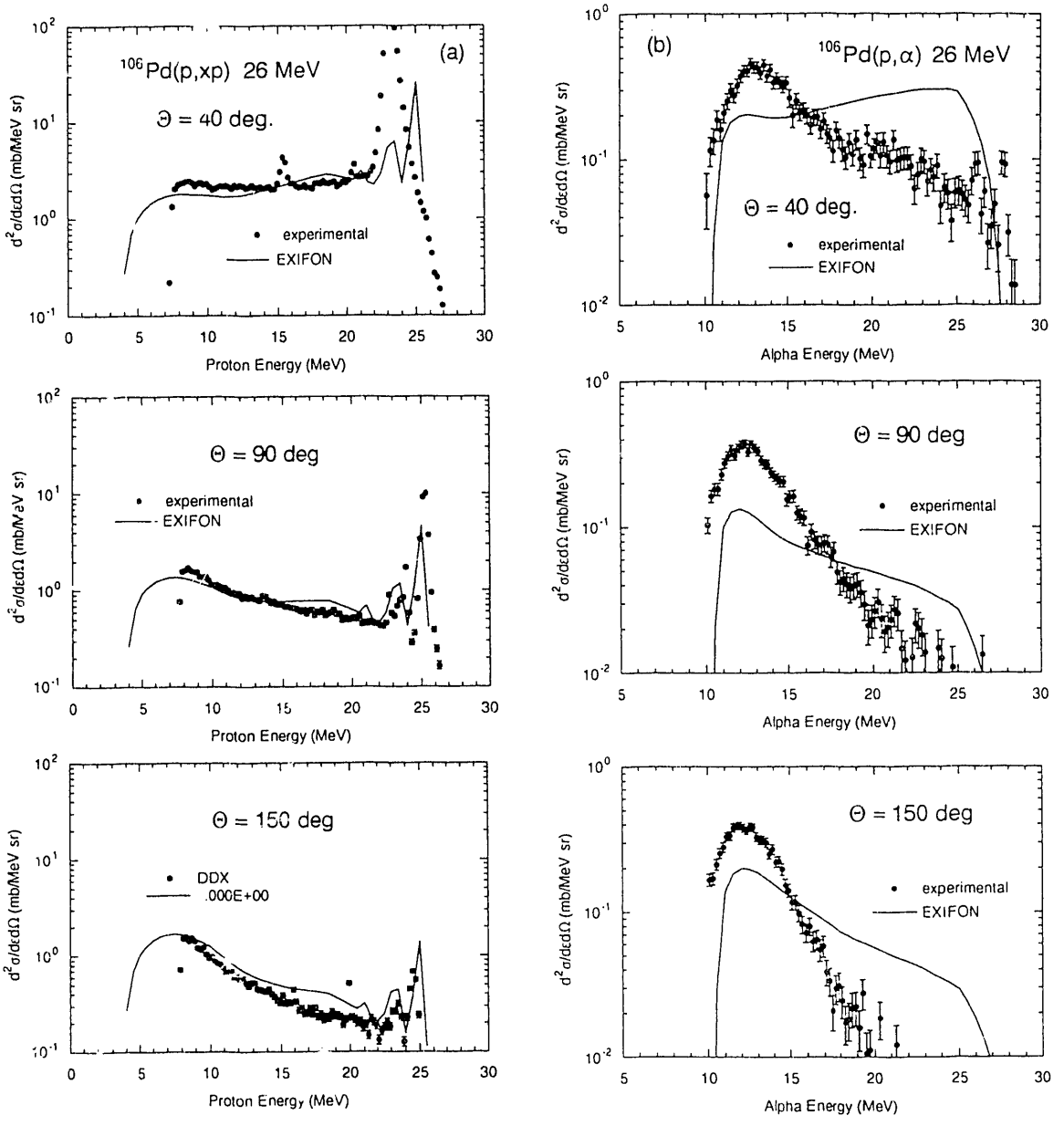

Fig. 2 Experimental double differential cross sections of (a) (p,xp) and (b) (p,α) reaction on ^{106}Pd at 26 MeV and those calculated using the code EXIFON.

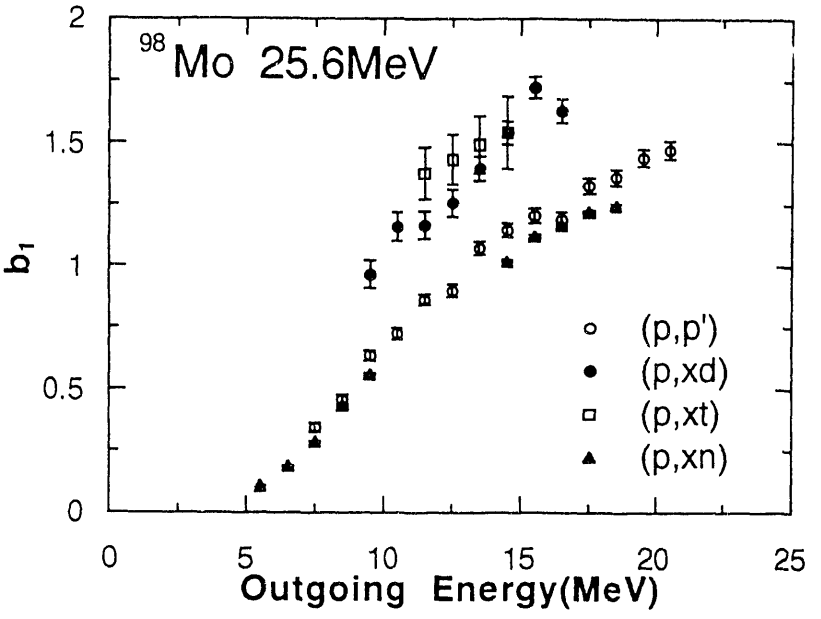

Fig. 3 Dependence of the Legendre coefficients $b_l(\varepsilon)$ on the kind of emitted particles for 25.6 MeV (p,xp) reaction with ^{98}Mo.

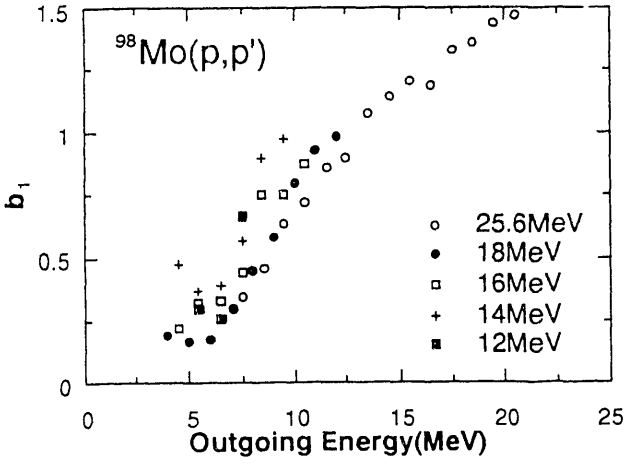

Fig. 4
Dependence of the Legendre coefficients $b_l(\varepsilon)$ on the incident energy for ^{98}Mo(p,p') reactions in the proton energy range from 12 to 25.6 MeV.

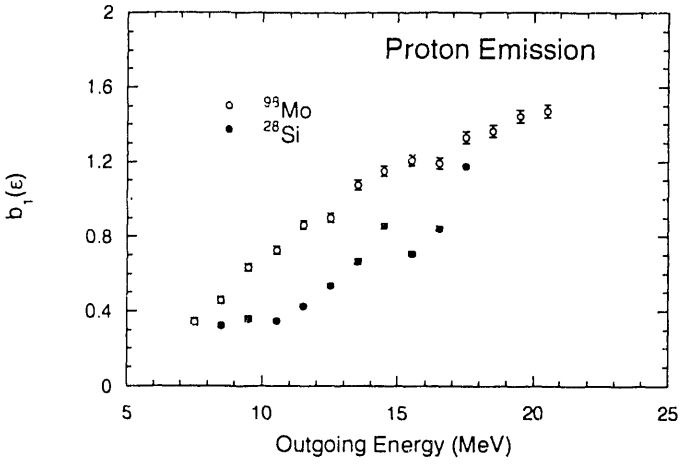

Fig. 5
Comparison of the Legendre coefficients $b_l(\varepsilon)$ between Si(p,p') reaction and ^{98}Mo(p,p') reaction at 25.6 MeV.

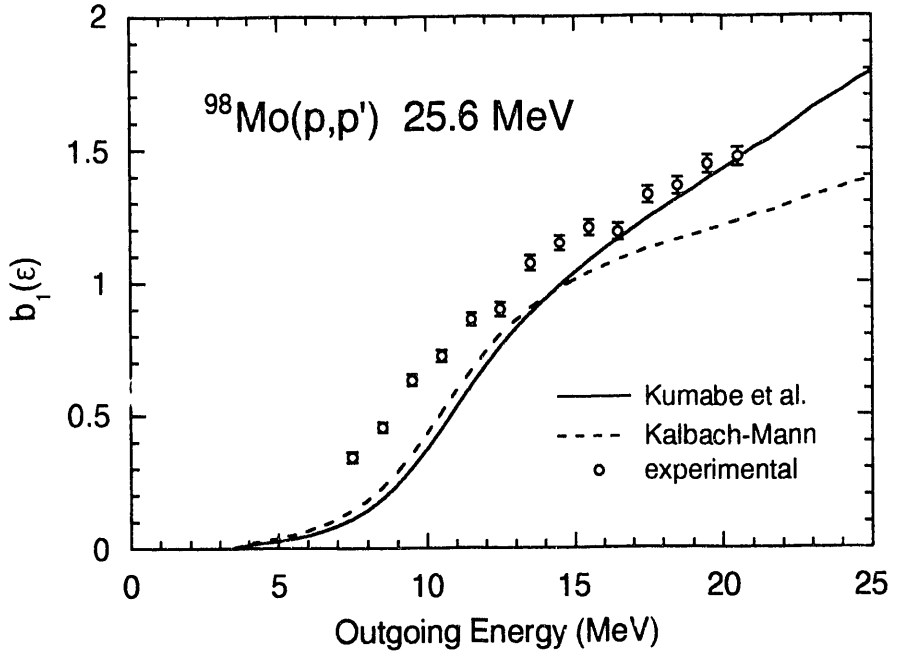

Fig. 6 Comparison between the experimental Legendre coefficients $b_l(\varepsilon)$ and the calculated ones for $^{98}Mo(p,p')$ at 25.6 MeV. The solid line is the values $b_l(\varepsilon)$ calculated using the systematics derived by Kumabe et al.[5] and the dashed line is those based on Kalbach-Mann systematics[4].

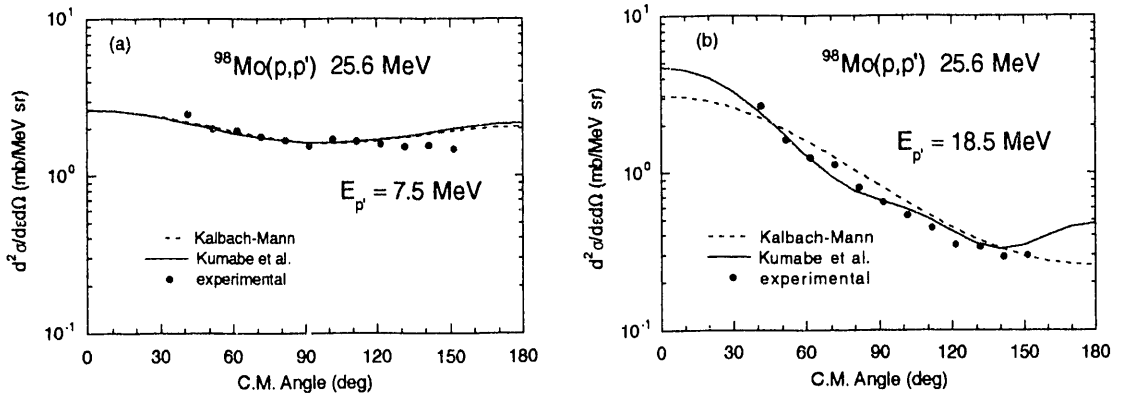

Fig. 7 Experimental and calculated angular distributions for $^{98}Mo(p,p')$ at outgoing proton energies of (a) 7.5 MeV and (b) 18.5 MeV. The solid and the dashed curves are angular distributions calculated using the systematics by Kumabe et al.[5] and Kalbach-Mann[4], respectively.

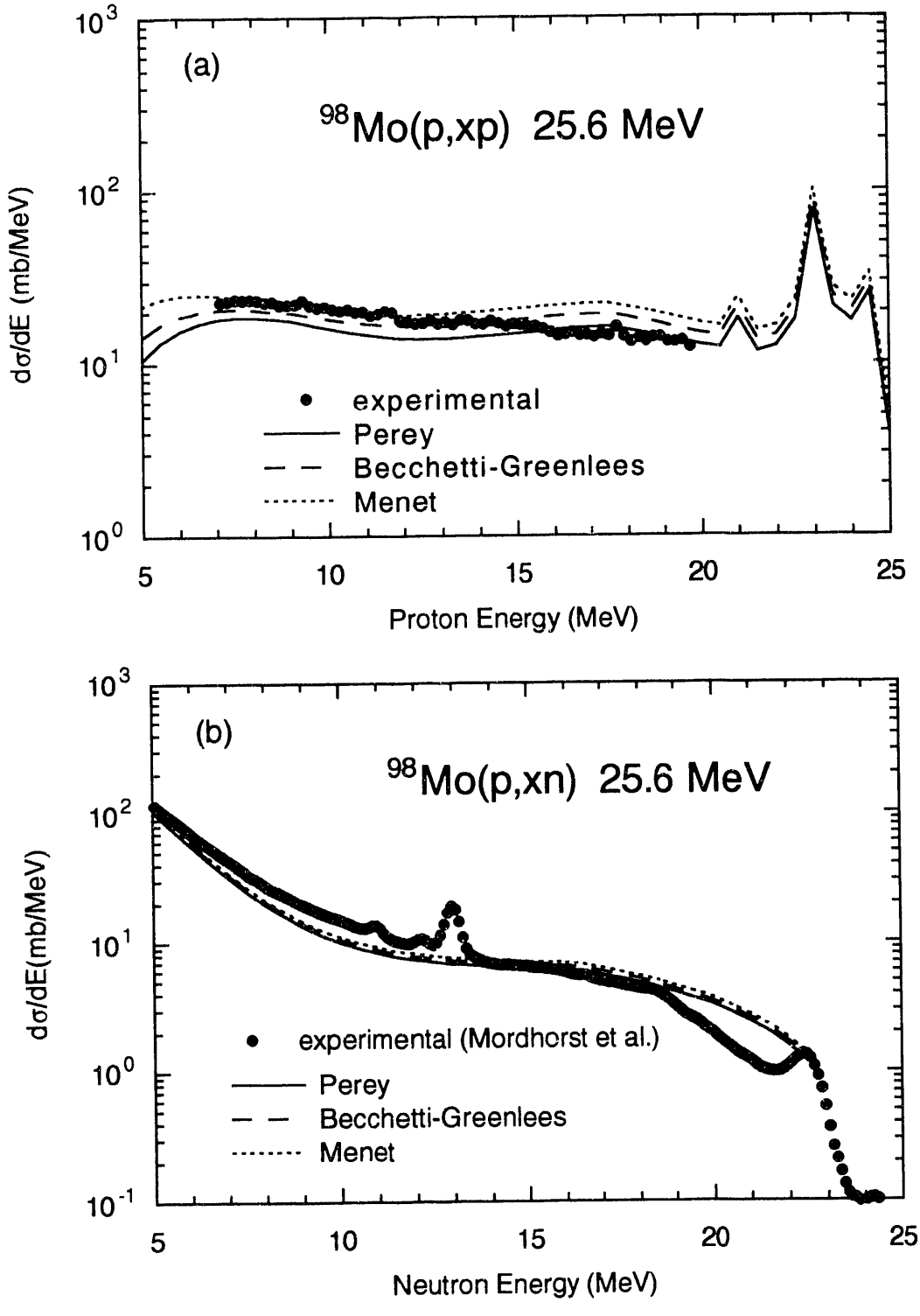

Fig. 8 Sensitivity of the proton optical model parameter to ^{98}Mo(p,xp) and (p,xn) spectra calculated using the EXIFON.

3.18 Elastic and Inelastic Proton Scattering from Light Nuclei (II) — ^{14}N and ^{16}O —

N. Koori, Y. Koyama*, Y. Watanabe*, H. Kashimoto*, H. Sakaki*,
H. Shinohara*, T. Michibata*, H. Ijiri*, A. Nohtomi**
K. Sagara+, H. Nakamura+, K. Maeda+, and T. Nakashima+

College of General Education, The University of Tokushima, Tokushima 770, Japan
**Department of Energy Conversion Engineering, Kyushu University, Kasuga, Fukuoka 816, Japan*
***Department of Nuclear Engineering, Kyushu University, Fukuoka 812, Japan*
+Department of Physics, Kyushu University, Fukuoka 812, Japan

Differential cross sections and analyzing powers of elastic and discrete inelastic proton scattering have been measured for ^{14}N and^{16}O with polarized protons of 14 and 16 MeV in order to investigate nucleon scattering from 1p-shell nuclei. These data are analyzed together with the previous data on ^{12}C using the spherical optical model and the coupled channels method.

1. Introduction

We have been studying the interaction of nucleon with light nuclei (1p-shell nuclei) in the incident energy range of 10-20 MeV in order to establish reliable theories and models for evaluation of neutron nuclear data for applications.[1-5] In the present work, differential cross sections and analyzing powers of elastic and discrete inelastic proton scattering from ^{14}N and ^{16}O have been measured at incident energies of 14 and 16 MeV. These data are compared with available neutron data, and analyzed on the basis of the spherical optical model (SOM) and the coupled-channels (CC) method. A result of reanalysis of the previous data[3,4] on ^{12}C is also reported.

2. Experimental procedures

These experiments have been carried out with a polarized proton beam from the Kyushu University tandem accelerator. The details of the experimental procedure have been described elsewhere[5]. Commercial nitrogen and oxygen were used as target gas: their purities are 99.9999% and 99.5%, respectively, and isotopic contents of ^{14}N and ^{16}O are 99.635% and 99.759%, respectively. The gas was filled at a pressure of 0.4 atm (at room temperature) in a gas cell of a stainless steel cylinder of 38 mm in diameter and of 34 mm in height. The cell

windows were 2.2 μm havar foils for the beam entrance and exit and 6 μm mylar foils for scattered protons. A counter telescope having three silicon surface barrier detectors with double slit geometry was used to detect the scattered protons: the first slit with opening of 2 mm was located 23.8 mm for ^{16}O experiment (or 24 mm for ^{14}N experiment) from the center of the gas cell and the second slit was located just in front of ΔE detector and the distance from the first slit was 178.2 mm (or 180 mm).

3. Experimental results and analyses

3.1 $^{14}N(\vec{p},p)$ and $(\vec{p},p')$ scattering at 14 and 16 MeV

Figures 1 shows experimental differential cross sections and analyzing powers of proton elastic scattering from ^{14}N at 14 and 16 MeV by solid circles. Seven low lying peaks corresponding to inelastic scattering were also processed, and differential cross sections and analyzing powers were obtained. These results are in reasonably good agreement with the previous 14.6 MeV data measured by Hansen et al.[6]

The experimental elastic scattering data were analyzed by the spherical optical model (SOM) using the potential of a standard form with a Woods-Saxon real volume term, surface derivative imaginary and spin-orbit terms. SOM fits were made to the elastic differential cross sections and analyzing powers using the code ECIS79[7]. The results of the SOM fits are shown in Fig.1 and the obtained OMP parameters are listed in Table I. The OMP parameter set derived by Dave and Gould[8] was used as an initial one (Set 0) after the fixed Coulomb correction $\Delta V=0.4Z/A^{1/3}$ was made in a real volume potential. A parameter set denoted by Set 1 is the result of all parameters research including potential well depth and geometrical parameters. There is a large difference between Set 0 and Set 1 in the spin-orbit term; the present search leads to remarkably small diffuseness. A parameter search was made again with all fixed geometrical parameters for 14 and 16 MeV. The result is given as Set 2. The agreement with the experimental data becomes rather worse at 14 MeV. Finally, OMP parameters were searched with the potential incorporating an imaginary spin-orbit term $W_{s.o}$. The fits to the experimental data are improved slightly at 14 MeV, but becomes worse in the differential cross sections at 16 MeV as shown in Fig.1 and Table I. The effect of resonance structure and coupling of the excited states is known to appear in nucleon scattering from light nuclei such as ^{14}N at low incident energies. Such effect should, therefore, be taken into account to draw a clear conclusion on the importance of $W_{s.o}$ term.

3.2 $^{16}O(\vec{p},p)$ and $(\vec{p},p')$ scattering at 14 and 16 MeV

Figure 3 shows experimental differential cross sections and analyzing powers of proton elastic scattering from ^{16}O at 14 and 16 MeV with the results of SOM fits. The procedure of the

SOM fits is the same as that for ^{14}N. The obtained SOM parameters are listed in Table I. The same parameter set [8] as for ^{14}N was input as the initial values given in the column Set 0. Overall good fits are obtained for both differential cross sections and analyzing powers. The parameters have small diffuseness of spin-orbit and surface imaginary terms. This is true of ^{14}N in Table I.

As shown in Fig.3, a remarkable difference between 14 and 16 MeV is observed in the measured analyzing powers around 90°. This may suggest strong resonance structure in the compound nucleus ^{17}F; a broad $f_{7/2}$ single particle level in ^{17}F around 17.5 MeV[9] and appreciably sharp resonance at 14.7 MeV in the elastic scattering excitation functions[10] have been reported. The experimental values are, however, reproduced fairly well by the SOM calculations using sets of parameters with potential well depths of imaginary and spin-orbit terms different largely between 14 and 16 MeV as shown in Table II.

The differential cross sections for 14 MeV (closed circles) are compared with neutron data[11] (open circle) in Fig.3. Both the proton and neutron data show fairly good agreement in shape as well as in magnitude, although there are some differences around 50° and at backward angles in elastic angular distributions.

3.3 Analysis of $^{12}C(\vec{p},p)$ and $(\vec{p},p')$ scattering at 14 and 16 MeV

SOM parameters for ^{12}C were searched again in the same manner as described for ^{14}N and ^{16}O. The result is shown in Fig.4 and Table III. Initial parameters (Set 0) were chosen to be the values taken from ref.12) with the correction of the Coulomb term. The agreement with the experimental analyzing powers is improved obviously in the case of a parameter set (Set 3) including an imaginary spin-orbit term.

Coupled-channels (CC) analysis was also performed using the code ECIS79. The coupling between the 0^+ ground state and the 2^+ excited state, as second member of the $K^\pi = 0^+$ rotational band, was taken into account in the calculation. Only the potential well depths and the quadrupole deformation parameters β_2 were searched with the geometrical parameters obtained from the SOM analysis. The result is shown in Fig.5 and Table IV. Both elastic and inelastic scattering data are reproduced fairly well by the CC calculation, although there is underestimation for inelastic scattering cross sections at forward angles. This disagreement may be due to the possible resonance influences.[8,12] Analyses including the effect of coupling with other states and of compound process would be required.

4. Concluding remarks

Differential cross sections and analyzing powers of proton elastic and inelastic scattering from ^{14}N and ^{16}O were measured at 14 and 16 MeV. Each optical potential parameter for ^{14}N and ^{16}O was derived from the SOM analysis. In the SOM fits, an effort was made to improve

the agreement with the experimental data by incorporating an imaginary spin-orbit potential. The previous data on ^{12}C were also analyzed with the SOM model, and then the CC analysis was applied to elastic and inelastic scattering ($J=2^+$,Q=-4.44 MeV) on ^{12}C using a rotational model. The result shows a reasonably good agreement between measured and calculated data. In future, it would be necessary to investigate the effects of resonance structure and compound nucleus process.

References

1) N. Koori et al., JAERI-M 89-167 (1989)
2) N. Koori et al., JAERI-M 91-009 (1991)
3) N. Koori et al., JAERI-M 92-029 (1992)
4) Y. Watanabe et al., *Proc. Int. Conf. on Nuclear Data for Science and Technology, May 13-17, 1991, Julich, Germany,* ed. S.M. Qaim , (Spring-Verlag, Berlin, 1992), p. 1002
5) N. Koori et al., *Proc. of the 1991 Symposium on Nuclear Data, Nov. 28-29, 1991, JAERI, Tokai, Japan,* JAERI-M 92-027 (1992)
6) L.F. Hansen et al., Phys. Rev. C **8**, 2072 (1973)
7) J. Raynal, code ECIS79, unpublished: J. Raynal, *Workshop on Applied Nuclear Theory and Nuclear Model calculations for Nuclear Technology Applications*, Trieste, Italy (1988), Ed. M.K. Mehta and J.J. Schmidt (World Scientific 1989), p.506
8) J.H. Dave and C.R. Gould, Phys. Rev. C **28**, 2212 (1983)
9) H.R. Hiddleston, J.A. Aymar and S.E. Darden, Nucl. Phys. **A242**, 323 (1975)
10) S. Kobayashi, J. Phys. Soc. Japan **15**, 1164 (1960)
11) M. Baba et al., Fast Neutron Laboratory Report NETU-50, Tohoku University (1988)
12) E.Woye et al., Nucl. Phys. **A394**, 139 (1983)

Table I A list of the SOM parameters obtained in the present analysis for ^{14}N. Each parameter set is as follows: ref.7) (Set 0), all parameter search (Set 1), search with a fixed geometrical parameter (Set 2), and the same as Set 2 except the inclusion of imaginary spin-orbit term (Set 3). Potential well depths in MeV and geometrical parameters in fm.

	Set0		Set1		Set2		Set3	
	14MeV	16MeV	14MeV	16MeV	14MeV	16MeV	14MeV	16MeV
V_R	51.62	51.61	50.48	50.61	52.26	50.67	53.00	48.96
r_R	1.209	1.209	1.245	1.247	1.246	1.246	1.246	1.246
a_R	0.573	0.573	0.623	0.524	0.573	0.573	0.573	0.573
W_D	21.91	23.32	18.27	14.53	16.95	15.60	17.14	16.71
r_I	1.415	1.415	1.497	1.423	1.460	1.460	1.460	1.460
a_I	0.105	0.105	0.103	0.130	0.116	0.116	0.116	0.116
$V_{S.O.}$	5.500	5.500	4.115	4.480	3.738	3.947	4.319	4.832
$W_{S.O.}$							0.056	0.413
$r_{S.O.}$	1.150	1.150	0.955	0.955	0.955	0.955	0.955	0.955
$a_{S.O.}$	0.500	0.500	0.180	0.033	0.180	0.180	0.180	0.180
$(\chi 2/N)\sigma$			1.063	0.830	3.730	0.757	3.451	1.134
$(\chi 2/N)A_y$			19.75	17.30	29.31	13.37	28.65	3.566
$(J/A)_V$	527.9	527.8	581.6	534.4	575.6	558.1	583.7	539.3
$(J/A)_D$	96.4	102.6	88.2	80.1	87.7	80.7	88.7	86.5
$(J/A^{1/3})_{V_{S.O.}}$	159.0	159.0	98.8	107.5	89.7	94.7	103.7	116.0
$(J/A^{1/3})_{W_{S.O.}}$							1.34	9.91

Table II A list of the SOM parameters obtained in the present analysis for ^{16}O. Same as Table I for each column.

	Set0		Set1		Set2		Set3	
	14MeV	16MeV	14MeV	16MeV	14MeV	16MeV	14MeV	16MeV
V_R	48.78	48.67	53.70	49.46	48.82	54.62	48.78	54.33
r_R	1.255	1.255	1.201	1.276	1.238	1.238	1.238	1.238
a_R	0.536	0.536	0.479	0.621	0.550	0.550	0.550	0.550
W_D	12.20	13.31	6.724	15.83	7.409	13.17	7.480	13.89
r_I	1.352	1.352	1.346	1.426	1.386	1.386	1.386	1.386
a_I	0.205	0.205	0.212	0.152	0.182	0.182	0.182	0.182
$V_{S.O.}$	5.5	5.5	6.392	2.828	5.064	3.153	5.098	2.884
$W_{S.O.}$							-0.056	0.305
$r_{S.O.}$	1.15	1.15	0.935	1.237	1.086	1.086	1.086	1.086
$a_{S.O.}$	0.5	0.5	0.385	0.260	0.322	0.322	0.322	0.322
$(\chi 2/N)\sigma$			3.35	8.26	9.93	21.45	9.90	20.33
$(\chi 2/N)A_y$			6.23	52.61	28.57	44.38	28.52	34.74
$(J/A)_V$	543	541	505	623	532	595	532	592
$(J/A)_D$	101.8	111.1	57.5	108	57.5	102	58.0	107
$(J/A^{1/3})_{V_{S.O.}}$	159	159	150	87.9	138	86.1	139	78.7
$(J/A^{1/3})_{W_{S.O.}}$							-1.53	8.32

Table III A list of the SOM parameters obtained in the present analysis for ^{12}C. Same as Table I for each column except Set 0, an initial parameter set taken from ref.12.

	Set0		Set1		Set2		Set3	
	14MeV	16MeV	14MeV	16MeV	14MeV	16MeV	14MeV	16MeV
V_R	55.52	54.92	74.83	67.70	58.38	58.44	57.48	57.22
r_R	1.06	1.06	0.882	1.000	1.06	1.06	1.06	1.06
a_R	0.54	0.54	0.656	0.612	0.54	0.54	0.54	0.54
W_D	6.66	6.34	8.026	20.560	8.570	6.390	8.041	6.371
r_I	1.54	1.54	1.457	1.451	1.54	1.54	1.54	1.54
a_I	0.28	0.28	0.912	0.090	0.28	0.28	0.28	0.28
$V_{S.O.}$	7.88	7.12	7.605	7.185	8.690	7.743	8.800	7.952
$W_{S.O.}$	0.83	0.83					1.190	0.793
$r_{S.O.}$	0.76	0.76	0.002	0.884	0.76	0.76	0.76	0.76
$a_{S.O.}$	0.36	0.36	-0.08	0.276	0.36	0.36	0.36	0.36
$(\chi 2/N)\sigma$			11.98	52.08	81.15	101.1	38.21	85.63
$(\chi 2/N)A_y$			33.04	81.60	83.17	280.7	30.33	192.1
$(J/A)_V$	412	408	439	483	434	434	427	425
$(J/A)_D$	99.1	94.4	425	86.1	128	95.1	120	94.8
$(J/A^{1/3})_{V_{S.O.}}$	15.1	136	0.382	160	166	148	168	152
$(J/A^{1/3})_{W_{S.O.}}$	15.9	15.9					22.7	15.1

Table IV Numerical results from the CC analysis of p-^{12}C scattering. Potential well depths in MeV and geometrical parameters in fm.

E_p	14 MeV	16 MeV
V_R	61.97	57.57
r_R	1.06	1.06
a_R	0.54	0.54
W_D	1.994	2.862
r_I	1.54	1.54
a_I	0.28	0.28
$V_{s.o.}$	6.233	5.746
$W_{s.o.}$	0.986	0.401
$r_{s.o.}$	0.76	0.76
$a_{s.o.}$	0.36	0.36
β_2	-0.74	-0.59

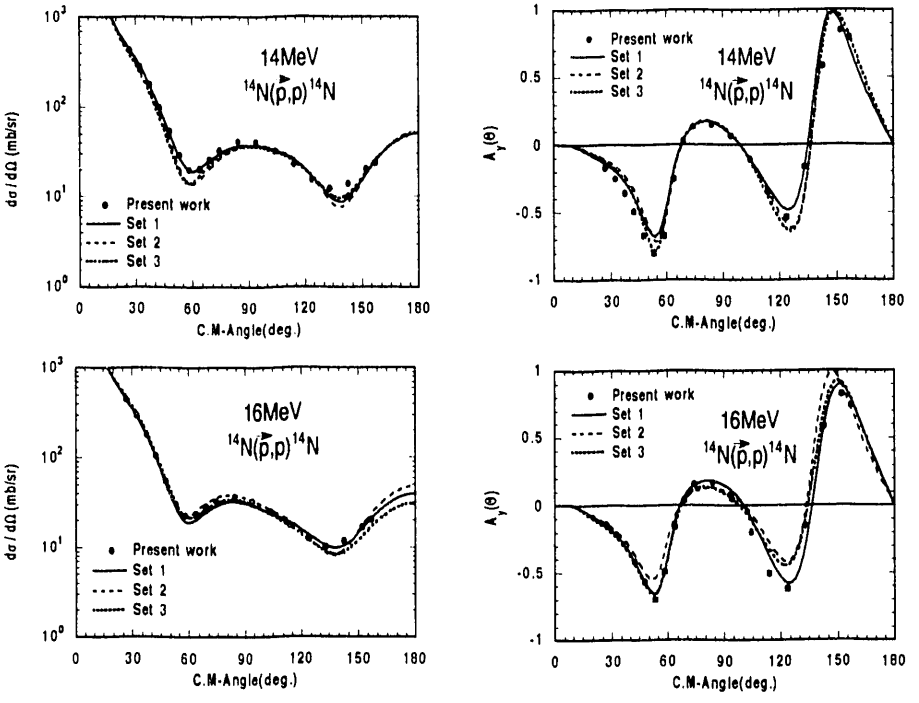

Fig. 1 Experimental differential cross sections and analyzing powers of ^{14}N(p,p) scattering at 14 and 16 MeV and SOM fits.

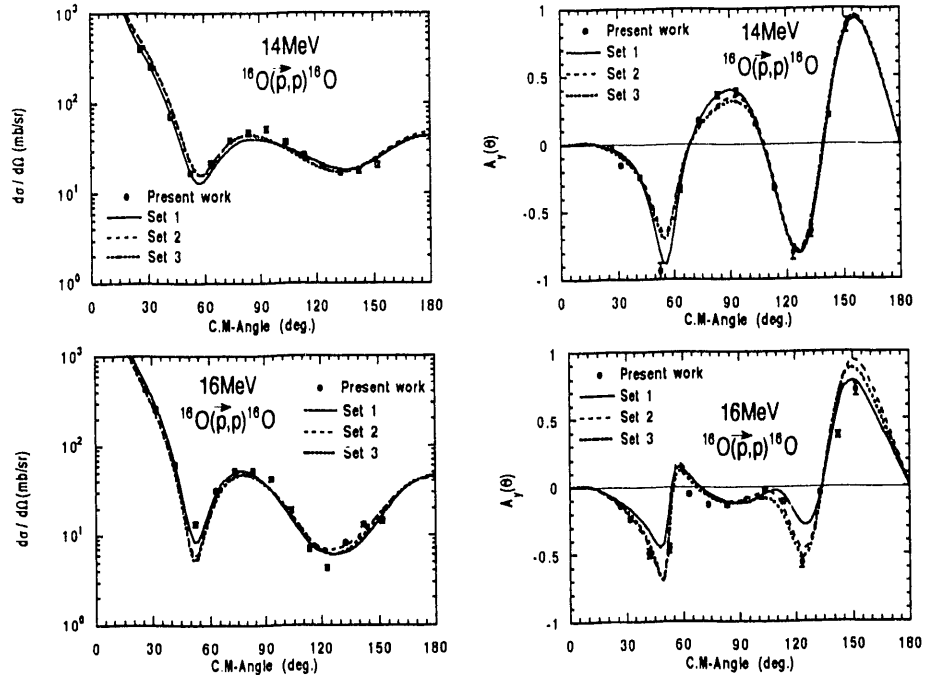

Fig. 2 Same as Fig. 1, except for ^{16}O.

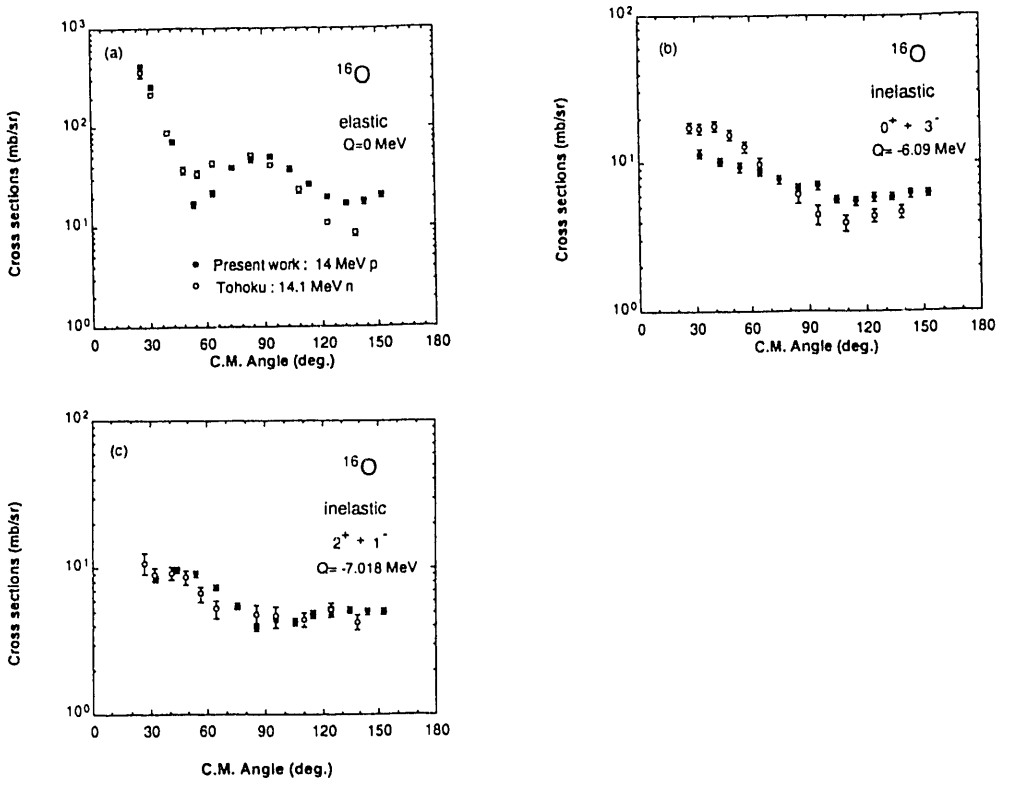

Fig. 3 Comparison between proton and neutron scattering from ^{16}O at 14 MeV. Closed and open circles show the present proton data and the neutron data taken from ref.10, respectively.

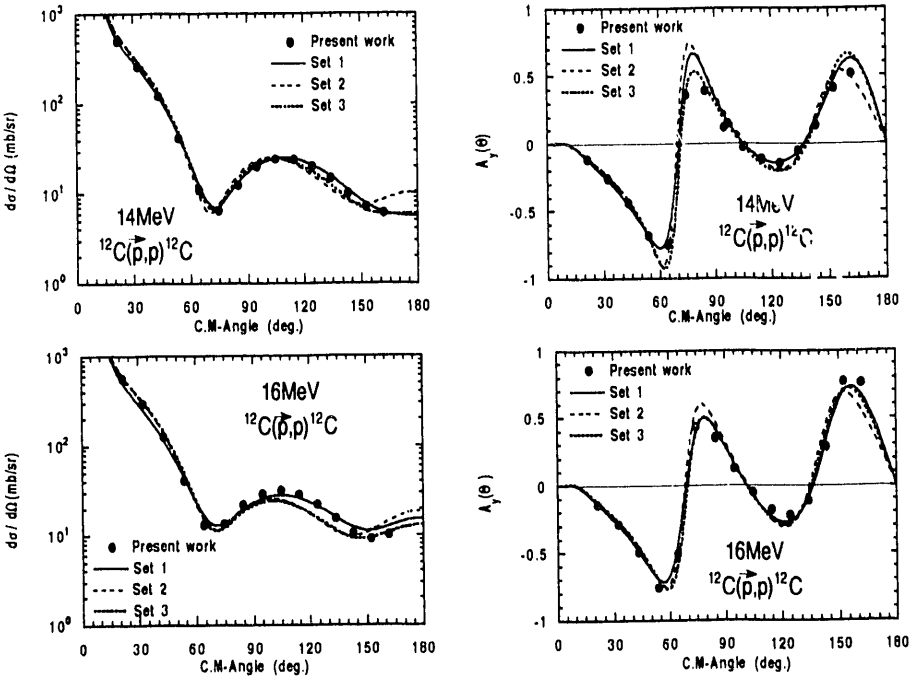

Fig. 4 Same as Fig. 1, except for ^{12}C.

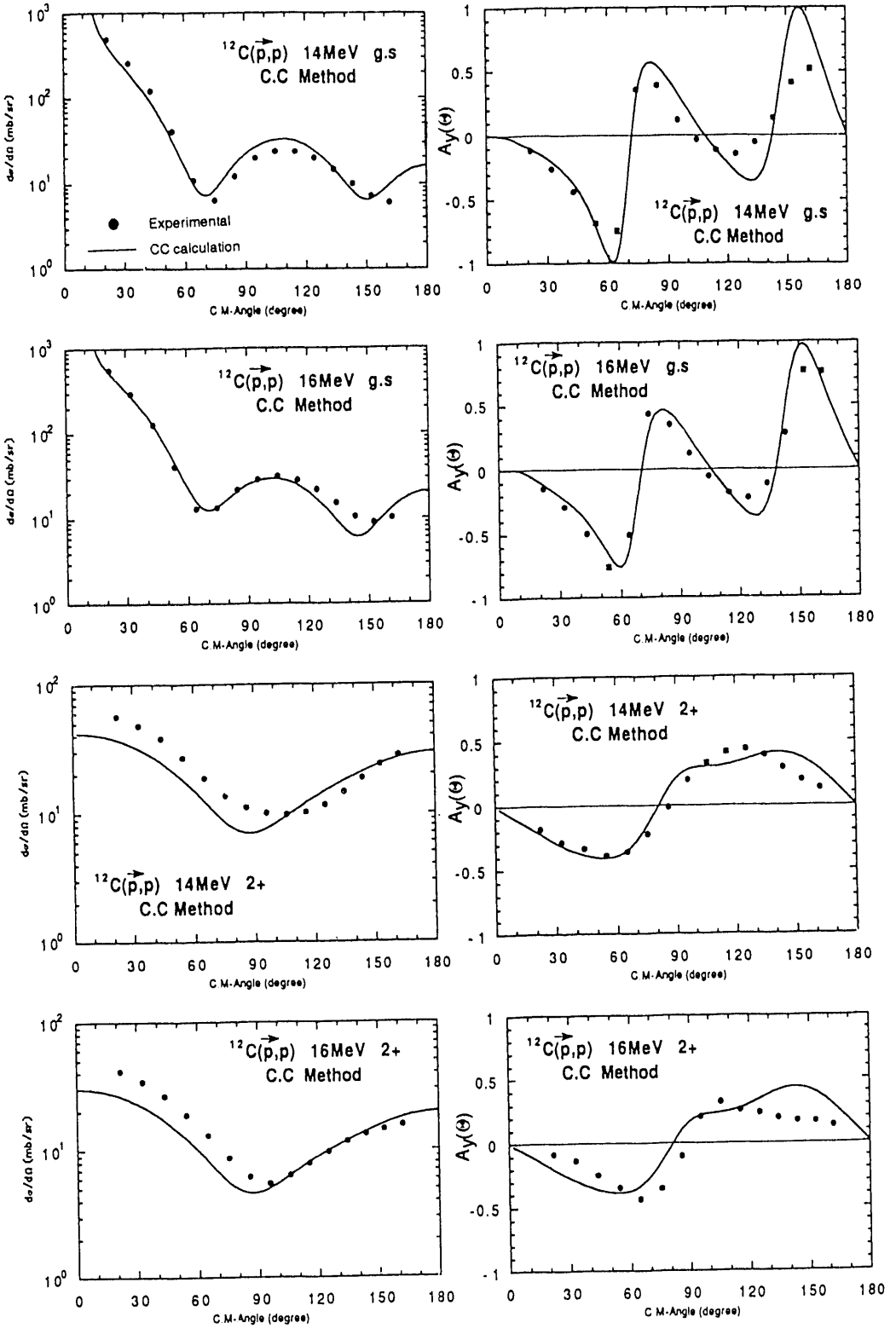

Fig. 5 Comparison of experimental data with coupled channels calculations for p-^{12}C elastic and inelastic scattering (the first 2^+) at 14 and 16 MeV.

3.19 An Experimental Study on Neutron Sputtering at 14.9 MeV — Measurement of Recoiled Radioactivities —

Y. Ikeda and C. Konno

Japan Atomic Energy Research Institute, Tokai-mura, Ibaraki-ken 319-11, Japan

Abstract: In view of the importance of induced radioactivity as well as material damage researches, we have started a systematic measurement of neutron sputtering yield (S_n) by using the D-T neutron source FNS (Fusion Neutronics Source) facility with particular attention on the partial reaction process with the radioactivity emissions. This paper describes the first result for S_n of recoiled atom due to (n,2n), (n,p) and (n,α) reactions in Al, Fe and Nb at 14.9 MeV. Recoil radioactivities subjected were ^{24}Na via ^{27}Al(n,α)^{24}Na for Al, ^{56}Mn via ^{56}Fe(n,p)^{56}Mn for Fe, and ^{92m}Nb and ^{90m}Y via ^{93}Nb(n,2n)^{92m}Nb and ^{93}Nb(n,α)^{90m}Y, respectively, for Nb. In order to give a overall guide line for S_n from a nuclear reaction point of view, S_ns were reduced by using corresponding cross section values. A systematics of S_n as a function of the proton number (Z) of target materials is demonstrated for the first time.

1. Introduction

During the decade of 1970, many material scientists had extensively investigated "neutron sputtering yield" (S_n) not only by experimental measurements with fast neutron irradiation [1-10], but also from theoretical treatment [11-13]. Materials subjected, however, were rather limited for particular elements on niobium and gold, and some other structural materials. Furthermore the data reported by different authors were in a poor agreement each other. In particular, Kaminsky reported an extremely large S_n of 2.5 x 10^{-1} for Nb due to 14 MeV neutron irradiation. The value was explained by the chunk emission [2,3]. Several different authors reported the S_ns of Nb for D-T neutrons, giving values of orders of 10^{-4} to 10^{-5}; most of them resulted in a convergency to be 10^{-5}.[15,16] The data could, however, give only the upper limit and showed large discrepancies with the theoretical predictions [16]. In the decade of 1980, there have been no clear effort on this subject. Major reason for the experimental deficiency is attributable to the lack of appropriate neutron sources for this purpose and to no significant progress in the measuring technique with better sensitivity for deposited atoms.

From the view point of fusion reactor design, a critical problem concerning the induced

radioactivity has been pointed out by Thomas et al. [8]. Basing on the experimental values, they investigated a serious increase of radioactivity inventory in a cooling channel of a D-T fusion reactor. The development of fusion energy is in steady progress, major part of which is leaded by ITER (International Thermonuclear Experimental Reactor) project [17]. In the engineering design phase, it is critically needed to establish more substantial experimental data base for the S_n concerning not only basic material damage studies but induced radioactivity inventory evaluations.

In view of the criticality, we have started a systematic measurement of S_n by using the FNS (Fusion Neutronics Source) facility [18] with particular attention on the partial reaction process with the radioactivity emissions. In this paper, we describe the first result for S_n of recoiled atom due to (n,2n), (n,p) and (n,α) reactions in Al, Fe and Nb at 14.9 MeV. A systematics of S_n as a function of the proton number (Z) of target materials is proposed for the first time to give a guide for estimation of S_n. All of previous experiments were carried out by using catcher foil in vacuum to eliminate the loss of recoil atom to be collected [1-10]. The present measurement was performed in air. This seems a drawback in terms of incomplete collection of recoiled atom due to attenuation by the air. Even though the distance is very short, stopping power for the high Z atom should attenuate significantly the emitted particle. A range of recoil atom of ^{92}Nb with kinetic energy of 200 keV in air was roughly estimated to be 0.3 mm. Assuming this value, it was suggested that some part of recoil atom with appreciably high kinetic energy could be detectable. Changing the distance between the target and collector, you will get different number depending on the attenuation in the air. In this regard, as the first trial, we employed the sample configuration in the air.

2. Experimental

The D-T neutrons were generated using FNS [18] by bombarding tritium target with deuterium beam (d^+) with 20 mA and 350 keV. The cold worked foils of aluminum, iron and niobium with thickness of 5, 20 and 12.5 μm, respectively, were used as the target materials subjected. The collector materials of plastic tape were placed in both front and back sides of the target foils using rather thick plastic holder at the distance of 0.2, 0.5, 1.0 and 2.0 mm (3.0 mm was added for Nb). The diameter of target materials was 10 mm. The samples were placed at distances of 10 to 15 mm from the neutron source in the direction of 0° with respect to d^+ beam and were irradiated with D-T neutrons of 14.9 MeV. A schematic drawing of the irradiation configuration is given in **Fig. 1**. The D-T neutron fluence at each foil was determined from the activation rates for ^{27}Al(n,α)^{24}Na, ^{56}Fe(n,p)^{56}Mn and ^{93}Nb(n,2n)^{92m}Nb dosimetry reactions adopting the cross sections of 112, 104 and 459 mb, respectively. After irradiation, the activities in the collectors were measured with a Ge detector. The numbers of radioactive recoil atoms deposited were determined from their activation rates assuming 100 % collection efficiency. Background activity due to impurity or unexpected contamination was examined by irradiating the samples by inserting a mask with different materials between the target material and collector. As a

result, no corresponding activity of concerned was observed in the collector.

3. Results

Recoil radioactivities subjected were ^{24}Na via ^{27}Al(n,α)^{24}Na for Al, ^{56}Mn via ^{56}Fe(n,p)^{56}Mn for Fe, and ^{92m}Nb and ^{90m}Y via ^{93}Nb(n,2n)^{92m}Nb and ^{93}Nb(n,α)^{90m}Y, respectively, for Nb. The g-ray spectra associated with activities deposited on catcher foils for Al, Fe and Nb targets are shown in **Figs. 2.1, 2.2 and 2.3**, respectively.

As defined commonly, the S_n is given as the number of recoil atoms emitted from the target per incident neutron. For the forward direction, the measured data are plotted in **Fig. 3** along with a range of available data of ^{92m}Nb reported by Behrich [4] and Thomson et al. [8]. **Figure 3** indicates that the number of recoil atom, in general, decreases as the distance increases. The forward S_n were deduced by extrapolating the data at different distance to the point at 0.1 mm distance.

4. Discussion

The determined S_n for ^{92m}Nb ranged 0.8 x 10^{-7} to 1.4 x 10^{-7}, resulting in good agreement with data reported in Refs. [4,8]. Concerning ^{24}Na, ^{56}Mn and ^{90m}Y, the S_ns have been measured for the first time. They are 9 x 10^{-7}, 7 x 10^{-8} and 3 x 10^{-9}, respectively. At present, experimental errors are estimated to be within ± 30 %. The S_n for ^{90m}Y is 20 times smaller than that of ^{92m}Nb. This is simply due to the small reaction cross section of 5 mb for ^{93}Nb(n,α)^{90m}Y around 14 MeV energy region [21], while the cross section for ^{93}Nb(n,2n)^{92m}Nb is 459 mb [20]. The S_n of ^{24}Na is 6 times higher than that of ^{92m}Nb. The cross section of 113 mb at 14.6 MeV for ^{27}Al(n,α)^{24}Na is, however, 4 times lower than that for ^{93}Nb(n,2n)^{92m}Nb. The enhanced Sn for ^{24}Na to this order of magnitude is explained by that large momentum transfer and low stopping power for ^{24}Na in Al. The range of recoil atom is determined by the kinetic energy and stopping power in the air. As a significant aspect of measurement in the air, **Figure 3** suggests us a possibility to extract information for primary energy spectrum of recoiled atoms.

There was clear difference in S_n for forward and backward direction with respect to the neutron current. For ^{24}Na, ^{56}Mn and ^{92m}Nb, the ratios of S_n were found to be 20, 130 and 32.1, respectively. These values were simply obtained from the activity ratios in the collectors on both sides of targets. The value of 32.1 for ^{92m}Nb was much less than the ratio of 139 reported by Thomas et al.[8]. This difference could be attributable to the difference in the experimental geometrical configuration. A theoretical prediction of the ratio for Nb sputtered by 15 MeV neutrons gave value of 22 [14], being consistent with the present data.

In order to give a overall guide line for S_n from a nuclear reaction point of view, S_ns were reduced by using corresponding cross section values. The reduced S_ns, are plotted in **Fig. 4** with respect to the proton number (Z) of target material. Hereafter, we denote the reduced Sn as **RS**. Some of experimental data are referred in the literature for total S_n, and (n,2n) and (n,p) for Mo,

Cr, Ni and Au [4,6,7,8] In **Fig. 4**, it was found that **RS** present a strong correlation with Z though the number of data is not sufficient. In general, **RS** decrease with increase of Z. This is understandable by taking the large momentum transfer in light element and the higher stopping power in the higher Z material into account. For (n,p) and (n,2n), **RS**s are identical, while **RS**s for (n,α) show slightly higher value than that for (n,2n). The **RS** for the total S_n gives much higher than those for other non-elastic reactions and the curve for the systematic trend shows slower decrease. The difference between the curves for (n,2n) and (n,α) could be explained by the difference in the momentum transfer in the recoil process; kinematic energy of recoil atom associated with alpha particle is expected two to four times larger than that associated with two neutron or one proton emission.

5. Summary

Still, there is large uncertainty to finalize this approach to formulate the systematic trends of **RS**s for the specific reactions, because experimental data is deficient. Even though, it is worthwhile to investigate any systematics for the S_n and the present approach encourages us to do further experiment on different elements. The other outcome in the present study is due for demonstrating a possibility to estimate energy spectrum of recoiled particles, by detecting emitted radioactivity depositions on collectors through different layer of air. The further investigation on this subject is underway.

References

[1] K. Keller, Plasma Physics, 10 (1968) 195-199.

[2] M. Kaminsky, J. H. Peavey and S. K. Das, Phys. Rev. Lett. 32, [11] (1974) 599.

[3] M. Kaminsky and S. K. Das, J. Nucl. Mater. 53 (1974) 162-170.

[4] R. Behrisch, R. Gahler and J. Kalus, J. Nucl. Mater. 53 (1974)183-188.

[5] M. A. Kark, T. H. Blewitt, A. C. Klank and T. L. Scott, J. Nucl. Mater. 53 (1974) 179-182.

[6] O. K. Harling, M. T. Thomas, R. L. Brodzinski and L. A. Rancitelli, Phys. Rev. Lett. 34, [21] (1975) 1340.

[7] L. H. Jenkins, G. J. Smith, J. F. Wendelken and M. J. Saltmarsh, J. Nucl. Mater. 63 (1976) 438-442.

[8] M. T. Thomas, O. K. Harrling, R. L. Brodzinski and L. A. Rancitelli, J. Nucl. Mater. 63 (1976) 448-453

[9] R. G. Meisenheimer, J. Nucl. Mater. 63 (1976) 429-431

[10] K. Nishizawa, Y. Morita, Y. Sensui and T. Matsuura, J. Nucl. Sci. and Technol. 16 (1979) 684-689.

[11] M. Guinan, J. Nucl. Mater. 53 (1974) 171-178.

[12] J. E. Robinson, B. S. Yarlagadda and R. A. Sacks, J. Nucl. Mater. 63 (1976) 432 - 437.

[13] J. B. Roberto, M. T. Robinson and C. Y. Fu, J. Nucl. Mater. 63 (1976) 460-465.

[14] H. H. Anderson, J. Nucl. Mater. 76&77 (1978) 190-192.

[15] O. K. Harling, M. T. Thomas, R. L. Bradzinski and L. A. Rancitelli, J. Nucl. Mater. 63 (1976) 422-428.

[16] R. Behrisch, J. Nucl. Mater. 108 & 109 (1982) 73-82.

[17] "ITER Conceptual Design Report," IAEA, ITER-DS-No 18 (Vienna, 1991)

[18] T. Nakamura, H. Maekawa, Y. Ikeda, Y. Oyama and J. Kusano, "Present Status of the Fusion Neutronics Source (FNS)," Proc. 4th Symp. on Accelerator Sci. and Technol., RIKEN, Saitama, 24 - 26, November 1982, pp.155-156.

[19] Y. Ikeda, C. Konno, K. Oishi, T. Nakamura, H. Miyade, K. Kawade, H. Yamamoto and T. Katoh, "Activation Cross Section Measurements for Fusion Reactor Structural Materials at Neutron Energy from 13.3 to 15.0 MeV Using FNS Facility," JAERI-1312 (1988).

[20] T. B. Ryves, "A Simultaneous Evaluation of Some Important Cross Sections at 14.7 MeV," Proc. of a Specialists' Meeting on Neutron Activation Cross Sections for Fission and Fusion Energy Applications, 13 - 15 September, 1989 Argonne National Laboratory, USA, (1989) pp. 293-307.

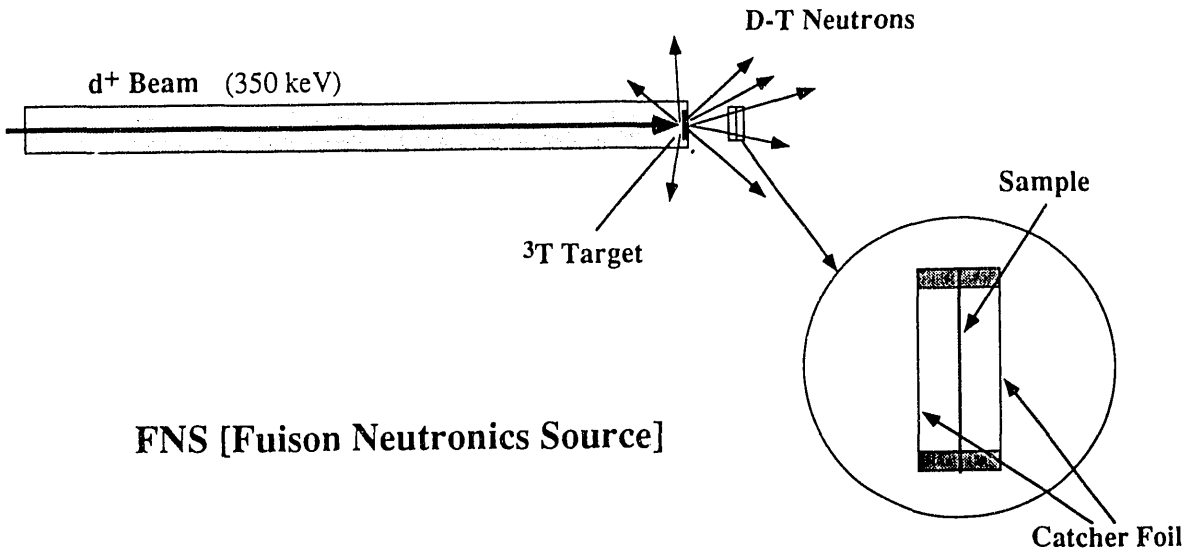

Fig. 1 Irradiation configuration of recoiled radioactivities measurement.

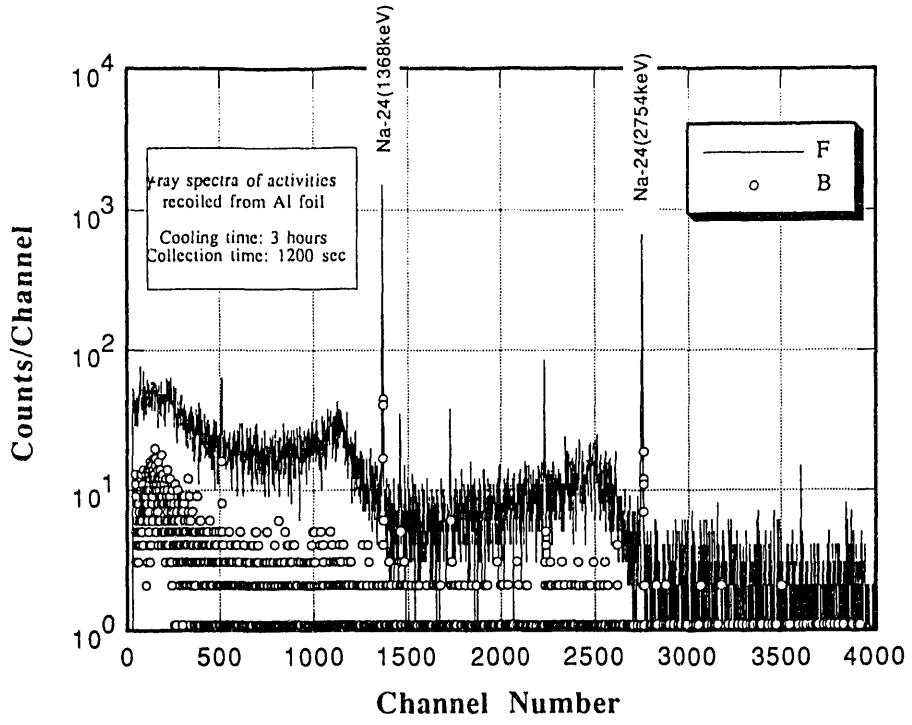

Fig. 2.1 Gamma-ray spectrum of radioactivities emitted from aluminium target irradiated with 14.9 MeV neutrons.

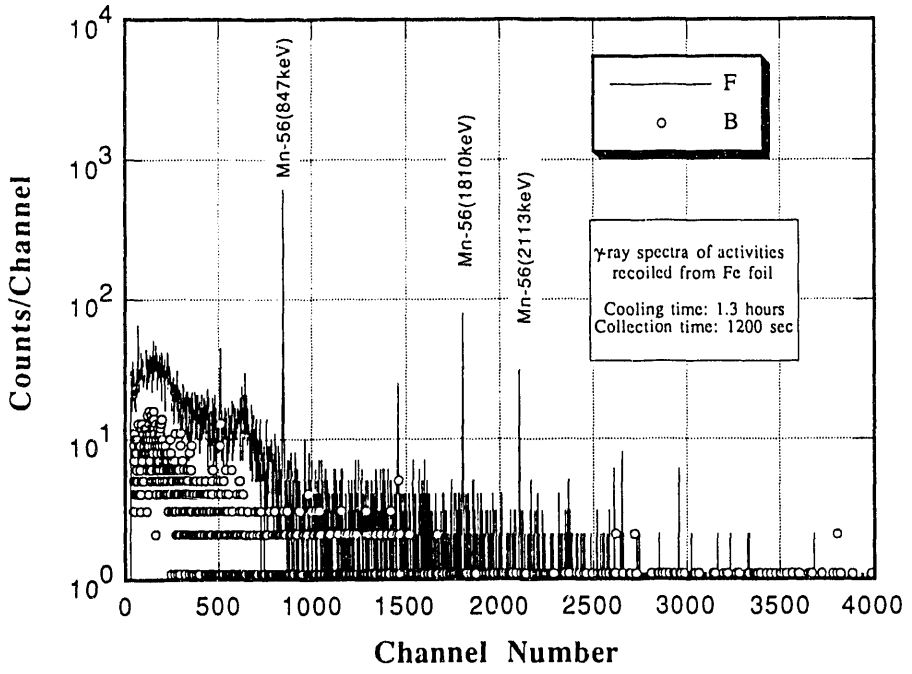

Fig. 2.2 Gamma-ray spectrum of radioactivities emitted from iron target irradiated with 14.9 MeV neutrons.

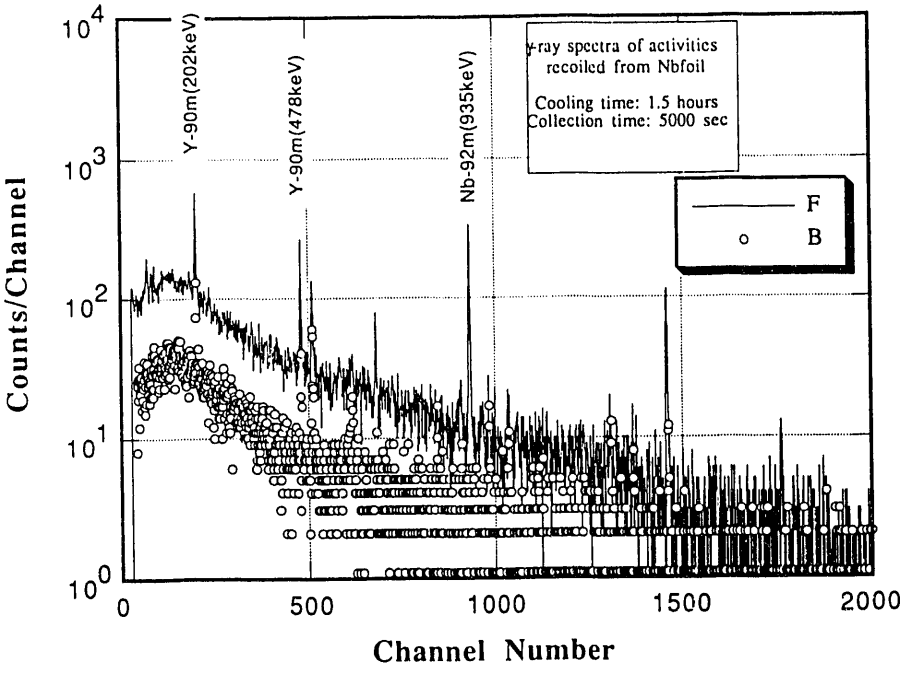

Fig. 2.3 Gamma-ray spectrum of radioactivities emitted from niobium target irradiated with 14.9 MeV neutrons.

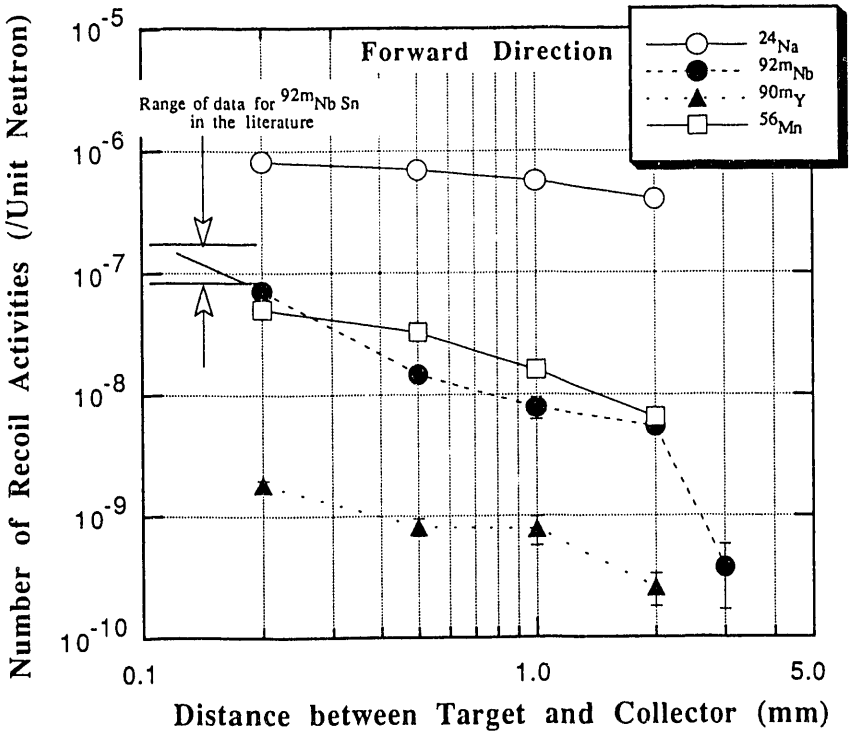

Fig. 3 Dependency of activity intensities on distances between target materials and catcher foils.

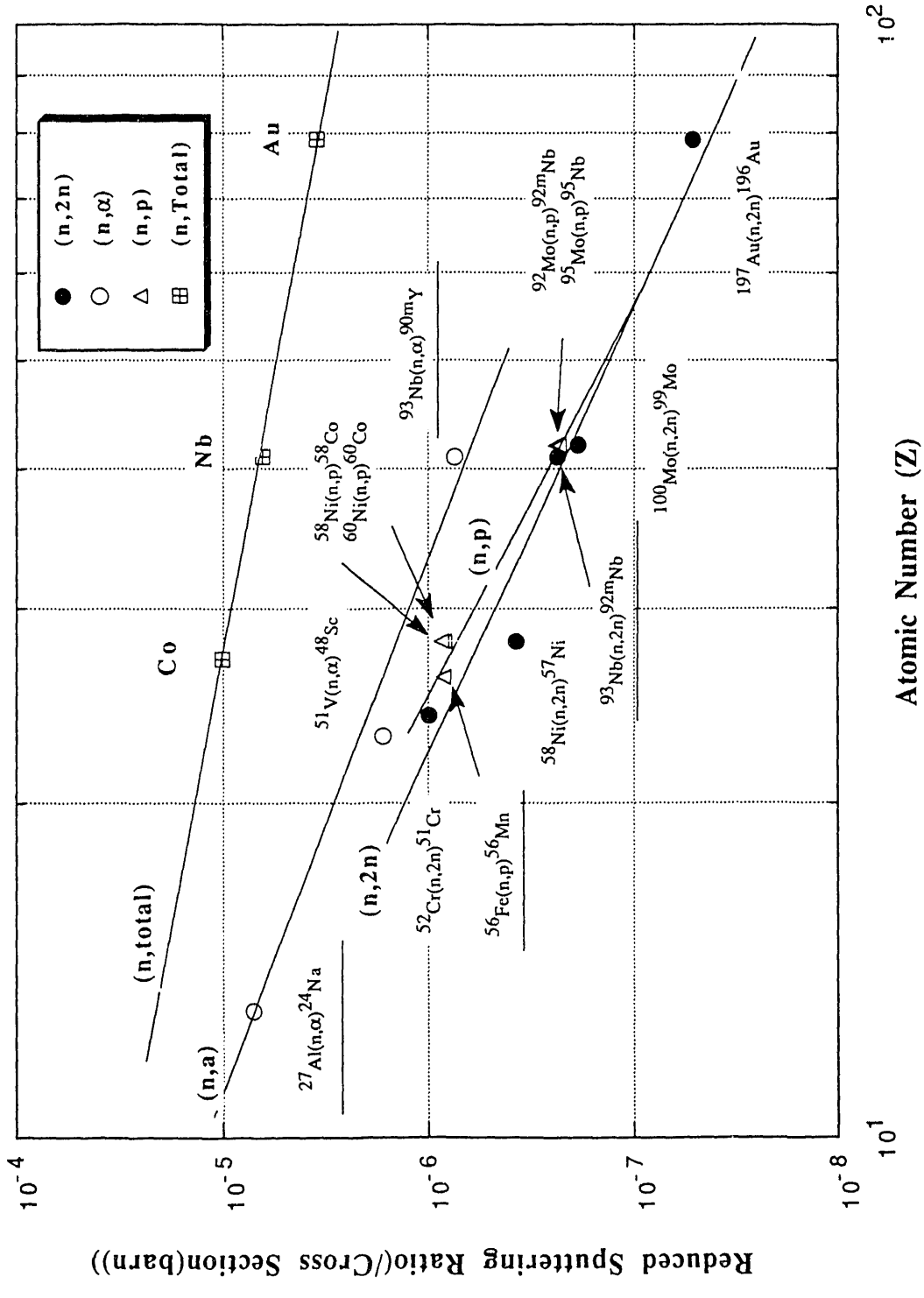

Fig. 4 Systematic trends of sputtering yields for specific reactions as a function of proton numbers (Z) of target materials.

3.20 Measurement of Double Differential Alpha Particle Emission Cross Sections of Beryllium for 14.1 MeV Incident Neutron

Y.Murakami, A.Takahashi and H.Nishizawa

Department of Nuclear Engineering,Faculty of Engineering, Osaka University, Yamadaoka 2-1, Suita, Osaka-565, Japan

Alpha particle spectra from $^{9}Be(n,2n)2\alpha$ reaction were measured with 14.1 MeV neutrons for 30-105 deg angle points. Employing the E-TOF two dimensional data acquisition system , measurement with good S-N ratio was undertaken. In order to deduce DDX data from raw spectrum, Monte-Carlo simulations which took locations of sample and energy loss into consideration were done. Using the result of calculation, corrections for raw data were made. The results of experiments were compared with evaluated nuclear data ENDF/B-VI, and some discrepancies were found. On the other hand, we performed statistical calculations based upon reaction kinematics which assumed 3body sequential decay. The calculated DDXs were compared with experimental data for alpha particles and neutrons to study consistency. From this analysis, it was suggested that the 3-body sequential decay could describe the continuum of the alpha-particle spectra, without assumption for unknown reaction channels as in the case of ENDF/B-VI.

1. INTRODUCTION

Neutron induced $^{9}Be(n,2n)$ reaction has a large cross section around 14MeV. Nuclear data for this reaction are considered as high priority data for fusion reactor blanket application. Since this reaction consists of sequential decay processes and direct multi-body decay processes, it is, however, difficult to estimate accurately angular-energy distribution for secondarily emitted particles. Recently in the evaluated nuclear data set ENDF/B-VI the DDXs for alpha particle were evaluated in addition to DDXs for neutron. This evaluation was very suggestive to understand the reaction mechanism, because final products of $^{9}Be(n,2n)$ reaction are 2 neutrons and 2 alpha particles. When ^{9}Be was bombarded with 14.1MeV neutrons, following reaction may contribute to total cross section.

1) $^{9}Be + n \rightarrow {}^{9}Be_{gs} + n_0$

2) $^{9}Be + n \rightarrow {}^{9}Be_{Ex>=2.43} + n_1$

2a) $^{9}Be_{Ex>=2.43} \rightarrow \alpha_1 + {}^{5}He$

$^{5}He \rightarrow \alpha_2 + n_2$

2b) $^{9}Be_{Ex>=2.43} \rightarrow n_2 + {}^{8}Be_{gs}$

$^{8}Be_{gs} \rightarrow \alpha_1 + \alpha_2$

2c) $^{9}Be_{Ex>=2.43} \rightarrow n_2 + {}^{8}Be_{3.}$

$^{8}Be_{3.} \rightarrow \alpha_1 + \alpha_2$

3) $^{9}Be + n \rightarrow {}^{6}He_{gs} + \alpha_0$

4) $^{9}Be + n \rightarrow \alpha_1 + {}^{6}He_{Ex>=1.8}$

$^{6}He_{Ex>=1.8} \rightarrow n_1 + {}^{5}He$

$^{5}He \rightarrow \alpha_2 + n_2$

5) $^{9}Be + n \rightarrow {}^{5}He_1 + {}^{5}He_2$

$^{5}He_{1,2} \rightarrow \alpha_{1,2} + n_{1,2}$

6) $^{9}Be + n \rightarrow \alpha_1 + nl_1 + {}^{5}He$

$^{5}He \rightarrow \alpha_2 + n_2$

In the evaluation of ENDF/B-VI, branches from 1) to 5) had been considered to contribute, but 3-body sequential decay 6) had not been taken into account. And the reaction 2) were evaluated for many different levels of ^{9}Be, which depend on many unknown parameters.

Therefore, verification by measured DDXs not only for neutrons but also for alpha particles is needed. DDXs had been measured for the (n,α) reaction by Ferenc et al.[1]. They had introduced reaction 6) in the analyze of alpha and neutron spectra at 14MeV incident neutrons.

At OKTAVIAN, measurement of DDXs for emitted neutrons about has been done for ^{9}Be in 1986 and 1987. In the first experiment using ring sample, the energy of incident neutrons varied according to the change of angle point. But in 1987, the 85deg TOF line had been constructed, and we could measure DDX for neutron at fixed incident neutron energy of 14.1MeV. Using the 85deg line, DDXs of emitted neutrons had been measured from 15deg to 160deg angle-points, for the energy region over 1MeV.

Recently the measuring system for DDXs of charged parti-

cles was built. We measured energy spectra of emitted alpha particles for the $^{9}Be(n,2n)2\alpha$ reaction at 5 angle-points, for the energy region over 2MeV, and made corrections on raw data by Monte-Carlo simulation to reduce DDXs data. In analysis, we based on Ref.[1] but we used new DDXs data of neutrons(87's). And present experimental DDXs of alpha particles were compared to DDXs of Ferenc et al.

2. EXPERIMENT

The pulsed D-T neutron source of OKTAVIAN was operated with <2 ns pulse width at FWHM and 1MHz repetition frequency. A CsI(Tl) scintillation detector , a collimator and a Be sample were set up (Fig.1) in a vacuum chamber, pressure of which was about 0.1 Torr. Because of evacuation of the air, energy loss of alpha particles in the air could be neglected.The size of Be sample were 20 micron x 6.0cm,(7.0cm or 8.0cm) diameter and these purity were 99.9%. To measure data at backward angle, larger samples were used. The sample was fixed by a surrounding gold wire (low alpha background). The distance between detector and Be sample i.e. flight path was varied from 32.0 to 56.7cm (Fig.2a) according to the change of emission angle set up.

The block diagram of this measuring system is shown in Fig.3. We made two dimensional data acquisition for pulse height of dynode signals which corresponded to energy(E) and time-of-flight(TOF) signals using fast anode signals. Both signals were gated by logic signals from pulse shape particle discrimination circuits. An example of measured results of 2-d E-TOF distributions is shown in Fig.4. For estimating background, measurement without sample was done. To integrate this contour distribution corresponding to alpha particle signals with respect to TOF, energy spectra were obtained.

For energy calibration, ^{252}Am and several kind of Al foils were used. The energy threshold of this experiment is about 2.0 MeV. These spectra were normalized by standard measurement of recoil protons from a polyethylene sample (40 micron x 2.5cm diameter) at 45deg in laboratory system.

3. RESULTS

3.1 Raw data and Monte-Carlo simulation

The size of sample broadens angular resolution at each angle points (Fig.2b). Moreover the energy loss of charged particle in the sample can not be neglected (Fig.5). For example, an alpha particle having 6MeV as initial energy

should lose its energy from 0 to 3.0MeV according to its path through the Be foil. Therefore Monte-Carlo simulation which took locations of sample and energy loss into consideration was done. The evaluated nuclear data ENDF/B-VI were used in the calculation. Calculated spectra and present experimental spectra (raw) were compared in Fig.6.

3.2 Data correction

In the Monte-Carlo calculation, mean path of alpha particle through the Be foil was calculated at the same time. To correct energy of alpha particles, Bethe formula and mean path were used. The energy of experimental raw data and calculated spectrum were corrected to be a little fit too higher. To compare the calculated spectra, of which energy was shifted, and DDX of ENDF/B-VI at each angle points, correction factors were obtained. Using these correction factors, we made corrections on energy corrected experimental data to deduce DDX data. Necessity of latter correction is caused by two reasons. One is that low-energy alpha particles stop in the foils. Another is that alpha particles should be slowed down to wider energy region than its energy bin according to these path ($0<x<25$ micron) through the foil. But deduced DDXs by the latter corrections depended upon evaluated nuclear data. If it is necessary to avoid dependence on evaluated nuclear data, there is nothing else to do comparing raw data with result of simulation calculation using the DDX needed to be evaluated. In Table.1, the locations of sample, D-T source, detector were shown.

Corrected DDX data and experimental data of Ferenc et al. were shown in the upper part of Fig.7 in comparison with evaluated ENDF/B-VI data. In the lower part of Fig.7 correction factors were shown. ADX (Angler Differential alpha particle emission Cross section) over 3MeV is shown in Fig.8. The errors shown in both data are based on only statistical errors.

4. Discussion

As a result of comparison with evaluated data, some discrepancies and agreements were found. In the high energy part of alpha spectrum, evaluated nuclear data ENDF/B-VI showed overestimation, especially near the discrete peak created by reaction 3) at backward angle. From comparison in Fig.8, present experiment supports the experiment of Ferenc et al rather than ENDF/B-VI and it suggests that alpha-particles tend to be emitted in more forward angle region. Moreover, low energy alpha-particles contribute to this tendency (see

Fig.7,30deg).

From the comparison with ENDF/B-VI and experimental data of emitted neutrons, the inelastic scattering peaks at Q=-2.43 MeV and so on show good agreements. But underestimation is found shown in the low energy part of spectra at backward angles (see Fig.9b).

The reason why there were discrepancies in DDXs between ENDF/B-VI and experiment was thought to be due to the treatment of continuum spectrum. In ENDF/B-VI, many different levels had been assumed to describe the continuum (ref.[2]). On the other hands, the 3-body sequential decay was assumed in the present analysis. Then we assumed reaction 6) which had not been taken into account in ENDF/B-VI. Using statistical method based upon reaction kinematics, DDX for alpha particles and neutrons were calculated. Obtained DDX data were compared with experimental DDX data in Fig.9. For experimental data of emitted neutrons, DDXs which had been measured in 1987 were used. At that experiment incident energy of neutrons was 14.1MeV, which was just same as the present experiment. Calculated DDX was normalized properly so as not to exceed the "height" of experimental data. For alpha particles, spectral shapes were in good agreements at all angle points. For neutrons, the calculation could describe well the shape of low energy part of spectra. Since the CM angular distribution has been assumed as isotropic, there were however found some angle-points where we had underestimation.

5. CONCLUSION

Alpha particle spectrum from ^{9}Be foil which was bombarded with 14.1 MeV neutrons were measured for 5 angle-points in 30-105 deg . The present measuring technique provided good S-N condition and satisfactory counting statistics. In order to deduce DDX data from raw spectrum, Monte-Carlo simulation which took locations of sample and energy loss into consideration was done and correction factors were estimated. Comparing evaluated data with corrected experimental DDX data, both were in agreement as a whole, although some discrepancies were found. To rule out the discrepancies, the 3-body sequential decay process was assumed and spectra for neutrons and alpha particles were calculated by statistical method based upon kinematics. Comparing this calculation with experimental DDX data for both particles, this process could describe the continuum of DDXs for alpha particles, and was not inconsistent to DDXs for neutrons. If this reaction could be considered

to have significant contribution, $^{9}Be(n,2n)2\alpha$ reaction can be described accurately, and it can rule out assumptions for many hitherto unclarified channels.

REFERENCE

[1] Ferenc et al.,Nucl.Sci.Eng., 101,1 (1989).
[2] Parkins et al.,Nucl.Sci.Eng.,90,83 (1985).

Table 1 Geometrical locations for present experiment, where θ_s is the emission angle, (Sx, Sy, Sz) is the coordinates at the center of Be foil when the center of scintillator is placed on the origin of the coordinates. Rs is the radius of a Be sample. θ_d is the angle between surface of Be foil and a normal line of surface of the scintillator.

θ_s (deg)	(Sx, Sy, Sz) (cm)	Rs (cm)	θ_d (deg)
30	(27.7,16.0,0)	3.0	60.0
45	(35.5,20.5,0)	3.5	67.5
60	(40.0,23.1,0)	3.5	60.0
75	(43.4,25.1,0)	4.0	52.5
105	(49.1,28.4,0)	4.0	135.0

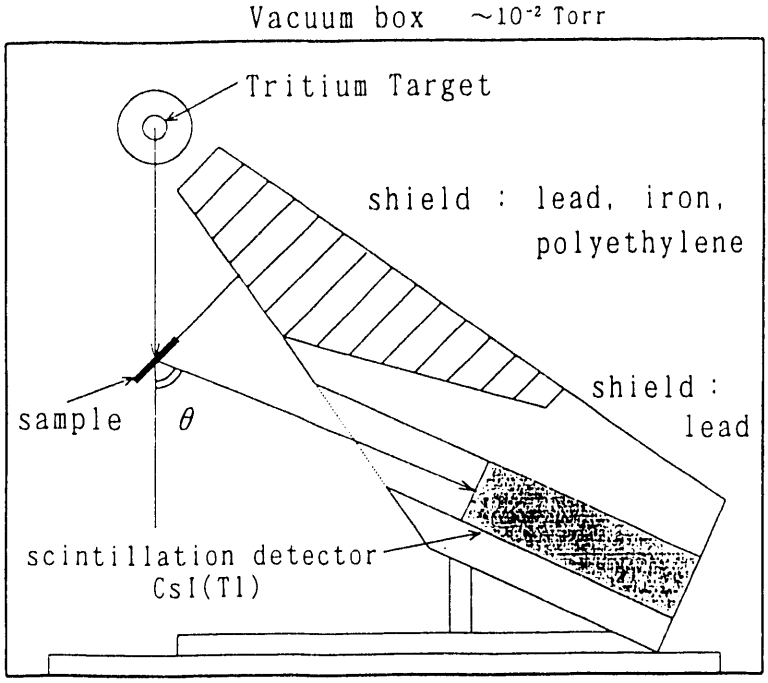

Fig. 1 Schematic view of experiment.

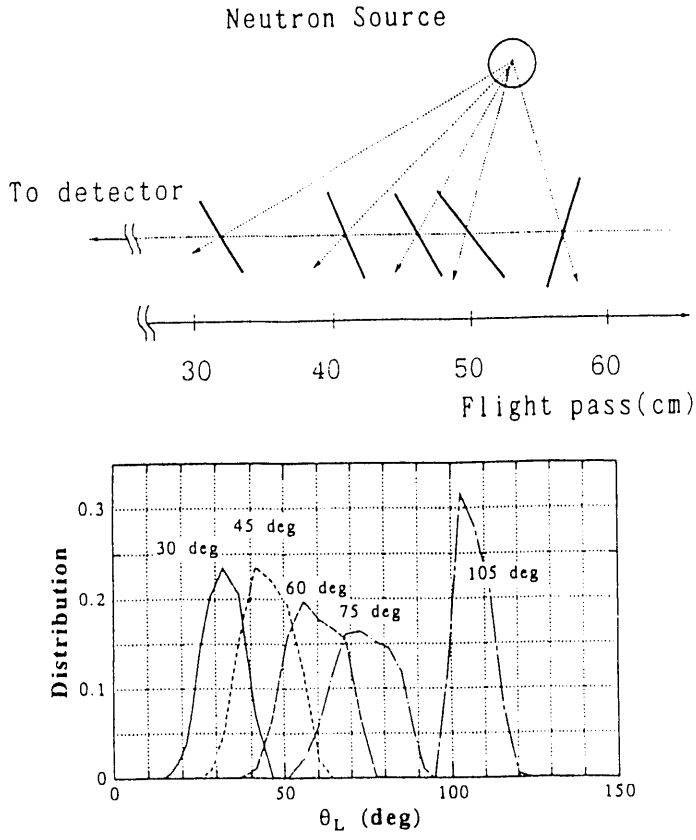

Fig. 2 (a) Location of Be samples for 30°, 45°, 60°, 75° and 105° in L.S.. (b) Broadening of angular resolution according to size of sample at each angle point.

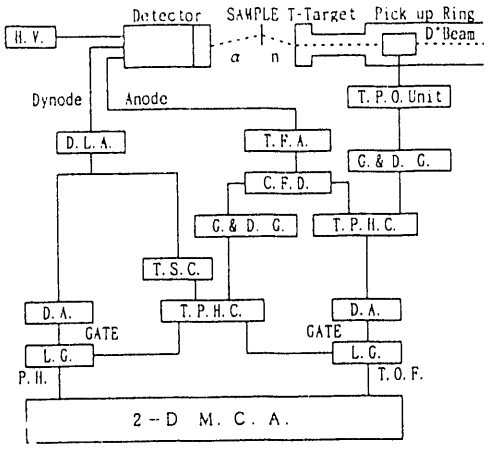

Fig. 3 Block diagram of measurement.

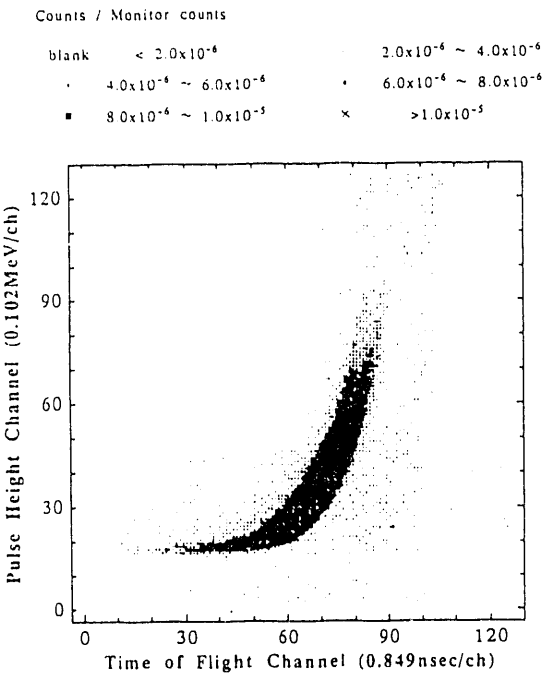

Fig. 4 Two-dimensional E-TOF distribution (fore ground).

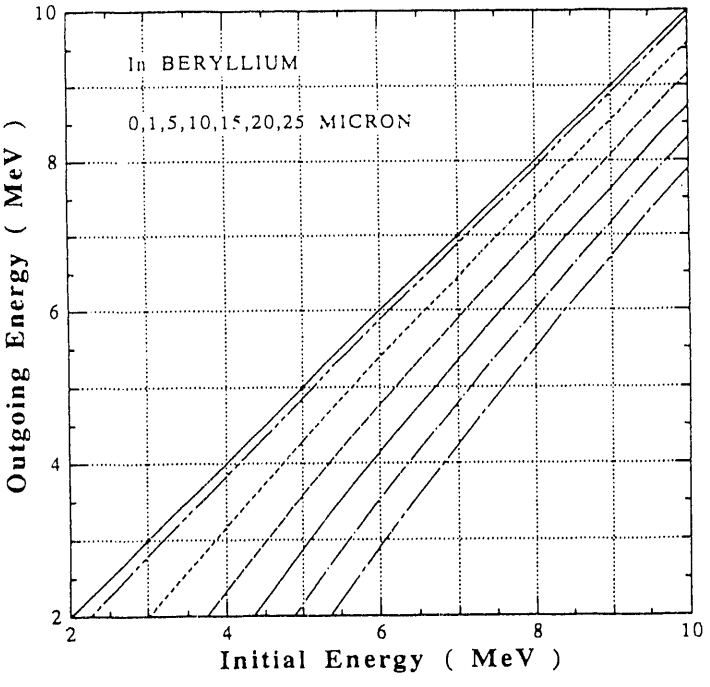

Fig. 5 Energy loss through Be foils from Bethe formula. The range through Be foils are 0, 5, 10, 15, 20 and 25 micron.

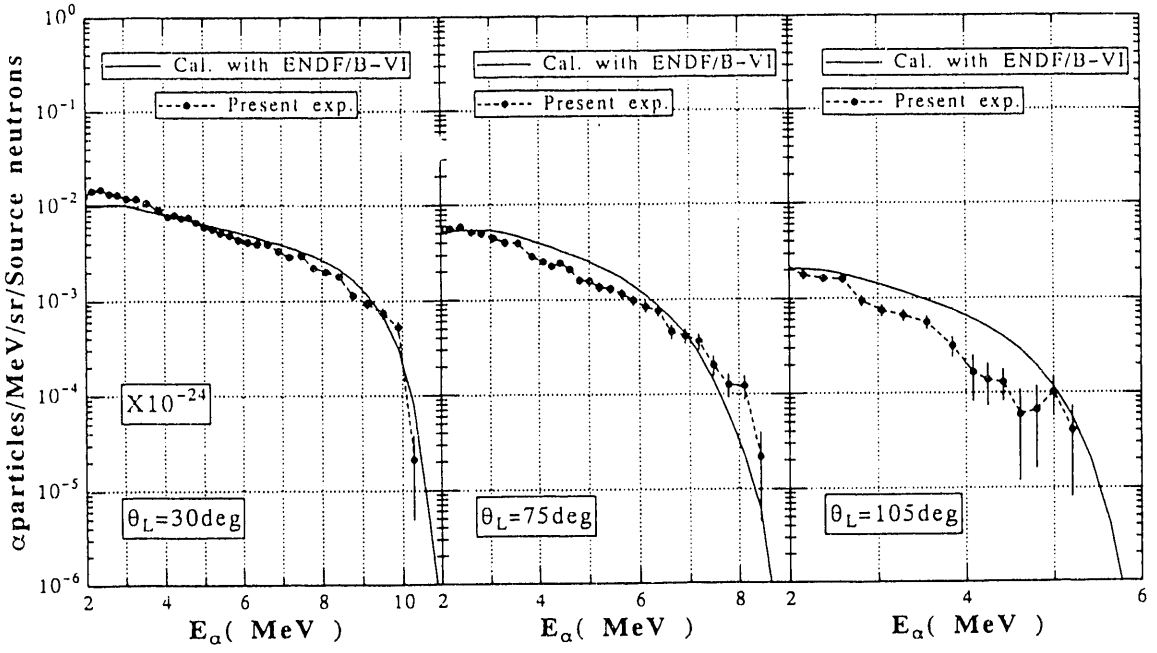

Fig. 6 Raw data (black circles) and Monte-Carlo simulation spectrum at 30°, 75° and 105° in laboratory system.

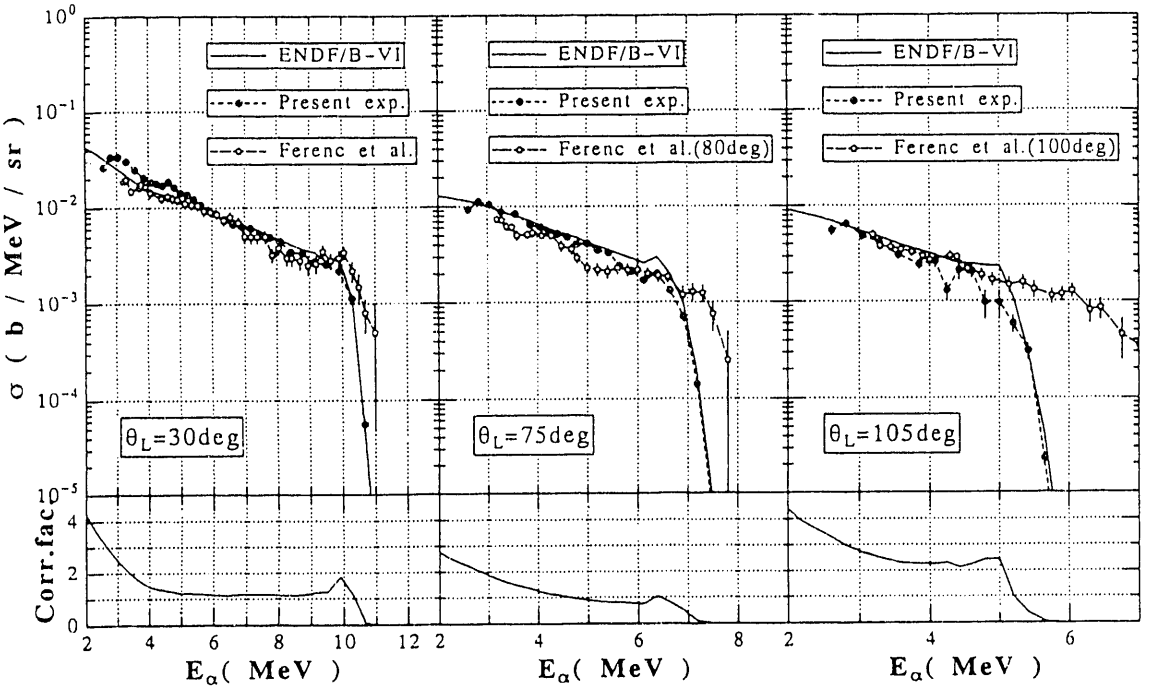

Fig. 7 Correction factor and DDX for ^{9}Be(n,2n)2α with En=14.1 MeV at 45°, 75° and 105° in laboratory system (solid points). Experiment of Ferenc et al. (pentagons) and ENDF/B-VI.

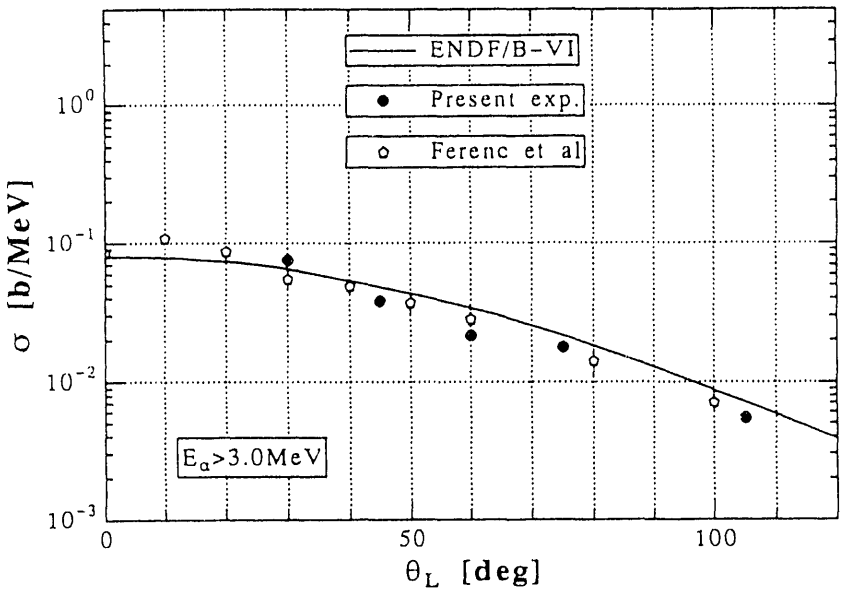

Fig. 8 ADX for Be compared with experiment of Ferenc and evaluated data ENDF/B-VI.

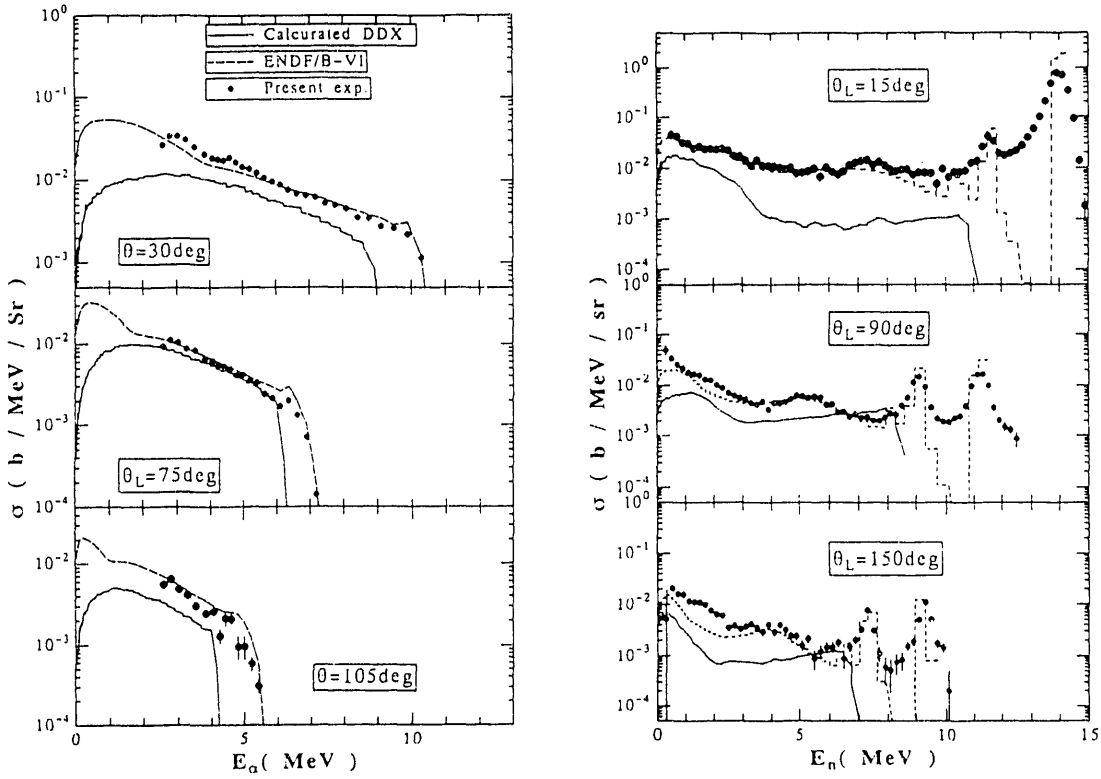

Fig. 9 (a) DDX for Alpha particle in L.S. Calculated data are compared with the experimental data and the evaluated data ENDF/B-VI. (b) DDX for neutron in L.S. Experimental data are those measured at OKTAVIAN in 1987.

3.21 Measurements of Double-differential α-particle Production Cross Sections of Fe and Ni Using Gridded Ionization Chamber

N.Ito, M.Baba, S.Matsuyama, I.Matsuyama and N.Hirakawa
Department of Nuclear Engineering, Tohoku University, Sendai.

S.Chiba, T.Fukahori, M.Mizumoto and K.Hasegawa
Japan Atomic Energy Research Institute, Tokai.

Double-differential α-particle production cross sections of Fe and Ni were measured for neutron energy region between 4 and 14 MeV using a gridded ionization chamber. The method applied in this work enables us to measure the double-differential cross sections at various incident neutron energies because of the high efficiency and background suppression capability of the gridded ionization chamber. The double-differential cross sections, the energy-differential cross sections and the excitation functions were obtained for the (n,xα) reactions of Fe and Ni and are compared with the previous experiments and evaluated data.

1. Introduction

The gas production reactions cause radiation damage and nuclear heating for structural materials of fusion reactors. For the estimation of these effects, the data of energy-angular distribution of emitted charged-particles are required as well as the data of reaction cross section. The (n,α) cross section data for Fe and Ni, however, are scarce since the activation method is difficult to apply for these reactions. Thus, large discrepancies exist among the evaluations[1]. Therefore, experimental data for the (n,α) cross sections of Fe and Ni are required for the region of wide incident neutron energy up to 14 MeV.

For the study of gas production reactions, we developed a gridded ionization chamber (GIC)[2,3] which has large geometrical efficiency with capability of energy-angle determination. The use of krypton as counting gas achieves high stopping power and low background production. The spectrometer using the GIC enables us to measure the double-differential cross sections at various incident energies because of its high efficiency with good S/N ratio.

We have reported the production cross sections of α-particle of Ni for incident energies of 4.3 ~ 6.5 and 14.1 MeV[3]. We extended the measurements of Ni for En = 7 ~ 10, 14.1 MeV and of Fe for En = 5.5 ~ 10, 14.1 MeV. The double-differential cross sections, the energy-differential cross sections and

the reaction cross sections were deduced and are compared with the previous experimental and evaluated data.

2. Experimental Procedure

The details of the GIC construction and experimental method have been reported in Ref. 2 and 3. The GIC applied in this work is shown in Fig. 1 schematically. If the charged particle emitted from a sample on cathode is stopped between the cathode and the Frisch grid, signals of the anode and the cathode, P_a and P_c respectively, are represented by the following equations[4];

$$P_a = E(1 - \sigma\frac{\bar{x}}{d}\cos\theta) \sim E \qquad (1)$$

$$P_c = E(1 - \frac{\bar{x}}{d}\cos\theta) \qquad (2)$$

where

E, θ = energy and angle of emitted particle, respectively,

σ = grid inefficiency of the GIC (~5.9%),

$\bar{x}$ = distance from the beginning of the ionization to the center of the gravity of the charge distribution of the trace,

d = spacing between the cathode and the Frisch grid.

Therefore, we can obtain the emission energy and the angle by analyzing the two-dimensional data of the signals of the anode versus the cathode according to the above equations.

Sample foils of natural nickel and iron, each 3 μm thick, were placed between the two cathode plates on a rotatable sample changer which can be operated outside of the chamber to avoid deterioration of gas purity. For the sample-out measurements, a tungsten foil of 50 μm thick or a gold foil of 1 μm thick was placed at the sample position. A polypropylene film of 10 μm thick was used for neutron fluence determination by counting protons from the H(n,p) reaction. In addition, ^{241}Am samples or ^{6}LiF samples were located on the sample changer for the calibration of energy scale using monoenergetic α-particles from ^{241}Am or tritons from the ^{6}Li(n_{th},t)α reaction.

Gas mixture of Kr+5%CH_4 was used in the measurements for neutron energies up to 10 MeV to avoid backgrounds due to the O(n,α) reaction, while Kr+3%CO_2 gas mixture was used in the earlier measurements[3]. For the measurements at 14 MeV, Kr+2%CO_2 gas mixture was used since the C(n,α) reaction is the main background at this neutron energy. The gas pressure was adjust-

ed so that to stop the emitted α-particle between the cathode and the Frisch grid. For the neutron fluence determination using the H(n,p) reaction, Kr+CO_2 counting gas was used since CH_4 produces large backgrounds due to recoil protons.

For incident neutron energies between 4.2 and 10.6 MeV, monoenergetic neutron beam was obtained by the D(d,n) reaction at Tohoku University Dynamitron Facility and JAERI Tandem Accelerator Facility. Background due to the D(d,np) breakup neutrons was proved to be negligible up to En = 10.6 MeV by auxiliary experiment with ^{3}He(d,np) neutron source[5]. Neutron beam of 14.1 MeV was obtained by the T(d,n) reaction at Tohoku University Dynamitron Facility. The neutron beam was collimated by a copper collimator so that the diameter of the beam was same as that of the sample to reduce the backgrounds generated by the bombardment of the chamber materials and a counting gas with neutrons. A NE213 detector was placed on the neutron beam axis to monitor the source neutrons.

A block diagram of the electronics is illustrated in Fig. 2. The events generated in forward- and backward- hemisphere were analyzed simultaneously. Coincidental pulse height data of the cathode and the anode were stored in a three parameter data acquisition system. Signals from the ring electrodes were used to reject events by particles having lower ionization density than α-particles such as protons.

The absolute value of the cross section was determined relative to the H(n,p) cross sections. In the incident energy range lower than 6 MeV, the normalization was made by measuring the recoil protons from the polypropylene sample placed in the GIC with the same counting systems. This normalization was extended up to 10.6 MeV using a NE213 detector with its known relative efficiency. In the 14.1 MeV measurements, neutron fluences were determined using a recoil proton counter telescope placed instead of the GIC, since the GIC cannot be applied to the measurement of the H(n,p) reaction owing to its incomplete stopping power to stop 14 MeV protons.

3. Measurements and Data Reduction

Figure 3-a shows a two-dimensional spectrum for the Ni(n,α) cross section measurement at 7.9 MeV of neutron energy. α-particles appear in the area between two lines corresponding to 0-deg. and 90-deg. of emission angle which are determined by the equation (1) and (2). Backgrounds due to recoil protons from CH_4 are seen only in the region of lower pulse height since gas pressure is optimized for the α-particles and protons deposit only a part of their energies in the counting gas. Figure 3-b shows the anode spectrum

corresponding to the α-particle area between 0-deg. and 90-deg. lines. Good S/N ratio is achieved in higher pulse height region where α-particles are observed, since proton background due to recoil protons and the Ni(n,p) reaction appear only in lower pulse height region.

Measuring time of several to 10 hours for each run is enough to obtain sufficient statistics owing to the high efficiency and good S/N ratio of the GIC spectrometer. The double-differential α-particle production cross sections were obtained by the two-dimensional data processing according to equations of (1) and (2). The energy-differential cross sections and the reaction cross sections were derived from integrating the double-differential cross sections.

4. Results and Discussion

Figure 4 shows the double-differential Ni(n,α) cross sections at 7.9 MeV incident neutron energy compared with those by ENDF/B-VI. The present results show peaking at forward and backward angles in the high energy region of the spectra, while ENDF/B-VI does not provide such structure. In addition, experimental data indicate spectrum shift because of the kinematical effect, i.e. harder spectrum at forward angle than that at backward angle. On the contrary, ENDF/B-VI gives angle-independent spectra in laboratory system.

Figure 5 shows the energy-differential Ni(n,xα) cross sections in center of mass system at En = 7.9, 9.7 and 14.1 MeV compared with experimental results by Graham et al.[6], Grimes et al.[7] and the evaluations of ENDF/B-VI. The present spectrum at En = 9.7 MeV is slightly softer than that by Graham et al., but agrees at En = 14.1 MeV with that by Grimes et al. within the quoted errors. The present result at En = 14.1 MeV is in good agreement with the spectrum of ENDF/B-VI, while our absolute values at En = 7.9 and 9.7 MeV are much lower than those of ENDF/B-VI.

Figure 6 shows the Ni(n,xα) cross sections compared with those by Paulsen et al.[8], Wattecamps[9], Graham et al[6]. and Grimes et al.[7] and evaluations of ENDF/B-VI and JENDL-3. The present data are in agreement with those by Paulsen et al. and JENDL-3 except for the incident energy of 9.7 MeV where our data show depression and are close to those by Wattecamps and Graham et al.. The reconfirmation will be necessary for our data at 9.7 MeV to clarify the excitation function of the Ni(n,xα) reaction.

Figure 7 shows the double-differential Fe(n,xα) cross sections at 14.1 MeV compared with those of ENDF/B-VI. Because of their small cross sections, uncertainties of our data are fairly larger compared with for Ni. Agreement between the present data and ENDF/B-VI is reasonably well except for the spectrum shift because of the kinematical effect which is not considered in

the ENDF/B-VI evaluation.

Figure 8 shows the energy-differential Fe(n,xα) cross sections in center of mass system at En = 9.7, 10.6 and 14.1 MeV compared with those by Saraf et al.[10], Grimes et al.[7] and ENDF/B-VI. The present spectrum at En = 10.6 MeV agrees with the data by Saraf et al., while the absolute values of our data at En = 9.7 MeV are too larger than their data. At En = 14.1 MeV, present spectrum is in good agreement with that by Grimes et al.. The present spectra agree with those of ENDF/B-VI for these three neutron energy points.

Figure 9 shows the Fe(n,xα) cross sections compared with those by Paulsen et al.[8], Wattecamps et al.[11], Saraf et al.[10], Grimes et al.[6], JENDL-3 and ENDF/B-VI. Although scatter of the experimental data is noticeable due to their large uncertainties, our data agree with those by Paulsen et al. and Wattecamps et al. within their quoted errors. The data measured by Saraf et al. are much smaller than the other data at En = 8.0 and 9.5 MeV. The present data seem to support the cross section values of ENDF/B-VI as well as their spectra as mentioned above.

5. Conclusion

Taking advantages of very high efficiency and good S/N ratio of the present spectrometer, the present measurements provided new data for the double-differential cross sections, the energy distributions and excitation functions for the Fe, Ni(n,xα) reactions in the neutron energy region of 4~14 MeV where only very few data had been reported.

Acknowledgment

The authors wish to thank Messrs. T.Takahashi, K.Komatsu and T.Nagaya for their supports in fabrication of the detector system and to thank Messrs. T.Iwasaki, S.Meigo, R.Sakamoto, M.Fujisawa and operating crew of JAERI Tandem Accelerator for their help during experiments.

References

1) C.Y.Fu, D.C.Larson, D.M.Hetrick, H.Vonach, J.Kopecky, S.Iijima, N.Yamamuro and G.Maino, Proc. Int. Conf. on Nucl. Data for Sci. and Tech., Jülich, Germany (1991) pp.857.
2) M.Baba, N.Ito, S.Matsuyama and N.Hirakawa, Proc. Int. Conf. on Nucl. Data for Sci. and Tech., Jülich, Germany (1991) pp.477.
3) N.Ito, M.Baba, F.Huang, S.Matsuyama and N.Hirakawa., JAERI-M, 92-027, 257 (1992).

4) C.Budtz-Jørgensen, H.-H.Knitter, Ch.Straede, F.J.Hanbsch and R.Vogt, Nucl. Instr. and Meth., A258, 209 (1987).
5) S.M.Grimes, P.Grabmayr, R.W.Finlay, S.L.Graham, G.Randers-Pehrson and J.Rapaport, Nucl. Instr. and Meth., 203, 269 (1982).
6) S.L.Graham, M.Armad, S.M.Grimes, H.Satyanarayana and S.K.Saraf, Nucl. Sci. Eng., 95, 60 (1987).
7) S.M.Grimes and R.C.Height, Phys. Rev. C19, 2127 (1979).
8) A.Paulsen, H,Liskin, F.Arnotte and R.Widera, Nucl. Sci. Eng., 78, 377 (1981).
9) E.Wattecamps, Proc. Int. Conf. on Nucl. Data for Sci. and Tech., Jülich, Germany (1991) pp.310.
10) S.K.Saraf, C.E.Brient, P.M.Egun, S.M.Grimes, V.Mishra and R.S.Pedroni, Nucl. Sci. Eng., 107, 365 (1991).
11) E.Wattecamps, H.Liskin, and F.Arnotte, Proc. Int. Conf. on Nucl. Data for Sci. and Tech., Antwerp, Belgium (1982) pp.156.

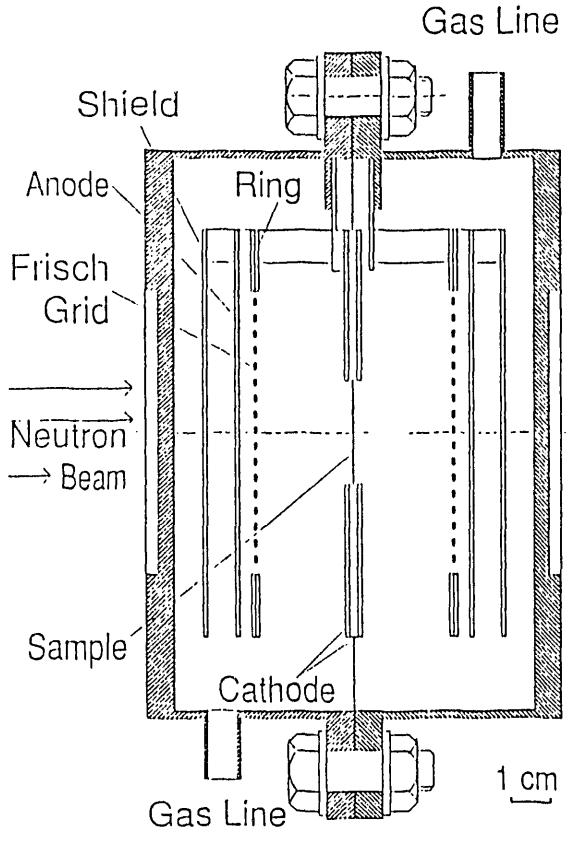

Fig. 1 Schematic view of the gridded ionization chamber (GIC).

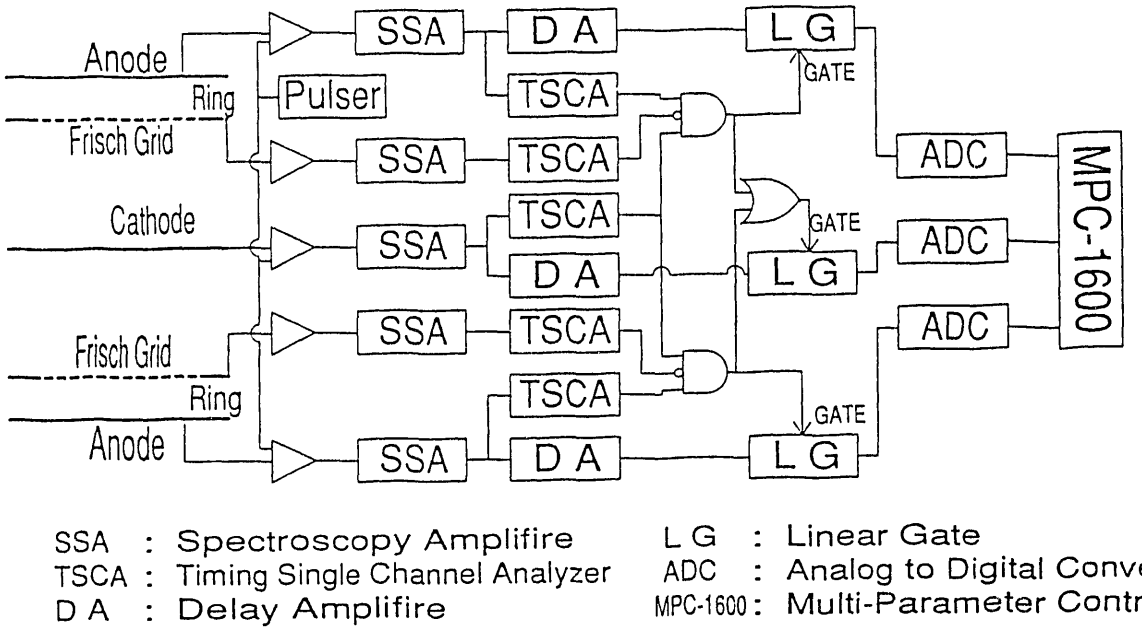

Fig. 2 Block diagram of the counting electronics.

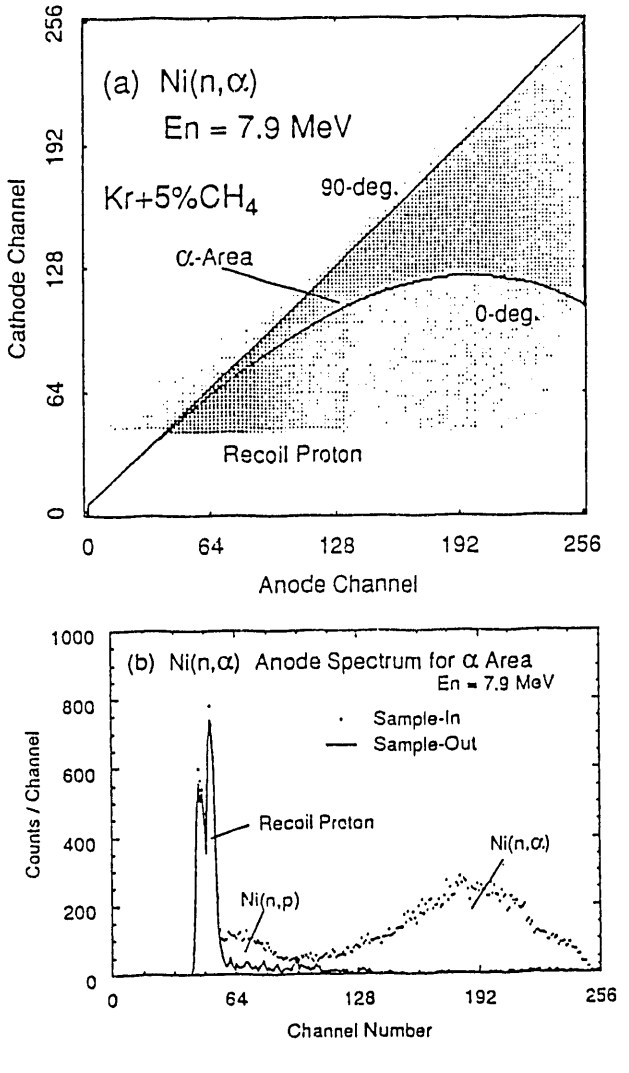

Fig. 3 Two dimensional spectrum and anode spectrum corresponding to the α-particle area for the Ni(n,α) measurement at En=7.9 MeV.

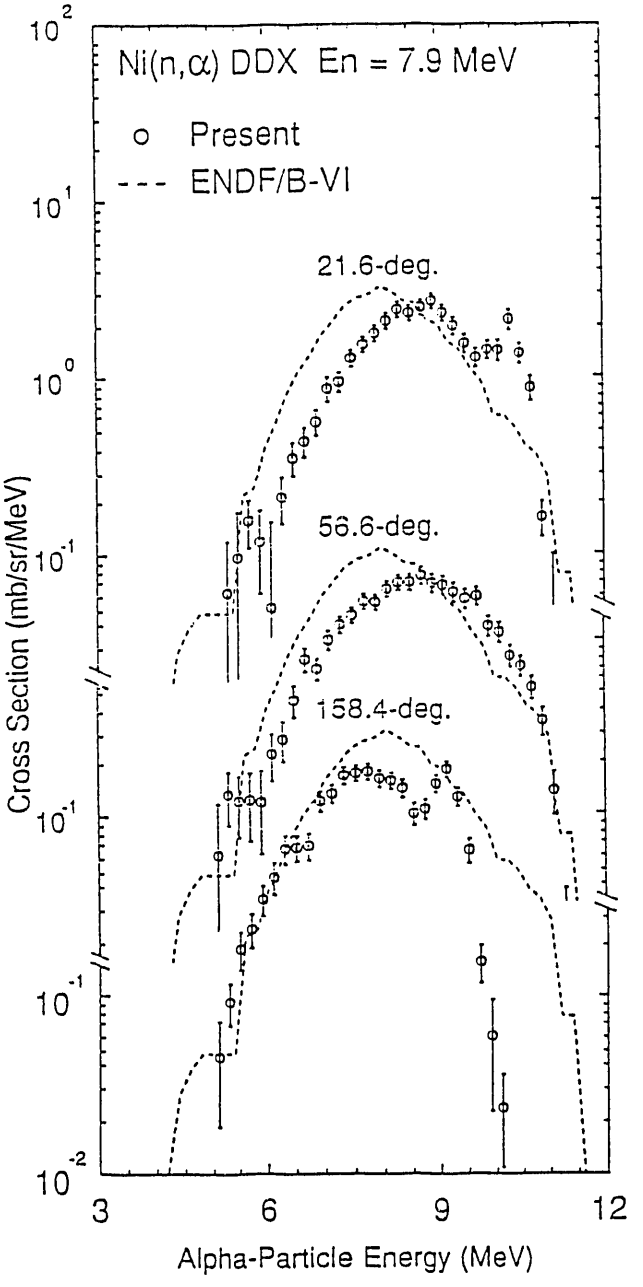

Fig. 4 The double-differential (n,α) cross sections at En=7.9 MeV.

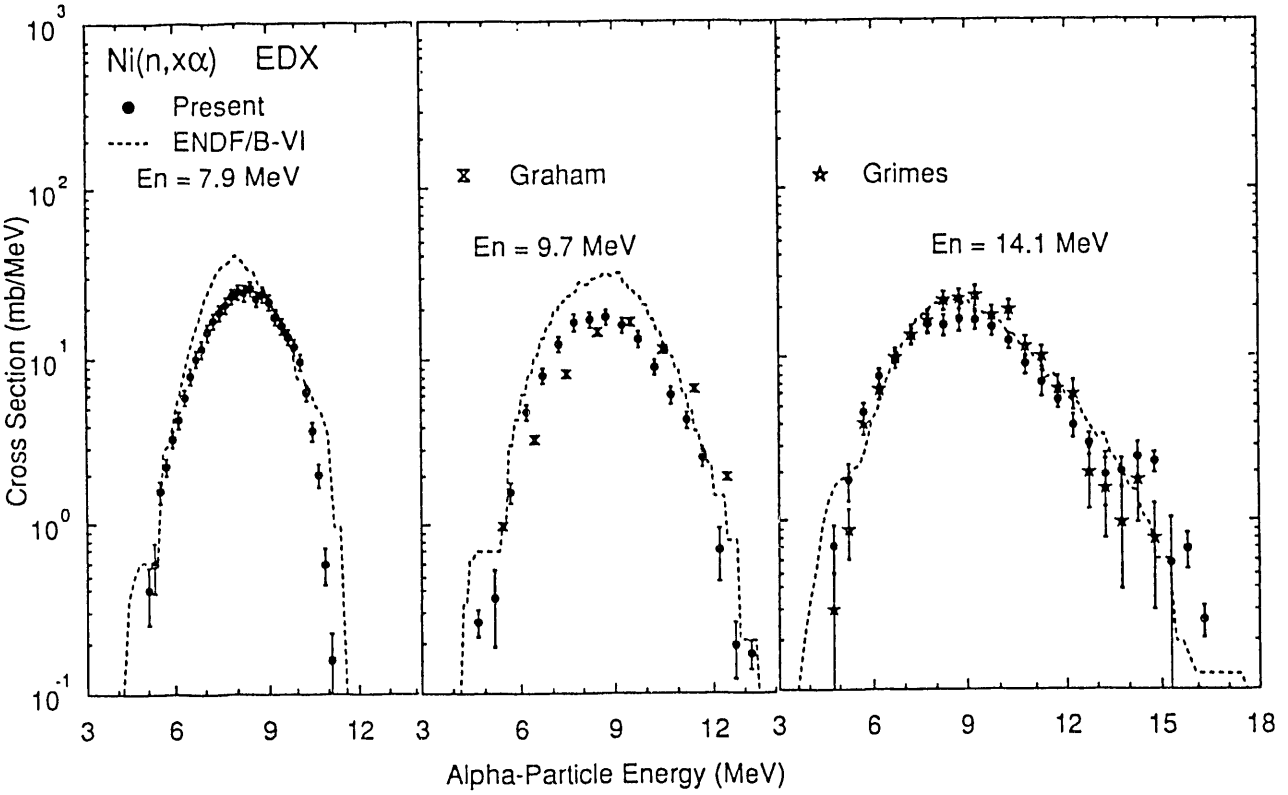

Fig. 5 The energy-differential Ni(x,xα) cross sections at En=7.9, 9.7 and 14.1 MeV.

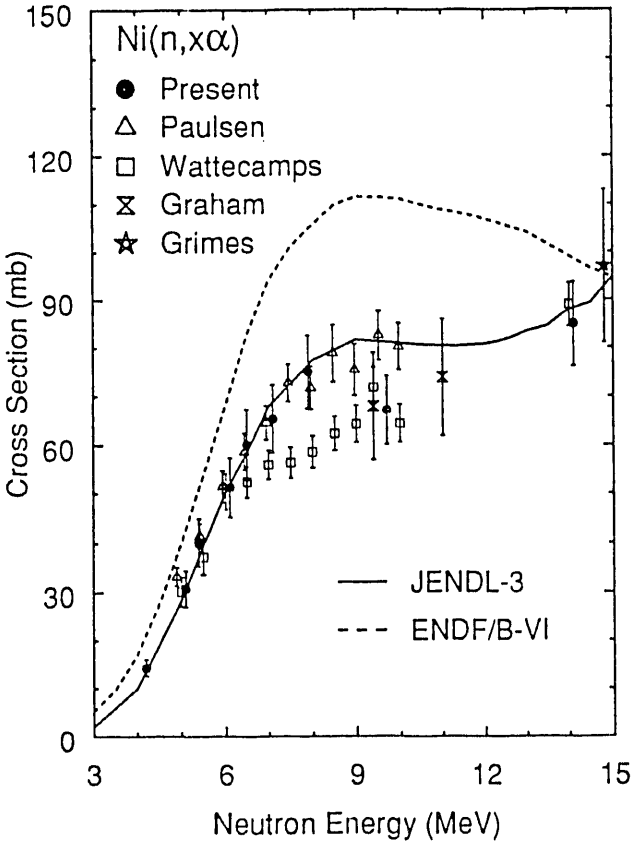

Fig. 6 The integrated Ni(n,xα) cross sections.

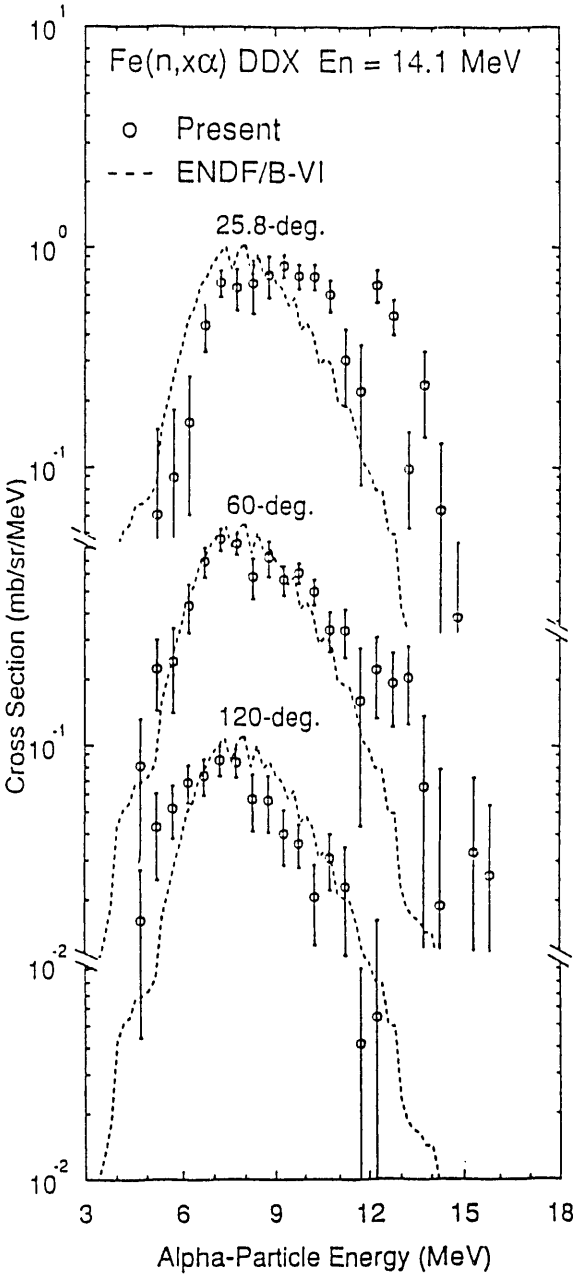

Fig. 7 The double-differential Fe(n,xα) cross sections at En=14.1 MeV.

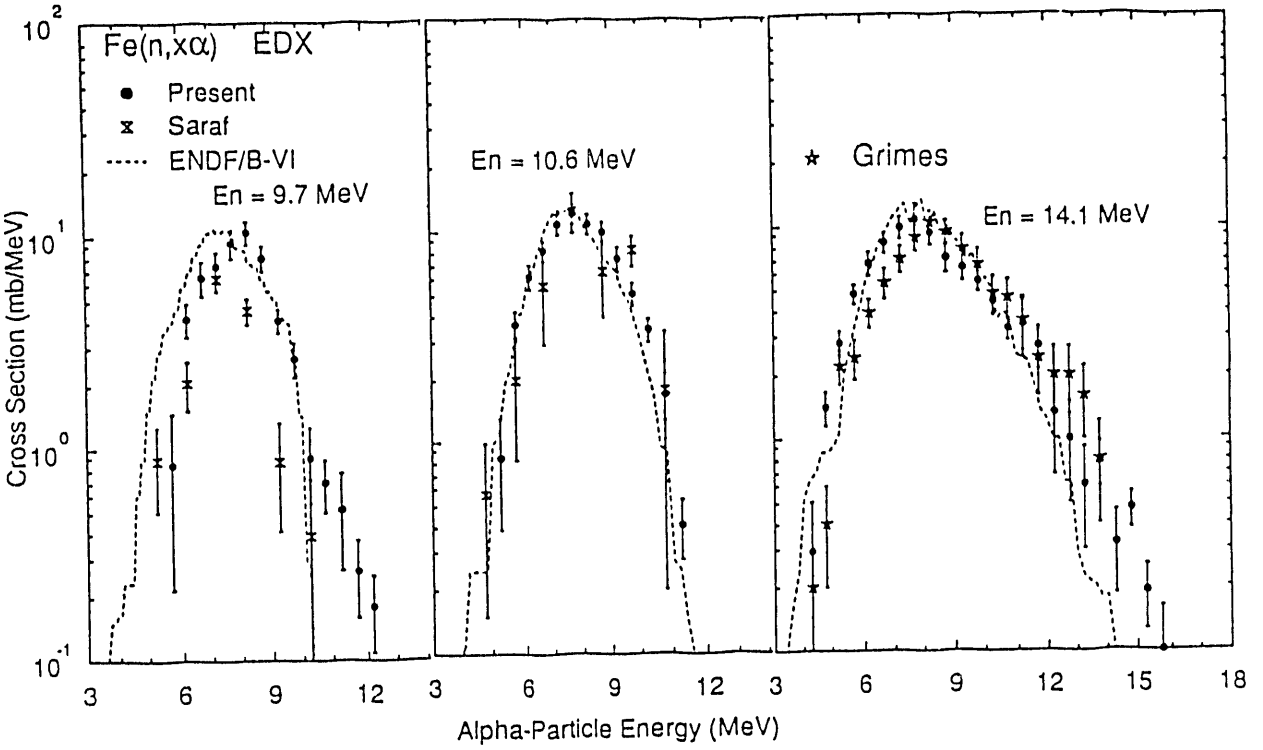

Fig. 8 The energy-differential Fe(n,xα) cross sections at En=9.7, 10.6 and 14.1 MeV.

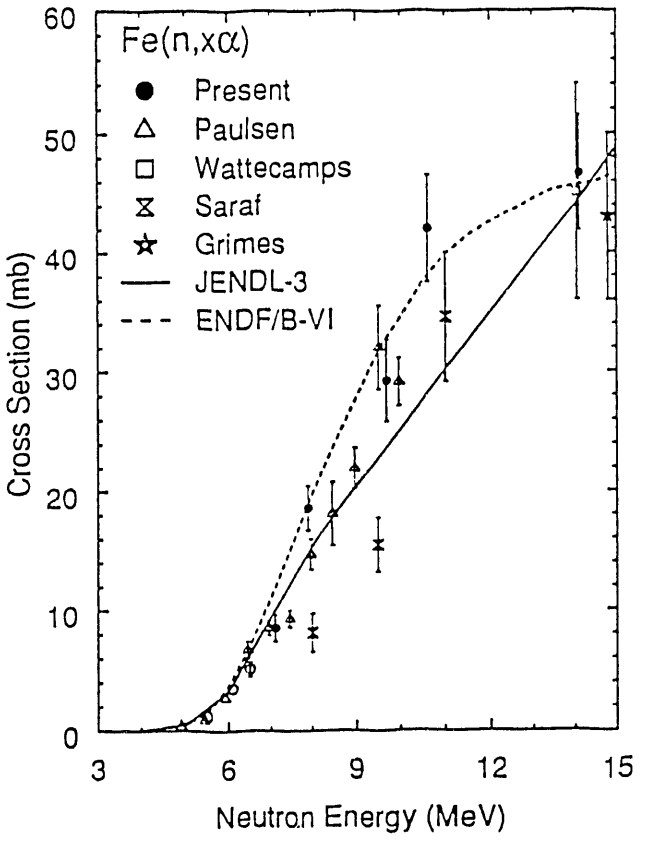

Fig. 9 The integrated Fe(n,xα) cross sections.

3.22 Measurements of Double-differential Neutron Emission Cross Sections of Mo, Ta and W

S.Matsuyama, T.Okubo, M.Baba, T.Ito, T.Akiyama, N.Ito, and N.Hirakawa
Department of Nuclear Engineering, Tohoku University
Aoba, Aramaki, Aoba-ku, Sendai 980, Japan

Double-differential neutron emission cross sections (DDXs) of Mo,Ta and W have been measured for 14 MeV incident neutrons using Tohoku University Dynamitron time-of-flight spectrometer.

DDX data were obtained 8-10 angles for secondary neutron energy range down to 0.7 MeV. Furthermore we deduced angle-integrated spectra and angular distributions of continuum neutrons.

The present results of DDXs for these nuclides are in good agreement with other experimental data. On the other hand, they show discrepancies from the data derived from the evaluated nuclear data of JENDL-3 and ENDF/B-VI. The angular distributions of continuum neutrons are compared with the systematics proposed by Kalbach-Mann and Kalbach.

1. Introduction

Double-differential neutron emission cross sections (DDXs) are important for designs of fusion and fission reactors, applications for radiobiology and high-energy accelerator technology, since these are the basic data in evaluating neutron transport, radiation damage and nuclear heating. In addition, DDXs are indispensable for the verification of theoretical calculations.

In this work, we have measured the double-differential neutron emission cross sections of Mo, Ta and W for 14.1 MeV neutrons and derived angle-integrated neutron emission spectra and angular distributions of continuum neutrons. The neutron emission spectra of these nuclides are expected as the reference data for the theoretical calculations.

2. Experiments

The experiments were performed using Tohoku University 4.5 MV Dynamitron pulsed neutron generator and associated time-of-flight spectrometer. The experimental method has been described previously /1,2/.

Primary 14.1 MeV neutrons were obtained via the T(d,n) reaction at emission angle of 97.5-degree. Pulsed deuteron beam with duration less than 2 nsec and 1 MHz repetition rate bombarded a metallic tritium target of tritium loaded

titanium, 1.5 cm diam and 4.5 Ci/cm^2 thick, which was mounted in a low-mass chamber.

The scattering samples were metallic cylinders of molybdenum, tantalum and tungsten, 3 cm diam and 5 cm long, and suspended vertically at a distance of 12 cm from the target.

Scattered neutrons were detected by a NE213 liquid scintillator, 14 cm-diam and 10 cm thick, coupled to a fast-timing photomultiplier tube (Hamamatsu R1250). It was placed in a massive shield that could be positioned at the scattering angles from 0 to 160-degree. In the present measurements, the flight path length was 6.5 m and an additional preshield was employed to suppress room-returned neutrons. For gamma-ray reduction, high- and low-bias pulse shape discriminator (PSD) systems were employed to achieve good neutron-gamma separation for wide neutron energy range. Threshold levels of high- and low-bias PSD systems were 2 MeV and 0.3 MeV proton, respectively. Energy dependent detector efficiency was determined by the calculation using O5S code for the energy region higher than 4 MeV and by measuring time-of-flight spectrum of fission neutrons from ^{252}Cf for the low energy region. Absolute cross section was determined referring the elastic scattering cross section of hydrogen.

Time-of-flight method was used to determine neutron energy. Fast timing signals from the detector were converted to fast logic signals by a wide dynamic-range constant-fraction timing discriminator. The time differences between the detector pulses and delayed beam pick-off signals were measured by a time-to-amplitude converter.

Another small NE213 scintillator, 2" diam and 2" thick, was used to provide the normalizations between sample-in and sample-out runs and to monitor time-correlated parasitic neutrons.

The neutron emission spectra were measured at several angles between 30 and 150-degree. For each measurement, sample-in and sample-out runs were carried out without stopping the beam using a remotely-controlled sample-changer.

3. Data Analysis

The procedure of data analysis has been described in detail elsewhere /1,2/. The experimental time-of-flight spectra were converted to energy spectra after applying corrections for detector efficiency and sample-out background. Then, these energy spectra were corrected for the effects of finite sample size and backgrounds caused by parasitic and target-scattered neutrons. The effects of finite sample size were estimated by Monte-Calro

calculations using a program SYNTHIA /3/. The JENDL-3 data were used for the corrections of Mo and Ta, and the ENDF-B/IV data were used for W. However the neutron emission spectra derived from the nuclear data did not reproduce the experimental data. Therefore, we modified the data by combining the evaluated nuclear data and the experimental data with the help of the Kalbach-Mann (KM) /4/ or Kalbach systematics /5/.

4. Results and Discussions

Data Comparison

Figures 1-3 show the angle integrated neutron emission spectra of Mo, Ta and W in comparison with the experimental data at OKTAVIAN /6/, the evaluation by A.Pavlic & H.Vonach /7/, and the evaluated nuclear data of JENDL-3 and ENDF/B-VI. Double-differential neutron emission cross sections are shown in Figs. 4-6, compared with those derived from the evaluated nuclear data of JENDL-3 and ENDF/B-VI.

The experimental spectra consist of an elastic peak and continuum neutrons and are very similar to each other except for the strength of collective state. Experimental spectra show isotropic distribution in the lower energy region and forward-peaked angular distribution in the higher energy region.

The present data are in good agreement with those taken at OKTAVIAN and the A.Pavlic & H.Vonach's evaluations except for the high energy region of Mo. In comparing the experimental data with the nuclear data, following points are pointed out: 1)the experimental data are higher than the JENDL-3 and ENDF/B-VI data in 5-10 MeV energy region and 2)the experimental spectra are very close to both nuclear data in the low energy region where the (n,2n) reaction is the main component, except for ENDF/B-VI of Mo.

There are large discrepancies between the experimental data and the evaluated nuclear data in forward angles, since angular dependence of both nuclear data is given as isotropic in laboratory system. In case of Mo, both nuclear data do not include collective peaks. The ENDF/B-VI data of Ta and W provide forward peaked angular distribution for the (n,continuum) reaction and show somewhat better agreement with the experimental data. However, there exists discontinuity in neutron emission spectra of ENDF/B-VI between isotropic (n,2n) reaction and anisotropic (n,continuum) reaction.

Angular distributions of Continuum Neutrons

Angular distributions of continuum neutrons are shown in Figs. 7-9 compared with the systematics proposed by Kalbach-Mann (KM) and Kalbach. For the calculation of those systematics, a statistical multistep reaction code EXIFON /6/ is used to divide the cross sections into multistep statistical compounds (MSD) and multistep statistical direct (MSD) components. Both systematics reproduce consistently the experimental angular distributions. Figure 10 shows the calculated angle-integrated neutron emission spectra using the EXIFON for Mo, Ta and W together with the experimental data. This code reproduces well the experimental spectra both for the shape and the magnitude.

In previous studies /1,2/, we noted that the KM systematics described well for heavy nuclides while the Kalbach systematics reproduced the results better for light and medium-heavy nuclides if we assumed the Blann-Lanzafame's exciton spectrum /9/ for MSD and the Weisskopf-Ewing's evaporation /10/ or the Lecouteur-Lang's emission spectrum /1/ for MSC (referred as semi-classical modeling in the following). This observation suggests the existence of mass dependence in the angular distributions of continuum neutrons.

The neutron emission spectrum of MSC component is harder than that of semi-classical modeling (see Fig. 11); therefore, angular distributions by both systematics are affected by the method of separation of MSD/MSC ratio especially in the energy region where MSD and MSC magnitudes are comparable. In the present studies, we applied the EXIFON code for the partition of MSD/MSC (referred as MSD/MSC model) and investigated the systematic behavior of the angular distributions.

For this purpose, we use reduced Legendre coefficient $B_1(=a_1/a_0$, where a_0 and a_1 are the zero-th and 1-st order Legendre coefficients for the experimental angular distributions): it is an index of the strength of forward peaking of angular distributions. Figure 12 shows the comparison between the experimental B_1 values (circle) and ones expected from the KM systematics; the results of semi-classical modeling (square) are shown as well as those of MSD/MSC model (triangle).

The experimental B_1 values increase with mass number and those by the KM systematics with MSD/MSC model show similar tendency. The KM systematics with MSD/MSC model describes better the experimental B_1 values than that with semi-classical modeling especially for medium-heavy nuclides. Figure 13 shows the similar comparison for the angular distributions of V, Cr and Zr. The KM systematics with MSD/MSC model reproduces better the experimental angular distributions. However the experimental B_1 values show differences from those by

the KM systematics and should be traced back further for better understanding.

5. Summary

We have measured double-differential neutron emission cross sections of molybdenum, tantalum and tungsten, and derived 1)double-differential neutron emission cross sections, 2) angle-integrated neutron emission cross sections and 3)angular distributions of continuum neutrons. Present data are in good agreement with other experimental data. However, evaluated nuclear data library of JENDL-3 and ENDF/B-VI show discrepancies from the experimental data especially in the high energy region.

Angular distributions of continuum secondary neutrons are reproduced by Kalbach & Mann systematics using the EXIFON for derivation of MSD/MSC ratios. Angle integrated neutron emission spectra calculated by using the code EXIFON are in good agreement with experimental data. Therefore, it is very useful to use the Kalbach and Mann systematics in combination with the EXIFON for the evaluation of continuum angular distributions.

Acknowledgment

The authors express their thanks to Dr.H.Kalka of T.U.Dresden and Dr.Y.Watanabe of Kyusyu University for providing us with the EXIFON code.

1. S.Matsuyama et.al. ;JAERI-M, 92-027, p.309(1992).
2. M.Baba et.al. ;J. Nucl. Sci. Technol., 27(7) p.601(1990).
3. T.Sakase ;Private communication.
4. C.Kalbach and F.M.Mann ;Phys. Rev., C23(1) p112(1981).
5. C.Kalbach ;Phys. Rev., C37(6) p.2350(1988).
6. H.Kalka ;Z.Phy.,A341 298(1992) and private communication
7. A.Takahashi et.al ;Private communication.
8. A.Pavlik & H.Vonach ;ISSN 0344-8401, No.13-4(1988).
9. M.Blann & F.M.Lanzafame ;Nucl. Phys., A142 p.559(1970).
10. D.Hermsdorf et.al. ;J. Nucl. Eng.,27 p.747(1973).
11. M.Lecouteur & D.W.Lang ;Nucl.Phys., 13 p32(1959).

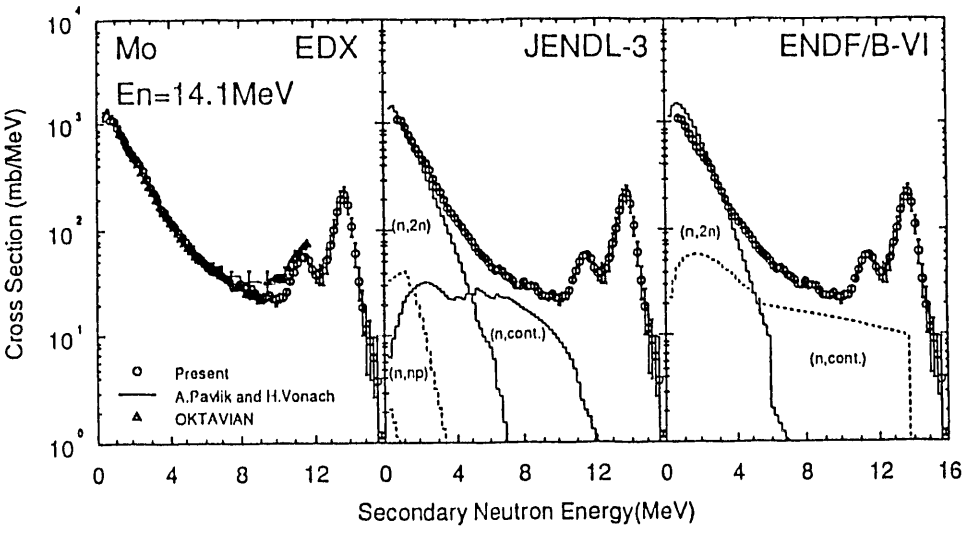

Fig. 1 Angle-integrated neutron emission spectra of Mo.

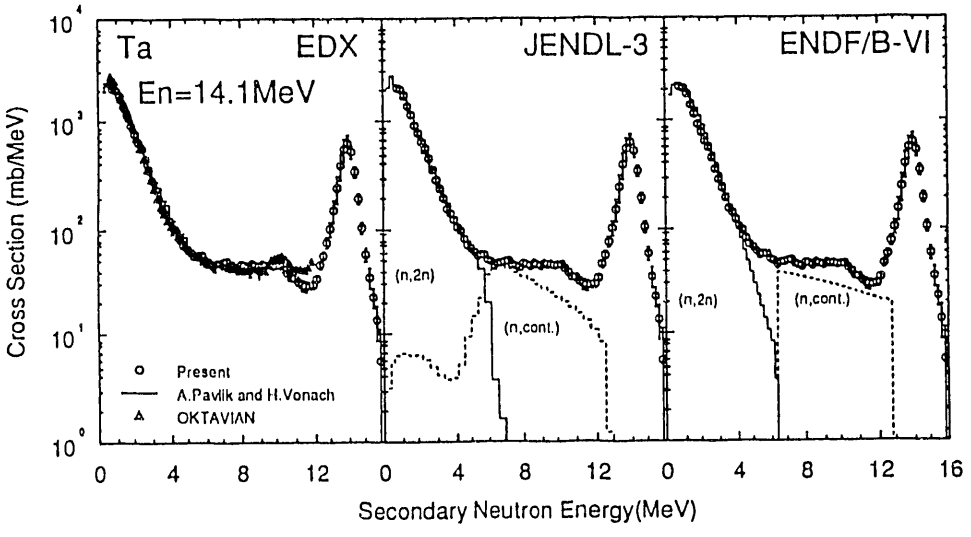

Fig. 2 Angle-integrated neutron emission spectra of Ta.

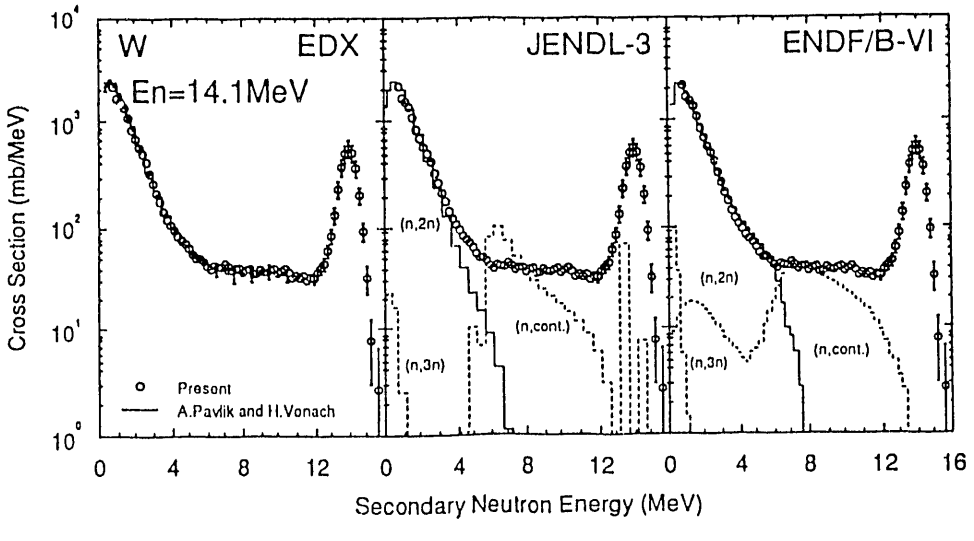

Fig. 3 Angle-integrated neutron emission spectra of W.

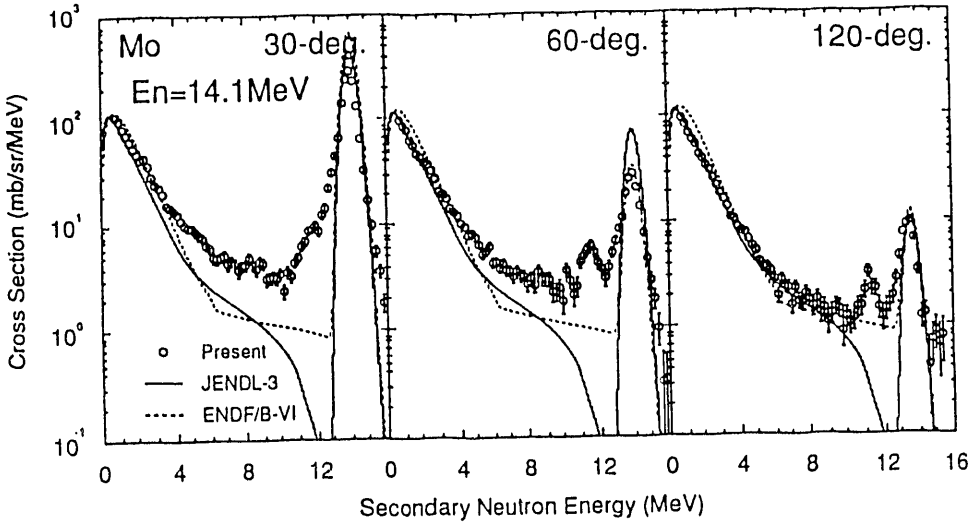

Fig. 4 Double-differential neutron emission cross sections of Mo.

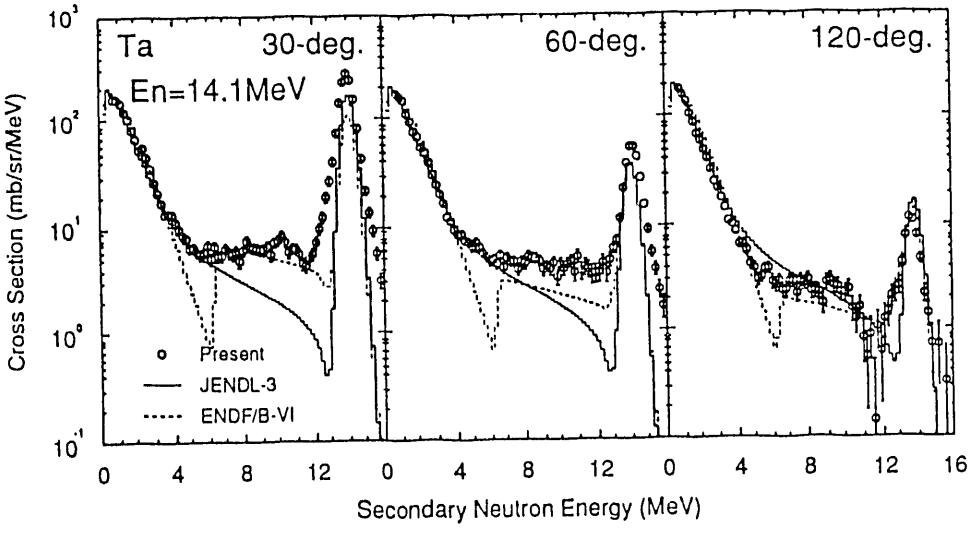

Fig. 5 Double-differential neutron emission cross sections of Ta.

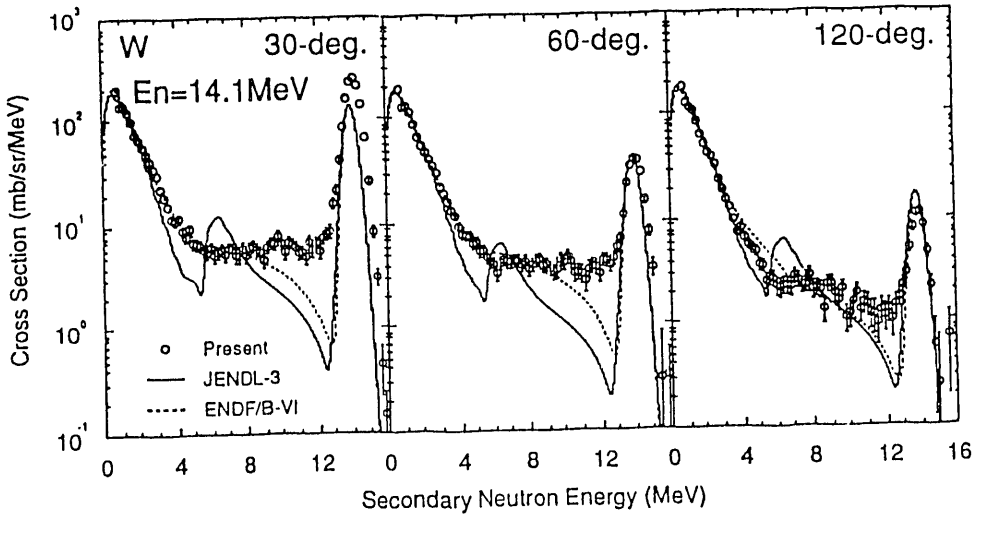

Fig. 6 Double-differential neutron emission cross sections of W.

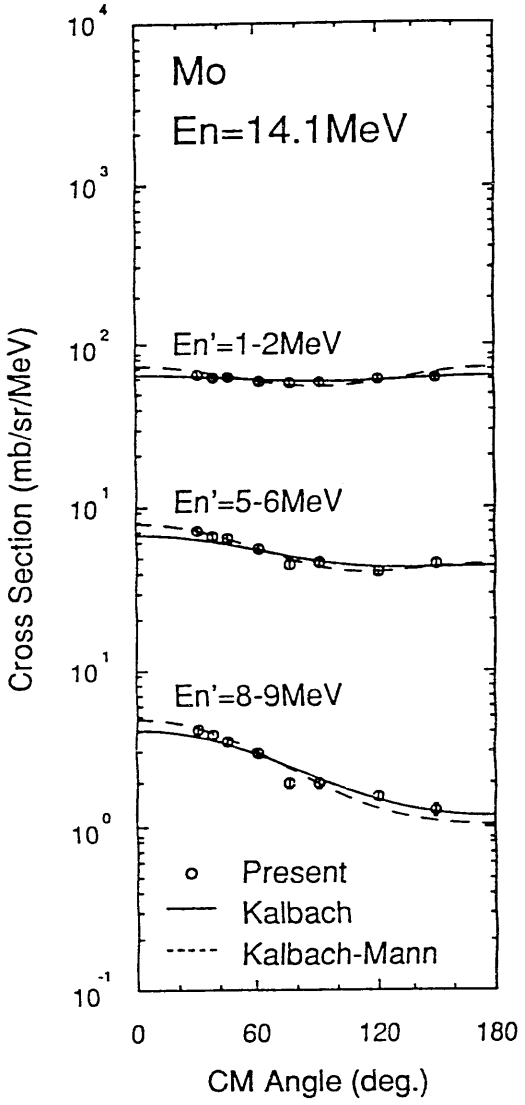

Fig. 7 Angular distributions of continuum neutrons of Mo, compared with Kalbach & Mann and Kalbach systematics.

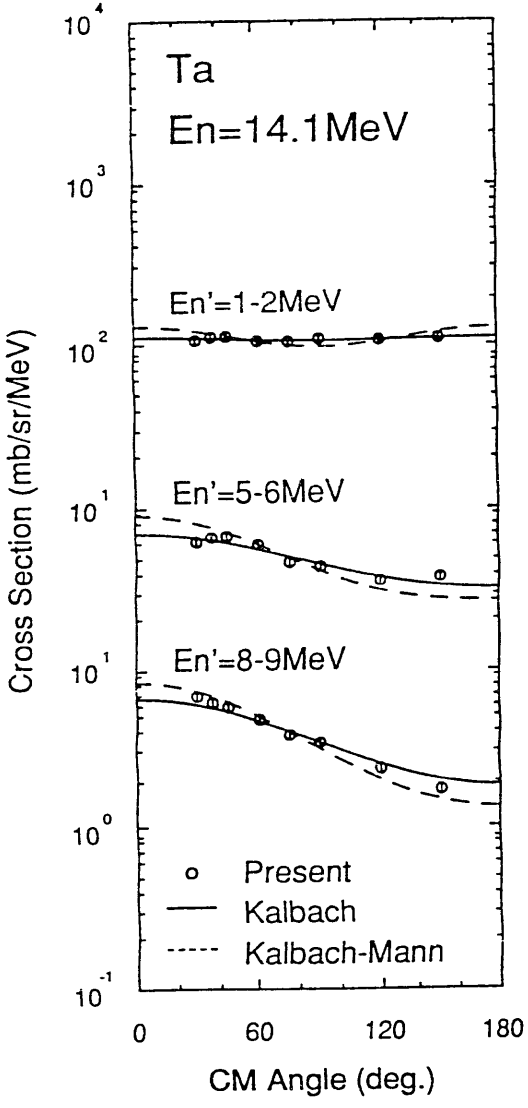

Fig. 8 Angular distributions of continuum neutrons of Ta, compared with Kalbach & Mann and Kalbach systematics.

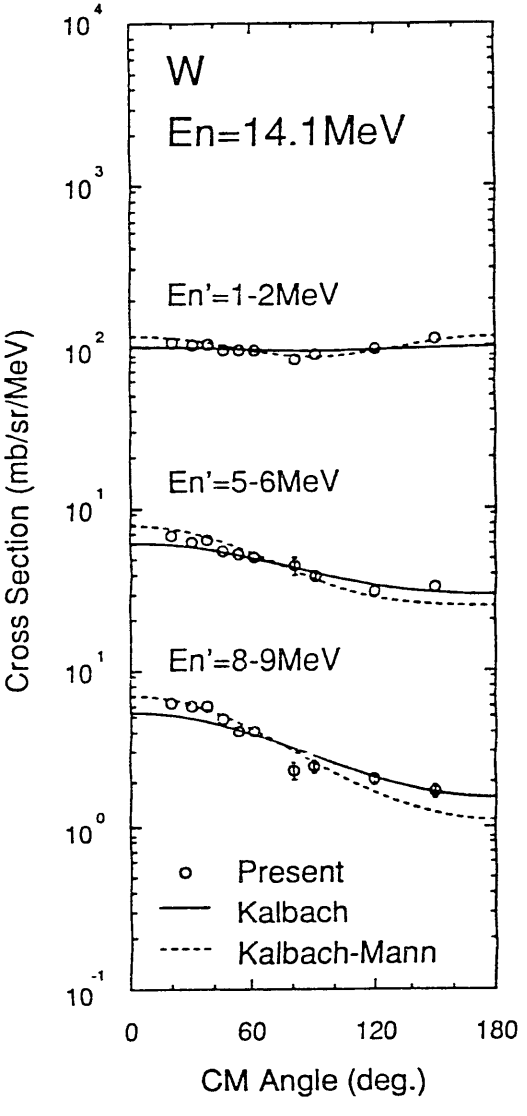

Fig. 9 Angular distributions of continuum neutrons of W, compared with Kalbach & Mann and Kalbach systematics.

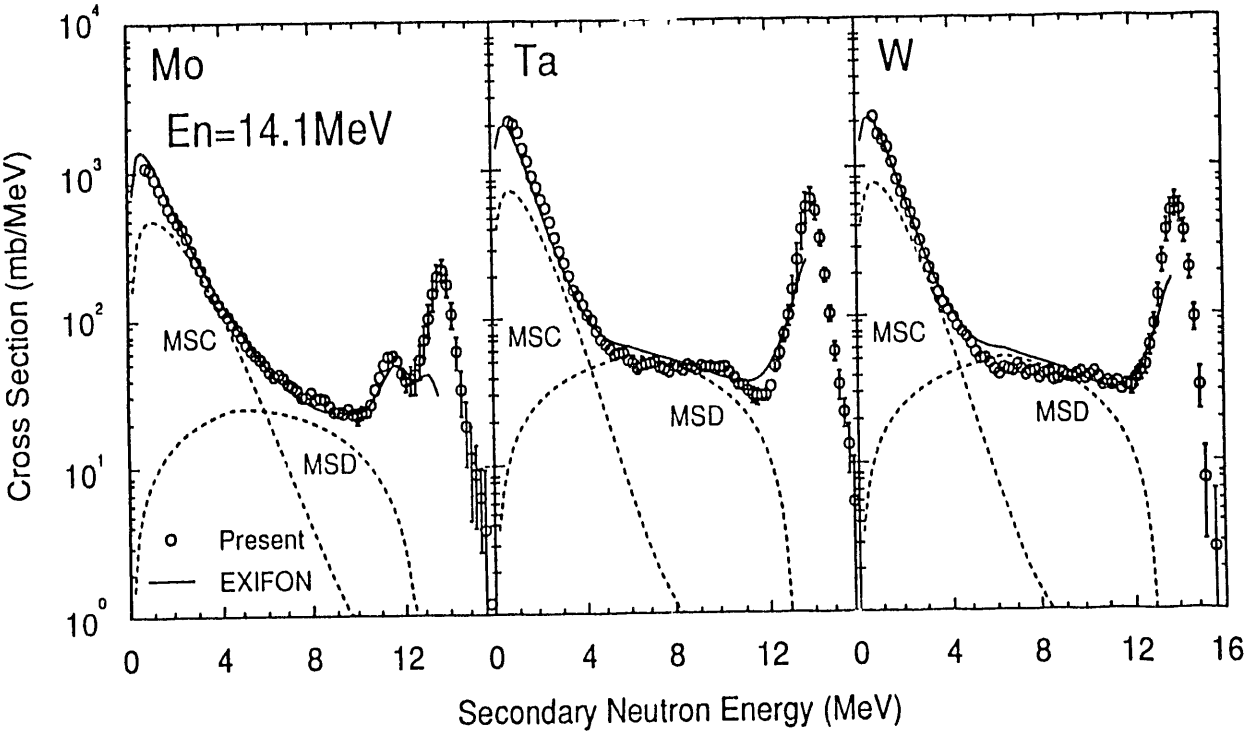

Fig. 10 Angle-integrated neutron emission spectra of Mo, Ta and W, compared with the calculated results of EXIFON.

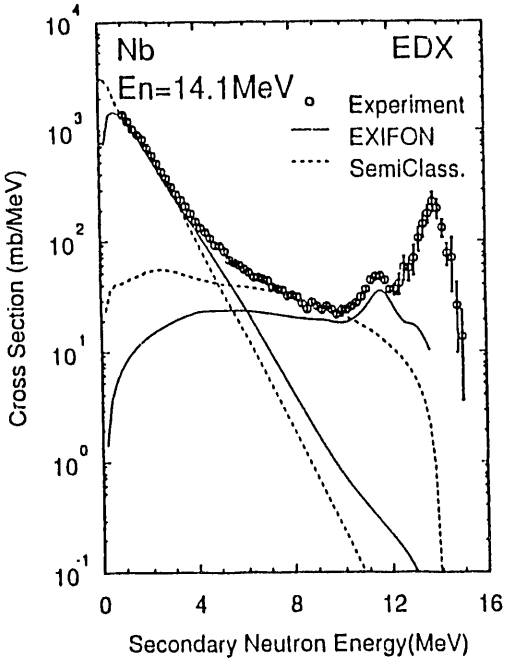

Fig. 11 Angle-integrated cross sections and each component of reactions, which are analyzed with EXIFON and semi-classical modeling.

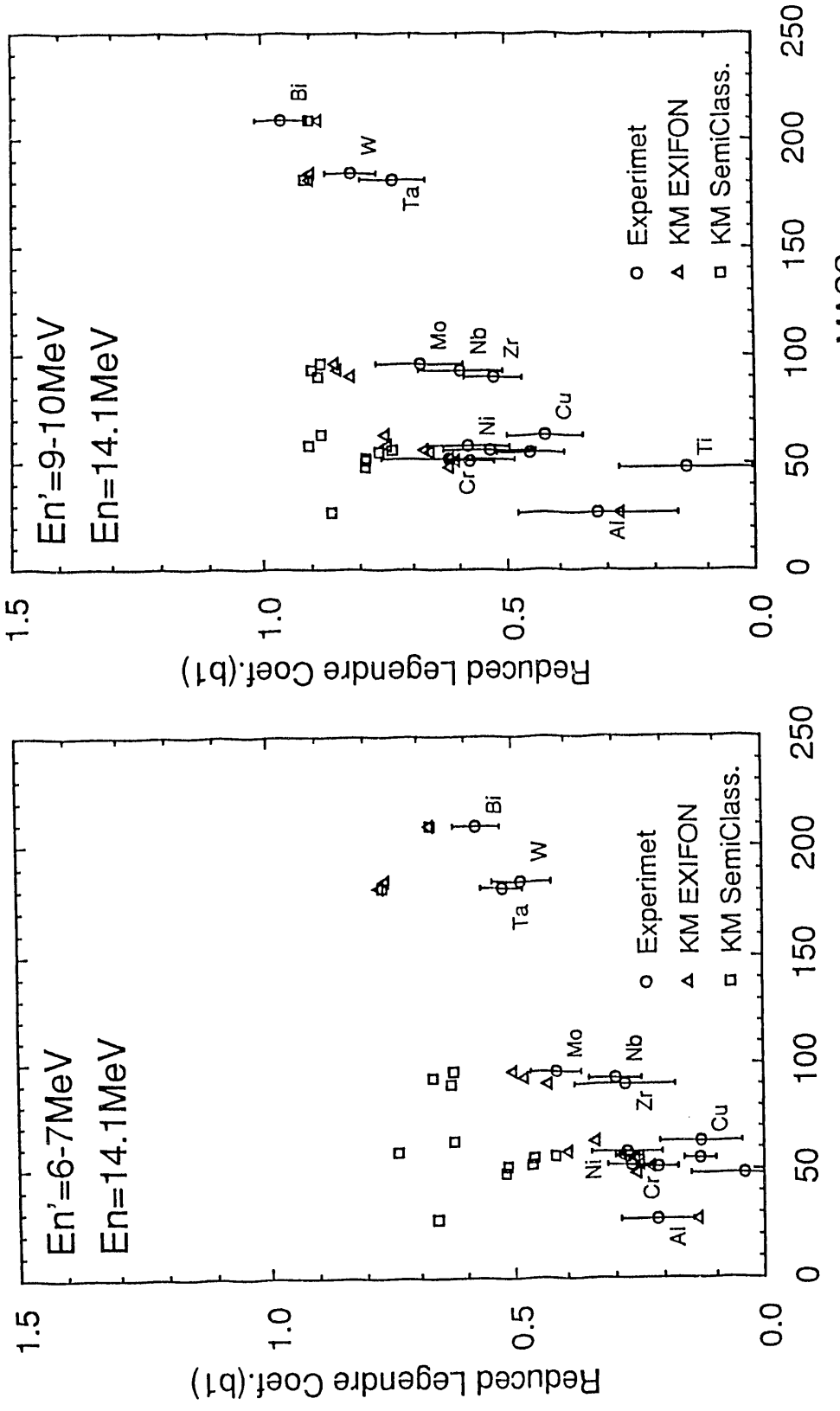

Fig. 12 Reduced Legendre coefficients of B1 for continuum neutrons, compared with calculations using Kalbach & Mann systematics with MSD/MSC partitions by EXIFON and semi-classical model.

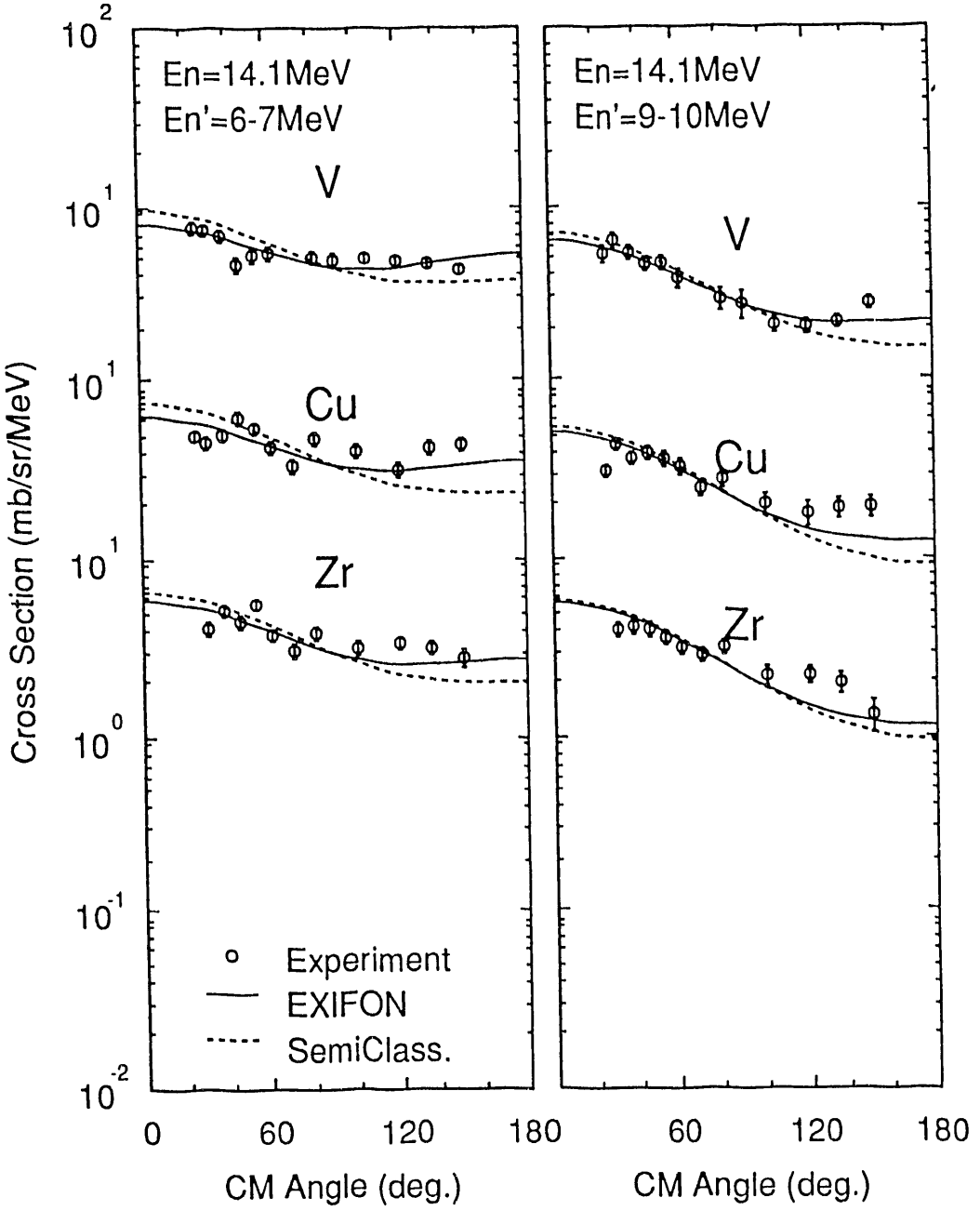

Fig. 13 Angular distributions of continuum neutrons compared with calculations using Kalbach & Mann systematics with MSD/MSC partitions by EXIFON and semi-classical model.

3.23 Measurement of Fission Cross Section of ^{237}Np in Resonance Region with Electron Linac Driven Lead Slowing-down Spectrometer (KULS)

Itsuro KIMURA, Akihiro YAMANAKA, Satoshi KANAZAWA, Yoshiaki FUJITA*
Katsuhei KOBAYASHI*, Yoshihiro NAKAGOME*, Shuji YAMAMOTO* and
Tadaharu TAMAI*

Department of Nuclear Engineering, Kyoto University
Yoshida, Sakyo, Kyoto 606-01
*Research Reactor Institute, Kyoto University
Kumatori, Sennan, Osaka 590-04

The fission cross section of Np-237 relative to that of U-235 from about 1eV to about 5 keV with energy resolution ($\Delta E/E$) of about 40% was measured with back-to-back type double fission chambers using a lead slowing-down neutron spectrometer driven by an electron linear accelerator.

The result shows that the shape of the present energy dependent cross section agrees with that of ENDF/B-VI, that of JENDL-3 below 130 eV and that of Plattard et al's data, the absolute values of the present data are about 3 times larger than those of the above three, but are rather closer to those measured by Hoffman et al..

A lead neutron slowing down spectrometer was installed beside the electron linear accelerator (electron linac) of Research Reactor Institute, Kyoto University. At the center of the spectrometer, we set an air-cooled Ta photoneutron target to generate pulsed neutrons. This spectrometer was named KULS. We obtained its performance, namely the relation between the slowing-down time t and the neutron energy E and the energy resolution $\Delta E/E$, using a BF_3 counter or a Ar gas proportional counter with a resonance filter of several elements. Good linearity was observed between $1/\sqrt{E}$ and t, and the energy resolution was determined to be about 40%. Details about the characteristics of KULS will be written elsewhere [1].

By making use of KULS, we measured the cross section for the ^{237}Np

(n, f) reaction relative to that for $^{235}U(n, f)$ from about 1 eV to about 5 keV. Back-to-back type double fission chambers were employed[2] for the fission cross section measurement. As the electrodes of the chambers, we electrodeposited $^{237}NpO_2$ and $^{235}UO_2$ layers on stainless steel plates 28 mm in diameter and 0.2 mm thick. The diameter of the deposits was 2 cm. After the electrodeposition, each plate was sintered and set into the chambers. The number of atoms in the deposits was determined by the alpha ray spectrometry with a Si surface barrier detector. The chambers were filled with a mixed gas of 97% Ar and 3% N_2 at 1 atm, and then put into a Bi covered experimental hole of KULS.

By an operation of the electron linac for about 50 hours, the cross section for the $^{237}Np(n, f)$ reaction was obtained, in which only the statistical error was taken into account. In Fig. 1, the present result is compared with the values in two newly evaluated nuclear data files, JENDL-3[3] and ENDF/B-VI[4]. The present result is compared with two earlier experimental data by Hoffman et al.[5] and Plattard et al'.[6] in Fig. 2. Since the energy resolution of the original files and earlier data is much higher than that of the present experiment, we processed those data by multiplying a resolution function of a Gaussian with 40% of its full width at half maximum.

From these two figures, it is seen that (1) the gross shape of the present result is similar to that of ENDF/B-VI in all energy range and to that of JENDL-3 below 120eV, (2) the absolute value of present result is about 3 times larger than the values in both JENDL-3 and ENDF/B-VI, and (3) the absolute value of the present data is rather closer to the Hoffman et al.'s. Therefore, it is recommended to reevaluate of the $^{237}Np(n, f)$ cross section in resonance and intermediate region in both files.

The authors are deeply thankful to Prof. M. Nakazawa of University of Tokyo and Dr. M. Nakano of Japan Atomic Energy Research Institute for their kind support. This work is partly supported by the Grant-in-Aid for Scientific Research from the Ministry of Education, Science and Culture.

References :

(1) Kobayashi, K., et al. : to be published.

(2) Obu, M., et al. : JAERI-M 9757 (1981).

(3) Shibata, K., Nakagawa, T., Asami, T. et al. : JAERI 1319 (1990).

(4) Rose, R. F. (ed) : BNL-NCS-17541 (4th ed.) (1991).

(5) Semon, M. D., Hoffman, M. and Sanders, W. M. : Bull. American Phys. Soc. 21 , 655 (1976). Their data are recorded in EXFOR in which it marked as Hoffman+.

(6) Plattard, S., Blons, J. Paya, D. : Nucl. Sci Eng. 61 , 477 (1976).

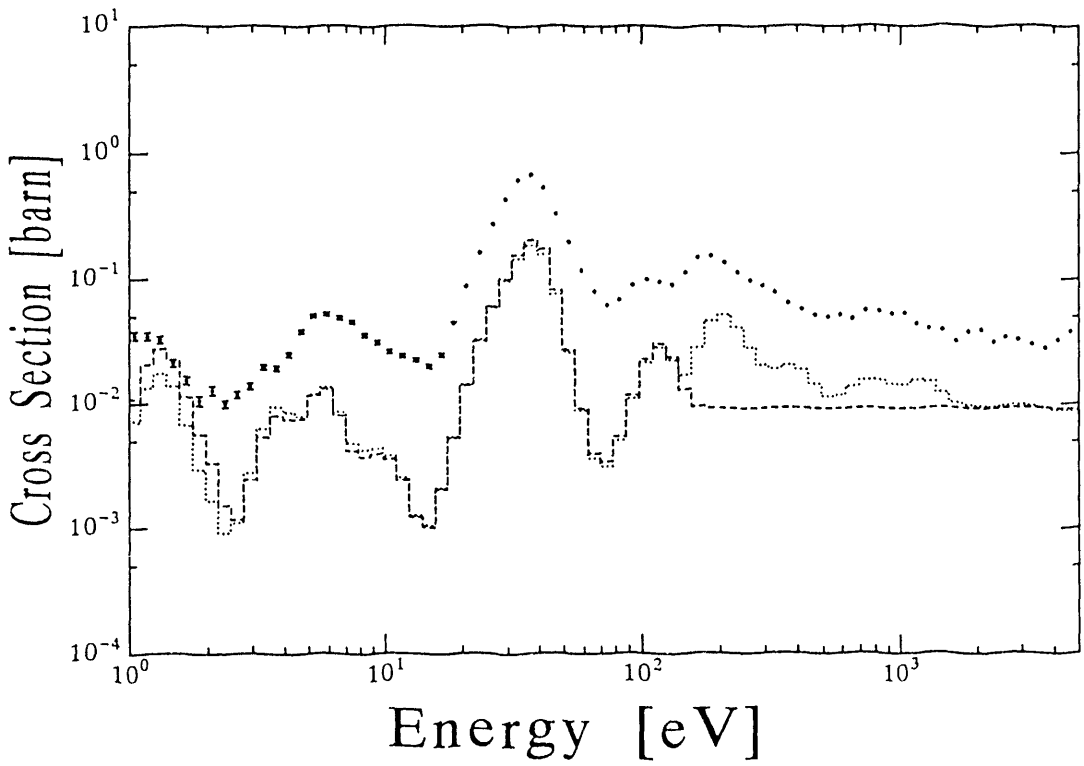

Fig. 1 Experimentally obtained cross section for the $^{237}Np(n,f)$ reaction compared with those in two newly evaluated nuclear data files. (I I I I I : Present result, ... : ENDF/B-VI, ---------- : JENDL-3).

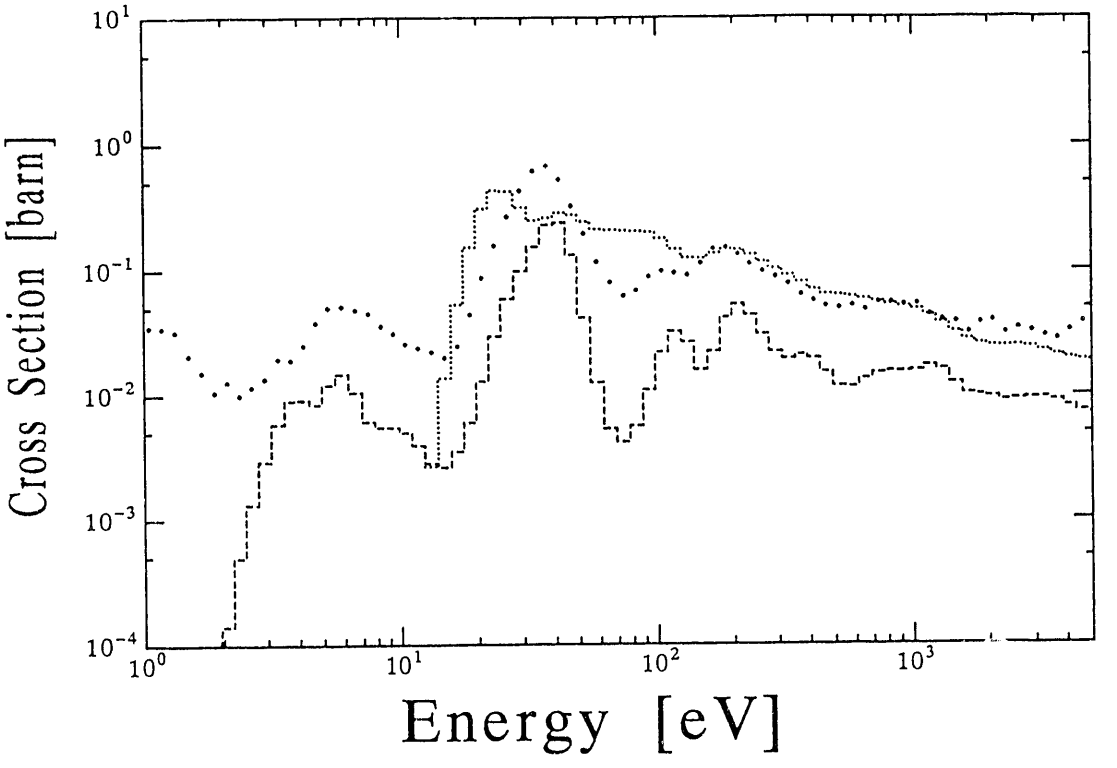

Fig. 2 Experimentally obtained cross section for the ^{237}Np(n,f) reaction (•••.• : Present result, ····· : Hoffman et al., --------- : Plattard et al.)

3.24 Characteristic Behavior of Neutrons in the Lead Slowing-down Spectrometer Coupled to Electron Linac

K.Kobayashi[1], Y.Nakagome[1], A.Yamanaka[2], S.Yamamoto[1],
Y.Fujita[1], T.Tamai[1], S.Kanazawa[2] and I.Kimura[2]

[1] Research Reactor Institute, Kyoto University
Kumatori-cho, Sennan-gun, Osaka 590-04, Japan
[2] Department of Nuclear Engineering, Kyoto University
Yoshidahonmachi, Sakyo-ku, Kyoto 606-01, Japan)

A lead slowing-down spectrometer was installed coupling to the 46 MeV electron linear accelerator (linac) at the Research Reactor Institute, Kyoto University (KURRI). With the Kyoto University Lead Slowing-down Spectrometer(KULS), characteristics for (1) the relation between neutron slowing-down time and energy, (2) energy resolution, and (3) neutron energy spectrum were obtained by the experiments using neutron resonance filters and/or the linac time-of-flight (TOF) method, and by the continuous energy Monte Carlo code MCNP including time-dependent process.

For the KULS, the slowing-down constant K in the relation $E=K/t^2$ was 190 ± 2 and 156 ± 2 (keV μsec^2) for bismuth and lead experimental holes, respectively. The energy resolution was around 40 % for both experimental holes in the relevant energy region. The neutron spectra in the KULS calculated with ENDF/B-IV, JENDL-3 and ENDL-85 libraries were in general agreement with those measured by the linac TOF method.

1. Introduction

Lead is one of the heavy mass elements and its neutron total cross section mainly consists of elastic scattering cross section. Therefore, when pulsed fast neutrons are put into the central region of the large lead assembly, the elastic scattering process takes most part of the slowing-down process because the absorption

cross section is very small. Neutrons are slowed down keeping an asymptotic form with the neutron time-dependent spectrum[1]. Hence the lead slowing-down spectrometer has almost constant energy resolution in wide energy range from a few one-tenth eV to several hundreds keV. There exists the relation of $E=K/t^2$ between the neutron energy E in keV and the slowing-down time t in μsec[1]. K is slowing-down constant.

In the present work, characteristic behavior of neutrons have experimentally been investigated with the lead slowing-down spectrometer coupled to the electron linear accelerator (linac) at the Research Reactor Institute, Kyoto University (KURRI). Resonance filters were applied for the determination of the relation between the neutron slowing-down time and energy, and of neutron energy resolution in the lead slowing-down spectrometer. Measurement of the neutron energy spectrum with the spectrometer was also made by the linac time-of-flight (TOF) method. Calculations were performed by the continuous energy Monte Carlo code MCNP[2] with time-dependent process, and the results were compared with the above characteristic measurements.

2. Lead Slowing-Down Spectrometer

A lead slowing-down spectrometer was recently installed coupling to the 46 MeV linac at KURRI. Specific features of the Kyoto University Lead Slowing-down Spectrometer (KULS) are as follows:

1) The KULS is a cube of 1.5 x 1.5 x 1.5 m^3 and about 40 tons, which is set on a platform car in the linac target room so that it can be removed when the normal neutron TOF measurements are made, as shown in Fig.1.

2) Number of the lead blocks used was about 1600 (size: 10 x 10 x 20 cm^3, and purity: 99.9 %). Each block was completely cleaned with alcohol or acetone and piled up to make a cube without structural steel.

3) The photoneutron target is made of tantalum plates and cooled by compressed air. The target system is separated from the linac vacuum system to prevent troubles by which the linac machine is disturbed. During the KULS experiments, linac beam power on the target was about 200 to 500 W.

4) For the multi-purpose and/or parallel measurements, eight experimental/irradiation holes were added, as seen in Fig.1, to the originally designed spectrometer[3], which was firstly set at the University of Tokyo and transferred to KURRI in Janu-

ary 1991. One of the holes was covered by bismuth layers of 10 to 15 cm thickness to shield high energy (6 to 7 MeV) gamma−rays by the Pb(n,γ) reaction in the spectrometer.

3. Experiments

3.1. Slowing−down Time and Energy

We have measured the relation between neutron slowing−down time and energy in the bismuth hole and the lead hole at the opposite upper position to the bismuth hole, as displayed in Fig.1. At first, a BF_3 counter (12 mm in diam., 50 mm long, 1 atm.) covered with resonance filter was employed for the measurement of slowing−down time spectrum by the neutron filter transmission method. A dip structure was observed in the time spectrum corresponding to the resonance energy. Table 1 lists the resonance filters used in the present measurement and their resonance energies. Since the resonance energies for these filters are well known[4], we can calibrate the relation between the slowing−down time t and energy E, as an equation of $E=K/(t+t_0)^2$, where K is slowing−down constant and t_0 is zero time correction constant. Event signals from the BF_3 counter were stored in the multi−channel analyzer of 4096−channel as a function of time. The channel width was selected to be 62.5 nsec, 125 nsec and 250 nsec as the need arose. Figure 2 illustrates a typical time spectrum from the Co filter. An Ar gas counter (0.5" in diam., 2.5" long, 1 atm.) was also covered with resonance filter to perform a capture gamma−ray measurement. Figure 3 displays a typical example of the time spectrum measured by Au−cylinder whose peak corresponds to the resonance energy at 4.9 eV. Figure 4 shows the curves which were obtained, by the least squares method, from the neutron slowing−down time and the resonance energy using the BF_3 and the Ar gas counters.

3.2. Energy Resolution

The time spectra which were measured with BF_3 and Ar gas counters were used to derive energy resolution of the KULS. For the transmission measurement with resonance filters using the BF_3 counter, a dip structure in the time spectrum may be broadened due to the certain width in the resonance peak and/or to the certain thickness of the filter. Then, some corrections are required to fit the dip spectrum with a Gaussian function and to obtain the full width at half maximum (FWHM).

From these facts, it would be better for the determination of energy resolution to apply a sharp resonance like a delta function. We have used a thin cylinder or plate-type filter having sharp resonances at 230 and 579 eV for Cu and 27.5 eV for Cd, respectively, as seen in Fig.3. The bumped spectral shape data were also fitted with a Gaussian function to derive the energy resolution.

3.3 Neutron Spectrum

As one of the characteristic behavior of neutrons in the KULS, the neutron spectrum has been measured by the linac TOF method using the 22 m station. The experimental procedures are almost similar to the previous measurements[5], and ^{6}Li glass scintillator and ^{10}B-vaseline plug NaI(Tl) detectors were used as neutron detectors[6]. The KULS has a horizontal through hole of 8 cm in diameter for a reentrant hole to extract neutrons from the central region. We have measured angular neutron fluxes emitted to 90 degree direction from the bottom of the reentrant hole made at 15 cm distant from the photoneutron target in the KULS. Below 1 keV, supplemental measurement was made with a BF_3 counter as a 1/v detector.

4. Calculations

Neutron time behavior in the KULS was investigated by the continuous energy Monte Carlo code MCNP[2]. The calculations were performed with three dimensional cartesian coordinate and a few 100,000 neutron random histories. The geometrical parameters and/or size of the KULS were referred to the actual one. Not only the steady state neutron spectrum but also the time-dependent neutron spectrum can be obtained by the MCNP code.

As an initial neutron spectrum for the calculation, energy spectrum from the tantalum photoneutron target was taken from the experimental data which were previously obtained by the neutron TOF method[5]. The MCNP code has its own nuclear data libraries, which were generated from the evaluated nuclear data files of ENDF/B-IV[7] and ENDL-85[8]. New data library[9] generated recently from JENDL-3 became available for the MCNP calculations.

In the present calculations, we have firstly obtained the neutron time behavior or the slowing-down time spectrum in the KULS. After that, the time-dependent neutron spectrum was integrated over a few tens milli-seconds from the linac burst

trigger to get the steady state neutron spectrum from about 0.1 eV to 20 MeV. Figure 5 shows the time-dependent neutron spectrum at 40 cm in the bismuth hole distant from the photoneutron target. The time behavior spectrum seems to be asymptotic form in 10 μsec in the KULS and after that, its form is kept in the slowing-down process, as seen in Fig.5.

5. Results

On the assumption that the resonance dip or bump in the slowing-down time spectrum is a Gaussian function, we have determined the central channel of the resonance structure, namely the slowing-down time against the known resonance energy and also derived the energy resolution by the FWHM. The relation between the slowing-down time and the resonance neutron energy is summarized in Fig.4. By the least squares fitting with these measured data, the slowing-down constants for bismuth and lead experimental holes in the KULS were obtained to be 192±2 and 156±2 (keV μsec^2), respectively.

Neutron energy resolution in the KULS was also determined by the Gaussian function fitted to the time-dependent spectrum measured with Ar gas counter using sharp resonances at 230 and 579 eV for Cu and at 27.5 eV for Cd. A BF_3 counter was supplementally used for the resolution measurements, although the corrections for filter thickness and resonance width were needed. Energy resolutions obtained in the present measurements are almost constant and about 40 % at FWHM from a few eV to about 1 keV, as given in Table 2. In the higher and lower energy regions, the resolution values increase a little as seen in the table.

The slowing-down constants and the energy resolutions calculated by the MCNP code were in good agreement with the present measurements for the bismuth and lead experimental holes.

Neutron spectrum in the KULS has been measured from a few eV to about 10 MeV by the linac TOF method. The spectra measured by the ^{6}Li glass scintillator and ^{10}B-vaseline plug NaI(Tl) detectors are shown in Fig.6, and both experimental results are in good agreement. The MCNP calculations were performed with the evaluated nuclear data libraries of ENDF/B-IV, JENDL-3 and ENDL-85. General agreement is seen between the calculated and the measured spectra, as shown in Fig.6. However, the ENDF/B-IV spectrum seems to be higher than the others below about 10 keV.

6. Summary

A lead slowing-down spectrometer was installed coupling to the 46 MeV electron linear accelerator at the Research Reactor Institute, Kyoto University. The characteristic behavior of neutrons in the spectrometer has been obtained by the time-dependent Monte Carlo code MCNP and by the experiments with BF_3 and Ar gas counters and the linac TOF method.

The slowing-down constant K in the relation of $E=K/t^2$ has experimentally been determined to be 190 ± 2 (keV μsec^2) for bismuth and 156 ± 2 (keV μsec^2) for lead hole. The energy resolution of the KULS has been obtained with Ar gas counter for the sharp resonances at 230 and 579 eV of Cu and at 27.5 eV of Cd, and with BF_3 counter by the neutron transmission method using resonance filters. The MCNP calculations and the measured energy resolution in the spectrometer are in good agreement, and the FWHM values are around 40 % in the relevant energy region for bismuth and lead holes.

The neutron energy spectra from a few eV to about 10 MeV measured by the TOF method were compared with those calculated by the MCNP code using the ENDF/B-IV, JENDL-3 and ENDL-85 cross section data. In general, the calculations were in good agreement with the measurements. However, the ENDF/B-IV spectrum seems to be rather higher below about 10 keV.

References:

1) A.A.Bergman, et al., Proc. 1st Int. Conf. on Peaceful Uses At. Energy, United Nations, 4, 135 (1955).
2) F.Briesmeister (ed.), "MCNP - A General Monte Carlo Code for Neutron and Photon Transport, Version 3A", LA-7396-M, Rev2, Los Alamos National Laboratory (1986).
3) H.Wakabayashi, et al., J. Nucl. Sci. Technol., 6,487 (1970).
4) S.F.Mughabghab, "Neutron Cross Sections, Vol.1, Neutron Resonance Parameters and Thermal Cross Sections", Parts A and B, Academic Press Inc., New York 1984.
5) K.Kobayashi, et al., Nucl. Sci. Eng., 99, 157 (1988).
6) I.Kimura, et al., Nucl. Instr. Meth., 137, 85 (1976).
7) The library is appeared in Ref. 2).

8) "LLNL Evaluated Nuclear Data Library", UCRL-50400 (1985).
9) K. Kosako, et al., JAERI-M 91-187 (1991).

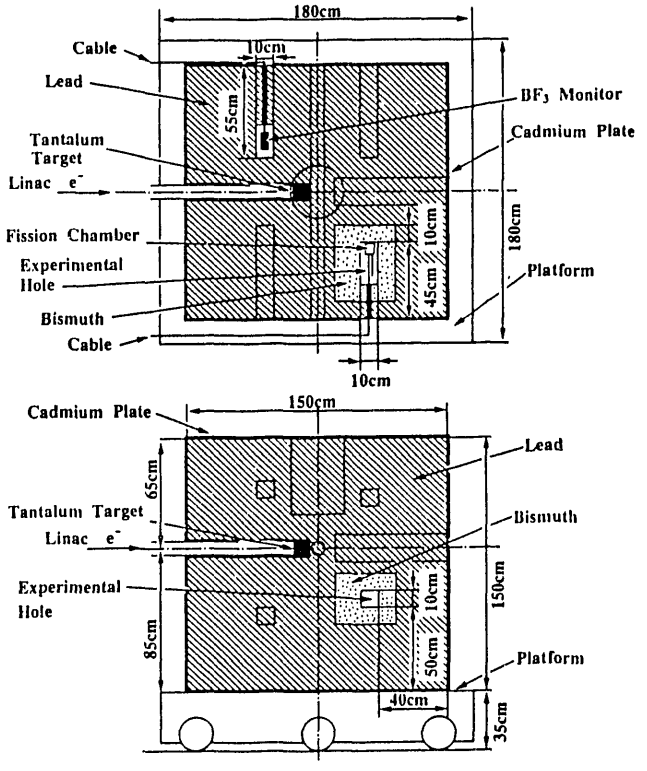

Fig. 1 Cross sectional view of Kyoto University Lead Slowing-down Spectrometer, KULS.

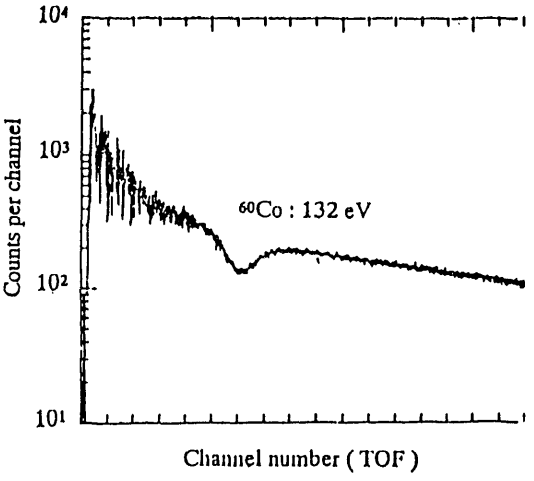

Fig. 2 Time spectrum measured by Co-filter using BF_3 counter.

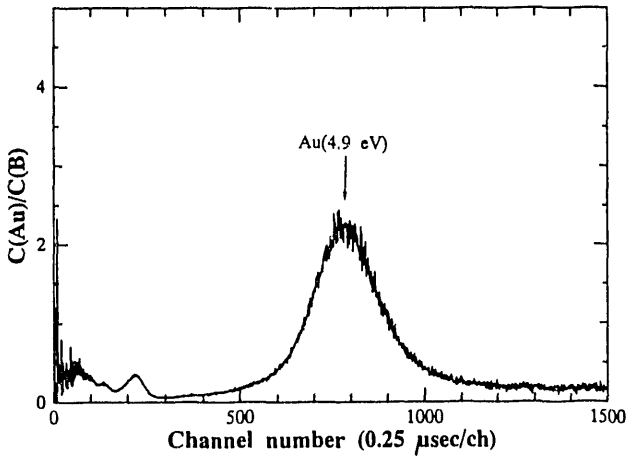

Fig. 3 Time spectrum measured by Au-cylinder using Ar gas counter.

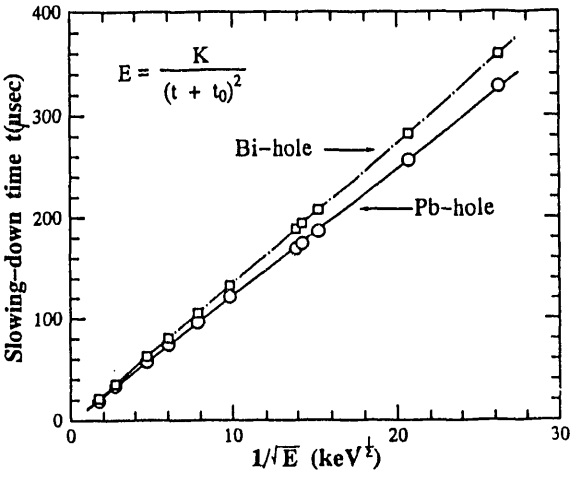

Fig. 4 Relation between slowing-down time and energy in the Bi and Pb holes.

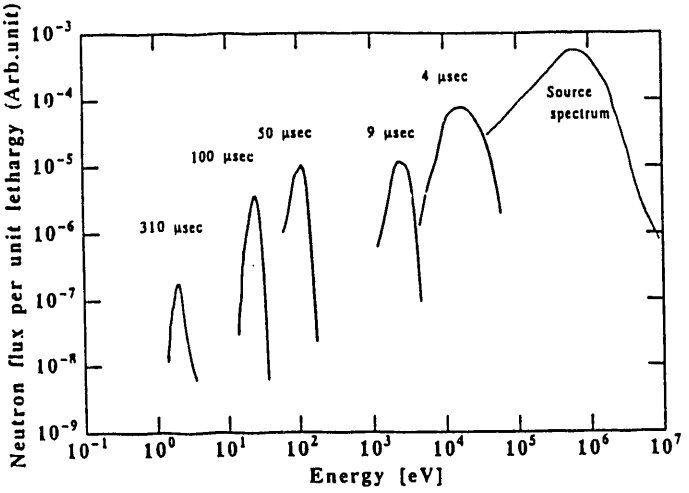

Fig. 5 Time dependent neutron spectrum in the KULS.

Table 1 Resonance filters

Material	Energy (eV)	Thickness (mm)	Form
In	1.46	0.2	foil
Te	2.33	7.0	powder
Ta	4.28	0.2	foil
	10.4		
Au	4.91	0.05	cylinder
Ag	5.19	0.5	cylinder
	16.3		
Cd	27.5	0.3	cylinder
Mo	44.9	7.0	powder
Co	132	0.3	cylinder
Cu	230	1.0	cylinder
	579		
Mn	336	7.0	powder

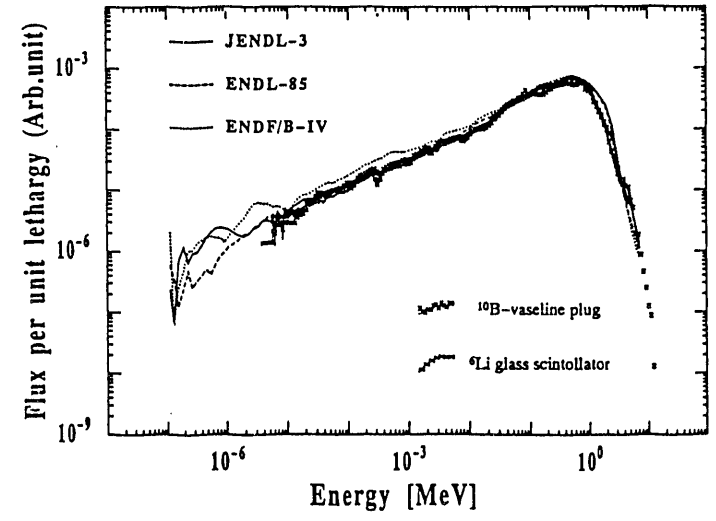

Fig. 6 Comparison of neutron spectra measured and calculated in the KULS.

Table 2 Energy resolution in Bi and Pb holes

Energy (eV)	Resolution (%) Exp. Ar counter	Exp. BF_3 counter	Calc. MCNP
1.46		51+3	56
4.9		40+2	40
10.4		43+1	34
27.5	39+2(Bi)		
27.5	38+2(Pb)		
44.9		38+1	36
132		41+2	44
230	38+3(Bi)		
230	41+3(Pb)		
336		40+3	44
579	42+3(Bi)		
2370		53+3	45

3.25 Testing of JENDL-3.1 and ENDF/B-VI-based WIMS Cross Section Libraries Processed by NJOY91

Jung-Do Kim, Choong-Sub Gil and Hee-Kyung Kim

Korea Atomic Energy Research Institute
P.O.Box 7, Daeduk-danji, Daejon, 305-606, Korea

The JENDL-3.1 and ENDF/B-VI-based 69-group cross section libraries for WIMS-D code were processed by using the latest version 91.38 of NJOY code system. The two multigroup libraries were intercompared by analyzing LWR critical experiments. By and large, the basic libraries show a similar tendency in the calculations of multiplication factor and integral lattice parameter.

1. Introduction

In the recent years, the new versions of evaluated nuclear data libraries have been released by Japan and USA. In order to test the quality and applicability of basic evaluated nuclear data libraries to light water reactors(LWR), 69-group constant libraries for WIMS code were generated by using the NJOY 91.38 nuclear data processing system with the JENDL-3.1[1] and ENDF/B-VI[2], and an intercomparison work for the two multigroup libraries was performed by analyzing a number of LWR benchmark experiments recommended by the cross Section Evaluation Working Group(CSEWG)[3].

2. Processed Data

Processed nuclides in JENDL-3.1 and ENDF/B-VI for this work are the followings:

Nuclide	Identification Number	
	JENDL-3.1	ENDF/B-VI
1-H-1*	3011	125
8-O-16	3081	825
13-Al-27	3131	1325
92-U-235	3924	9228
92-U-238	3926	9237

* Scattering Law Data (H in H_2O) : ENDF/B-III

3. Data Processing

NJOY[4] is well known as the most general purpose and versatile nuclear data processing code system, and the NJOY91.38 is the latest version released by the Los Alamos National Laboratory through the Radiation Shielding Information Center. The capabilities for processing ENDF-6 format file are almost complete.

To eliminate the differences due to the use of different processing method, input model, or definitions of multigroup constants as needed by the WIMS cross section library, two basic libraries were processed by using the NJOY91.38 with a same input option.

The specifications of multigroup processing used in the NJOY91.38 runs to provide WIMS library is given below and the processing scheme is shown in Figure 1.

- Reconstruction, linearization and thinning tolerence : 0.1%
- Temperature : 300^0K
- Weighting function : mid-life PWR flux (IWT=5 in GROUPR)
- Computed flux range : 0.1 eV ~ 48.052 eV for U-235; 0.1 eV ~ 367.26 eV for U-238
- Dilution factor (σ_0) : 10^0, 10^1, 10^2, 10^3, 10^4, 10^5 and 10^{10} barns for U-235; 10^{-1}, 10^0, 10^1, 5×10^1, 10^2, 10^3 and 10^{10} barns for U-238

4. Benchmark Problem

The CSEWG has recommended a variety of integral experiments for checking the data of interest for thermal reactor calculations. The experiments selected in this study include TRX and BAPL-UO_2 series with a simple geometric configuration.

The Westinghouse experiments known as the TRX lattices are frequently quoted as standards for benchmark calculations. The lattices were H_2O-moderated, and fully reflected simple assemblies operated at room temperature. The fuel rods were of uranium metal clad in aluminum. Those of BAPL-UO_2 series were of high density uranium oxide. Brief characteristics of the lattices are summarized below.

Lattice	Fuel	Clad.	Fuel rad. (cm)	H_2O/Fuel Volume Ratio
TRX-1	1.3% enriched	Al	0.4915	2.35
TRX-2				4.02
BAPL-1	1.3% enriched UO_2	Al	0.4864	1.43
BAPL-2				1.78
BAPL-3				2.40

The following integral parameters were measured at the center of each lattices :

Ratio of epithermal to thermal U-238 capture rate(ρ^{28}),
ratio of epithermal to thermal U-235 fission rate(δ^{25}),
ratio of U-238 fission to U-235 fission rate(δ^{28}) and
ratio of U-238 capture to U-235 fission rate(C*).

5. Calculation

WIMS code[5] is one of the most widely used thermal reactor codes and is of interest especially to reactor physicists in developing countries. WIMS-KAERI (a KAERI version of WIMS-D4) calculations were performed using cylindrical cell model, 69 groups, discrete ordinates, S_{12}, and B-1 method for leakage. The calculated data are multiplication factors and integral lattice parameters.

6. Self-shielding of Elastic Scattering

In WIMS-type codes (CASMO or EPRI-CPM), self-shielding for absorption and fission reactions can be treated explicitly through resonance integral tabulations. However, resonance scattering cannot be taken into account in the same way. In order to consider the self-shielding effect of elastic scattering of U-238, another cross section set for U-238, which include fully self-shielded(dilution factor : 1.0 barn) scattering cross sections in the 69-group table(slowing-down power, transport cross section and scattering matrix), were generated.

7. Dilution Factor Grid

The dilution factor grid values should be chosen (by experience) to be concentrated in the σ_0 range where the shielded cross section changes the most. To survey the sensitivity of calculated benchmark parameters to different dilution factor grid, another set with ten grids were processed with JENDL-3.1.

8. Results and Discussion

8.1 Effect of Dilution Factor Grid

Table 1 gives the influence of the grid. The 7 grids set gives a slightly higher K_{eff}, and lower δ^{28} and C* as compared with 10 grids set.

8.2 Multiplication Factor

Calculated eigenvalues are compared in Table 2. There are no significant differences in the K_{eff} values obtained with each of JENDL-3.1 and ENDF/B-VI, comparing with the large difference of computer running time for data processing (Table 3).

8.3 Integral Lattice Parameter

Intercomparison of reaction rate ratios, as well as calculated to experimental ratios (C/E), are summarized in Tables 4 ~ 7. The differences between JENDL-3.1 and ENDF/B-VI are about 1% or so.

8.4 Effect of Self-shielded Scattering

The calculated eigenvalues using the fully self-shielded U-238 scattering data are given in Table 8. The relative difference of K_{eff} values between no-shielded and fully-shielded scattering data are within 0.4 ~ 1.0%. In Table 9, the influence of U-238 self-shielded scattering on integral lattice parameters is summarized for JENDL-3.1. The relative changes in calculated parameters due to the self-shielded U-238 scattering are within 0.3 ~ 2.0%. Detailed results are given in Table 10.

8.5 Comparison of 69-group Data

69-group data processed with JENDL-3.1 and ENDF/B-VI are intercompared in Figures 2 ~12. Potential cross sections for O-16 and Al-27 give some differences. The ENDF/B-VI data of O-16 are about 3% larger and while those of Al-27 are approximately 5% smaller than the JENDL-3.1 data. Both libraries show a different shape for Al-27 absorption cross sections. Globally, U-235 capture cross sections of ENDF/B-VI show a lower tendency comparing with JENDL-3.1. Two libraries give -23 to 60% difference for U-235 capture cross sections and -19 to 44% difference for U-238 fission cross sections.

9. Conclusion

The JENDL-3.1 and ENDF/B-VI-based 69-group cross sections for WIMS library were processed by using the NJOY 91.38 system and the two libraries were intercompared by analyzing LWR critical experiments.

By and large, two libraries (JENDL-3.1 and ENDF/B-VI) show a similar tendency. The relative differences of K_{eff} and integral lattice parameters intercompared are within or not too far from the experimental uncertainty. The range of differences is within 0.2% on K_{eff} and around 1% on integral lattice parameters. The influence of self-shielded U-238 scattering on K_{eff} are within 0.4 ~ 1.0%. The K_{eff} values obtained with fully self-shielded U-238 scattering are underestimated.

References

1) K. Shibada, et al. : JAERI-1319 (1990).
2) P. F. Rose : BNL-NCS-17541 4th ed. (1991).
3) "CSEWG Benchmark Specification", ENDF-202, BNL-19302 (1974).
4) R. E. MacFarlane, et al. : LA-9303-M, Vol. 1 (1982).
5) J. R. Askew, et al. : J. British Nuclear Energy Soc. 5, 564 (1966).

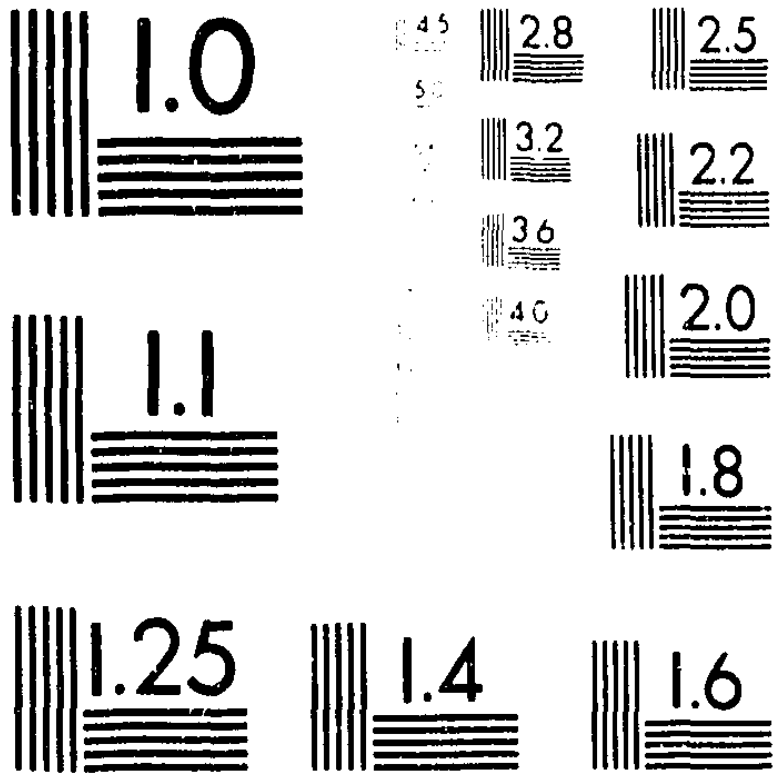

Table 1 Effect due to different dilution factor grids

Lattice	No. of σ_0 grid		Percent difference
	7*	10**	
	K-effective		
TRX -1	0.9996	0.9988	+0.08
TRX -2	0.9979	0.9974	+0.05
BAPL-1	1.0035	1.0031	+0.04
BAPL-2	1.0025	1.0023	+0.02
BAPL-3	1.0015	1.0015	+0.00
	ρ^{28}		
TRX -1	1.3237	1.3292	-0.41
TRX -2	0.8322	0.8359	-0.44
BAPL-1	1.3903	1.3929	-0.19
BAPL-2	1.1591	1.1603	-0.10
BAPL-3	0.9128	0.9130	-0.02
	C*		
TRX -1	0.7881	0.7899	-0.23
TRX -2	0.6375	0.6388	-0.20
BAPL-1	0.8036	0.8044	-0.10
BAPL-2	0.7331	0.7335	-0.05
BAPL-3	0.6561	0.6562	-0.02

* U-235 : 1, 10, 100, 10^3, 10^4, 10^5, 10^{10}
U-238 : 0.1, 1, 10, 50, 100, 10^3, 10^{10}

** U-235 : 10, 50, 100, 150, 300, 500, 700, 10^3, 10^4, 10^{10}
U-238 : 0.1, 0.5, 1, 10, 30, 50, 70, 100, 10^3, 10^{10}

Table 2 Calculated eigenvalues (using no-shielded scattering)

Lattice	K-infinite		K-effective	
	JENDL-3.1	ENDF/B-VI	JENDL-3.1	ENDF/B-VI
TRX -1	1.1782	1.1807 (+0.21)*	0.9996	1.0006 (+0.10)
TRX -2	1.1637	1.1646 (+0.08)	0.9979	0.9984 (+0.05)
BAPL-1	1.1416	1.1391 (-0.22)	1.0035	1.0012 (-0.23)
BAPL-2	1.1456	1.1432 (-0.21)	1.0025	1.0005 (-0.20)
BAPL-3	1.1319	1.1298 (-0.19)	1.0015	1.0000 (-0.15)

* percent difference relative to JENDL-3.1

Table 3 Statistics of uranium data processing

Content	Nuclide	Temperature	JENDL-3.1	ENDF/B-VI	Ratio
Number of X-section points processed with RECONR and BROADR routine	U-235	0°K	16,844 (16,114)*	381,820 (381,461)	22.7 (23.7)
		300°K	12,936	72,247	5.6
	U-238	0°K	325,542 (325,173)	551,910 (551,633)	1.7 (1.7)
		300°K	117,258	181,732	1.5
Computer running time(sec), Cyber 960-31 OS : NOS/VE	U-235	300°K	1,425	30,105	21.1
	U-238	300°K	24,908	83,130	3.3

* Data in parenthesis are the number of resonance points

Table 4 Calculated and C/E values for ratio of epithermal to thermal U-238 capture rate(ρ^{28})

(using no-shielded scattering)

Lattice	JENDL-3.1		ENDF/B-VI	
	Calculated	C/E	Calculated	C/E
TRX -1	1.3237E+0	1.0028	1.3226E+0	1.0020 (-0.08)*
TRX -2	8.3221E-1	0.9943	8.3098E-1	0.9928 (-0.15)
BAPL-1	1.3903E+0	1.0002	1.4075E+0	1.0126 (+1.24)
BAPL-2	1.1591E+0	1.0349	1.1742E+0	1.0468 (+1.15)
BAPL-3	9.1285E-1	1.0076	9.2189E-1	1.0175 (+0.99)

* percent difference relative to JENDL-3.1

Table 5 Calculated and C/E values for ratio of epithermal to thermal U-235 fission rate(δ^{25})

(using no-shielded scattering)

Lattice	JENDL-3.1		ENDF/B-VI	
	Calculated	C/E	Calculated	C/E
TRX -1	9.4027E-2	0.9527	9.4549E-2	0.9579 (+0.56)*
TRX -2	5.7829E-2	0.9418	5.8149E-2	0.9471 (+0.56)
BAPL-1	7.9631E-2	0.9480	8.0229E-2	0.9551 (+0.75)
BAPL-2	6.5032E-2	0.9563	6.5511E-2	0.9634 (+0.74)
BAPL-3	5.0060E-2	0.9627	5.0419E-2	0.9696 (+0.72)

* percent difference relative to JENDL-3.1

Table 6 Calculated and C/E values for ratio of U-238 to U-235 fission rate(δ^{28})

(using no-shielded scattering)

Lattice	JENDL-3.1		ENDF/B-VI	
	Calculated	C/E	Calculated	C/E
TRX -1	9.6925E-2	1.0249	9.6099E-2	1.0169 (-0.78)*
TRX -2	6.9189E-2	0.9984	6.8430E-2	0.9874 (-1.10)
BAPL-1	7.5331E-2	0.9658	7.4574E-2	0.9561 (-1.00)
BAPL-2	6.4866E-2	0.9276	6.4120E-2	0.9160 (-1.15)
BAPL-3	5.3270E-2	0.9346	5.2564E-2	0.9222 (-1.33)

* percent difference relative to JENDL-3.1

Table 7 Calculated and C/E values for ratio of U-238 capture to U-235 fission rate(C*)

(using no-shielded scattering)

Lattice	JENDL-3.1		ENDF/B-VI	
	Calculated	C/E	Calculated	C/E
TRX -1	7.8810E-1	0.9888	7.8708E-1	0.9876 (-0.13)*
TRX -2	6.3749E-1	0.9853	6.3687E-1	0.9843 (-0.10)
BAPL-1	8.0357E-1		8.0898E-1	(+0.67)
BAPL-2	7.3311E-1		7.3747E-1	(+0.59)
BAPL-3	6.5614E-1		6.5931E-1	(+0.48)

* percent difference relative to JENDL-3.1

Table 8 Calculated eigenvalues (using fully-shielded U-238 scattering)

Lattice	K-infinite		K-effective	
	JENDL-3.1	ENDF/B-VI	JENDL-3.1	ENDF/B-VI
TRX -1	1.1748	1.1772 (+0.20)*	0.9901	0.9908 (+0.07)
TRX -2	1.1616	1.1624 (+0.07)	0.9920	0.9924 (+0.04)
BAPL-1	1.1402	1.1376 (-0.23)	0.9975	0.9952 (-0.23)
BAPL-2	1.1445	1.1420 (-0.22)	0.9972	0.9951 (-0.21)
BAPL-3	1.1310	1.1288 (-0.19)	0.9976	0.9960 (-0.16)

percent difference relative to no-shielded scattering

Lattice	K-infinite		K-effective	
	JENDL-3.1	ENDF/B-VI	JENDL-3.1	ENDF/B-VI
TRX -1	-0.29	-0.30	-0.95	-0.98
TRX -2	-0.18	-0.19	-0.59	-0.60
BAPL-1	-0.12	-0.13	-0.60	-0.60
BAPL-2	-0.10	-0.10	-0.53	-0.54
BAPL-3	-0.08	-0.09	-0.39	-0.40

* percent difference relative to JENDL-3.1

Table 9 Influence of U-238 self-shielded scattering on lattice parameters (JENDL-3.1)

(percent difference relative to no-shielded scattering)

Lattice	ρ^{28}	δ^{25}	δ^{28}	C*
TRX -1	+1.98	+1.60	+1.07	+0.99
TRX -2	+1.79	+1.41	+0.64	+0.73
BAPL-1	+0.79	+0.63	+0.65	+0.41
BAPL-2	+0.77	+0.60	+0.57	+0.37
BAPL-3	+0.71	+0.56	+0.42	+0.31

Table 10 C/E values for integral lattice parameters (using fully-shielded U-238 scattering)

Lattice	JENDL-3.1	ENDF/B-VI	JENDL-3.1	ENDF/B-VI
	ρ^{28}		δ^{25}	
TRX -1	1.0227	1.0224	0.9679	0.9736
TRX -2	1.0120	1.0111	0.9552	0.9607
BAPL-1	1.0081	1.0209	0.9540	0.9613
BAPL-2	1.0428	1.0551	0.9621	0.9694
BAPL-3	1.0147	1.0251	0.9680	0.9751
	δ^{28}		C^*	
TRX -1	1.0358	1.0281	0.9986	0.9976
TRX -2	1.0048	0.9940	0.9925	0.9918
BAPL-1	0.9720	0.9624		
BAPL-2	0.9319	0.9213		
BAPL-3	0.9385	0.9261		

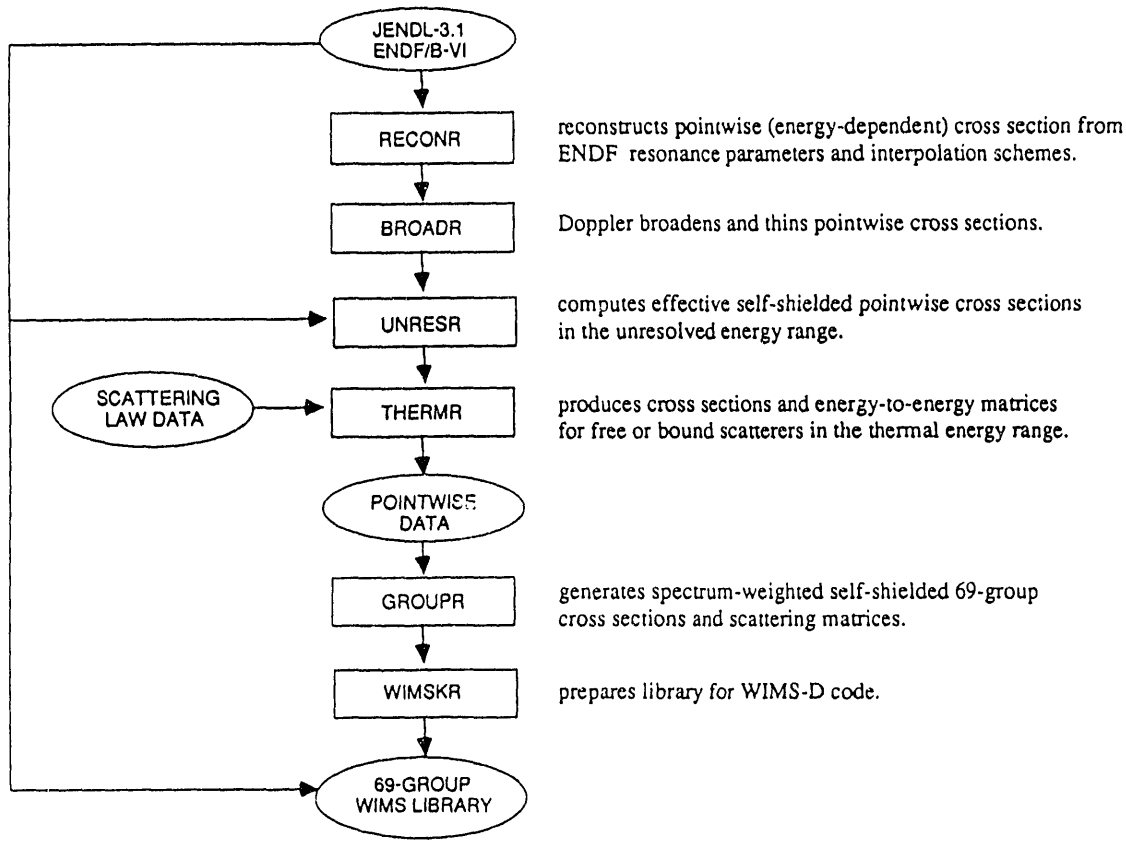

Fig. 1 Flow diagram for generating 69-group library of WIMS-D code.

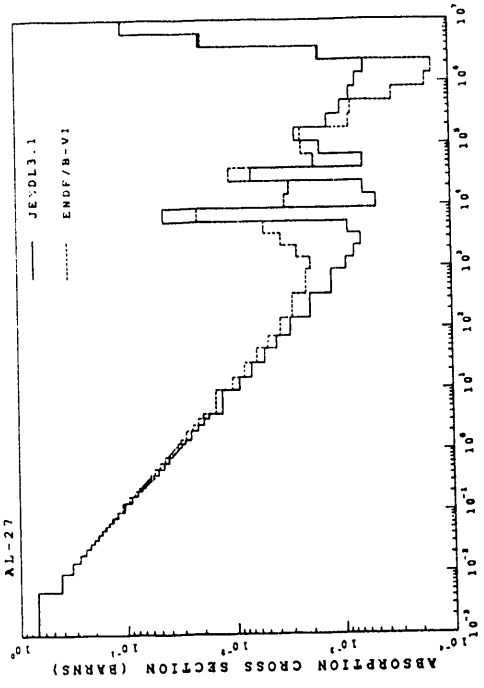

Fig. 3 Comparison of O-16 scattering cross sections.

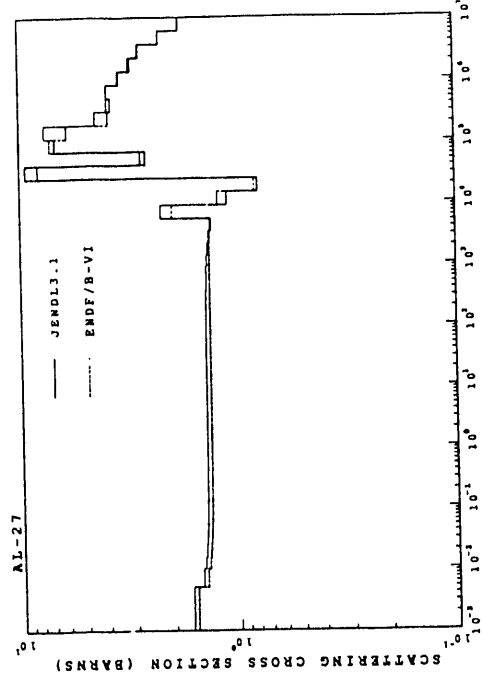

Fig. 5 Comparison of Al-27 scattering cross sections.

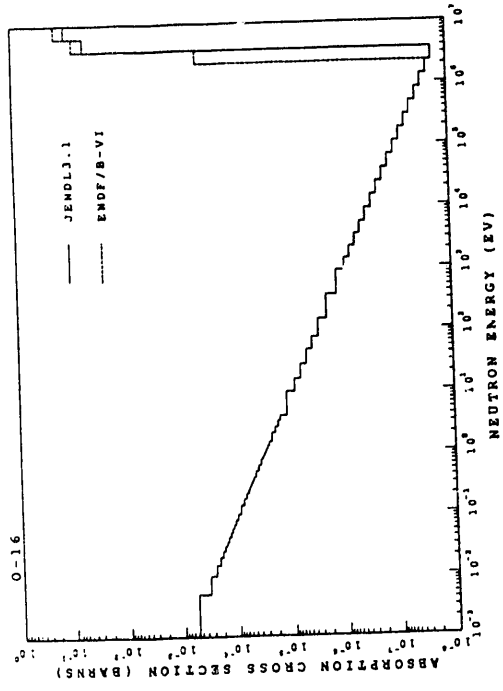

Fig. 2 Comparison of O-16 absorption cross sections.

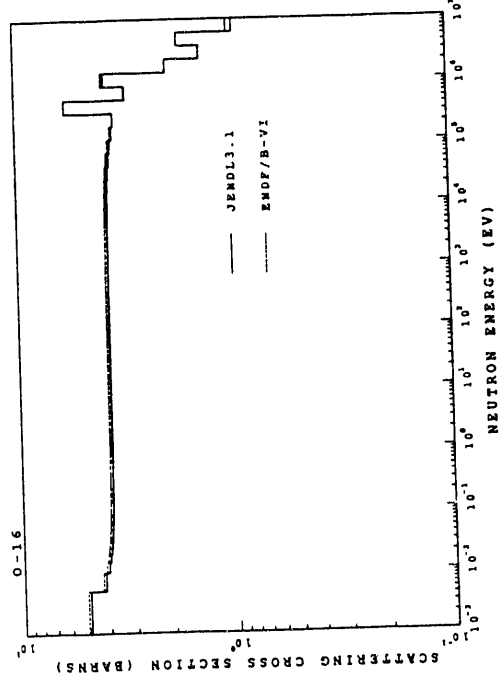

Fig. 4 Comparison of Al-27 absorption cross sections.

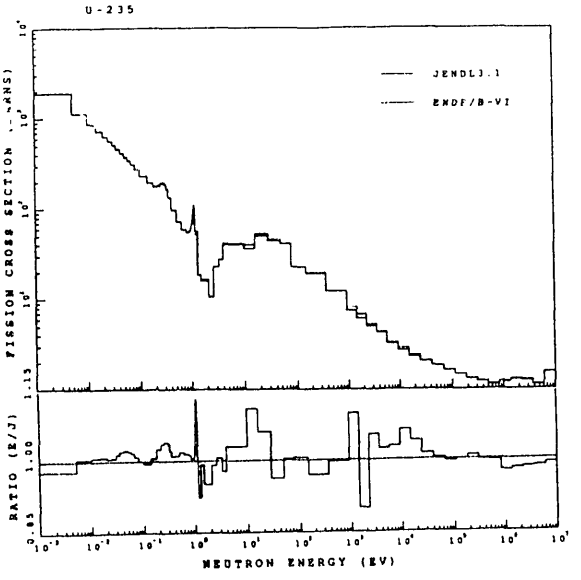

Fig. 6 Comparison of U-235 fission cross sections.

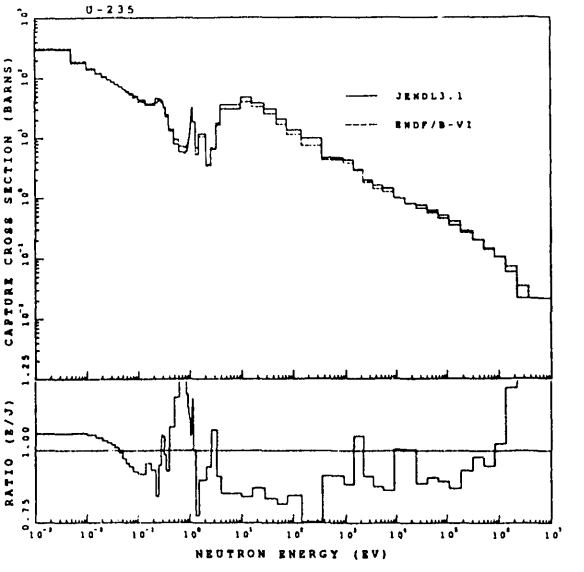

Fig. 7 Comparison of U-235 capture cross sections.

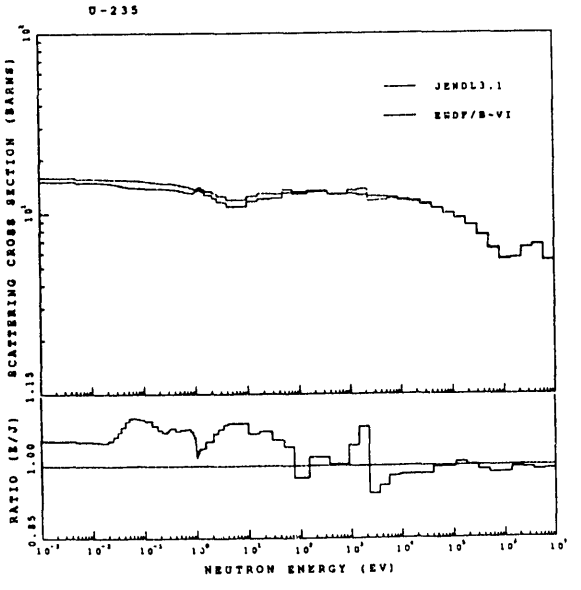

Fig. 8 Comparison of U-235 scattering cross sections.

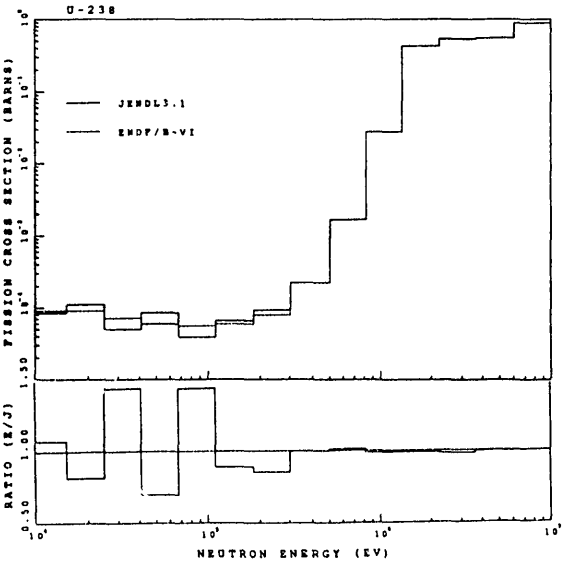

Fig. 9 Comparison of U-238 fission cross sections.

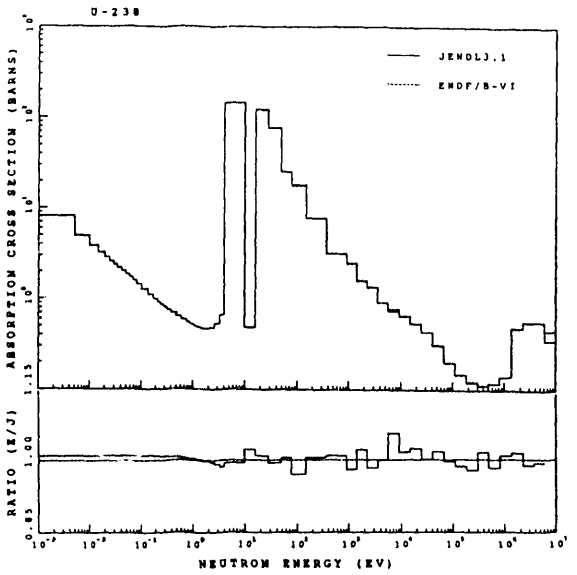

Fig. 10 Comparison of U-238 absorption cross sections.

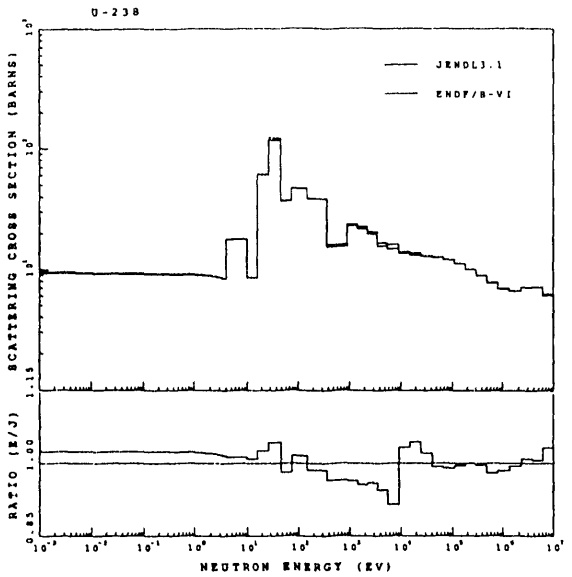

Fig. 11 Comparison of U-238 scattering cross sections.

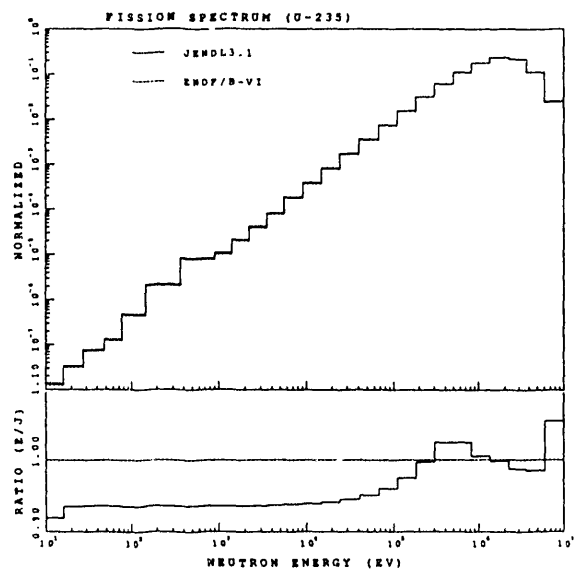

Fig. 12 Comparison of U-235 fission spectrum.

国際単位系(SI)と換算表

表1 SI基本単位および補助単位

量	名称	記号
長さ	メートル	m
質量	キログラム	kg
時間	秒	s
電流	アンペア	A
熱力学温度	ケルビン	K
物質量	モル	mol
光度	カンデラ	cd
平面角	ラジアン	rad
立体角	ステラジアン	sr

表2 SIと併用される単位

名称	記号
分, 時, 日	min, h, d
度, 分, 秒	°, ′, ″
リットル	l, L
トン	t
電子ボルト	eV
原子質量単位	u

1 eV = 1.60218×10^{-19} J
1 u = 1.66054×10^{-27} kg

表3 固有の名称をもつSI組立単位

量	名称	記号	他のSI単位による表現
周波数	ヘルツ	Hz	s^{-1}
力	ニュートン	N	$m \cdot kg/s^2$
圧力, 応力	パスカル	Pa	N/m^2
エネルギー, 仕事, 熱量	ジュール	J	N·m
工率, 放射束	ワット	W	J/s
電気量, 電荷	クーロン	C	A·s
電位, 電圧, 起電力	ボルト	V	W/A
静電容量	ファラド	F	C/V
電気抵抗	オーム	Ω	V/A
コンダクタンス	ジーメンス	S	A/V
磁束	ウェーバ	Wb	V·s
磁束密度	テスラ	T	Wb/m^2
インダクタンス	ヘンリー	H	Wb/A
セルシウス温度	セルシウス度	℃	
光束	ルーメン	lm	cd·sr
照度	ルクス	lx	lm/m^2
放射能	ベクレル	Bq	s^{-1}
吸収線量	グレイ	Gy	J/kg
線量当量	シーベルト	Sv	J/kg

表4 SIと共に暫定的に維持される単位

名称	記号
オングストローム	Å
バーン	b
バール	bar
ガル	Gal
キュリー	Ci
レントゲン	R
ラド	rad
レム	rem

1 Å = 0.1 nm = 10^{-10} m
1 b = 100 fm^2 = 10^{-28} m^2
1 bar = 0.1 MPa = 10^5 Pa
1 Gal = 1 cm/s^2 = 10^{-2} m/s^2
1 Ci = 3.7×10^{10} Bq
1 R = 2.58×10^{-4} C/kg
1 rad = 1 cGy = 10^{-2} Gy
1 rem = 1 cSv = 10^{-2} Sv

表5 SI接頭語

倍数	接頭語	記号
10^{18}	エクサ	E
10^{15}	ペタ	P
10^{12}	テラ	T
10^{9}	ギガ	G
10^{6}	メガ	M
10^{3}	キロ	k
10^{2}	ヘクト	h
10^{1}	デカ	da
10^{-1}	デシ	d
10^{-2}	センチ	c
10^{-3}	ミリ	m
10^{-6}	マイクロ	μ
10^{-9}	ナノ	n
10^{-12}	ピコ	p
10^{-15}	フェムト	f
10^{-18}	アト	a

(注)

1. 表1-5は「国際単位系」第5版, 国際度量衡局 1985年刊行による。ただし, 1 eV および 1 u の値は CODATA の1986年推奨値によった。
2. 表4には海里, ノット, アール, ヘクタールも含まれているが日常の単位なのでここでは省略した。
3. bar は, JISでは流体の圧力を表わす場合に限り表2のカテゴリーに分類されている。
4. EC閣僚理事会指令では bar, barn および「血圧の単位」mmHg を表2のカテゴリーに入れている。

換算表

力	N(=10^5 dyn)	kgf	lbf
	1	0.101972	0.224809
	9.80665	1	2.20462
	4.44822	0.453592	1

粘度 1 Pa·s(N·s/m^2) = 10 P(ポアズ)(g/(cm·s))
動粘度 1 m^2/s = 10^4 St(ストークス)(cm^2/s)

圧力	MPa(=10 bar)	kgf/cm^2	atm	mmHg(Torr)	lbf/in^2(psi)
	1	10.1972	9.86923	7.50062×10^3	145.038
	0.0980665	1	0.967841	735.559	14.2233
	0.101325	1.03323	1	760	14.6959
	1.33322×10^{-4}	1.35951×10^{-3}	1.31579×10^{-3}	1	1.93368×10^{-2}
	6.89476×10^{-3}	7.03070×10^{-2}	6.80460×10^{-2}	51.7149	1

エネルギー・仕事・熱量	J(=10^7 erg)	kgf·m	kW·h	cal(計量法)	Btu	ft·lbf	eV
	1	0.101972	2.77778×10^{-7}	0.238889	9.47813×10^{-4}	0.737562	6.24150×10^{18}
	9.80665	1	2.72407×10^{-6}	2.34270	9.29487×10^{-3}	7.23301	6.12082×10^{19}
	3.6×10^6	3.67098×10^5	1	8.59999×10^5	3412.13	2.65522×10^6	2.24694×10^{25}
	4.18605	0.426858	1.16279×10^{-6}	1	3.96759×10^{-3}	3.08747	2.61272×10^{19}
	1055.06	107.586	2.93072×10^{-4}	252.042	1	778.172	6.58515×10^{21}
	1.35582	0.138255	3.76616×10^{-7}	0.323890	1.28506×10^{-3}	1	8.46233×10^{18}
	1.60218×10^{-19}	1.63377×10^{-20}	4.45050×10^{-26}	3.82743×10^{-20}	1.51857×10^{-22}	1.18171×10^{-19}	1

1 cal = 4.18605 J(計量法)
= 4.184 J(熱化学)
= 4.1855 J(15℃)
= 4.1868 J(国際蒸気表)

仕事率 1 PS(仏馬力)
= 75 kgf·m/s
= 735.499 W

放射能	Bq	Ci
	1	2.70270×10^{-11}
	3.7×10^{10}	1

吸収線量	Gy	rad
	1	100
	0.01	1

照射線量	C/kg	R
	1	3876
	2.58×10^{-4}	1

線量当量	Sv	rem
	1	100
	0.01	1

(86年12月26日現在)